The Design and Synthesis of Photoresponsive Molecules for the Sequential Modulation of Biomolecules

Reuben Breetveld

PhD

University of York

Chemistry

September 2025

Abstract

Spatiotemporal control over growth factor signalling is fundamental to tissue development and regeneration. However, many current biomaterial systems lack the precision required to replicate the complex biochemical signalling processes observed *in vivo*. This thesis addresses these limitations through the design, synthesis, and characterisation of photoresponsive molecules capable of wavelength-selective activation.

A series of photocages and photocleavable linkers based on coumarin and BODIPY scaffolds were synthesised. Literature synthetic routes were optimised with scalability in mind, enabling access to gram-scale quantities of key compounds. In parallel, novel photoresponsive molecules with tuned absorption properties were developed to enable photoactivation at discrete visible wavelengths.

Photochemical kinetic studies were undertaken to evaluate decaging efficiency across visible wavelengths. Under all conditions examined, photorelease proceeded *via* first-order kinetics, enabling quantitative comparison of decaging performance between compounds and irradiation wavelengths.

Preliminary peptide functionalisation studies were also performed. A lysine residue within a model peptide was selectively photocaged using an orthogonal deprotection strategy, and the installed photocage retained photolytic activity following irradiation at 365 nm. A synthetic workflow for photocaging glutamic acid residues was also developed, although full photochemical evaluation was not completed.

Overall, this work provides a chemical foundation for the future development of photoresponsive biomaterials capable of dynamically regulating biomolecular interactions, with potential applications in stem cell control and tissue engineering.

List of Contents

1. Introduction

2. The synthesis of coumarin and BODIPY photocages

3. The synthesis of photocleavable linkers

4. Decaging studies and Peptide functionalisation

5. Future work

Declaration

I declare that this thesis is a presentation of original work, and I am the sole author. This work has not previously been presented for an award at this, or any other, University. All sources are acknowledged as references.

Acknowledgments

I would first like to thank my supervisor, Dr. Christopher Spicer, for his invaluable mentorship, support, and insight throughout the past four years. His guidance greatly shaped my development as a scientist, and the friendly, welcoming environment he created ensured I thoroughly enjoyed my time at the University of York. I am also grateful to the Department of Chemistry for funding this project.

I sincerely thank the Spicer group, especially Nick Rose, Lydia Barber, and Laetitia Raynal, for helping me settle in and feel at home in my first year, alongside the wider Chemical Biology community for their ideas, support, and camaraderie, which ensured there was never a dull moment in the lab. I am particularly indebted to Dr. Nicholas Yates, whose scientific knowledge (and love of newts) was invaluable to me both inside and outside of the lab.

My gratitude extends to all of the technical staff at York, including Imam, Julia, Roksana, and Helen, for their tireless work, and to Heather Fish, Ed Bergstrom, and Karl Heaton for their essential contributions to the characterisation of my products.

Beyond the lab, I thank the UoY darts society and York darting community as a whole for providing such an enjoyable outlet during difficult times. Thanks also to James (x2), Matt, Josh, and Connor for their help with the Monster Tower, a highlight of my time in York.

Thank you to my family, Mum, Sadie and Denis, for supporting me during my writing period at home, even in the toughest of times.

Finally, I would like to thank Jamie Wood, whose friendship was crucial not only to my sanity but also to the success of this work.

A Dhaid,

Ní raibh aon lá nach raibh tú i mo smaointe. Tá súil agam gur chuir mé bród ort. Beidh tú i mo chroí go deo.

Chapter 1

Introduction

1.1 Project basis

1.1.1 Biomaterials for tissue engineering

Tissue engineering (TE) is a multidisciplinary field, that has emerged since the late 1980s which aims to exploit the human body's capacity for growth and repair in order to cultivate tissues for therapeutic purposes. The field combines principles from developmental biology, materials science, synthetic chemistry, and biophysics to harness the underlying biological mechanisms that determine cell fate.[1] One key mechanism that is routinely exploited is biochemical signalling, with growth factors such as bone morphogenetic protein (BMP) and fibroblast growth factor (FGF) commonly utilised to direct processes including osteogenesis,[2,3] and chondrogenesis.[4–6] A second widely exploited mechanism is mechanotransduction at the cell-matrix interface, whereby cells sense and respond to the stiffness and architecture of their surrounding extracellular matrix leading to changes in gene expression and phenotype. For example, stiff matrices tend to direct stem cells toward osteogenic lineages,[7] whereas more flexible matrices promote the formation of softer tissues such as neurons.[8] By controlling these biochemical and mechanical cues, either statically or dynamically, tissue engineering strategies capable of guiding complex cell behaviours including differentiation and proliferation can be developed and translated into powerful therapeutic technologies.

TE is an incredibly diverse field, encompassing a wide array of technologies from cell culture to genetic manipulation, to protein engineering. Consequently, from this point onwards, we will focus on the area of most importance to this thesis, biomaterials (BMs). BMs themselves are incredibly diverse, encompassing any natural or synthetic scaffold, which has been created to interact with a biological system. As such, BMs can be used for a wide variety of applications, ranging from metallic implants such as artificial hip joints,[9] to implantable biosensors,[10] to hydrogels that provide a scaffold for cell growth[11] as seen in figure 1 below.

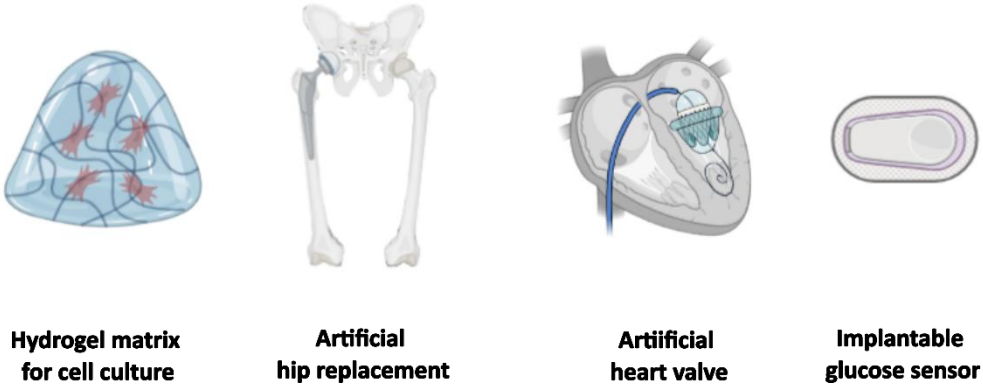

Figure 1: A selection of the possible diverse applications of biomaterials.

In the context of scaffolds for cell growth, biomaterials serve as three-dimensional frameworks capable of driving tissue formation. Beyond providing mechanical support for cell adhesion and proliferation, these scaffolds can also deliver biochemical signals that help guide cellular differentiation.[12,13] This is advantageous, as *in vivo* cell fate is regulated by biochemical signalling cascades that are under strict spatiotemporal control.[14] Incorporating such control into biomaterial scaffolds enables the presentation of defined gradients of signalling molecules, thereby allowing greater regulation over cell behaviour and improved control of the tissue development process.[3,15] The structure and composition of biomaterials are bespoke, and they can be engineered with a specific purpose in mind, such as modulating cell proliferation or differentiation, either through the selection of particular polymers,[16] or through functionalisation with bioactive molecules designed to activate specific cellular signalling pathways.[17,18] In this way these scaffolds can be engineered to mimic key features of the extracellular matrix (ECM), which is the native structural support network produced by cells *in vivo*.[19,20] The ECM is composed mainly of water, fibrous proteins such as collagen, and proteoglycans, forming a matrix that supports cellgrowth,[21,22] and is critical to their survival and development. Not only does the ECM provide a three-dimensional structure, promoting

tissue development, but it also acts as a reservoir, harbouring a myriad of essential biomolecules.[23] These range from structural proteins such as elastin which provides elasticity to tissues like skin,[24] to metalloproteinases which facilitate wound healing,[25] to biological signalling molecules including growth factors and cytokines which drive cellular differentiation.[26] By providing structural support alongside spatiotemporally regulated biochemical signals, the ECM plays a central role in directing tissue development. Accordingly, biomaterials capable of recapitulating these functions represent an important tool for controlling cell fate in vitro.

One of the most prevalent classes of BMs used for this purpose are hydrogels. Hydrogels, consist of a three-dimensional polymer network which is hydrophilic in nature and as such, capable of retaining large amounts of water. This large water content, coupled with their inherent mechanical elasticity arising from their crosslinked polymer architecture, enables hydrogels to mimic the structural properties of the ECM, making them an ideal scaffold for TE.[27] Furthermore, the crosslinked nature of the polymer network creates a porous structure, which facilitates the diffusion of nutrients, biomolecules, and metabolic waste products into and out of the developing tissue.[28] Hydrogels can be created from a wide array of polymers, from natural polymers such as collagen and alginate to synthetic alternatives such as polyethylene glycol (PEG) and polyacrylamide. These polymers impart different properties on the final hydrogel formed and as such the chemical and mechanical properties of a hydrogel are tunable, simply by selecting a specific polymer.[29] The properties of the hydrogel can then be further refined through the modulation of parameters such as the polymer to water ratio, to the degree of crosslinking, allowing for the creation of a bespoke scaffold tailored to a specific biological application of interest.[27,30] The polymers within a hydrogel can also be functionalised with molecules that allow them to interact with the surrounding environment.

This creates a structure capable of enriching specific biomolecules of interest, improving their ability to drive tissue development even further.[2]

1.1.2 Growth factors

As mentioned above, hydrogels can be functionalised to allow them to interact with specific biomolecules of interest, helping to drive tissue formation. Perhaps the most powerful biomolecules for driving tissue formation are growth factors (GFs).[31] These are soluble, cell-secreted peptides or proteins, which bind to, and activate receptors present on the cell surface. The binding of a GF to its specific receptor results in the activation of signalling cascades within the cell, which ultimately results in the activation of proteins known as transcription factors, altering gene expression, and leading to a change in cell function and/or morphology in a process known as signal transduction.[32,33] Biological environments are complex, and cellular processes are controlled by vast networks of these GF signalling cascades, which interact with, and influence, each other as seen in figure 2 below. *In vivo,* these interactions are under strict spatio-temporal control, which allows for proper cell function, as well as the development of the correct tissue types at discrete locations within the body. This temporal control is complex and operates *via* several different underlying mechanisms including negative feedback, enzymatic activation, receptor endocytosis and controlled release from within the ECM.[34–37] Consequently, it has been challenging to effectively mimic these signalling pathways *in vitro* using current TE technologies, making it difficult to gain control over the tissue development process.

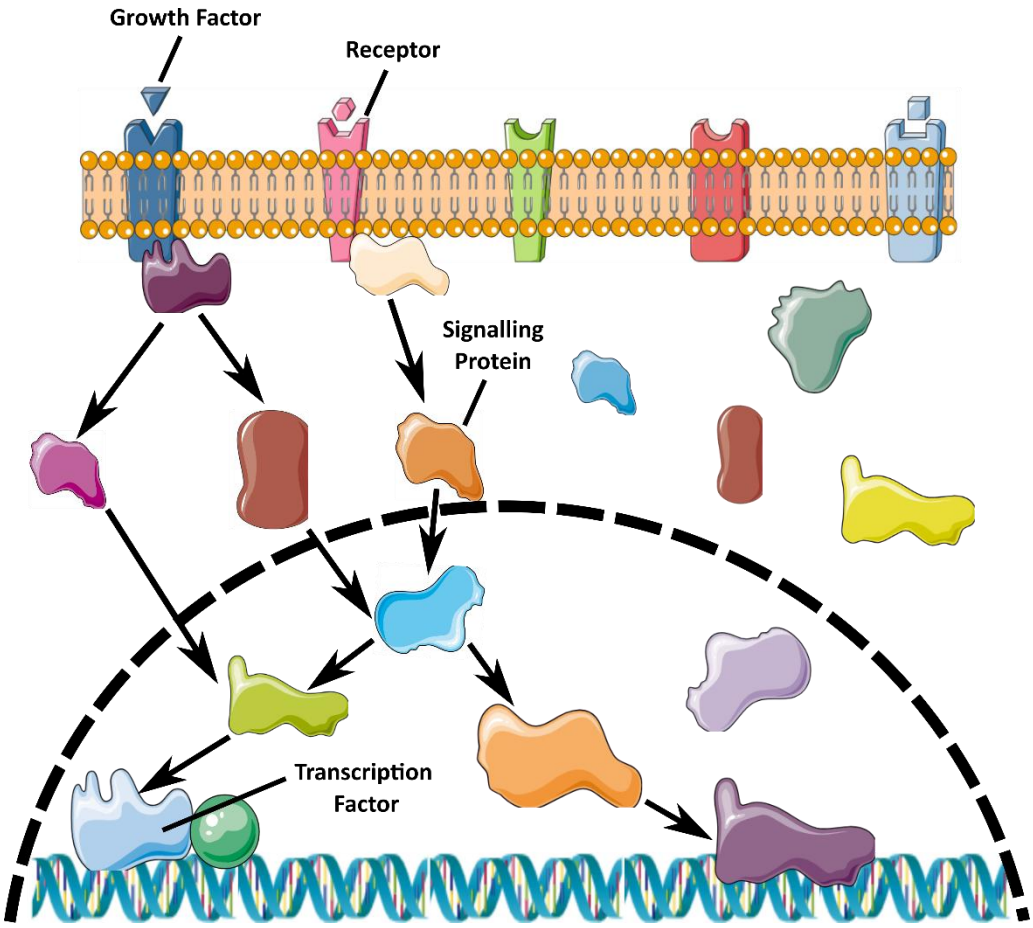

Figure 2: A simplified schematic of the signal transduction process following GF binding to a cell-surface receptor. Ligand binding induces receptor activation, which in turn triggers intracellular signalling cascades involving sequential protein-protein interactions. These cascades culminate in the activation of transcription factors which regulate gene expression leading to a change in cellular function and/or morphology.

1.1.3 Functionalised hydrogels for growth factor enrichment

As mentioned in the previous section, GF signalling is key to driving tissue differentiation. *In vivo* stem cells are exposed to specific GFs at discrete points in time leading to them developing into a desired cell type.[38,39] Although precise control over these signalling pathways is difficult to achieve, efforts have been made to enrich important GFs during cellular development in order to drive the formation of a tissue of interest. In particular, functionalised

hydrogels have proven to be extremely useful for this purpose. By seeding cells on a hydrogel functionalised with a molecule that selectively binds to, and sequesters a key developmental GF, the cells can be encouraged to descend down a desired lineage, driving the formation of a tissue of interest.[31]

One of the earliest examples of this was demonstrated by Stupp et al.[40] In their work, peptide amphiphile nanofibers were produced which contained an epitope with high affinity for transforming growth factor β-1 (TGFβ-1). To identify this epitope, phage display was performed against recombinant TGF-β1 using a random peptide library, yielding a short sequence capable of binding and sequestering this GF. This sequence was incorporated into a peptide amphiphile using solid-phase peptide synthesis, which enabled the formation of a hydrogel consisting of self-assembled nanofibers that retained TGF-β1 for significantly longer than non-functionalised controls. *In vivo*, this material was tested within a rabbit model containing a chondral defect, where it was shown that it accelerated cartilage regeneration relative to non-functionalised controls. Additionally, chondrogenesis was observed, even in the absence of exogenous TGF-β1, demonstrating the ability of this material to recruit endogenous GFs. This allowed for a single-injection treatment, potentially allowing for the development of non-invasive therapies in the future.[40]

Following on from this work, Stupp et al, set out to create a similar hydrogel capable of sequestering bone morphogenetic protein-2 (BMP-2), in the hope of driving osteogenesis.[2] Once again phage display was performed, this time against BMP-2 which identified a peptide sequence capable of binding it with high affinity, and this sequence was incorporated into a peptide amphiphile using solid-phase peptide synthesis. A functionalised hydrogel, consisting of these peptide amphiphile fibres was then created and shown to drive spinal fusion within

a rat posterolateral lumbar fusion model. Remarkably, a spinal fusion rate of 100% was achieved within two weeks, whilst simultaneously requiring 10-fold less exogenous BMP-2 than a collagen sponge control. Additionally, a fusion rate of 42% was observed in the absence of exogenous BMP-2, once again demonstrating the potential of these functionalised hydrogels to recruit endogenous GFs.[2]

The work of this group,[2,40] demonstrates the potential for GF sequestering materials to drive tissue formation. By seeding cells on a material and sequestering a specific GF of interest, the localised concentrations of this GF can be greatly increased allowing for the activation of a desired signalling pathway. This ultimately leads to the upregulation of genes that drive tissue formation, providing increased control over cell fate. A simplified schematic of this process in figure 3 below.

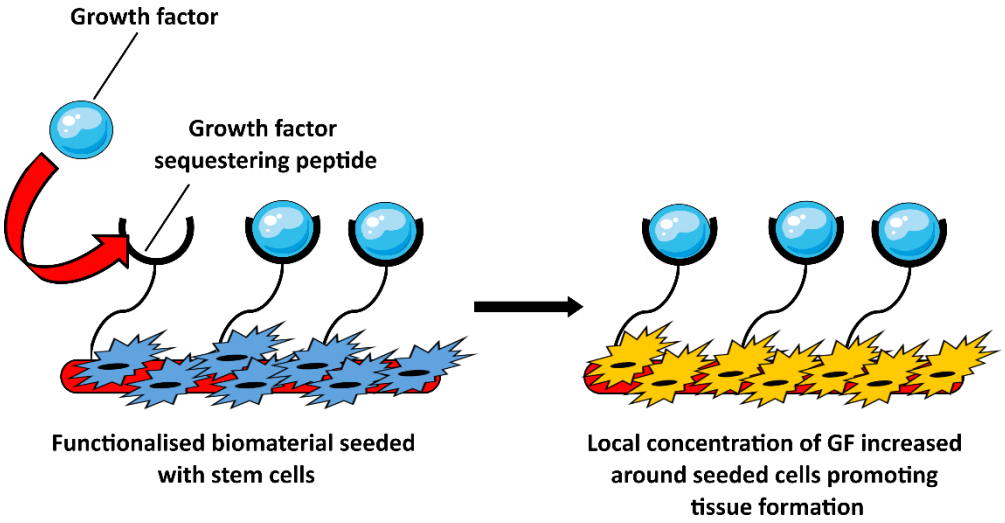

Figure 3: Simplified schematic of a functionalised hydrogel driving tissue formation. The hydrogel is functionalised with a peptide capable of sequestering a GF, thereby increasing its local concentration around seeded stem cells. Elevated GF availability enhances activation of the corresponding signalling pathway, promoting stem cell differentiation and subsequent formation of the desired tissue.

Although the materials discussed above demonstrated the ability to sequester specific GFs, they lacked dynamic functionality, meaning that growth factor sequestration could not be activated or deactivated at specific points in time.[2,40] As such, temporal control over the signal transduction process was not achieved. Whilst this limitation is acceptable for more broad developmental processes such as osteogenesis, whereby BMP-2 is one of the primary signalling pathways activated during this process, it represents a significant obstacle to overcome in the development of more specialised TE techniques such as organogenesis. *In vivo*, the development of these more specialised tissues and organs requires precise spatio-temporal control over multiple signalling pathways,[41,42] meaning that if more bespoke tissues are to be developed using *in vitro* techniques, spatio-temporal control over GF signalling is a key consideration.

This limitation was addressed by Broguiere et al., who in their work, developed a material capable of sequestering nerve growth factor (NGF) to promote axonal growth.[15] In contrast to the materials discussed previously, the system developed in this work allowed for spatio-temporal control over NGF enrichment, through the application of a technique known as photocaging. Photocaging involves the use of a photolabile, small-molecule chromophore covalently bonded to, and inhibiting the activity of, a biomolecule of interest. Upon activation with light this chromophore, or 'cage' is removed, returning activity.[43] In this way, photocages are analogous to protecting groups used in synthetic chemistry to inhibit the reactivity of promiscuous functional groups. However, unlike these more traditional protecting groups, which often require harsh chemical or physical conditions for cleavage, photocages can be removed simply by irradiation with light, allowing the photocaged biomolecule to be activated in an inherently more non-invasive and biocompatible manner, particularly if the photocage can be cleaved using low-energy, visible light. Furthermore, the use of a focused light delivery

system such as a LASER, allows for a high degree of spatial precision, allowing for localised activation of a specific biomolecule of interest.

In their work, Broguiere et al. incorporated a photocaged Sortase A glycine donor motif into a hydrogel, which initially prevented recognition by the enzyme Sortase A.[15] Upon irradiation with light, the photocage was removed allowing Sortase A to ligate this motif to a corresponding donor motif linked to NGF *via* an avidin-biotin carrier system. This led to a local increase in NGF concentration at irradiated regions, affording excellent spatio-temporal control. Using this strategy, axonal growth could be guided through a three-dimensional brain-mimetic matrix simply by irradiating a specific pathway with light, thus demonstrating the potential of this system for driving tissue development. A simplified schematic of this system can be seen in figure 4 below.

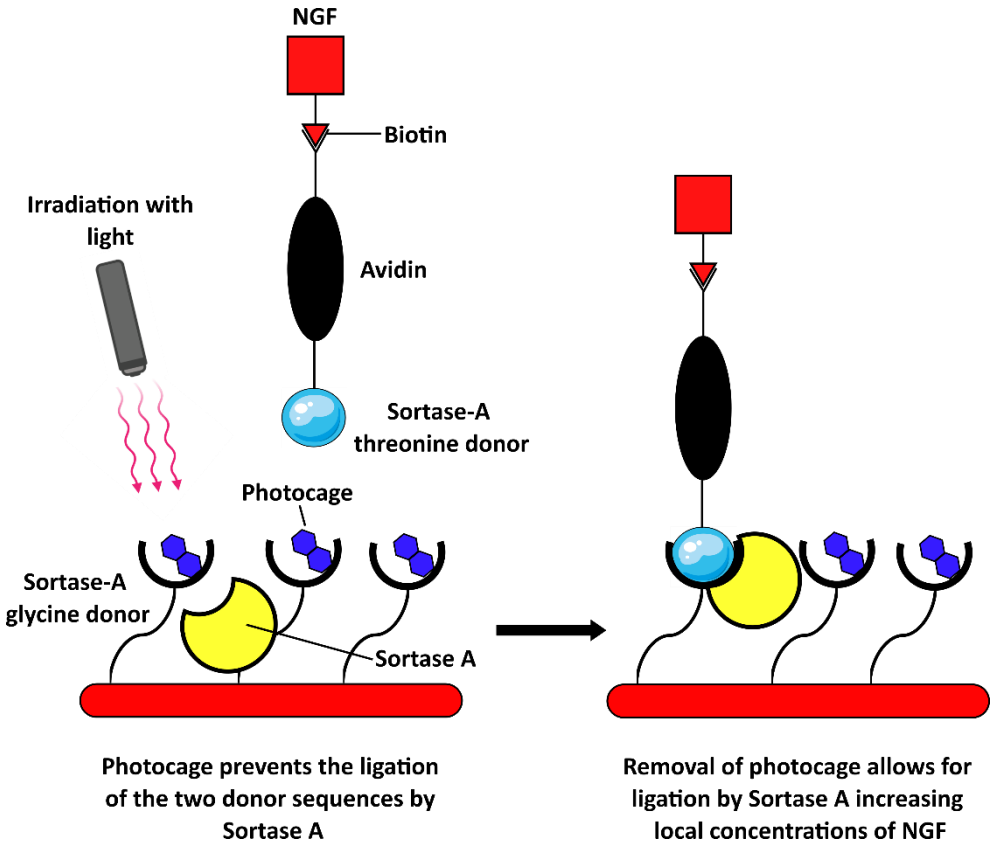

Figure 4: Schematic of the system developed by Broguiere et al. Light-triggered cleavage of a photocaged Sortase A glycine donor enabled NGF carrier ligation and local enrichment of NGF.[15]

The system developed by Broguiere et al, allowed for precise spatio-temporal activation of NGF signalling simply by targeting specific regions within the hydrogel using LASER irradiation.[15] However, a notable limitation of this system, was that it only allowed for the enrichment of a single GF. Whilst this was not detrimental to axonal growth, it may limit the applications of this technology were it to be used to engineer tissues which require the sequential activation of multiple different GF signalling pathways.

In contrast to this, Azagarsamy & Anseth developed a hydrogel system which provided spatio-temporal control over the sequential release of multiple different GFs.[3] This approach

exploited wavelength-controlled photocleavage through the use of photocleavable linkers, which incorporated a click handle to tether biomolecules to the hydrogel matrix and subsequently permit their photorelease. Two orthogonally cleavable linkers, based on the *o*-nitrobenzyl and coumarin scaffolds, were synthesised and used to attach BMP-2 and BMP-7 to a hydrogel seeded with human mesenchymal stem cells (hMSCs). While tethered, the GFs remained inactive, however, photolysis of their corresponding photocleavable linker released them into the surrounding media, facilitating the activation of their associated signalling pathways. Orthogonal release was achieved by first irradiating at 405 nm, cleaving the nitrobenzyl linker to release BMP-2, followed several days later by irradiation at 365 nm to release BMP-7, *via* the photolysis of the coumarin linker. Sequential exposure to these GFs significantly enhanced osteogenic differentiation compared to delivery of either BMP-2 or BMP-7 alone, demonstrating the potential of wavelength-controlled, sequential photorelease as a powerful strategy to drive tissue differentiation.[3] A schematic overview of this system is provided in figure 5 below.

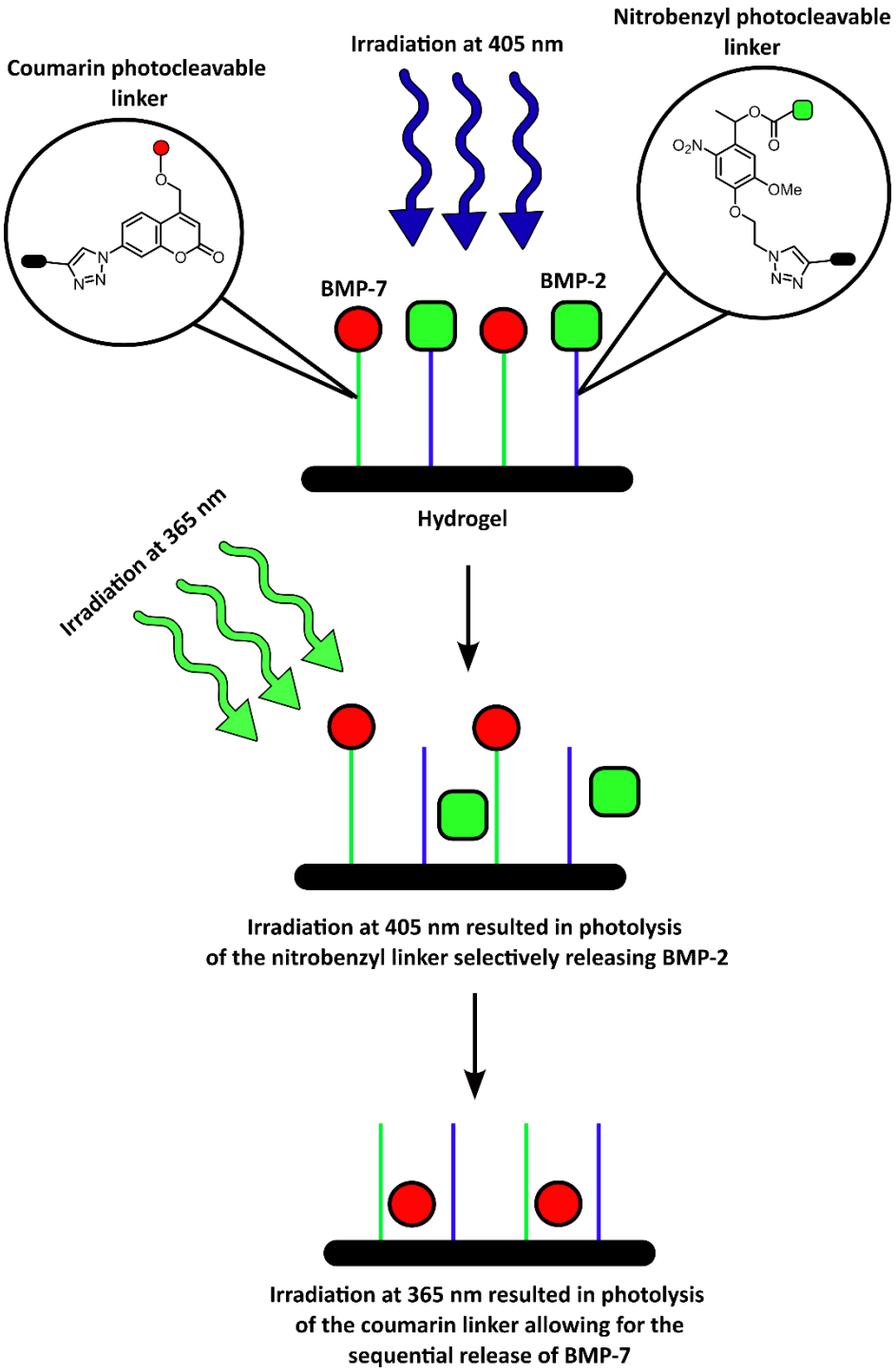

Figure 5: Schematic of the system developed by Azagarsamy and Anseth. BMP-2 and BMP-7 were tethered to a hydrogel via orthogonal photocleavable linkers (nitrobenzyl and coumarin, respectively). Irradiation at 405 nm selectively released BMP-2, followed by 365 nm irradiation to release BMP-7 sequentially.[3]

The systems discussed above all enrich GFs helping to drive tissue differentiation, but each does so in a distinct manner. Stupp et al., employed GF sequestering peptides to recruit specific GFs to the hydrogel surface, increasing local concentrations and helping to activate a specific signalling pathway of interest to drive tissue formation.[2,40] Although this is sufficient for broader developmental processes such as osteogenesis, the lack of temporal control afforded by these systems limits their applications, as for more complex developmental processes, increased spatio-temporal control is often required. Broguiere et al, addressed this issue by functionalising a hydrogel with a photocaged Sortase A glycine donor, enabling localised GF enrichment in response to light.[15] The major limitation of this system was that due to the nature of the avidin carrier, (which binds to biotin with femtomolar affinity) only a single GF could be enriched, meaning that sequential enrichment of multiple different GFs could not be achieved. In contrast to this, Azargasamy & Anseth utilised two orthogonally cleavable photocleavable linkers, based on the o-nitrobenzyl and coumarin scaffolds which facilitated the sequential release of the GFs BMP-2 and BMP-7.[3] Selective photorelease was achieved by irradiating the hydrogel using different wavelengths of light, and the resulting sequential enrichment significantly enhanced osteogenic differentiation in hMSCs, demonstrating the utility of this approach to drive tissue formation.

In our work, we aim to build on all of the above systems, incorporating aspects of each in order to create a material capable of sequentially activating and deactivating the signalling pathways of several unique GFs, in the hope of creating a system which more closely mimics the signal transduction process that occurs *in vivo*. If a system like this could be created, it would be a powerful tool for TE, helping to drive the development of more complex tissues and organs and the creation of personalised therapeutic strategies. The system which we wish to develop is discussed in the following section.

1.1.4 Functionalised hydrogels capable of the sequential activation and deactivation of multiple growth factors

The system developed by Stupp et al. involved the functionalisation of a material with a single GF sequestering peptide, thereby enabling the selective enrichment of a specific GF of interest.[2,40] However, for more complex TE applications it would be beneficial to create a material capable of enriching multiple different GFs. Despite this, the straightforward incorporation of multiple GF sequestering peptides into a hydrogel matrix may introduce significant challenges. Specifically, such an approach would likely result in the simultaneous enrichment of all target GFs. As previously discussed, GF signalling relies on the precise modulation of multiple different GF signalling cascades, each requiring strict temporal control. Consequently, the simultaneous enrichment of multiple GFs, without the capability for spatio-temporal control, would fail to recreate native signalling complexity. This unnatural signalling could result in the development of heterogenous cell populations,[44] severely impacting tissue development as seen in figure 6 below.

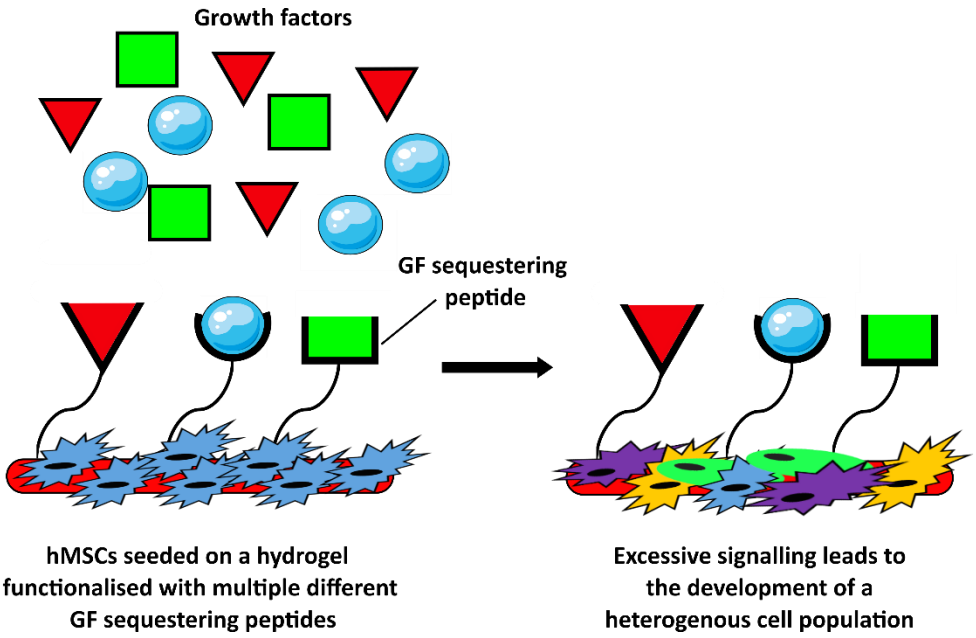

Figure 6: The enrichment of multiple GFs concurrently can lead to excessive signalling and the generation of heterogeneous cell populations.

In order to address this issue, we propose to regulate the affinity of these peptides for their respective GFs using light. This will be accomplished by installing photocages onto each peptide which can be cleaved by orthogonal wavelengths of light, thereby temporarily inhibiting their binding activity. Each GF can then be selectively enriched simply by removing the photocage present on its corresponding peptide with the correct wavelength of light. In this way, spatio-temporal control can be gained over the enrichment of multiple GFs, allowing them to be activated in a sequential manner more closely mimicking the biological signalling cascades seen *in vivo*. An overview of this system is provided in figures 7 and 8 below.

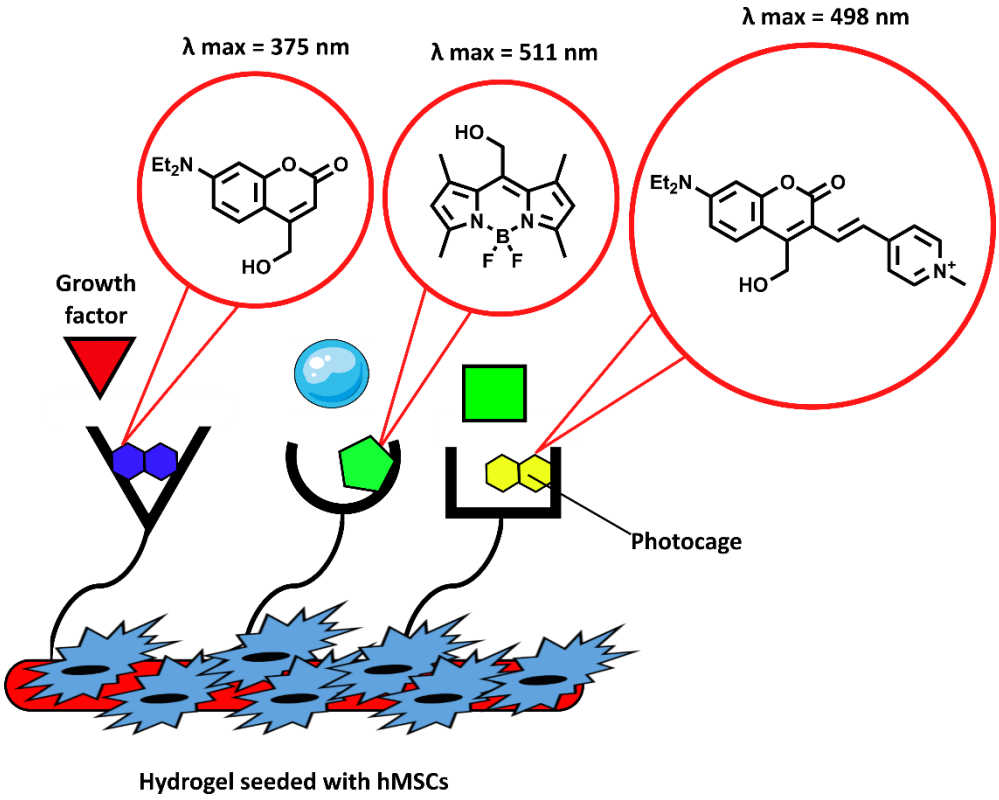

Figure 7: A schematic of a hydrogel seeded with hMSCs and functionalised with photocaged GF sequestering peptides. The photocages render the peptides inactive until light-induced cleavage.

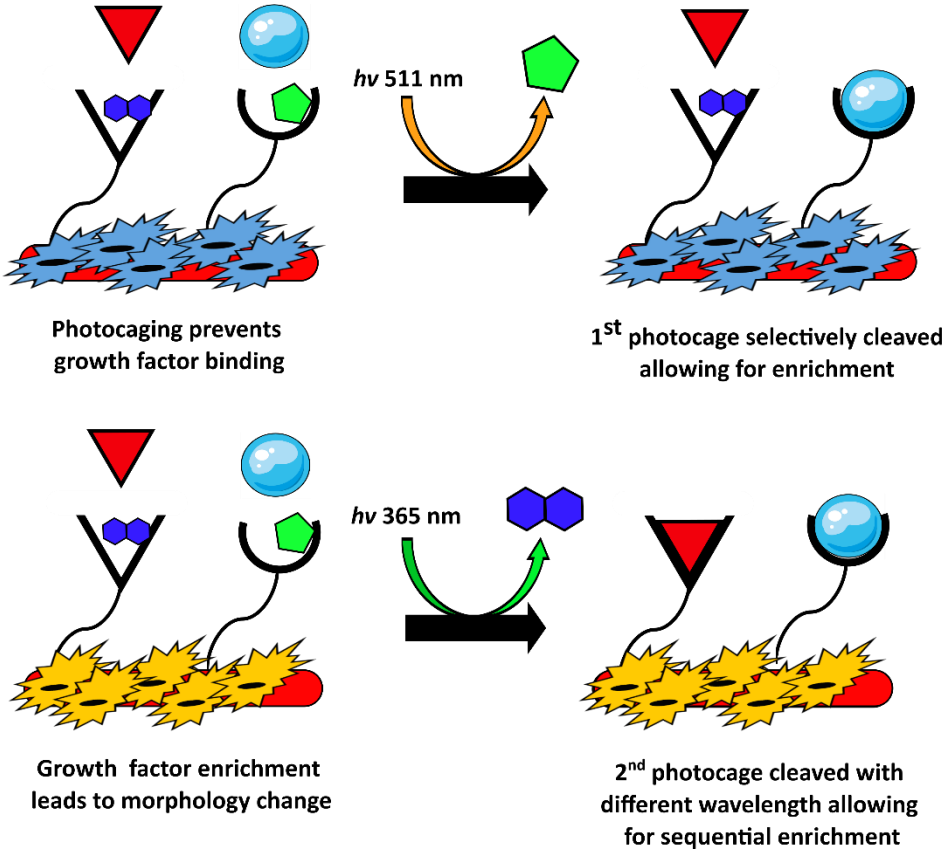

Figure 8: Schematic of a hydrogel system incorporating orthogonally cleavable photocages for sequential GF enrichment. Initially, irradiation at 511 nm selectively cleaves the first photocage, enabling the binding and enrichment of the first GF. Following the observation of a desired morphology change, irradiation at 365 nm cleaves the second photocage, sequestering the second GF, thereby facilitating sequential enrichment.

The system proposed above allows for the sequential enrichment of multiple different GFs using light. However, a major limitation of this system is the irreversible nature of the decaging reaction. Once a photocage is cleaved, and its corresponding GF sequestering peptide activated, there is no means of deactivating or "turning off" this peptide, meaning that this GF will be enriched for the remainder of the tissue culture process. *In vivo*, the dynamic nature of signalling pathways means that both the activation and deactivation of GFs are key to

driving tissue development.[45,46] Consequently, in order to mimic the signal transduction processes that occur *in vivo*, a means of deactivating GF signalling is also required.

In the work discussed in the previous section, Anseth & Azagarsamy utilised photocleavable linkers to tether GFs to hydrogel matrix and sequentially increase their concentrations through irradiation with specific wavelengths of light.[3] However, if these linkers were instead used to tether GF sequestering peptides to the hydrogel network, photocleavage would result in the release of the peptide from the material, thereby abolishing its capacity to sequester its target GF at the hydrogel surface. This would effectively terminate the enrichment of the target GF within the matrix and, consequently, deactivate the associated signalling pathway. Moreover, by incorporating multiple orthogonally cleavable linkers, each responsive to a distinct wavelength of light and coupled to a different GF-sequestering peptide, it would be possible to achieve wavelength-specific and selective deactivation of multiple GF signalling pathways simply by irradiating the material with light of the appropriate wavelength. A schematic representation of this proposed strategy is shown in Figure 9.

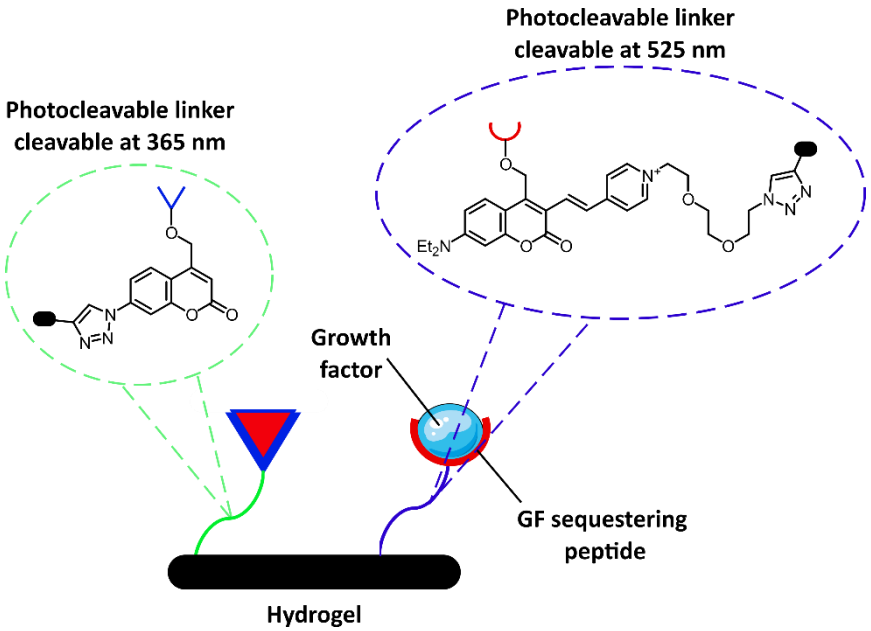

Figure 9: A schematic of a hydrogel functionalised with two different GF sequestering peptides each tethered via an orthogonally cleavable photocleavable linker. Irradiation at the appropriate wavelength induces photocleavage, releasing the targeted peptide from the hydrogel matrix and thereby terminating the enrichment of its corresponding GF at the surface.

In this work we aim to combine the above system, with the system depicted in figure 8 above. Thus, creating a photoresponsive material capable of sequentially activating and deactivating the enrichment of multiple different GFs. This approach would mimic the dynamics of signalling cascades in vivo, affording excellent spatio-temporal control over biochemical signalling. Such a system would provide precise regulation of tissue development process, enabling controlled differentiation and representing a powerful tool for TE. A schematic overview of the proposed system can be seen in figure 10 below.

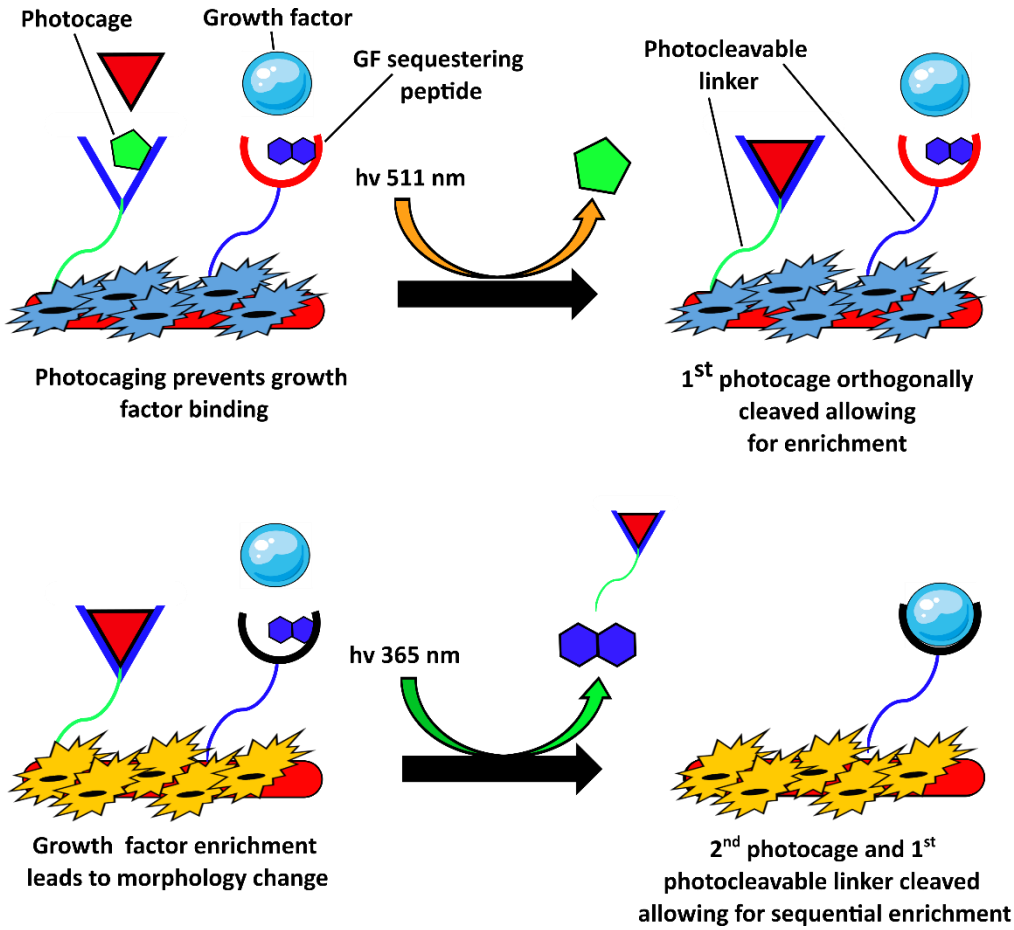

Figure 10: A schematic of the system to be developed during this work. A hydrogel seeded with hMSCs is functionalised with photocaged GF-sequestering peptides tethered via photocleavable linkers. Irradiation at 511 nm selectively removes the first photocage, facilitating the enrichment of the targeted GF. Subsequent irradiation at 365 nm activates the second peptide whilst simultaneously cleaving the linker of the first, thereby initiating enrichment of the second GF and terminating the enrichment of the first.

1.2 Photo-responsive chemistry

1.2.1 Light

Electromagnetic radiation was first described by Maxwell in 1864 and refers to radiation which travels through space in the form of oscillating electric and magnetic fields. This is described by Maxwell's equations and the resulting waves span a wide range of wavelengths and

frequencies which are collectively known as the electromagnetic spectrum.[47] The concept of light refers to the visible (and near-visible) portion of this spectrum. The properties of light are dictated by two key factors, wavelength (λ) and frequency (*v*). The wavelength of light refers to the distance between two consecutive crests (or troughs) in a wave and is typically measured in nanometres (nm). Frequency on the other hand refers to the number of wave cycles that pass through a point in space per unit time. Typically, this is measured in hertz (Hz) whereby 1 Hz is equal to one cycle per second. These properties are linked through equation 1 seen below which describes the speed of light (*c*). The speed of light is constant and has a value of 3 x 10^8 ms^{-1} within a vacuum. As such, there is an inverse relationship between wavelength and frequency, whereby as the wavelength of light increases, its frequency decreases.

$$c = \lambda \cdot v$$

Equation 1: The speed of light (c) is equal to the product of the wavelength and frequency [47]

Maxwell's equations provided a comprehensive description of light as an electromagnetic wave, a theory which remained widely accepted for several decades. However, in 1905, Albert Einstein observed a phenomenon which could not be described using classical wave theory alone. When a metallic surface was irradiated with light, it was observed that electrons were ejected, a phenomenon which was later termed the photoelectric effect. Crucially, this ejection of electrons only occurred if the incident light was of a frequency above a certain threshold value, irrespective of its intensity. Conversely, if the incident light was of a frequency below the required threshold value, the surface failed to eject electrons regardless of how intense the irradiation was. Classical electromagnetism had previously predicted that increasing light intensity should increase the energy imparted to the electrons, and as such

these findings were found to be contradictory. To account for this, Einstein proposed that light must also exhibit particle-like behaviour, consisting of discrete, quantised packets of energy which he termed photons.[48] Prior to this discovery, Max Planck had already introduced the idea that energy was quantised and could only exist as multiples of the smallest fundamental unit of energy.[49] He called this unit Planck's energy, and Einstein applied this principle to photons, describing their energy as being equal to the product of frequency and Planck's constant as seen in equation 2 below.

$$E = h \cdot v$$

Equation 2: Planck's equation describes the energy of a photon

As a result, light can not only be described as a wave, but also as a particle. This behaviour is a central concept of quantum mechanics and is referred to as the wave-particle duality.[48] Taking both of the previous equations into account, it can now be seen that the energy of a photon is directly linked to its frequency, which in turn is dependent on its wavelength. Light with a short wavelength has high frequency, and so it is these photons that are highest in energy. Conversely, light with a long wavelength has a low frequency meaning that it is lower in energy. As a result, it can be said that light in the red region of the visible light spectrum, which exhibits the longest wavelength, is lowest in energy. At the other end of the spectrum, light in the violet/blue region has a shorter wavelength, and as such is higher in energy. This is an important consideration when applying light to the study of biological systems as longer wavelength, lower energy light typically offers enhanced biocompatibility *vs* its shorter wavelength, higher energy counterparts.[50,51] A schematic depicting the electromagnetic spectrum can be seen in figure 11 below.

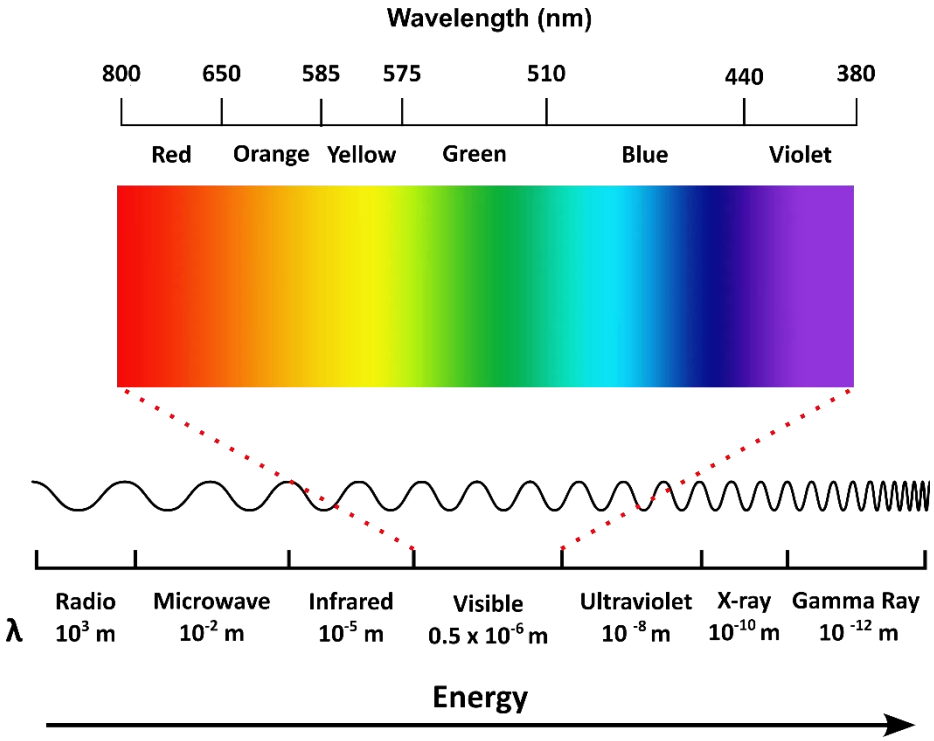

Figure 11: A schematic of the electromagnetic spectrum with the visible region expanded. Increasing wavelength corresponds to decreasing photon energy, which enhances biocompatibility.

1.2.2 Chromophores and the absorption of light

A molecule, or a specific region of a molecule, that is capable of absorbing light within the ultraviolet (UV), visible or infrared (IR) regions of the electromagnetic spectrum is referred to as a chromophore. This selective absorption results in the reflection or transmission of the remaining wavelengths of visible light, giving rise to the observed colour of the compound.[52] Prior to light absorption, a chromophore exists in its electronic ground state whereby its electrons occupy the lowest available energy levels. Upon exposure to light of suitable energy, an electronic transition can occur, whereby an electron is promoted from the ground state to a higher-energy electronic excited state.[53] This process is most commonly illustrated using a Jablonski diagram,[54] which schematically depicts the various electronic states of a molecule and the transitions that can occur between them, as shown in Figure 12. Looking at this

Jablonski diagram, it can be seen that each energy level (denoted with an S) has a number of associated energy levels. This is due to the existence of vibrational energy levels. These levels arise from the quantised vibrational motion of the chemical bonds within the molecule. Consequently, light absorption is not restricted to a single discrete energy gap but can occur from several different vibrational sublevels of the ground electronic state to various vibrational sublevels of the excited state. This gives rise to a distribution of possible absorption transitions, allowing the chromophore to absorb over a range of wavelengths rather than at a single, sharply defined value.[53]

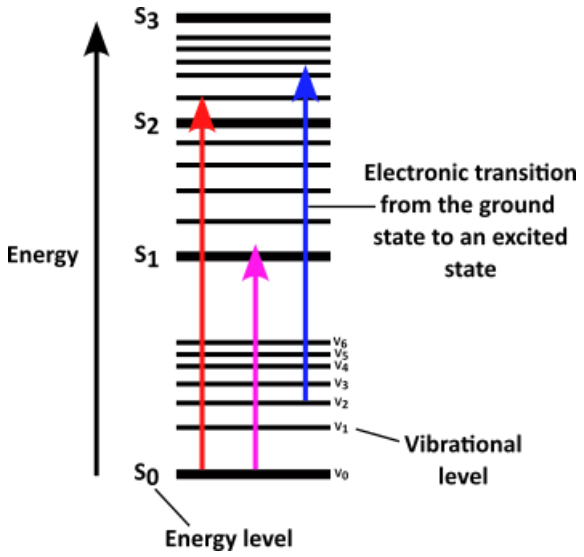

Figure 12: A Jablonski diagram.

1.2.3 Energy dissipation from the excited state

Upon the absorption of a photon, a chromophore is promoted from its electronic ground state to an electronic excited state. This higher energy state imparts electronic instability and as such, the molecule undergoes a series of relaxation processes in order to dissipate energy and return to its ground state. Energy can be dissipated through a variety of different pathways, and these can be radiative, whereby energy is released in the form of light, or non-radiative, whereby energy is released in the form of heat or vibrational motion.[53]

Fluorescence is a classic example of a radiative relaxation process, wherein an electron in its excited state seeks to return to the ground state through the emission of a photon. During absorption, an electron is promoted from the ground state (S_0) to the excited state (S_1). Due to the Franck–Condon principle,[55,56] this transition typically occurs to a higher vibrational level of the excited state, as electronic excitation proceeds vertically on the potential energy surface with minimal nuclear displacement. Following excitation, the electron rapidly relaxes to the lowest vibrational level of S_1 through a process known as vibrational relaxation whereby energy is dissipated as heat to the surrounding environment. From this lowest available vibrational state, the electron then returns to the ground state by emitting a photon, a process known as fluorescence.[53] However, due to the fact that energy has already been lost through vibrational relaxation, the energy of the emitted photon is lower than that of the photon that was originally absorbed. Consequently, the wavelength of the emitted light is higher than that of the absorbed light. This difference in energy between the absorbed and emitted light is known as the Stokes shift.[57]

In contrast to radiative processes, non-radiative processes do not dissipate energy in the form of light. Rather they release energy in the form of heat or vibrational motion.[53] An example of this occurs with internal conversion, whereby an electron transitions from the excited state to a lower energy state, by increasing the vibrational energy of the molecule or nearby species releasing energy in the form of heat. Another non-radiative process that can occur is intersystem crossing, whereby an electron in the excited state undergoes an inversion of spin, changing from a paired-spin configuration (singlet) to an unpaired-spin configuration (triplet) resulting in the formation of the excited triplet state. Once in the excited triplet state, the molecule can undergo non-radiative decay, returning it to the singlet ground state with the release of heat to the surroundings. It can also dissipate energy through the emission of a

photon, in a process known as phosphorescence. This process is similar to fluorescence, however, due to the spin-disallowed nature of the transition it occurs over a longer time period.[58,59]

In addition to the radiative and non-radiative relaxation pathways discussed above, a molecule in the excited state may also seek to dissipate energy through heterolytic bond cleavage.[60–62] This photochemical process is of central importance to this work. As discussed previously, a photocage is a small-molecule chromophore that is covalently attached to and used to temporarily inactivate a biomolecule of interest. Upon irradiation with light within the absorption range of the photocage, an electron is promoted, resulting in the formation of the excited state.[60] Whilst relaxation pathways such as fluorescence, internal conversion, and intersystem crossing may also occur, competing with the desired bond cleavage pathway, photocages are designed such that the excited state decays by undergoing heterolytic cleavage of the bond which attaches the photocage to the aforementioned biomolecule. As such, the decay of the excited state leads to the release of the caged biomolecule, restoring its native activity. This light-induced process is known as decaging and is essential to the success of this project. A schematic overview of the above processes is provided on the Jablonski diagram in figure 13 below.

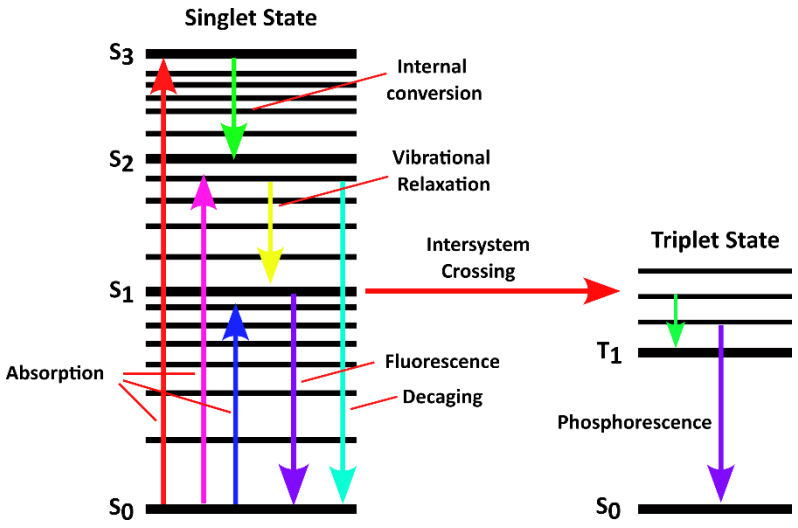

Figure 13: Jablonski diagram illustrating a range of possible photophysical and photochemical transitions that may occur following the absorption of a photon.[58]

1.3 Photocaging

1.3.1 Applications and limitations of photocaging

As discussed in Section 1.2.1, the energy of light is inversely proportional to its wavelength. Consequently, cleavage wavelength is an important consideration when developing a photocaging strategy for biological applications. Photocages that are cleavable at longer, visible wavelengths are inherently more biocompatible than those which require high energy UV light. Irradiation with UV can induce detrimental processes such as photobleaching, DNA damage, or generation of reactive oxygen species, all of which compromise cell viability.[63–65] Consequently, the selection of a photocage that undergoes efficient photolysis under low-energy light is essential for applications involving live cells or tissues.[66] In this context, photocages responsive to red light offer distinct advantages over those cleavable by higher-energy blue or violet light.

The principal benefit of photocaging lies in the spatio-temporal control it provides over the activation of biological systems, by utilising light as a non-invasive and highly controllable

external stimulus.[67] Targeted delivery systems such as LASERs, allow light to be delivered with exceptional spatial control, allowing for rapid and selective activation of a species of interest whilst simultaneously minimising damage to surrounding tissues. Within the broader context of chemical biology, photocaging has been utilised to gain control over a wide range of molecular processes. These include the temporally controlled activation of enzymes,[68] nucleotides[69] and neurotransmitter release,[70] to name but a few. They have also been applied to synthetic chemistry with photocages such as *o*-nitrobenzyls being used extensively to protect promiscuous moieties such as amines and alcohols to allow for multi-step chemical syntheses.[71] As such it can be said that the applications of photocaging are broad, and it can be implemented in a wide range of fields, from developmental biology to synthetic chemistry.

Despite these advantages, photocaging is not without its limitations. Photocages requiring photolysis at higher energy cleavage wavelengths such as those in the UV or near-UV range can compromise cell health through processes such as photobleaching and DNA damage, which can result in cell death.[63–65] Moreover, the byproducts formed by certain decaging reactions may themselves be problematic. A classic example of this is the photolysis of *o*-nitrobenzyls, which generates o-*n*itrosobenzaldehyde, a species that is both cytotoxic and strongly absorbing, thus competing for incident light and diminishing the decaging efficiency of the parent photocage.[60]

An additional challenge is the need for the photocage to be soluble in the experimental medium. Photocages often take the form of small organic molecules which have planar aromatic components and as such the aqueous solubility of these compounds can be problematic when they are applied to biological systems.[60] However, in recent years efforts

have been made to create photocages with superior solubility profiles so that they are easier to apply to biological systems.[72,73]

Finally, in the context of creating a system of sequential activation, whereby multiple photocages are utilised to cage several different biomolecules of interest, it is important that the overlap in their absorption profiles is minimised, so that they are cleavable orthogonally using different wavelengths of light.[74] This limits selection of photocages which can be used in tandem with each other, and often requires difficult chemical syntheses in order to produce selectively cleavable photocages. Nonetheless ongoing developments in photocage design, including improvements in photophysical properties and solubility profiles continue to expand the scope and versatility of this technology for biological applications.[72,73]

1.3.2 Decaging cross section and decaging efficiency

The ability for a photocage to absorb light at the irradiation wavelength is critical to determining decaging efficiency. This light absorbing capacity is quantified by the molar extinction coefficient (ε) which is a measure of how strongly a chromophore absorbs at a given wavelength.[60,75]

Although the extinction coefficient of a photocage provides insight into the accessibility of the excited state upon irradiation at a given wavelength, it does not provide insight into the nature of the excited state that is formed. As mentioned previously, photon absorption can lead to the promotion of an electron to a number of discrete, quantised energy levels, depending on the energy of the incident light. Once the excited state is formed, the molecule may relax through a variety of competing decay pathways. Whilst heterolytic bond cleavage is the productive pathway associated with photocaging, it is important to note that other, non-productive, processes such as fluorescence and internal conversion also occur competing with

the desired decaging reaction. The preference of the excited state to decay through one of these competing processes is strongly influenced by the nature of the excited state that is populated upon the absorption of photon. Consequently, the likelihood of an excited state to decay though heterolytic bond cleavage is an important consideration.[76,77] The decaging quantum yield (Q_u), quantifies the probability that an absorbed photon will result in bond cleavage and cargo release. It is defined as the number of decaging events that occur per photon absorbed.

Consequently, the overall efficiency of the decaging process is not solely linked to the absorption capabilities of the photocage. Rather, it is determined by two key factors, the accessibility of the excited state upon irradiation at a particular wavelength, and the likelihood that this state will decay productively *via* heterolytic bond cleavage. In order to quantify this relationship, a metric known as the decaging cross section, σ_d is used.[78] This parameter provides a wavelength-dependent measure of decaging efficiency and is defined as the product of the molar extinction coefficient and decaging quantum yield as seen in equation 3 below. Photocages with high decaging cross sections at a given wavelength, undergo efficient photolysis under these conditions, making them particularly useful for biological applications as their efficiency may allow for rapid cleavage using low-intensity light, limiting the exposure of cells to light.[78]

$$\sigma_d = \varepsilon \cdot \Phi$$

Equation 3: The product of the extinction coefficient and decaging quantum yield gives rise to the decaging cross section

1.4 The development of photocaging

Up to this point, the general principles underlying the photocaging process have been discussed. However, a detailed examination of the distinct classes of photocages and their development over time has not yet been provided. Consequently, this section will explore the three most widely utilised classes of photocages *o*-nitrobenzyl derivatives, coumarins and boro-dipyrromethenes (BODIPYs). The rational design strategies employed to enhance the photophysical properties of these photocages for biological applications will be discussed, alongside the mechanisms of the respective decaging reactions. The general structures of these classes of photocages are provided in figure 14 below.

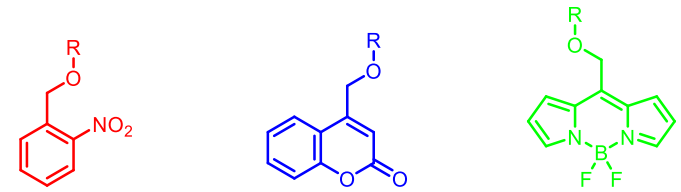

***o*-Nitrobenzyl** **Coumarin** **BODIPY**

Figure 14: The general structures of the three most widely used classes of photocage.

1.4.1 The development of *o*-nitrobenzyl photocages

1.4.1.1 Structural considerations

-Nitrobenzyl photocages consist of a benzyl core scaffold, which is substituted at the *ortho*-position by a nitro group.[79] The caged molecule is typically linked *via* a carbon-oxygen bond at the benzylic carbon, allowing for photolysis upon irradiation with light. In order to facilitate this coupling, o-nitrobenzyl photocages are typically synthesised in their benzyl alcohol form, as they can then undergo etherification or esterification with the desired cargo in order to cage it. The general structure of this class of photocage, including positional numbering is provided in figure 15 below.

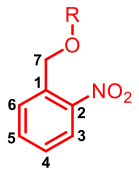

***o*-Nitrobenzyl**

Figure 15: The numbered structure of the o-nitrobenzyl scaffold.

1.4.1.2 Mechanistic considerations

As discussed in Section 1.2.3, the decaging reaction that occurs upon irradiation of a photocage with light is initiated by the decay of an electronically excited state *via* heterolytic bond cleavage. However, the precise mechanistic details of this process differ significantly among the various classes of photocages. In the case of *o*-nitrobenzyl derivatives, photolysis proceeds through the formation of a reactive aci-nitro intermediate.[80] A general overview of this photocleavage mechanism is illustrated in Figure 16 below. The absorption of a photon by compound **(1)** upon irradiation with light, results in the excitation of the nitro-group, which subsequently undergoes an intramolecular proton abstraction with the adjacent benzylic carbon resulting in the formation of aci-nitro tautomer **(2)**, which exists in rapid equilibrium

with its ionic form **(3)**. Initially, it was believed that cyclisation predominantly occurred from the anionic intermediate **(3)**, however, more recent studies have shown that cyclisation of the neutral aci-tautomer **(2)** is the dominant pathway. Nonetheless, both intermediates are capable of undergoing intramolecular cyclisation, leading to the formation of the cyclic intermediates **(4)** and **(5**), respectively. The final decaging step then occurs *via* the elimination of the caged molecule, which also results in the formation of *o*-nitrosobenzaldehyde derivative **(6).**[62]

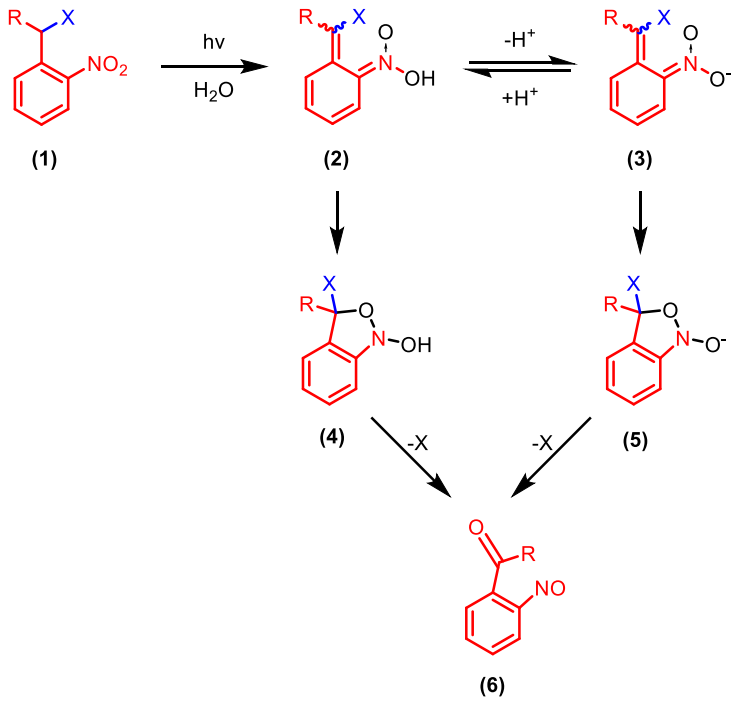

Figure 16: A schematic of the proposed mechanism of photocleavage upon the irradiation of o-nitrobenzyl photocages with light.[62]

1.4.1.3 The birth of a field

An ortho-nitrobenzyl derivative was utilised in the first ever example of biological photocaging. This was reported by Hoffman et al. in 1978 who in their work attached an *o*-nitrobenzyl derivative **(7)** to the terminal phosphate group of the biological energy carrier

adenosine triphosphate (**ATP**) creating **(8)** as seen in figure 17 below.[79] The presence of this photocage, rendered the caged ATP inactive as a substrate for the enzyme Na^+,K^+-ATPase, thereby creating a stable, inactive reservoir of this important biomolecule. Upon exposure to light at 340 nm, photolysis of the carbon-oxygen bond attaching the photocage to the terminal phosphate group occurred, resulting in the generation of *o*-nitrosobenzaldehyde **(9)** and the release of native ATP **(10)**, as seen in figure 17. The photolysis of **(8)**, restored the ability of the ATP to act as a substrate for Na^+,K^+-ATPase, resulting in the activation of Na^+,K^+-ATPase cycle, in what was the first example of utilising photocaging to modulate a biological system. This illustrated the ability of photocaging to gain spatio-temporal control over biomolecular signalling in a non-invasive manner.

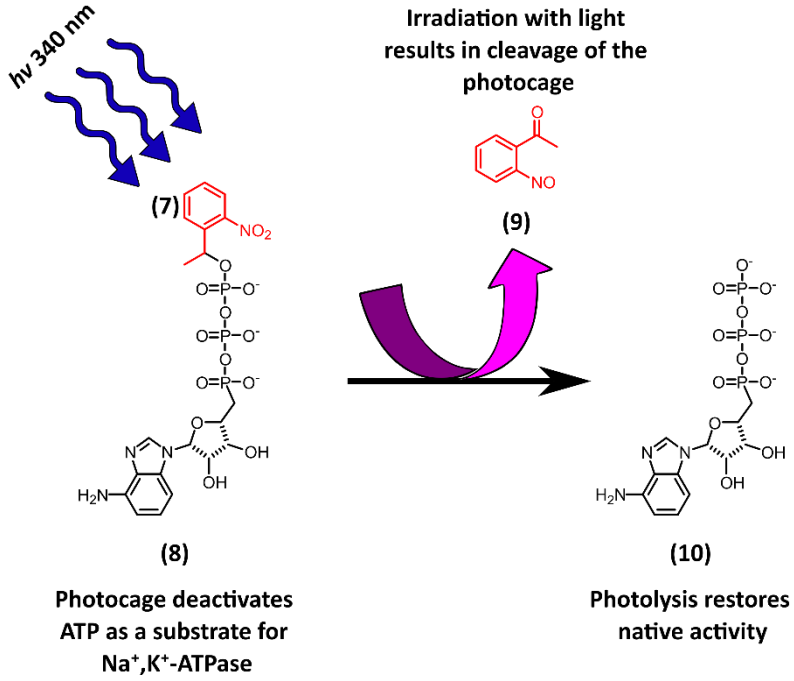

*Figure 17: Schematic representation of the original photocaging system developed by Hoffman et al. In this system, an o-nitrobenzyl photocage **(7)** was conjugated to the terminal phosphate group of ATP, thereby preventing its hydrolysis by the enzyme Na^+,K^+-ATPase. Upon irradiation at 340 nm, the C–O bond linking the photocage to ATP was cleaved, releasing native ATP and restoring its ability to act as a substrate for Na^+,K^+-ATPase.[79]*

Although **(8)** was successful at releasing its cargo upon irradiation with light, several key difficulties existed. First and foremost, cleavage was achieved using light at 340 nm. As mentioned in section 1.2.1 above, a photons wavelength is inversely proportional to its wavelength. Consequently, in order for photocaging to be biocompatible technology, decaging should be achieved using light that falls within the visible range (>380 nm). As such, the compound developed by Hoffman et al., was not suited for use with living cells, as the high-energy nature of the UV light required for photolysis may compromise their viability. Additionally, the decaging efficiency of this compound was not optimal, with only about 80% of theoretical free ATP release observed over the duration of the experiment.[79] This was likely due to the compound exhibiting a poor decaging quantum yield within the UV range. If the structure of these compounds could be altered, so that they could be cleavable in the visible range, with an improved decaging quantum yield, it would greatly broaden their biological applications.

1.4.1.4 The development of 4,5-dimethoxy ortho-nitrobenzyl photocages

The first attempt to red-shift the absorbance of o-nitrobenzyl photocages was made by Lester et al.[81] In their work, methoxy groups were introduced at the 4- and 5- positions of the nitrobenzyl scaffold creating photocage **(11)** as seen in figure 18 below. These groups had an electron donating effect on the o-nitrobenzyl scaffold, thus increasing the electron density in the aromatic π-system through resonance. As such the energy of the ground state was increased, reducing the HOMO-LUMO energy gap and producing a shift in absorption maximum to 340 nm, a significant improvement over **(7)**, which absorbed maximally at approximately 250 nm. **(11)** was employed in the caging of the cyclic nucleotides cyclic AMP and cyclic GMP and it was found that decaging could be achieved at wavelengths of up to 420

nm. This wavelength was significantly more biocompatible than the 340 nm utilised by Hoffman et al, greatly expanding the biological applications for this class of compound.

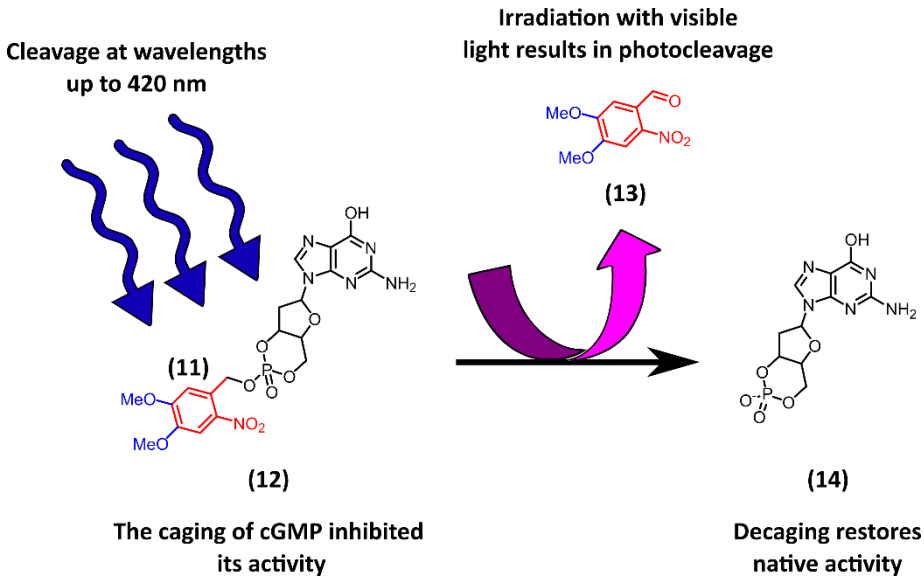

*Figure 18: Schematic representation of the o-nitrobenzyl photocage **(11)** developed by Lester et al. for the caging of cGMP. The methoxy substituents of this photocage red-shifted its absorption profile allowing for efficient decaging at wavelengths of up to 420 nm.*[81]

1.4.1.5 The development of nitrodibenzofuran photocages

In the decades following the work of Hoffman et al. and Lester et al., no significant leaps in *ortho*-nitrobenzyl based photocage design were made.[79,81] Applications were broadened and this class of photocage was used in the caging of many important biomolecules such as neurotransmitters,[70,82] peptides,[83] proteins,[84] and nucleotides,[85,86] however, the photocages employed in these studies were largely based on either the original *ortho*-nitrobenzyl scaffold or the 4,5-dimethoxy-2-nitrobenzyl scaffold. Thus, the photochemical properties of this class of photocages remained largely unchanged during this period. In 2006, Davies et al. sought to resolve this.[87] Their work introduced a novel class of nitrobenzyl photocages based on the nitrodibenzofuran scaffold which can be seen in figure 19 below. This novel scaffold retained the essential *o*-nitrobenzyl core but incorporated an additional fused benzofuran motif. The

inclusion of this extended aromatic system significantly enhanced the photophysical properties of the resulting photocages. Notably, a significant improvement to the molar extinction coefficient (ε) was afforded with **(15)** having a value of 18,400 $M^{-1}cm^{-1}$ at its λ_{max} of 330 nm. This represented an improvement of up to 43-fold compared to the original o-nitrobenzyl photocage, and up to 4.3-fold relative to the most widely used 4,5-dimethoxy-2-nitrobenzyl derivative at the time.

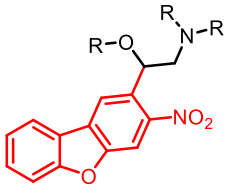

(15)

Figure 19: The structure of the novel nitrobenzofuran photocage produced by Davies et al. [87]

Davies et al utilised **(15)** to photocage Ca^{2+} ions in solution. Rather than directly caging these ions, they instead attached **(15)** to the Ca^{2+} ion chelator ethylene glycol-bis(β-aminoethyl ether)-N,N,N',N'-tetraacetic acid (**EGTA**) as seen in figure 20 below. In the case of this work, the caged form of EGTA **(16)** was capable of chelating Ca^{2+} ions, however, upon irradiation at 347 nm photolysis of the nitrobenzofuran photocage, resulted in the degradation of EGTA inhibiting its ability to sequester Ca^{2+} ions. This had the effect of increasing Ca^{2+} ions in solution. This system was applied to cardiac muscle cells, whereby an increase in Ca^{2+} concentration in solution would result in muscle contraction. Upon irradiation at 347 nm for 0.2 seconds almost complete contraction of the cardiac muscle was observed, indicating almost total release of Ca^{2+} ions. Photolysis of a corresponding ortho-nitrobenzyl-chelator complex on the other hand resulted in only a small percentage of maximal tension, suggesting that very little Ca^{2+} release had occurred, therefore demonstrating the enhanced efficiency of nitrodibenzofuran photocages.[87] Interestingly, it was found that the decaging quantum yield

of 0.7 was similar to the quantum yield recorded for the original o-nitrobenzyl photocage **(7)** produced by Hoffman et al.,[79] meaning that the improved efficiency was exclusively as a result of the improved absorption properties of **(15)**.

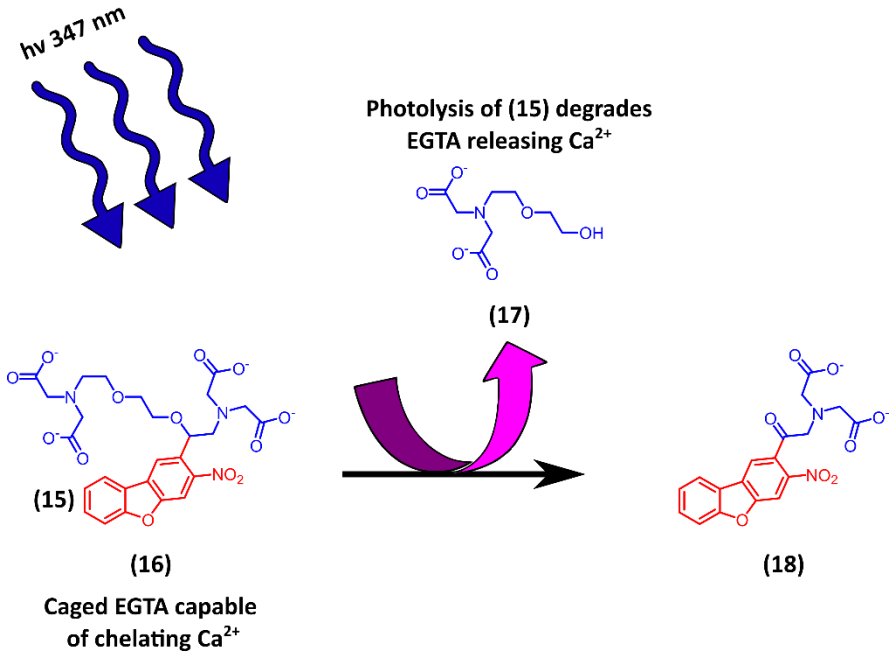

*Figure 20: Schematic representation of the nitrobenzofuran photocage **(16)** that was employed in the caging of EGTA. Photolysis of **(15)** resulted in the degradation of **(16)** ceasing its ability to chelate Ca^{2+} ions from solution.*

1.4.1.4 The development of nitrodibenzocarbazole photocages

Although the nitrobenzofuran photocage **(15)** developed by Davies et al. had a large extinction coefficient of 18,400 $M^{-1}cm^{-1}$ at its λ_{max}, this absorption maximum was at 330 nm which lay within the UV range.[87] Martin & Wang hypothesised that exchanging the furan core of nitrodibenzofuran for a carbazole moiety would positively impact the photochemical properties, since comparing the UV-vis spectra of dibenzofuran and carbazole, a clear red-shift in λ_{max} from 300 nm to 350 nm is observed.[88] The nitrogen atom present on the carbazole ring also provides a handle for additional functionalisation, allowing for the introduction of hydrophilic groups in order to boost water-solubility, which would further enhance the

biocompatibility of this class of photocage.[88] Two nitrocarbazole based photocages **(19),** and its isomer **(20)** were produced as seen in figure 21.

(19) **(20)**

Figure 21: The nitrodibenzocarbazole photocages produced by Martin & Wang. [88]

Benzoate esters of the above photocages were prepared alongside a benzoate ester of **(15)**, dissolved in THF and irradiated at 400 nm. Upon examination of the results, it was determined that at this wavelength **(19)** was four times as efficient at decaging than the nitrobenzofuran derivative **(15)**. From these results it was decided to use a nitrodibenzocarbazole photocage to cage a fluoroquinolone antibiotic in order to gain photoactivatable control over the death of *Escherichia coli*. The photocage used in this study was also modified to boost its aqueous solubility. This was achieved through the alkylation of the *N*-position of the carbazole ring with hydrophilic moiety creating **(21)** as seen in figure 22 below. The resulting caged antibiotic **(22)** was shown to exhibit a ten-fold increase in aqueous solubility in comparison to its nitrodibenzofuran caged counterpart. Decaging studies of the nitrodibenzocarbazole-caged fluoroquinolone showed that upon irradiation at 400 nm, 58% of the desired antibiotic was released within 30 mins. Biological testing then confirmed that upon photoactivation with light, the released cargo was capable of inhibiting the growth of *E. coli* cells. Following on from this, **(21)** was then utilised in the photocaging of tyrosine. Traditionally, phenols are much more difficult to cage than carboxylic acids due to the fact they are poorer leaving groups. Thus, phenols are typically attached to a caging group *via* a carbonate linker in order to create a better leaving group and boost efficiency. There are, however, stability issues associated

with this due to the hydrolytic instability of carbonates, particularly *in vivo* and so direct caging of phenol groups is desirable. A protected tyrosine was caged with **(21)**, and solutions of this caged compound were irradiated at 360, 370, 380, 390 and 400 nm for 1 hour. At 360 nm, 81% decaging was observed, however, as the wavelength was increased, conversion dropped considerably and at 400 nm only 16% conversion was observed.[88] This decrease in efficiency relative to the photorelease of fluoroquinolone was likely due to the nature of the leaving group, with phenols being more difficult to release.

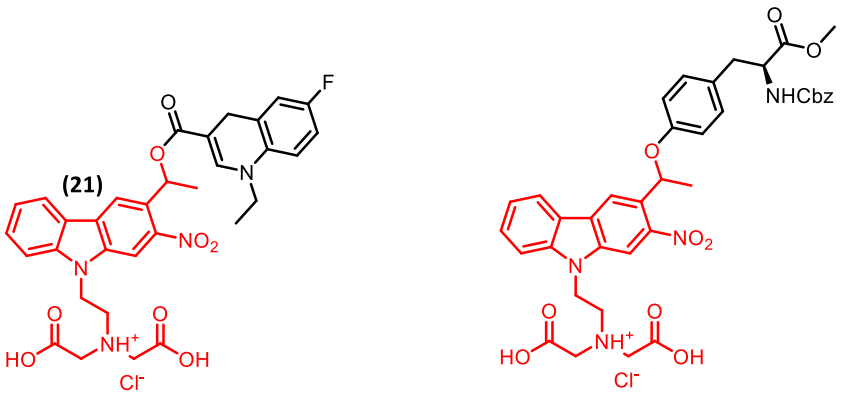

(22) **(23)**

*Figure 22: The structure of the water-soluble nitrodibenzocarbazole photocage **(21)**, developed by Martin and Wang, and employed for the caging of both fluoroquinolone and tyrosine.[88]*

1.4.1.5 *ortho*-Nitrobenzyl photocages, a timeline

The above sections have outlined the evolution of o-nitrobenzyl photocages following their initial application in the late 1970s, when Hoffman et al. employed **(7)** in the photocaging of ATP. This early derivative had a λ_{max} of approximately 265 nm, which necessitated the use of high energy UV-light to achieve photolysis, restricting its use in biological systems.[79] In order to enhance the biocompatibility of this class, Lester et al. introduced methoxy substituents at the 4 and 5 positions of the aromatic ring in the mid-1980s, producing photocage **(11).** The

introduction of these groups led to a red-shift in absorbance towards the visible range which allowed for efficient decaging at wavelengths up to 420 nm.[81] Despite, this significant advancement, no significant improvements to the photophysical properties of this class of photocage were made until the mid-2000s. At this time, Davies et al. incorporated a benzofuran moiety into the o-nitrobenzyl scaffold, affording photocage **(15)**. The introduction of this fused ring system dramatically improved the molar extinction coefficient (ε) allowing for more efficient absorption and thus more efficient decaging.[87] This work was further refined by Martin & Wang, who in the early-2020s replaced the benzofuran scaffold for a carbazole moiety resulting in the production of **(21)**.[88] The incorporation of this group maintained the high extinction coefficient, but red-shifted the absorbance towards the visible range allowing for photolysis with lower energy light. Additionally, the introduction of this group provided a handle for nitrogen alkylation, which had the effect of enhancing the aqueous solubility of this class compound. A schematic overview of these developments is provided in figure 23 below.

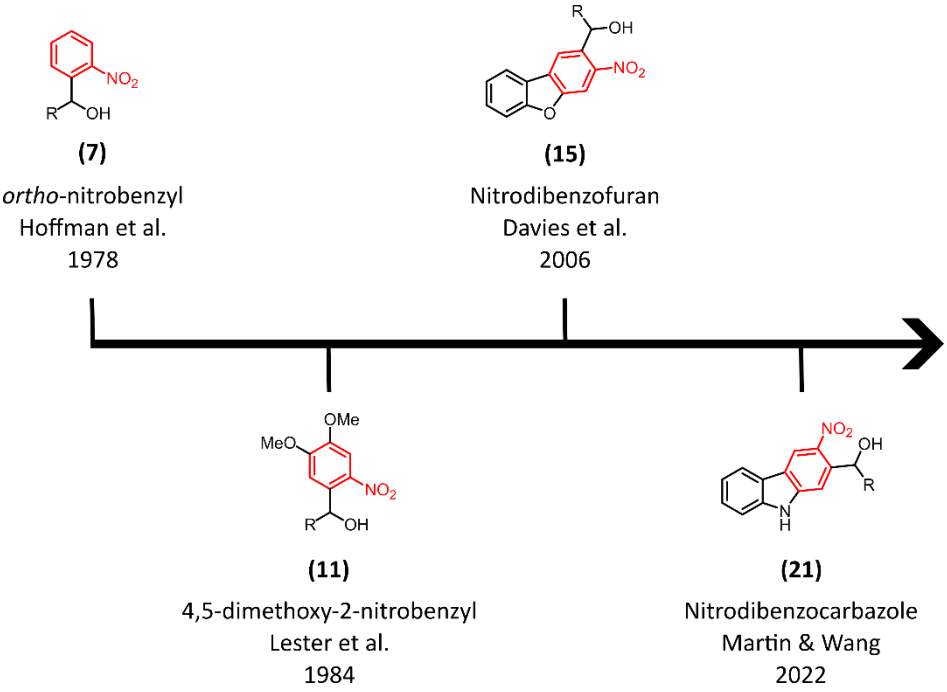

Figure 23: A timeline of the development of o-nitrobenzyl photocages.

1.4.1.6 The benefits and limitations of ortho-nitrobenzyl photocages

The characteristic properties of *o*-nitrobenzyl photocages, afford several key benefits and limitations. Their simplistic structure, with early derivatives consisting solely of a nitro-substituted benzyl group, renders them synthetically accessible and practical for use across a wide range of disciplines. Moreover, *o*-nitrobenzyl photocages can be utilised in the photocaging a wide variety of functional groups including amines, alcohols, carboxylic acids and phosphates.[71] These groups are present in a wide array of different biomolecules allowing these photocages to be used for a multitude of biological applications.

In contrast to other classes of photocages such as coumarins and BODIPYs, *o*-nitrobenzyls are inherently non-fluorescent.[60] This eliminates an unproductive decay pathway upon the formation of the excited state, potentially increasing decaging efficiency. Additionally, it allows this class of photocage to be utilised in conjunction with fluorescence-based imaging techniques such as fluorescence microscopy. This is an important advantage, when real-time monitoring of a biological process is required.

Alongside this, the wavelengths that are typically utilised to cleave this class of photocage lie within the UV-range (340-365 nm). Although this limits biological applications, it also offers a practical benefit, in that it allows decaging to be performed using UV-light sources. These are commonly found in a laboratory setting, negating the need for specialised equipment, and making the photocleavage of these compounds readily accessible to a wide range of scientific disciplines.

Despite these advantages, several limitations restrict the broader use of *o*-nitrobenzyl photocages. Most significantly, their absorption profile is centred around the high-energy UV region of the electromagnetic spectrum. Irradiation at these wavelengths can cause cellular

damage through photobleaching and other associated processes.[65] Although some derivatives, such as the 4,5-dimethoxy o-nitrobenzyl photocage **(11)** produced by Lester et al, are cleavable at wavelengths of up to 420 nm,[81] decaging efficiency at this wavelength is limited, especially in comparison to other classes of photocage such as coumarins and BODIPYs.

Although, work has been performed in order to enhance the decaging efficiency of *o*-nitrobenzyl photocages, this work is mostly related to improving the molar extinction coefficient of this class of compound.[87] Consequently, the quantum yield of this class remains poor, especially relative to more modern classes of photocages. As such the decaging efficiency of the class is limited, often requiring longer irradiation times, exacerbating phototoxic effects and limiting biocompatibility.

Finally, the decaging mechanism of *o*-nitrobenzyl photocages leads to the formation of cytotoxic byproducts such as *o*-nitrosobenzaldehyde. This contrasts with other photocage classes such as coumarins which typically produce inert byproducts.[60] Consequently, these classes are often preferred for biological applications.

In summary, *ortho*-nitrobenzyl photocages are synthetically accessible, versatile, and compatible with a broad range of functional groups, making them widely applicable in both chemical and biological research. The ability to perform photocleavage with readily available UV light sources is a practical benefit. However, the limitations associated with their UV absorption profile, low quantum yields, and generation of toxic byproducts restrict their use in biological settings, typically restricting this class of photocage to *in vitro* applications.

1.4.2 The development of coumarin photocages

1.4.2.1 Structural considerations

Coumarins are aromatic compounds consisting of a fused benzene and α-pyrone ring numbered as seen in figure 24 below. The caged molecule is typically coupled at the 4-position through a carbon-oxygen bond and as such, coumarin photocages are typically synthesised in their 4-methyl hydroxy form in order to facilitate coupling of the cargo.

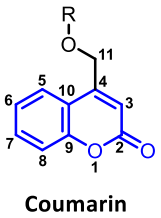

Coumarin

Figure 24: The numbered structure of the coumarin scaffold.

1.4.2.2 Mechanistic considerations

The decaging of (coumarin-4-yl)methyl esters is a multi-step process, with several competing reaction pathways as illustrated in figure 25 below. Upon irradiation with light, the coumarin-cargo complex (CM-C), absorbs a photon, promoting an electron to the LUMO and forming the excited singlet state ^{1}[CM-C]*. This excited state can be deactivated by fluorescence and other non-radiative processes returning the complex to the ground state ^{1}[CM-C]. However, the excited state can also dissipate energy *via* heterolytic bond cleavage, forming the singlet ion pair ^{1}[CM^{+} C^{-}]. These ions can recombine to forming the original CM-C ground state. However, they can also proceed to escape their solvent cage forming the solvent separated ions CM^{+} and C^{-}. At this point, the positively charged CM^{+} reacts rapidly with a surrounding water molecule forming the hydroxymethyl coumarin CM-OH.[61]

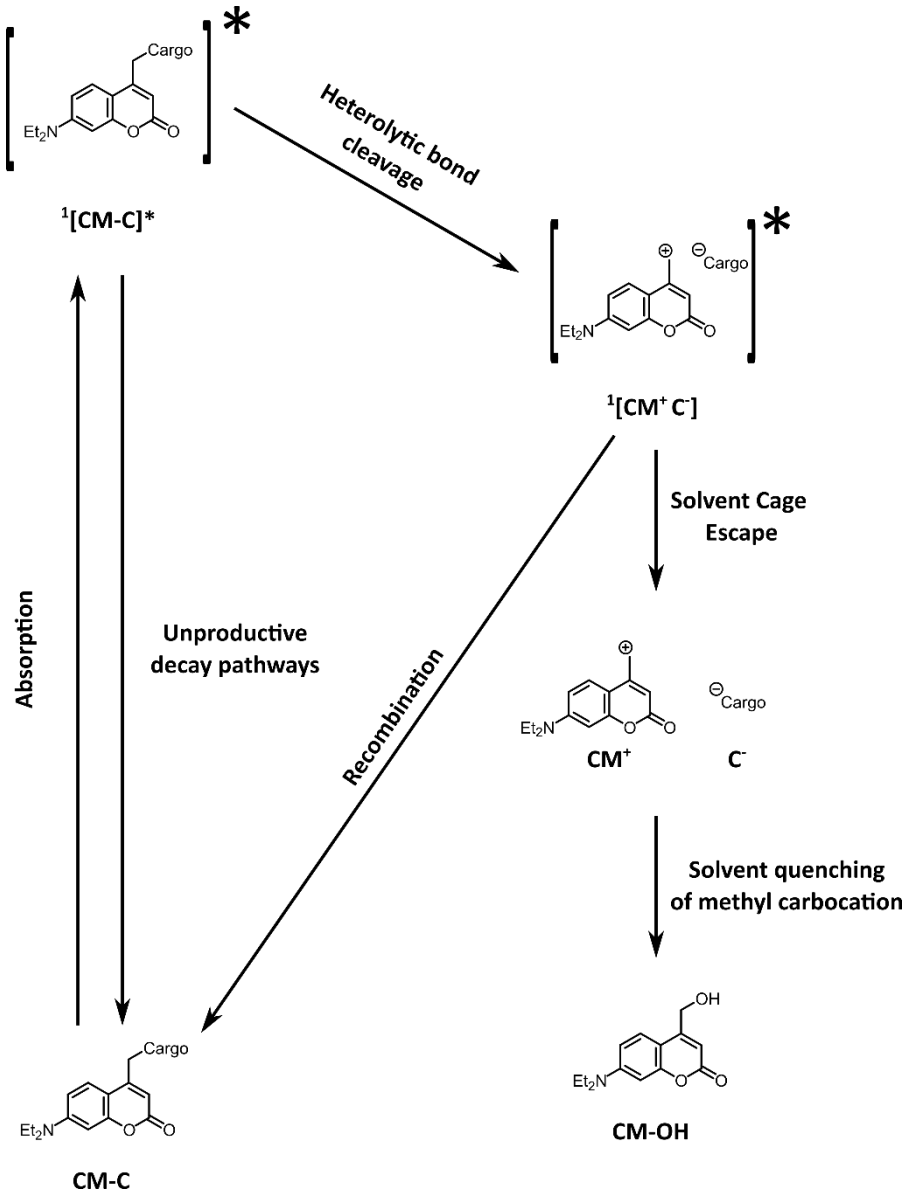

Figure 25: A schematic representation of the decaging process of coumarin photocages. [61]

Looking at the schematic above, it is evident that the decaging efficiency is governed by three key steps. The first is the absorption of a photon, which promotes the photocage from the ground state to an electronically excited state. This step is determined by the absorption characteristics of the coumarin chromophore, which are intrinsically linked to its structure. Consequently, structural modification of the coumarin scaffold in order to enhance its absorption properties, particularly at longer, more biologically compatible wavelengths, has been a major consideration in the development of modern coumarin photocages.[72,89,90]

The second step of the decaging process is the decay of the excited state. Although the absorption of a photon provides access to the state, it does not dictate how energy is dissipated. In terms of a decaging reaction, heterolytic bond cleavage is the desired productive pathway. However, it is important to note that processes such as fluorescence, internal conversion, and intersystem crossing can compete with this productive pathway, thus diminishing decaging efficiency.[61] Thus, the design of efficient coumarin photocages requires not only favourable absorption properties, but also minimisation of excited state losses through radiative and non-radiative decay.

The third step involves the escape of the ion pair from the solvent cage, leading to the release of the caged cargo in its anionic form. This process is influenced by both the nature of the surrounding solvent environment and by the stability of the ion pair that is generated upon photolysis. Ion pairs that are short-lived are prone to rapid recombination and are likely to undergo unproductive decay, hence negatively impacting the decaging quantum yield. In order to prevent this, significant efforts have been made to stabilise the coumarin methyl carbocation intermediate, thereby enhancing the probability of successful cargo release.[76,77] Alongside this, the nature of the leaving group is also a key factor in determining decaging efficiency, with groups with low pK_a values such as carboxylic acids typically being easier to release than groups such as phenols due to their anionic form being inherently more stable.

1.4.2.3 Early developments

The first coumarin derivative was isolated from tonka beans in 1820.[91] Subsequently, a plethora of derivatives have been produced synthetically for a wide range of purposes. Coumarins are widely used in the perfume industry, as well as in the pharmaceutical industry where the coumarin-based drug warfarin is an important anticoagulant, the sales of which

exceed $100M per year.[92,93] More importantly to us, coumarins have also been extensively employed in photocaging. The first example of coumarin photocaging was performed by Matuszewski & Givens in 1984. In this work, it was shown that 7-methoxy coumarin **(24)** could efficiently cage phosphodiester derivatives. With decaging occurring upon irradiation at 360 nm.[94]

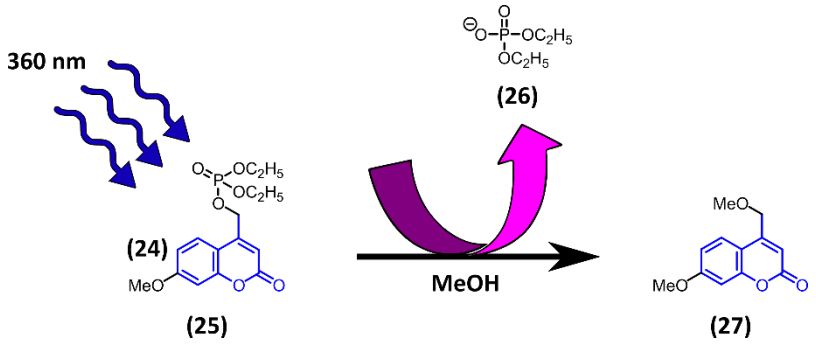

Figure 26: Schematic of the 7-methoxy coumarin photocage (24) which was employed by Matuszewski & Givens in the caging of a phosphodiester.[94]

The first significant attempt to modify the coumarin scaffold, in order to improve its photophysical properties was made by Tsien et al. in 1999.[95] In their work, a bromo group was introduced at the 6-position and the 7-methoxy group was replaced with a hydroxyl group producing **(28)** as seen in figure 27 below.

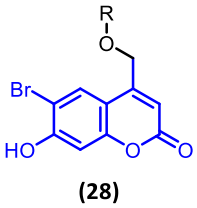

*Figure 27: The structure of the 6-bromo,7-hydroxy coumarin photocage **(28)** developed by Tsien et al.[95]*

The photocage pictured above was specifically designed to enhance the two-photon absorption cross section within this class of compounds. As discussed in Section 1.2.2,

conventional absorption involves the promotion of an electron from the ground state to an excited state by a single photon whose energy matches the electronic transition energy. In contrast, two-photon absorption is a nonlinear optical process whereby two photons of lower energy are absorbed simultaneously to achieve the same electronic excitation.[96] While the energy of each individual photon is insufficient to bridge the energy gap alone, their combined energy enables excitation to the same electronic state accessible *via* one-photon absorption. In this way the excited state becomes accessible at significantly longer wavelengths, improving biocompatibility.[97]

Due to the requirement for the simultaneous absorption of two-photons, two-photon absorption is inherently more difficult to achieve than conventional one-photon absorption and typically requires the use of high-intensity pulsed LASERs to deliver high numbers of photons to the chromophore.[98] Consequently, the design of a molecule capable of efficient two-photon excitation necessitated careful structural optimisation. The photocage developed by Tsien et al. was based on the 7-hydroxycoumarin chromophore, which had previously been shown to exhibit favourable two-photon fluorescence characteristics.[99] In order to further enhance its two-photon absorption properties, the 6-position was brominated, with the electron-withdrawing nature of the bromine atom decreasing the pK_a of the 7-hydroxy group, which promoted the formation of the anionic species at physiological pH. This anionic form possessed a higher two-photon absorption cross section, thereby improving excitation efficiency under two-photon conditions.[95] In addition to its effect on absorption, the heavy bromine atom was also expected to facilitate intersystem crossing to the triplet excited state due to the heavy atom effect. The triplet state is typically longer-lived than the singlet state, thereby increasing the probability of productive decay and enhancing decaging efficiency.[95]

(28) was employed in the caging of glutamate and upon irradiation at 365 nm, almost full decaging was observed within 2 minutes. More importantly, it was also shown that this compound exhibited good two-photon decaging as upon irradiation with a 740 nm pulsed LASER for 1 h, almost 90% of the glutamate cargo as released as seen in figure 28 below.[95]

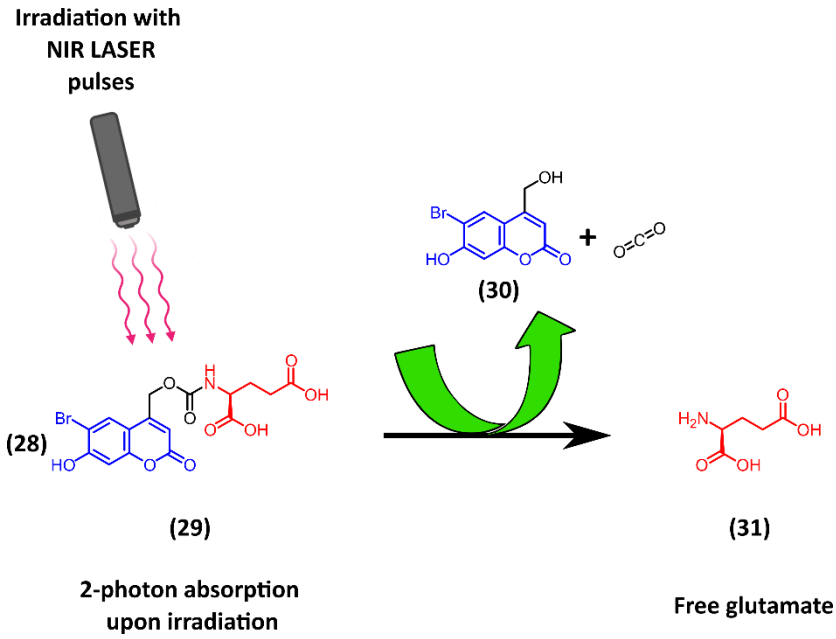

*Figure 28: Schematic of the decaging of **(29)** upon irradiation using NIR LASER pulses. The 7-bromine atom of **(28)** facilitated intersystem crossing allowing for efficient decaging at these wavelengths.*[95]

Upon verification of the favourable two-photon properties of **(28)**, it was once again utilised to photocage glutamate, but this time within rodent brain slices. Caged glutamate was shown to be biologically inert prior to decaging. Upon irradiation with femtosecond LASER pulses at 740 nm, efficient photorelease of glutamate was achieved, resulting in localised receptor activation. By systematically scanning the neurons within the brain slice in 3-D, a detailed map of neuronal sensitivity to glutamate was generated, allowing functional receptor distributions to be charted with high spatial resolution. This demonstrated the high degree of spatial precision afforded by the two-photon decaging of **(28)**. The use of an irradiation wavelength

of 740 nm was a significant development at the time as this represented one of the longest wavelengths ever used in photocaging within a biological system up to this point. Not only did this wavelength offer improved biocompatibility due to its low-energy nature, but it is also poorly absorbed by chromophores present within tissues, meaning that it features improved tissue penetration depths.[95] Consequently, the development of **(28)** was a key advancement in the field of photocaging at the time.

1.4.2.4 Dialkylamino coumarin photocages

Although **(28)**, was capable of undergoing two-photon decaging at 740 nm, this process required femtosecond pulsed LASERs and was therefore not accessible to standard laboratories.[95] Whilst it was capable of undergoing one-photon decaging at wavelengths of up to 365 nm, this was still within the UV range, and hence not ideal for biological applications. If the absorption profile of this class of photocage could be red-shifted towards the visible range, it would allow for photocleavage at longer, more biocompatible wavelengths, greatly expanding the applications of this class of photocage.

One strategy to improve the absorption properties of coumarin photocages is through the introduction of an electron-donating group (EDG) at the 7-position of the coumarin scaffold. As mentioned in section 1.4.4.1, the coumarin scaffold is a conjugated system consisting of a benzene ring fused to an α-pyrone. Within this scaffold, the carbon atoms adopt trigonal planar geometries, with each employing three sp^2-hybridized orbitals to form σ-bonds, while retaining an unhybridized p orbital oriented perpendicular to the molecular plane. In a carbon–carbon double bond, σ-bonds arise from head-on overlap of sp^2 orbitals, while π-bonds form *via* side-on overlap of adjacent p orbitals. The π-bond is higher in energy than the

σ-bond, and the energy gap between the bonding π orbital and the antibonding π* orbital is relatively small, enabling electronic excitation with lower-energy (longer-wavelength) light.[100]

Consequently, the tuning of the absorption properties of a coumarin derivative typically involves the introduction of substituents that raise the energy of the bonding π orbital (HOMO) in order to decrease the HOMO-LUMO energy gap to allow for the absorption of a lower energy photon. Introducing an EDG to the coumarin scaffold allows electron density to be donated into the bonding π orbital, allowing the energy of the HOMO to be raised, reducing the energy HOMO–LUMO gap and resulting in a red-shift in absorbance.[89,101]

One of the most significant examples EDG substitution of the coumarin scaffold was performed at the 7-position substitution by Kaupp et al. In their initial work in 2001, they explored the effect of substituting the 7-position of the coumarin scaffold with a variety of different functionalities, in the hope of achieving high decaging efficiency at visible wavelengths.[102] A number of different groups, were trialled as seen in figure 29 below, but it was found that substitution of this position with a 7-diethylamino group **(32)** had the most profound effect on the photophysical properties. Not only was the λ_{max} of this photocage red shifted by more than 70 nm relative to photocage **(33)** but when utilised in the caging of cAMP and cGMP, this compound was shown to efficiently decage at wavelengths between 360 – 400 nm.[102]

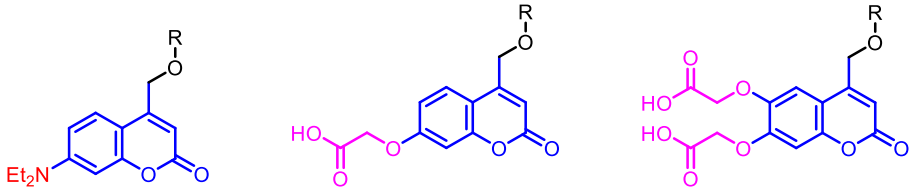

(32)

λ_{max1}= 402 nm
λ_{max1}= 396 nm

(33)

λ_{max1}= 326 nm
λ_{max1}= 325 nm

(34)

λ_{max1}= 346 nm
λ_{max1}= 347 nm

Figure 29: Schematic of the structures and λ_{max} of the photocages developed by Kaupp et al.[102]

This work was built upon in 2003, when Kaupp et al. utilised **(32)** and dimethylamino coumarin derivative **(35)** in the caging of 8-bromo-substituted cyclic nucleotides.[90] A more in depth analysis of the photochemical properties of these photocages was performed and it was hoped that these derivatives would combine rapid photorelease, with high solvolytic stability whilst simultaneously exhibiting red-shifted absorption maxima with high extinction coefficients.

Upon analysis of these compounds, it was found that both the **(32)**-caged and **(35)**-caged nucleotides were stable under aqueous conditions with neither degrading within a 24 h period when dissolved in aqueous pH 7.2 buffer.[90] An investigation into the photophysical properties of these compounds revealed that the **(35)**-caged nucleotides were found to exhibit absorption maxima in the range of 386 – 398 nm with corresponding molar extinction coefficients at these wavelengths of 16,000 – 17,000 $Lmol^{-1}cm^{-1}$. The **(32)**-caged nucleotides on the other hand, exhibited absorption maxima between 395 – 406 nm with improved molar extinction coefficients of 17,000 – 20,000 $Lmol^{-1}cm^{-1}$.[90] These values represented a marked improvement over the 6-bromo-7-hydroxy coumarin photocage **(28)** developed by Tsien et al, which although possessing a comparably high molar extinction coefficient of 17,470 $Lmol^{-1}cm^{-1}$ at its $\lambda_{max,}$ this maximum lay at 368 nm which is further into the UV region.[95]

Notably, **(28)** was shown to have an extinction coefficient of just 5,400 $Lmol^{-1}cm^{-1}$ at 400 nm, which is almost 3-fold lower than the dialkylamino derivatives produced by Kaupp et al., further demonstrating the improved visible-light absorption properties of these compounds as seen in figure 30 below.

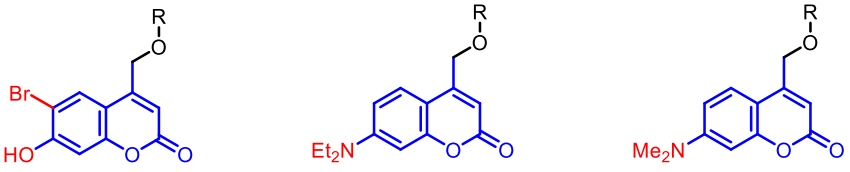

(28) **(32)** **(35)**

ε = 5,400 **ε = 17,000 - 20,000** **ε = 16,000 - 17,000**

*Figure 30: The molar extinction coefficients (in Lmol-1cm-1) of **(28)** vs the dialkylamino derivatives **(32)** and **(35)** at approximately 400 nm. The dialkylamino derivatives feature much stronger absorption at this wavelength due to their red-shifted absorption maxima.*[90,95]

The decaging quantum yields of **(32)** and **(35)** were then measured, with values of up to 0.31 and 0.28. respectively, recorded for the photorelease of 8-bromo-cGMP.[90] Once again these values represented a significant improvement over **(28)** which recorded a decaging quantum yield of just 0.019 for the release of glutamate upon irradiation at 365 nm.[95] Furthermore, compounds **(32)** and **(35)** demonstrated efficient decaging of 8-bromo-cGMP at wavelengths as long as 436 nm, with up to 98% cargo release achieved within 6 minutes. This was a marked enhancement in visible-light photorelease efficiency relative to earlier generations of photocages, such as dimethoxy-ortho-nitrobenzyl **(11)** which was shown to release less than 1% of its cargo at this wavelength over the same time period.[90]

The biological applicability of these compounds *in vivo* was then demonstrated. Caged 8-bromo-cGMP was confirmed to be inactive as an agonist for cyclic nucleotide-gated ion

channels. Upon light activation, both **(32)** and **(35)** effectively released free 8-bromo-cGMP, leading to Ca^{2+} influx through these channels. Notably, up to 10% cargo release was achieved using a single 50-ms pulse at 405 nm, illustrating the capacity of these derivatives for rapid and efficient photorelease at long wavelengths within biological systems.[90]

Consequently, it can be said that the introduction of a dialkylamino group at the 7-position of the coumarin scaffold was a key advancement in the development coumarin photocages. Not only did this moiety red-shift absorption maxima into the visible range whilst maintaining similar molar extinction coefficients to previous derivatives, but it also allowed for rapid and efficient photocleavage at wavelengths of up to 436 nm. This was a significant improvement relative to other available photocages at the time and greatly widened the biological applications of this field. The 7-dialkylamino group was so important to the photophysical properties of coumarin photocages that it remains an essential component of many of the "next-generation" coumarin photocages seen today.

1.4.2.5 Extended coumarin photocages

In the previous section, the red-shifting effect of 7-dialkylamino groups on the absorption maxima of coumarin photocages was discussed. This red-shift in absorbance was brought about by the electron donating effect of the nitrogen atom, whose lone pair was conjugated with the aromatic system, increasing electron density and increasing the energy of the HOMO and thus reducing the energy required to bridge the HOMO-LUMO gap. In 2012, Zhu et al, tried a different approach, introducing a styryl group at this position.[89] Not only did this moiety, extend the conjugated π-system of the coumarin scaffold, resulting in a higher energy HOMO, but it could also be substituted with electron donating substituents to further decrease the HOMO-LUMO gap. Several substituents were trialled including a para-ethoxy

group, and it was found that once again, a dimethylamino group was best at red-shifting absorbance, with an absorbance maximum of 407 nm recorded for **(36)**. This derivative was then used in the photocaging of adenosine as seen in figure 31 below, with efficient photolysis being achieved at wavelengths of up 475 nm, representing a significant red-shift compared to the dialkylamino photocages **(32)** and **(35)** developed by Kaup et al, which were cleavable at wavelengths of up to 436 nm.[89,90]

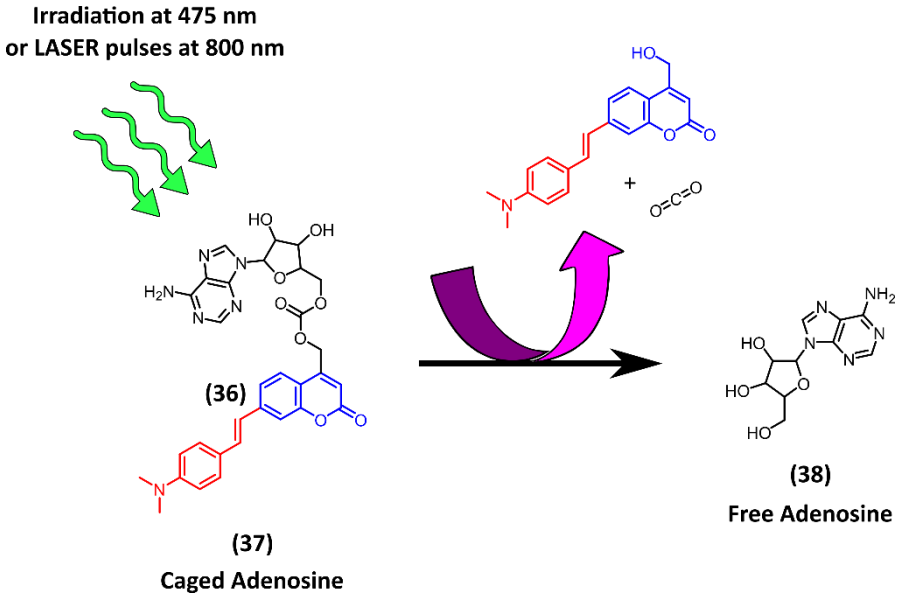

*Figure 31: Schematic of extended coumarin derivative **(36)** developed by Zhu et al. and utilised in the caging of adenosine. The introduction of the para-dimethylamino group at the 7-position red-shifted absorbance allowing for one photon cleacage at 475 nm and two-photon cleavage at 800 nm.[89]*

In contrast to photocage **(36)** designed by Zhu et al. which red-shifted the absorption maximum through the introduction of a styryl group at the 7-position,[89] Davies et al. decided to extend conjugation through the modification of the 3-position, resulting in the development of **(39)** as seen in figure 32 below.[103] This modification resulted in a red-shift in the absorption maximum to 450 nm, once again allowing for photolysis with low-energy

visible light. Crucially, this shift also resulted in minimal absorption within the UV region of the electromagnetic spectrum. As such, **(39)** was proposed as a candidate for sequential, wavelength-selective activation of biomolecules when used in tandem with a photocage cleavable with UV light.[104] For this purpose, *o*-nitrobenzyl derivative **(40)** was chosen as it had previously been shown to exhibit efficient decaging at 365 nm.[105]

To validate this approach, **(39)** and **(40)** were employed to cage the inhibitory and excitatory neurotransmitters GABA and glutamate, respectively.[104] The caged compounds were then applied to hippocampal CA1 neurons. Upon irradiation at 365 nm, selective photolysis of **(40)** occurred, triggering the release of glutamate and the generation of an action potential. Subsequent irradiation at 470 nm induced the photolysis of **(39)**, releasing GABA and terminating the action potential due to its inhibitory effect.[104] In this way, precise temporal control over the process of neurotransmission had been achieved, simply by irradiating the sample using different wavelengths of light, representing a significant advancement in the field of photocaging.

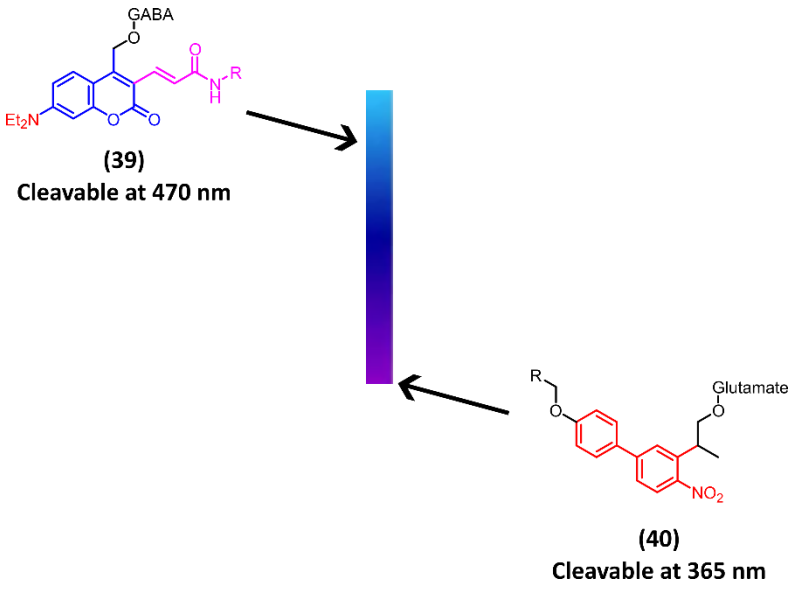

Figure 32: Schematic view of the photocages utilised by Davies et al. for the orthogonal and sequential decaging of glutamate and GABA.[104]

Building on the work of Davies et al., Blanchard-Desce et al. aimed to develop a series of coumarin photocages with enhanced two-photon properties.[106] **(39)** had been shown to exhibit good two-photon decaging efficiencies upon irradiation at 900 nm. It was postulated that this was due to the donor-π-acceptor nature of this molecule. This created a push-pull system whereby the 7-diethylamino group donated electron density into the coumarin scaffold, which then acted as a bridge, facilitating the flow of electrons into the 3-vinyl group. This lowered the HOMO-LUMO energy gap through a process known as intramolecular charge transfer (ICT). This is a process whereby upon the absorption of a photon and the formation of the excited state, electron density flows from the donor group to the acceptor group through the conjugated π-system resulting in the formation of a polarised excited state which is partially positive near the donor and partially negative near the acceptor. In polar solvents such as H_2O, this charge-separated excited state is further stabilized by dipole–dipole interactions, which reduce its energy relative to that of a typical π–π* excited state, resulting

in a red-shift in absorption.[106–108] Alongside this red-shift in absorbance, ICT also promotes two-photon absorption as the formation of the excited state leads to a large change in the molecular dipole moment, which in turn improves transition probability through increased interaction with the electromagnetic field of incoming photons.[106]

Consequently, Blanchard-Desce et al., postulated that if they could increase the acceptor nature of the conjugated system at the 3-position, then they could increase ICT creating a more polarised excited state. Not only would this red-shift absorption, but it would also potentially improve the two-photon absorption properties. A selection of derivatives synthesised during this work can be seen in figure 33 below. Looking at these compounds it can be seen that they all feature a red-shift in their absorption maxima *vs* **(39)** which can be attributed to their superior acceptor capabilities at the 3-position.[106]

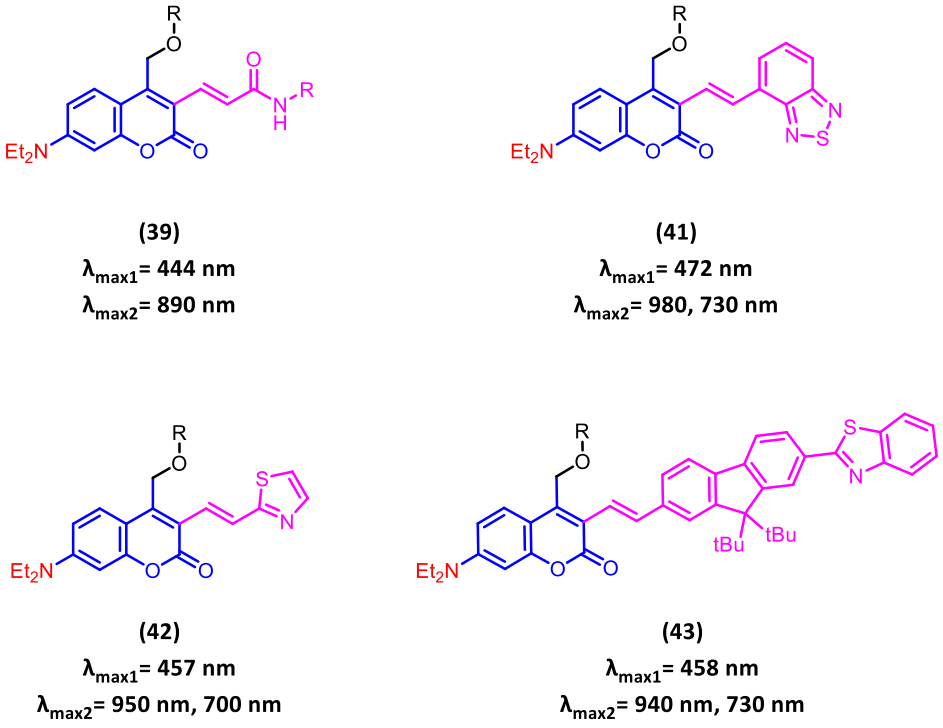

Figure 33: The absorption maxima of the photocages developed by Blanchard-Desce et al were red-shifted through the introduction of a donor-π-acceptor system across the coumarin scaffold. [106]

In addition to exhibiting red-shifted absorption maxima, the compounds described above also featured two distinct two-photon absorption bands, offering an alternative excitation window for two-photon photolysis. Among them, the fluorenyl-substituted photocage **(43)** displayed the most favourable two-photon properties and was therefore selected for further study. This compound was used to photocage Fmoc-Gly-OH and its performance *vs* photocages with similar two-photon absorption bands was investigated. Upon irradiation at 730 nm, **(43)** exhibited a seven-fold increase in decaging efficiency compared to its parent compound, the diethylamino coumarin derivative **(32)**. Furthermore, its efficiency at 940 nm was tested against compound **(39)** and revealed a two-fold enhancement in two-photon decaging efficiency at this wavelength. [106]

The ability of the above compounds to undergo one-photon decaging was also investigated. Once again, Fmoc-Gly-OH was utilised as a model cargo molecule and the decaging study was performed at 455 nm. Interestingly, in comparison to **(39)**, it was found that these extended photocages exhibited lower decaging efficiencies and it was found that increasing the electron withdrawing nature of the vinyl group at the 3-position had a detrimental effect on photolysis rates.[104,106] As mentioned in 1.4.2.2, coumarin decaging involves the formation of an ion pair which then must escape its surrounding solvent cage in order to decage successfully.[61] Increasing the electron withdrawing nature of the acceptor moiety, removes electron density from the coumarin scaffold restricting its ability to stabilise the coumarin methyl carbocation that is formed upon heterolytic bond cleavage. As a result, the ion pair is more likely to recombine unproductively impacting the decaging quantum yield. As decaging efficiency is defined as the product of the extinction coefficient and the decaging quantum yield this has the effect of decreasing decaging efficiency. During two-photon decaging, this is compensated for by the far superior two-photon absorption properties of **(43)** vs **(32)** and **(39).** However,

the one-photon absorption properties are not sufficient to counteract the impact of the lower quantum yield meaning that these compounds are less efficient at 455 nm.

Despite the successes of the above work, there were several key issues to be addressed. Firstly, these photocages, despite having red-shifted absorbances, suffered from poor one-photon decaging efficiencies. Alongside this, as the pi-system was extended, aqueous solubility was diminished, making the application of these photocages in biological settings increasingly difficult. Kele et al. sought to address these problems through the development of a series of 3-vinyl photocages, containing heteroaromatics bearing a quaternary, cationic nitrogen atom.[72] The introduction of this cationic nitrogen allowed for aqueous solubilities of greater than 0.25 mM representing a significant improvement over the photocages developed by Blanchard-Desce et al.[106] Alongside this, the increased electron withdrawing ability afforded by this moiety caused a red-shift in the absorbance with the absorption maxima of the synthesised photocages all lying between 482 and 538 nm which is within the green light range. Additionally, all of the developed photocages maintained good molar extinction coefficients at these maxima as seen in figure 34 below.

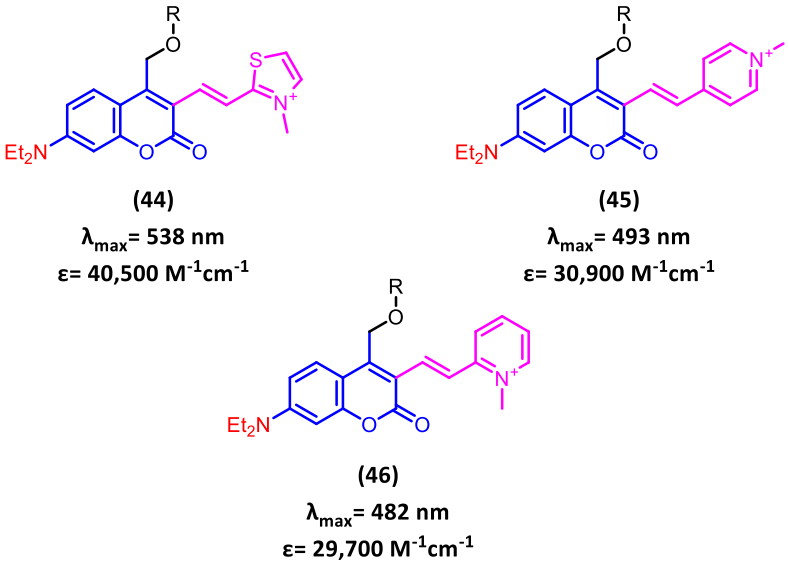

Figure 34: The introduction of a quaternary nitrogen containing heteroaromatic by Kele et al improved the aqueous solubility of the synthesised coumarins alongside red-shifting absorbance.[72]

The above photocages were utilised in the caging of 3,5-dimethylbenzoic acid, and their decaging efficiencies upon irradiation with green light was investigated. Photocages **(45)** and **(46)** both exhibited near-quantitative decaging within 20 minutes of irradiation, representing a significant improvement in one-photon decaging efficiency *vs* the photocages developed by Blanchard-Desce et al.[106] Although **(44)**, only exhibited 20% cargo release under the same conditions, it was shown to release approximately 25% of its cargo within 20 mins upon irradiation with orange light (600 nm). This was a significant advancement as this was the highest wavelength ever used in the one-photon decaging of a coumarin photocage at the time, with orange light being inherently more biocompatible due to its low-energy nature. Additionally, this wavelength is poorly absorbed by biological chromophores, allowing for deeper tissue penetration.[72]

1.4.2.6 Improving the quantum yield of coumarin photocages

Up to this point, the discussed developments in coumarin photocages have focused on red-shifting the absorption maxima of this class of compound so that decaging can be achieved using low energy, visible light. However, as discussed in section 1.3.2, the decaging cross section, which is a measure of decaging efficiency, is determined by the product of both the molar extinction coefficient and the decaging quantum yield. As such, the decaging quantum yield is also an important consideration when attempting to develop efficient photocages.

As mentioned, previously, coumarin photocages, particularly those with a donor-π-acceptor systems, undergo ICT resulting in the formation of a polarised excited state. Whilst this does enhance the two-photon absorption properties of these photocages it is also important to note that this state can negatively impact the decaging quantum yield. Upon formation of the polarised excited state, rotation around the C-N bond of the donor moiety can occur, which results in the non-radiative release of energy to the surrounding medium and consequently unproductive decay.[77] Heckel et al. noted that **(47),** which had previously been shown to exhibit a 90% fluorescence quantum yield in aqueous solution,[109] prevented this bond rotation from occurring through the installation of a restricted ring system at the 3 and 7 positions of the coumarin scaffold. Consequently, they postulated that if this restricted ring system could be applied to coumarin photocages, it would provide an enhancement in the decaging quantum yield by preventing twisting of the excited state.[77] Four of these restricted derivatives were synthesised and can be seen in figure 35 below. Looking at this figure it can be seen that derivatives **(48)** and **(49)** contained an additional unsaturated bond in order to add further rigidity to the ring system. Additionally, derivatives **(49)** and **(50)** contained an ethyl group on the nitrogen atom. Upon formation of the polarised excited state, the partially positive donor may release energy through hydrogen bonding with the surrounding solvent.

It was hoped that the addition of this group would prevent this, deactivating an additional unproductive decay channel. [77]

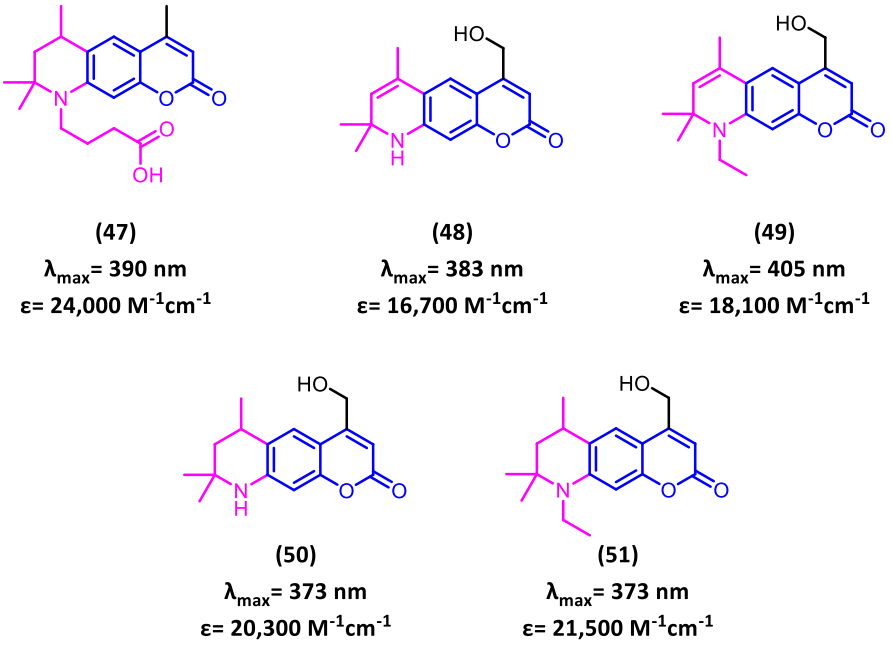

*Figure 35: A summary of the photophysical properties of the original dye **(47)** and the 4 photocages based on its structure developed by Heckel et al.* [77]

The above photocages were utilised in the caging of histamine and their efficiency vs the 7-diethylamino coumarin photocage **(32)** was investigated. The reference photocage **(32)** exhibited a quantum yield of just 5.6×10^{-3} when irradiated at 405 nm. With the fully unsaturated derivatives **(50)** and **(51)** a significant increase to 1.6×10^{-2} and 9.6×10^{-3} was observed representing approximately a two-fold increase in quantum yield. This improved even further with the introduction of an unsaturated bond into the ring system with **(48)** and **(49)** exhibiting quantum yields of 2.6×10^{-2} and 3.0×10^{-2}.[77] This was over a five-fold improvement in quantum yield *vs* **(32)** demonstrating the ability of a restricted ring system to enhance quantum yield. The quantum yields were then used to calculate decaging cross sections and it was found that the best performing photocage **(49)** had a decaging cross section at 405 nm of 617 $M^{-1}cm^{-1}$. This was more than twelve times the value calculated for

(32), representing a significant improvement in decaging efficiency.[77] Not only would this be beneficial for increased temporal control, but it would also allow for increased biocompatibility due to lower irradiation times. The results of this experiment are summarised in figure 36 below.

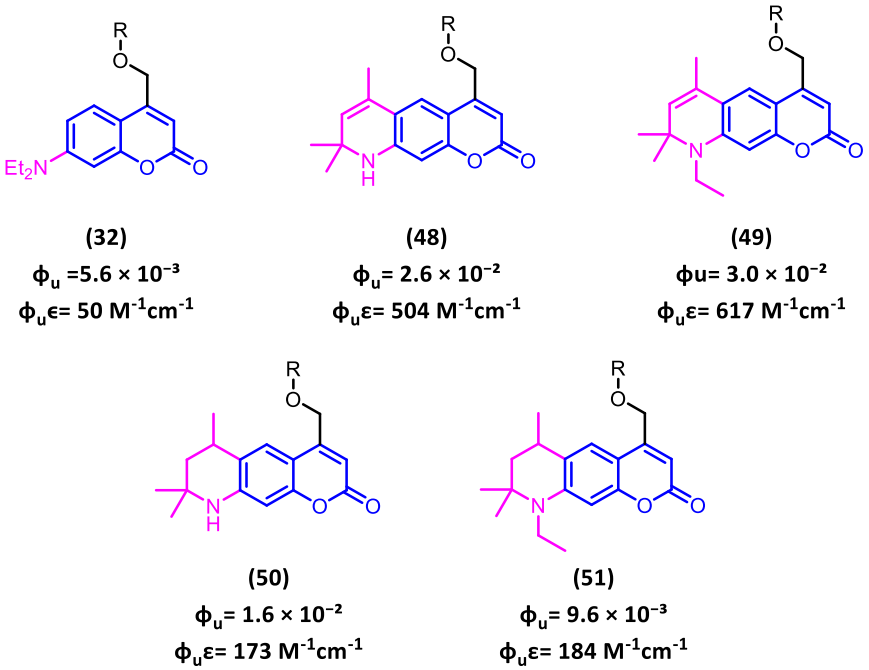

*Figure 36: The quantum yields and decaging cross sections at 405 nm of the photocages developed by Heckel et al, compared to reference compound (**32**).* [77]

An alternative strategy for improving the quantum yield of coumarin photocages is through the stabilisation of the coumarin methyl carbocation that forms as a result of heterolytic bond cleavage. As mentioned in section 1.4.2.2, upon photolysis of the coumarin-cargo bond, an ion pair is formed which then subsequently escapes its surrounding solvent cage to release the cargo in its anionic form. However, if the methyl carbocation is unstable, unproductive recombination can occur diminishing the decaging quantum yield.

Feringa et al., sought to stabilise the coumarin methyl carbocation formed during decaging through substitution at the 11-position.[76] It was hypothesised that this position could accommodate groups capable of stabilising the developing positive charge *via* hyperconjugation or resonance, thereby improving the efficiency of photorelease. A number of coumarin photocages were synthesised and their ability to release a caged acetic acid upon irradiation at 400 nm was investigated. Among the various substituents investigated it was found that the vinyl-substituted derivative **(54)** demonstrated the most pronounced enhancement in quantum yield, with its quantum yield of 0.27 being almost 15 times greater than the quantum yield of model photocage **(32).** The findings of this work are summarised in figure 37 below.[76]

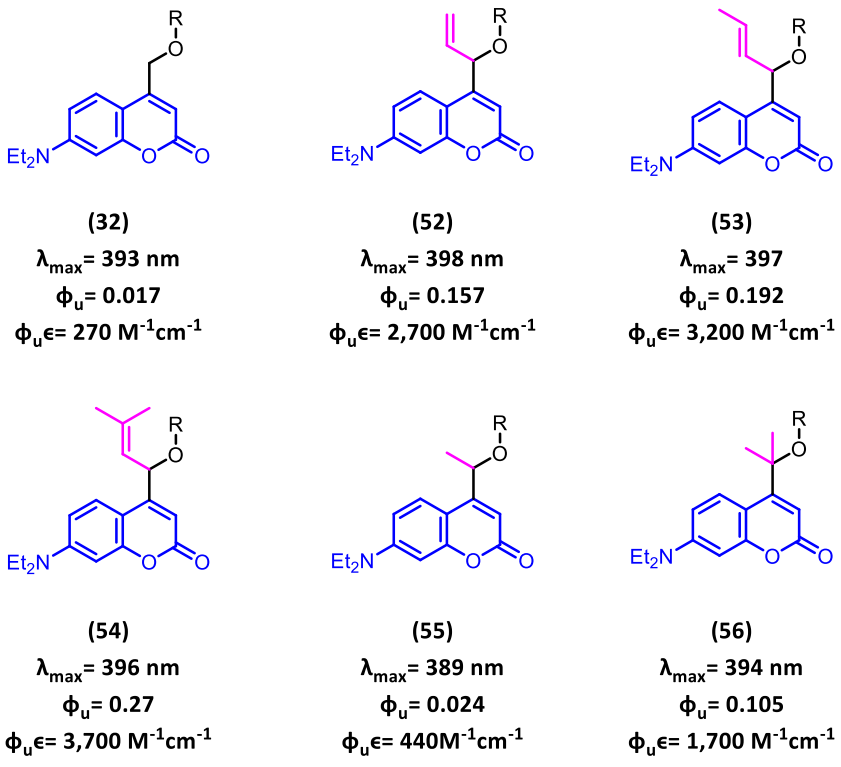

*Figure 37: A summary of the quantum yields and decaging cross sections of the 11-substituted coumarin photocages produced by Feringa et al. vs model compound **(32)**.*[76]

Feringa et al., then applied this strategy to extended coumarin photocage **(45)** developed by Kele et al., producing **(57)**.[72,110] It was hypothesised that the poor quantum yield of **(45)** was due to the electron withdrawing effect of the 3-vinyl pyridinium group, leading to less electron density available in the π-system to stabilise the positive charge formed during heterolytic bond cleavage. Thus, it was postulated that the introduction of a prenyl substituent would significantly increase quantum yield. These photocages were utilised in the photocaging of acetic acid and upon irradiation at 530 nm, a 7.5-fold increase in quantum yield was observed for **(57)** *vs* **(45),** as seen in figure 38 below. This was a significant advancement, as this simple structural modification allowed for much more efficient decaging at long wavelengths.

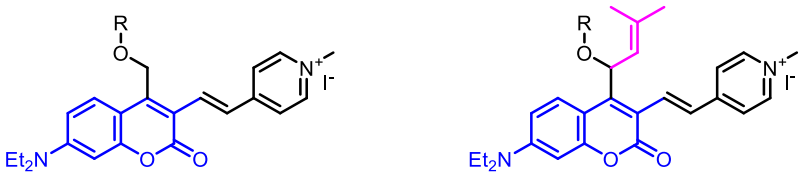

(45)
λ_{max}= 499 nm
ϕ_u= 2.0× 10^{-3}

(57)
λmax= 494 nm
ϕ_u= 1.5 × 10^{-2}

*Figure 38: The presence of a prenyl subsituent on the 4-methyl group of **(57)** allowed for a 7.5-fold increase in quantum yield vs the original photcage **(45)** developed by Kele et al.*[72,110]

1.4.2.7 A timeline of the development of coumarin photocages

Since their initial development by Matuszewski & Givens in 1984,[94] coumarin photocages have undergone extensive structural modifications aimed at optimising their photophysical and photochemical performance. Following the enhancement of two-photon absorption properties through the development of compound **(28)** by Dantzker et al.,[95] subsequent efforts primarily focused on red-shifting the absorption maxima of the coumarin scaffold to

improve compatibility with biologically relevant wavelengths. A key advancement was reported in 2001 by Kaupp et al., who introduced a diethylamino substituent at the 7-position of the coumarin scaffold.[102] This modification significantly red-shifted absorption maxima, enabling efficient one-photon decaging at wavelengths of up to 436 nm. This moiety was so effective at red-shifting the absorption profile of coumarin photocages, that it remains a key feature of many of the next generation coumarin photocages seen today.

Building on this, Zhu et al. further red-shifted the absorption profile by incorporating a styryl group at the 3-position, which extended the π-conjugation of the coumarin scaffold.[89] This allowed for efficient decaging at wavelengths up to 475 nm. Davies et al. subsequently modified the 3-position with a vinyl substituent, achieving an absorption maximum near 450 nm. Notably, this design eliminated absorption in the UV region, thereby allowing orthogonal decaging alongside UV-absorbing photocages such as o-nitrobenzyl derivative **(40).**[104]

Further refinement of the coumarin scaffold was carried out by Blanchard-Desce et al., who introduced a donor–π–acceptor system through the simultaneous installation of an electron-withdrawing vinyl group at the 3-position and an electron-donating diethylamino group at the 7-position.[106] This architecture facilitated ICT, resulting in a polarised excited state and enhanced two-photon absorption cross-sections. Kele et al. expanded on this design by incorporating a quaternary nitrogen-containing heteroaromatic group at the terminus of the 3-vinyl substituent. This further improved water solubility and enabled one-photon decaging at wavelengths extending to 600 nm.[72]

Whilst the above modifications significantly improved absorption properties, subsequent efforts turned toward enhancing decaging quantum yields. Heckel et al. addressed this by incorporating the nitrogen atom of the 7-substituent into a constrained ring system.[77] This

structural restriction limited C–N bond rotation in the excited state, thereby suppressing non-productive decay pathways and resulting in up to a 12-fold increase in decaging efficiency.

Finally, Feringa et al., improved quantum yield through the introduction of a prenyl substituent at the 11-position of the coumarin scaffold. This allowed for stabilisation of the methyl carbocation formed during the excited state.[76] When incorporated into one of the extended derivatives produced by Kele et al it was found to increase the quantum yield by 7.4 fold dramatically improving decaging efficiency.[110] A timeline of these key developments can be seen in figure 39 below.

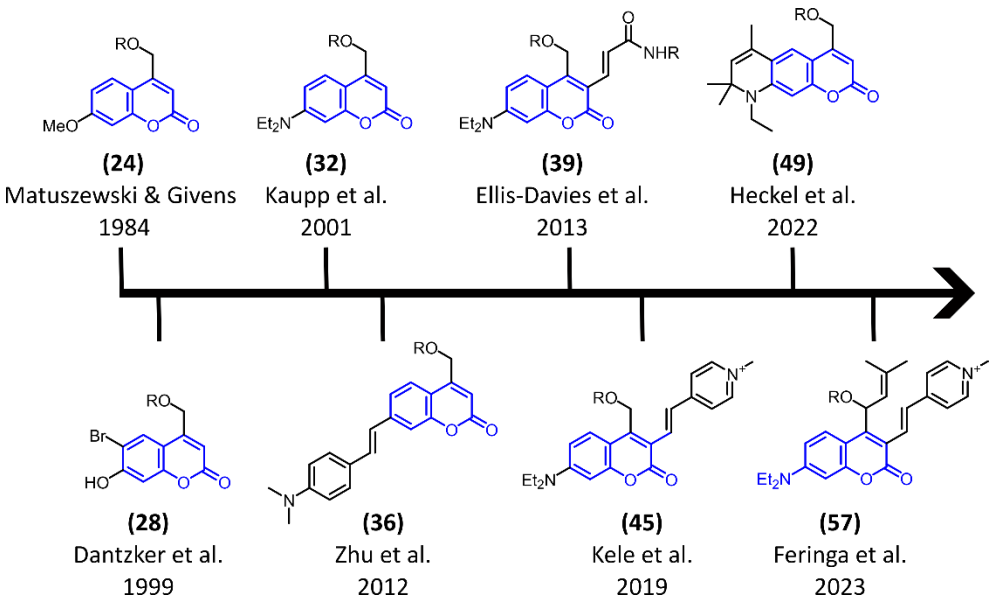

Figure 39: A timeline schematic detailing the development of coumarin photocages.

1.4.2.8 Benefits and limitations of coumarin photocages

Coumarin photocages have emerged as a versatile class of photolabile protecting groups owing to their favourable photophysical properties, tunable chemical structure, and broad applicability in biological systems. However, their utility is not without constraints, and several limitations must also be considered prior to their use. The key benefits and limitations of coumarin photocages are discussed below.

Perhaps the most obvious benefit of this class of compound, is their excellent absorption profiles relative to the aforementioned *o*-nitrobenzyls. The absorption profiles of coumarin photocages are typically red-shifted compared to this class of compound facilitating efficient one-photon photocleavage within the visible range. Many coumarin photocages also exhibit favourable two-photon absorption properties allowing them to be cleaved with high efficiency at near-infrared (**NIR**) wavelengths of up to 940 nm.[95,106] Not only are these wavelengths low in energy, enhancing biocompatibility, but they are also poorly absorbed by biological chromophores, therefore allowing for enhanced tissue penetration depth. Alongside this, two-photon decaging is typically achieved using LASER systems, which allow for a high degree of spatial resolution, limiting off-target effects. This high spatial resolution makes two-photon decaging particularly attractive for applications requiring subcellular or deep-tissue targeting, such as neurobiology and developmental biology. However, the widespread adoption of two-photon photocaging strategies is restricted by the high cost and technical complexity of the requisite LASER systems, which can limit accessibility.

Another key benefit of coumarin photocages, is the non-toxic nature of their byproducts. Photolysis of a coumarin photocage results in the release of the cargo molecule in its anionic form alongside the coumarin methyl carbocation which is rapidly quenched by surrounding solvent. This hydroxy-coumarin byproduct (in water) is typically non-toxic allowing for enhanced biocompatibility, particularly for *in vivo* applications. This is in contrast to *o*-nitrobenzyl photocages which form *o*-nitrosobenzaldehyde based byproducts upon photolysis which have been shown to be cytotoxic.[60]

Coumarin photocages are also incredibly versatile. The presence of a 4-hydroxymethyl group facilitates easy coupling of many functionalities, either directly or through the use of a linker

molecule. Coumarins have been used to photocage alcohols,[89] phosphates,[111] and amines[112] to name but a few, facilitating the photocaging of a wide variety of biomolecules, including peptides,[113] nucleotides,[90] proteins[114] and neurotransmitters.[104] Alongside this, the coumarin scaffold has also been extensively modified in order to allow for photocleavage at a wide range of different wavelengths. Not only has this allowed for orthogonal photocleavage of multiple photocages within a system but it also facilitates the selection of a particular photocage for that has been optimised for specific experimental conditions.[72,89,95]

Although, coumarin photocages have a large number of associated benefits, they do also suffer from a number of limitations. Some derivatives, particularly those with strongly electron withdrawing substituents at the 3-position, suffer from low-decaging quantum yields, which limits decaging efficiency.[106] Although, efforts have been made to increase the quantum yields of these derivatives, they have not been universally rectified meaning that many of the most red-shifted coumarin derivatives suffer from poor efficiency.

Coumarin photocages are also inherently fluorescent. Whilst this can be used to track decaging processes within a biological system, it may also act as a competitive decay pathway for the excited state, limiting quantum yields. Fluorescence also restricts the use of these photocages alongside techniques such as fluorescence microscopy, limiting applications.

Coumarin photocages also exhibit limited aqueous solubility. Although certain derivatives such as those developed by Kele et al. which contain a quaternary nitrogen containing heteroaromatic, feature enhanced solubility profiles,[72] the extended aromatic system of coumarin photocages makes them relatively hydrophobic. This can pose problems when attempting to apply these photocages to biological systems, particularly when high-local concentrations of photocaged molecules are required.

Finally, coumarin photocages are also more synthetically complexity *than* other classes of photocage such as *o*-nitrobenzaldehydes. Whilst basic derivatives such as 7-diethylamino-4-hydroxymethyl coumarin **(32)**, are readily synthetically accessible and often commercially available,[90] more complex derivatives such as those which feature extended conjugation or rigidified ring systems,[77] often require elaborate multi-step synthetic routes. These syntheses can be difficult and time consuming, limiting accessibility to these derivatives and impacting their widespread applicability.

1.4.3 The development of BODIPY photocages

1.4.3.1 Structural considerations

Boron-dipyrromethene (BODIPY) photocages consist of a central dipyrromethene scaffold, in which the two nitrogen atoms of the pyrrole rings chelate a central boron at its core. A number of different substituents can be present on the boron atom but the most commonly seen is fluorine, which forms a BF_2 moiety. The BODIPY scaffold is numbered as seen in figure 40 below, and cargo can be attached at multiple positions including directly to the boron atom at position 4 and at the α positions (3 and 5). However, the *meso* position (position 8) has been by far the most explored for cargo attachment and as such, it is this class of photocage that will be considered from here on out.

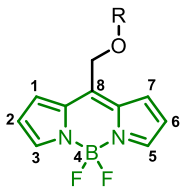

Figure 40: The numbered structure of the BODIPY scaffold.

1.4.3.2 Mechanistic Considerations

There are a number of different decaging mechanisms that can occur depending on the site of attachment. The decaging of a *meso*-methyl BODIPY occurs *via* a photochemical S_N1 reaction.[115] The cargo molecule is typically attached through an ester bond at this site and upon the absorption of a photon and subsequent generation of the excited state, energy is dissipated through heterolytic cleavage of the C-O bond. This releases the cargo molecule in its anionic form and forms a meso-methyl carbocation on the BODIPY. This carbocation is then rapidly quenched by surrounding solvent as seen in figure 41 below. In this way this mechanism is similar to the decaging mechanism of coumarin photocages previously discussed in section 1.4.2.2.

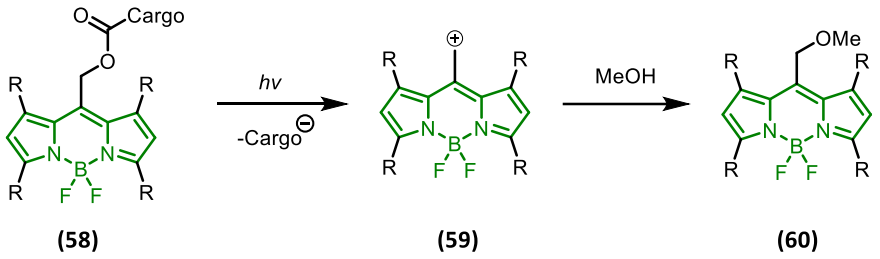

(58) **(59)** **(60)**

Figure 41: The general decaging mechanism of meso-methyl BODIPY photocages in methanol.[115]

1.4.3.3 Initial development

BODIPYs are a versatile class of organic dye and have had a major impact on modern science.[116] They play an important role as fluorescent probes due to their high fluorescence quantum yields and absorption coefficients and have been utilised in the study of many biological systems.[117] As such, many commercial derivatives exist today for this specific application. BODIPYs also have applications as fluorescent sensors and can be used to sense physical changes such as pH.[118] Relevant to this work, BODIPYs have also been utilised as photocages and exhibit favourable properties when applied in biological systems as they

typically absorb in the green region of the visible spectrum at approximately 500 nm which is non-toxic to cells.[119]

Although BODIPY dyes have been commonly used as fluorophores since their initial development in 1968,[120] it was not until 2014 that their photocaging capabilities were demonstrated by Urano et al. By substituting one of the fluorine atoms present on the central boron atom with an aryloxy group, they found that photolysis of the B-O was possible using visible light.[119] Following on from this discovery, a BODIPY derivative was used in the caging of histamine *via* a benzyloxycarbonyl linker attached at the central boron atom. Although initial *in vitro* studies produced positive results, they were unable to generate a histamine response in HeLa cells. Upon visualisation of the cells using fluorescence microscopy, it was shown that the hydrophobic nature of the BODIPY photocage was causing localisation within the cell membrane. Subsequently, a more hydrophilic derivative based on a dicarboxy-BODIPY scaffold was utilised and was shown to successfully release histamine within HeLa cells upon irradiation with visible light (460-500 nm) as seen in figure 42 below. This first work highlighted two attractive properties of BODIPY photocages. Firstly, they undergo single-photon decaging upon irradiation with visible light, at wavelengths which are equal to, if not greater than the wavelengths used to cleave coumarin photocages that have been previously discussed. Additionally, their inherent fluorescence allows them to be visualised within a biological setting using standard microscopy techniques, which is highly advantageous when troubleshooting decaging systems intracellularly or *in vivo.*[119] Although it Is important to note that this process directly competes with the productive heterolytic bond cleavage pathway required for decaging and so it may diminish efficiency.

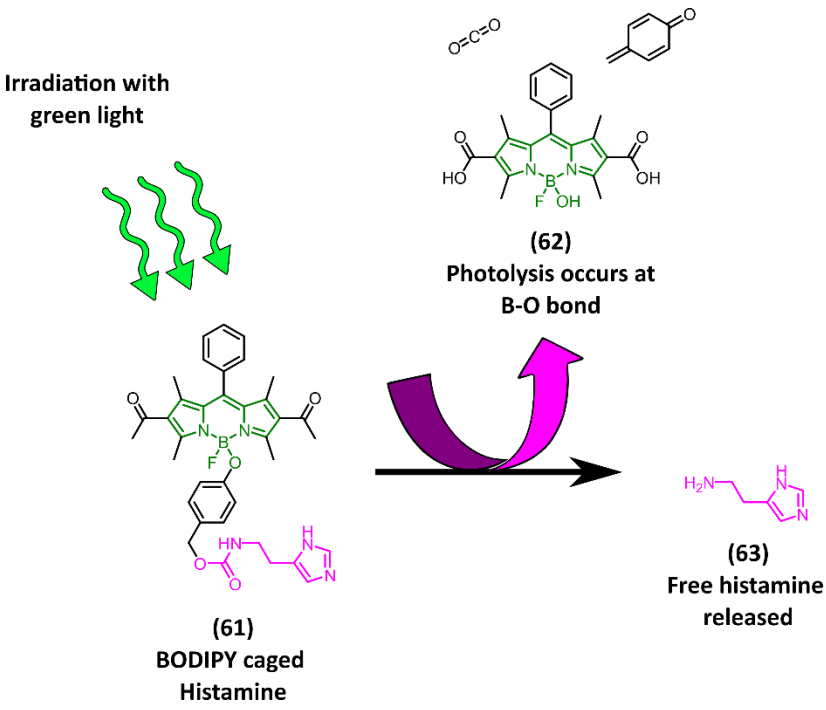

Figure 42: A schematic depicting the release of histamine from the initial BODIPY photocage developed by Urano et al.[119]

1.4.3.4 The development of *meso*-methyl BODIPY Photocages

Building on the work of Urano et al., Winter et al. performed a time dependent density functional theory (TD-DFT) calculations to predict photocage structures with easily accessible carbocation states. It was during this study, that they discovered that carbocations attached to BODIPY scaffold at the meso-position, which are generated by C-O bond scission, have low lying excited states, indicating that they are easily accessible upon irradiation with light.[115] Based on this finding they set out to synthesise a library of meso-methyl BODIPY derivatives. These derivatives were utilised in the photocaging of acetic acid as a model cargo, and their performance upon irradiation with light at 532 nm was investigated as seen in figure 43 below. During this study it was found that the decaging quantum yield of compounds **(64)** – (**68),** was less than or comparable, to the most popular *o*-nitrobenzyl and coumarin based photocages at the time,[60] however this was compensated for by the large molar extinction coefficients of

the synthesised BODIPYs meaning that the decaging cross sections of the synthesised compounds was still practical for use.[115] Of the library synthesised only **(69)** was found to be not useful, as it was found to be unstable due to alternative decay pathways. Additionally, the λ_{max} of the synthesised photocages were all equal to or above 515 nm, meaning that photocleavage was achievable using green light. It is important to note that this work was reported in 2015, 4 years prior to the development of the red-shifted coumarin photocages synthesised by Kele et al.,[72] meaning that these BODIPY derivatives were some of the earliest photocages capable of undergoing efficient decaging upon irradiation with green light, representing a significant advancement in the field.[115] Of the synthesised derivatives, it was found that the iodinated derivative **(68)** had the best decaging cross section with a value of 117 $M^{-1}cm^{-1}$ recorded upon irradiation at 532 nm, an improvement of almost 1.7-fold over the next best performing derivative **(65)**. This was attributed to its excellent quantum yield afforded by the introduction of the iodine atoms. It was postulated that these atoms facilitated intersystem crossing (ISC) upon formation of the excited state, allowing for the formation of a longer-lived triplet state, increasing the probability of productive decay of the excited state.[115]

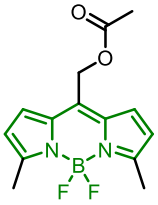

(64)

λ_{max}= 519 nm

ε= 57,000 $M^{-1}cm^{-1}$

Φ_u= 6.4 × 10^{-4}

$\Phi_u\varepsilon$= 37 $M^{-1}cm^{-1}$

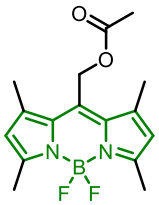

(65)

λ_{max}= 515 nm

ε= 71,000 $M^{-1}cm^{-1}$

Φ_u= 9.9 × 10^{-4}

$\Phi_u\varepsilon$= 70 $M^{-1}cm^{-1}$

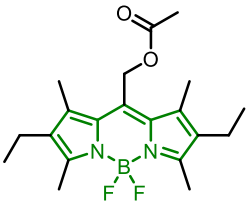

(66)

λ_{max}= 544 nm

ε= 62,000 $M^{-1}cm^{-1}$

Φ_u= 9.5 × 10^{-4}

$\Phi_u\varepsilon$= 59 $M^{-1}cm^{-1}$

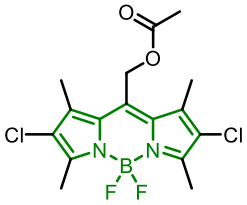

(67)

λ_{max}= 544 nm

ε= 48,000 $M^{-1}cm^{-1}$

Φ_u= 4.0 × 10^{-4}

$\Phi_u\varepsilon$= 19 $M^{-1}cm^{-1}$

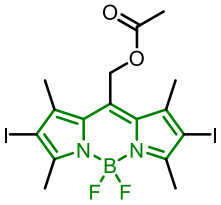

(68)

λ_{max}= 553 nm

ε= 49,000 $M^{-1}cm^{-1}$

Φ_u= 2.38 × 10^{-3}

$\Phi_u\varepsilon$= 117 $M^{-1}cm^{-1}$

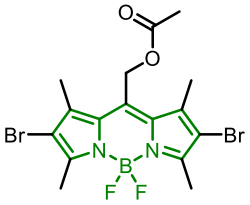

(69)

λ_{max}= 545 nm

ε= -

Φ_u= -

$\Phi_u\varepsilon$= -

Figure 43: A summary of the photophysical properties of the BODIPY library developed by Winter et al.[115]

Following this initial study, **(65)** was used to cage 2,4-dinitrobenzoic acid, a known fluorescence quencher for BODIPY dyes. The resulting compound was incubated with drosophila S2 cells and studied using fluorescence microscopy. Initially low levels of fluorescence were detected due to the presence of the quencher. However, upon irradiation at 500 nm, fluorescence rapidly intensified due to successful photorelease of the cargo as seen in figure 44 below, demonstrating the potential of BODIPYs as cages for intracellular cargoes.[115]

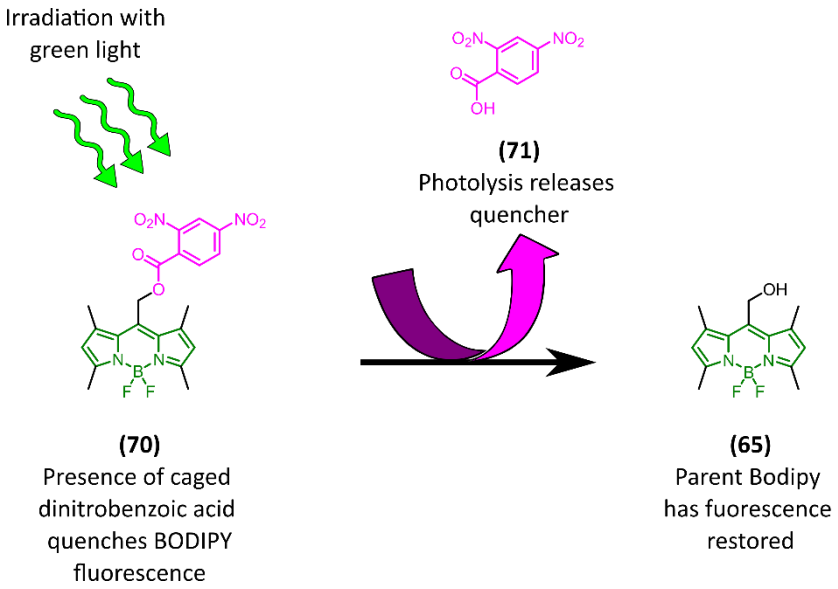

*Figure 44: Schematic of the decaging of **(70)** upon irradiation with green light. Photolysis of the BODIPY-cargo bond released the fluorescence quencher **(71)**, restoring the fluorescence of the parent BODIPY **(65)**.*

1.4.3.5 The optimisation of *meso*-methyl BODIPY Photocages

Building on the initial success of their *meso*-methyl BODIPY derivatives, Winter et al. embarked on a systematic study of structure activity relationships on this class of compound to elucidate which motifs were important in maximising photorelease efficiency and allow for rational design of next generation BODIPY photocages. This study was performed using both computational and spectroscopic methods, and several structural modifications were investigated in the hope of producing a final BODIPY derivative with superior decaging efficiency.[121]

The first structural modification to a BODIPY photocage to be studied was 2,6-dihalogen substitution. As discussed previously, the presence of heavy atoms on a chromophore promotes ISC upon excitation, resulting in the formation of the excited triplet state upon irradiation with light. This state is longer lived than the corresponding singlet state, thus increasing the probability of productive decay resulting in decaging. Consequently, it was

hypothesised that the introduction of heavy atoms to the BODIPY scaffold would positively influence decaging efficiency. Chlorinated, brominated and iodinated BODIPY derivatives were produced and their decaging activity upon irradiation at 507 nm was investigated. During this study it was found that the higher the atomic number of the substituted halogen, the higher the efficiency of the decaging process. In fact, 2,6-diiodo BODIPY derivatives exhibited a 10-20-fold increase in photo-release efficiency in comparison to their non-halogenated counterparts, which was consistent with the results they had previously observed during their initial study discussed in the previous section.[121]

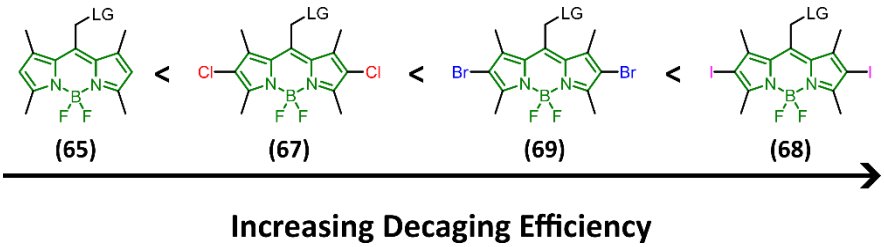

Figure 45: A schematic of the 2,6-dihalogenated BODIPY derivatives developed by Winter et al. Decaging efficiency was found to increase with increasing atomic number of the substituted halogen.[121]

The next structural motif to be studied was modification at the primary *meso*-methyl carbon.[121] Since the initial discovery of these molecules as photocages in 2015, it had been postulated that the decaging process proceeds *via* an S_N1 type reaction, resulting in the formation of a primary carbocation as seen in figure 41 above.[115] For S_N1 type reactions, carbocation formation is the rate determining step and so it was hypothesised that if the carbocation intermediate could be stabilised, decaging efficiency could be increased. This stabilisation would be achieved through the introduction of an additional methyl group at the *meso*-methyl carbon. Upon decay, a secondary carbocation would now be formed, with enhanced stability in comparison to the primary carbocation of previous derivatives due to

the effects of hyperconjugation. Methyl substituted *meso*-methyl BODIPY derivative **(72)**, seen in figure 46 below, was synthesised and its decaging efficiency upon irradiation at 507 nm was investigated. However, this modification did not have the desired effect of increasing decaging rate. It was proposed that this was because the additional methyl group imparted an out of plane geometry onto the otherwise rigid BODIPY scaffold, allowing for energy to be dissipated non-radiatively through vibrational relaxation. This competed with the productive decaging decay pathway, thus reducing efficiency.[121]

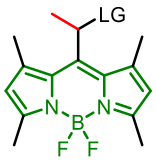

(72)

*Figure 46: The meso-methyl substituted BODIPY **(72)** developed by Winter et al.[121]*

Another important factor to consider during the decaging process is the quality of the leaving group. According to the mechanism proposed in figure 41 above, the leaving group is eliminated in its anionic form.[115] Thus, the ability for the leaving group to be eliminated correlates with the pK_a of the conjugate acid it forms. The lower the pK_a of a leaving group conjugate acid, the more stable in its anionic form, and the more likely it is to be eliminated *via* an S_N1 type mechanism. In order to investigate the effect of leaving group quality on decaging rate, Winter et al. synthesised BODIPY derivatives bearing a chlorine, acetate, or methoxy group at the *meso*-methyl position as seen in figure 47 below.[121] These groups have pK_a values of -7.0, 4.76 and 15.5 respectively and upon examination of their decaging quantum yields it was found that as predicted decaging efficiency decreased dramatically with increasing pK_a. This finding provided further corroboration to the theory that BODIPY decaging operates via an S_N1 type mechanism. It also highlighted the importance of the leaving group

to decaging efficiency, suggesting that in order to cage poorer leaving groups such as alcohols and amines, linker molecules in the form of carbonates and carbamates would be required in order to boost efficiency.[121]

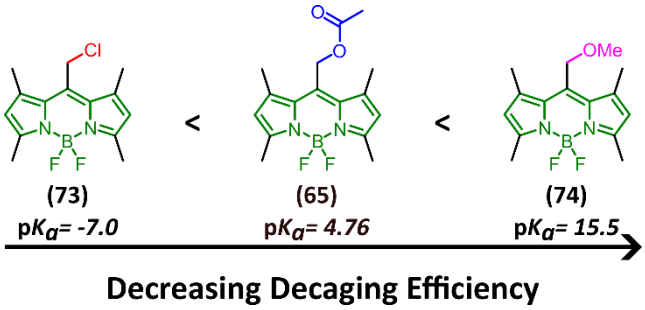

Figure 47 The decaging efficiency of BODIPY photocages can be increased by decreasing the pK_a of the leaving group[121]

Finally, Winter et al. investigated the effect of varying Boron substitution on decaging efficiency. Fluorine is the most electronegative element and thus exerts a strong electron-withdrawing effect when bound to the boron centre of BODIPY. Replacing these atoms with electron-donating groups was therefore hypothesised to increase electron density within the scaffold and stabilise the carbocation intermediate formed during decaging. Winter *et al.* achieved this substitution using Grignard reagents to install alkyl and aryl groups as seen in figure 48 below. Photophysical evaluation revealed an inverse relationship between steric bulk and decaging efficiency, with methyl-substituted derivative **(75)** outperforming ethyl analogue **(76)**, which in turn exceeded aryl variant **(77)**. As observed for meso-methyl substitution, increased steric congestion around boron likely disrupts scaffold planarity, promoting non-radiative decay pathways. Notably, the optimal derivative **(75)** displayed up to a 30-fold enhancement in decaging efficiency relative to the parent BF_2 analogue **(65)**, highlighting boron alkylation as a highly effective strategy for improving photoreactivity.[121]

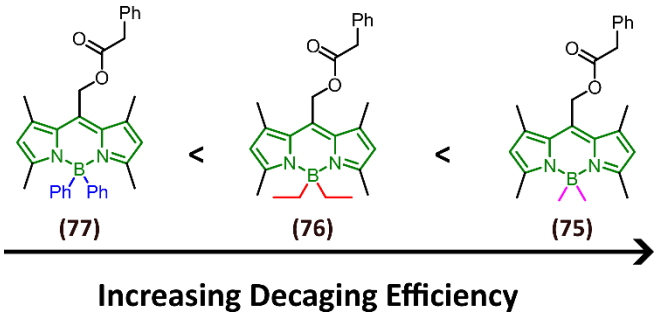

Figure 48: The boron-substituted BODIPYs developed by Winter et al. Decaging efficiency was found to increase with decreasing steric bulk.[121]

Now that a systematic study on the structure activity relationship of the BODIPY scaffold had been performed, researchers combined favourable substituents in order to determine if their effects were additive. A 2,6-diiodo *B*-dimethyl BODIPY **(78)** was synthesised and used to cage a variety of different leaving groups as seen in figure 49 below. Upon irradiation with green light, it was shown that these changes were indeed additive, and this novel photocage showed a marked increase in its decaging quantum yield. An increase in quantum yield of up to 12- and 2.5-fold was observed in comparison to the original diiodo **(68)** and original *B*-dimethyl **(75)** BODIPY photocages respectively, indicating that it was indeed advantageous to combine these structural motifs. The importance of this study is emphasised by comparing the quantum yield to the original "first generation" BODIPY photocage **(65)**, with an increase in decaging efficiency of over two orders of magnitude. In fact, the final derivative was calculated to have a one photon cross section of 40,000 $M^{-1}cm^{-1}$ the highest of any visible light absorbing photocage at the time.[121]

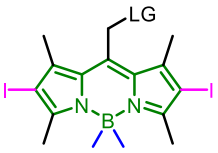

(78)

Figure 49: The optimised "second-generation" BODIPY photocage (78) developed by Winter et al. as a result of their SAR study.[121]

1.4.3.6 Red-shifting the absorbance of *meso*-methyl BODIPY photocages

The next generation photocage **(78)** described in the previous section had a λ_{max} of 538 nm.[121] If this could be shifted further into the red region, cleavage with higher wavelength, lower energy light could be achieved, increasing biocompatibility further and providing scope for the orthogonal decaging of multiple different photocages within the same mixture. Extension of the π-system had already been proven to be highly successful in providing a bathochromic shift for coumarin-based photocages and so Winter et al., applied the same strategy to BODIPY photocages.[72,106,122] Extending the π-systems at these positions allows for conjugation with the core BODIPY scaffold, thus allowing for increased electron delocalisation and a reduction in the HOMO-LUMO gap, red shifting absorbance. A library of extended BODIPY photocages was synthesised and their photophysical properties were then investigated as seen in figure 50 below.[122] It was found that the extension of the π-system did in fact lead to a red-shift in absorption. Expectedly, the extent to which the π-system was extended, was key to determining the λ_{max} of each compound, with derivatives that were only extended at one position having absorption maxima at lower wavelengths than di-substituted derivatives. It was also found that replacing the fluorine atoms present on the central boron atom with electron donating methyl groups had a positive effect on decaging efficiency, with alkylated derivative **(83)** experiencing over a 15-fold improvement in decaging cross section *vs* its

fluorinated counterpart **(82).** Thus, the library synthesised had given rise to a series of red-shifted BODIPY photocages, capable of efficient decaging at distinct wavelengths. In combination with the derivatives already synthesised by this group discussed in the previous section,[121] there were now BODIPY-derived photocages cleavable across a range of wavelengths between 450-700 nm. Additionally, the narrow nature of the absorption bands of this class of compound allowed for minimal overlap, meaning that there was now a realistic possibility of achieving selective, orthogonal, decaging within a mixture, simply by irradiating the sample with different wavelengths of light.[122]

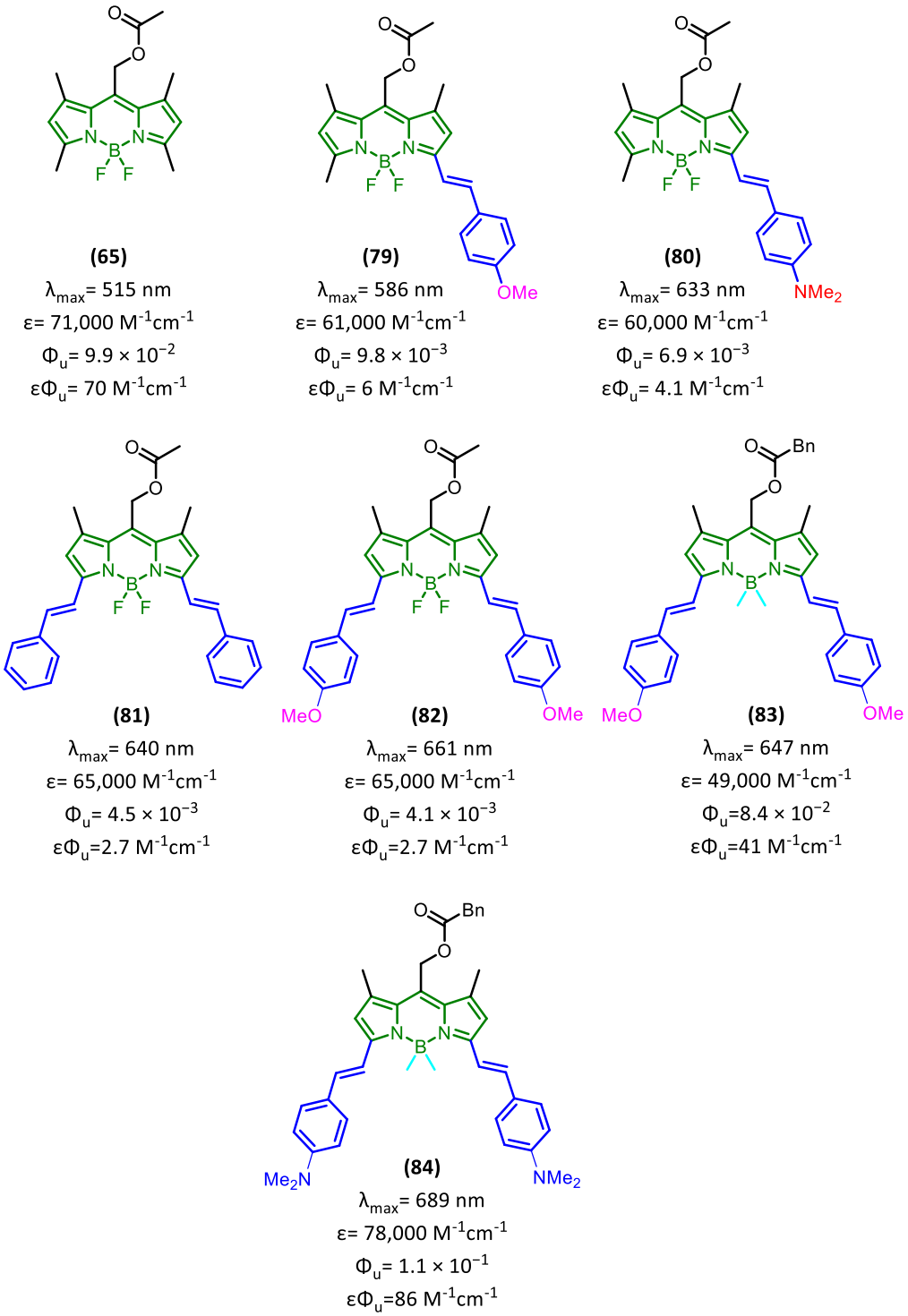

Figure 50: A summary of the photophysical properties of the red-shifted BODIPY derivatives developed by Winter et al.[122]

In biological settings, strict temporal control is often required over different biomolecules, in order to achieve a desired response. Thus, if a system whereby sequential activation of key

biomolecules at discrete points in time could be developed, it would present itself as a powerful tool in triggering biological processes. Now that a library of distinctly absorbing BODIPY photocages had been created, this technology had become a realistic possibility, and Winter et al. embarked on a proof-of-concept study, whereby they attempted to gain selective activation within a mixture, simply by using several photocages with distinct absorption profiles and irradiating the sample with different wavelengths of light. In order to ensure the greatest chance of success, three photocages with dramatically different absorption profiles were chosen, a 7-diethylamino-4-methyl coumarin cage **(32)** (λ_{max}≈ 380 nm), a dimethyl boron BODIPY **(65)** (λ_{max}≈ 520 nm), and a π-extended BODIPY derivative **(84)**(λ_{max}≈ 690 nm), and each was used to cage succinic acid.[74] It was hoped that the unique absorption bands of these photocages would allow for selective, wavelength-dependent, release upon irradiation with light. Whilst these photocages did not demonstrate complete orthogonality, they did exhibit high selectivity when sequentially irradiated with the longest wavelength first. Thus, when the final system in which all three photocages were present was trialled, the mixture was irradiated with light in order of decreasing wavelength, allowing for each photocage to be sequentially activated as seen in figure 51 below.[74] Whilst this work, represents an early model demonstration of this concept, it was a significant advancement in the field of photocaging as selective decaging of three distinctly absorbing photocages using visible wavelengths of light had been achieved for the first time. If this system can in the future be implemented in a biological setting it would allow for excellent spatiotemporal over multiple biomolecules within the same system, allowing for precise regulation of a biological process of interest.

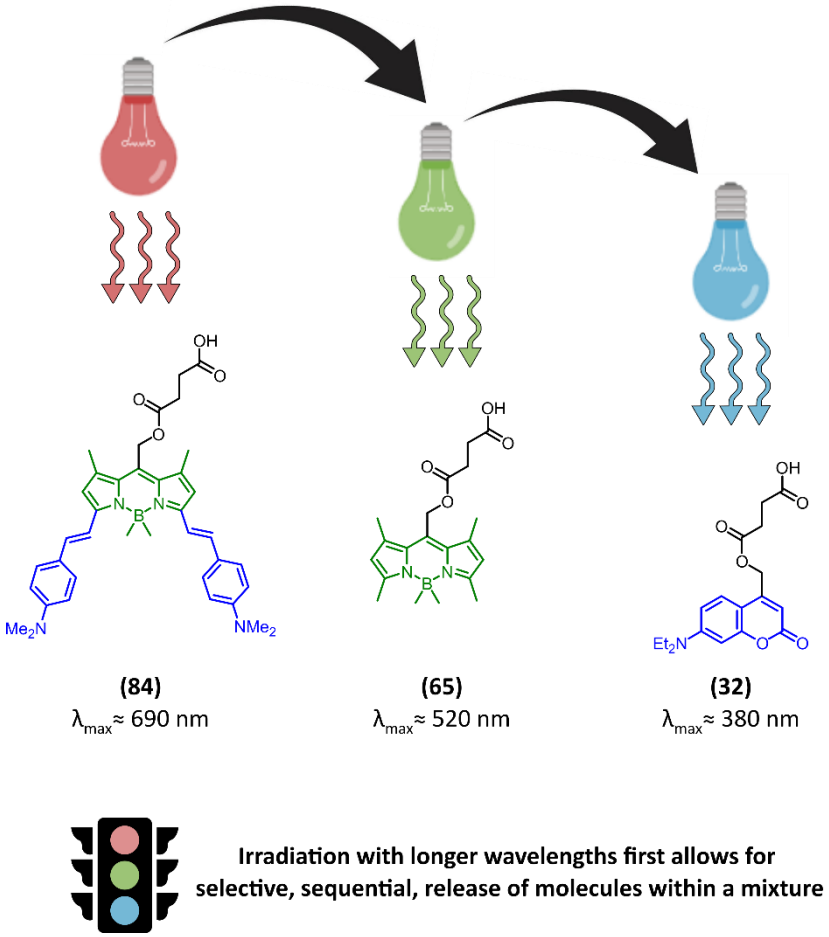

Figure 51: A schematic of the sequential decaging system developed by Winter et al.[74]

1.4.3.7 A timeline of the development of BODIPY photocages

Although brief, the field of BODIPY photocaging has expanded rapidly over the past decade. Since the initial discovery by Urano et al. that the B-O bond was cleavable using visible light,[119] the photochemical properties of the class have improved dramatically through the development of *meso*-methyl BODIPY photocages by Winter et al.[115] The SAR study performed on these *meso*-methyl photocages gave rise to derivatives bearing methyl groups on the boron atom which were the most efficient, visible light absorbing photocages developed to date.[121] The applications of these "2nd generation" BODIPY photocages were then expanded through the extension of the π-system, giving rise to highly efficient BODIPY photocages that were

cleavable with virtually every wavelength of visible light.[122] This work was highly significant as it allowed for the sequential activation of different photocages within a mixture simply by irradiating the sample with different wavelength of light.[74] This represents a key development for the biological applications of photocaging as it provides scope for the future sequential activation of biomolecules *in vivo*, which would allow for excellent temporal control over biochemical signalling. A timeline of the development of BODIPY photocages can be seen in figure 52 below.

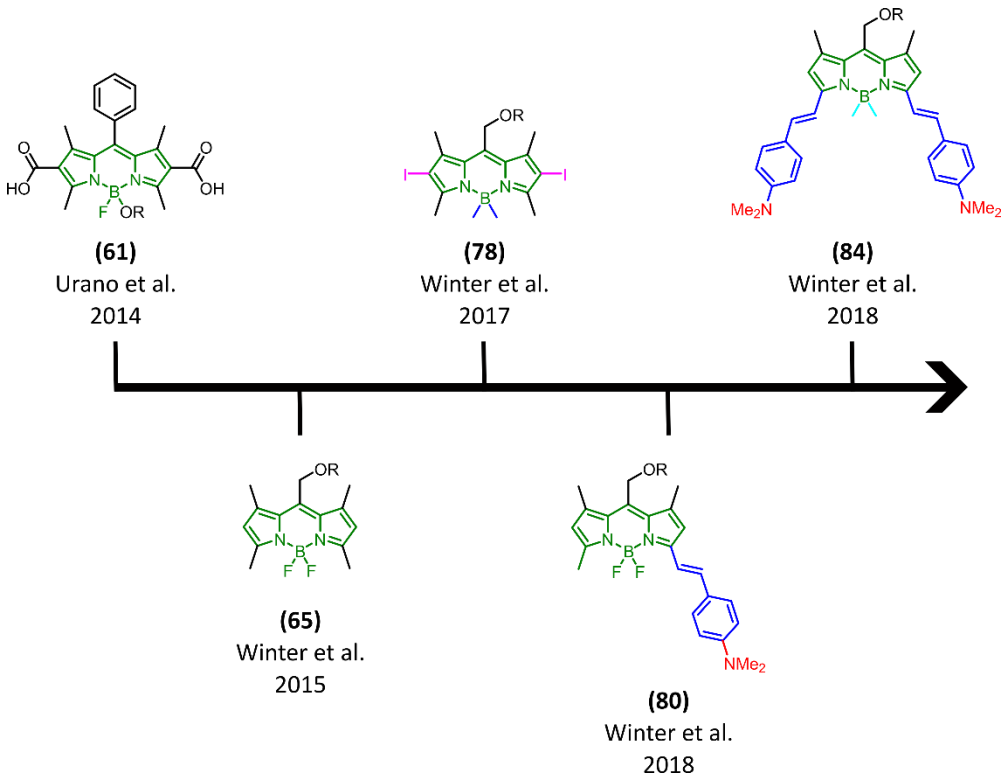

Figure 52: A timeline of the development of BODIPY photocages

1.4.3.8 The benefits and limitations of BODIPY photocages

Since their initial implementation by Urano et al. in 2014,[119] BODIPY photocages have rapidly developed into one of the premier classes of photocage currently in use. These photocages are characterised by favourable absorption profiles, with simple derivatives typically

exhibiting absorption maxima between 500 – 550 nm, well within the visible region of the electromagnetic spectrum. This coupled with high molar extinction coefficients at these wavelengths has facilitated efficient decaging at biocompatible wavelengths, making this class of photocage attractive for use in a biological setting.

The BODIPY scaffold has also been modified in order to red-shift absorption profiles. In particular, π-system extension at the 3- and 5-positions has proven highly effective for this purpose. Notably, derivatives **(81)** and **(85)**, developed by Winter *et al.*, exhibited absorption maxima of 633 nm and 689 nm, respectively.[122] This red-shift in absorbance facilitated decaging using red light, which is not only low in energy and therefore more biocompatible, but also poorly absorbed by biological chromophores allowing for increased tissue penetration.

The absorption bands of BODIPY chromophores are also narrow and intense. The nature of these bands, alongside the tunability of the absorbance profile of the BODIPY scaffold, has allowed for orthogonal decaging of a number of different BODIPY photocages within a mixture.[74] This offers the potential for the sequential activation of distinct biomolecules in complex biological environments.

Although, BODIPY photocages afford a number of key benefits, there are also limitations associated with this class of compound which must be considered. Many derivatives within this family exhibit strong fluorescence. This can compete with the desired photochemical decaging process by introducing a non-productive excited state decay pathway, thereby negatively impacting the overall decaging quantum yield.

Whilst the modularity of the BODIPY scaffold has allowed for the systematic tuning of photophysical properties across a wide range of wavelengths, this structural flexibility often

comes at the cost of synthetic accessibility. The preparation of extended or heavily substituted BODIPY derivatives often involves difficult, multi-step syntheses thereby limiting accessibility.[122] As such, broader application of extended BODIPY derivatives across a range of disciplines has been hindered up to this point.

The hydrophobic nature of the BODIPY scaffold means that the aqueous solubility of this class of compound is limited. Whilst the introduction of hydrophilic groups such as sulfonates, has been shown to improve solubility profiles,[73] their solubility in biological environments remains limited, often restricting their use to *in vitro* applications. Additionally, the BODIPY scaffold is acid sensitive, with treatment with acid often leading to the decomplexation of the central BORON atom.[123] Although the addition of substituents such as methyl or cyano groups has been utilised to increase acid stability,[124] compatibility with techniques such as solid phase peptide synthesis remains limited due to the acidic conditions required for cleavage.[125]

1.5 Thesis aims

Having now outlined the development of the field of photocaging, and its broader applicability to biomaterials, it is now possible to consider the specific aims of this work. As discussed in section 1.1.4, the ultimate goal of this project is to create photoresponsive materials, capable of sequentially activating and deactivating GF signalling pathways, thereby providing spatiotemporal control over tissue development. Realising this goal will require a multi-faceted approach, involving the design and synthesis of photoresponsive molecules, the verification of their photoreactivity and their subsequent functionalisation for incorporation into biomaterials. To realise this goal, this thesis is structured around three research objectives, each addressed in a dedicated results chapter.

The first objective, discussed in Chapter 2, is the synthesis of a library of photocages with discrete absorption profiles to enable orthogonal decaging under user-defined irradiation conditions. As discussed in section 1.4, substitution of the coumarin and BODIPY scaffolds at strategic positions provides a means of tuning their photophysical properties, red-shifting absorption profiles and minimising spectral overlap.[72,89,102,103,122] However, many reported photocages have only been synthesised on small scale or in proof-of-concept studies, which limits their applicability to materials. As such, we aim to develop, reliable, high-yielding, synthetic routes toward a range of coumarin and BODIPY photocages thus expanding their relevance in a materials setting.

The second objective, addressed in Chapter 3, is the development of photocleavable linkers capable of tethering biomolecules to material surfaces prior to wavelength-dependent release. While conventional photocages are well established, linkers that enable controlled attachment and subsequent photorelease of biomolecules remain comparatively underdeveloped. This chapter therefore focuses on both optimising synthetic access to established photocleavable linkers and designing novel derivatives with discrete absorption profiles to facilitate the sequential photorelease of biomolecules from material scaffolds.

The third objective, addressed in Chapter 4, is to validate the photoreactivity of the synthesised photocages and photocleavable linkers and assess their suitability for biomaterials applications. This will be achieved by performing a series of kinetic decaging studies, which will allow for quantitative determination of first order rate constants. These studies will be complemented by the development of bioconjugation strategies, enabling photocages and photocleavable linkers to be coupled to model peptide, laying a foundation of the future caging of GF sequestering peptides.

Collectively, these studies will lay the foundation for the ultimate aim of this work, the integration of photocages and photocleavable linkers into biomaterial scaffolds to enable the sequential activation and deactivation of GF signalling. By combining synthetic chemistry, bioconjugation and kinetic analysis, this thesis seeks to establish the groundwork for a future photoresponsive platform, capable of exerting precise spatiotemporal control over biological signalling and ultimately stem cell fate and tissue development.

1.6 References

1. Esdaille, C. J.; Washington, K. S.; Laurencin, C. T. Regenerative engineering: A review of recent advances and future directions. *Regen. Med.* **2021**, *16* (5), 495–512.
2. Lee, S. S.; Hsu, E. L.; Mendoza, M.; Ghodasra, J.; Nickoli, M. S.; Ashtekar, A.; Polavarapu, M.; Babu, J.; Riaz, R. M.; Nicolas, J. D.; Nelson, D.; Hashmi, S. Z.; Kaltz, S. R.; Earhart, J. S.; McKee, J. S.; Bairstow, S. F.; Shah, R. N.; Hsu, W. K.; Stupp, S. I. Gel scaffolds of BMP-2-binding peptide amphiphile nanofibers for spinal arthrodesis. *Adv. Healthc. Mater.* **2015**, *4* (1), 131–141.
3. Azagarsamy, M. A.; Anseth, K. S. Wavelength-controlled photocleavage for the orthogonal and sequential release of multiple proteins. *Angew. Chem., Int. Ed.* **2013**, *52* (51), 13803–13807.
4. Correa, D.; Somoza, R. A.; Lin, P.; Greenberg, S.; Rom, E.; Duesler, L.; Welter, J. F.; Yayon, A.; Caplan, A. I. Sequential exposure to fibroblast growth factors (FGF) 2, 9 and 18 enhances hMSC chondrogenic differentiation. *Osteoarthritis Cartilage* **2015**, *23* (3), 443–453.
5. Worster, A. A.; Brower-Toland, B. D.; Fortier, L. A.; Bent, S. J.; Williams, J.; Nixon, A. J. Chondrocytic differentiation of mesenchymal stem cells sequentially exposed to transforming growth factor-β1 in monolayer and insulin-like growth factor-I in a three-dimensional matrix. *J. Orthop. Res.* **2001**, *19* (4), 738–749.
6. Garcia-Ruiz, A.; Sánchez-Domínguez, C. N.; Moncada-Saucedo, N. K.; Pérez-Silos, V.; Lara-Arias, J.; Marino-Martínez, I. A.; Camacho-Morales, A.; Romero-Diaz, V. J.; Peña-Martinez, V.; Ramos-Payán, R.; Castro-Govea, Y.; Tuan, R. S.; Lin, H.; Fuentes-Mera, L.; Rivas-Estilla, A. M. Sequential growth factor exposure of human Ad-MSCs improves chondrogenic differentiation in an osteochondral biphasic implant. *Exp. Ther. Med.* **2021**, *22* (5), 1282.
7. Lakmal Elvitigala, K. C. M.; Sakai, S. MSC-derived osteogenic cell sheets on stiffness-tuned hyaluronic acid–gelatin hydrogels. *J. Mater. Chem. B* **2026**, ASAP.

8. Sun, Y.; Xu, Z.; Wang, M.; Lv, S.; Wu, H.; Chi, G.; Li, L.; Li, Y. Soft matrix combined with BMPR inhibition regulates neurogenic differentiation of human umbilical cord mesenchymal stem cells. *Front. Bioeng. Biotechnol.* **2020**, *8*, 791.
9. Davis, R.; Singh, A.; Jackson, M. J.; Coelho, R. T.; Prakash, D.; Charalambous, C. P.; Ahmed, W.; da Silva, L. R. R.; Lawrence, A. A. A comprehensive review on metallic implant biomaterials and their subtractive manufacturing. *Int. J. Adv. Manuf. Technol.* **2022**, *120* (3–4), 1473–1530.
10. Sagdic, K.; Fernández-Lavado, E.; Mariello, M.; Akouissi, O.; Lacour, S. P. Hydrogels and conductive hydrogels for implantable bioelectronics. *MRS Bull.* **2023**, *48* (5), 495–505.
11. Yue, S.; He, H.; Li, B.; Hou, T. Hydrogel as a biomaterial for bone tissue engineering: A review. *Nanomaterials* **2020**, *10* (8), 1511.
12. Norouzi, S.; Saveh Shemshaki, N.; Norouzi, E.; Latifi, M.; Azimi, B.; Danti, S.; Qiao, X.; Miao, Y.; Yang, S.; Gorji, M.; Petrovic, V.; Aboudzadeh, M. A.; Bagherzadeh, R. Recent advances in biomaterials for tissue-engineered constructs: Essential factors and engineering techniques. *Mater. Today Chem.* **2024**, *37*, 102016.
13. Langer, R.; Vacanti, J. P. Tissue engineering. *Science* **1993**, *260* (5110), 920–926.
14. Valls, P. O.; Esposito, A. Signalling dynamics, cell decisions, and homeostatic control in health and disease. *Curr. Opin. Cell Biol.* **2022**, *75*, 102066.
15. Broguiere, N.; Lüchtefeld, I.; Trachsel, L.; Mazunin, D.; Rizzo, R.; Bode, J. W.; Lutolf, M. P.; Zenobi-Wong, M. Morphogenesis guided by 3D patterning of growth factors in biological matrices. *Adv. Mater.* **2020**, *32* (25), 1908299.
16. Shoichet, M. S. Polymer scaffolds for biomaterials applications. *Macromolecules* **2010**, *43* (2), 581–591.
17. Li, G.; Luo, Y.; Hu, Z.; Shi, Z.; Cao, X.; Xu, R.; Mi, Y.; Yao, Y.; Mao, H.; Zhang, H.; Zhu, Y. Recent advances in peptide-functionalized hydrogels for bone tissue engineering. *ACS Biomater. Sci. Eng.* **2025**, *11* (4), 1970–1989.
18. Dawson, E.; Mapili, G.; Erickson, K.; Taqvi, S.; Roy, K. Biomaterials for stem cell differentiation. *Adv. Drug Deliv. Rev.* **2008**, *60* (2), 215–228.
19. Chen, Z.; Du, C.; Liu, S.; Liu, J.; Yang, Y.; Dong, L.; Zhao, W.; Huang, W.; Lei, Y. Progress in biomaterials inspired by the extracellular matrix. *Giant* **2024**, *19*, 100323.
20. Raspa, A.; Gelain, F. Mimicking extracellular matrix via engineered nanostructured biomaterials for neural repair. *Curr. Neuropharmacol.* **2021**, *19* (12), 2110–2124.
21. Frantz, C.; Stewart, K. M.; Weaver, V. M. The extracellular matrix at a glance. *J. Cell Sci.* **2010**, *123* (24), 4195–4200.
22. Naahidi, S.; Jafari, M.; Logan, M.; Wang, Y.; Yuan, Y.; Bae, H.; Dixon, B.; Chen, P. Biocompatibility of hydrogel-based scaffolds for tissue engineering applications. *Biotechnol. Adv.* **2017**, *35* (5), 530–544.
23. Brown, B. N.; Badylak, S. F. Extracellular matrix as an inductive scaffold for functional tissue reconstruction. *Transl. Res.* **2014**, *163* (4), 268–285.
24. Kielty, C. M.; Sherratt, M. J.; Shuttleworth, C. A. Elastic fibres. *J. Cell Sci.* **2002**, *115* (Pt 14), 2817–2828.

25. Pilcher, B. K.; Dumin, J. A.; Sudbeck, B. D.; Krane, S. M.; Welgus, H. G.; Parks, W. C. The activity of collagenase-1 is required for keratinocyte migration on a type I collagen matrix. *J. Cell Biol.* **1997**, *137* (6), 1445–1457.
26. Karamanos, N. K.; Theocharis, A. D.; Piperigkou, Z.; Manou, D.; Passi, A.; Skandalis, S. S.; Vynios, D. H.; Orian-Rousseau, V.; Ricard-Blum, S.; Schmelzer, C. E. H.; Duca, L.; Durbeej, M.; Afratis, N. A.; Troeberg, L.; Franchi, M.; Masola, V.; Onisto, M. A guide to the composition and functions of the extracellular matrix. *FEBS J.* **2021**, *288* (24), 6850–6912.
27. Cao, H.; Duan, L.; Zhang, Y.; Cao, J.; Zhang, K. Current hydrogel advances in physicochemical and biological response-driven biomedical application diversity. *Signal Transduct. Target. Ther.* **2021**, *6* (1), 426.
28. Nguyen, K. T.; West, J. L. Photopolymerizable hydrogels for tissue engineering applications. *Biomaterials* **2002**, *23* (22), 4307–4314.
29. Spicer, C. D. Hydrogel scaffolds for tissue engineering: The importance of polymer choice. *Polym. Chem.* **2020**, *11* (2), 184–219.
30. Zhang, X.; Zhang, R.; Wu, S.; Sun, Y.; Yang, H.; Lin, B. Physically and chemically dual-crosslinked hydrogels with superior mechanical properties and self-healing behavior. *New J. Chem.* **2020**, *44* (23), 9903–9911.
31. Teixeira, S. P. B.; Domingues, R. M. A.; Shevchuk, M.; Gomes, M. E.; Peppas, N. A.; Reis, R. L. Biomaterials for sequestration of growth factors and modulation of cell behavior. *Adv. Funct. Mater.* **2020**, *30* (44), 1909011.
32. Stone, W. L.; Bhimji, S. S. Physiology, growth factor. *StatPearls* [Internet]; StatPearls Publishing: Treasure Island, FL, 2018–; accessed 2025-09-24.
33. Brivanlou, A. H.; Darnell, J. E. Transcription: Signal transduction and the control of gene expression. *Science* **2002**, *295* (5556), 813–818.
34. Lake, D.; Corrêa, S. A. L.; Müller, J. Negative feedback regulation of the ERK1/2 MAPK pathway. *Cell. Mol. Life Sci.* **2016**, *73* (23), 4397–4413.
35. Lu, L.; Feng, M.; Gu, J.; Xia, Z.; Zhang, H.; Zheng, S.; Duan, Z.; Hu, R.; Wang, J.; Shi, W.; Ji, C.; Shen, Y.; Chen, G.; Zheng, S. G.; Han, Y. P. Restoration of intrahepatic regulatory T cells through MMP-9/13-dependent activation of TGF-β is critical for immune homeostasis following acute liver injury. *J. Mol. Cell Biol.* **2013**, *5* (6), 369–379.
36. Hynes, R. O. The extracellular matrix: Not just pretty fibrils. *Science* **2009**, *326* (5957), 1216–1219.
37. Sorkin, A.; von Zastrow, M. Endocytosis and signalling: Intertwining molecular networks. *Nat. Rev. Mol. Cell Biol.* **2009**, *10* (9), 609–622.
38. Discher, D. E.; Mooney, D. J.; Zandstra, P. W. Growth factors, matrices, and forces combine and control stem cells. *Science* **2009**, *324* (5935), 1673–1677.
39. Jaeger, I.; Arber, C.; Risner-Janiczek, J. R.; Kuechler, J.; Pritzsche, D.; Chen, I.-C.; Naveenan, T.; Ungless, M. A.; Li, M. Temporally controlled modulation of FGF/ERK signaling directs midbrain dopaminergic neural progenitor fate in mouse and human pluripotent stem cells. *Development* **2011**, *138* (20), 4363–4374.
40. Shah, R. N.; Shah, N. A.; Lim, M. M. D. R.; Hsieh, C.; Nuber, G.; Stupp, S. I. Supramolecular design of self-assembling nanofibers for cartilage regeneration. *Proc. Natl. Acad. Sci. U.S.A.* **2010**, *107* (8), 3293–3298.
41. Sampath Kumar, A.; Tian, L.; Bolondi, A.; Hernández, A. A.; Stickels, R.; Kretzmer, H.; Murray, E.; Wittler, L.; Walther, M.; Barakat, G.; Haut, L.; Elkabetz, Y.; Macosko, E. Z.;

Guignard, L.; Chen, F.; Meissner, A. Spatiotemporal transcriptomic maps of whole mouse embryos at the onset of organogenesis. *Nat. Genet.* **2023**, *55* (7), 1176–1185.
42. Arnold, S. J.; Robertson, E. J. Making a commitment: Cell lineage allocation and axis patterning in the early mouse embryo. *Nat. Rev. Mol. Cell Biol.* **2009**, *10* (2), 91–103.
43. Li, Y.; Wang, M.; Wang, F.; Lu, S.; Chen, X. Recent progress in studies of photocages. *Smart Mol.* **2023**, *1* (1), e20220003.
44. Iwamoto, K.; Shindo, Y.; Takahashi, K. Modeling cellular noise underlying heterogeneous cell responses in the epidermal growth factor signaling pathway. *PLoS Comput. Biol.* **2016**, *12* (11), e1005222.
45. Chandarlapaty, S. Negative feedback and adaptive resistance to the targeted therapy of cancer. *Cancer Discov.* **2012**, *2* (4), 311–319.
46. Locasale, J. W. Signal duration and the time scale dependence of signal integration in biochemical pathways. *BMC Syst. Biol.* **2008**, *2* (1), 108.
47. Maxwell, J. C. A dynamical theory of the electromagnetic field. *Philos. Trans. R. Soc. Lond.* **1865**, *155*, 459–512.
48. Einstein, A. Über einen die erzeugung und verwandlung des lichtes betreffenden heuristischen gesichtspunkt. *Ann. Phys.* **1905**, *322* (6), 132–148.
49. Planck, M. Ueber das gesetz der energieverteilung im normalspectrum. *Ann. Phys.* **1901**, *309* (3), 553–563.
50. Dani, S.; Schütz, K.; Dikici, E.; Bernhardt, A.; Lode, A. The effect of continuous long-term illumination with visible light in different spectral ranges on mammalian cells. *Sci. Rep.* **2024**, *14* (1), 9444.
51. Françon, A.; Behar-Cohen, F.; Torriglia, A. Wavelength-dependency of the impact of light on proliferation and DNA damage of corneal cells in vitro. *J. Photochem. Photobiol., B* **2025**, *264*, 113118.
52. Shukla, R.; Dubey, A.; Pandey, V.; Golhani, D.; Jain, A. P. Chromophore—An utility in UV spectrophotometer. *Inventi Rapid Pharm. Ana. Qual. Assur.* **2012**, *2012* (3), 1–4.
53. Jaffé, H. H.; Miller, A. L. The fates of electronic excitation energy. *J. Chem. Educ.* **1966**, *43* (9), 469–475.
54. Jablonski, A. Efficiency of anti-Stokes fluorescence in dyes. *Nature* **1933**, *131* (3319), 839–840.
55. Franck, J. Elementary processes of photochemical reactions. *Trans. Faraday Soc.* **1926**, *21*, 536–542.
56. Condon, E. A theory of intensity distribution in band systems. *Phys. Rev.* **1926**, *28* (6), 1182–1201.
57. Stokes, G. G. On the change of refrangibility of light. *Philos. Trans. R. Soc. Lond.* **1852**, *142*, 463–562.
58. Wardle, B. *Principles and Applications of Photochemistry*; Wiley: Chichester, 2009.
59. Turro, N. J.; Ramamurthy, V.; Scaiano, J. C. *Principles of Molecular Photochemistry: An Introduction*; University Science Books: Sausalito, CA, 2009.
60. Klán, P.; Šolomek, T.; Bochet, C. G.; Blanc, A.; Givens, R.; Rubina, M.; Popik, V.; Kostikov, A.; Wirz, J. Photoremovable protecting groups in chemistry and biology: Reaction mechanisms and efficacy. *Chem. Rev.* **2013**, *113* (1), 119–191.
61. Schmidt, R.; Geissler, D.; Hagen, V.; Bendig, J. Mechanism of photocleavage of (coumarin-4-yl)methyl esters. *J. Phys. Chem. A* **2007**, *111* (27), 5768–5774.

62. Il'ichev, Y. V.; Schwörer, M. A.; Wirz, J. Photochemical reaction mechanisms of 2-nitrobenzyl compounds: Methyl ethers and caged ATP. *J. Am. Chem. Soc.* **2004**, *126* (14), 4581–4595.
63. Clydesdale, G. J.; Dandie, G. W.; Muller, H. K. Ultraviolet light induced injury: Immunological and inflammatory effects. *Immunol. Cell Biol.* **2001**, *79* (6), 547–568.
64. Hart, R. W.; Setlow, R. B.; Woodhead, A. D. Evidence that pyrimidine dimers in DNA can give rise to tumors. *Proc. Natl. Acad. Sci. U.S.A.* **1977**, *74* (12), 5574–5578.
65. McMillan, T. J.; Leatherman, E.; Ridley, A.; Shorrocks, J.; Tobi, S. E.; Whiteside, J. R. Cellular effects of long wavelength UV light (UVA) in mammalian cells. *J. Pharm. Pharmacol.* **2008**, *60* (8), 969–976.
66. Josa-Culleré, L.; Llebaria, A. In the search for photocages cleavable with visible light: An overview of recent advances and chemical strategies. *ChemPhotoChem* **2021**, *5* (4), 309–329.
67. Xiong, H.; Xu, Y.; Kim, B.; Rha, H.; Zhang, B.; Li, M.; Yang, G.-F.; Kim, J. S. Photo-controllable biochemistry: Exploiting the photocages in phototherapeutic window. *Chem* **2023**, *9* (1), 29–64.
68. Cheung, J. W.; Kinney, W. D.; Wesalo, J. S.; Reed, M.; Nicholson, E. M.; Deiters, A.; Cropp, T. A. Genetic encoding of a photocaged histidine for light-control of protein activity. *ChemBioChem* **2023**, *24* (7), e202200721.
69. Pinheiro, A. V.; Baptista, P.; Lima, J. C. Light activation of transcription: Photocaging of nucleotides for control over RNA polymerization. *Nucleic Acids Res.* **2008**, *36* (14), e90.
70. Rossi, F. M.; Margulis, M.; Tang, C. M.; Kao, J. P. Y. N-nmoc-L-glutamate, a new caged glutamate with high chemical stability and low pre-photolysis activity. *J. Biol. Chem.* **1997**, *272* (52), 32933–32939.
71. O'Hagan, M. P.; Duan, Z.; Huang, F.; Laps, S.; Dong, J.; Xia, F.; Willner, I. Photocleavable ortho-nitrobenzyl-protected DNA architectures and their applications. *Chem. Rev.* **2023**, *123* (10), 6839–6887.
72. Bojtár, M.; Kormos, A.; Kis-Petik, K.; Kellermayer, M.; Kele, P. Green-light activatable, water-soluble red-shifted coumarin photocages. *Org. Lett.* **2019**, *21* (23), 9410–9414.
73. Kand, D.; Liu, P.; Navarro, M. X.; Fischer, L. J.; Rousso-Noori, L.; Friedmann-Morvinski, D.; Winter, A. H.; Miller, E. W.; Weinstain, R. Water-soluble BODIPY photocages with tunable cellular localization. *J. Am. Chem. Soc.* **2020**, *142* (11), 4970–4974.
74. Peterson, J. A.; Yuan, D.; Winter, A. H. Multiwavelength control of mixtures using visible light-absorbing photocages. *J. Org. Chem.* **2021**, *86* (14), 9655–9664.
75. Bardhan, A.; Deiters, A. Development of photolabile protecting groups and their application to the optochemical control of cell signaling. *Curr. Opin. Struct. Biol.* **2019**, *57*, 164–175.
76. Schulte, A. M.; Alachouzos, G.; Szymański, W.; Feringa, B. L. Strategy for engineering high photolysis efficiency of photocleavable protecting groups through cation stabilization. *J. Am. Chem. Soc.* **2022**, *144* (27), 12105–12115.
77. Klimek, R.; Asido, M.; Hermanns, V.; Junek, S.; Wachtveitl, J.; Heckel, A. Inactivation of competitive decay channels leads to enhanced coumarin photochemistry. *Chem.–Eur. J.* **2022**, *28* (35), e202200647.
78. Zhao, Y.; Zheng, Q.; Dakin, K.; Xu, K.; Martinez, M. L.; Li, W.-H. New caged coumarin fluorophores with extraordinary uncaging cross sections suitable for biological imaging applications. *J. Am. Chem. Soc.* **2004**, *126* (14), 4653–4663.

79. Kaplan, J. H.; Forbush, B.; Hoffman, J. F. Rapid photolytic release of adenosine 5'-triphosphate from a protected analogue: Utilization by the Na:K pump of human red blood cell ghosts. *Biochemistry* **1978**, *17* (10), 1929–1935.
80. Walbert, S.; Pfleiderer, W.; Steiner, U. E. Photolabile protecting groups for nucleosides: Mechanistic studies of the 2-(2-nitrophenyl)ethyl group. *Helv. Chim. Acta* **2001**, *84* (6), 1601–1611.
81. Nerbonne, J. M.; Richard, S.; Nargeot, J.; Lester, H. A. New photoactivatable cyclic nucleotides produce intracellular jumps in cyclic AMP and cyclic GMP concentrations. *Nature* **1984**, *310* (5972), 74–76.
82. Ramesh, D.; Wieboldt, R.; Niu, L.; Carpenter, B. K.; Hess, G. P. Photolysis of a protecting group for the carboxyl function of neurotransmitters within 3 μs and with product quantum yield of 0.2. *Proc. Natl. Acad. Sci. U.S.A.* **1993**, *90* (23), 11074–11078.
83. Walker, J. W.; Gilbert, S. H.; Drummond, R. M.; Yamada, M.; Sreekumar, R.; Carraway, R. E.; Ikebe, M.; Fay, F. S. Signaling pathways underlying eosinophil cell motility revealed by using caged peptides. *Proc. Natl. Acad. Sci. U.S.A.* **1998**, *95* (4), 1568–1573.
84. Rothman, D. M.; Petersson, E. J.; Vázquez, M. E.; Brandt, G. S.; Dougherty, D. A.; Imperiali, B. Caged phosphoproteins. *J. Am. Chem. Soc.* **2005**, *127* (3), 846–847.
85. Ghosn, B.; Haselton, F. R.; Gee, K. R.; Monroe, W. T. Control of DNA hybridization with photocleavable adducts. *Photochem. Photobiol.* **2005**, *81* (4), 953–959.
86. Chaulk, S. G.; MacMillan, A. M. Separation of spliceosome assembly from catalysis with caged pre-mRNA substrates. *Angew. Chem., Int. Ed.* **2001**, *40* (11), 2149–2152.
87. Momotake, A.; Lindegger, N.; Niggli, E.; Barsotti, R. J.; Ellis-Davies, G. C. R. The nitrodibenzofuran chromophore: A new caging group for ultra-efficient photolysis in living cells. *Nat. Methods* **2006**, *3* (1), 35–40.
88. Wang, Z.; Martin, S. F. Design, synthesis and evaluation of novel carbazole-derived photocages. *Chem.–Eur. J.* **2022**, *28* (18), e202200311.
89. Bao, C.; Fan, G.; Lin, Q.; Li, B.; Cheng, S.; Huang, Q.; Zhu, L. Styryl conjugated coumarin caged alcohol: Efficient photorelease by either one-photon long wavelength or two-photon NIR excitation. *Org. Lett.* **2012**, *14* (2), 572–575.
90. Hagen, V.; Frings, S.; Wiesner, B.; Helm, S.; Kaupp, U. B.; Bendig, J. [7-(Dialkylamino)coumarin-4-yl]methyl-caged compounds as ultrafast and effective long-wavelength phototriggers of 8-bromo-substituted cyclic nucleotides. *ChemBioChem* **2003**, *4* (5), 434–442.
91. Lončar, M.; Jakovljević, M.; Šubarić, D.; Pavlić, M.; Buzjak Služek, V.; Cindrić, I.; Molnar, M. Coumarins in food and methods of their determination. *Foods* **2020**, *9* (5), 645.
92. Matos, M. J.; Santana, L.; Uriarte, E.; Abreu, O. A.; Molina, E.; Yordi, E. G. Coumarins—An important class of phytochemicals. In *Phytochemicals: Isolation, Characterisation and Role in Human Health*; InTech: Rijeka, 2015.
93. Fan, P.; Gao, Y.; Zheng, M.; Xu, T.; Schoenhagen, P.; Jin, Z. Recent progress and market analysis of anticoagulant drugs. *J. Thorac. Dis.* **2018**, *10* (3), 1392–1397.
94. Givens, R. S.; Matuszewski, B. Photochemistry of 2-nitrobenzyl derivatives. *J. Chem. Soc., Chem. Commun.* **1984**, (16), 106–107.
95. Furuta, T.; Wang, S. S. H.; Dantzker, J. L.; Dore, T. M.; Bybee, W. J.; Callaway, E. M.; Denk, W.; Tsien, R. Y. Brominated 7-hydroxycoumarin-4-ylmethyls: Photolabile protecting groups with biologically useful cross-sections for two-photon photolysis. *Proc. Natl. Acad. Sci. U.S.A.* **1999**, *96* (4), 1193–1200.

96. Göppert-Mayer, M. Über elementarakte mit zwei quantensprüngen. *Ann. Phys.* **1931**, *401* (3), 273–294.
97. Luu, P.; Fraser, S. E.; Schneider, F. More than double the fun with two-photon excitation microscopy. *Commun. Biol.* **2024**, *7* (1), 624.
98. Diaspro, A.; Bianchini, P.; Vicidomini, G.; Faretta, M.; Ramoino, P.; Usai, C. Multi-photon excitation microscopy. *Biomed. Eng. Online* **2006**, *5*, 36.
99. Parma, L.; Omenetto, N. Two-photon absorption of 7-hydroxycoumarine. *Chem. Phys. Lett.* **1978**, *54* (3), 460–463.
100. Atkins, P. W.; de Paula, J.; Keeler, J. *Atkins' Physical Chemistry*, 11th ed.; Oxford University Press: Oxford, 2018.
101. Sánchez-de-Armas, R.; San-Miguel, M. A.; Oviedo, J.; Sanz, J. F. Molecular modification of coumarin dyes for more efficient dye-sensitized solar cells. *J. Chem. Phys.* **2012**, *136* (19), 194702.
102. Hagen, V.; Bendig, J.; Frings, S.; Eckardt, T.; Helm, S.; Reuter, D.; Kaupp, U. B. Highly efficient and ultrafast phototriggers for cAMP and cGMP by using long-wavelength UV/Vis activation. *Angew. Chem., Int. Ed.* **2001**, *40* (6), 1045–1048.
103. Amatrudo, J. M.; Olson, J. P.; Lur, G.; Chiu, C. Q.; Higley, M. J.; Ellis-Davies, G. C. R. Wavelength-selective one- and two-photon uncaging of GABA. *ACS Chem. Neurosci.* **2014**, *5* (1), 64–70.
104. Passlick, S.; Kramer, P. F.; Richers, M. T.; Williams, J. T.; Ellis-Davies, G. C. R. Two-color, one-photon uncaging of glutamate and GABA. *PLoS One* **2017**, *12* (11), e0187732.
105. Kantevari, S.; Passlick, S.; Kwon, H. B.; Richers, M. T.; Sabatini, B. L.; Ellis-Davies, G. C. R. Development of anionically decorated caged neurotransmitters: In vitro comparison of 7-nitroindolinyl- and 2-(p-phenyl-o-nitrophenyl)propyl-based photochemical probes. *ChemBioChem* **2016**, *17* (10), 938–946.
106. Klausen, M.; Dubois, V.; Clermont, G.; Tonnelé, C.; Castet, F.; Blanchard-Desce, M. Dual-wavelength efficient two-photon photorelease of glycine by π-extended dipolar coumarins. *Chem. Sci.* **2019**, *10* (15), 4477–4484.
107. Cao, D.; Liu, Z.; Verwilst, P.; Koo, S.; Jangjili, P.; Kim, J. S.; Lin, W. Coumarin-based small-molecule fluorescent chemosensors. *Chem. Rev.* **2019**, *119* (18), 10403–10519.
108. Debnath, T.; Ghosh, H. N. An insight of molecular twisting of coumarin dyes. *ChemistrySelect* **2020**, *5* (30), 9461–9476.
109. Luo, D.; Kuang, C.; Liu, X.; Wang, G. Experimental investigations on fluorescence excitation and depletion of ATTO 390 dye. *Opt. Laser Technol.* **2013**, *45* (1), 488–493.
110. Schulte, A. M.; Smid, L. M.; Alachouzos, G.; Szymański, W.; Feringa, B. L. Cation delocalization and photo-isomerization enhance the uncaging quantum yield of a photocleavable protecting group. *Chem. Commun.* **2023**, *60* (5), 673–676.
111. Furuta, T.; Iwamura, M. New caged groups: 7-substituted coumarinylmethyl phosphate esters. In *Methods in Enzymology*; Caged Compounds; Academic Press: San Diego, 1998; Vol. 291, pp 50–63.
112. Banala, S.; Jin, X.-T.; Dilan, T. L.; Sheu, S.-H.; Clapham, D. E.; Drenan, R. M.; Lavis, L. D. Elucidating and optimizing the photochemical mechanism of coumarin-caged tertiary amines. *J. Am. Chem. Soc.* **2024**, *146* (30), 20627–20635.
113. Gandioso, A.; Cano, M.; Massaguer, A.; Marchán, V. A green light-triggerable RGD peptide for photocontrolled targeted drug delivery: Synthesis and photolysis studies. *J. Org. Chem.* **2016**, *81* (23), 11556–11564.

114. Luo, J.; Uprety, R.; Naro, Y.; Chou, C.; Nguyen, D. P.; Chin, J. W.; Deiters, A. Genetically encoded optochemical probes for simultaneous fluorescence reporting and light activation of protein function with two-photon excitation. *J. Am. Chem. Soc.* **2014**, *136* (44), 15551–15558.
115. Goswami, P. P.; Syed, A.; Beck, C. L.; Albright, T. R.; Mahoney, K. M.; Unash, R.; Smith, E. A.; Winter, A. H. BODIPY-derived photoremovable protecting groups unmasked with green light. *J. Am. Chem. Soc.* **2015**, *137* (11), 3783–3786.
116. Bañuelos, J. BODIPY dye, the most versatile fluorophore ever? *Chem. Rec.* **2016**, *16* (1), 335–348.
117. Waddell, P. G.; Liu, X.; Zhao, T.; Cole, J. M. Rationalizing the photophysical properties of BODIPY laser dyes via aromaticity and electron-donor-based structural perturbations. *Dyes Pigments* **2015**, *116*, 125–131.
118. Bañuelos, J.; Arbeloa, F. L.; Arbeloa, T.; Salleres, S.; Amat-Guerri, F.; Liras, M.; Arbeloa, I. L. Photophysical study of new versatile multichromophoric diads and triads with BODIPY and polyphenylene groups. *J. Phys. Chem. A* **2008**, *112* (43), 10816–10824.
119. Umeda, N.; Takahashi, H.; Kamiya, M.; Ueno, T.; Komatsu, T.; Terai, T.; Hanaoka, K.; Nagano, T.; Urano, Y. Boron dipyrromethene as a fluorescent caging group for single-photon uncaging with long-wavelength visible light. *ACS Chem. Biol.* **2014**, *9* (10), 2242–2246.
120. Treibs, A.; Kreuzer, F.-H. Difluorboryl-komplexe von di- und tripyrrylmethenen. *Justus Liebigs Ann. Chem.* **1968**, *718* (1), 208–223.
121. Slanina, T.; Shrestha, P.; Palao, E.; Kand, D.; Peterson, J. A.; Dutton, A. S.; Rubinstein, N.; Weinstain, R.; Winter, A. H.; Klán, P. In search of the perfect photocage: Structure–reactivity relationships in meso-methyl BODIPY photoremovable protecting groups. *J. Am. Chem. Soc.* **2017**, *139* (42), 15168–15175.
122. Peterson, J. A.; Wijesooriya, C.; Gehrmann, E. J.; Mahoney, K. M.; Goswami, P. P.; Albright, T. R.; Syed, A.; Dutton, A. S.; Smith, E. A.; Winter, A. H. Family of BODIPY photocages cleaved by single photons of visible/near-infrared light. *J. Am. Chem. Soc.* **2018**, *140* (23), 7343–7346.
123. Rumyantsev, E. V.; Alyoshin, S. N.; Marfin, Y. S. Kinetic study of BODIPY resistance to acids and alkalis: Stability ranges in aqueous and non-aqueous solutions. *Inorg. Chim. Acta* **2013**, *408*, 181–185.
124. Wang, M.; Vicente, M. G. H.; Mason, D.; Bobadova-Parvanova, P. Stability of a series of BODIPYs in acidic conditions: An experimental and computational study into the role of the substituents at boron. *ACS Omega* **2018**, *3* (5), 5502–5510.
125. Palomo, J. M. Solid-phase peptide synthesis: An overview focused on the preparation of biologically relevant peptides. *RSC Adv.* **2014**, *4* (62), 32658–32672.

Chapter 2

The synthesis of Coumarin and BODIPY Photocages

2.1 Photocage selection criteria

In this chapter, the synthesis of the photocages required for our approach is discussed. Before these photocages were synthesised there were several key factors to consider which governed their selection. Of the utmost importance was biocompatibility, due to the fact that we hoped to employ the synthesised photocages in a biological context. Consequently, it was imperative that the chosen photocages be cleavable using visible wavelengths of light. As mentioned in section 1.2.1 of the previous chapter, the energy of light is inversely proportional to its wavelength.[1,2] As such, longer wavelength, visible light is inherently more biocompatible than its UV counterpart, the high energy of which can impact cell viability through processes such as photobleaching and DNA damage.[3,4] As discussed in section 1.4 of the previous chapter, o-nitrobenzyl based photocages typically absorb within the UV region Although some derivatives have been cleavable at wavelengths of up to 420 nm which is within the visible range,[5] the maximum one-photon cleavage wavelengths of this class have stagnated at this point. Additionally, the decaging mechanism of this class of photocage results in the formation of *o*-nitrosobenzaldehyde which is a known cytotoxin.[6,7] As such we decided to disregard this class of compound in favour of coumarin and BODIPY-based photocages due to their typically longer cleavage wavelengths and inert nature of their respective byproducts.

Another key consideration was the fact that the system which we desired to develop necessitated the sequential activation of photocages, meaning that there was a requirement for orthogonal decaging. In order to maximise the potential for selective photocleavage, it was imperative that the absorption profiles of the selected photocages exhibit as minimal overlap as possible, as seen in figure 1 below. As discussed in section 1.4 of the previous chapter, coumarin and BODIPY photocages have undergone extensive derivatisation since their initial development, meaning that photocages cleavable from 380 nm all the way up to 700 nm exist

across these classes.[8,9] This makes these families of compounds potentially viable for sequential activation within mixtures.[10]

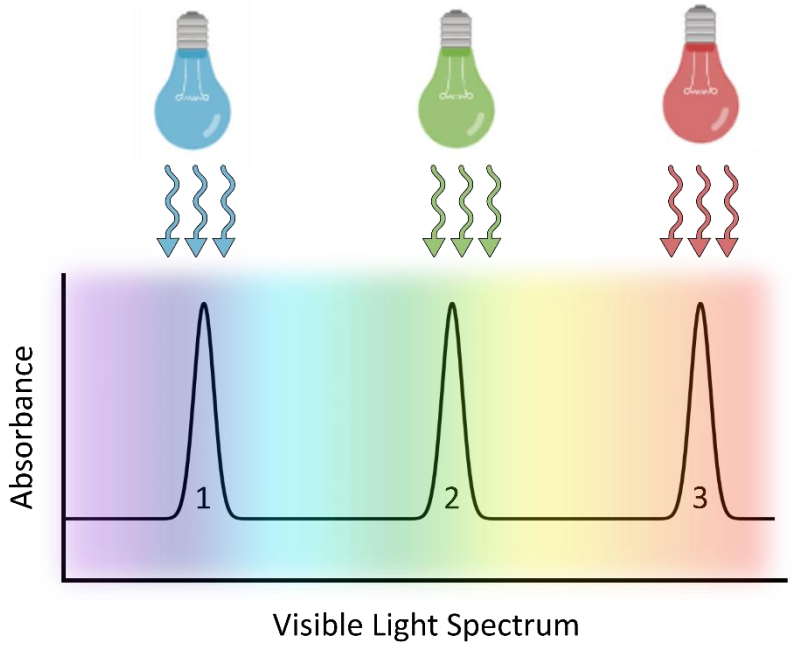

Figure 1: A schematic representation of the ideal photocage absorption profiles to allow for orthogonal decaging

Finally, although coumarin and BODIPY photocages have been developed that are cleavable across a broad range of visible wavelengths, the structures of red-shifted derivatives are often complex.[9,11,12] The synthesis of such derivatives typically involves multi-step procedures which can be difficult and time consuming. Additionally, many of these photocages have previously been made on mg scale, meaning that although their photoreactivity has been investigated, they have not been implemented functionally. Given the nature of our work, we required substantial quantities of each photocage to allow for optimisation of the final system in the future. Consequently, it was important that we optimised any synthetic routes that were low yielding or laborious, so that photocages could be produced at a reasonable scale.

2.2 The selection of coumarin photocages

Now that key selection criteria for the final photocages had been identified, it was time to select appropriate derivatives. 7-diethylamino-4-hydroxymethyl coumarin derivative **(1)**, had previously been developed by Kaupp et al. and had been shown to exhibit efficient decaging at wavelengths of between 360 – 440 nm.[8] This range lies just within the visible range of the electromagnetic spectrum making it ideal for orthogonal cleavage alongside red-shifted derivatives.[10] Additionally, **(1)** was a key intermediate in the synthesis of **(2)** by Kele et al.[11] **(2)** had a reported λ_{max} of 493 nm which is in the green region of the visible light spectrum allowing for efficient cleavage at wavelengths between 500 – 544 nm. Crucially **(1)** absorbs minimally in this range maximising the potential for orthogonal decaging. A scheme depicting the proposed synthetic route for the production of these compounds can be seen in scheme 1 below.

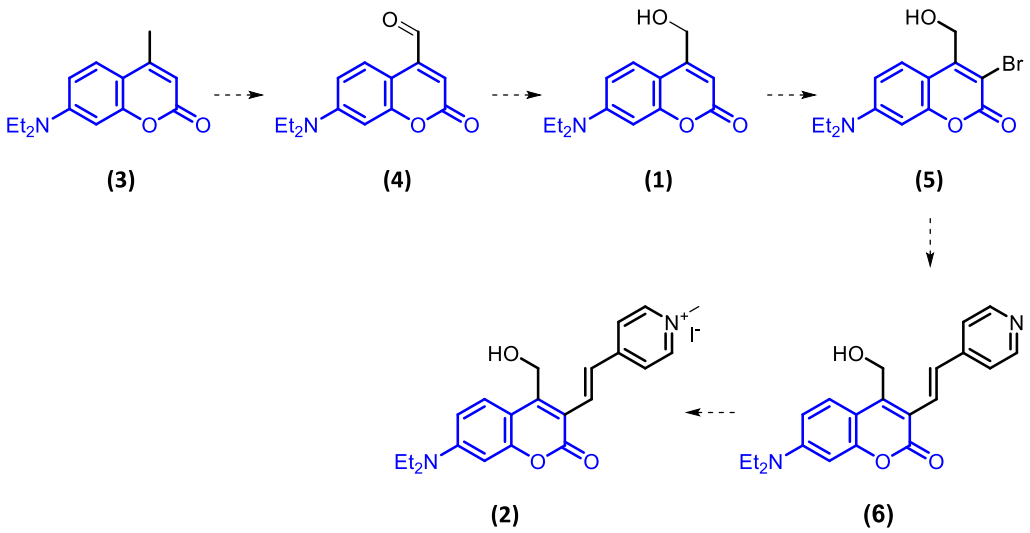

Scheme 1: A schematic of the proposed synthetic route for the production of the final coumarin photocages to be used in this work

2.3 The synthesis of coumarin photocages

2.3.1 The synthesis of **(1)**

The first photocage to be synthesised was 7-(diethylamino)-4-(hydroxymethyl)coumarin **(1)**. Initially, this was attempted *via* a selenium dioxide mediated Riley oxidation of 7-diethylamino-4-methyl coumarin to form **(4)** as previously described by Nakajima & Ito.[13] Following this, the resulting aldehyde was reduced to the desired alcohol using sodium borohydride as seen in scheme 2 below.

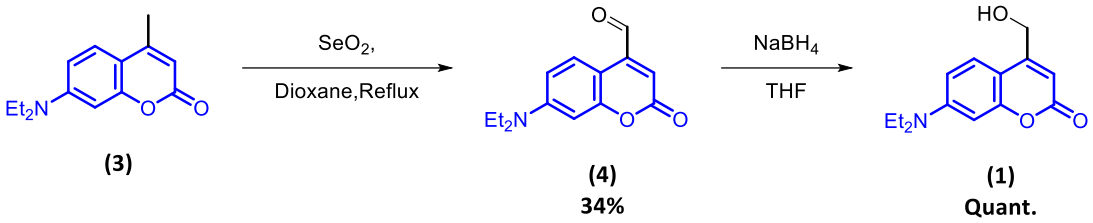

*Scheme 2: A schematic of the initial synthesis of **(1)** via an SeO_2 mediated oxidation followed by reduction with $NaBH_4$.*

Although the above synthesis was successful, it presented several problems. Most notably, the initial Riley oxidation resulted in the formation of selenium-based byproducts. Although not characterised, these byproducts were presumed to be a mixture of unreacted selenium dioxide alongside other organoselenium species such as selenous acid. These impurities formed a dark, viscous residue which adhered strongly to the reaction vessel as well as the product mixture. The resulting mixture exhibited poor resolution upon attempting flash column chromatography, meaning that purification of the desired product was difficult. This had a negative impact on yield, with a highest recorded yield of 34%. Additionally, this issue was exacerbated at scales above 1g, posing a significant obstacle to scalability, therefore limiting our ability to produce sufficient quantities of this compound for our research purposes.

This challenge had also previously been encountered by Göbel et al,[14] who proposed an alternative synthetic route involving an initial condensation of **(3)** with N,N-dimethylformamide dimethyl acetal (DMF-DMA) to form the corresponding enamine **(7)** which then readily undergoes conversion to the corresponding aldehyde **(4)** *via* oxidation with sodium periodate. The desired alcohol **(1)** could then be obtained once again by reduction with $NaBH_4$.

We set about following the above literature route,[14] making several alterations to maximise yield and throughput. In the literature route the crude product of this oxidation step **(4)** was reduced directly and then purified by column chromatography. However, during our synthesis we found that the main impurity present during this process was unreacted enamine **(7)**, which was similar in polarity to the final alcohol **(1)** making purification by column chromatography at the end of the route difficult. Thus, we decided to remove this impurity by performing column chromatography following the oxidation step. The aldehyde **(4)** formed as a result of this reaction was significantly less polar than the enamine starting material **(7)** and so purification was easily achieved using column chromatography. Following this purification, the reduction could be carried out, and upon quenching of the $NaBH_4$ using saturated aqueous $NaHCO_3$ solution, the product could be isolated in quantitative yields without the need for further purification. The final synthetic route is described in scheme 3 below. This optimisation enabled a maximum yield over three steps of 57% to be obtained, and reactions could be performed on up to a 20 g scale which was much greater than previous attempts. This not only provided us with sufficient quantities of **(1)** for future peptide photocaging, as discussed in Chapter 4 but also provided us with sufficient quantities of starting material for the synthesis of red-shifted derivative **(2)** which is discussed in the following sections. Notably the acetate form of **(1)**, which was used for the decaging studies discussed in chapter 4 was

synthesised by brominating the 4-methyl group followed by nucleophilic attack by KOAc as discussed in section 3.5 of the next chapter.

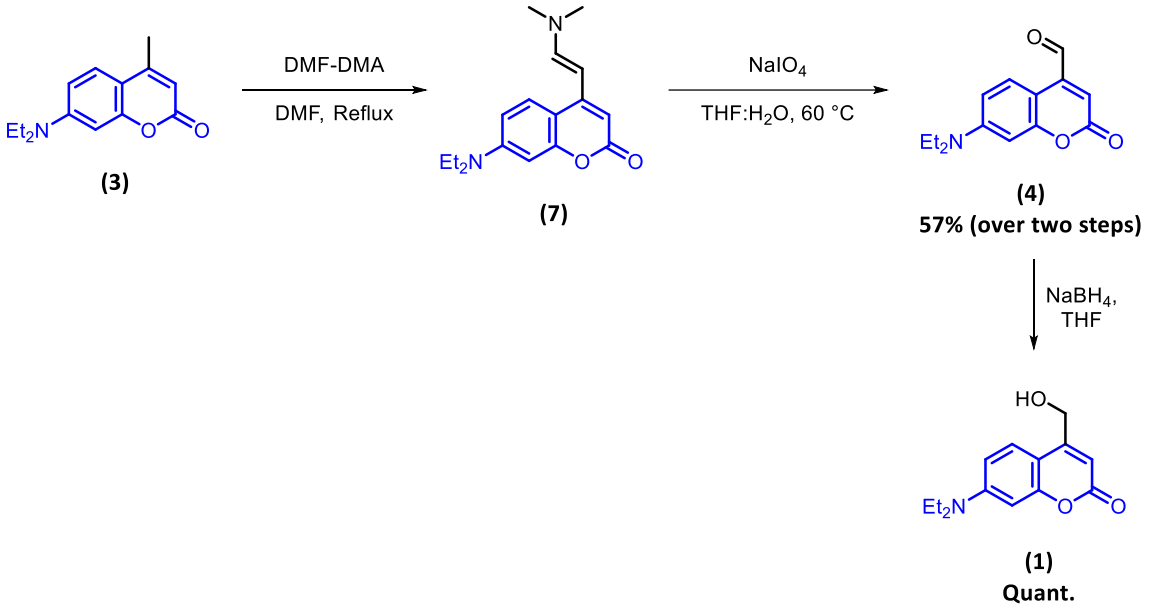

*Scheme 3: A schematic of the optimised synthetic route for the production of **(1)***

2.3.2 The synthesis **(5)**

Following the successful synthesis of **(1)**, the synthesis of the brominated derivative **(5)** was attempted. The addition of a bromine atom at the 3-position provides a handle for palladium cross coupling, allowing for the future production of red-shifted coumarin derivatives as seen in scheme 1 above. Prior to brominating **(1)**, it was decided that conditions would first be trialled using **(3),** in order to prevent wastage of valuable material**.** Initially, the bromination was attempted using Br_2 and triethylamine following the procedure of Pereira et al. as seen in scheme 5 below.[15] Although this bromination was successful, selectivity was poor which resulted in the suspected bromination of several other positions and the production of multiple side products. Purification by column chromatography was successful but unfortunately a yield of just 30% was obtained. As such, a more selective bromination reaction was required. Kele et al. had previously utilised *N*-bromosuccinimide (NBS) as a mild source

of electrophilic bromine and thus this reagent was trialled.[11] Not only did this reagent achieve excellent selectivity, with only bromination of the desired 3-position observed, but it also proceeded much more quickly, going to completion within 30 mins rather than the overnight reaction conditions which were required during the previous synthesis. Following purification, a yield of 84% was obtained which represented a significant increase in comparison to the original conditions as seen in scheme 4 below.

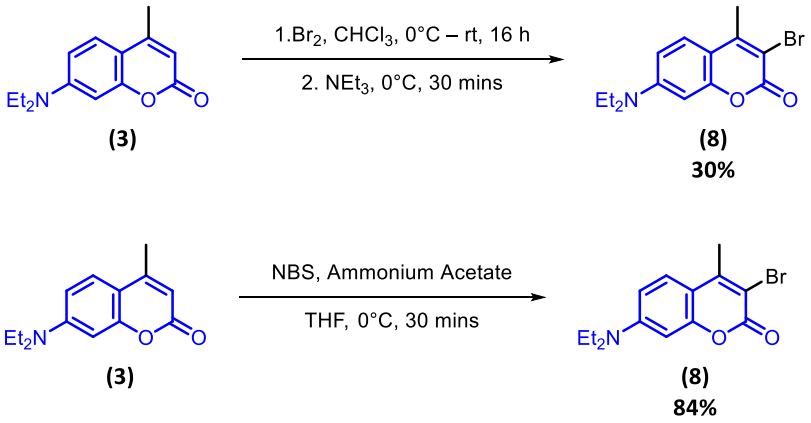

*Scheme 4: A schematic of the conditions trialled for the bromination of **(3)***

Following on from this optimisation, the chosen conditions were used to brominate **(1)**. This reaction was once again successful and a yield of 70% was obtained following purification. This scheme is seen in scheme 5 below.

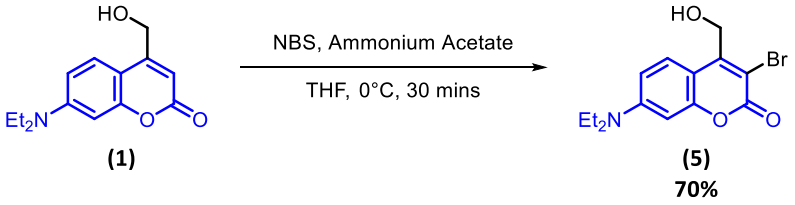

*Scheme 5: The final conditions used in the bromination of **(3)***

2.3.3 The synthesis of (6)

Following the successful installation of the bromine atom at the 3-position, it was time to attempt to couple the coumarin scaffold to a 4-vinyl pyridine group *via* a palladium-mediated Heck coupling. As discussed in section 1.4.2.5 of the previous chapter, the introduction of a vinyl group at the 3-position allows for the extension of the π-system, lowering the HOMO-LUMO energy gap and leading to a red-shift in absorbance.[16,17] This effect is amplified by forming a donor-π-acceptor system whereby the 7-diethylamino group can donate electron density across the π-system and into an electron acceptor, which in the case of this molecule is the pyridine ring (especially once N-alkylated as discussed in the following section).[11,18]

Once again, we first attempted to optimise conditions using methyl coumarin **(8)**, in order to avoid wastage of valuable material. This reaction was performed under microwave conditions and utilised Q-Phos as a coordinating ligand as described by Kele et al, with the product **(9)** being isolated as an orange solid with a yield of 38% as seen in scheme 6 below.[11] Although this reaction was successful, Q-Phos is a relatively expensive ligand costing approximately £70 per 100 mg. Thus, if this reaction were to be repeated at greater scale, a more cost-effective source of phosphine ligand would be preferable. As such, we decided to repeat the reaction under identical conditions but varying the phosphine ligand from Q-Phos to PPh_3. Not only was this reaction still successful, but it also provided an increase in yield from 38% to 60%.

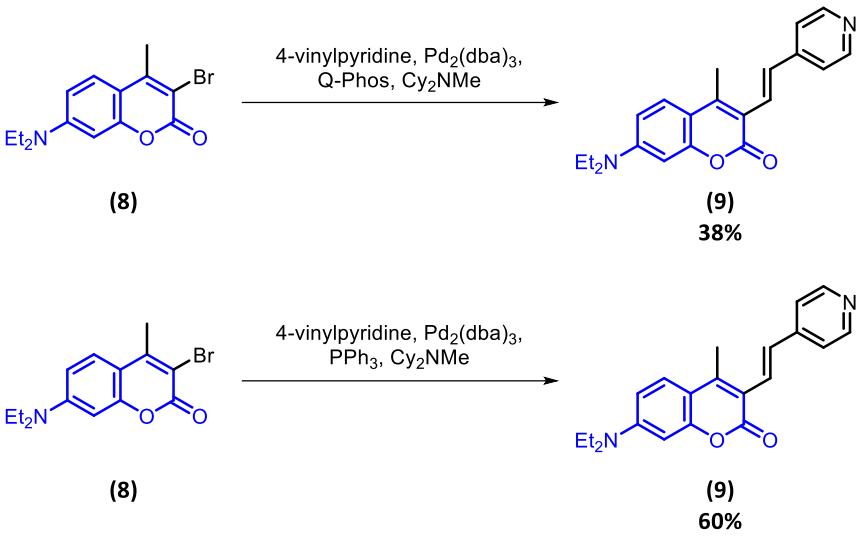

Scheme 6: A schematic of the conditions trialled for the palladium mediated Heck coupling

The optimised conditions were then applied to **(5)** affording the desired product **(6)** in a 61% yield as seen in scheme 7 below.

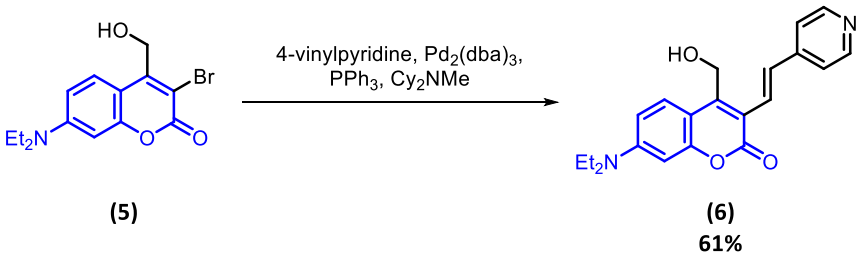

*Scheme 7: The final conditions for the synthesis of **(6)***

2.3.4 The synthesis of **(2)**

Following the successful synthesis of **(6)**, it was now time to attempt an *N*-alkylation in order to form the desired red-shifted photocage **(2)**. Again, this was first optimised using the methyl version **(9)** and was attempted using methyl iodide using conditions described by Kele et al. as seen in scheme 8 below.[11] Unfortunately, upon attempting this synthesis we quickly encountered issues. Firstly, it was found that purification by column chromatography was extremely difficult due to the polar nature of **(10)**, with an eluent system of 20% MeOH in DCM failing to elute it from a silica column. Thus, we had to explore alternative methods of

purification. Reverse-phase chromatography was first trialled, however, it was found that once again we were unable to elute **(10)** from the column. Following this, we attempted to precipitate the product using ice-cold diethyl ether. This method was more successful and afforded the product as a red/purple solid with a yield of 41 %.

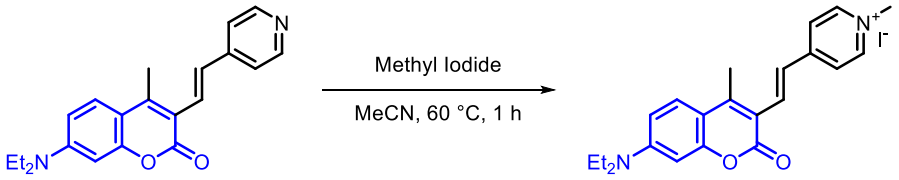

(9) **(10)** **41%**

*Scheme 8: The synthesis of **(10)** using the conditions described by Kele et al.*[11]

Although, the above synthesis was successful, it was at this point that we encountered another issue with this compound, its lack of solubility in NMR solvents and therefore difficulty of analysis. Although mass spectrometry did provide some evidence that the correct product had been formed, we found it impossible to obtain an NMR spectrum of **(10)**. Kele et al. had utilised a mixture of $CDCl_3$:CD_3OD 1:1 *v:v* for analysis of the related compound **(11).**[11] However, when we attempted to use this system, it was found that our compound remained insoluble. Other NMR solvents such as deuterated DCM, D_2O, and DMSO (d_6) were all trialled, however, it was found that **(10)** was insoluble in all available deuterated solvents, meaning that full characterisation was not obtained.

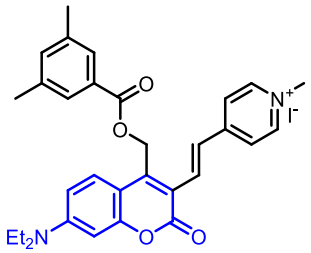

(11)

Figure 2: The structure of the extended coumarin photocage utilised in the caging of 3,5-dimethylbenzoic acid by Kele et al [11]

Although, we were unable to fully characterise **(10)**, we decided to continue with the synthesis of **(2)** in the hope that it would be more soluble due to the presence of its hydroxyl group. Upon attempting this synthesis, a yield of 66% was observed as seen in scheme 9, however, once again we failed to obtain an NMR spectrum due to the insolubility of **(2)** in the available NMR solvents.

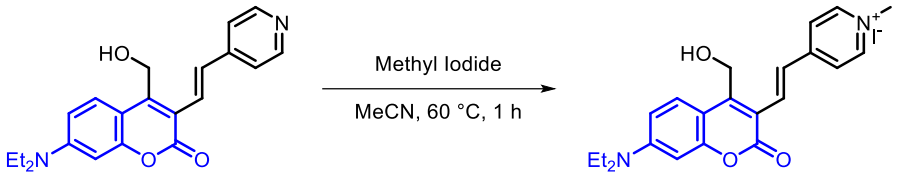

(6) **(2)** **66%**

*Scheme 9: Schematic of the conditions employed for the initial synthesis of **(2)***

In order to address the problems presented by the insolubility of **(2)**, it was rationalised that if a different counterion could be introduced, it may lead to an increase in solubility. We initially explored the trifluoromethanesulfonate (triflate) anion in the hope that this would aid solubility. Rather than attempting salt metathesis in order to achieve counterion exchange, we instead opted to repeat the synthesis again using methyl triflate rather than methyl iodide. Immediately the effect of this new reagent could be seen. Rather than requiring heating at 60 °C for 1 h with methyl iodide, full conversion was achieved after just 15 mins at 0 °C as seen in

scheme 10 below. Following successful purification by precipitation from diethyl ether, we found that the triflate counterion enhanced solubility in MeCN allowing NMR characterisation. This synthesis proved robust and reproducible, and was routinely performed on a 100 mg scale, providing sufficient quantities of the final compound for our research purposes.

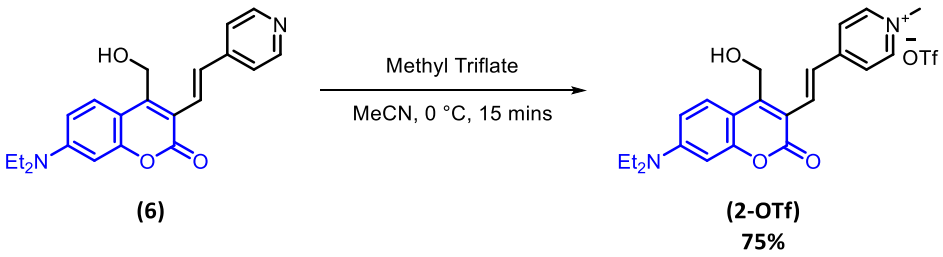

(6) **(2-OTf)** **75%**

*Scheme 10: Schematic of the conditions utilised for the of **(2-OTf)**.*

Additionally, following a successful crystallisation from MeCN, a crystal structure of **(2-OTf)** was also obtained which can be seen in figure 3 below, further confirming the formation of the desired product. Looking at this crystal structure, it can be seen that structure of this molecule is rigid, maintaining a planar structure throughout. This planar nature allows for extended conjugation of the π-system, which facilitates the red-shift in absorbance relative to photocage (**1).**

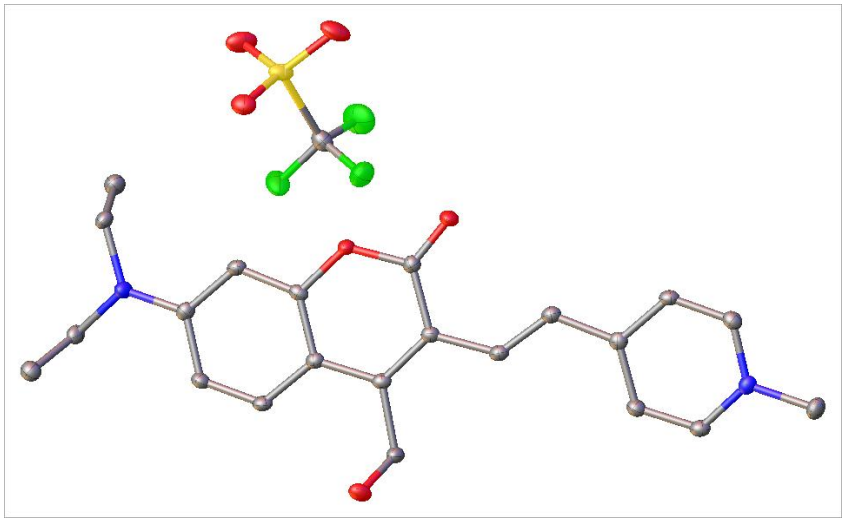

*Figure 3: The crystal structure generated based on the XRD data obtained for **(2).***

Following the successful synthesis of **(2-OTf)**, we set out to synthesise its acetate form for use in the decaging study discussed in section 4.5 of Chapter 4. The final route is described in scheme 11 below.

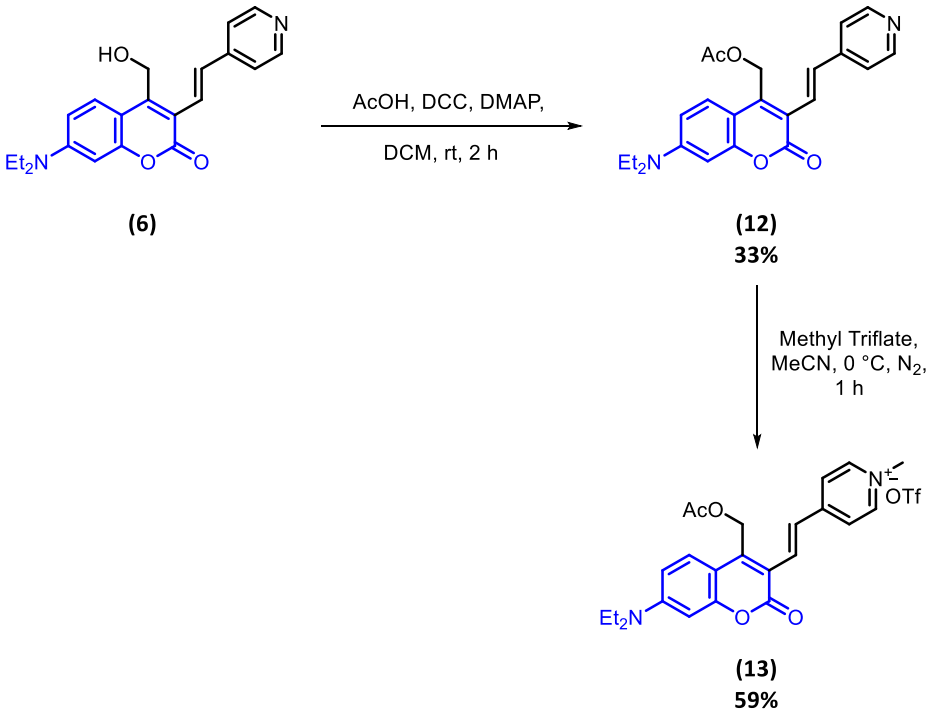

*Scheme 11: Schematic of the synthetic route for the production of **(13)**, which will be used as a substrate for the decaging study of **(2-OTf)** in Chapter 4.*

2.4 The selection of BODIPY photocages

Following the successful synthesis of coumarin photocages **(1)** and **(2-OTf)**, we aimed to synthesise photocages based on the BODIPY scaffold. The aforementioned photocages had absorption maxima at 380 and 500 nm respectively, as discussed later, and thus photocages with absorption maxima beyond this range were required. The initial target was **(15),** a BODIPY photocage produced by Winter et al.[19] Although, this photocage has an absorption maximum at 510 nm which is similar to **(2)** (501 nm), it absorbs over a much narrower range, which may allow for more selective photocleavage. Additionally, it serves as a starting material for the production of the extended derivative **(17)** which has a reported maximum of 661 nm, much further into the red range.[9] The proposed synthetic routes for the production of these photocages are seen in scheme 12 below.

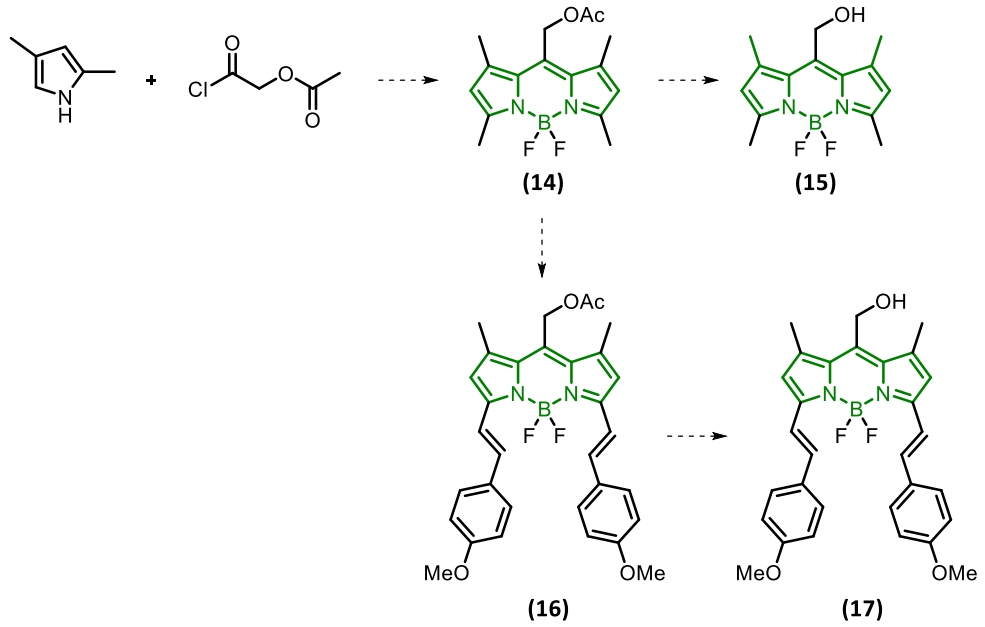

*Scheme 12: A schematic of the proposed synthetic route toward BODIPY photocages **(15**) and **(17)***

2.5 The synthesis of BODIPY photocages

2.5.1 The synthesis of **(14)**

Synthesis of the BODIPY photocages began with the production of the acetoxy BODIPY starting material **(14).** This synthesis involved a condensation reaction between 2,4-dimethylpyrrole and acetoxyacetyl chloride to produce the dipyrromethene backbone followed by a base catalysed *in situ* complexation of $BF_3.OEt_2$ forming **(14)** as described by Cosa & Krumova.[20] This reaction had a reported yield of 75%, however, when we attempted this synthesis a yield of just 11% was recorded. This low yield could be attributed to the large amount of polypyrrole that was formed as a result of pyrrole polymerisation. Some of this side product could be attributed to impurities present within the starting material, however, upon monitoring the reaction by TLC, it was clear that a significant quantity was also being formed during the initial condensation reaction. Not only did this competing polymerisation side reaction negatively impact yield *via* a competing reaction pathway, but the polymer formed was difficult to remove by column chromatography which further impacted yield. Thus, it was clear that some optimisation of the reaction conditions was required to reduce polymerisation. During their synthesis Cosa & Krumova performed the initial condensation reaction at reflux in DCM.[20] It was rationalised that heating the reaction mixture may have been contributing to the polypyrrole formation and thus we decided to perform this initial reaction at 0 °C. Upon monitoring the reaction progression by TLC, it was found that a significantly smaller quantity of polymer was being formed. As such, we also decided to perform the following complexation step at 0 °C. Upon completion of the reaction and subsequent purification, a yield of 36% was recorded as seen in scheme 13 below. Although this was significantly lower than the yield reported by Cosa and Krumova,[20] the fact that this step was at the beginning of the synthetic

route and could be easily repeated in order to gain access to more material meant that it was acceptable for our purposes. As such we decided to continue along the synthetic route.

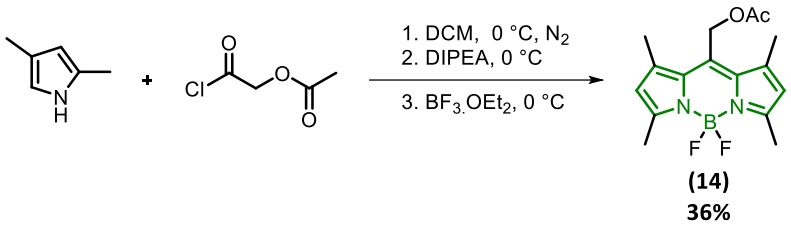

*Scheme 13: The final conditions used for the synthesis of **(14)***

2.5.2 The synthesis of (15)

Following the successful synthesis of the key intermediate **(14)**, we attempted to synthesise photocage **(15)**. Once again, we initially attempted this synthesis following the conditions published by Cosa & Krumova as seen in scheme 14 below.[20]

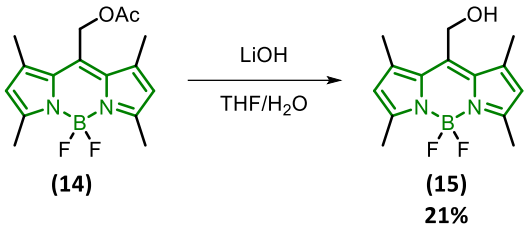

*Scheme 14: The initial conditions used for the synthesis of **(15)***

A yield of 21% was obtained which was significantly lower than the literature yield of 70%. Characterisation of the crude product revealed that decomplexation of the central boron atom had occurred, resulting in the formation of a significant quantity of the corresponding dipyrrin. Not only did its unwanted formation compete with the desired reaction pathway, but it also increased the difficulty of purification impacting yield to an even greater extent. Previous reports have demonstrated that bases such as potassium *tert*-butoxide and hydrazine can promote removal of the complexed boron from the BODIPY scaffold. Although these

transformations typically require harsher microwave conditions,[21,22] they nonetheless demonstrate the potential for boron decomplexation under basic conditions. Consequently, it is conceivable that the lithium hydroxide utilised in the above reaction was causing degradation of the BODIPY scaffold resulting in the observed loss in yield. Thus, we postulated that if milder deprotection conditions could be employed, the formation of this undesirable side product could be limited improving yields. We first attempted a Zemplén deacetylation, using sodium methoxide in methanol.[23] However, this reaction was unsuccessful, and once again resulted in the formation of the dipyrrin species through decomplexation of the central boron atom. Potassium carbonate in methanol is widely used as a mild deprotection system in oligonucleotide and carbohydrate chemistry, particularly for removal of protecting groups such as Fmoc and acetates.[24,25] Accordingly, K_2CO_3/MeOH was evaluated as a milder deprotection protocol for the synthesis of **(15)**. These conditions proved to be much more effective and afforded the product in a yield of 83%, without the need for additional purification as seen in scheme 15. This represented a significant improvement over the initial conditions detailed in scheme 14.

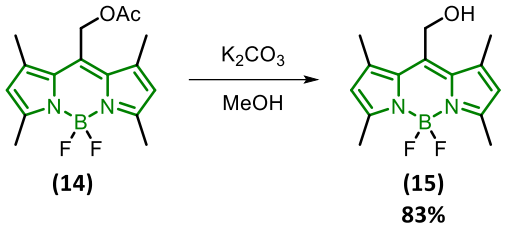

(14) **(15)** **83%**

Scheme 15: K_2CO_3 in methanol provided a milder source of methoxide ions for acetate deprotection affording the desired product in an 83% yield.

2.5.3 The synthesis of **(16)**

Subsequent to the successful synthesis of **(15)** we attempted to synthesise the π-extended derivative **(16).** The extension of the π-system was achieved through the installation of methoxystyrene groups at the 3- and 5- positions of the BODIPY core. This has the effect of closing the HOMO-LUMO energy gap allowing for the promotion of an electron using lower-energy, higher-wavelength light as explained in section 1.4.3.6 of the introductory chapter. The synthesis of this compound was achieved using the procedure outlined by Winter et al. with a yield of 93% achieved as seen in scheme 16 below.[9] This reaction operates *via* a Knoevenagel condensation mechanism,[26] whereby the α-methyl group of the BODIPY scaffold is deprotonated and acts as a nucleophile, attacking the carbonyl group of the *p*-anisaldehyde, before undergoing dehydration to form the desired alkene. This process exists in equilibrium and so the reaction was performed under vacuum, removing water as it was formed and shifting the equilibrium towards product formation in order to maximise yield.

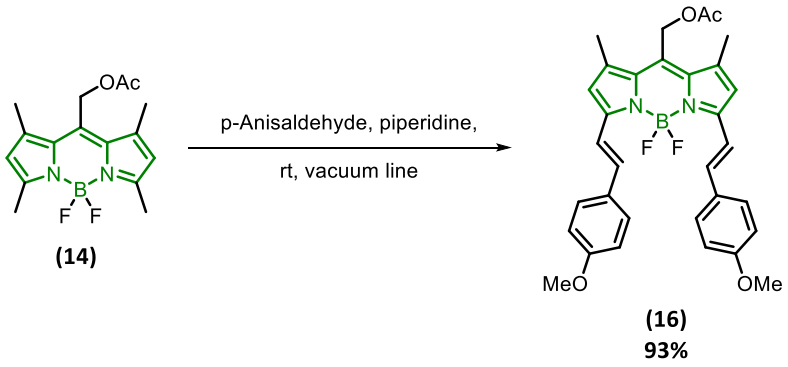

*Scheme 16: A schematic depicting the conditions used for the synthesis of **(16)***

2.5.4 The synthesis of alternative BODIPY photocages

During this work, a number of additional BODIPY photocages were synthesised in order to provide alternative photocaging options and to circumvent some of the synthetic complications detailed above. The synthesis of **(15)** had previously presented problems as the

LiOH mediated hydrolysis of the acetate group had led to decomplexation of the central boron atom as discussed in section 2.5.2. Previously Winter et al. had achieved this hydrolysis by treating **(14)** with methyl magnesium bromide.[27] This method not only avoided boron decomplexation but also exchanged the fluorines present on the boron atom for methyl groups resulting in the formation of **(18)**. Unlike fluorine, which is strongly electron withdrawing, the methyl substituents are electron donating, facilitating stabilisation of the methyl carbocation formed during heterolytic bond cleavage, and thus increasing the decaging quantum yield.[27] The synthesis of BODIPY photocage **(18)** is described in scheme 17 below. Not only was the desired product afforded in a quantitative yield, but no further purification was required following extraction of the aqueous layer with DCM, representing a significant improvement over the original synthesis of **(15)**.

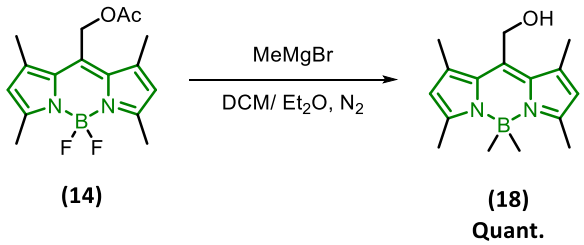

(14) **(18)** **Quant.**

*Scheme 17: Schematic of the conditions utilised for the synthesis of **(18).**[27]*

In addition to the difficulties faced during the synthesis of **(15)**, we also experienced challenges whilst synthesising its precursor **(14)**, with a maximum recorded yield of 36% recorded following optimisation. The reaction used to form **(14)** involved a condensation reaction between 2,4-dimethylpyrrole and acetoxyacetyl chloride to produce the dipyrromethene backbone followed by a base catalysed *in situ* complexation of $BF_3.OEt_2$. This is the most commonly employed reaction in the production of BODIPYs,[19,20,27,28] however,

meso-benzyl alcohol BODIPY **(19)** had previously been produced using an alternative synthetic route.[29] Although this BODIPY scaffold, was different to the *meso*-methyl derivatives that have been considered up to this point, it was hoped that the planar nature of the aromatic ring would maintain the rigidity of the BODIPY scaffold, limiting its effect on the photophysical properties of the compound and facilitating decaging.

Our synthesis began with the production of aromatic aldehyde **(20)** *via* a $NaBH_4$ mediated reduction of terephthalaldehyde **(21)**. Initially this reduction was attempted at rt using 1 eq. of $NaBH_4$, however it was found that the reaction proceeded too quickly resulting in the formation of the di-hydroxy product. Each equivalent of $NaBH_4$ contains 4 equivalents of hydride and so in the hope of improving selectivity, the number of equivalents of $NaBH_4$ was reduced to 0.25 eq. Additionally the reaction was also performed at -20 °C. These changes dramatically increased selectivity for the mono-hydroxy product and following purification a yield of 74% was obtained. Following the successful synthesis of **(20)**, **(19)** was successfully produced using the conditions seen in scheme 18 below.

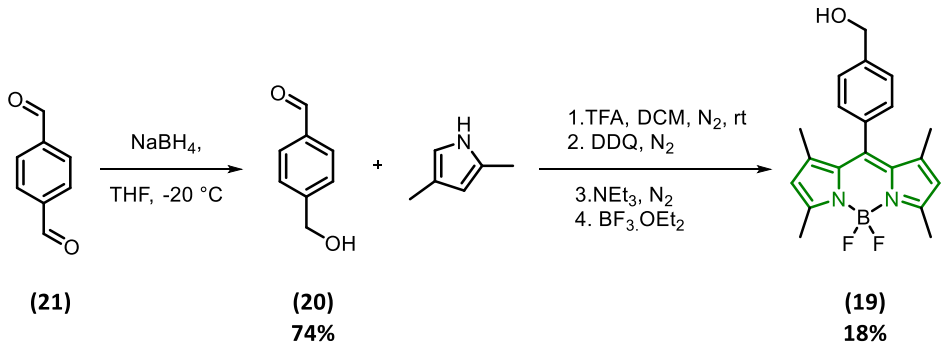

(21) **(20)** **74%** **(19)** **18%**

*Scheme 18: A schematic of the synthetic route utilised for the production of **(19)***

Following successful purification, **(19)** was dissolved in a minimum amount of DCM and allowed to crystallise at 4 °C over the course of several weeks. The resulting crystals formed were subjected to XRD analysis producing the crystal structure seen in figure 4 below. Looking

at this crystal structure, it can be seen that the *meso*-benzyl alcohol moiety lies perpendicular to the core BODIPY scaffold, thus interrupting the planar nature of this molecule. Similar interruptions to the planarity of the BODIPY scaffold had previously been shown to allow for non-radiative decay upon formation of the excited state resulting in a reduction in decaging quantum yield due to the existence of competing pathways.[27] Alongside this, the synthesis of this compound was once again low yielding due to the formation of polypyrrole, which required two columns to completely remove. As such, it was deemed that the synthesis of **(19)** did not provide any benefits over the synthesis of **(14)** described in section 2.5.1, meaning that we chose to optimise the synthesis of **(14)** rather than continuing to pursue this compound.

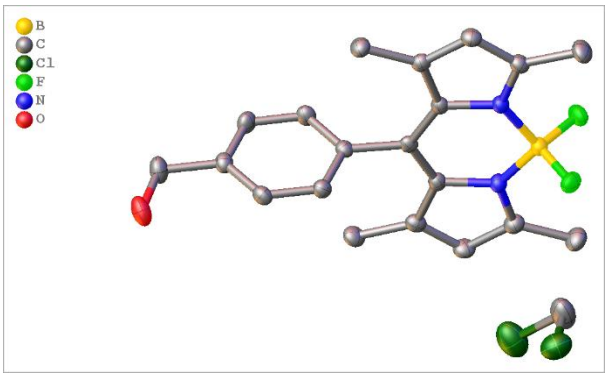

*Figure 4: The crystal structure generated from the XRD data obtained for **(19)***

2.6 UV-Vis spectra of the final photocages

Now that the desired photocages had been successfully synthesised, photophysical characterisation was required in order to confirm that they had distinct absorption profiles. The absorption spectra of the final photocages in methanol can be seen in figure 5 below. Looking at these spectra it can be seen that whilst there is some overlap in absorbance, the absorption maxima of these compounds lie within three distinct regions of the visible light spectrum. **(1)** has a λ_{max} of 375 nm which lies within the blue region, just inside the visible light

spectrum. Compounds **(2-OTf)**, **(15)** and **(18)** on the other hand have λ_{max} of 498, 511 and 507 nm respectively, which all lie within the green region. Crucially, at the absorption maxima of these compounds (498 – 511 nm) compound **(1)**, exhibits minimal absorption. This in turn maximises the potential for orthogonal decaging of the aforementioned compounds upon irradiation with green light, as **(1)** would not be expected to decage at these wavelengths due to its minimal absorbance in this region. Finally, compound **(16)** had a λ_{max} of 660 nm which is within the red region of the visible light spectrum. Once again, all of the aforementioned compounds exhibit minimal absorption in this region maximising the potential for orthogonal photocleavage of **(16)** upon irradiation with red light. As such, a sequential decaging system can be envisioned whereby a mixture of caged compounds can first be irradiated with red light in order to decage **(16)**, followed by green light to decage a green light absorbing compound such as **(2)**, before finally irradiating with blue light resulting in the photolysis of **(1).** The potential of such a system to allow for orthogonal, sequential decaging has previously been demonstrated by Winter et al.[10] However, with the optimised synthesis of these compounds as discussed throughout this chapter, we hope to produce sufficient quantities of material whereby this system can eventually be applied to the activation of peptides rather than small molecule model compounds. Decaging studies using these compounds are discussed in Chapter 4 of this thesis.

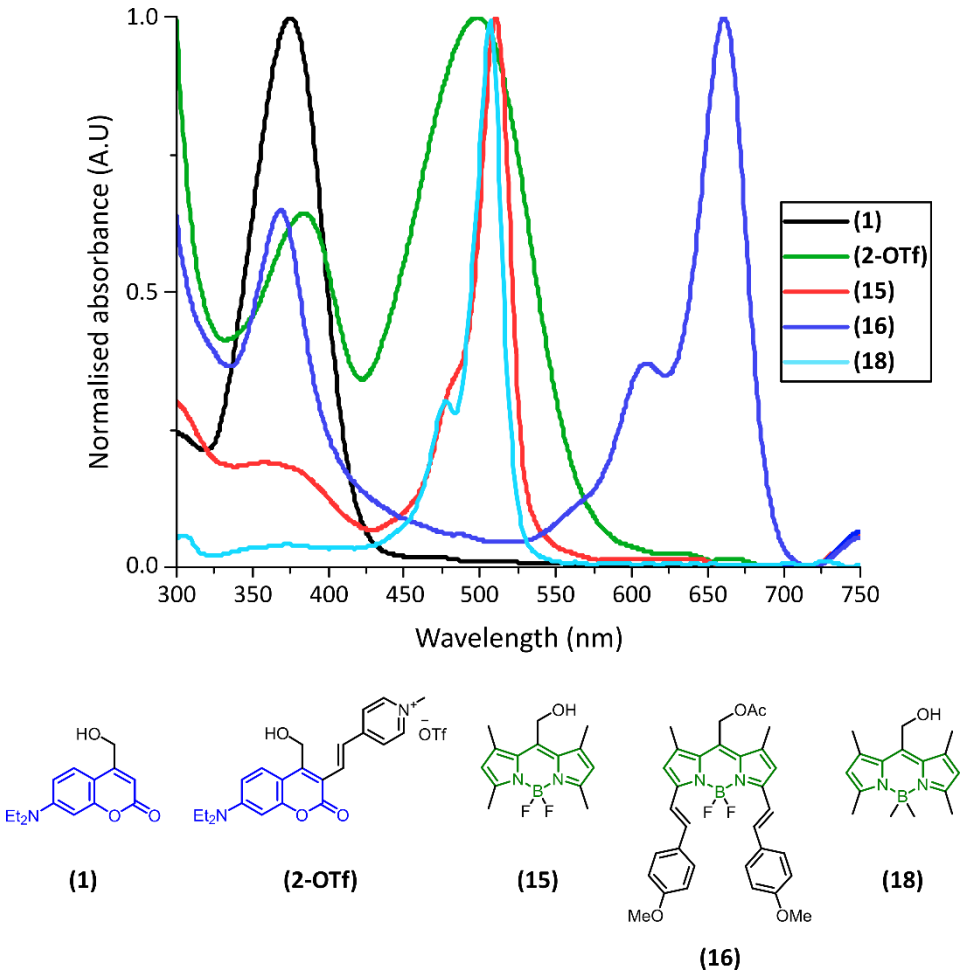

Figure 5: UV-Vis absorption spectra in MeOH of the final photocages produced in this work.

Photocage	λ_{max}	Visible Light Region
(1)	375 nm	Blue
(2-OTf)	498 nm	Green
(15)	511 nm	Green
(16)	660 nm	Red
(18)	507 nm	Green

Table 1: The absorption maxima in MeOH of the final photocages produced during this work.

2.7 Conclusion

The goal of this chapter was to optimise and complete the synthesis of distinctly absorbing photocages. Work began with the synthesis of coumarin photocage **(1)**. Initially synthesis of

this compound was challenging due to poor yields and purification difficulties, primarily arising from selenium-based byproducts generated during the initial Riley oxidation of the methyl group. These challenges were successfully overcome by implementing an alternative synthetic route developed by Göbel et al.,[14] in which the methyl group was first converted to enamine **(7)**, then oxidised to an aldehyde **(4)**, and finally reduced to the desired alcohol **(1)**. This revised route not only allowed for the production of **(1)** in a 57% yield over 3 steps, but it also allowed for better scalability, with this synthesis being completed at scales of up to 20 g, representing a significant improvement over the previous synthesis.

Following the successful synthesis of **(1)**, brominated derivative **(5)** was prepared and subjected to palladium-mediated Heck coupling in order to extend the π-system and generate vinyl-substituted photocage **(6)**. Subsequent *N*-alkylation led to the formation of red-shifted derivative **(2).** Initially the poor solubility of this compound prevented full characterisation. However, his issue was resolved through the use of methyl triflate instead of methyl iodide as an alkylating agent. This afforded the triflate salt of this compound **(2-OTf)** which improved solubility in MeCN, allowing for NMR and crystallographic characterisation of this compound.

Following the successful synthesis of the above coumarin photocages, efforts shifted to the synthesis of BODIPY photocages. Initial synthesis of the acetate-protected BODIPY **(14)** suffered from low yields due to the formation of polypyrrole which acted not only as a competing reaction pathway but also made purification of this compound more difficult as it was difficult to remove using column chromatography. However, performing the condensation and complexation steps at low temperature reduced the formation of this undesirable byproduct, allowing for an improvement in yield alongside better reproducibility due to easier purification. Deacetylation of **(14)** to yield **(15)** initially resulted in decomplexation of the

boron centre, limiting yield, which was attributed to the use of LiOH as a base in this reaction. This challenge was overcome by employing potassium carbonate in methanol, which enabled mild and efficient deprotection. The extended π-system derivative **(16)** was then synthesised *via* a Knoevenagel condensation, and yield was improved by removing water under vacuum to drive the reaction forward.

Following this, alternative BODIPY photocages were also explored. Photocage **(18)** was synthesised by treatment of **(14)** with methyl magnesium bromide, providing an alternative to BODIPY photocage **(15)**.

The synthesis of *meso*-phenol derivative **(19)**, experienced similar challenges to the synthesis of **(14)** in that purification was difficult due to pyrrole polymerisation. Additionally, crystallographic data obtained for this compound indicated that the *meso*-phenol moiety lay perpendicular to the BODIPY scaffold. This imparted an out of plane geometry which could potentially allow for non-radiative decay upon formation of the excited state, negatively impacting decaging quantum yield. For these reasons, we decided not to continue to pursue this compound.

UV-Vis spectra were then obtained for the above photocages. These spectra can be seen in figure 5 above and it was observed that the absorption maxima of these compounds were distributed across three key regions of the visible light spectrum, blue, green and red. It is hoped that the minimal overlap between the absorption profiles of these photocages would allow for sequential, orthogonal decaging of these compounds in the future. However, prior to this decaging studies are required which are discussed in chapter 4 of this thesis.

2.8 Experimental

2.8.1 General Considerations

Proton nuclear magnetic resonance (^{1}H NMR) spectra were recorded on a Jeol ECX-400 (400 MHz) or Bruker AVIIIHD (500 MHz) spectrometer. Carbon nuclear magnetic resonance (^{13}C NMR) spectra were recorded on a Jeol ECX-400 (100 MHz) spectrometer. NMR shifts were assigned using COSY, HSQC and HMBC spectra. All chemical shifts are quoted on the δ scale in ppm using residual solvent as the internal standard (^{1}H NMR: $CDCl_3$ = 7.26; MeOD = 3.31; D_2O = 4.69; DMSO-d_6 = 2.50 and ^{13}C NMR: $CDCl_3$ = 77.16, MeOD = 49.00, DMSO-d_6 = 39.52). Coupling constants (*J*) are reported in Hz with the following splitting abbreviations: s = singlet, d = doublet, t = triplet, q = quartet, sept = septet, m = multiplet, app = apparent, br = broad. High resolution electrospray ionisation (ESI) mass spectra (HRMS) were recorded on a Bruker Campact TOF-MS or a Jeol AccuTOF GCx-plus spectrometer. Nominal and exact *m/z* values are reported in Daltons. Single-crystal X-ray diffraction data were collected on a Rigaku Oxford Diffraction SuperNova diffractometer equipped with an Eos CCD detector using Cu Kα radiation (λ = 1.54184 Å) at low temperature. Data were collected using omega scans and processed using CrysAlisPro. Absorption corrections were applied using standard Gaussian methods.

Structures were solved using direct methods and refined by full-matrix least-squares on F^2 using SHELXL. Molecular graphics and preparation of publication materials were carried out using Olex2.

Thin layer chromatography (TLC) was carried out using aluminium backed sheets coated with 60 F_{254} silica gel (Merck). Visualization of the silica plates was achieved using a UV lamp (λ_{max} = 254, 302, or 366 nm), and/or ammonium molybdate (5% in 2M H_2SO_4), and/or potassium

permanganate (5% $KMnO_4$ in 1M NaOH with 5 % potassium carbonate), and/or ninhydrin (1.5% ninhydrin, 3% AcOH in *n*-butanol), and/or bromocresol green (0.4% bromocresol green in ethanol, basified till blue with 0.1 M NaOH). Flash column chromatography was carried out using Geduran Si 60 (40-63 μm) (Merck). Mobile phases are reported as % volume of more polar solvent in less polar solvent.

Anhydrous solvents were dried using a PureSolv MD 7 Solvent Purification System. Deionized water was used for chemical reactions. All other solvents were used as supplied (Analytical or HPLC grade), without prior purification. Reagents were purchased from Sigma-Aldrich and used as supplied, unless otherwise indicated. Brine refers to a saturated solution of sodium chloride. Petrol refers to the fraction of petroleum ether boiling in the range 40-60 °C. Anhydrous magnesium sulfate ($MgSO_4$) was used as the drying agent after reaction workup unless otherwise stated.

2.8.2 Synthesis

The synthesis of **(4)**: SeO_2 Method

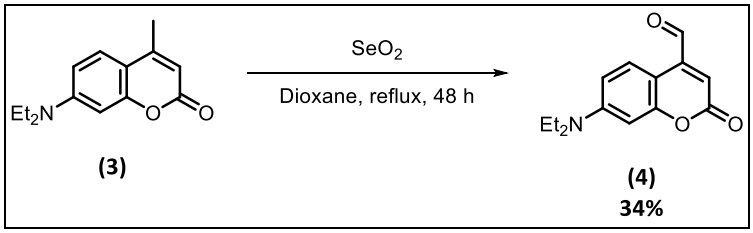

Selenium dioxide (2.2 g, 19.4 mmol) was added to a solution of 7-diethylamino-4-methylcoumarin (3.0 g, 12.9 mmol) in dioxane (75 ml) and the mixture was refluxed for 48 h. After cooling to room temperature, the resulting mixture was filtered through celite and concentrated *in vacuo*. The residue was then purified by flash chromatography (25 % EtOAc: petrol), and pure fractions were combined and concentrated *in vacuo* to afford the product as a red solid with a yield of 1.07 g, 4.4 mmol (34%).

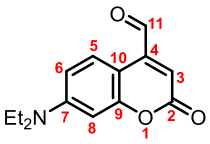

^{1}H NMR (400 MHz, $CDCl_3$) δ 10.02 (s, 1H, C**H**O, H_{11}), 8.31 (d, *J* = 9.1 Hz, 1H, Ar**H**$_5$), 6.64 (dd, *J* = 9.1, 2.6 Hz, 1H, Ar**H**$_6$), 6.53 (d, *J* = 2.6 Hz, 1H, Ar**H**$_8$), 6.45 (s, 1H, Ar**H**$_3$), 3.42 (q, *J* = 7.1 Hz, 4H, N(C**H**$_2$CH$_3$)$_2$), 1.29–1.10 (m, 6H, N(CH$_2$C**H**$_3$)$_2$).

Spectroscopic data were in agreement with [14]

The synthesis of **(4)**: DMF-DMA method

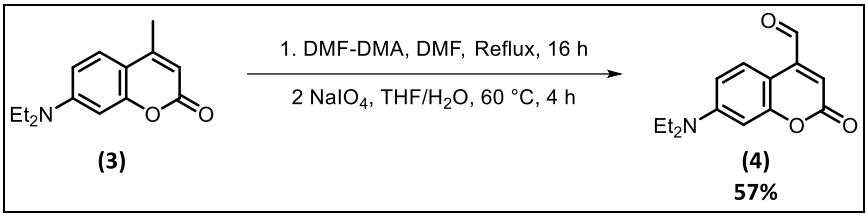

N,*N*-Dimethylformamide dimethyl acetal (2.56 ml, 17.2 mmol, 2 eq.) was added to a solution of 7-diethylamino-4-methyl coumarin (2.0 g, 8.6 mmol, 1 eq.) in DMF (8 ml) and the resulting mixture was refluxed for 16 h. After cooling to rt, sat. aqueous $NaHCO_3$ solution (50 ml) was added. The aqueous was extracted with DCM (3 × 50 ml) and the combined organic layers dried over $MgSO_4$, filtered, and concentrated *in vacuo*. The resulting brown solid was dissolved in THF:H_2O (60 ml, 1:1) prior to the addition of $NaIO_4$ (5.5 g, 25.8 mmol, 3 eq.). The reaction mixture was stirred at 60 °C for 4 h and the resulting precipitate was removed by filtration and washed with EtOAc (50 ml). Sat. aqueous $NaHCO_3$ solution (50 ml) was added to the filtrate and the aqueous was extracted with EtOAc (3 × 50ml). The combined organic layers were dried over $MgSO_4$, filtered, and concentrated *in vacuo.* The residue was then purified using flash chromatography (10% EtOAc: petrol) and pure fractions were combined and concentrated *in vacuo* affording the product as a red solid with a yield of 1.2 g, 4.9 mmol (57%).

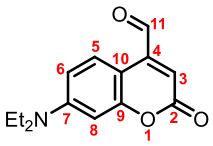

^{1}H NMR (400 MHz, $CDCl_3$) δ 9.99 (s, 1H, C**H**O, H_{11}), 8.26 (d, *J* = 9.1 Hz, 1H, Ar**H**$_5$), 6.60 (dd, *J* = 9.1, 2.6 Hz, 1H, Ar**H**$_6$), 6.48 (d, *J* = 2.6 Hz, 1H, Ar**H**$_8$), 6.41 (s, 1H, Ar**H**$_3$), 3.40 (q, *J* = 7.1 Hz, 4H, N(C**H**$_2$CH$_3$)$_2$), 1.19 (t, *J* = 7.1 Hz, 6H, N(CH$_2$C**H**$_3$)$_2$)

Spectroscopic data were in agreement with [14]

The synthesis of **(1)**

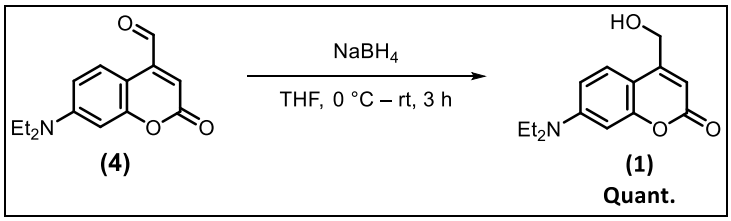

Sodium borohydride (370 mg, 9.8 mmol, 2 eq.) was added in small portions over a 5-minute period to a stirred solution of **(4)** (1.2 g, 4.9 mmol, 1 eq.) in THF (20 ml) at 0 °C [CARE: evolution of hydrogen gas]. The reaction was then warmed to room temperature and stirred for 3 h prior to quenching *via* dropwise addition of sat. $NaHCO_3$ aqueous solution until gas evolution had ceased. Further sat. $NaHCO_3$ solution (50 ml) was then added, and the aqueous was extracted with EtOAc (2 × 100 ml). The combined organics were dried over $MgSO_4$, filtered, and concentrated *in vacuo* to afford the product as a yellow solid with a yield of 1.22 g, 4.9 mmol, (quantitative).

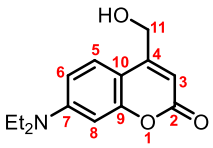

^{1}H NMR (400 MHz, $CDCl_3$) δ 7.30 (d, *J* = 9.1 Hz, 1H, Ar**H**$_5$), 6.55 (dd, *J* = 9.1, 2.6 Hz, 1H, Ar**H**$_6$), 6.49 (d, *J* = 2.6 Hz, 1H, Ar**H**$_8$), 6.25 (s, 1H, Ar**H**$_3$), 4.82 (s, 2H, C**H**$_2$, H_{11}), 3.39 (q, *J* = 7.2 Hz, 4H, N(C**H**$_2$CH$_3$)$_2$)), 1.19 (t, *J* = 7.2 Hz, 6H, N(CH$_2$C**H**$_3$)$_2$).

Spectroscopic data were in agreement with [30]

The synthesis of **(8)**

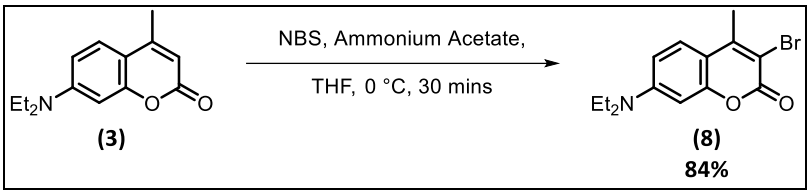

(3) (1 g, 4.3 mmol, 1 eq.) was dissolved in THF (15 ml), cooled to 0 °C and placed under a nitrogen atmosphere. NBS (840 mg, 4.7 mmol, 1.1 eq.) and ammonium acetate (33 mg, 0.4 mmol, 0.1 eq.) were then added at which point a colour change from pale yellow to dark brown was observed. After stirring for 30 mins the reaction mixture was diluted with H_2O (40 ml). The aqueous was extracted with EtOAc (3 × 30 ml) and the combined organic layers were dried over MgSO4, filtered and concentrated *in vacuo*. The crude product was purified by flash column chromatography (0–30% EtOAc: petrol) and the pure fractions were combined and concentrated *in vacuo* to afford the product as a yellow solid with a yield of 1.13 g, 3.6 mmol (84%).

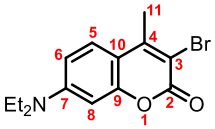

^{1}H NMR (400 MHz, $CDCl_3$) δ 7.35 (d, *J* = 9.1 Hz, 1H, Ar**H**$_5$), 6.55 (dd, *J* = 9.1, 2.6 Hz, 1H, Ar**H**$_6$), 6.39 (d, *J* = 2.6 Hz, 1H, Ar**H**$_8$), 3.36 (q, *J* = 7.1 Hz, 4H, N(C**H**$_2$CH$_3$)$_2$), 2.45 (s, 3H, C**H**$_3$, H$_{11}$), 1.16 (t, *J* = 7.1 Hz, 6H, N(CH$_2$C**H**$_3$)$_2$).

Spectroscopic data were in agreement with [31]

The synthesis of **(9)**

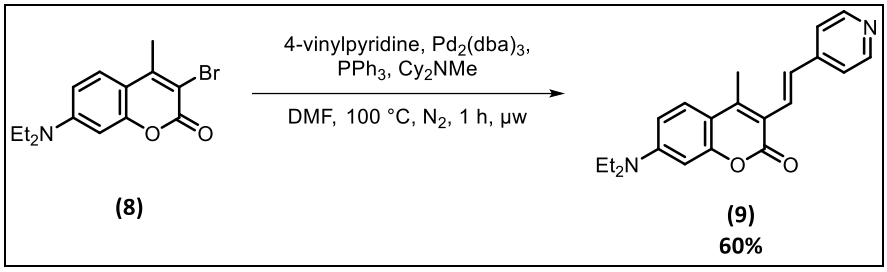

A mixture of **(8)** (50 mg, 0.16 mmol, 1 eq.), $Pd_2(dba)_3$ (7 mg, 0.008 mmol, 0.05 eq.), triphenylphosphine (2 mg, 0.008 mmol, 0.05 eq.), *N,N*-dicyclohexylmethylamine (70 µl, 0.32 mmol, 2 eq.) and 4-vinylpyridine (17 µl, 0.16 mmol, 1 eq.) in DMF (3 ml) was purged with N_2 for 15 mins in a microwave-compatible reaction vessel. The vessel was then placed in a microwave reactor and irradiated at 100 °C for 1 h. After cooling to rt the solvent was removed *in vacuo* and the residue was dry-loaded onto a silica pad and washed with 30% (EtOAc: petrol) to remove unreacted starting material. The product was then eluted with 10% (MeOH: DCM) and concentrated *in vacuo* to afford the product as a brown/orange solid in a yield of 32 mg, 0.096 mmol (60%).

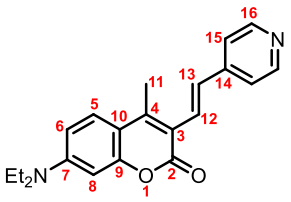

^{1}H NMR (400 MHz, $CDCl_3$) δ 8.54 (d, *J* = 5.9 Hz, 2H, Pyridine-H, **H**$_{16}$), 7.67 (d, *J* = 16.1 Hz, 1H, CC**H**$_{12}$), 7.50 (d, *J* = 9.1 Hz, 1H, Ar**H**$_5$), 7.40 – 7.30 (Overlapping, 3H, H_{13}, H_{15}), 6.62 (dd, *J* = 9.1, 2.6 Hz, 1H, Ar**H**$_6$), 6.49 (d, *J* = 2.6 Hz, 1H, Ar**H**$_8$), 3.42 (q, *J* = 7.1 Hz, 4H, N(C**H**$_2$CH$_3$)$_2$), 2.53 (s, 3H, CH_3, H_{11}), 1.21 (t, *J* = 7.1 Hz, 9H, N(CH_2C**H**$_3$)$_2$).

The synthesis of **(5)**

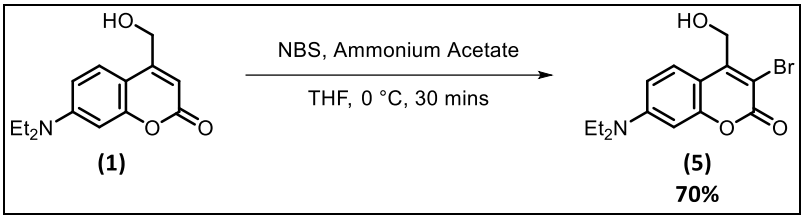

N-Bromo-succinimide (960 mg, 5.4 mmol, 1.1 eq.) and ammonium acetate (38 mg, 0.49 mmol, 0.1 eq.) were added to a stirred solution of **(1)** (1.24 g, 4.9 mmol, 1 eq.) in THF (20 ml) at 0 °C. The mixture was stirred for 30 mins before being quenched *via* the addition of sat. $Na_2S_2O_3$ aqueous solution (20 ml). The aqueous was extracted with EtOAc (3 × 30 ml) and the combined organic layers were dried over $MgSO_4$, filtered and concentrated *in vacuo* and the residue purified by flash chromatography (0-30% EtOAc: petrol). Pure fractions were concentrated *in vacuo* affording the product as a yellow solid with a yield of 1.11 g, 3.4 mmol (70%).

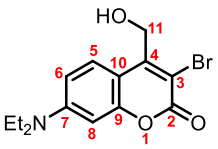

^{1}H NMR (400 MHz, $CDCl_3$) δ 7.65 (d, *J* = 9.1 Hz, 1H, Ar**H**$_5$), 6.61 (dd, *J* = 9.1, 2.6 Hz, 1H, Ar**H**$_6$), 6.46 (d, *J* = 2.6 Hz, 1H, Ar**H**$_8$), 4.94 (s, 2H, C**H**$_2$OH, H_{11}), 3.40 (q, *J* = 7.1 Hz, 4H, N(C**H**$_2$CH$_3$)$_2$), 1.19 (t, *J* = 7.1 Hz, 6H, N(CH_2C**H**$_3$)$_2$).

Spectroscopic data were in agreement with [11]

The synthesis of (6)

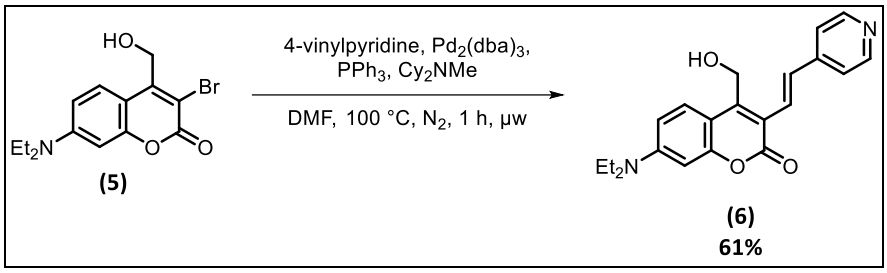

A mixture of **(5)** (578 mg, 1.8 mmol, 1 eq.), $Pd_2(dba)_3$ (82 mg, 0.09mmol, 0.05 eq.), triphenylphosphine (47 mg, 0.09 mmol, 0.05 eq.), *N,N*-dicyclohexylmethylamine (770 µl, 3.6 mmol, 2 eq.) and 4-vinylpyridine (190 µl, 1.8 mmol, 1 eq.) in DMF (6 ml) was purged with N_2 for 15 mins in a microwave-compatible reaction vessel. The vessel was then placed in a microwave reactor and irradiated at 100 °C for 1 h. After cooling to rt the solvent was removed *in vacuo* and the residue was purified by flash column chromatography (0-4% MeOH: DCM). Pure fractions were concentrated *in vacuo*, affording the product as an orange solid with a yield of 390 mg, 1.1 mmol (61%).

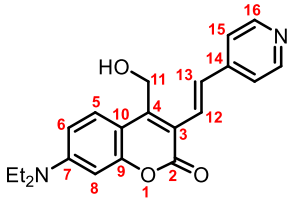

^{1}H NMR (400 MHz, $CDCl_3$) δ 8.35 (d, *J* = 6.1 Hz, 2H, Pyridine-**H,** H_{16}), 7.71 (d, *J* = 9.2 Hz, 1H, Ar**H**$_5$), 7.58 (d, *J* = 16.0 Hz, 1H, CC**H,** H_{12}), 7.32 (d, *J* = 16.0 Hz, 1H, CC**H**, H_{13}), 7.17 (d, *J* = 6.1 Hz, 2H, Pyridine-**H,** H_{15}), 6.60 (dd, *J* = 9.2, 2.6 Hz, 1H, Ar**H**$_6$), 6.41 (d, *J* = 2.6 Hz, 1H, Ar**H**$_8$), 4.92 (s, 2H, C**H**$_2$OH, H_{11}), 3.39 (q, *J* = 7.1 Hz, 4H, N(C**H**$_2$CH$_3$)$_2$), 1.19 (t, *J* = 7.1 Hz, 6H, N(CH$_2$C**H**$_3$)$_2$).

HRMS ESI *m/z*: calc for $C_{21}H_{22}N_2O_3$ $[M+H]^+$ 351.1703, $[M+Na]^+$ 373.1523; Obs $[M+H]^+$ 351.1707, $[M+Na]^+$ 373.1517

Spectroscopic data were in agreement with [11]

The synthesis of **(2-OTf)**

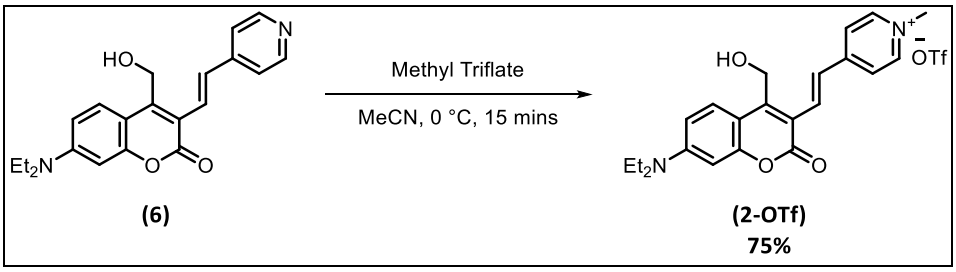

Methyl triflate (46 µL, 0.40 mmol, 1 eq.) was added to a stirring solution of **(6)** (140 mg, 0.40 mmol, 1 eq.) in MeCN (5 ml) at 0 °C. An immediate colour change from orange to dark pink was observed and the reaction was stirred for 15 mins. At this point the reaction mixture was added dropwise to cold diethyl ether (15 ml). The precipitated product was collected by centrifugation (4,000 rpm, 6 mins) and the supernatant was removed, affording the purified product as red/purple solid in a yield of 100 mg, 0.30 mmol (75%).

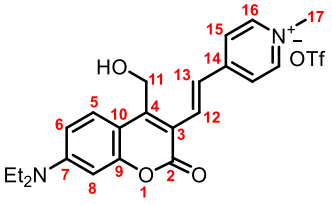

^{1}H NMR (400 MHz, MeCN-d_3) δ 8.37 (d, *J* = 6.9 Hz, 2H, Pyridine-**H**$_{16}$), 8.00 – 7.90 (overlapping, 4H, H$_{12}$, H$_{13}$, H$_{15}$), 7.75 (d, *J* = 9.3 Hz, 1H, Ar**H**$_5$), 6.75 (dd, *J* = 9.3, 2.6 Hz, 1H, Ar**H**$_6$), 6.50 (d, *J* = 2.6 Hz, 1H, Ar**H**$_8$), 4.92 (d, *J* = 5.7 Hz, 2H, C**H**$_2$OH, **H**$_{11}$), 4.15 (s, 3H, **H**$_{17}$), 3.77 (t, *J* = 5.7 Hz, 1H, OH), 3.47 (q, *J* = 7.1 Hz, 4H, N(C**H**$_2$CH$_3$)$_2$), 1.19 (t, *J* = 7.1 Hz, 6H, N(CH$_2$C**H**$_3$)$_2$).

^{19}F NMR (376 MHz, MeCN-d_3) δ -79.05 (s, 1F, Triflate).

HRMS ESI m/z: calc for $C_{22}H_{25}N_2O_3$ $[M]^+$ 365.1860; Obs 365.1867

The synthesis of **(12)**

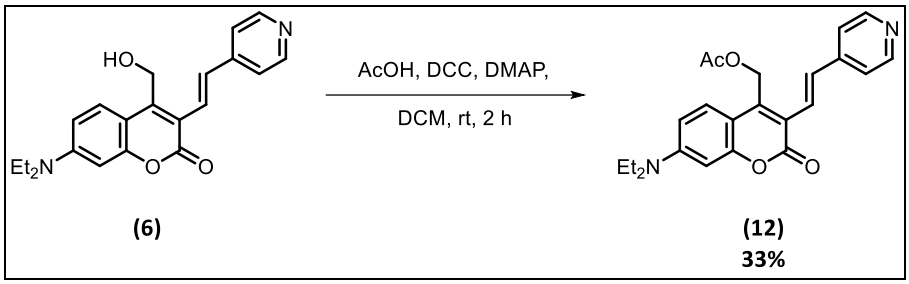

(6) **(12)**
33%

(6) (50 mg, 0.14 mmol, 1 eq.) was dissolved in DCM (15 ml) and protected from light. DCC (35 mg, 0.17 mmol, 1.2 eq.), DMAP (21 mg, 0.17 mmol, 1.2 eq.) and AcOH (10 µl, 0.17 mmol, 1.2 eq.) were added and the reaction was stirred at rt for 2 h. At this point full conversion was indicated by TLC (5% MeOH in DCM) and the reaction was quenched *via* the addition of sat. aqueous $NaHCO_3$ solution (15 ml). The product was extracted with DCM (2 × 15 ml) and the combined organics were washed with brine prior to being dried over $MgSO_4$, filtered and concentrated *in vacuo*. The crude product was dissolved in cold MeCN and filtered in order to remove any dicyclohexylurea which had formed as a side product of the reaction. The product was then further purified by flash column chromatography (0 – 10% MeOH: DCM) affording the product as an orange solid with a yield of 18 mg, 0.046 mmol (33%).

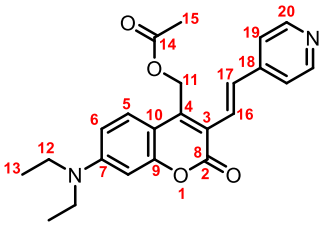

^{1}H NMR (400 MHz, $CDCl_3$) δ 8.55 (d, *J* = 4.9 Hz, 2H, Pyr**H**$_{20}$), 7.66 (d, *J* = 16.0 Hz, 1H, AlkeneH**,** **H**$_{16}$), 7.53 (d, *J* = 9.2 Hz, 1H, Ar**H**$_5$), 7.44 (d, *J* = 16.0 Hz, 1H, Alkene**H,** H$_{17}$), 7.38 – 7.32 (m, 2H, Pyr**H**$_{19}$), 6.63 (dd, *J* = 9.2, 2.6 Hz, 1H, Ar**H**$_6$), 6.49 (d, *J* = 2.6 Hz, 1H, Ar**H**$_8$), 5.41 (s, 2H, C**H**$_2$OAc,

H$_{11}$), 3.42 (q, *J* = 7.1 Hz, 4H, N(C**H**$_2$CH$_3$)$_2$, H$_{12}$), 2.11 (s, 3H, OCOC**H**$_3$, H$_{15}$), 1.21 (t, *J* = 7.1 Hz, 6H, N(CH$_2$C**H**$_3$)$_2$, H$_{13}$).

HRMS ESI *m/z*: calc for $C_{23}H_{24}N_2O_4$ $[M+H]^+$ 393.1809, $[M+Na]^+$ 415.1628; Obs $[M+H]^+$ 393.1822, $[M+Na]^+$ 415.1652

Spectroscopic data were in agreement with [6]

The synthesis of (13)

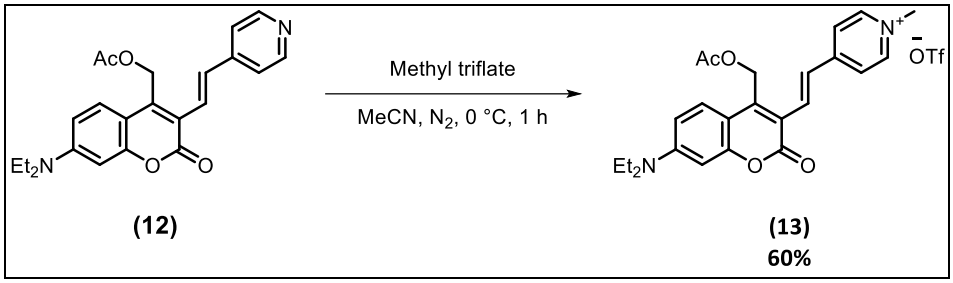

(12) (65 mg, 0.17 mmol, 1 eq.) was dissolved in anhydrous MeCN (10 ml), placed under nitrogen atmosphere, cooled to 0 °C, and protected from light. In a separate vessel, a solution of methyl triflate (19 µl, 0.17 mmol, 1 eq.) in anhydrous MeCN (5 ml) was created purged with N_2 and cooled to 0 °C. The methyl triflate solution was then added dropwise to the stirring solution of **(12)** over the course of 5 mins. Upon complete addition of this solution, the reaction mixture was stirred for 1 h at 0 °C. At this point the reaction was quenched by the dropwise addition of sat. aqueous $NaHCO_3$ solution. The product was extracted with EtOAc (3 × 20 ml), and the combined organics were concentrated in vacuo. The crude product was redissolved in MeCN (5 ml) and added dropwise to cold diethyl ether (90ml) in two 50 ml falcon tubes to precipitate the product, which was then pelleted by centrifugation (4,000 RPM, 6 mins) and the supernatant removed, affording the purified product as red solid with a yield of 57 mg, 0.10 mmol (59%).

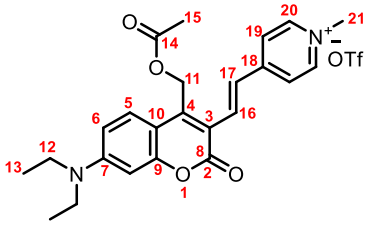

^{1}H NMR (400 MHz, MeCN-d_3) δ 8.41 (d, *J* = 6.9 Hz, 2H, Pyr**H**, H_{20}), 7.98 (d, *J* = 6.9 Hz, 2H, Pyr**H** , H_{19}), 7.96 – 7.86 (m, 2H, Alkene**H**, $H_{16,17}$), 7.67 (d, *J* = 9.3 Hz, 1H, Ar**H**, H_5), 6.78 (dd, *J* = 9.3, 2.6 Hz, 1H, Ar**H**, H_6), 6.53 (d, *J* = 2.6 Hz, 1H, Ar**H**, H_8), 5.48 (s, 2H, C**H**$_2$OAc, H_{11}), 4.17 (s, 3H, NC**H**$_3$, H_{21}), 3.49 (q, *J* = 7.1 Hz, 4H, N(C**H**$_2$CH$_3$)$_2$, H_{12}), 2.04 (s, 3H), 1.19 (t, *J* = 7.1 Hz, 6H, N(CH$_2$C**H**$_3$)$_2$, H_{13}).

^{13}C NMR (101 MHz, MeCN-d_3) δ 170.43 (C_{14}), 159.85 (C_2), 156.21 (C_9), 154.41 (C_{18}), 152.18 (C_7), 148.82 (C_4), 144.51 (C_{20}), 133.86 ($C_{16/17}$), 127.85 (C_5), 125.73 ($C_{16/17}$), 123.80 (C_{19}), 113.81 (C_3), 110.15 (C_6), 108.09 (C_{10}), 96.67 (C_8), 57.45 (C_{11}), 47.14 (C_{21}), 44.69 (C_{12}), 20.07 (C_{15}), 11.86 (C_{13}).

^{19}F NMR (400 MHz, MeCN-d_3) δ -79.24 (Triflate)

HRMS ESI *m/z*: calc for $C_{24}H_{27}N_2O_4$ $[M]^+$ 407.1965; Obs $[M]^+$ 407.1970

The synthesis of **(14)**

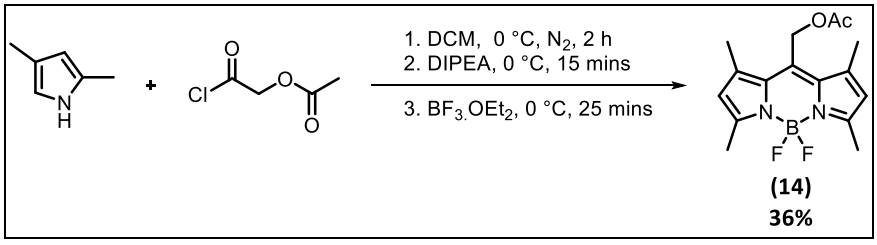

To a stirring solution of acetoxyacetyl chloride (0.32 ml, 3.0 mmol, 1.2 eq.) in anhydrous DCM (20 ml) at 0 °C under N_2 was added 2,4-dimethylpyrrole (0.54 mL, 5.0 mmol, 2 eq.) dropwise over the course of 5 mins. The reaction was stirred at 0 °C for 2 h by which point a colour

change from colourless to red had been observed. DIPEA (1.70 ml, 10.0 mmol, 4 eq.) was then added, which was accompanied by a colour change from red to dark green and the reaction was allowed to progress for a further 15 mins. $BF_3.OEt_2$ (1.23 ml, 10.0 mmol, 4 eq.) was then added with a colour change from dark green to purple and the reaction mixture was stirred for a further 15 mins prior to washing with saturated aqueous $NaHCO_3$ (50 ml). The aqueous was then extracted with DCM (3 × 50 ml). The combined organic layers were combined and dried over magnesium sulfate, prior to filtration and concentration *in vacuo*. The crude product was then purified by flash column chromatography (30% EtOAc: petrol). Pure fractions were concentrated *in vacuo* to afford the product as an orange/green solid with a yield of 291 mg, 0.91 mmol (36%).

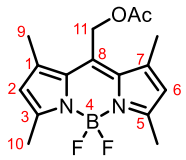

^{1}H NMR (400 MHz, $CDCl_3$) δ 6.08 (s, 2H, Pyrrole-**H**, H_2, H_6), 5.29 (s, 2H, C**H**$_2$, H_{11}), 2.53 (s, 6H, C**H**$_3$, H_9), 2.35 (s, 6H, C**H**$_3$, H_{10}), 2.13 (s, 3H, OCOC**H**$_3$).

Spectroscopic data were in agreement with [20]

The synthesis of **(15)**

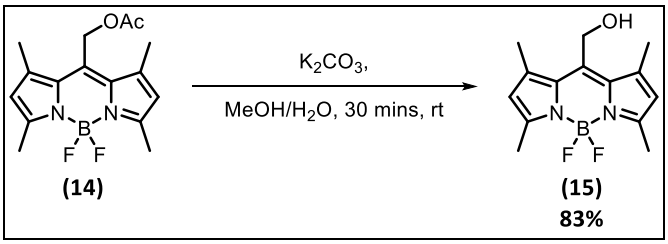

To a solution of **(14)** (185 mg, 0.58 mmol, 1 eq.) in MeOH/H_2O (5:1, 12 ml) was added K_2CO_3 (80mg, 0.58 mmol, 1 eq.). The reaction mixture was stirred at room temperature for 30 mins

prior to the removal of the solvent *in vacuo*. The residue was then suspended in DCM (50 ml) and the organics washed with saturated aqueous $NaHCO_3$ solution (50 mL). The aqueous was extracted with DCM (2 × 20 ml) and the combined organic layers were dried over magnesium sulfate before filtering and concentration *in vacuo* which afforded the product as a red solid with a yield of 134 mg, 0.48 mmol (83%).

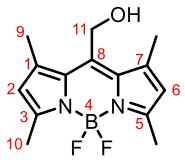

^{1}H NMR (400 MHz, $CDCl_3$) δ 6.07 (s, 2H, Pyrrole-**H,** H_2**,** H_6), 4.89 (s, 2H, C**H**$_2$OH, H_{11}), 2.50 (overlapping, 12H, H_9, H_{10}).

HRMS ESI *m/z*: calc for $C_{14}H_{17}BF_2N_2O$ $[M+H]^+$ 279.1475, $[M+Na]^+$ 301.1294, $[M+K]^+$ 317.1034; Obs $[M+H]^+$ 279.1489, $[M+Na]^+$ 301.1306, $[M+K]^+$ 317.1040

Spectroscopic data were in agreement with [28]

The synthesis of **(16)**

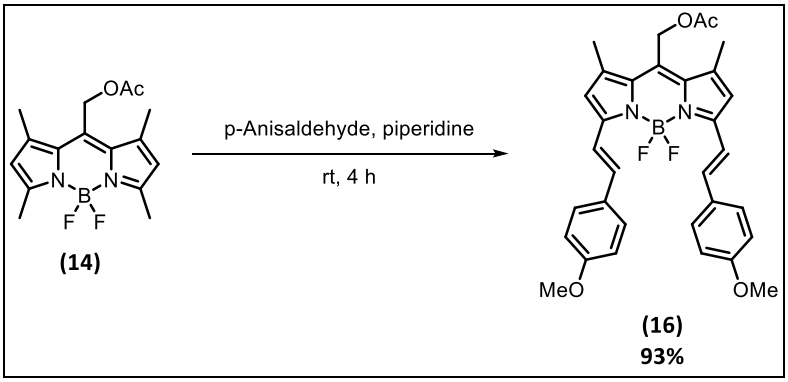

(14) (50 mg, 0.15 mmol, 1eq.) was dissolved in *p*-anisaldehyde (0.3 ml, 3.75 mmol, 15 eq.) and a drop of piperidine was added. The reaction vessel was placed under vacuum and stirred for 4 h at room temperature with the observation of a colour change from orange to dark

blue/green as the reaction progressed. Following this, the solvent was removed *in vacuo* and the residue purified by flash column chromatography (0 – 100% DCM: petrol) and pure fractions were combined and concentrated affording the product as a dark blue solid with a yield of 75 mg, 0.14 mmol (93%).

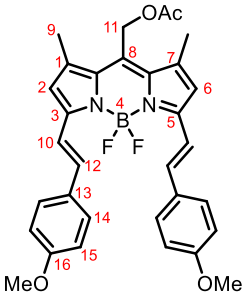

^{1}H NMR (400 MHz, CHLOROFORM-*D*) δ 7.61 – 7.52 (overlap, 6H, H_{15}/H_{12}/H_{10}), 6.92 (Alkene-H, H_{14}, d, *J* = 8.8 Hz, 4H), 6.71 (s, 2H, Pyrrole-**H**, H_2, H_6), 5.33 (s, 2H, C**H**$_2$, H_{11}), 3.85 (s, 6H, OC**H**$_3$), 2.40 (s, 6H, **H**$_9$), 2.14 (s, 3H, COC**H**$_3$).

Spectroscopic data were in agreement with [9]

The synthesis of **(18)**

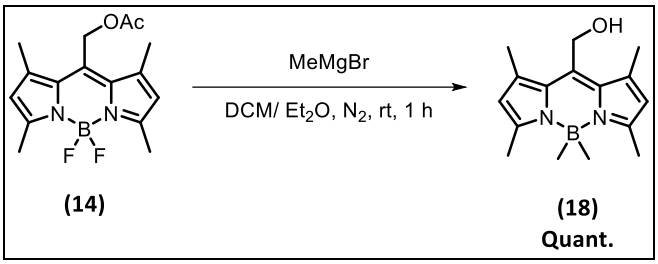

To a stirring solution of **(14)** (100 mg, 0.30 mmol, 1 eq.) in anhydrous DCM (10 ml) under N_2 was added a solution of methyl magnesium bromide (3 M in diethyl ether, 1.1 ml, 3.3 mmol, 11 eq.). The reaction mixture was stirred at rt for 1 h prior to quenching with dropwise addition of aqueous ammonium chloride solution (50 ml, CARE: effervescence observed, exothermic). The aqueous was then extracted with DCM (3 × 50 ml) and the combined organic

layers were washed with brine (100 ml), dried over $MgSO_4$, filtered and concentrated *in vacuo.* The residue was purified by flash column chromatography (DCM) and pure fractions were combined and concentrated to afford the product as an orange solid with a yield of 85 mg, 0.30 mmol (quantitative).

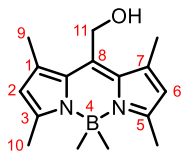

^{1}H NMR (400 MHz, $CDCl_3$) δ 6.07 (s, 2H, Pyrrole-**H**, H_2, H_6), 4.94 (s, 2H, C**H**$_2$, H_{11}), 2.51 (s, 6H, C**H**$_3$, H_9), 2.45 (s, 6H, C**H**$_3$, H_{10}), 0.17 (s, 6H, BC**H**$_3$).

Spectroscopic data were in agreement with [32]

The synthesis of (20)

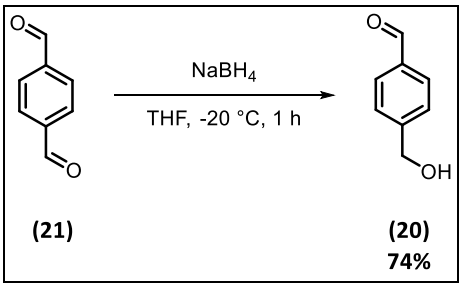

To a stirring solution of terephthaldehyde (5.00 g, 37.3 mmol, 1 eq.) in dry THF (50 ml) at -20 °C was added $NaBH_4$ (352 mg, 9.3 mmol, 0.25 eq.) in small portions over the course of 5 mins. The reaction mixture was stirred at -20 °C until complete conversion by TLC (60% EtOAc: petrol) was observed. Upon reaching completion the reaction mixture was warmed to rt and quenched *via* dropwise addition of saturated aqueous $NaHCO_3$ solution (50 mL). The aqueous was extracted with ethyl acetate (3 × 50 ml) and the combined organic layers were combined and dried over magnesium sulfate prior to filtration and concentration *in vacuo.* The crude

product was purified by flash column chromatography (0-60% EtOAc in Petrol) and the pure fractions were combined and concentrated to afford the product as a yellow solid with a yield of 3.75 g, 27.5 mmol (74%).

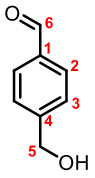

^{1}H NMR (400 MHz, DMSO-d_6) δ 9.94 (s, 1H, C**H**O, H_6), 7.83 (d, *J* = 7.7 Hz, 2H, Ar**H**, H_2), 7.50 (d, *J* = 7.7 Hz, 2H, Ar**H**, H_3), 5.39 (td, *J* = 5.7, 2.0 Hz, 1H, CH_2O**H**), 4.56 (d, *J* = 5.7 Hz, 2H, C**H**$_2$OH, H_5).

Spectroscopic data was in agreement with [33]

The synthesis of **(19)**

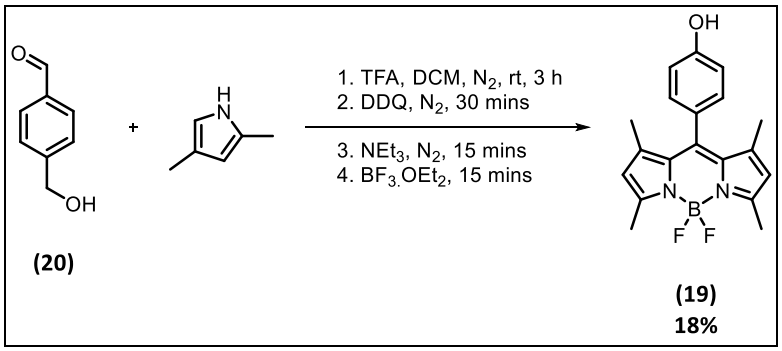

To a stirring solution of **(20)** (200 mg, 1.46 mmol, 1 eq.) in anhydrous DCM (50 ml), under N_2 was added 2,4-dimethylpyrrole (300 µl, 2.92 mmol, 2 eq.). The resulting solution was stirred at rt for 5 mins, prior to the addition of 3 drops of trifluoroacetic acid which was accompanied by a colour change from colourless to red. Following a further 3 h of stirring at rt, a solution of 2,3-dichloro-5,6-dicyano-1,4-benzoquinone (330 mg, 1.46 mmol, 1 eq.) in anhydrous DCM (10 ml) was added dropwise with a colour change from red to dark purple observed. Following

further stirring for 30 min, NEt_3 (4.4 ml, 31.6 mmol, 22 eq.) was added in a dropwise manner with a colour change from purple to dark green. Stirring was continued for a further 15 mins before dropwise addition of $BF_3.Et_2O$ (4.4 ml, 35.6 mmol, 24 eq.) with a colour change from dark green to purple. The reaction was allowed to progress for a further 15 mins prior to quenching with saturated aqueous $NaHCO_3$ solution (50 ml). The aqueous was then extracted with DCM (3 × 50 ml) and the organic layers combined and dried over $MgSO_4$ prior to filtration and concentration *in vacuo.* The crude product was then purified by flash column chromatography, first with (100% DCM) as eluent, followed by a second column using (0 – 30% EtOAc: petrol) with pure fractions being combined and concentrated to afford the product as an orange solid with a yield of 92 mg, 0.27 mmol (18%).

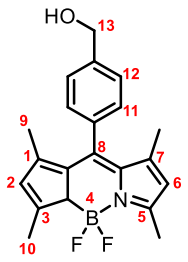

^{1}H NMR (400 MHz, $CDCl_3$) δ 7.47 (d, *J* = 7.9 Hz, 2H, Ar**H**, H_{11}), 7.24 (d, *J* = 7.9 Hz, 2H, Ar**H**, H_{12}), 5.96 (s, 2H, Pyrrole-H, H_2, H_6), 4.78 (s, 2H, C**H**$_2$, H_{13}), 2.53 (s, 6H, C**H**$_3$, H_{10}), 1.36 (s, 6H, CH_3, **H**$_9$).

Spectroscopic data were in agreement with [34]

2.8.3 NMR Spectra of Novel Compounds

NMR Spectra of **(2-OTf)**

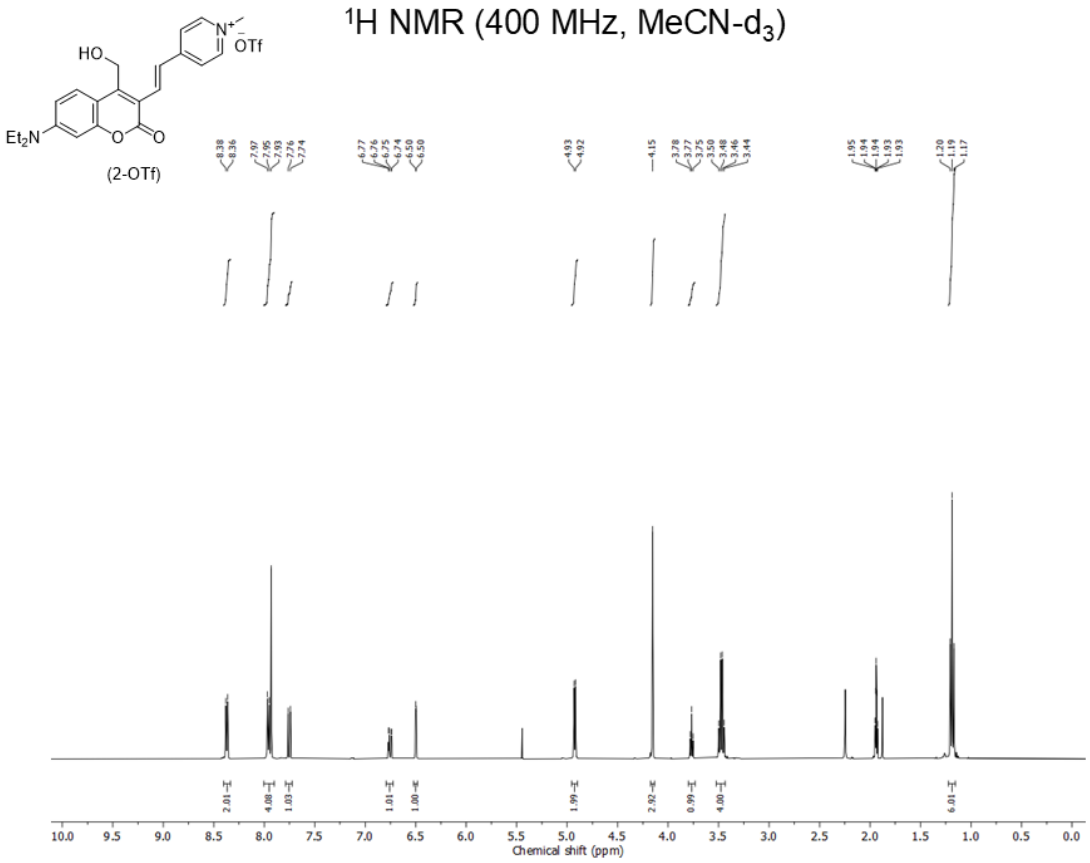

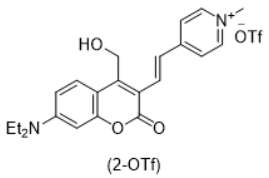

(2-OTf)

^{19}F NMR (400 MHz, MeCN-d_3)

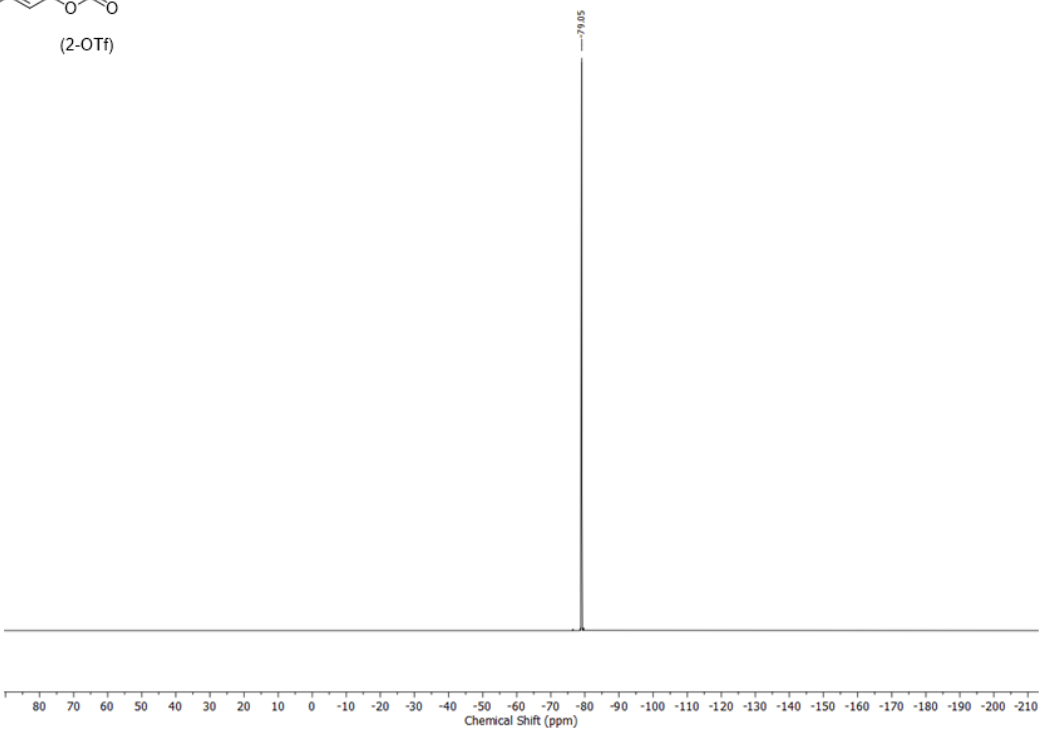

NMR Spectra of **(13)**

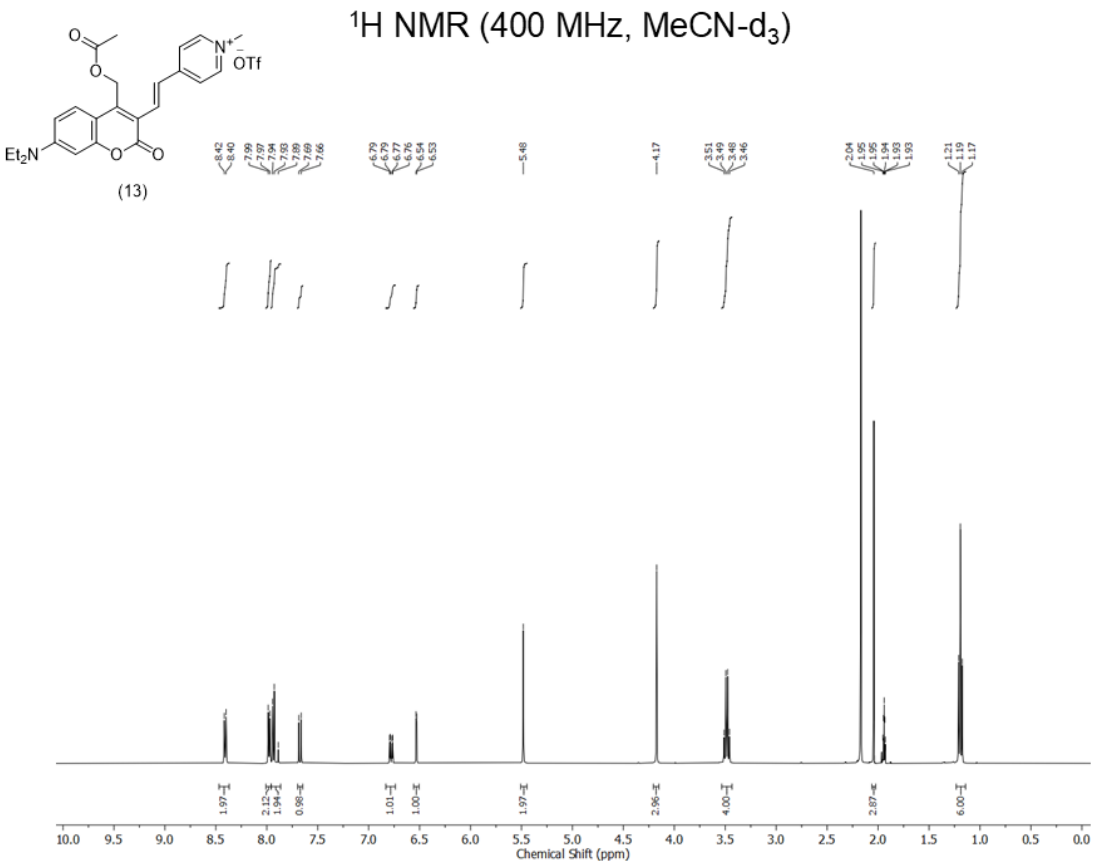

^{13}C NMR (100 MHz, MeCN-d_3)

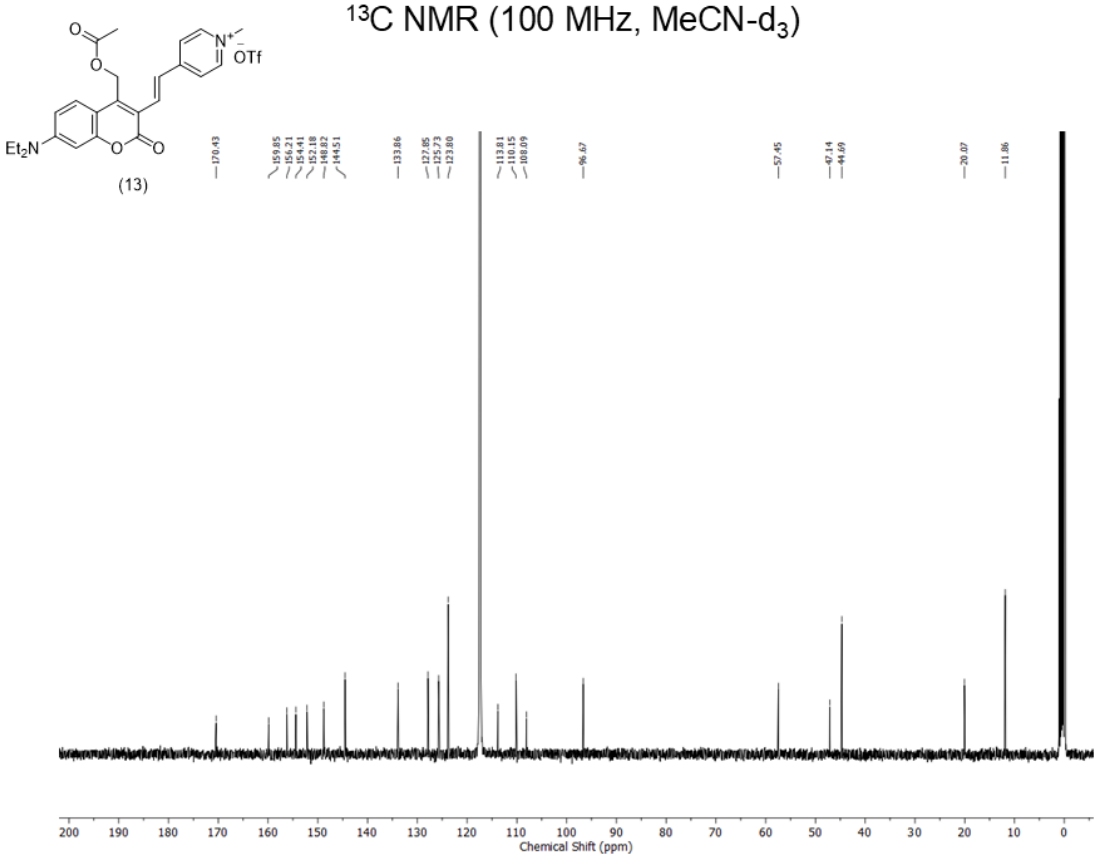

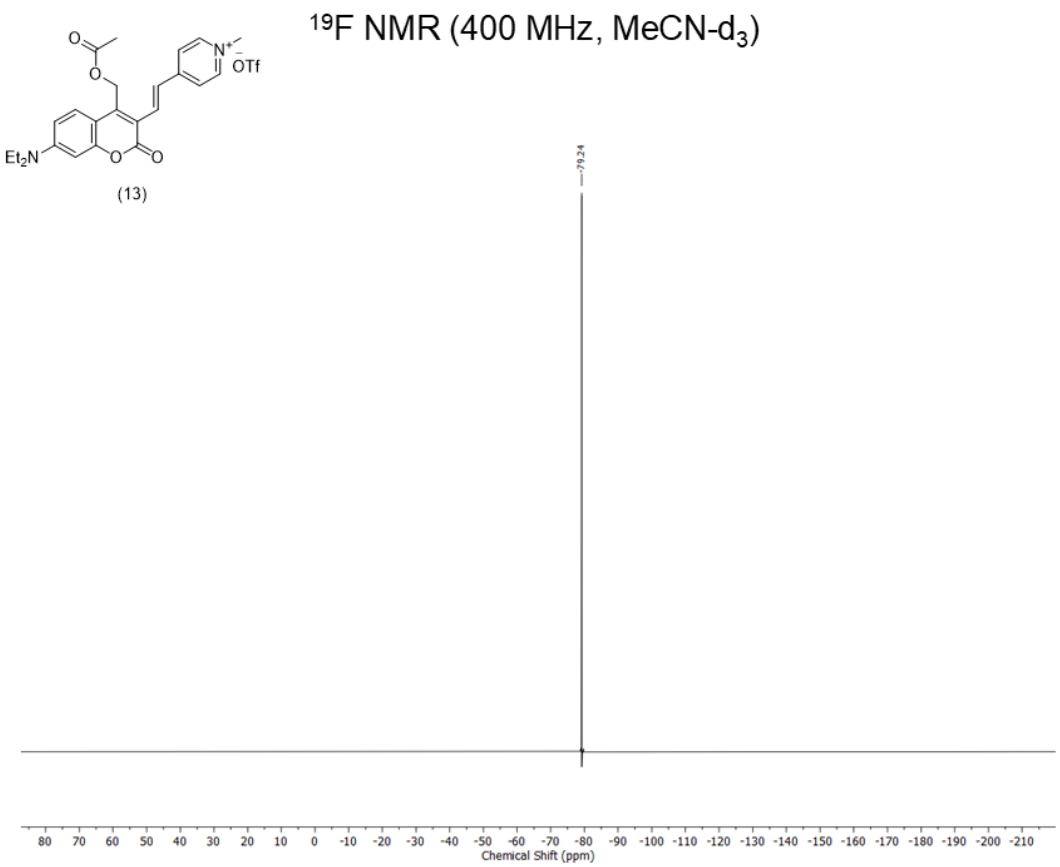

2.9 References

1. Einstein, A. Über einen die erzeugung und verwandlung des lichtes betreffenden heuristischen gesichtspunkt. *Ann. Phys.* **1905**, *322* (6), 132–148.
2. Planck, M. Ueber das gesetz der energieverteilung im normalspectrum. *Ann. Phys.* **1901**, *309* (3), 553–563.
3. Clydesdale, G. J.; Dandie, G. W.; Muller, H. K. Ultraviolet light induced injury: Immunological and inflammatory effects. *Immunol. Cell Biol.* **2001**, *79* (6), 547–568.
4. McMillan, T. J.; Leatherman, E.; Ridley, A.; Shorrocks, J.; Tobi, S. E.; Whiteside, J. R. Cellular effects of long wavelength UV light (UVA) in mammalian cells. *J. Pharm. Pharmacol.* **2008**, *60* (8), 969–976.
5. Nerbonne, J. M.; Richard, S.; Nargeot, J.; Lester, H. A. New photoactivatable cyclic nucleotides produce intracellular jumps in cyclic AMP and cyclic GMP concentrations. *Nature* **1984**, *310* (5972), 74–76.
6. Il'ichev, Y. V.; Schwörer, M. A.; Wirz, J. Photochemical reaction mechanisms of 2-nitrobenzyl compounds: Methyl ethers and caged ATP. *J. Am. Chem. Soc.* **2004**, *126* (14), 4581–4595.
7. Klán, P.; Šolomek, T.; Bochet, C. G.; Blanc, A.; Givens, R.; Rubina, M.; Popik, V.; Kostikov, A.; Wirz, J. Photoremovable protecting groups in chemistry and biology: Reaction mechanisms and efficacy. *Chem. Rev.* **2013**, *113* (1), 119–191.

8. Hagen, V.; Bendig, J.; Frings, S.; Eckardt, T.; Helm, S.; Reuter, D.; Kaupp, U. B. Highly efficient and ultrafast phototriggers for cAMP and cGMP by using long-wavelength UV/Vis activation. *Angew. Chem., Int. Ed.* **2001**, *40* (6), 1045–1048.
9. Peterson, J. A.; Wijesooriya, C.; Gehrmann, E. J.; Mahoney, K. M.; Goswami, P. P.; Albright, T. R.; Syed, A.; Dutton, A. S.; Smith, E. A.; Winter, A. H. Family of BODIPY photocages cleaved by single photons of visible/near-infrared light. *J. Am. Chem. Soc.* **2018**, *140* (23), 7343–7346.
10. Peterson, J. A.; Yuan, D.; Winter, A. H. Multiwavelength control of mixtures using visible light-absorbing photocages. *J. Org. Chem.* **2021**, *86* (14), 9655–9664.
11. Bojtár, M.; Kormos, A.; Kis-Petik, K.; Kellermayer, M.; Kele, P. Green-light activatable, water-soluble red-shifted coumarin photocages. *Org. Lett.* **2019**, *21* (23), 9410–9414.
12. Bao, C.; Fan, G.; Lin, Q.; Li, B.; Cheng, S.; Huang, Q.; Zhu, L. Styryl conjugated coumarin caged alcohol: Efficient photorelease by either one-photon long wavelength or two-photon NIR excitation. *Org. Lett.* **2012**, *14* (2), 572–575.
13. Ito, K.; Nakajima, K. Selenium dioxide oxidation of alkylcoumarins and related methyl-substituted heteroaromatics. *J. Heterocycl. Chem.* **1988**, *25* (2), 553–558.
14. Weinrich, T.; Gränz, M.; Grünewald, C.; Prisner, T. F.; Göbel, M. W. Synthesis of a cytidine phosphoramidite with protected nitroxide spin label for EPR experiments with RNA. *Eur. J. Org. Chem.* **2017**, 2017 (3), 425–432.
15. Martins, S.; Candeias, A.; Caldeira, A. T.; Pereira, A. 7-(Diethylamino)-4-methyl-3-vinylcoumarin as a new important intermediate to the synthesis of photosensitizers for DSSCs and fluorescent labels for biomolecules. *Dyes Pigments* **2020**, *174*, 108026.
16. Olson, J. P.; Kwon, H. B.; Takasaki, K. T.; Chiu, C. Q.; Higley, M. J.; Sabatini, B. L.; Ellis-Davies, G. C. R. Optically selective two-photon uncaging of glutamate at 900 nm. *J. Am. Chem. Soc.* **2013**, *135* (16), 5954–5957.
17. Amatrudo, J. M.; Olson, J. P.; Lur, G.; Chiu, C. Q.; Higley, M. J.; Ellis-Davies, G. C. R. Wavelength-selective one- and two-photon uncaging of GABA. *ACS Chem. Neurosci.* **2014**, *5* (1), 64–70.
18. Klausen, M.; Dubois, V.; Clermont, G.; Tonnelé, C.; Castet, F.; Blanchard-Desce, M. Dual-wavelength efficient two-photon photorelease of glycine by π-extended dipolar coumarins. *Chem. Sci.* **2019**, *10* (15), 4477–4484.
19. Goswami, P. P.; Syed, A.; Beck, C. L.; Albright, T. R.; Mahoney, K. M.; Unash, R.; Smith, E. A.; Winter, A. H. BODIPY-derived photoremovable protecting groups unmasked with green light. *J. Am. Chem. Soc.* **2015**, *137* (11), 3783–3786.
20. Krumova, K.; Cosa, G. BODIPY dyes with tunable redox potentials and functional groups for further tethering: Preparation, electrochemical, and spectroscopic characterization. *J. Am. Chem. Soc.* **2010**, *132* (49), 17560–17569.
21. Crawford, S. M.; Thompson, A. Conversion of 4,4-difluoro-4-bora-3a,4a-diaza-s-indacenes (F-BODIPYs) to dipyrrins with a microwave-promoted deprotection strategy. *Org. Lett.* **2010**, *12* (7), 1424–1427.
22. Smithen, D. A.; Baker, A. E. G.; Offman, M.; Crawford, S. M.; Cameron, T. S.; Thompson, A. Use of F-BODIPYs as a protection strategy for dipyrrins: Optimization of BF_2 removal. *J. Org. Chem.* **2012**, *77* (7), 3439–3453.
23. Zemplén, G.; Kunz, A. Studien über amygdalin, IV: Synthese des natürlichen l-amygdalins. *Ber. Dtsch. Chem. Ges.* **1924**, *57* (8), 1357–1359.

24. Yadav, A. K.; Shen, D. L.; Shan, X.; He, X.; Kermode, A. R.; Vocadlo, D. J. Fluorescence-quenched substrates for live cell imaging of human glucocerebrosidase activity. *J. Am. Chem. Soc.* **2015**, *137* (3), 1181–1189.
25. Reese, C. B.; et al. Synthesis of well-defined phosphate-methylated DNA fragments: The application of potassium carbonate in methanol as deprotecting reagent. *Nucleic Acids Res.* **1990**, *18* (17), 5197–5204.
26. Knoevenagel, E. Condensation von malonsäure mit aromatischen aldehyden durch ammoniak und amine. *Ber. Dtsch. Chem. Ges.* **1898**, *31* (3), 2596–2619.
27. Slanina, T.; Shrestha, P.; Palao, E.; Kand, D.; Peterson, J. A.; Dutton, A. S.; Rubinstein, N.; Weinstain, R.; Winter, A. H.; Klán, P. In search of the perfect photocage: Structure–reactivity relationships in meso-methyl BODIPY photoremovable protecting groups. *J. Am. Chem. Soc.* **2017**, *139* (42), 15168–15175.
28. Kaufmann, J.; Müller, P.; Andreadou, E.; Heckel, A. Green-light activatable BODIPY and coumarin 5'-caps for oligonucleotide photocaging. *Chem.–Eur. J.* **2022**, *28* (36), e202200477.
29. Liu, J.-Y.; Yeung, H.-S.; Xu, W.; Li, X.; Ng, D. K. P. Highly efficient energy transfer in subphthalocyanine–BODIPY conjugates. *Org. Lett.* **2008**, *10* (23), 5421–5424.
30. Schönleber, R. O.; Bendig, J.; Hagen, V.; Giese, B. Rapid photolytic release of cytidine 5'-diphosphate from a coumarin derivative: A new tool for the investigation of ribonucleotide reductases. *Bioorg. Med. Chem.* **2002**, *10* (1), 97–101.
31. Fejzagić, A. V.; Myllek, S.; Hogenkamp, F.; Greb, J.; Pietruszka, J.; Classen, T. A fluorescence-based assay system for the determination of haloperoxidase activity using a two-dimensional calibration approach. *ChemistryOpen* **2020**, *9* (9), 959–966.
32. Umeda, N.; Takahashi, H.; Kamiya, M.; Ueno, T.; Komatsu, T.; Terai, T.; Hanaoka, K.; Nagano, T.; Urano, Y. Boron dipyrromethene as a fluorescent caging group for single-photon uncaging with long-wavelength visible light. *ACS Chem. Biol.* **2014**, *9* (10), 2242–2246.
33. Shruthi, T. G.; Subramanian, S.; Eswaran, S. Design, synthesis and study of antibacterial and antitubercular activity of quinoline hydrazone hybrids. *Heterocycl. Commun.* **2020**, *26* (1), 84–92.
34. Matsumoto, T.; Urano, Y.; Takahashi, Y.; Mori, Y.; Terai, T.; Nagano, T. In situ evaluation of kinetic resolution catalysts for nitroaldol by rationally designed fluorescence probe. *J. Org. Chem.* **2011**, *76* (10), 3616–3625.

Chapter 3

The synthesis of photocleavable linkers

3.1 Introduction

The previous chapter discussed the synthesis of photocages capable of undergoing orthogonal decaging across the visible light spectrum. The distinct absorption profiles of the synthesised photocages facilitates the sequential release of cargo molecules within a mixture, through irradiation with photocage specific wavelengths, at discrete points in time.[1] As discussed in Section 1.1.4 of the introductory chapter, the ultimate goal of this project is to employ these photocages as part of a tissue engineering strategy whereby they would be used to inactivate a series of growth factor sequestering peptides tethered to a hydrogel seeded with stem cells. Selective activation using light, would then facilitate sequential enrichment of a series of growth factors thus influencing cell fate.

However, in order to more closely mimic the complexity of signalling cascades observed *in vivo*, a means of deactivating these peptides is also required. We aim to achieve this by employing another class of photo-responsive molecule, photocleavable linkers. As with conventional photocages, the cargo molecule is attached covalently and subsequently released upon irradiation with an appropriate wavelength of light. However, photocleavable linkers bear an additional reactive moiety that facilitates their incorporation into materials. Most commonly, an azide or alkyne group is introduced, allowing the linker to undergo a click reaction with a complementary functionality present on a material of interest. In this way the linker tethers the cargo molecule to a surface until photolysis is induced, thereby releasing the cargo molecule from the surface.

Using orthogonally cleavable, photocleavable linkers to tether a series of cargo molecules to a surface would allow for sequential release of these cargo molecules from the surface, in a similar fashion to the sequential decaging systems discussed previously.[2] In the context of this

work, it would facilitate the sequential release of a series of growth factor sequestering peptides from a hydrogel surface. As these peptides enhance growth factor signalling through sequestration, releasing them from the surface would cease this function thus providing a means of deactivating growth factor signalling. A schematic of how photocleavable linkers function is provided in figure 1 below.

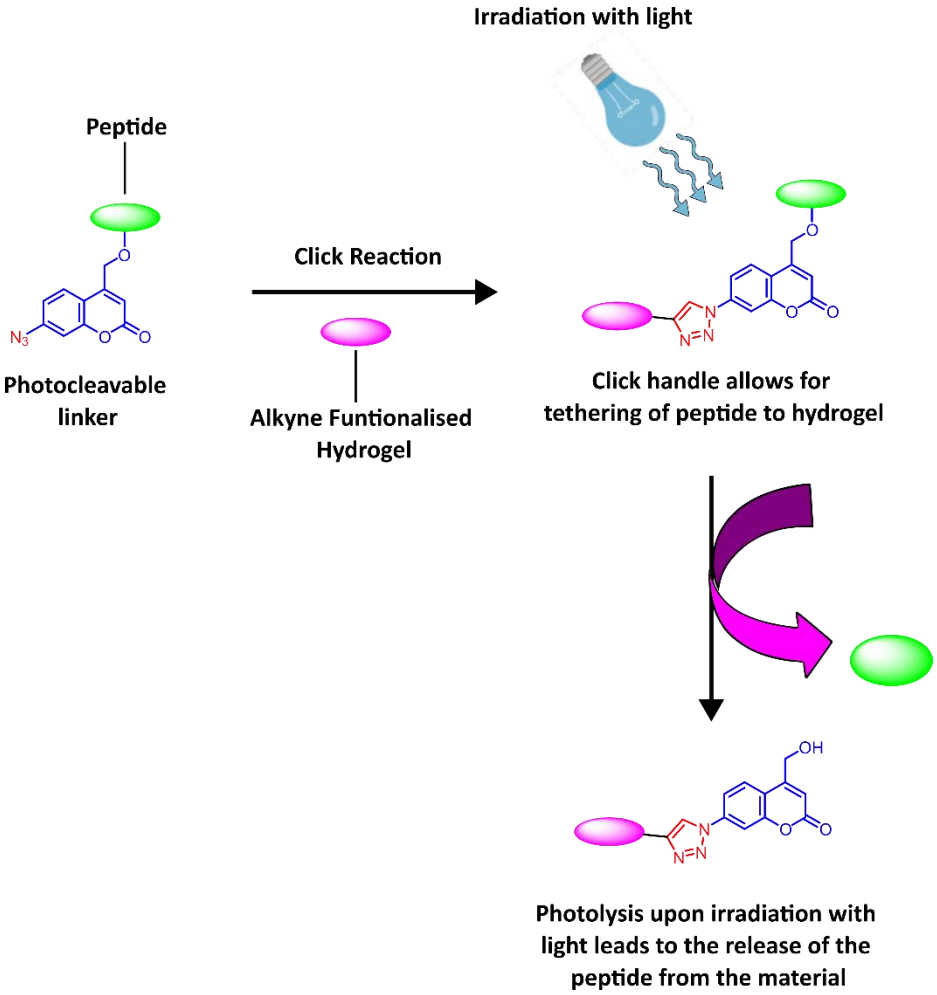

Figure 1: A schematic summary of how a photocleavable linker tethers a cargo molecule to a material, before releasing it upon irradiation with an appropriate wavelength of light.

3.2 Photocleavable linker selection criteria

In section 2.1 of the previous chapter, the selection criteria for photocages to be used in this work were discussed and for the most part these criteria remained the same for

photocleavable linker selection. Briefly, biocompatibility was a key consideration, meaning that any photocleavable linkers produced needed to be cleavable using low-energy, visible light so as to limit phototoxicity. There was also a requirement for orthogonal photocleavage, meaning that the absorption profiles of the selected photocleavable linkers needed to exhibit as minimal overlap as possible in order to facilitate selective photolysis. Due to the nature of this work and desire to integrate the molecules into bulk materials, we also required substantial quantities of final compounds (> 500 mg) for our research purposes. Consequently, it was important that the synthetic routes used in the production of any photocleavable linkers were optimised to allow for the production of sufficient quantities of material.

3.3: The selection of photocleavable linkers

7-azido-4-hydroxymethyl coumarin **(1),** which had previously been developed by Anseth & Azagarsamy,[2] presented itself as a potential candidate for our purposes. This molecule had been shown to efficiently release BMP-7 from a hydrogel matrix upon irradiation at 365 nm, which lies just within the visible range, as previously demonstrated in figure 1 above. Additionally, this molecule was also shown to undergo orthogonal photocleavage in tandem with *o*-nitrobenzyl photocleavable linker (**2)**. Irradiation at 405 nm, was shown to selectively cleave **(2)**, in the presence of **(1)** followed by sequential cleavage of **(1)** by irradiation at 365 nm.[2] This demonstrated the potential of **(1)** to undergo orthogonal photocleavage with more red-shifted photocleavable linkers. Furthermore, the presence of the 7-azido moiety allowed conjugation to the hydrogel using the strain-promoted azide-alkyne cycloaddition **(SPAAC)** click reaction. This is a variant of the copper-catalysed azide-alkyne cycloaddition **(CuAAC)** developed by Sharpless et al in 2001,[3] and involves the reaction of an azide with a strained cyclooctyne in order to form a 1,2,3-triazole linkage.[4] Not only is this reaction robust and high yielding, but it also readily proceeds under aqueous conditions without the need for a copper

catalyst, making it an ideal conjugation strategy for the tethering of biomolecules to hydrogels.[2,5] Additionally, the 1,2,3-triazole linkage is stable under physiological conditions,[6,7] which in the context of our work would ensure that cargo release from the material surface would be initiated solely by photolysis. The structures of the photocleavable linkers developed by Anseth & Azagarsamy can be seen in figure 2 below.

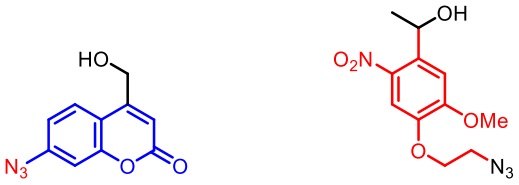

(1) **(2)**

Figure 2: The structures of the photocleavable linkers employed by Anseth & Azagarsamy.

Although Anseth & Azagarsamy achieved orthogonal cleavage of **(1)** and **(2)** by 1st irradiating the hydrogel at 405 nm to release **(2)** followed by irradiation at 365 nm to release **(1)**, this process was not fully selective and approximately 10% of **(1)** underwent cleavage following the initial irradiation at 405 nm. We reasoned, that if a more red-shifted photocleavable linker could be developed, we could increase the energy difference between cleavage wavelengths, thus maximising the potential for fully orthogonal photocleavage. In the previous chapter photocage **(3)** was synthesised based on the work of Kele et al.[8] This photocage had a λ_{max} of 498 nm and had previously been shown to undergo efficient decaging upon irradiation with green light 500 – 544 nm.[8] This represented over a 200 nm increase *vs* the 405 nm used to cleave **(2)** during the work of Anseth & Azagarsamy.[2] Thus, if a clickable version of this photocage could be developed, it would greatly increase the chances of orthogonal photocleavage when used in tandem with **(1)**. As described in section 2.3.4, the final step in the synthesis of **(3)** involved the *N*-alkylation of the pyridine ring using methyl triflate. We

postulated that if this reagent could be replaced with an alkylating agent bearing an azido group, a molecule could be created that would retain the photophysical properties of **(3)**, whilst simultaneously incorporating a moiety capable of undergoing click chemistry. This led to the proposal of **(4)** as a potential photocleavable linker as seen in figure 3 below.

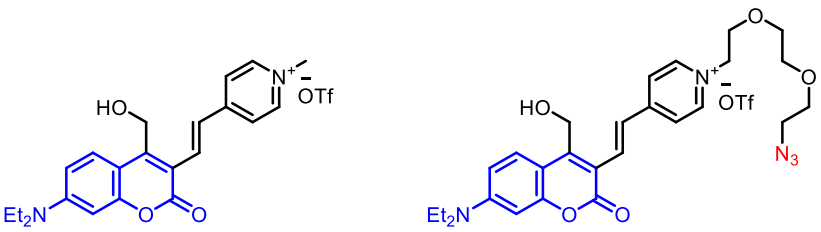

*Figure 3: The structures of photocage **(3)** which was synthesised in the previous chapter and its proposed photocleavable linker counterpart **(4).***

3.4 The synthesis of 7-azido-4-hydroxymethyl coumarin (1)

3.4.1Initial Attempt

In their work, Azagarsamy & Anseth described a three-step synthesis of **(1)**.[2] The initial step of this reaction involved the diazotisation of **(5)**, using tBuONO in the presence of $BF_3.OEt_2$. Following this they isolated the corresponding diazonium salt, prior to treatment with NaN_3 to form the desired azide **(6)** in a yield of 44%. However, diazonium salts are highly reactive species and are prone to decomposition.[9] Consequently, we opted to carry out a one-pot synthesis, whereby once the diazonium intermediate was formed it was then subsequently reacted with sodium azide to form **(6)** directly. Additionally, we chose to perform the initial diazotisation of the amino group using sodium nitrite in HCl rather than using tBuONO as had been utilised in the previous synthesis, as these conditions were harsher, ensuring full formation of the diazonium intermediate whilst simultaneously allowing for enhanced

scalability. These alterations allowed **(6)** to be isolated in quantitative yields at scales of up to 10 g without the need for further purification following aqueous workup, a significant improvement over the reported method.

Following the successful synthesis of **(6**), we attempted to synthesise the final compound **(1)** *via* a SeO_2-mediated Riley oxidation. This synthesis was once again attempted using the conditions described by Azagarsamy & Anseth.[2] In their work, a yield of 25% was reported for this synthesis. However, when we trialled these conditions a yield of just 7% was obtained as can be seen in scheme 1 below. Similar to the synthesis of 7-diethylamino-4-formyl coumarin described in section 2.3.1 of the previous chapter, many of the problems could be attributed to difficult purification as a result of the formation of selenium-based byproducts. Scalability once again posed a major problem as yields dropped even further at scales greater than 1 g, restricting our ability to synthesise sufficient quantities of **(1)** for our research purposes, where large quantities are required for material functionalisation. As such it was clear that in order to consistently produce **(1)** at greater scales, an alternative synthetic route was required.

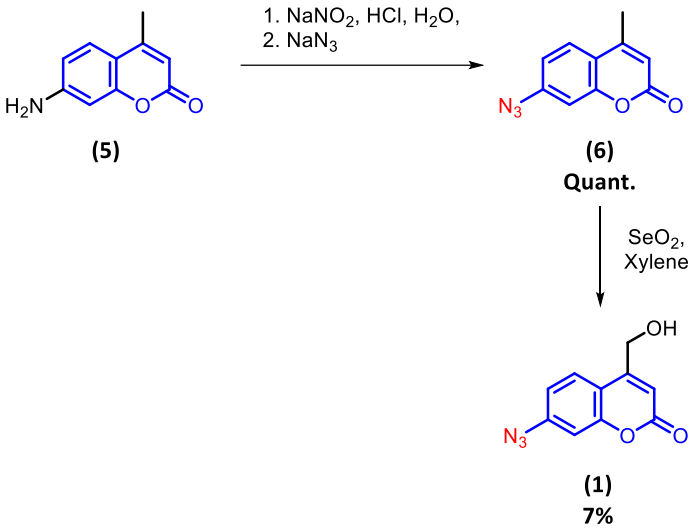

*Scheme 1: Our two-step synthesis of **(1)** based on the work of Anseth & Azagarsamy featured difficult purification following the SeO2 oxidation leading to a yield of just 7% over two steps.*[2]

3.4.2 Alternative routes

In the previous chapter, the issues associated with the SeO_2-mediated Riley oxidation of the methyl group of 7-diethylamino-4-methyl coumarin were overcome by replacing this reaction with a two-step synthesis involving an initial condensation of the 4-methyl group with DMF-DMA to form the corresponding enamine, followed by oxidation to the corresponding aldehyde using $NaIO_4$ as described by Gobel et al.[10] As such we decided to apply this methodology to **(6)** in the hope of producing final compound **(1)** as seen in scheme 2 below.

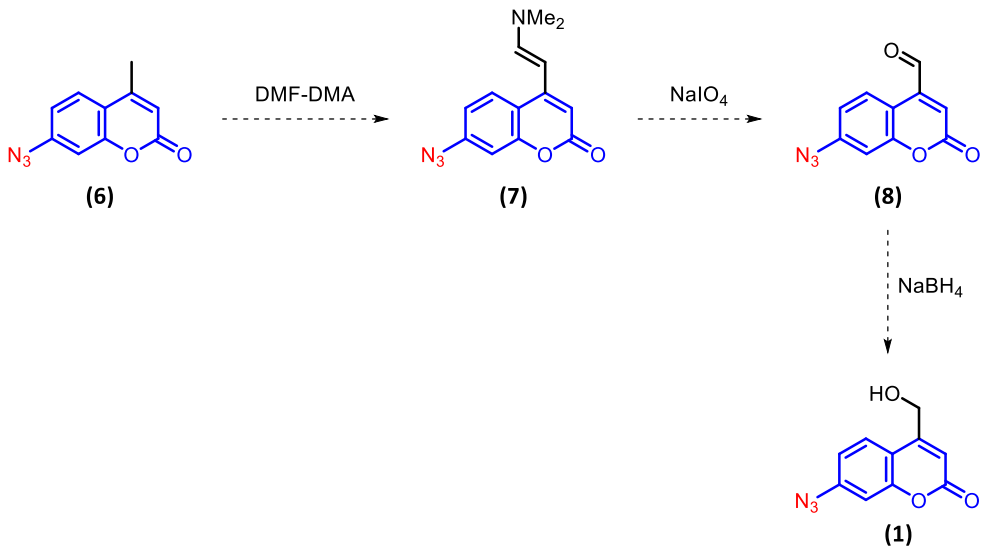

*Scheme 2: A proposed alternative route for the synthesis of **(1)**, based on the successful synthesis of 7-diethylamino-4-hydroxymethyl coumarin from the previous chapter.*

Unfortunately, upon attempting the initial condensation of **(6)** with DMF-DMA to form the corresponding enamine **(7)**, it was found that this reaction did not proceed, with only starting material present upon characterisation of the crude reaction mixture. We then attempted a similar route using 7-amino-4-methyl coumarin **(5)** as starting material in place of **(6)**, postulating that the azide functionality could be installed following the formation of the alcohol as seen in scheme 3 below. However, once again it was found that the initial condensation step of this route did not proceed, meaning that **(1)** could not be produced in this manner. As such it was clear that if sufficient quantities of **(1)** were to be synthesised, alternative methodology was required in order to overcome the shortcomings of the previous routes.

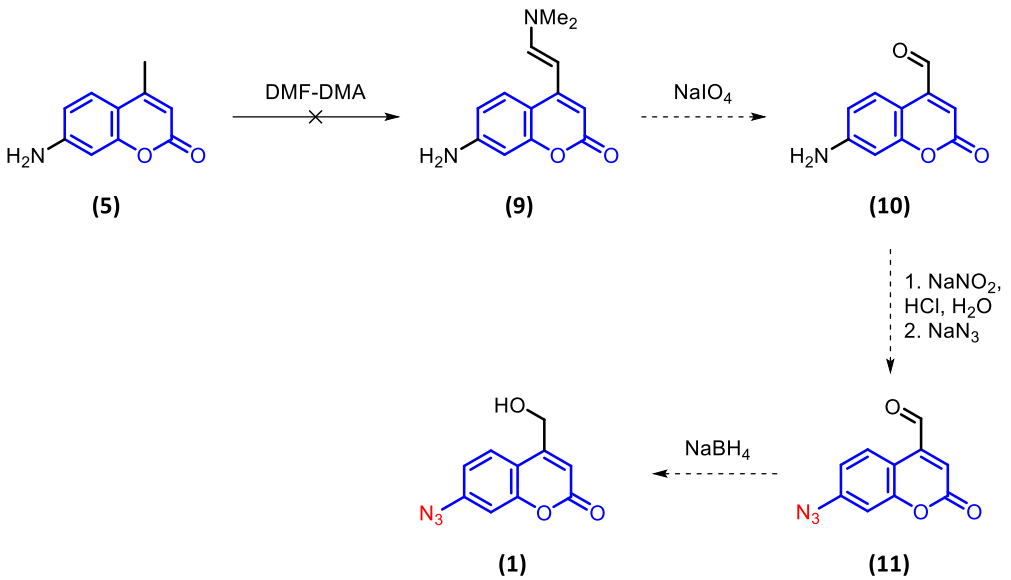

*Scheme 3: A 2nd alternative route for the production of **(1)**, which failed at the initial enamine formation step.*

3.4.3 Retrosynthetic Analysis of (1)

Following the previous difficulties associated with the synthesis of **(1)**, it was decided that a retrosynthetic analysis would be performed. We decided to avoid any disconnections or functional group interconversions which would require the use of an oxidant such as SeO_2, as it was this reagent which had caused the greatest challenge during the initial synthesis of **(1)** described in section 3.3.1. With this consideration in mind, we developed the retrosynthetic analysis seen in scheme 4 below.

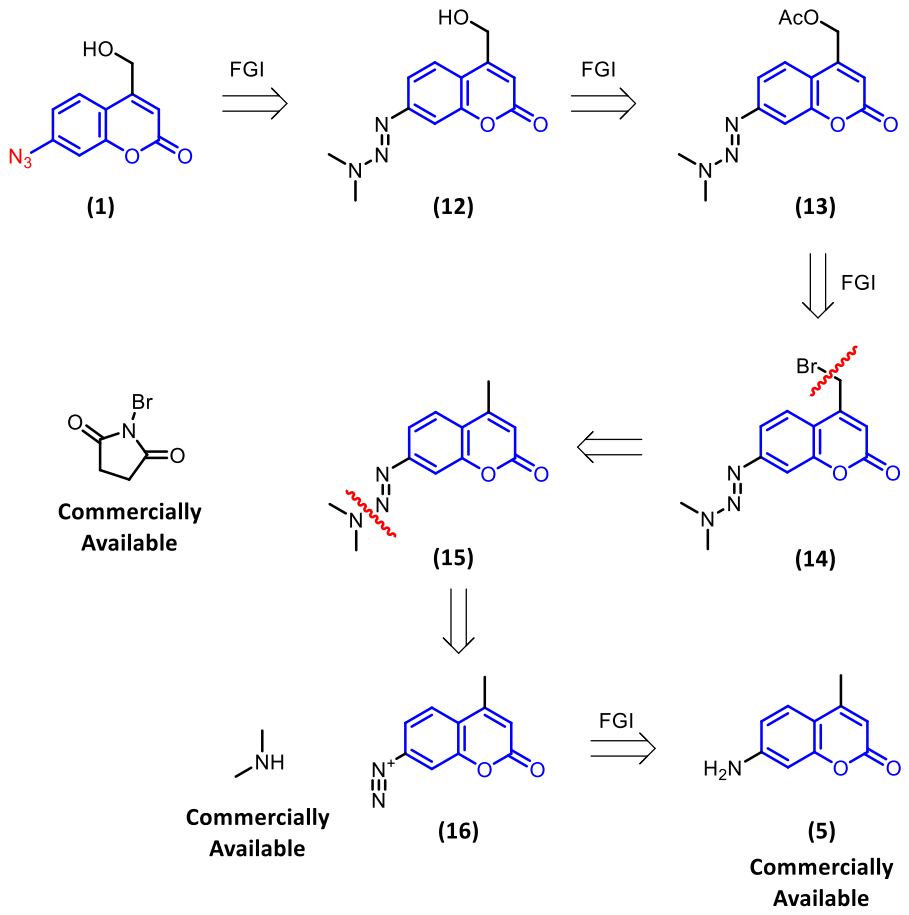

*Scheme 4: A retrosynthetic analysis of **(1)**, from commercially available 7-amino coumarin derivative **(5).***

Looking at the above retrosynthetic analysis, several key differences were planned in comparison to the previous synthesis of **(1).** Firstly, rather than installing the azide functionality at the beginning of the route by diazotisation of the corresponding aniline, followed by nucleophilic attack by sodium azide, the azide is introduced during the final synthetic step. This is facilitated by the introduction of a triazene at the beginning of the route. Aryl triazenes can be employed as a latent form of the reactive diazonium and are bench stable, isolable and compatible with a wide range of reaction conditions. They are readily formed by reacting a diazonium salt with a secondary amine, a strategy which was 1st identified as a useful protection strategy by Gross et al. in 1993.[11] Since this time, they have

been extensively employed as a diazonium protection strategy and have been shown to withstand conditions which would decompose the corresponding free diazonium such as cross-coupling reactions and halogen-metal exchanges.[11–13] In addition to this, they have also been shown to be inert towards strong electrophiles, which would otherwise undergo nucleophilic attack if the original aromatic amine were present.[12,13] At a desired late stage, the triazene can be converted to the desired diazonium salt under mild acidic conditions, which can then be converted to the desired azide by treatment with sodium azide.[11] This late-stage functionalisation has facilitated syntheses which would otherwise have proven problematic if the diazonium were free, such as the synthesis of the natural product ellipticine, whereby late-stage azido installation was crucial to the success of the synthesis.[12]

In addition to this new protecting group strategy, the need for a strong oxidant was also eliminated. By brominating the 4-methyl group, an electrophilic carbon centre would be created which allows for nucleophilic attack by an acetate anion, introducing an acetate group which could then be hydrolysed to the desired alcohol. A similar strategy had previously been utilised in the production of 7-diethylamino-4-methyl coumarin by Zhang et al.,[14] and as such we were confident that we could successfully apply this methodology to our synthesis.

3.4.4 A novel synthetic route toward 7-azido-4-hydroxymethyl coumarin (1)

Now that a retrosynthetic analysis had been performed, it was time to attempt to synthesise **(1)**. The desired product was synthesised successfully according to the route outlined in scheme 5 below.

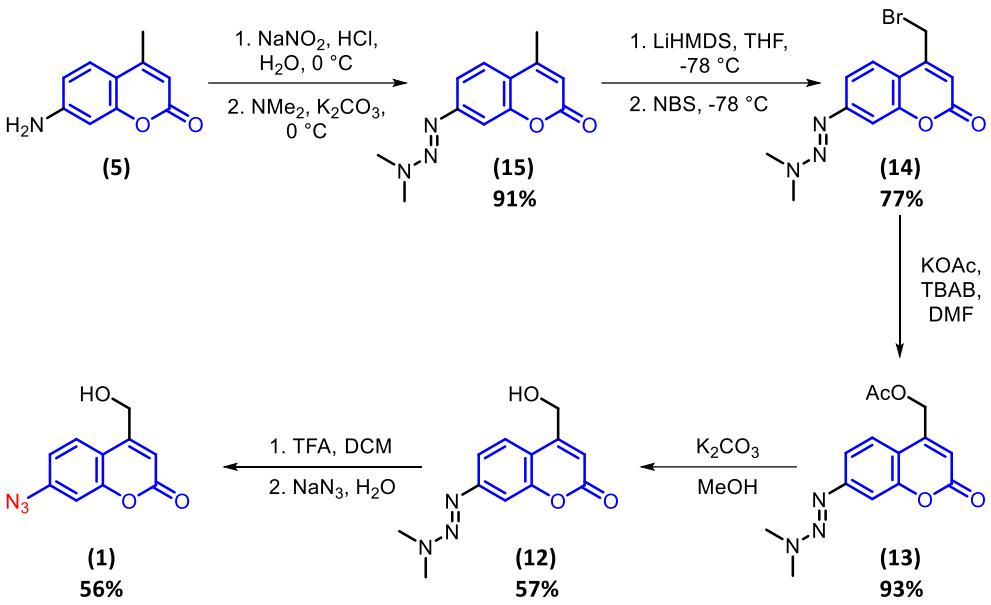

*Scheme 5: Our successful five-step synthesis of **(1)** starting from 7-amino-4-methyl coumarin **(5)**.*

Looking at scheme 6 above it can be seen that the route began with the synthesis of **(15)** from the amino coumarin starting material **(5)**. The 7-amino group of **(5)** was converted to its corresponding diazonium salt by treatment with sodium nitrite in the presence of HCl. The diazonium was then subjected to nucleophilic attack by dimethylamine to form the desired triazene **(15)** in a yield of 91%.

Following the successful synthesis of **(15)**, it was time to install the bromine atom at the 4-methyl position. In the previous chapter, 7-diethylamino-4-methyl-3-bromo coumarin was synthesised by treatment of 7-diethylamino-4-methyl coumarin with *N*-bromosuccinimide and triethylamine as described in section 2.3.2. As such, it was clear that selective bromination of the 4-methyl position was going to require conditions that activated the methyl carbon. Rivera-Fuentes et al. had previously achieved bromination at this position by initially deprotonating the methyl group with LiHMDS, followed by bromination with NBS.[15] The

triazene moiety which had been installed during the previous step, has been shown to be stable to the use of organolithium reagents in the past,[12] and as such we decided to employ these conditions for the synthesis of **(14).** This was successful and following purification, afforded the desired product in a yield of 77%.

Treatment of **(14)** with KOAc replaced the bromide with an acetate in a 93% yield, without the need for column chromatography. This moiety was then hydrolysed to the desired alcohol **(12)**, using K_2CO_3 in MeOH, once again affording the desired product without the need for purification by column chromatography. Notably the recorded yield of 57% indicated that a significant amount of product had been lost during aqueous workup.

Following the formation of the alcohol **(12)** in the previous step, it was now time to convert the triazene group at the 7-position to its corresponding azide. Compound **(12)** was dissolved in TFA: DCM (1:1), converting the triazene to its diazonium form. Treatment with NaN_3 then resulted in the formation of the desired azide **(1)** with a yield of 56% following purification.

The above synthetic route successfully produced **(1)**, with a yield of 21% recorded over five steps. This was a significant improvement over the reported literature yield of 11% over two steps reported by Azagarsamy & Anseth.[2] Additionally our route featured easy purification, only requiring two column chromatography purifications across the five-step synthesis. This was in contrast to the original route, which featured a difficult column chromatography purification following the oxidation of the methyl group due to the presence of selenium-based byproducts. Overall, this allowed us to consistently produce sufficient quantities of **(1)** for our research purposes, satisfying one of the key selection criteria outlined in section 3.2 above.

Additionally, the installation of the triazene moiety at the 7-position creates the opportunity for future late-stage functionalisations of the coumarin scaffold. As mentioned previously, the triazene moiety tolerates a wide array of organic transformations, making it an ideal candidate as a protecting group for diazonium chemistry. Treatment of the triazene with acid converts it back into its diazonium form *in situ,* providing access to a large-array of possible functionalities through the reaction with nucleophiles *via* a Sandmeyer-type reaction as can be seen in scheme 7 below.

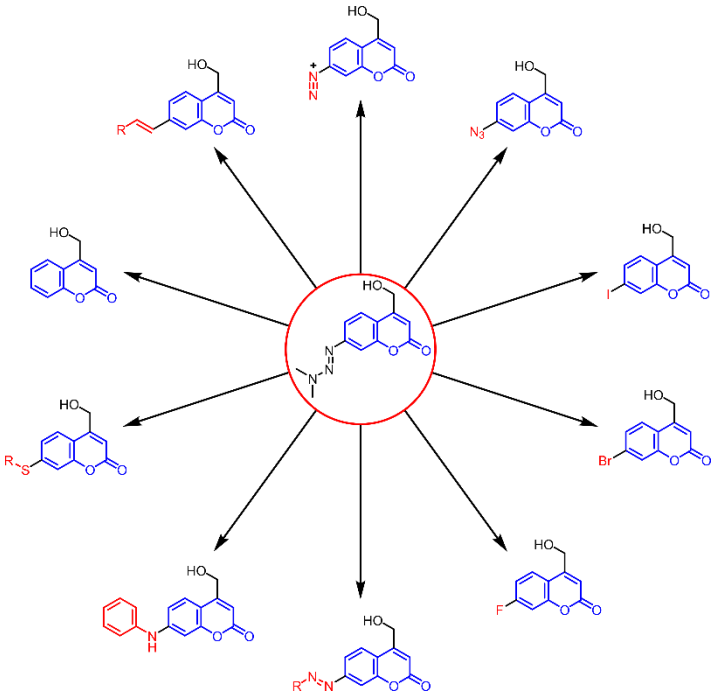

Scheme 6: A selection of the possible transformations available following diazotisation of a triazene-containing coumarin.[16]

3.5 Decaging studies of photocleavable linker (**1**)

Now that **(1)** had been successfully synthesised, we decided to perform proof-of-concept photo-decaging studies in order to verify that this compound behaved as intended. In their work, Anseth & Azagarsamy employed **(1)** in the caging of Boc-β-alanine as seen in figure 4 below.[2] The caged compound was dissolved in a mixture of MeCN: PBS (4:1) and irradiated at

365 nm for 20 minutes. The reaction progress was tracked using HPLC and approximately 80% of the cargo was stated to be released at the conclusion of the experiment. This conversion was determined by tracking the disappearance of the starting material peak and the appearance of a new peak on the UV chromatogram. However, no further characterisation of this peak was performed meaning that it could have arisen due to degradation of the aryl azide rather than successful decaging. As such we decided to use LC-MS during our decaging studies as this technique provides mass spectra which correspond to any UV peaks generated, which would allow us to determine the identity of any products formed with a higher degree of certainty.

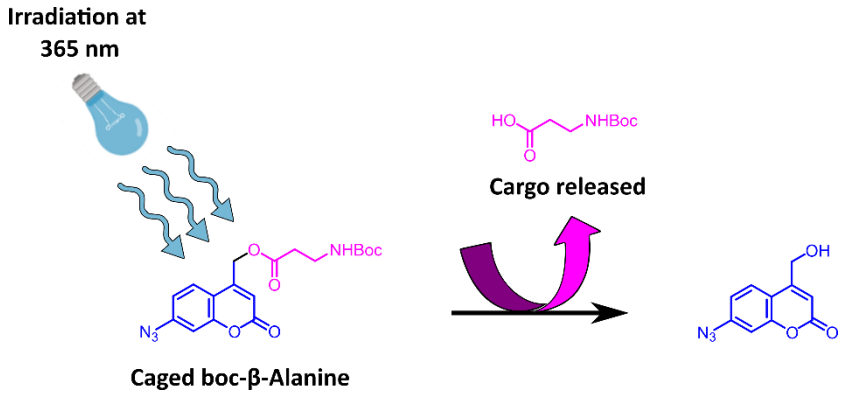

Figure 4: A schematic view of the release of Boc-β-alanine by ***(1)****, following irradiation at 365 nm as reported by Anseth & Azagarsamy.* [2]

In our experiments, acetic acid was selected as the caged substrate rather than Boc-β-alanine. This was motivated by the fact that triazene derivative **(13)** bearing an acetate group had already previously been synthesised as seen in scheme 5 above. Conversion of the triazene to the corresponding azide was then easily achieved through diazotisation with HCl, followed by treatment with NaN_3 to form the desired azide (**16).** We also reasoned that upon incorporating **(16)** into a material using CuAAC, the azide would undergo cycloaddition with an alkyne forming a triazole linkage. In order to more accurately reflect this transformation,

we decided to incorporate "clicked" linker **(17)**. Finally, we decided to incorporate 7-diethylamino coumarin derivative **(18)** into our study as a positive control. The decaging ability of this compound upon irradiation at 365 nm has been well documented in literature, and as such it would serve as a suitable benchmark against which the decaging ability of the other compounds could be assessed.[17,18] The synthesis of these compounds is described in scheme 7 below.

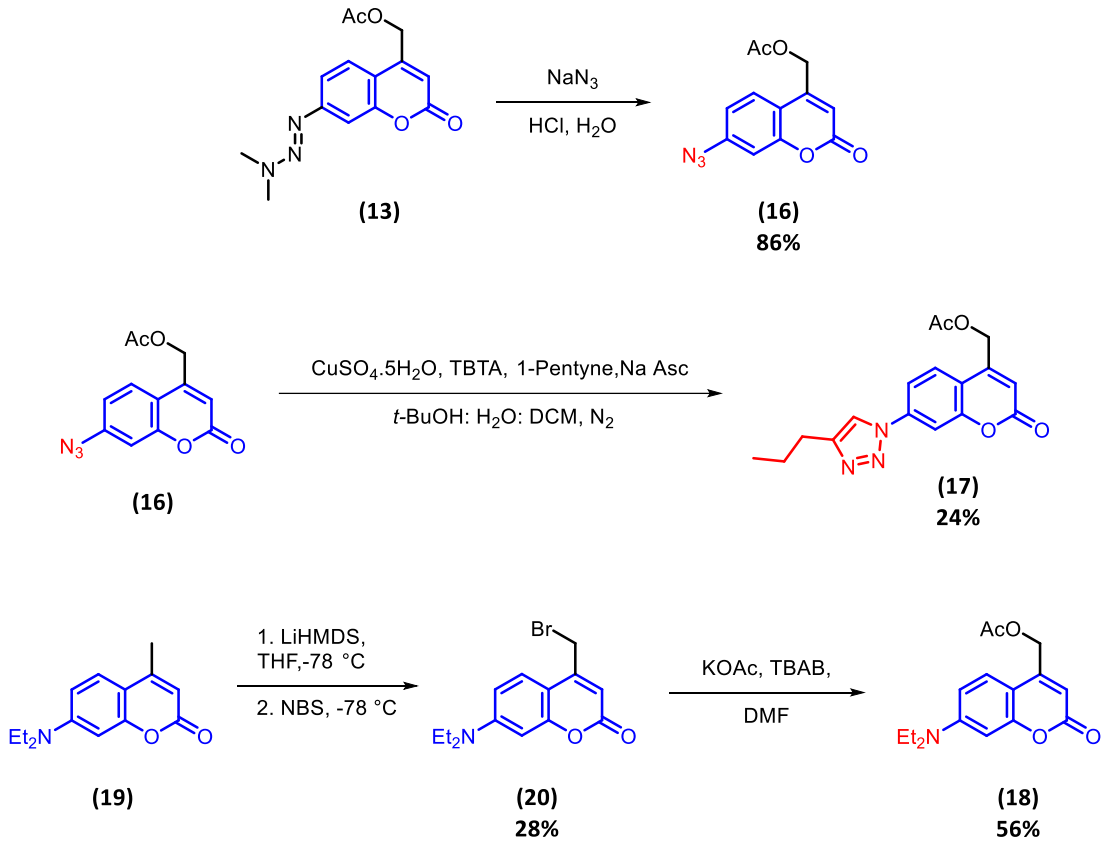

Scheme 7: A schematic of the synthetic routes employed for the production of the compounds to be used in our decaging study.

0.1 mM solutions of the above final compounds in a mixture of MeOH and H_2O (1:4) were irradiated at 365 nm. This was in contrast to the solvent system of MeCN and PBS (1:4) utilised by Anseth & Azagarsamy,[2] and was chosen as the above compounds exhibited higher solubility

in MeOH than MeCN. The samples were irradiated for 5 mins with an aliquot removed every 30 seconds and analysed by LC-MS. Figure 5 below shows the UV (210 – 400 nm) chromatograms generated for the positive control **(18)**, at t_0 and t = 5 min. Looking at these chromatograms, it can be seen that starting material peak **(A)** reacted to form to product peaks **(B)** and **(C)**. An additional peak **(D)** was also observed on the chromatogram recorded at 5 mins. This could have been indicative of unreacted starting material as it appeared at a similar retention time to peak **(A)**. However, it could also have been an additional decaging product.

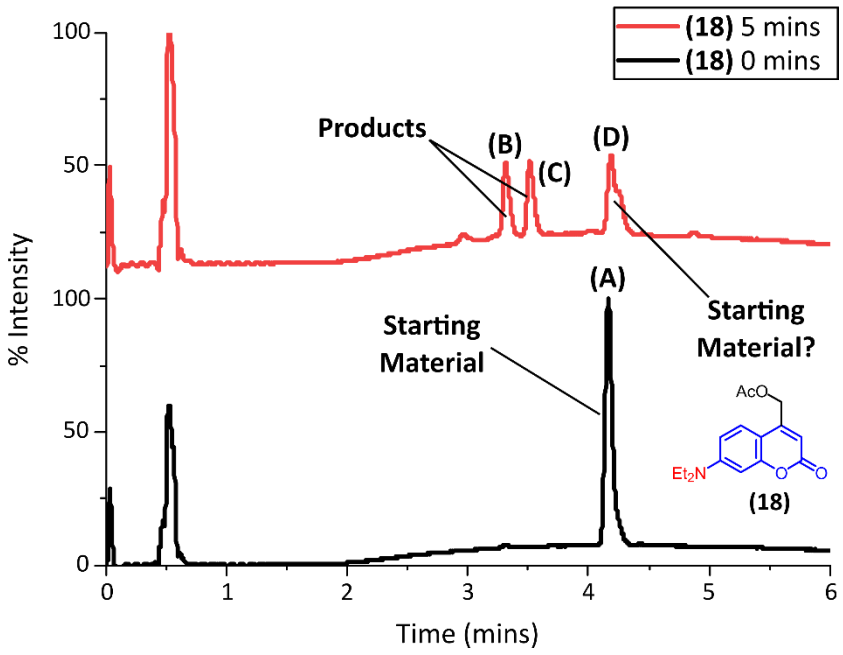

*Figure 5: The UV 210 – 400 nm chromatograms obtained for **(18)** at t_0 and t= 5 mins.*

In order to determine the identity of the products on the above chromatogram, analysis of the corresponding mass spectra was required. As mentioned in section 1.4.2.2 of the introductory chapter, coumarin decaging operates *via* an S_N1-type mechanism, whereby the excited state decays *via* heterolytic cleavage of the C-O bond, releasing the cargo in its anionic form and forming a methyl coumarin carbocation which is then quenched by surrounding

solvent.[19] The solvent used during our experiment was MeOH:H_2O. As such a number of coumarin-based products would be expected, depending on which surrounding solvent molecules quenched the carbocation upon its formation.

Figure 6 below depicts the corresponding mass spectra for the UV-chromatogram of **(18)**, following 5 mins of irradiation. Looking at this chromatogram, three peaks **(B)**, **(C)** and **(D)** are observed. The recorded mass spectrum for peak **(B)** consisted of two peaks, 247.78 and 517.09. These matched the expected values $[M+H]^+$ and dimer $[M+Na]^+$ for the hydroxy coumarin decaging product depicted in the yellow box, which arose due to quenching of the methyl carbocation by surrounding water.

Peak **(C)** also has a mass spectrum comprising of two peaks, 277.83 and 577.12. Although the exact identity of this compound could not be identified, the mass was consistent with the hemiacetal form of product **(B)**. Although it was not clear how this could have formed, there was O_2 present during irradiation meaning that, **(B)** could have been oxidised to its corresponding aldehyde, prior to forming the hemiacetal during LC-MS analysis.

Peak **(D)**, had a similar retention time as peak **(A)**, suggesting that it may be unreacted starting material as seen in figure 5 above. However, looking at the mass spectrum obtained for this peak Masses of 261.81 and 545.11 are obtained, matching the expected $[M+H]^+$ and dimeric $[M+Na]^+$ for the methoxy coumarin derivative seen in the purple box, which arises from quenching of the methyl carbocation by surrounding methanol. Additionally, the presence of starting material is also indicated by the presence of a peak at 289.83. This was significant as it meant that we were unable to fully determine conversion. However, the presence of the three aforementioned products did confirm that decaging was occurring to some degree and thus the ability of the experimental set-up to trigger decaging was validated.

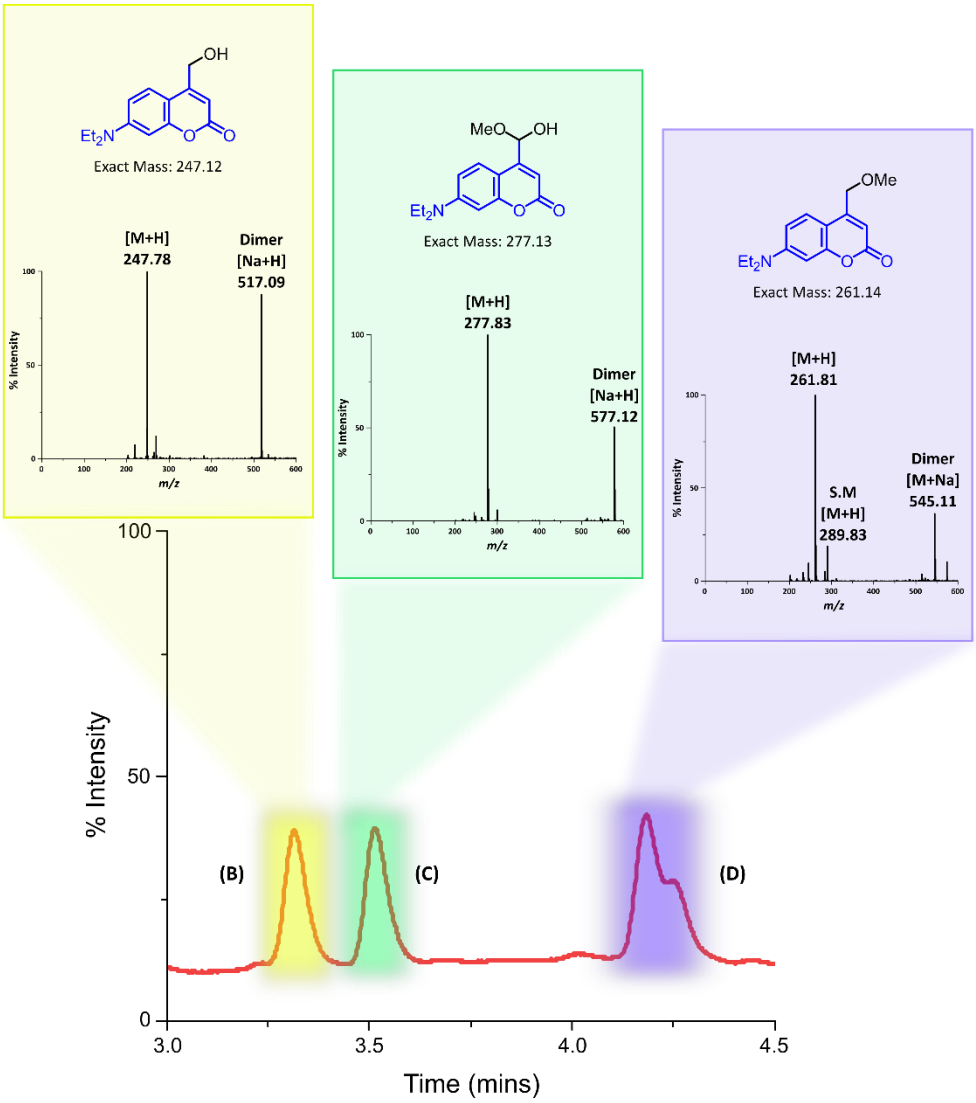

*Figure 6: The corresponding mass spectra for peaks **(B)**, **(C)** and **(D)** on the UV 210 – 400 nm obtained for **(18)** at t= 5 mins.*

Now that our experimental set-up had been shown to successfully cause decaging, we set out to analyse the results generated for **(16)** and **(17)**. The UV 210 – 400 nm chromatograms generated for **(16)** at t_0 and t = 5 min can be seen in figure 7 below. Looking at these chromatograms it can be seen that starting material peak **(A)**, was almost fully converted into products **(B, C & D)** following 5 mins of irradiation at 365 nm.

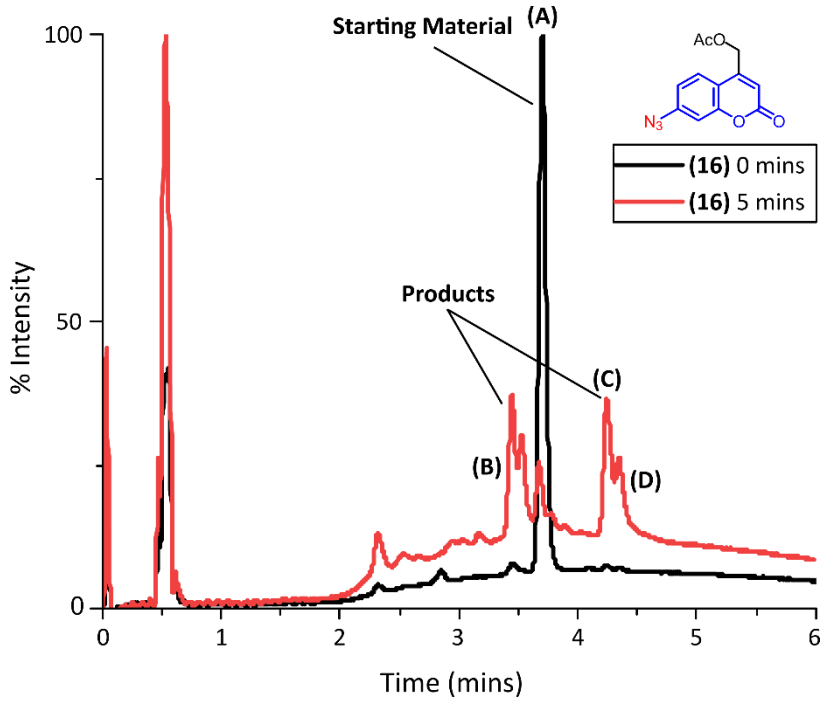

*Figure 7: The UV 210 – 400 nm chromatograms obtained for **(16)** at t_0 and t= 5 mins.*

Upon analysis of the corresponding mass spectra however, it became evident that the observed products were not the result of decaging but rather arose from the activation of the aryl azide. Aryl azides have been extensively used in photoaffinity labelling since the late 1960s due to their inherent photosensitivity.[20–22] Upon exposure to UV (or near UV) light, they decompose to liberate N_2, generating a highly reactive nitrene, which can then undergo bond insertion with proximal functionalities labelling a site of interest.[23] The inherent reactivity of the nitrene makes it highly promiscuous, meaning that a diverse range of products can be formed depending on the surrounding chemical environment. Solvent quenching is common, along with dimerisation, whereby the nitrene first enters its triplet state *via* intersystem crossing, forming a radical which then reacts with another triplet nitrene to form a diazo bridge.[23,24] A schematic summary of these processes is provided in figure 8 below.

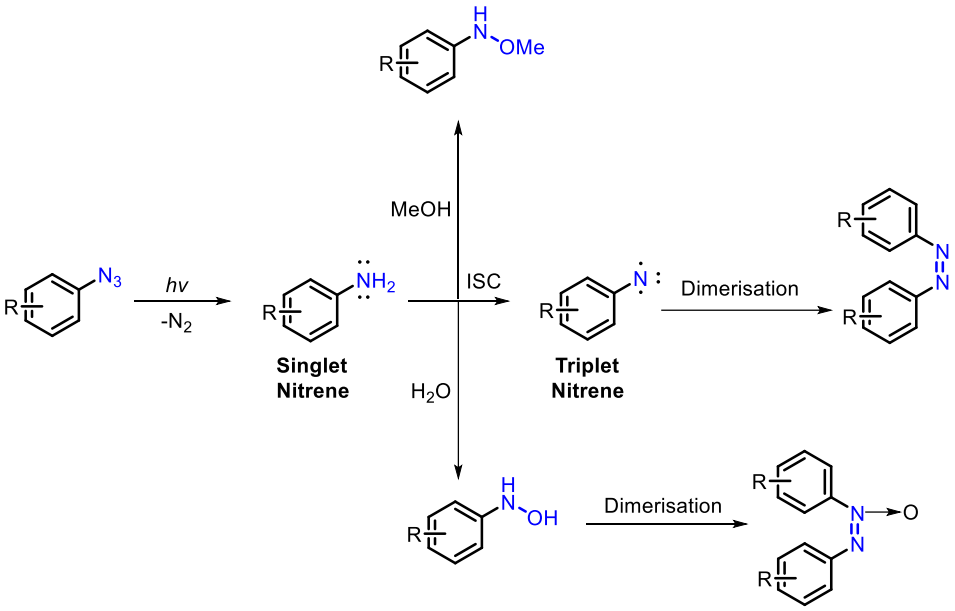

Figure 8: A selection of the possible reaction pathways upon photolysis of an aryl azide with light. [23,24]

Figure 9 below depicts the UV 210 – 400 nm chromatogram generated at t = 5 mins for **(16)** alongside the corresponding mass spectra. Looking at this chromatogram it is observed that peak **(B)** corresponded to an *m/z* of 263.72, which aligned with the expected $[M+H]^+$ for the methoxyamine-coumarin depicted in the yellow box. This product likely resulted from the quenching of the singlet nitrene by methanol. Peak **(C)** exhibits two *m/z* values, 479.02 and 501.00, which corresponded to the anticipated $[M+H]^+$ and $[M+Na]^+$ for the oxygenated dimer shown in the green box. Finally, peak **(D)** displayed an *m/z of* 463.05, consistent with the $[M+H]^+$ of the dimer indicated in the purple box. A second peak at 479.05 is also observed, which can be attributed to the partial resolution of peaks **(C)** and **(D)**, as this *m/z* value matches the $[M+H]^+$ of the oxygenated dimer seen in peak **(C).**

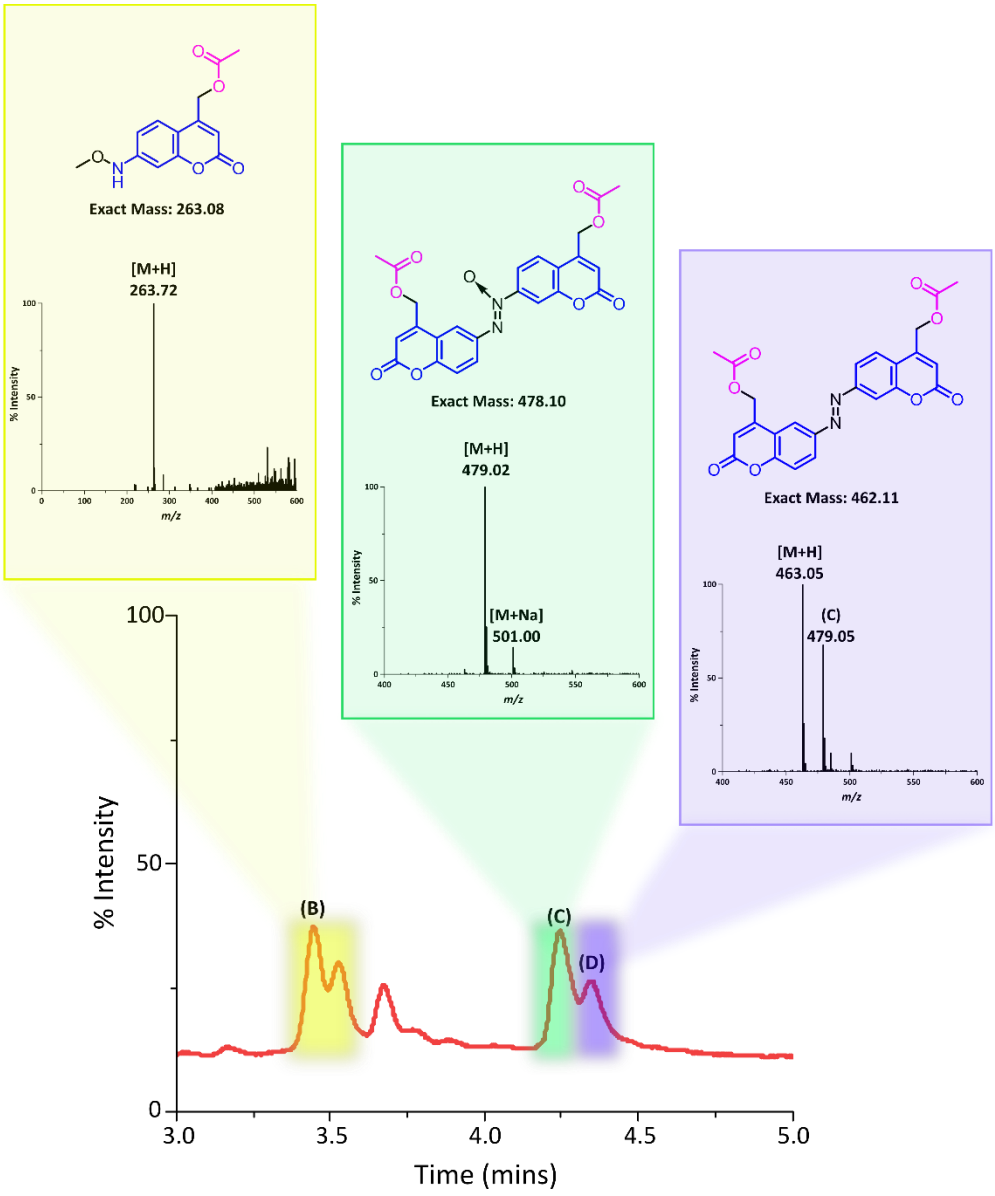

*Figure 9: The corresponding mass spectra for peaks **(B)**, **(C)** and **(D)** on the UV 210 – 400 nm obtained for **(16)** at t= 5 mins.*

Although the data obtained for **(16)** indicated that decaging was not occurring, this could have been due to the side-reactivity of the aryl azide. The triazole containing (**17)**, is more representative of the structure that would be formed after CuAAC or SPAAC of the azide. The UV 210 – 400 nm chromatograms obtained for **(17)** at t_0 and t = 5 mins can be seen in figure 10, along with the corresponding mass spectra. Looking at this figure it can be seen that a single starting material peak exists at T_0. Following 5 mins of irradiation at 365 nm this peak

remains, indicating that no decaging had taken place. This was then corroborated by the corresponding mass spectra obtained for these peaks, which indicated that both were indeed representative of the starting material. Consequently, **(17)** was stable to irradiation at 365 nm for 5 mins, releasing none of its cargo.

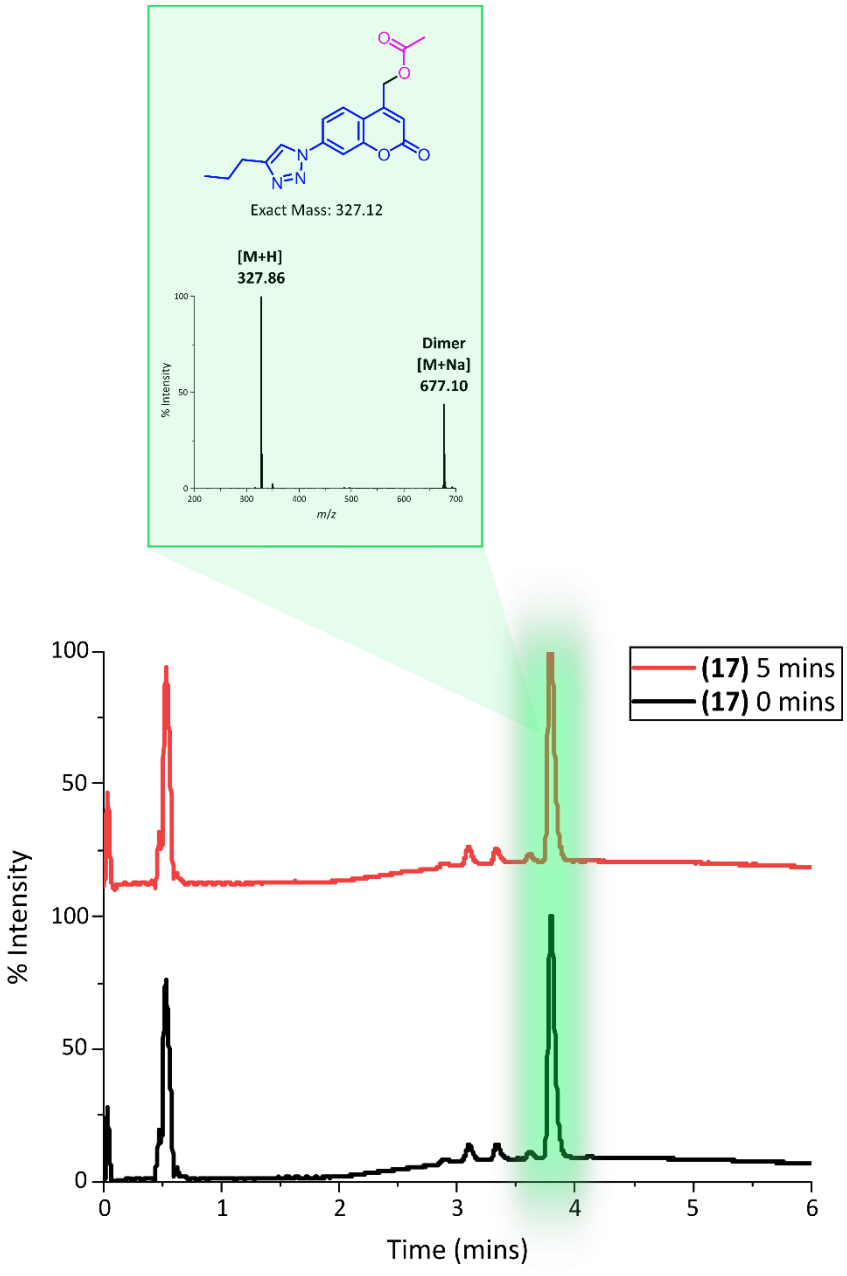

*Figure 10: The UV 210 – 400 nm chromatograms obtained for **(17)** at t_0 and t= 5 mins alongside the corresponding mass spectrum of the sole peak present.*

The above result highlighted a key limitation of the study performed by Anseth & Azagarsamy.[2] In their work, conversion was monitored solely by UV-Vis spectroscopy, and changes in absorbance were attributed to decaging without concrete product characterisation. Consequently, it is likely that photodegradation of the aryl azide chromophore was misinterpreted as decaging. In contrast to this, our results clearly demonstrated that aryl azide **(16)** underwent rapid photodegradation upon irradiation at 365 nm, with no evidence of decaging having occurred, as can be seen in figure 9 above. This finding was corroborated by irradiation of the corresponding triazole **(17)**, which was a more representative model of how **(16)** would behave once incorporated into a material, and once again did not exhibit any decaging activity following 5 mins of exposure under identical conditions as can be seen in figure 10 above. We considered the possibility that 5 min of irradiation might have been insufficient to observe decaging and therefore extended the irradiation time to 2 h. However, as shown in the UV chromatograms 210–400 nm and corresponding mass spectra depicted in Figure 11 below, compound **(17)** remained stable under irradiation at 365 nm over this time period.

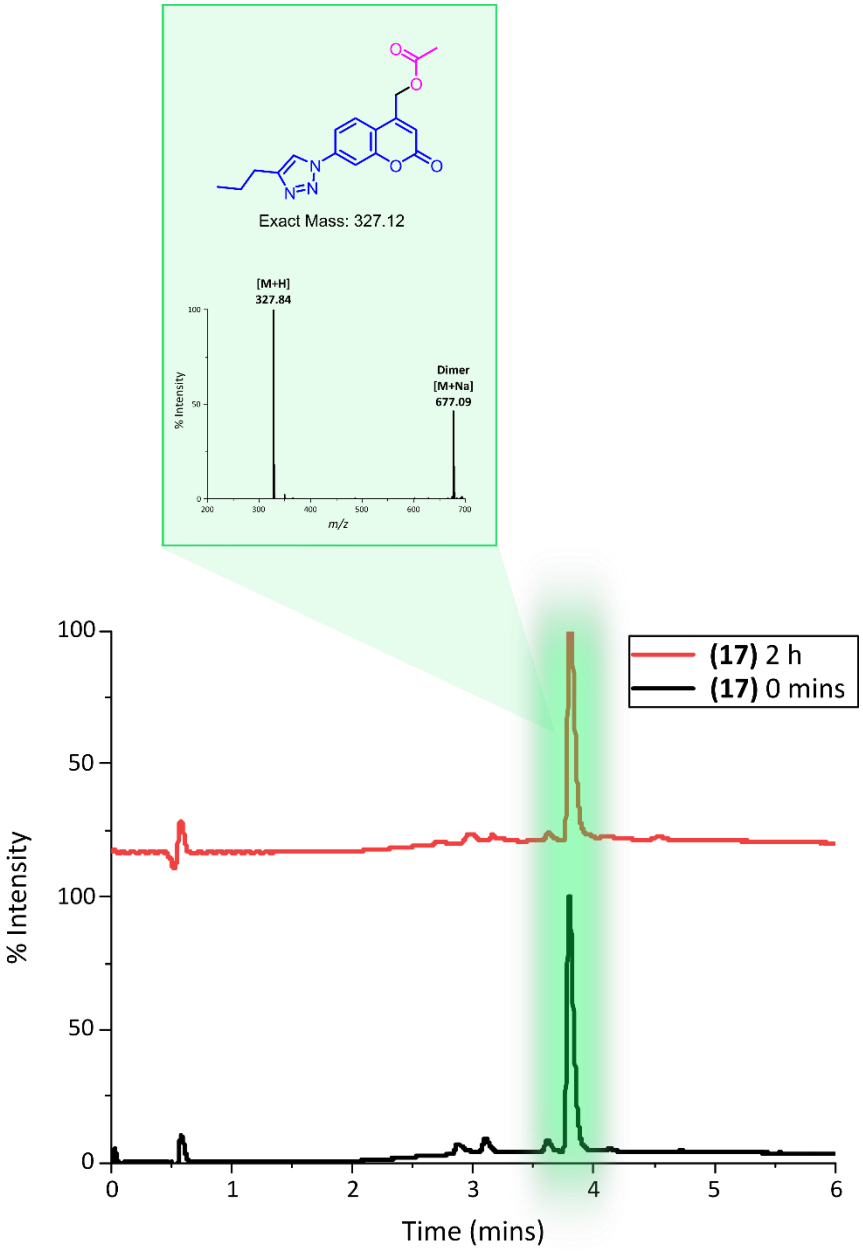

*Figure 11: The UV 210 – 400 nm chromatograms obtained for **(17)** at t_0 and t= 2 h alongside the corresponding mass spectrum of the sole peak present.*

From the above experiments, it can be seen that the 7-azido coumarin chromophore, did not undergo photo-decaging upon irradiation at 365 nm under our experimental conditions, making it unsuitable for our intended application. In order to design a future potential photocleavable linker to satisfy our needs, we needed to gain an understanding as to why this was the case. The absorbance spectra of the compounds used in this study depicted in figure

12 below, provide useful insight into the lack of decaging activity observed for **(16)** and **(17)**. As explained in section 1.3.2 of the introductory chapter decaging efficiency is quantified using a metric known as the decaging cross section. This parameter provides a wavelength-dependent measure of decaging efficiency and is defined as the product of the molar extinction coefficient and decaging quantum yield.[25] Hence, the capacity for a photocage to absorb light at the irradiation wavelength is critical, as it is this absorption capacity that facilitates access to the excited state from which decaging can occur. Looking at figure 12, it can be seen that the absorption profiles of **(16)** and **(17)** exhibit minimal overlap with the irradiation wavelength of 365 nm, absorbing at just 14% and 2% of their λ_{max} at this wavelength respectively. As such, their ability to enter the excited state at this wavelength is severely restricted, leading to the lack of decaging observed during our experiments. **(18)** on the other hand, was shown to successfully decage during our study and looking at its absorption profile it can be seen that it absorbs strongly at 365 nm, absorbing at approximately 83% of its λ_{max}. As such the excited state of this molecule is much more accessible at 365 nm, allowing for more efficient decaging to occur. Thus, when designing a novel photocleavable linker for our intended purpose it was critical that the absorption profile overlapped as maximally as possible with wavelength of irradiation.

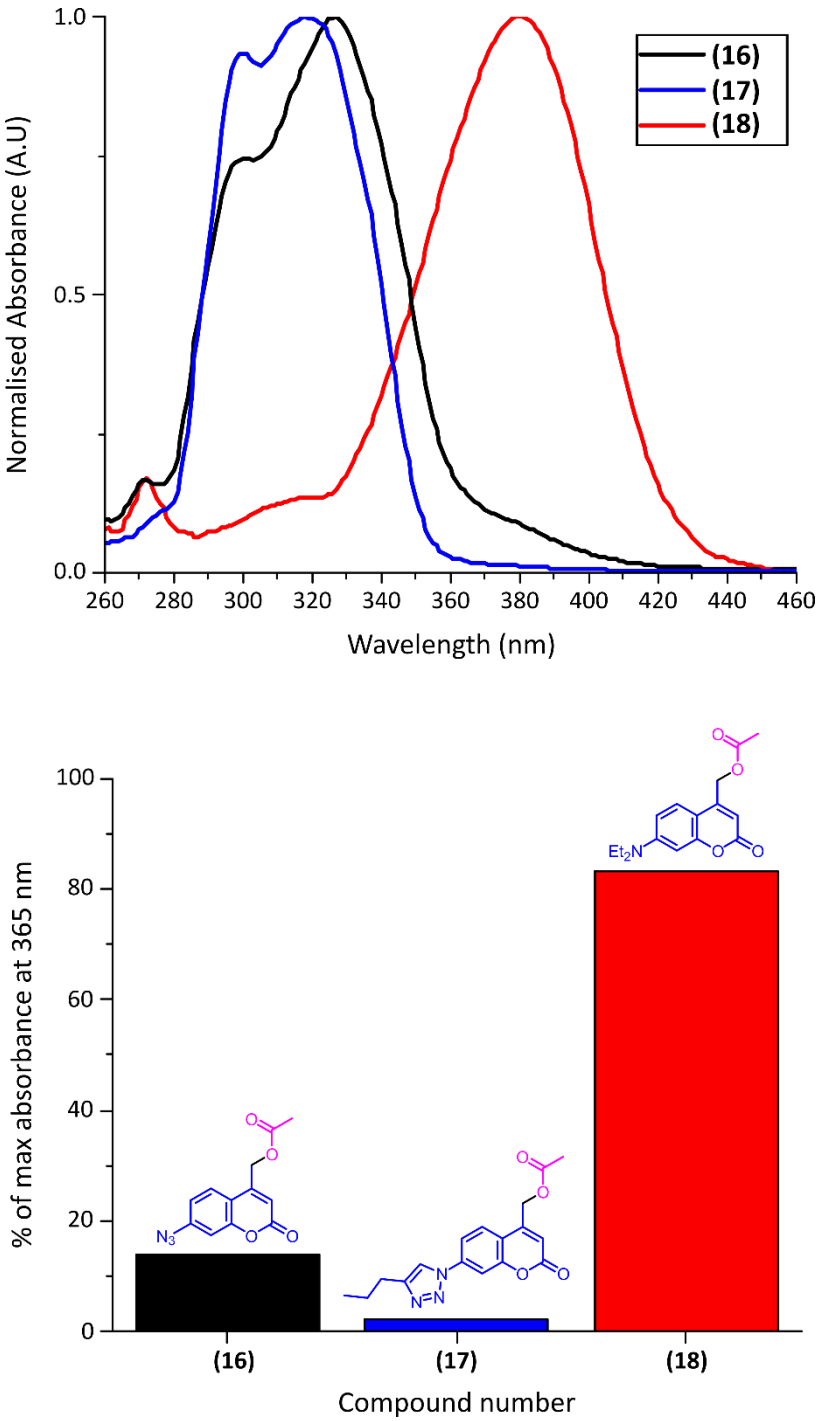

Figure 12: The absorption spectra of the compounds studied during our decaging study alongside a graph depicting their relative absorbances at the wavelength of irradiation (365 nm).

Although in our work, we were unable to successfully decage **(1)** at 365 nm, Anseth & Azagarsamy had previously shown that this molecule was capable of releasing BMP-7 from a

hydrogel matrix.[2] The light source that was utilised during our decaging study was an LED sourced from Hepato chem which had been shown to have a narrow emission band around 365 nm. However, it is possible that the light source used during the work of Anseth & Azagarsamy, featured a wider emission band which extended further into the UV range. If this band extended far enough into the UV range, it is possible that the irradiation wavelengths exhibited some overlap with the absorption profile of **(1)** allowing for decaging to occur.

3.6 The development of alternative photocleavable linker (21)

3.6.1 The design of (21)

From the previous experiment, it was clear that photocleavable linker (**1)** did not undergo decaging upon irradiation at 365 nm. Consequently, a novel photocleavable linker, capable of absorbing at this wavelength was required. The obvious structural difference between the studied compounds occurred at the 7-position of the coumarin scaffold, with the 7-diethylamino coumarin derivative **(18)** being considerably red-shifted, in comparison to the azide and triazole containing compounds **(16)** and **(17)**. As discussed in section 1.4.2.4, the nitrogen atom of this group contains a lone pair which can conjugate with the π-system of the coumarin scaffold. This has the effect of narrowing the HOMO-LUMO energy gap, resulting in a red-shift in absorbance.[17,18] This moiety was found to be so beneficial to red-shifting absorbance that it has remained as a key component of many of the “next generation” red-shifted coumarin photocages seen today.[8,26–28] As such we decided that this moiety should be incorporated into any photocleavable linker s to be designed. With this in mind, we designed the derivative **(21)** seen in figure 13 below. This compound incorporated the azido group at the 3-position of the coumarin scaffold, whilst maintaining the electron-donating diethylamino group at the 7-position. As such, it was hoped that the absorbance of this compound would be shifted toward the red range whilst still maintaining its azide click handle.

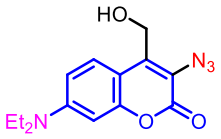

(21)

Figure 13: The structure of the 7-diethylamino containing proposed photocleavable linker ***(21).***

3.6.2 The synthesis of **(21)**

Liang et al. had previously reported an Ullman-type coupling capable of converting aryl halides to their corresponding azides under mild conditions.[29] The synthesis of 7-diethylamino-3-bromo coumarin **(22)** was reported in section 2.3.2 of the previous chapter,[8] and the methodology developed by Liang et al. was applied directly to it as seen in scheme 8 below. Unfortunately, rather than forming the desired azido product **(21)**, dehalogenation was observed resulting in the formation of **(23)**.

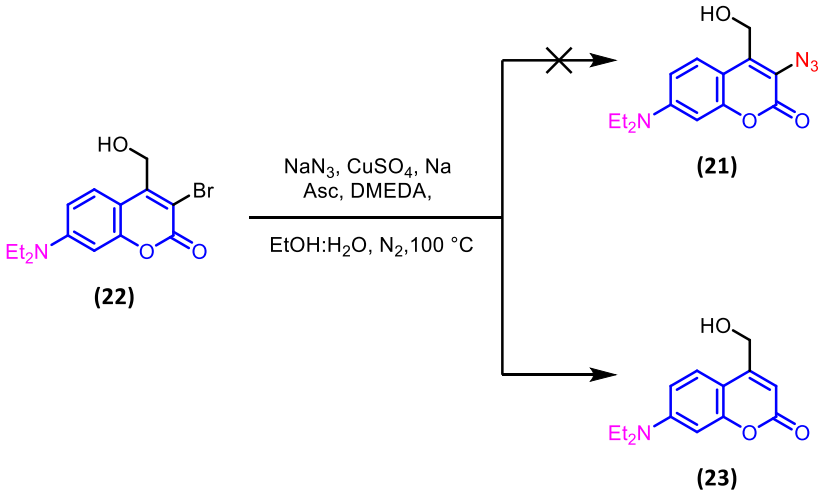

Scheme 8: The attempted Ullman-type coupling performed on ***(22)****, resulted in dehalogenation rather than the production of the desired azido product* ***(21).***

Following the failure of the above reaction, it was obvious that different methodology was required in order to synthesise **(21).** We reasoned that if **(23)** could be nitrated at the 3-position forming **(24)**, we could then reduce this moiety to form the corresponding aryl amine

(25). We could then perform a diazotisation followed by treatment with NaN_3 to produce the desired compound **(21)** as seen in scheme 9 below.

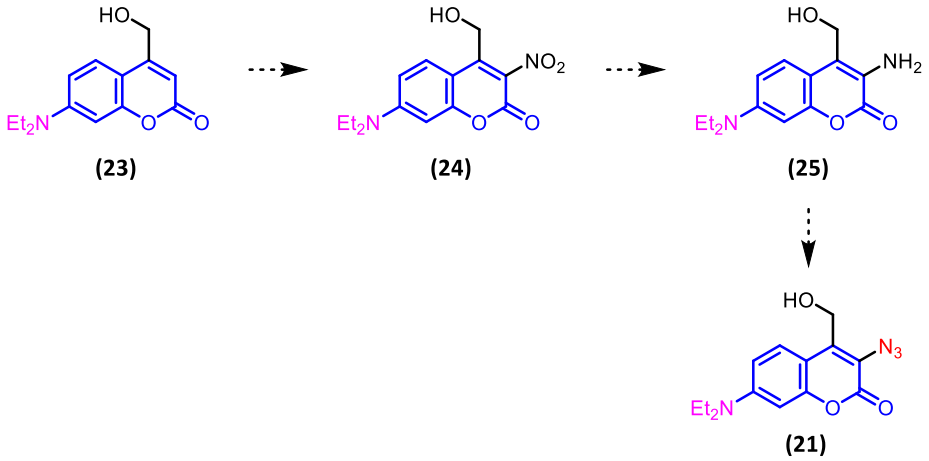

*Scheme 9: An alternative route for the production **(21)** which relied on the nitration of the 3-position of **(23).***

Nitration of 7-diethylamino-4-methyl coumarin **(26)** had previously been optimised by Luk'yanets et al.[30] In this work **(26)** was nitrated at the 3-position using H_2SO_4/HNO_3 to form 3-nitro derivative **(27)** as seen in scheme 10 below. When they performed this synthesis, the desired product was precipitated by pouring the reaction mixture into ice-cold water at the conclusion of the reaction. However, when we applied this methodology to **(23)**, it was found that the product did not precipitate upon addition of the reaction mixture to water. As such we were required to extract the product from the aqueous mixture. Although this was initially successful allowing **(24)** to be isolated in a 16% yield following purification, this extraction proved extremely difficult to replicate, with the product often remaining in the aqueous layer. This extraction was attempted with a number of different solvents including EtOAc, DCM, Et_2O, and toluene, however, all attempts were unsuccessful. As such it was difficult to consistently produce sufficient quantities of **(24)** for our research purposes.

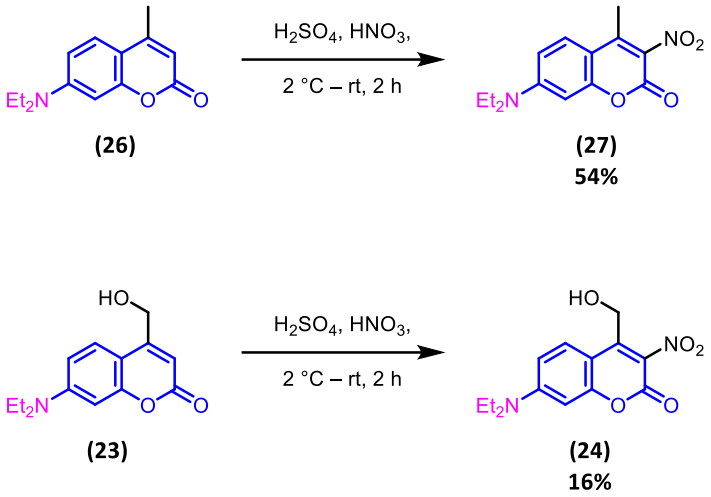

*Scheme 10: Schematic of the conditions utilised for the nitration of **(26)** and **(23)**. **(24)** was afforded in a considerably higher yield due to isolation issues.*

Although the above reaction was inconsistent, we still attempted to reduce **(24)** to the corresponding amine **(25)** before converting it to the desired azide **(21). (25)** was synthesised by performing a reduction on **(24)** using zinc in methanol and acetic acid which afforded the desired product in a yield of 45%. We then attempted to form the corresponding azide by diazotisation with $NaNO_2$ in the presence of HCl, followed by nucleophilic attack by NaN_3. However, rather than producing **(21)**, we instead observed that aldehyde **(28)** was formed. When treated with sodium nitrite under acidic conditions, benzylic alcohols can be converted to the corresponding alkyl nitrite.[31] This intermediate is unstable and rapidly equilibrates with the original alcohol. However, it can also decompose to form the corresponding aldehyde,[32] which would potentially explain why we observed the formation of **(28)** during our synthesis as seen in scheme 11 below.

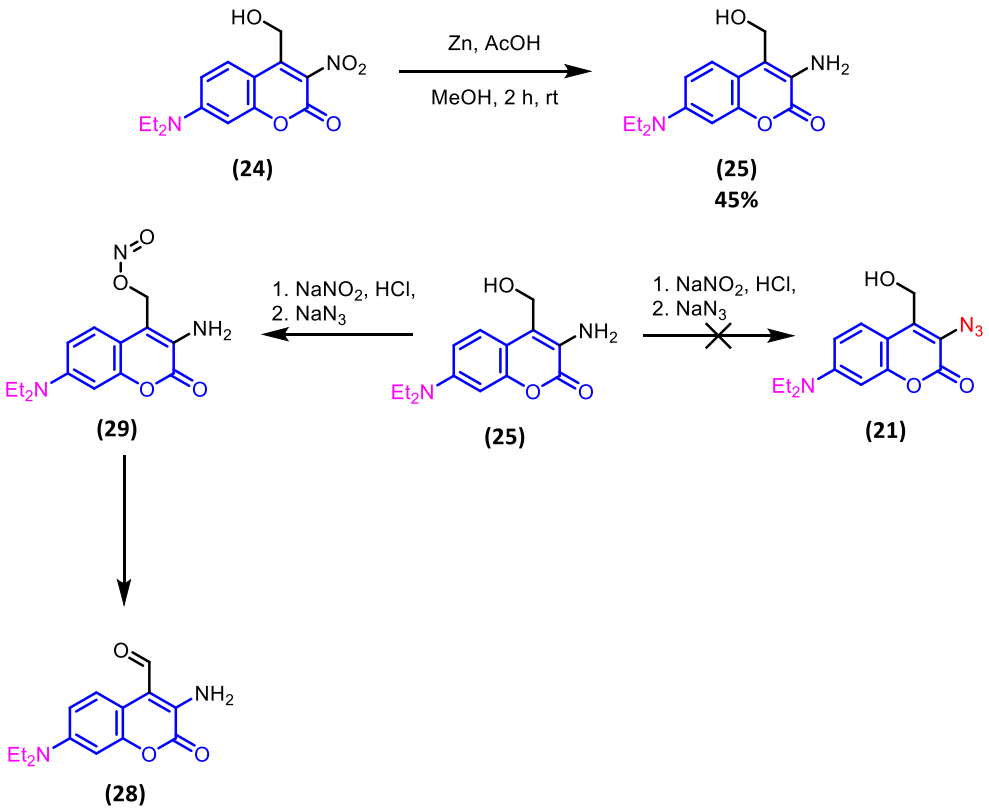

*Scheme 11: Schematic of the failed synthetic route for the production of **(21)**. Treatment of **(25)** with NaNO2 and NaN3 resulted in the formation of aldehyde **(28)** likely through alkyl nitrite intermediate **(29)**.*

Due to the failure of the above synthesis, we decided to 1st protect the alcohol in order to prevent the formation of the aldehyde side-product. As such we decided to attempt a nitration on **(18)** as seen in scheme 12 below. It was hoped that the added hydrophobicity of **(29)**, afforded by the acetate group would aid isolation from water. Unfortunately, upon trialling this reaction it was found that this was not the case, and we experienced the same isolation issues associated with the synthesis of **(21)**. In fact, we could not isolate this product at any point meaning that we could not confirm that it was being successfully formed.

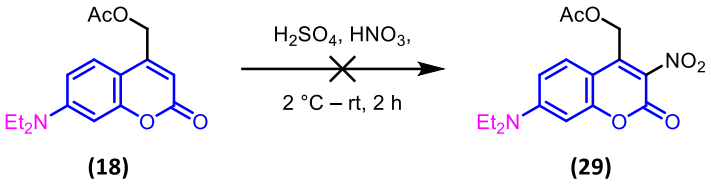

*Scheme 12: A schematic of the conditions employed during the failed nitration of **(18).***

From the failure of the above reaction, it was clear that an alternative method of nitration was required if the route were to succeed. Katayev et al. had recently reported on the nitration of aromatic compounds under mild conditions using *N*-nitrosaccharin.[33] This reagent acts as a mild source of the nitronium ion, avoiding the need for the harsh acidic conditions which had caused the issues associated with our previous syntheses. *N*-nitrosaccharin was synthesised as seen in scheme 13 below before being utilised in the attempted nitration of **(23).** Unfortunately, this nitration failed with no conversion detected by TLC, causing us to abandon this route.

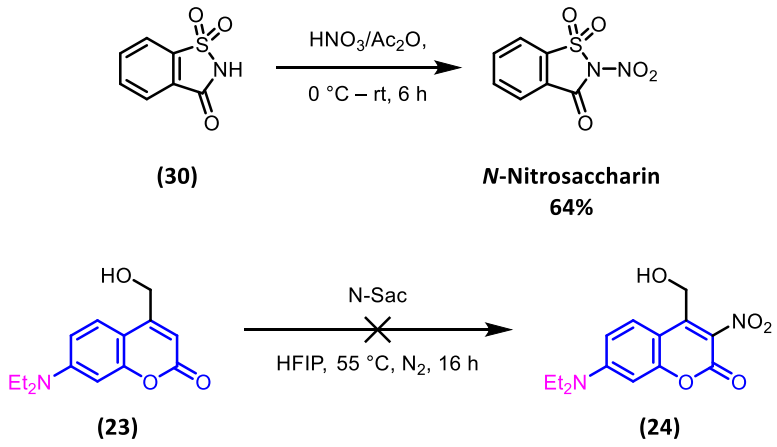

*Scheme 13: The attempted nitration of **(23)** using N-Nitrosaccharin did not proceed.*

Due to the failure of the synthetic routes described in this section, it was decided that alternative photocleavable linkers would be designed in the hope that they would be more synthetically accessible. This is discussed in the following section.

3.7 The development of novel photocleavable linker (31)

3.7.1 The design of (31)

Due to the failure of the above synthetic routes, it was clear that alternative photocleavable linker s, capable of absorbing in the visible range were required. 3-bromo coumarins had previously been shown to successfully undergo Suzuki-Miyaura cross coupling reactions in order to install an aryl group at this position.[34] Thus, we reasoned that if an aryl amine could be installed using this methodology, it could then be converted to the corresponding azide to provide a click handle. Additionally, unlike the π-extended coumarins discussed in section 1.4.2.5,[8,26,27,35] the aryl substituent would be free to rotate about its axis and would not conjugate with the aromatic system of the coumarin scaffold. Thus, it was predicted that the absorption profile of **(31)** would more closely resemble that of **(18)**, seen in figure 12 above, facilitating orthogonal cleavage with the green-light absorbing photocage **(3)** which had previously been shown to have a λ_{max} of 498 nm in section 2.6 of the previous chapter. The structure of the proposed photocleavable linker (**29)** is depicted in figure 14 below.

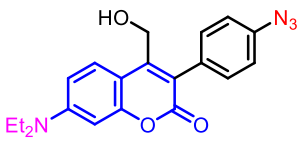

(31)

*Figure 14: The structure of proposed photocleavable linker (**29)** which incorporated a click handle via an aryl linker installed at the 3-position of the coumarin scaffold.*

3.7.2 Retrosynthetic analysis of **(31)**

Before **(31)** could be synthesised, a retrosynthetic analysis was required in order to plan a potential synthetic route. This is seen in scheme 14 below. Looking at the route it can be seen that the hydroxyl group present on previously synthesised coumarin **(23)** is protected with a silyl ether at the beginning of the route, which we chose as it tolerates the conditions required for cross coupling reactions and is easily cleavable using tertbutyl ammonium fluoride (TBAF).[36] The 3-position is then brominated, allowing the coumarin to undergo a Suzuki-Miyuara cross coupling reaction with the commercially available 4-aminophenylboronic acid, in order to install the aryl amine. The amine then undergoes diazotisation and subsequent conversion to the corresponding azide, whilst the hydroxyl group at the 4-position remains protected to prevent the formation of the alkyl nitrite which was previously suspected to occur in scheme 11 above. Finally, the silyl ether protecting group is cleaved, affording the desired compound **(31).**

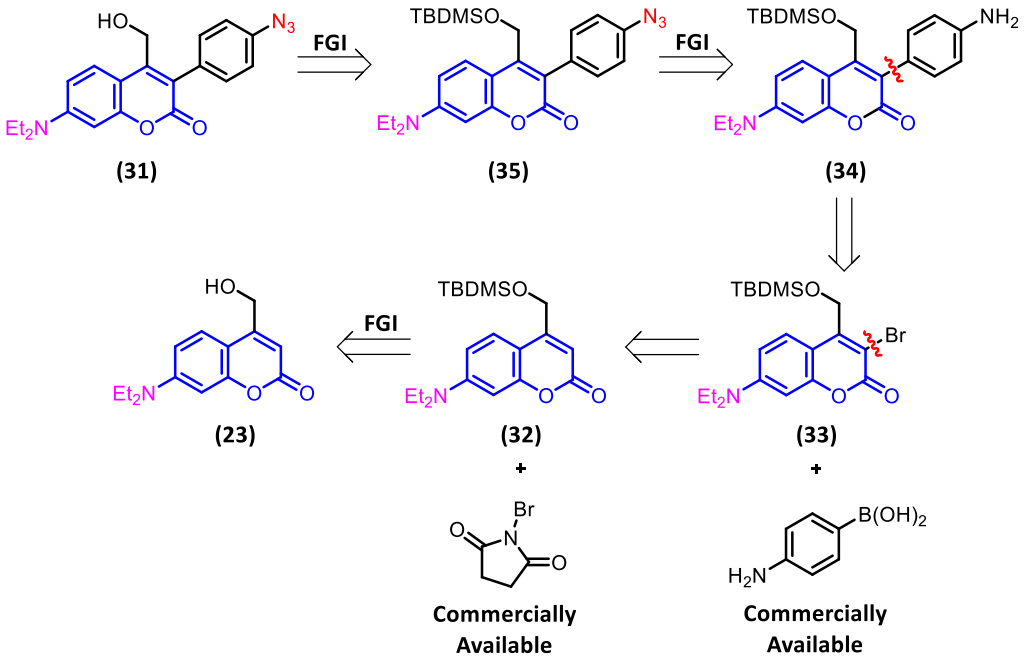

*Scheme 14: A retrosynthetic analysis of **(31)** from previously synthesised coumarin **(23).***

3.7.3 The forward synthesis of **(31)**

Now that a retrosynthetic analysis of **(31)** had been performed we could now attempt its synthesis. This synthesis was successful and afforded the desired product in a yield of 12% over five steps as outlined in scheme 15 below.

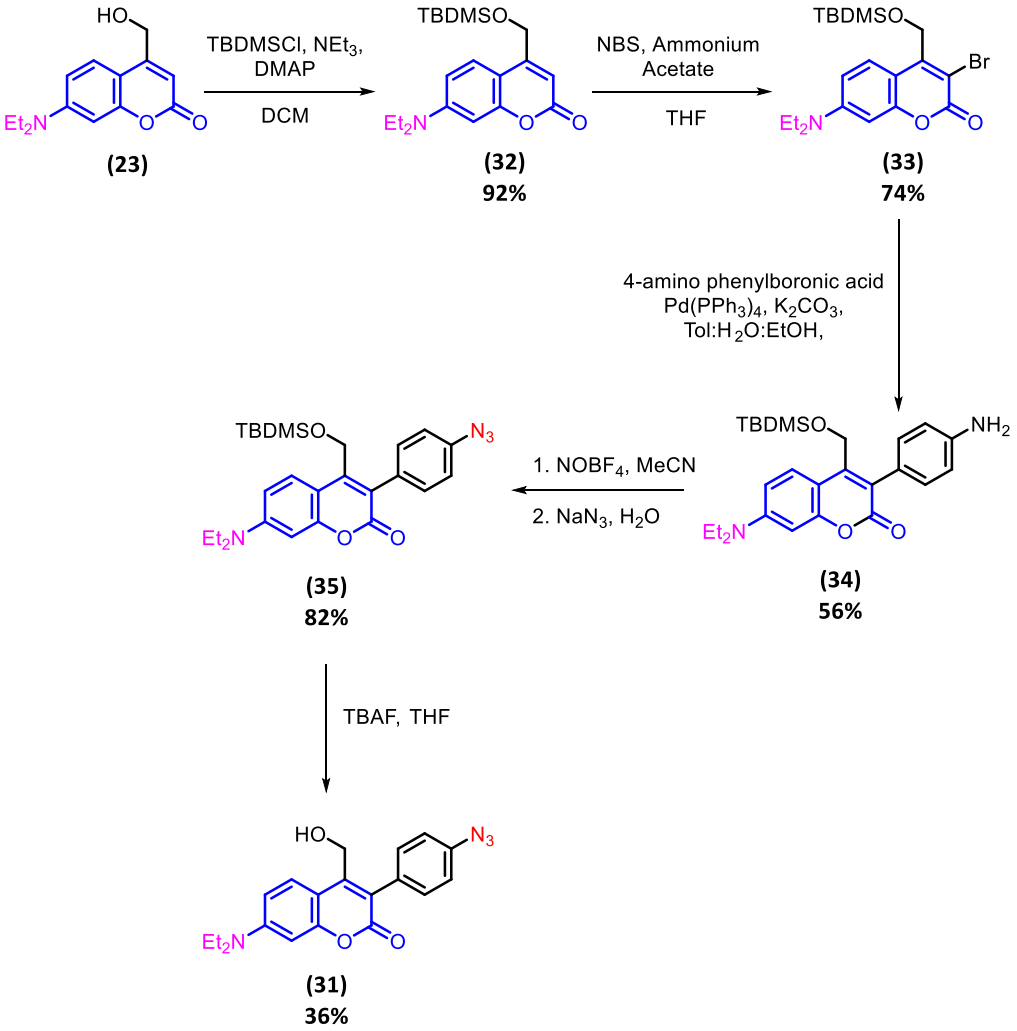

*Scheme 15: The successful synthetic route employed for the production of **(31)** which achieved a yield of 12% over five steps.*

The first step in the above synthetic route was the installation of a silyl ether protecting group, forming **(32)**. This synthesis was carried out following the procedure of Ellis-Davies et al.,[35] and afforded the desired product in a yield of 92%.

Following the successful synthesis of **(32)**, it was now time to brominate the 3-position of the coumarin scaffold. In the previous chapter, bromination of this position was achieved using *N*-bromosuccinimide as a source of electrophilic bromine according to the method of Kele et al.[8] As such, we decided to apply these conditions to **(32)**. Once again, this reaction was successful and afforded the desired product **(33)** in a yield of 74% following purification.

Now that the 3-position had been successfully brominated, the aryl amine could be installed at this position through a Suzuki-Miyaura cross coupling reaction with 4-aminophenylboronic acid forming **(34)**. Initially, purification presented a challenge as the triphenylphosphine oxide formed as a byproduct was difficult to remove using column chromatography. However, we were able to exploit the pK_a of the aryl ammonium to aid purification, with an acid-base extraction resulting in the complete removal of this impurity and allowing the product to be isolated in a yield of 56% following column chromatography.

Following the successful synthesis of **(34)**, conversion of the aryl amine to the corresponding azide was required. Generally, the synthesis of aryl azides involves the diazotisation of the amine followed by nucleophilic attack by NaN_3 to install the azide. Diazotisation is typically achieved by the *in situ* formation of nitrous acid by reacting sodium nitrite with a strong acid such as HCl.[37,38] This nitrous acid, can then undergo protonation, followed by dehydration yielding the nitrosonium ion $[NO]^+$ which acts as a highly electrophilic source of nitrogen, which the aryl amine then attacks to form the diazonium salt.[39] However, we were concerned that the harsh acidic conditions required for nitrosonium formation using this method would compromise the silyl ether protecting group resulting in the formation of undesirable side products. As such, an alternative diazotising reagent was required if this synthesis were to be successful. We opted to employ nitrosonium tetrafluoroborate. This reagent is the

nitrosonium salt of fluoroboric acid. Consequently, it acts as a source of the nitrosonium ion required for diazotisation. Diazotisation had previously been achieved solely by treating an aryl amine with this reagent in acetonitrile at low temperature,[40,41] significantly milder conditions than using $NaNO_2$ in HCl. **(34)** was dissolved in MeCN, placed under N_2 and cooled to -20 °C prior to treatment with $NOBF_4$ in order to diazotise the aryl amine. Subsequent treatment with NaN_3 afforded the desired product **(35)** with a yield of 82% without the need for further purification.

The final step of the synthesis was to cleave the silyl ether protecting group in order to liberate the desired alcohol. This was achieved by dissolving **(35)** in THF and subsequent treatment with TBAF. This reaction was successful, and the **(31)** was afforded in a 36% yield following purification.

The full synthetic route to final compound **(31)** consisted of five steps and afforded the desired product with a yield of 12% over five steps starting from (**23).** As such, a novel photocleavable linker had been successfully synthesised, overcoming the difficulties associated with the production of **(21)** described in section 3.7 above.

Following the successful synthesis of **(31)**, UV-Vis characterisation was required in order to confirm that it absorbed within the desired range. Before this could be done, a “clicked” version of this molecule was required, in order to provide a more representative model of its photophysical properties once incorporated into a material. The synthesis of this “clicked” version **(36)** can be seen in scheme 16 below. Similar to the compounds synthesised in section 3.5 above, we decided to synthesise this molecule in its acetate form so as to facilitate a decaging study which is discussed in section 4.4 of the following chapter. The UV-Vis characterisation of **(31)** and **(36)** is discussed in the following section.

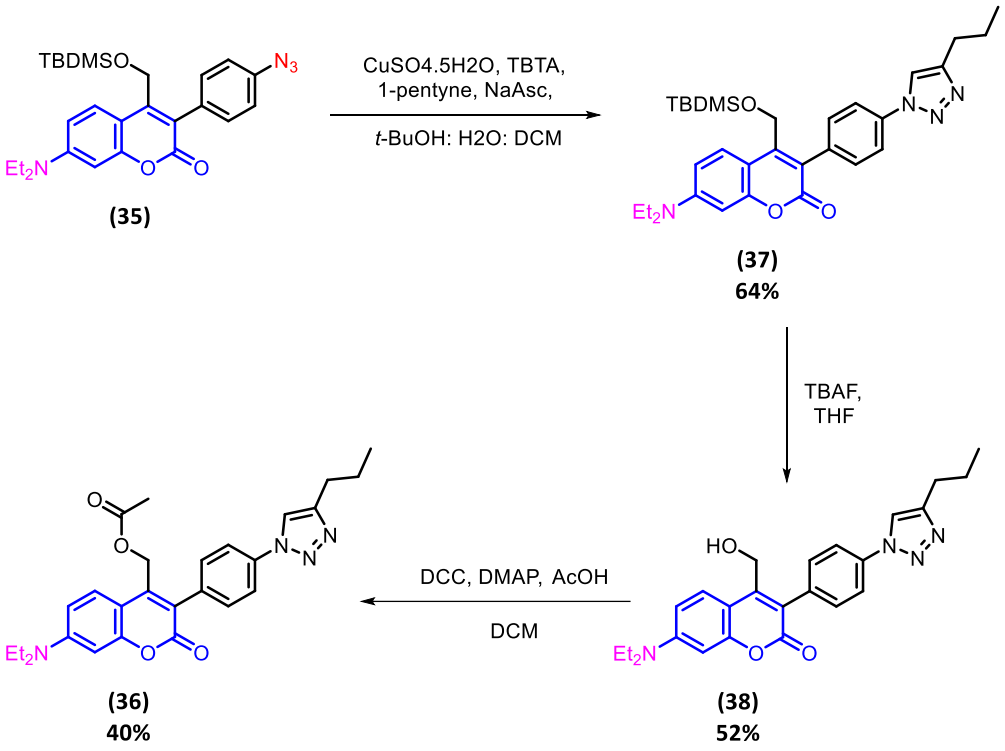

*Scheme 16: The three-step synthesis of "clicked" photocage **(36)** from **(35)**.*

3.7.4 UV-Vis characterisation of (31) and (36)

Now that **(31)**, and its clicked counterpart **(36)** had been successfully synthesised, UV-Vis spectroscopy was required in order to confirm that these molecules absorbed within the desired range of the visible light spectrum. The absorption spectra of these compounds can be seen in figure 15 below. Looking at these spectra it can be seen that the absorption profiles of these compounds are considerably red-shifted compared to those of **(16)** and **(17)** seen in. The λ_{max} of (**31)** and **(36)** were recorded as 396 and 403 nm, which we hoped would facilitate decaging not only at 365 nm, but also at 405 nm, which is further into the visible range and thus more biocompatible. The decaging studies performed on **(36)** is discussed in section 4.4 of the following chapter.

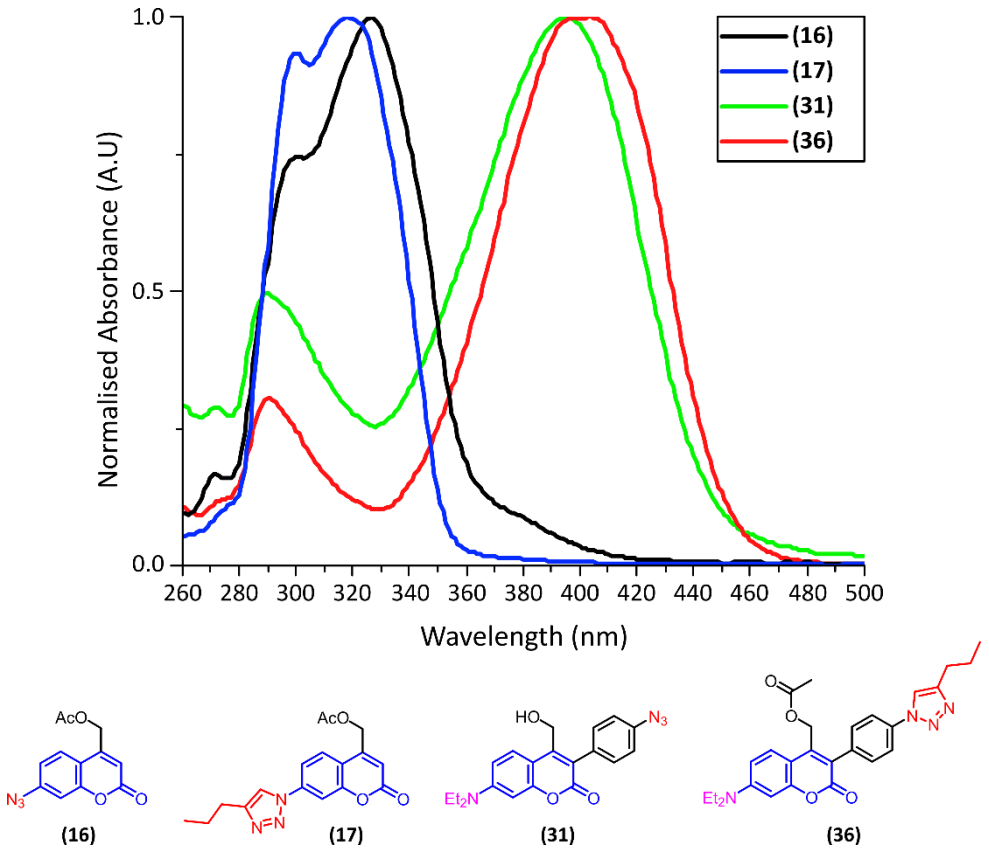

*Figure 15: The absorption spectra of photocleavable linker **(29)** and its clicked counterpart **(34).***

3.8 The development of red-shifted photocleavable linker **(4)**

3.8.1 The synthesis of **(4)**

Now that blue-light absorbing photocleavable linker **(29**) had been successfully synthesised, we set out to synthesise, a novel photocleavable linker **(4)** which we expected to be responsive to green light irradiation**.** In section 2.3.4 of the previous chapter, green-light absorbing coumarin photocage **(3)** was synthesised based on the work of Kele et al.[8] The final step of this synthesis involved the alkylation of the pyridine ring using methyl triflate. We reasoned that if this alkylating agent could be exchanged for one bearing an azido substituent, then we could alkylate the pyridine ring, red shifting absorbance, whilst simultaneously installing a click handle. The proposed synthetic route for the production of **(4)** can be seen in scheme 17 below.

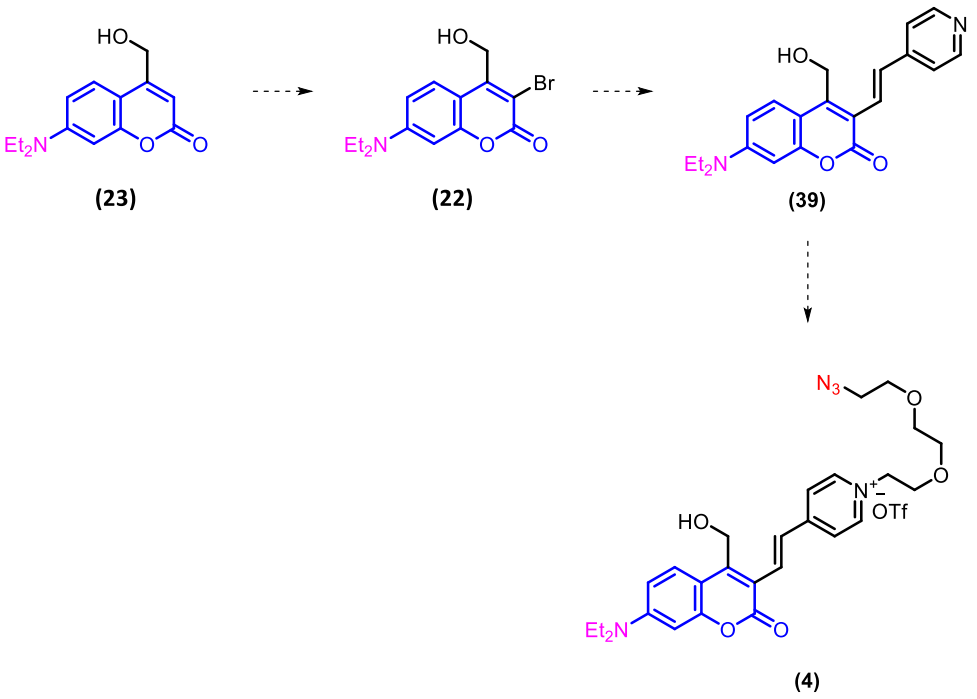

*Scheme 17: Schematic of the proposed synthetic route for the production of **(4)**, from the previously synthesised **(23)**.*

(39) had already been synthesised in the previous chapter as described in section 2.3.3. Triethylene glycol derivative **(40)** had previously been synthesised by Dr. Phathutshedzo Masithi as outlined in scheme 18 below. As such we planned to employ it as an alkylating agent by converting it to its corresponding triflate **(41)**.

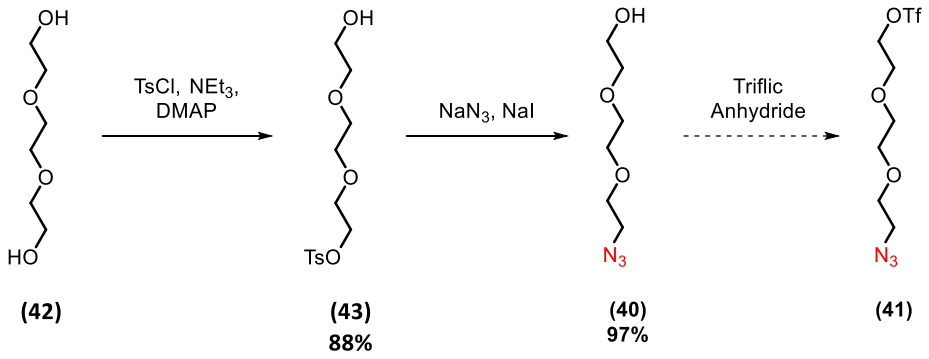

*Scheme 18: Schematic of the synthetic route employed to produce **(40).***

(41) was reacted directly without isolation due to its expected instability. This was achieved by treatment of **(40)** with triflic anhydride. Once formed, a solution of **(39)** in MeCN was added in a dropwise manner in order to form **(4)**. Purification was then achieved by precipitation in ice-cold diethyl ether, which afforded the desired product in a yield of 19% as seen in scheme 19 below.

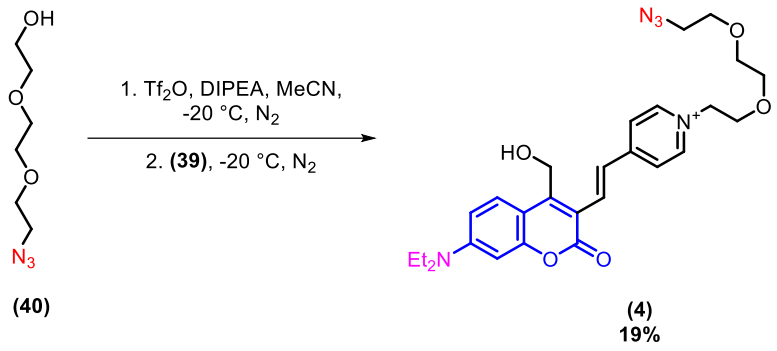

(40) **(4)** **19%**

*Scheme 19: Schematic of the conditions used for the synthesis of novel photocleavable linker **(4).***

Following the successful synthesis of **(4)**, its acetate version **(44)** was synthesised from previously produced **(45)**(section 2.3.4 of the previous chapter) according to conditions described in scheme 20 below.

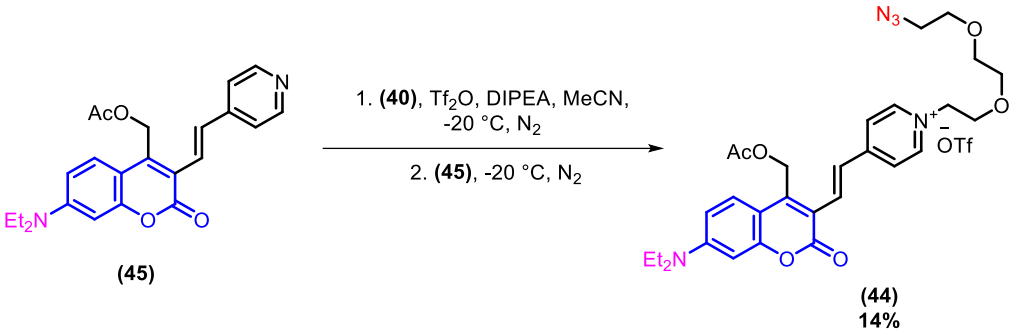

(45) **(44)** **14%**

*Scheme 20: Schematic of the conditions utilised for the production of **(43)**.*

3.8.2 UV-Vis characterisation of **(4)**

When **(4)** was designed, it was hoped that alkylation of its pyridine ring with an azido-terminal triethylene glycol chain would shift its absorbance into the green region, whilst simultaneously providing a clickable handle, allowing for its incorporation into materials. Looking at its absorption spectrum in figure 16 below, it can be seen that it has a λ_{max} of 504 nm, which lies just inside the green region. This is similar to **(3)**, the methyl version of this compound which has a λ_{max} of 498 nm, meaning that the extension of the alkyl chain did not have a significant effect on the photophysical properties of this compound. Consequently, it can be said that both the design and synthesis of **(4)** were a success, resulting in the production of a novel, red-shifted photocleavable linker. In fact, with a λ_{max} of 504 nm, **(4)** is the most red-shifted coumarin photocleavable linker reported and is the first to exhibit absorbance in the green-light region, representing a significant development for this class of compound.

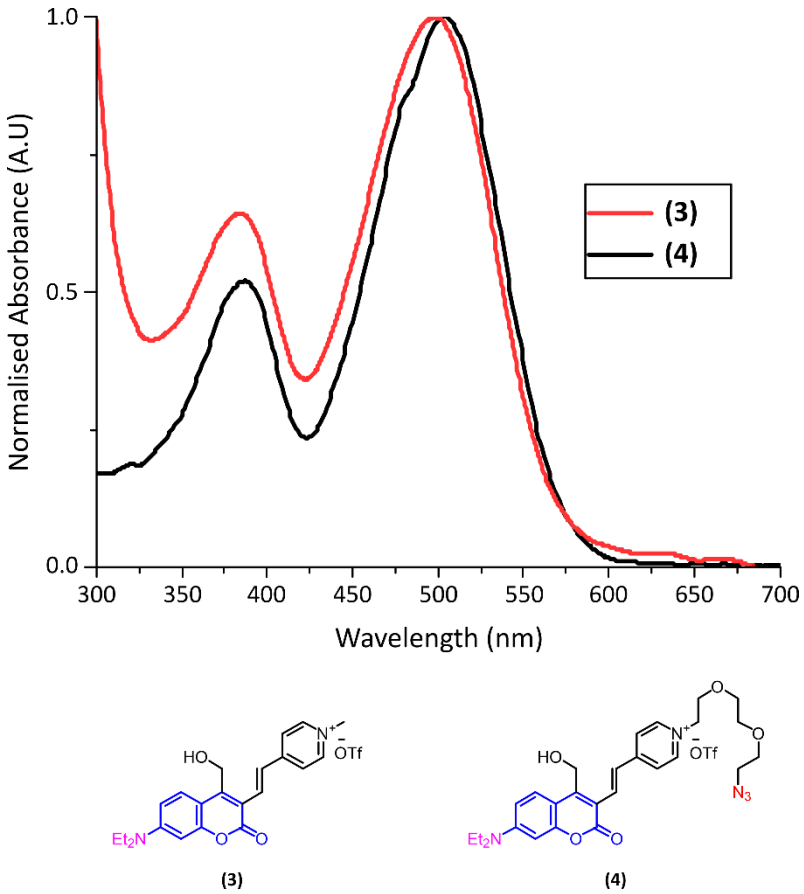

*Figure 16: The absorption spectra of **(3)** and novel photocleavable linker **(4)**.*

3.9: A summary of the photocleavable linkers produced during this work.

This chapter focused on the production of clickable, coumarin photocages to be used as photocleavable linkers for the incorporation of peptides into materials. In total, three photocleavable linkers were produced. Photocleavable linker **(1)** had been previously synthesised by Azagarsamy & Anseth.[2] Although we could not replicate their synthesis, an alternative route, capable of producing sufficient quantities of this compound consistently, was developed. The use of a triazene as a means of protecting the diazonium salt was key to the success of this route. This moiety also presents the opportunity for derivatisation in the future as it can be easily converted into a wide array of different functional groups simply by treatment with acid to form the reactive diazonium salt, followed by attack by a nucleophile

of choice to install the desired functionality. Unfortunately, whilst attempting to decage **(1)**, by irradiation with 365 nm, it was found that this compound did not undergo decaging. Upon further investigation of its photophysical properties, it was found that this was likely due to this compound absorbing in the UV region, with its absorption profile exhibiting minimal overlap with the wavelength of irradiation. Whilst decaging had previously been observed by Anseth & Azagarsamy,[2] this was likely due to the use of a light source which irradiated over a wider range of wavelengths, thus allowing for overlap with the absorption profile of **(1).**

As such, we decided to design **(21)**, which introduced the azido group at the 3-position and maintained the 7-diethylamino group which has previously been shown to conjugate with the π-system of the coumarin scaffold shifting absorbance into the visible range.[17] Although, this photocage could not be synthesised, we were able to design and synthesise **(31)**, which utilised a Suzuki-Miyaura cross coupling reaction to install an arylamine at the 3-position of the coumarin scaffold which was subsequently converted to the desired azide. This compound was shown to have a λ_{max} of 395 nm, which lies within the visible range. As such it was hoped that this compound would decage upon irradiation with 365 nm, with this experiment being discussed in section 4.4 of the following chapter.

Finally, red-shifted photocleavable linker (**4)** was designed and synthesised. This compound was shown to absorb maximally at 504 nm, within the green region of the visible light region. In fact, **(4)** exhibited the highest λ_{max} of any clickable coumarin photocage produced, representing a significant development for this class of compound. It was hoped that this compound would exhibit decaging upon irradiation with green light, with this experiment being discussed in section 4.6 of chapter 4 of this work. A comparison of the UV-Vis spectra of the compounds produced during this work is provided in figure 17 below. Looking at this

figure it can be seen that through careful design and planning, the λ_{max} of these compounds was shifted toward the red region.

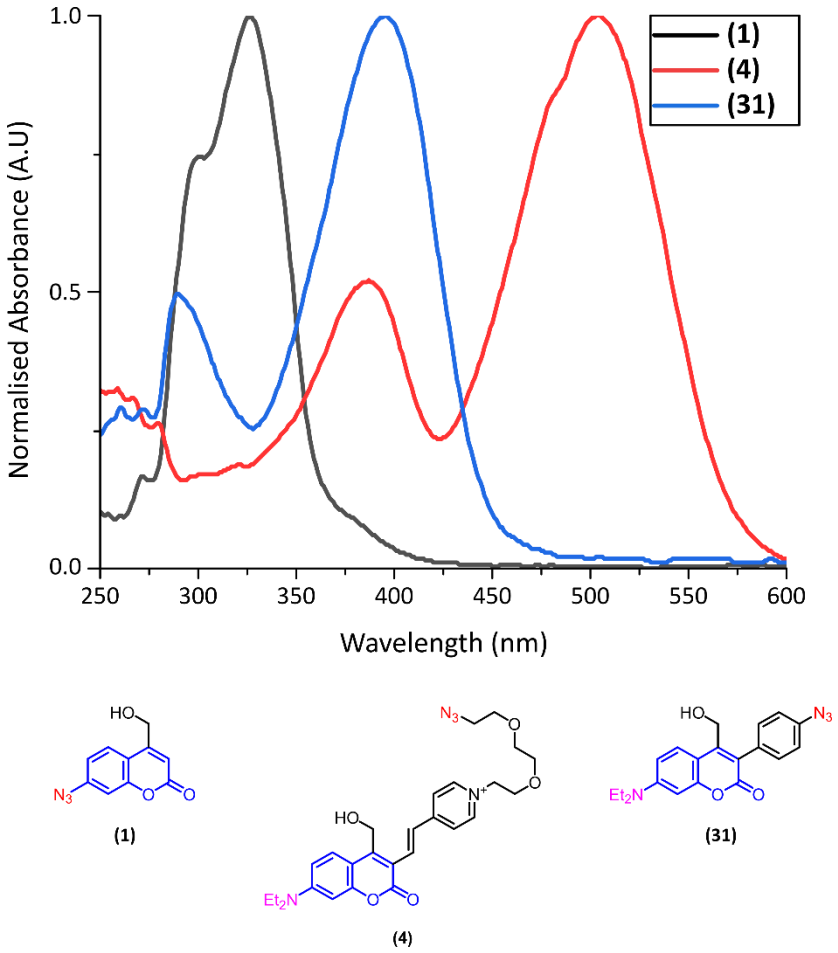

Figure 17: The absorption spectra of the final photocleavable linkers produced during this work.

3.10 Experimental

3.10.1 General Considerations

Proton nuclear magnetic resonance (^{1}H NMR) spectra were recorded on a Jeol ECX-400 (400 MHz) or Bruker AVIIIHD (500 MHz) spectrometer. Carbon nuclear magnetic resonance (^{13}C NMR) spectra were recorded on a Jeol ECX-400 (100 MHz) spectrometer. NMR shifts were assigned using COSY, HSQC and HMBC spectra. All chemical shifts are quoted on the δ scale in ppm using residual solvent as the internal standard (^{1}H NMR: $CDCl_3$ = 7.26; MeOD = 3.31; D_2O = 4.69; DMSO-d_6 = 2.50 and ^{13}C NMR: $CDCl_3$ = 77.16, MeOD = 49.00, DMSO-d_6 = 39.52). Coupling constants (*J*) are reported in Hz with the following splitting abbreviations: s = singlet, d = doublet, t = triplet, q = quartet, sept = septet, m = multiplet, app = apparent, br = broad. High resolution electrospray ionisation (ESI) mass spectra (HRMS) were recorded on a Bruker Campact TOF-MS or a Jeol AccuTOF GCx-plus spectrometer. Nominal and exact *m/z* values are reported in Daltons.

Thin layer chromatography (TLC) was carried out using aluminium backed sheets coated with 60 F_{254} silica gel (Merck). Visualization of the silica plates was achieved using a UV lamp (λ_{max} = 254, 302, or 366 nm), and/or ammonium molybdate (5% in 2M H_2SO_4), and/or potassium permanganate (5% $KMnO_4$ in 1M NaOH with 5 % potassium carbonate), and/or ninhydrin (1.5% ninhydrin, 3% AcOH in *n*-butanol), and/or bromocresol green (0.4% bromocresol green in ethanol, basified till blue with 0.1 M NaOH). Flash column chromatography was carried out using Geduran Si 60 (40 – 63 μm) (Merck). Mobile phases are reported as % volume of more polar solvent in less polar solvent.

Anhydrous solvents were dried using a PureSolv MD 7 Solvent Purification System. Deionised water was used for chemical reactions. All other solvents were used as supplied (Analytical or

HPLC grade), without prior purification. Reagents were purchased from Sigma-Aldrich and used as supplied, unless otherwise indicated. Brine refers to a saturated solution of sodium chloride. Petrol refers to the fraction of petroleum ether boiling in the range 40-60 °C. Anhydrous magnesium sulfate ($MgSO_4$) was used as the drying agent after reaction workup unless otherwise stated.

3.10.2 Synthesis

The synthesis of **(6)**

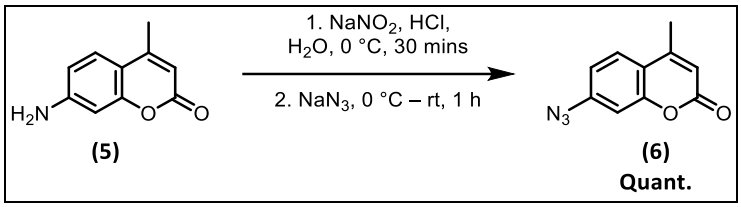

(5) **(6)**
Quant.

(5) (3.0 g, 17.1 mmol, 1 eq.) was dissolved in aqueous HCl (3 M, 200 ml) and cooled to 0 °C. A solution of $NaNO_2$ (1.4 g, 20.5 mmol, 1.2 eq.) in H_2O (10 ml) was added and the resulting mixture was stirred at 0 °C for 30 mins. At this point EtOAc (50 ml) was added prior to the dropwise addition of a solution of NaN_3 (3.3 g, 51.4 mmol, 3 eq.) in H_2O (10 ml). The reaction mixture was allowed to warm to room temperature and stirred for 2 h. The product was extracted with EtOAc (3 × 100 ml), and the combined organics were dried over $MgSO_4$, filtered, and concentrated *in vacuo* to afford the product as a brown solid with a yield of 3.44 g, 17.1 mmol (quantitative).

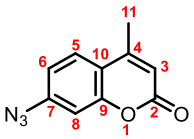

^{1}H NMR (400 MHz, $CDCl_3$) δ 7.56 (d, *J* = 8.3 Hz, 1H, Ar**H**$_5$), 7.01 – 6.87 (overlapping, 2H, Ar**H**$_{6,8}$), 6.22 (d, *J* = 1.3 Hz, 1H, A**rH**$_3$), 2.41 (d, *J* = 1.3 Hz, 3H, C**H**$_3$, H_{11}).

HRMS ESI *m/z*: calc for $C_{10}H_7N_3O_2$ $[M+Na]^+$: 224.0430; Obs: 224.0439

Spectroscopic data were in agreement with [42]

The synthesis of **(1)**: SeO2 method

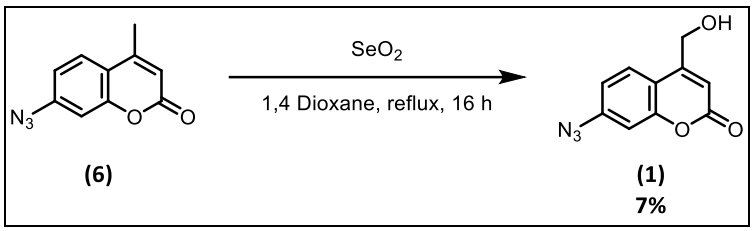

SeO_2 (1.1 g, 25.0 mmol, 5 eq.) was added to a stirring solution of **(6)** (1.0 g, 5.0 mmol, 1 eq.) in 1,4-dioxane (100 ml). The reaction mixture was refluxed at 16 h before cooling to rt, filtering through celite and concentrating *in vacuo,* affording a green/black residue. The crude product was suspended in hot 10% hexane in DCM (30 ml) prior to filtration, yielding a bright orange filtrate and black/green residue. The filtrate was concentrated *in vacuo* and the residue purified by flash column chromatography (0 – 3% MeOH: DCM). The pure fractions were combined and concentrated *in vacuo* affording the product as an orange solid with a yield of 73 mg, 0.34 mmol, (7%).

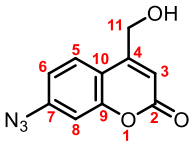

^{1}H NMR (400 MHz, $CDCl_3$) δ 7.49 (d, *J* = 8.5 Hz, 1H, Ar**H**$_5$), 6.97 (d, *J* = 2.2 Hz, 1H, Ar**H**$_8$), 6.93 (dd, *J* = 8.5, 2.2 Hz, 1H, Ar**H**$_6$), 6.56 (s, 1H, Ar**H**$_3$), 4.88 (d, *J* = 1.5 Hz, 2H, C**H**$_2$OH, **H**$_{11}$).

HRMS ESI *m/z*: calc for $C_{10}H_7N_3O_3$ $[M+Na]^+$ 240.0380; Obs $[M+Na]^+$ 240.0385

The Synthesis of **(15)**

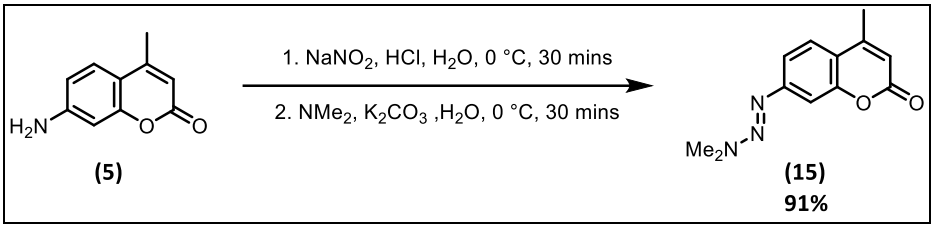

(5) (3.0 g, 17.1 mmol, 1 eq.) was dissolved in an aqueous HCl solution (3 M, 150 ml) and cooled to 0 °C. After stirring for 5 mins, a solution of $NaNO_2$ (1.3 g, 18.8 mmol, 1.1 eq.) in H_2O (100 ml) was added in small portions over the course of 5 mins with the observation of a colour change from light to dark brown. The reaction mixture was stirred for 30 mins at 0 °C prior to addition of EtOAc (50 ml). A solution of NMe_2 (20% solution in H_2O, 6.95 ml, 61.6 mmol, 3.6 eq.) and K_2CO_3 (9.0 g, 65.0 mmol, 3.8 eq.) in H_2O (100 ml) was added over the course of 5 mins with the observation of effervescence. Upon complete addition, the reaction mixture was stirred at room temperature for 30 mins. At this point the aqueous was extracted with EtOAc (3 × 150 ml) and the combined organics were washed with brine (200 ml). The organic layer was then dried over $MgSO_4$, filtered and concentrated *in vacuo,* to afford the product as a brown solid with a yield of 3.6 g, 15.5 mmol (91%).

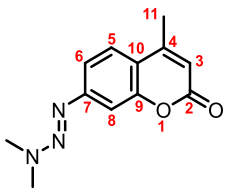

^{1}H NMR (400 MHz, $CDCl_3$) δ 7.53 (d, *J* = 9.1 Hz, 1H, Ar**H**$_5$), 7.39-7.35 (m, 2H, Ar**H**$_{6,8}$), 6.18 (d, *J* = 1.2 Hz, 1H, Ar**H**$_3$), 3.57 (s, 3H, NC**H**$_3$), 3.26 (s, 3H, NC**H**$_3$), 2.42 (d, *J* = 1.2 Hz, 3H, C**H**$_3$, H_{11}).

^{13}C NMR (101 MHz, $CDCl_3$) δ 161.68(**C**$_2$), 154.67 (**C**$_7$/**C**$_9$), 154.14 (**C**$_7$/**C**$_9$), 152.61 (**C**$_{10}$), 124.99 (**C**$_5$), 117.44 (**C**$_6$), 117.30 (**C**$_4$), 113.31 (**C**$_3$), 107.96 (**C**$_8$), 43.53(N**C**H$_3$), 36.48(N**C**H$_3$), 18.84 (**C**$_{11}$).

HRMS ESI *m/z*: calc for $C_{12}H_{13}N_3O_2$ $[M+H]^+$ 232.1081, $[M+Na]^+$ 254.0900; Obs $[M+H]^+$ 232.1078, $[M+Na]^+$ 254.0902

The synthesis of **(14)**

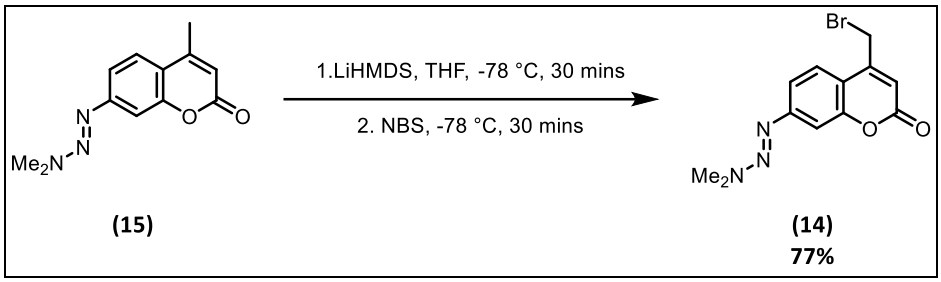

(15) (1.0 g, 4.3 mmol, 1 eq.) was dissolved in anhydrous THF (45 ml) and placed under a nitrogen atmosphere. This solution was cooled to -78 °C prior to the dropwise addition of LiHMDS (1.0 M in THF, 10.8 ml, 10.8 mmol, 2.5 eq.). The reaction mixture was then stirred at -78 °C for 30 mins. In the meantime, a solution of NBS (925 mg, 5.2 mmol, 1.2 eq.) in anhydrous THF (15 ml) was created and placed under nitrogen atmosphere. This solution was cooled to -78 °C and added to the above reaction mixture dropwise over the course of 5 mins. Upon complete addition, the reaction was allowed to proceed for 30 mins prior to warming to rt and quenching with aqueous HCL solution (1.0 M, 10 ml). The product was extracted with DCM (3 × 50 ml) and the combined organics washed with brine (150 ml). The organic layer was then dried over $MgSO_4$, filtered and concentrated *in vacuo.* The residue was then purified using flash column chromatography (0 – 3% MeOH: DCM), with the pure fractions being concentrated to afford the final product as a yellow solid with a yield of 1.0 g, 3.3 mmol, (77%).

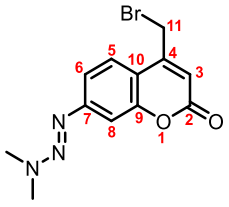

^{1}H NMR (400 MHz, $CDCl_3$) δ 7.64 (d, *J* = 8.5 Hz, 1H, Ar**H$_5$**), 7.42 (dd, *J* = 8.5, 1.9 Hz, 1H, Ar**H$_6$**), 7.38 (d, *J* = 1.9 Hz, 1H, Ar**H$_8$**), 6.40 (s, 1H, Ar**H$_3$**), 4.47 (s, 2H, C**H**$_2$Br, H_{11}), 3.58 (s, 3H, NC**H**$_3$), 3.26 (s, 3H, NC**H**$_3$)

^{13}C NMR (101 MHz, $CDCl_3$) δ 161.14 (**C**$_2$), 155.24(**C$_7$/C$_9$**), 154.61 (**C**$_7$/**C$_9$**), 150.14 (**C**$_4$), 124.89 (**C**$_5$), 117.69 (**C**$_6$), 114.37 (**C$_{10}$**), 114.17 (**C**$_3$), 108.31 (**C**$_8$), 43.65 (N**C**H$_3$), 36.39 (N**C**H$_3$), 27.07 (**C**$_{11}$).

HRMS ESI *m/z*: calc for $C_{12}H_{12}BrN_3O_2$ $[M+H]^+$ 310.0186, $[M+Na]^+$ 332.0005; Obs $[M+H]^+$ 310.0186, $[M+Na]^+$ 332.0002

The synthesis of **(13)**

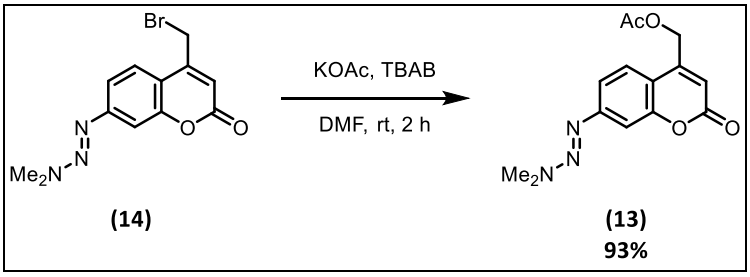

(14) (1.0 g, 3.3 mmol, 1 eq.) was dissolved in DMF (30 ml) prior to the addition of tetrabutylammonium bromide (53 mg, 0.17 mmol, 0.05 eq.) and KOAc (389 mg, 3.96 mmol, 1.2 eq.) and the reaction was stirred at room temperature for 2 h. The solvent was removed *in vacuo* and the residue redissolved in EtOAc (50 ml) and the organics washed with brine (50 ml). The organic layer was then dried over $MgSO_4$, filtered and concentrated *in vacuo* to afford the product as a yellow solid with a yield of 891 mg, 3.10 mmol (93%).

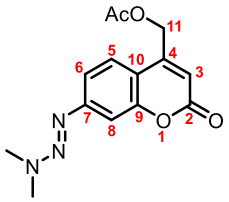

^{1}H NMR (400 MHz, CDCl_3) δ 7.41 (d, *J* = 9.0 Hz, 1H, Ar**H$_5$**), 7.36 (m, 2H, Ar**H$_{6,8}$**), 6.37 (s, 1H, Ar**H$_3$**), 5.27 (d, *J* = 1.5 Hz, 2H, C**H$_2$**OAc, H_{11}), 3.57 (s, 3H, NC**H$_3$**), 3.25 (s, 3H, NC**H$_3$**), 2.20 (s, 3H, OCC**H$_3$**).

^{13}C NMR (101 MHz, CDCl_3) δ 170.29 (O**C**OCH$_3$), 161.28 (**C$_2$**), 154.85(**C$_7$**/**C$_9$**), 154.43(**C$_7$**/**C$_9$**), 149.21 (**C$_4$**), 123.79 (**C$_5$**), 117.68 (**C$_6$**), 114.23 (**C$_{10}$**), 111.12 (**C$_3$**), 108.27 (**C$_8$**), 61.35 (**C$_{11}$**), 43.66 (N**C**H$_3$), 36.36 (N**C**H$_3$), 20.88 (OCO**C**H$_3$)

HRMS ESI *m/z*: calc for $C_{14}H_{15}N_3O_4$ $[M+H]^+$ 290.1135, $[M+Na]^+$ 312.0955; Obs $[M+H]^+$ 290.1130, $[M+Na]^+$ 312.0959

The synthesis of **(12)**

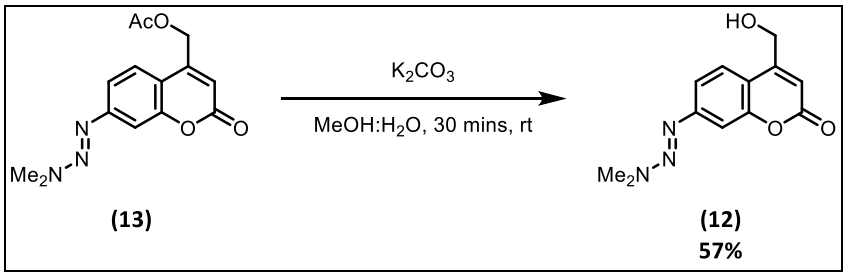

(13) (300 mg, 1.05 mmol, 1 eq.) was dissolved in MeOH:H_2O (30 ml, 9:1) and K_2CO_3 (144 mg, 1.05 mmol, 1 eq.) was added. The reaction mixture was then stirred at room temperature for 30 mins. The solvent was removed *in vacuo* and the residue resuspended in EtOAc (20 ml) and washed with brine (20 ml). The organic layer was then dried over $MgSO_4$, filtered and concentrated *in vacuo* to afford the product as a yellow solid with a yield of 148 mg, 0.60 mmol, (57%).

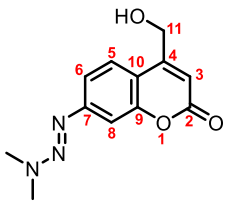

^{1}H NMR (400 MHz, $CDCl_3$) δ 7.44 (d, *J* = 8.5 Hz, 1H, Ar**H**$_5$), 7.39 (d, *J* = 1.9 Hz, 1H, Ar**H**$_8$), 7.36 (dd, *J* = 8.5, 1.9 Hz, 1H, Ar**H**$_6$), 6.53 (t, *J* = 1.5 Hz, 1H, Ar**H**$_3$), 4.92 (d, *J* = 3.8 Hz, 2H, C**H**$_2$OH, H$_{11}$), 3.58 (s, 3H, NC**H**$_3$), 3.26 (s, 3H, NC**H**$_3$)

The synthesis of **(1)**: Alternative method

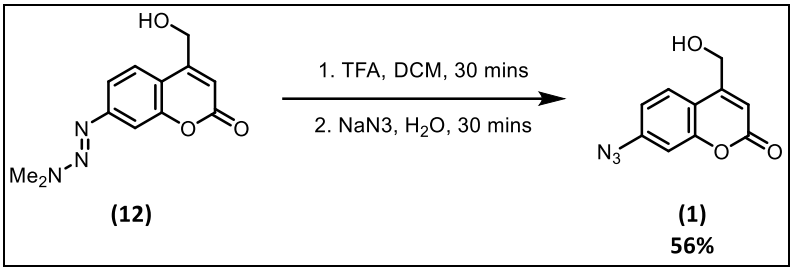

(12) (125 mg, 0.50 mmol, 1 eq.) was dissolved in DCM (15 ml) and TFA (15 ml) was added in a dropwise fashion. A colour change from yellow to dark brown was observed and the reaction mixture was allowed to stir for 30 mins. At this point it was cooled to 0 °C, and a solution of NaN_3 (98 mg, 1.50 mmol, 3 eq.) in H_2O (3 ml) was added dropwise. The reaction was stirred at 0 °C for 90 mins prior to the addition of saturated $NaHCO_3$ solution (30 ml). The product was extracted with DCM (3 × 50 ml), and the combined organic layers were washed with brine (50 ml), dried over $MgSO_4$ and filtered, before being concentrated *in vacuo*. The crude product was purified by flash column chromatography (0–5% MeOH:DCM) and the pure fractions were combined and concentrated to afford the product as a yellow/brown solid with a yield of 61 mg, 0.28 mmol, (56%).

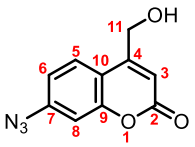

^{1}H NMR (400 MHz, $CDCl_3$) δ 7.49 (d, *J* = 8.5 Hz, 1H, Ar**H$_5$**), 7.00 (d, *J* = 2.3 Hz, 1H, Ar**H$_8$**), 6.93 (dd, *J* = 8.5, 2.3 Hz, 1H, Ar**H$_6$**), 6.56 (t, *J* = 1.5 Hz, 1H, Ar**H$_3$**), 4.88 (d, *J* = 4.8 Hz, 2H, C**H**$_2$OH, H$_{11}$).

HRMS ESI *m/z*: calc for $C_{10}H_7N_3O_3$ $[M+Na]^+$ 240.0380, $[M+K]^+$ 256.0119; Obs $[M+Na]^+$240.0385, $[M+K]^+$ 256.0123

The synthesis of **(16)**

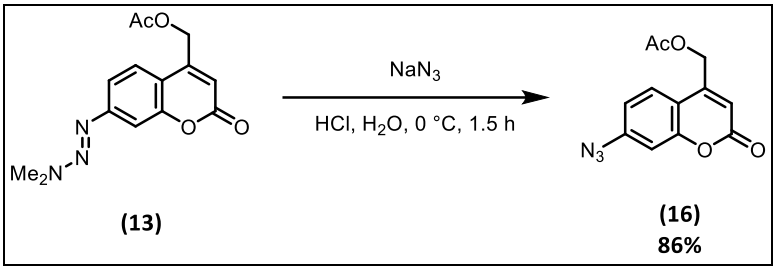

(13) (100 mg, 0.35 mmol, 1 eq.) was suspended in H_2O (50 ml) and cooled to 0 °C prior to the addition of NaN_3 (2.3 g, 35.0 mmol, 100 eq.). Conc. HCl (17.5 ml) was then added with significant effervescence observed. Alongside this the suspension fully dissolved with a colour change from orange/brown to green/yellow observed. The reaction was allowed to proceed at 0 °C for 90 mins before quenching by dropwise addition of NaOH solution (10 M, Aqueous). The aqueous was then extracted with EtOAc (3 × 25 ml). The combined organics were then washed with brine (50 ml), dried over $MgSO_4$, filtered and concentrated *in vacuo* affording a yellow oil. The residue was then purified by flash column chromatography (0–3% MeOH: DCM) and the pure fractions combined and concentrated to afford the product as a light-yellow solid with a yield of 77 mg, 0.30 mmol, (86%).

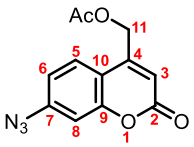

^{1}H NMR (400 MHz, $CDCl_3$) δ 7.49 (d, *J* = 8.5 Hz, 1H, Ar**H**$_5$), 7.01 (d, *J* = 2.2 Hz, 1H, Ar**H**$_8$), 6.97 (dd, *J* = 8.5, 2.2 Hz, 1H, Ar**H**$_6$), 6.43 (t, *J* = 1.4 Hz, 1H, Ar**H**$_3$), 5.24 (d, *J* = 1.5 Hz, 2H, C**H**$_2$COCH$_3$, H$_{11}$), 2.21 (s, 3H, CH$_2$COC**H**$_3$).

^{13}C NMR (101 MHz, $CDCl_3$) δ 170.20 (OCO**C**H_3), 160.12 (**C**$_2$), 155.00 (**C**$_7$/**C**$_9$), 148.72 (**C**$_4$), 144.53 (**C**$_7$/**C**$_9$), 125.07 (**C**$_5$), 115.77 (**C**$_6$), 114.28 (**C**$_{10}$), 112.32(**C**$_3$), 107.65 (**C**$_8$), 61.15 (**C**$_{11}$), 20.84 (OCO**C**H_3).

HRMS ESI *m/z*: calc for $C_{12}H_9N_3O_4$ $[M+Na]^+$ 282.048526; Obs 282.04589

The synthesis of **(17)**

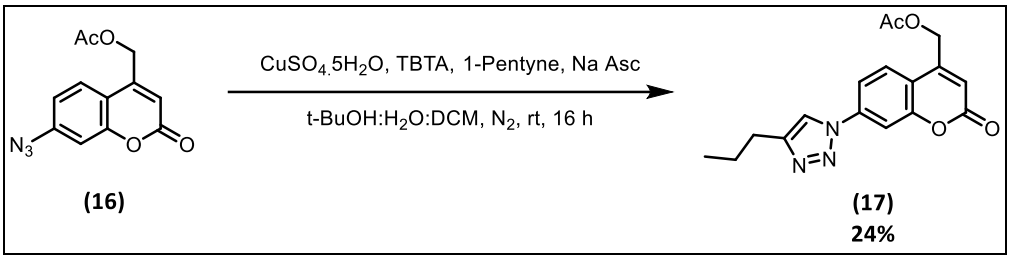

(16) (200 mg, 0.70 mmol, 1 eq.) and 1-pentyne (77 µl, 0.78 mmol, 1.1 eq.) were dissolved in a mixture of ^{t}BuOH: DCM (4 ml, 1:1) and placed under nitrogen atmosphere. In a separate reaction vessel tris((3-benzyl-1H-1,2,3-triazol-4-yl)methyl)amine (20 mg, 0.04 mmol, 0.06 eq.), $CuSO_4.5H_2O$ (47 mg, 0.19 mmol, 0.27 eq.) and sodium ascorbate (158 mg, 0.80 mmol, 1.1 eq.) were dissolved in H_2O (4 ml) and placed under nitrogen atmosphere. The contents of the 2nd flask were then added to the initial reaction vessel, and the reaction was stirred at room temperature for 16 h before the solvent was removed *in vacuo*. The residue was redissolved in EtOAc (25 ml) and the organics washed with brine (25 ml), dried over $MgSO_4$, filtered and concentrated *in vacuo*. The crude product was purified by flash column chromatography (50 – 90% EtOAc: hexane) and pure fractions were combined and concentrated to afford the product as a light-yellow solid with a yield of 58 mg, 0.17 mmol, (24%).

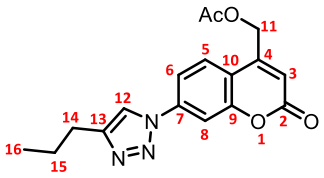

^{1}H NMR (400 MHz, $CDCl_3$) δ 7.84-7.77 (overlapping, 2H, Ar**H**$_{6,12}$), 7.72 (d, *J* = 2.2 Hz, 1H, Ar**H**$_8$), 7.64 (d, *J* = 8.6 Hz, 1H, Ar**H**$_5$), 6.54 (t, *J* = 1.5 Hz, 1H Ar**H**$_3$), 5.32 (d, *J* = 1.5 Hz, 2H, C**H**$_2$COCH$_3$, H$_{11}$), 2.80t, *J* = 2.4 Hz, 2H, CH$_3$CH$_2$C**H**$_2$, H$_{14}$), 2.23 (s, 3H, CH$_2$OCOC**H**$_3$, H$_{11}$), 1.78 (dt, *J1 = J2* = 7.4 Hz, 2H, CH$_3$C**H**$_2$CH$_2$**, H$_{15}$**), 1.03 (t, *J* = 7.4 Hz, 3H, C**H**$_3$CH$_2$CH$_2$, H$_{16}$).

^{13}C NMR (101 MHz, $CDCl_3$) δ 170.16 (CH$_2$**C**OCH$_3$), 159.77 (**C**$_2$), 154.55 (**C**$_7$/**C**$_9$), 149.89 (**C**$_{13}$), 148.48 (**C**$_4$), 139.63 (**C**$_7$/**C**$_9$), 125.28 (**C**$_5$), 118.67 (**C**$_{12}$), 116.85 (**C**$_{10}$), 116.13 (**C**$_6$), 113.88 (**C**$_3$), 108.45 (**C**$_8$), 61.09 (**C**$_{11}$), 27.75 (**C**$_{14}$), 22.75 (**C$_{15}$**), 20.84 (CH$_2$CO**C**H$_3$), 13.94 (**C**$_{16}$).

HRMS ESI *m/z*: calc for $C_{17}H_{17}N_3O_4$ $[M+H]^+$ 328.1292, $[M+Na]^+$ 350.1111; Obs $[M+H]^+$ 328.1300, $[M+Na]^+$ 350.1120

The synthesis of **(20)**

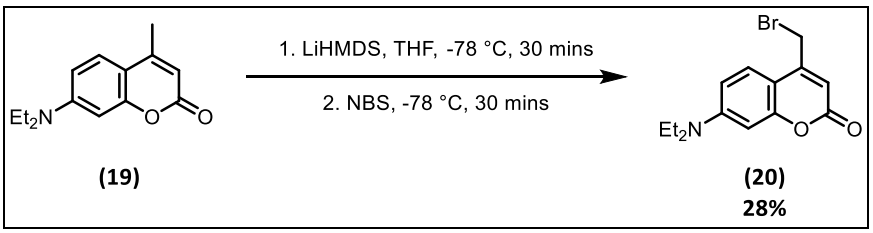

(19) (1.0 g, 4.3 mmol, 1 eq.) was dissolved in THF (25 ml) and cooled to -78 °C. LiHMDS (1.0 M in THF, 10.8 ml, 10.8 mmol, 2.5 eq.) was added dropwise and the reaction was stirred at -78 °C for 30 mins. At this point NBS (925 mg, 5.20 mmol, 1.2 eq.) was added and the reaction mixture was stirred at -78 °C for an additional 30 mins. The reaction mixture was then warmed to rt prior to being quenched by the dropwise addition of aqueous HCl solution (1.0 M). The aqueous was extracted with EtOAc (25 mL) and the organics washed with brine (25 mL) dried

over $MgSO_4$, filtered and concentrated *in vacuo*. The residue was purified by flash column chromatography (0 – 20% EtOAc: hexane) and the pure fractions were combined and concentrated to afford the product as a yellow/brown solid with a yield of 376 mg, 1.20 mmol, (28%).

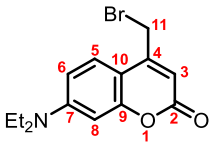

^{1}H NMR (400 MHz, $CDCl_3$) δ 7.46 (d, *J* = 9.0 Hz, 1H, Ar**H**$_5$), 6.60 (dd, *J* = 9.0, 2.6 Hz, 1H, Ar**H**$_6$), 6.47 (d, *J* = 2.6 Hz, 1H, Ar**H**$_8$), 6.10 (s, 1H, Ar**H**$_3$), 4.37 (s, 2H, C**H**$_2$Br, H$_{11}$), 3.39 (q, *J* = 7.1 Hz, 4H, N(C**H**$_2$CH$_3$)$_2$), 1.18 (t, *J* = 7.1 Hz, 6H, N(CH$_2$C**H**$_3$)$_2$).

HRMS ESI *m/z:* calc for $C_{14}H_{16}BrNO_2$ $[M+H]^+$ 310.0437, $[M+Na]^+$ 332.0257; Obs $[M+Na]^+$ 310.0430, $[M+Na]^+$ 332.0257

Spectroscopic data were in agreement with [43]

The synthesis of **(18)**

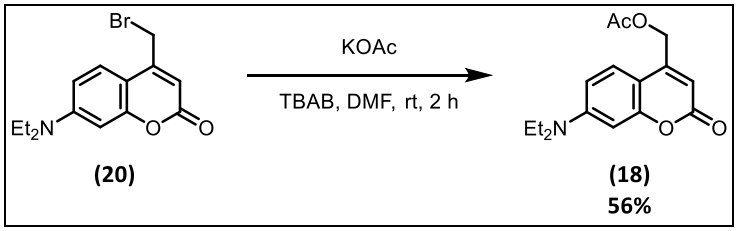

(20) (200 mg, 0.64 mmol, 1 eq.) and tetrabutylammonium bromide (10 mg, 0.03 mmol, 0.05 eq.) were dissolved in DMF (10 ml). KOAc (76 mg, 0.76 mmol, 1.2 eq.) was added and the reaction mixture was stirred at room temperature for 2 h. The solvent was removed *in vacuo,* and the residue was redissolved in EtOAc (25 ml), the organics washed with brine (25 ml) dried over $MgSO_4$, filtered and concentrated *in vacuo*. The residue was then purified by flash column

chromatography (0–80% EtOAc hexane) and the pure fractions were combined and concentrated to afford the product as a yellow solid with a yield of 103 mg, 0.36 mmol, (56%).

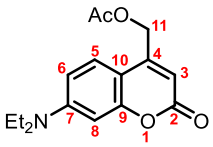

^{1}H NMR (400 MHz, $CDCl_3$) δ 7.28 (d, *J* = 9.0 Hz, 1H, Ar**H**$_5$), 6.59 (dd, *J* = 9.0, 2.6 Hz, 1H, Ar**H**$_6$), 6.53 (d, *J* = 2.6 Hz, 1H, Ar**H**$_8$), 6.13 (t, *J* = 1.3 Hz, 1H, Ar**H**$_3$), 5.21 (d, *J* = 1.3 Hz, 2H, C**H**$_2$COCH$_3$, H$_{11}$), 3.41 (q, *J* = 7.1 Hz, 4H, N(C**H**$_2$CH$_3$)$_2$), 2.18 (s, 3H, CH$_2$COC**H**$_3$), 1.20 (t, *J* = 7.1 Hz, 6H, N(CH$_2$C**H**$_3$)$_2$).

HRMS ESI *m/z*: calc for $C_{16}H_{19}NO_4$ $[M+H]^+$ 290.1387, $[M+Na]^+$312.1206; Obs $[M+H]^+$ 290.1382, $[M+Na]^+$ 312.1205

Spectroscopic data were in agreement with [44]

The synthesis of **(24)**

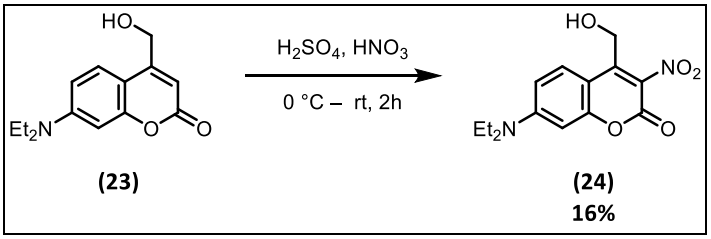

(23) (199 mg, 0.80 mmol, 1 eq.) was dissolved in conc. H_2SO_4 (5 ml) and sonicated to ensure full dissolution. The solution was then cooled to 0 °C and HNO_3 (70% reagent, 51 µl, 0.80 mmol, 1 eq.) was added with the observation of a colour change from orange to dark brown. The reaction was stirred at 0 °C for 1 h before warming to room temperature and stirring for an additional hour. The reaction was then quenched by the dropwise addition of ice-cold water, followed by sat. aqueous $NaHCO_3$ solution (10 ml). The product was then extracted

with EtOAc (3 × 25 ml), and the combined organics were washed with brine (50 mL), dried over $MgSO_4$, filtered and concentrated *in vacuo*. The residue was purified by flash column chromatography (DCM) with pure fractions being combined and concentrated to afford the product as an orange solid with a yield of 38 mg, 0.13 mmol, (16%).

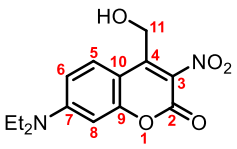

^{1}H NMR (400 MHz, $CDCl_3$) δ 7.70 (d, *J* = 9.3 Hz, 1H, Ar**H**$_5$), 6.71 (dd, *J* = 9.3, 2.6 Hz, 1H, Ar**H**$_6$), 6.49 (d, *J* = 2.6 Hz, 1H, Ar**H**$_8$), 4.76 (d, *J* = 6.3 Hz, 2H, C**H**$_2$OH, H$_{11}$), 3.46 (q, *J* = 7.2 Hz, 4H, N(C**H**$_2$CH$_3$)$_2$), 1.24 (t, *J* = 7.2 Hz, 6H, N(CH$_2$C**H**$_3$)$_2$).

HRMS ESI *m/z*: Calc for $C_{14}H_{16}N_2O_5$ $[M+H]^+$ 293.1132, $[M+Na]^+$ 315.0951, $[M+K]^+$ 331.0691; Obs $[M+H]^+$ 293.1133, $[M+Na]^+$ 315.0947, $[M+K]^+$ 331.0686

The synthesis of **(25)**

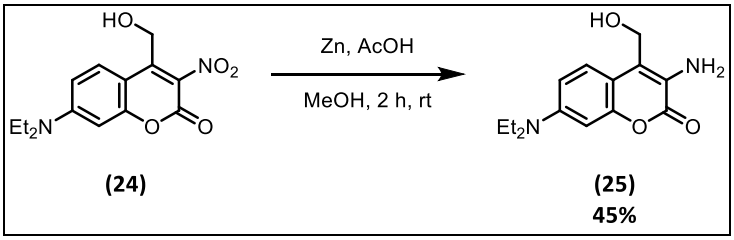

(24) (67 mg, 0.23 mmol, 1 eq.) was dissolved in MeOH (10 ml) and Zinc dust (150 mg, 2.30 mmol, 10 eq.) was added. The resulting mixture was stirred at rt for 5 mins prior to the addition of glacial AcOH (20 ml). The rection was allowed to progress for 2 h prior to being quenched *via* dropwise addition of sat. aqueous $NaHCO_3$. The zinc was subsequently removed by filtration through a celite pad, and the filtrate was extracted with EtOAc (3 × 25 ml). The combined organics were washed with brine, dried over $MgSO_4$, filtered and concentrated *in*

vacuo. The crude product was purified by flash column chromatography (0–15% MeOH: DCM) and pure fractions were combined and concentrated to afford the product as a yellow solid with a yield of 27 mg, 0.10 mmol, (45%).

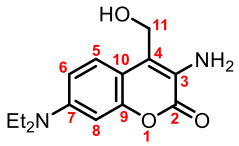

^{1}H NMR (400 MHz, $CDCl_3$) δ 7.32 (d, *J* = 8.9 Hz, 1H, Ar**H**$_5$), 6.64 (d, *J* = 8.9 Hz, 1H, Ar**H**$_6$), 6.56 (s, 1H, Ar**H**$_8$), 4.84 (s, 2H, C**H**$_2$OH, H_{11}), 3.37 (q, *J* = 7.1 Hz, 4H, N(C**H**$_2$CH$_3$)$_2$), 1.17 (t, *J* = 7.1 Hz, 6H, N(CH$_2$C**H**$_3$)$_2$).

HRMS ESI *m/z*: calc for $C_{14}H_{18}N_2O_3$ $[M+H]^+$ 263.1390, 285.1210 $[M+Na]^+$, $[M+K]^+$ 301.0949; Obs $[M+H]^+$ 263.1390, $[M+Na]^+$ 285.1207, $[M+K]^+$ 301.0949

The synthesis of **(32)**

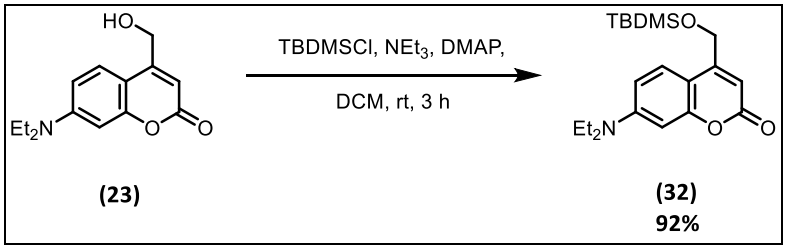

To a stirring solution of **(23)** (500 mg, 2.0 mmol, 1eq.) in DCM (25 ml), at rt, was added NEt_3 (0.4 ml, 3.0 mmol, 1.5 eq.), TBDMSCl (360 mg, 2.4 mmol, 1.2 eq.) and DMAP (12 mg, 0.10 mmol, 0.05 eq.). The reaction mixture was stirred at room temperature for 3 h at which point sat. aqueous $NaHCO_3$ (25 ml) was added. The aqueous was extracted with DCM (3 × 25 ml) before the combined organics were washed with brine (50 ml), dried over $MgSO_4$, filtered, and concentrated *in vacuo*. The residue was purified by flash column chromatography (40% EtOAc: hexane) and the pure fractions were combined and concentrated to afford the product as a light-yellow solid with a yield of 667 mg, 1.84 mmol, (92%).

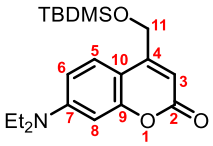

^{1}H NMR (400 MHz, $CDCl_3$) δ 7.23 (d, *J* = 8.9 Hz, 1H, Ar**H**$_5$), 6.53 (dd, *J* = 8.9, 2.5 Hz, 1H, Ar**H**$_6$), 6.49 (d, *J* = 2.5 Hz, 1H, Ar**H**$_8$), 6.26 (t, *J* = 1.5 Hz, 1H, Ar**H**$_3$), 4.80 (d, *J* = 1.5 Hz, 2H, C**H**$_2$OH, H_{11}), 3.39 (q, *J* = 7.1 Hz, 4H, N(C**H**$_2$CH$_3$)$_2$), 1.18 (t, *J* = 7.1 Hz, 6H, N(CH$_2$C**H**$_3$)$_2$), 0.94 (s, 9H, OSi(CH$_3$)$_2$C(C**H**$_3$)$_3$), 0.12 (s, 6H, Si(C**H**$_3$)$_2$C(CH$_3$)$_3$).

HRMS ESI *m/z*: Calc for $C_{20}H_{31}NO_3Si$ $[M+H]^+$ 362.2146, $[M+Na]^+$ 384.1965; Obs $[M+H]^+$ 362.2149, $[M+Na]^+$ 384.1971

Spectroscopic data were in agreement with [45]

The synthesis of **(33)**

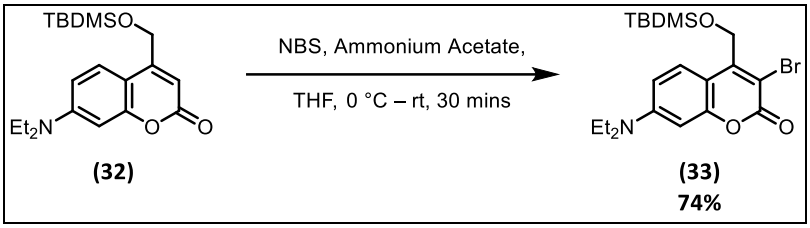

(32) (300 mg, 0.83 mmol, 1 eq.) was dissolved in THF (20 ml) and cooled to 0 °C. Ammonium acetate (6.4 mg, 0.083 mmol, 0.1 eq.) was then added followed by NBS (163 mg, 0.91 mmol, 1.1 eq.). The reaction mixture was stirred at 0 °C for 5 mins prior to warming to rt and stirring for an additional 25 mins. The reaction was quenched with sat. aqueous $Na_2S_2O_3$ solution (20 ml) prior to extraction with EtOAc (3 × 25 ml). The combined organic layers were washed with brine (50 ml), dried over $MgSO_4$, filtered and concentrated *in vacuo*. The crude product was purified by flash column chromatography (20% EtOAc: hexane) and the pure fractions were

combined and concentrated to afford the product as a yellow solid with a yield of 270 mg, 0.61 mmol, (74%).

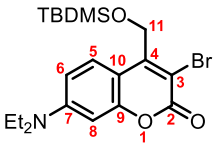

^{1}H NMR (400 MHz, $CDCl_3$) δ 7.74 (d, *J* = 9.1 Hz, 1H, Ar**H**$_5$), 6.59 (dd, *J* = 9.1, 2.6 Hz, 1H, Ar**H**$_6$), 6.45 (d, *J* = 2.6 Hz, 1H, Ar**H**$_8$), 4.97 (s, 2H, C**H**$_2$OTBDMS, H_{11}), 3.39 (q, *J* = 7.1 Hz, 4H, N(C**H**$_2$CH$_3$)$_2$)), 1.19 (t, *J* = 7.1 Hz, 6H, N(CH$_2$C**H**$_3$)$_2$)), 0.88 (s, 9H, OSi(CH$_3$)$_2$C(C**H**$_3$)$_3$), 0.12 (s, 6H, OSi(C**H**$_3$)$_2$C(CH$_3$)$_3$).

HRMS ESI *m/z*: calc for $C_{20}H_{30}BrNO_3Si$ $[M+H]^+$ 440.1251, $[M+Na]^+$ 462.1071; Obs $[M+H]^+$ 440.1267, $[M+Na]^+$ 462.1082

Spectroscopic data were in agreement with [35]

The synthesis of **(34)**

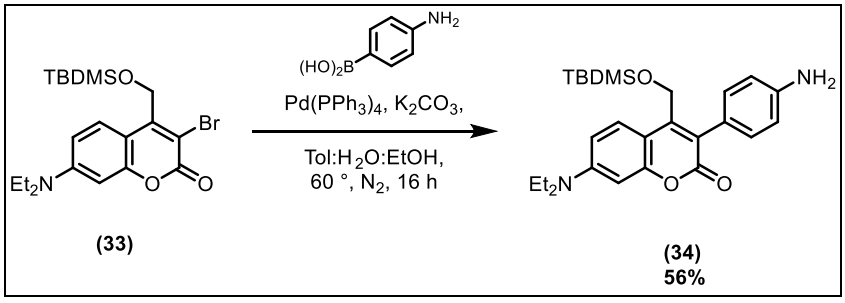

(33) (270 mg, 0.61 mmol, 1 eq.), 4-aminophenylboronic acid hydrochloride (212 mg, 1.22 mmol, 2 eq.), $Pd(PPh_3)_4$ (17 mg, 0.015 mmol, 0.025 eq.) and K_2CO_3 (253 mg, 1.83 mmol, 3 eq.) were added to a 3-necked flask fitted with a condenser and placed under N_2 atmosphere. A solvent mixture of toluene:H_2O:EtOH (1:2:1, 20 ml) purged with N_2 for 15 min was then added. and the reaction mixture was heated to 60 °C. After 16 h the reaction was cooled to rt and the

solvent removed *in vacuo*. The residue was dissolved in EtOAc (20 ml) and extracted with aqueous HCl solution (1.0 M, 20 ml). The aqueous layer was then adjusted to pH 10 *via* the addition of aqueous NaOH solution (1.0 M) before being extracted with EtOAc (3 × 25 ml) before being dried over $MgSO_4$, filtered, and concentrated *in vacuo.* The crude product was purified by flash column chromatography (40–60% EtOAc: petrol) and the pure fractions were combined and concentrated to afford the product as a brown/yellow solid with a yield of 153 mg, 0.34 mmol, (56%).

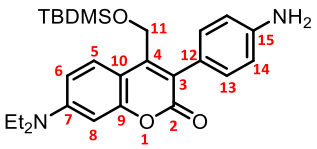

^{1}H NMR (400 MHz, $CDCl_3$) δ 7.68 (d, *J* = 9.1 Hz, 1H, Ar**H**$_5$), 7.20 – 7.10(m, 2H, Ph**H**$_{13}$), 6.75 – 6.67 (m, 2H, Ph**H**$_{14}$), 6.61 (dd, *J* = 9.1, 2.6 Hz, 1H, Ar**H**$_6$), 6.52 (d, *J* = 2.6 Hz, 1H, Ar**H**$_8$), 4.61 (s, 2H, C**H**$_2$OSiTBDMS, H_{11}), 3.76 (s, broad, 2H, N**H**$_2$), 3.41 (q, *J* = 7.1 Hz, 4H, N(C**H**$_2$CH$_3$)$_2$)), 1.21 (t, *J* = 7.1 Hz, 6H, N(CH$_2$C**H**$_3$)$_2$)), 0.87 (s, 9H, OSi(CH$_3$)$_2$C(C**H**$_3$)$_3$), -0.01 (s, 6H, OSi(C**H**$_3$)$_2$C(CH$_3$)$_3$).

^{13}C NMR (101 MHz, $CDCl_3$) δ 163.00(**C**$_2$), 155.58(**C**$_9$), 149.92 (**C**$_7$), 147.71 (**C**$_4$), 146.32 (**C**$_{12}$), 131.69 (**C**$_{14}$), 127.41 (**C**$_5$), 124.21 (**C**$_{15}$), 121.53 (**C**$_3$), 114.76 (**C**$_{13}$), 108.75(**C**$_{10}$), 108.63 (**C**$_6$), 97.45 (**C**$_8$), 60.27 (**C**$_{11}$), 44.80 N(**C**H$_2$CH$_3$)$_2$), 25.90 OSi(CH$_3$)$_2$C(**C**H$_3$)$_3$, 18.32 OSi(CH$_3$)$_2$**C**(CH$_3$)$_3$), 12.61 N(CH$_2$**C**H$_3$)$_2$), -5.26 OSi(**C**H$_3$)$_2$C(CH$_3$)$_3$.

HRMS ESI *m/z*: calc for $C_{26}H_{36}N_2NaO_3Si$ $[M+H]^+$ 453.2568, $[M+Na]^+$ 475.2387; Obs $[M+H]^+$ 453.2578, $[M+Na]^+$ 475.2391

The synthesis of **(35)**

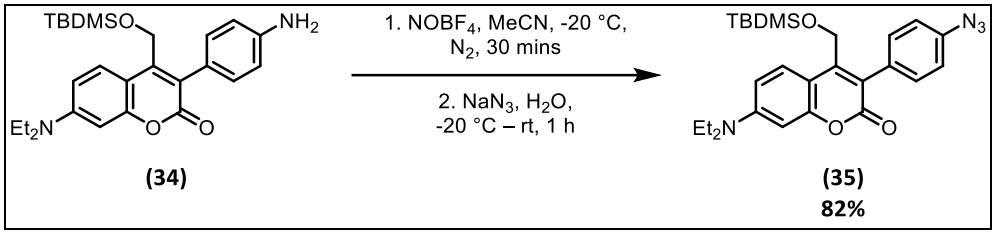

$NOBF_4$ (20 mg, 0.17 mmol, 1 eq.) was dissolved in anhydrous MeCN (5 ml) under N_2 and cooled to -20 °C. **(34)** (75 mg, 0.17 mmol, 1 eq.) was dissolved in anhydrous MeCN (10 ml) under N_2 and cooled to the same temperature. The solution of **(34)** was then added dropwise to the stirring solution of $NOBF_4$ and an instant colour change from yellow to dark red was observed. The reaction was allowed to proceed for 30 mins before being protected from light. At this point a solution of NaN_3 (13 mg, 0.20 mmol, 1.2 eq.) in H_2O (2 ml) was added dropwise. This was accompanied by a colour change from dark red to yellow. The reaction mixture was allowed to warm to rt and stirred for a further 1 h. At this point the mixture was diluted with EtOAc (15 ml) and the organics washed with HCl (1 M aqueous, 20 ml) and brine (20 ml). The organic layer was dried over $MgSO_4$, filtered and concentrated *in vacuo*, affording the product as a yellow/brown solid with a yield of 66 mg, 0.14 mmol, (82%).

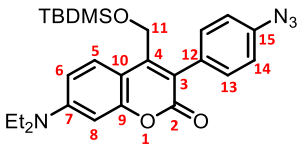

^{1}H NMR (400 MHz, $CDCl_3$) δ 7.67 (d, *J* = 9.0 Hz, 1H, Ar**H**$_5$), 7.40-7.33 (m, 2H, Ph**H**$_{13}$), 7.10-7.03 (m, 2H, Ph**H**$_{14}$), 6.63 (dd, *J* = 9.0, 2.6 Hz, 1H, Ar**H**$_6$), 6.53 (d, *J* = 2.6 Hz, 1H, Ar**H**$_8$), 4.56 (s, 2H, C**H**$_2$OTBDMS, H$_{11}$), 3.43 (q, *J* = 7.1 Hz, 4H, N(C**H**$_2$CH$_3$)$_2$), 1.22 (t, *J* = 7.1 Hz, 6H, N(CH$_2$C**H**$_3$)$_2$), 0.87 (s, 9H, OSi(CH$_3$)$_2$C(C**H**$_3$)$_3$), 0.00 (s, 6H, OSi(C**H**$_3$)$_2$C(CH$_3$)$_3$).

^{13}C NMR (101 MHz, $CDCl_3$) δ 162.59 (**C**$_2$), 155.90 (**C**$_9$), 150.38 (**C**$_7$), 148.59 (**C**$_4$), 139.79 (**C**$_{12}$), 132.31 (**C**$_{13}$), 131.18 (**C**$_{15}$), 127.53 (**C**$_5$), 120.33 (**C**$_3$) 118.86 (**C**$_{14}$), 108.86 (**C**$_6$), 108.40 (**C**$_{10}$), 97.49(**C**$_8$), 60.09 (**C**$_{11}$), 44.89 N(**C**$H_2$$CH_3$)$_2$, 25.91 (OSi($CH_3$)$_2$C(**C**$H_3$)$_3$, 18.35 (OSi($CH_3$)$_2$**C**($CH_3$)$_3$, 12.64 N($CH_2$**C**$H_3$)$_2$, -5.23(OSi(**C**$H_3$)$_2$C($CH_3$)$_3$.

HRMS ESI *m/z*: calc for $C_{26}H_{34}N_4O_3Si$ $[M+H]^+$ 479.2473 $[M+Na]^+$ 501.2292 $[M+K]^+$ 517.2032; Obs $[M+H]^+$ 479.2472, $[M+Na]^+$ 501.2302, $[M+K]^+$ 517.2029

The synthesis of **(31)**

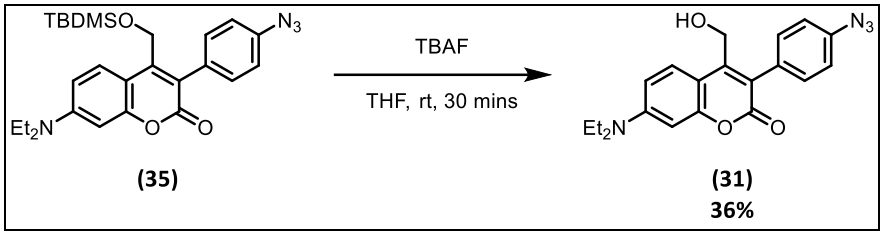

(35) (105 mg, 0.22 mmol, 1 eq.) was dissolved in THF (10 ml) and protected from light. TBAF (1.0 M in THF, 220 µl, 0.22 mmol, 1 eq.) was added dropwise and the reaction was stirred for 30 mins. Sat. aqueous $NaHCO_3$ solution (10 ml) was then added and the aqueous was extracted with EtOAc (3 × 25 ml). The combined organic layers were washed with brine (50 ml) and dried over $MgSO_4$, filtered and concentrated *in vacuo* affording the product as a yellow/brown solid in a yield of 38 mg, 0.08 mmol, (36%).

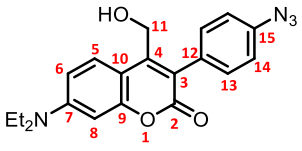

^{1}H NMR (400 MHz, $CDCl_3$) δ 7.69 (d, *J* = 9.1 Hz, 1H, Ar**H**$_5$), 7.40 – 7.29 (m, 2H, Ph**H**$_{13/14}$), 7.08 – 7.01 (m, 2H, Ph**H**$_{13}$/$_{14}$), 6.63 (dd, *J* = 9.1, 2.6 Hz, 1H, Ar**H**$_6$), 6.52 (d, *J* = 2.6 Hz, 1H, Ar**H**$_8$), 4.60 (s, 2H, C**H**$_2$OH, H$_{11}$), 3.42 (q, *J* = 7.1 Hz, 4H, N(C**H**$_2$$CH_3$)$_2$), 1.21 (t, *J* = 7.1 Hz, 6H, N(CH_2C**H**$_3$)$_2$).

^{13}C NMR (101 MHz, $CDCl_3$) δ 162.54 (**C**$_2$), 155.92 (**C**$_9$), 150.53 (**C**$_7$), 148.27 (**C**$_4$), 139.87 (**C**$_{12}$), 132.08 (**C**$_{13}$), 130.92 (**C**$_{15}$), 126.99 (**C**$_5$), 120.59 (**C**$_3$), 119.04 (**C**$_{14}$), 109.17 (**C**$_6$), 107.80 (**C**$_{10}$), 97.62 (**C**$_8$), 59.27 (**C**$_{11}$), 44.90 (N(**C**$H_2CH_3)_2$), 12.59(N(CH_2**C**$H_3)_2$).

HRMS ESI *m/z*: calc for $C_{20}H_{20}N_4O_3$ $[M+H]^+$ 365.1608, $[M+Na]^+$ 387.1428, $[M+K]^+$ 403.1167; Obs $[M+H]^+$ 365.1617, $[M+Na]^+$ 387.1436, $[M+K]^+$ 403.1175

The Synthesis of **(37)**

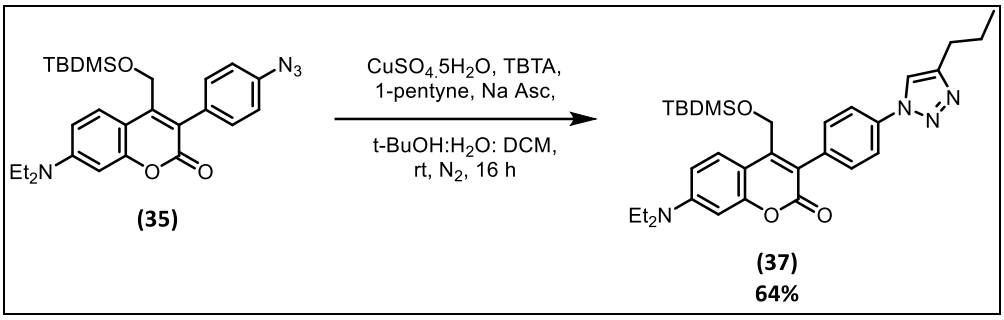

(35) (66 mg, 0.14 mmol, 1 eq.) was dissolved in mixture of *t*-BuOH:H_2O:DCM (1:2:1, 8ml) and protected from light. 1-pentyne (56 µL, 0.57 mmol, 4.1 eq.) was added and the mixture was stirred for 10 mins. TBTA (15 mg, 0.03 mmol, 0.2 eq.), sodium ascorbate (119 mg, 0.60 mmol, 4.25 eq.) and $CuSO_4.5H_2O$ (35 mg, 0.14 mmol, 1 eq.) were then added and the reaction was placed under N_2. The reaction was stirred at rt for 16 h at which point the solvent was removed *in vacuo.* The crude reaction mixture was then redissolved in EtOAc (20 ml) and the organics washed with sat. aqueous $NaHCO_3$ solution (20 ml) followed by brine (20 ml). The organic layer was dried over $MgSO_4$, filtered and concentrated *in vacuo*. The residue was then purified by flash column chromatography (20 – 40% EtOAc: petrol) and pure fractions concentrated *in vacuo* to afford the product as a yellow solid with a yield of 48 mg, 0.09 mmol (64%).

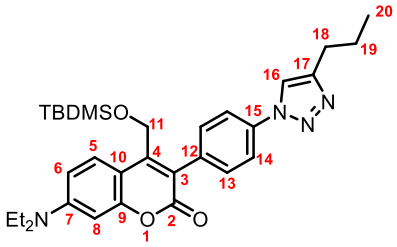

^{1}H NMR (400 MHz, $CDCl_3$) δ 7.79 – 7.76 (m, 2H, Ph**H**$_{,14}$), 7.75 (s, 1H, Triazole**H,** H_{16}), 7.69 (d, *J* = 9.1Hz, 1H, Ar**H**$_5$), 7.56 – 7.51 (m, 2H, Ph**H**$_{13}$), 6.64 (dd, *J* = 9.1, 2.6 Hz, 1H, Ar**H**$_6$), 6.54 (d, *J* = 2.6 Hz, 1H, Ar**H**$_8$), 4.59 (s, 2H, C**H**$_2$OSi, H_{11}), 3.44 (q, *J* = 7.1 Hz, 4H, N(C**H**$_2$CH$_3$)$_2$), 2.79 (t, *J* = 7.3 Hz, 2H, Triazole-C**H**$_2$CH$_2$CH$_3$, H_{18}), 1.78 (dt, J= 7.3, 7.3 Hz 2H, Triazole-CH$_2$C**H**$_2$CH$_3$, H_{19}), 1.23 (t, *J* = 7.3 Hz, 6H, N(C**H**$_2$CH$_3$)$_2$), 1.01 (t, *J* = 7.3 Hz, 3H, Triazole-CH$_2$CH$_2$C**H**$_3$, H_{20}), 0.87 (s, 9H, OSi(CH$_3$)$_2$C(C**H**$_3$)$_3$), 0.01 (s, 6H, OSi(C**H**$_3$)$_2$C(CH$_3$)$_3$).

^{13}C NMR (101 MHz, $CDCl_3$) δ 162.43 (**C**$_2$), 155.99(**C**$_9$), 150.53 (**C**$_7$), 149.19 (**C**$_{17}$), 148.96 (**C**$_4$), 136.84 (**C**$_{12}$), 134.82 (**C**$_{15}$), 132.22 (**C**$_{13}$), 127.59 (**C**$_5$), 120.07 (**C**$_{14}$), 119.78 (**C**$_3$), 118.97 (**C**$_{16}$), 108.95 (**C**$_6$), 108.26 (**C**$_{10}$), 97.44 (**C**$_8$), 60.02 (**C**$_{11}$), 44.89(N(**C**H$_2$CH$_3$)$_2$), 27.82 (**C**$_{18}$), 25.88 (Si(CH)$_2$C(**C**H)$_3$), 22.82 (**C**$_{19}$), 18.32 (Si(CH)$_2$**C**(CH)$_3$, 13.96 (**C**$_{20}$), 12.62 (N(CH$_2$**C**H$_3$)$_2$), -5.21 (Si(**C**H)$_2$C(CH)$_3$.

The Synthesis of **(38)**

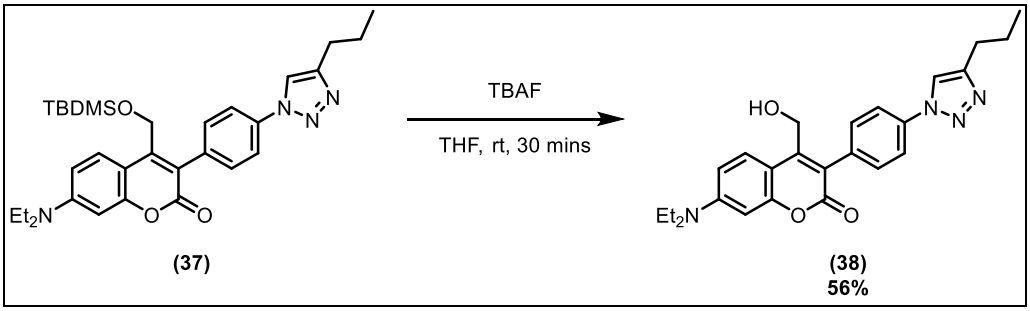

(37) (48 mg, 0.09 mmol, 1 eq.) was dissolved in THF (10 ml) and protected from light. TBAF (1.0 M in THF, 90 µL, 0.09 mmol, 1 eq.) was added dropwise and the reaction was stirred for 30 mins. At this point, the reaction was quenched *via* the dropwise addition of sat. aqueous

$NaHCO_3$ solution (10 ml) and the product was extracted with EtOAc (3 × 25 ml). The combined organic layers were washed with brine (50 ml), dried over $MgSO_4$, filtered and concentrated *in vacuo* affording the product as a yellow/brown solid with a yield of 20 mg, 0.05 mmol (56%).

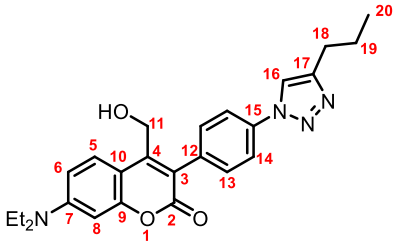

^{1}H NMR (400 MHz, $CDCl_3$) δ 7.79 (d, *J* = 9.1 Hz, 1H, Ar**H**$_5$), 7.72 (s, 1H, Triazole**H**, H_{16}), 7.70 – 7.66 (m, 2H, Ph**H**$_{14}$), 7.51 – 7.45 (m, 2H, Ph**H**$_{13}$), 6.65 (dd, *J* = 9.1, 2.6 Hz, 1H, Ar**H**$_6$), 6.52 (d, *J* = 2.6 Hz, 1H, Ar**H**$_8$), 4.65 (s, 2H, C**H**$_2$OH, H_{11}), 3.42 (q, *J* = 7.1 Hz, 4H, N(C**H**$_2$CH$_3$)$_2$), 2.73 (t, *J* = 7.5 Hz, 2H, AlkylH, **H**$_{18}$), 1.78 – 1.68 (m, 2H, Alkyl**H**, H_{19}), 1.21 (t, *J* = 7.1 Hz, 6H, N(C**H**$_2$CH$_3$)$_2$), 0.98 (t, *J* = 7.4 Hz, 3H, H_{20}).

^{13}C NMR (101 MHz, $CDCl_3$) δ 162.51 (**C**$_2$), 156.00(**C**$_9$), 150.64 (**C**$_7$), 149.26 (**C**$_4$), 149.04 (**C**$_{17}$), 136.56 (**C**$_{12}$), 134.89 (**C**$_{15}$), 132.13 (**C**$_{13}$), 127.49 (**C**$_5$), 120.16 (**C**$_{14}$), 119.76 (**C**$_3$), 119.09 (**C**$_{16}$), 109.25 (**C**$_6$), 107.97 (**C**$_{10}$), 97.47 (**C**$_8$), 59.05 (**C**$_{11}$), 44.92 (N(**C**H$_2$CH$_3$)$_2$), 27.66 (**C**$_{18}$), 22.71 (**C**$_{19}$), 13.91 (**C**$_{20}$), 12.60 (N(CH$_2$**C**H$_3$)$_2$).

HRMs ESI *m/z*: calc for $C_{25}H_{28}N_4O_3$ $[M+H]^+$ 433.2234, $[M+Na]^+$ 455.2054; Obs $[M+H]^+$ 433.2241, $[M+Na]^+$ 455.2053

The Synthesis of **(36)**

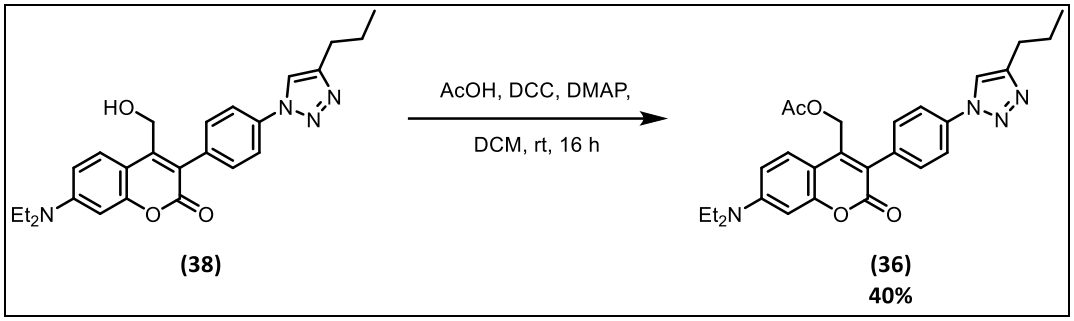

(38) (20 mg, 0.05 mmol, 1 eq.) was dissolved in DCM (5 ml) and protected from light. AcOH (4 µL, 0.06 mmol, 1.2 eq.), DCC (12 mg, 0.06 mmol, 1.2 eq.) and DMAP (7 mg, 0.06 mmol, 1.2 eq.) were added. The reaction was allowed to proceed at room temperature for 16 h prior to quenching with sat. aqueous $NaHCO_3$ solution (5 ml). The product was extracted with DCM (3 × 25 ml) and the combined organics were washed with brine before being dried over $MgSO_4$, filtered and concentrated *in vacuo.* The DCU formed as a result of the reaction was then removed by redissolving the crude product in cold MeCN (10 ml) followed by filtration. The residue was then further purified by flash column chromatography (20 – 60% EtOAc: petrol) affording the product as a yellow solid with a yield of 10 mg, 0.02 mmol, (40%).

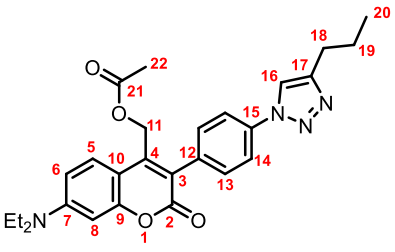

^{1}H NMR (400 MHz, $CDCl_3$) δ 7.81 – 7.77 (m, 2H, Ph**H**$_{14}$), 7.74 (s, 1H, Triazole**H**$_{16}$), 7.52 – 7.47 (m, 2H, Ph**H**$_{13}$), 7.44 (d, *J* = 9.1 Hz, 1H, Ar**H**$_5$), 6.64 (dd, *J* = 9.1, 2.6 Hz, 1H, Ar**H**$_6$), 6.56 (d, *J* = 2.6 Hz, 1H, Ar**H**$_8$), 5.04 (s, 2H, C**H**$_2$OAc, H$_{11}$), 3.44 (q, *J* = 7.1 Hz, 4H, N(C**H**$_2$CH$_3$)$_2$,), 2.79 (t, *J* = 7.6 Hz, 2H, Triazole-C**H**$_2$CH$_2$CH$_3$, H$_{18}$), 2.08 (s, 3H, OCOC**H**$_3$), 1.82 – 1.73 (m, 2H, Triazole-

$CH_2C\mathbf{H}_2CH_3$, H_{19}), 1.23 (t, *J* = 7.1 Hz, 6H, $N(CH_2C\mathbf{H}_3)_2$), 1.02 (t, *J* = 7.3 Hz, 3H, Triazole-$CH_2CH_2C\mathbf{H}_3$, H_{20}).

^{13}C NMR (101 MHz, $CDCl_3$) δ 170.30 (**C**$_{21}$), 161.88 (**C**$_2$), 155.90 (**C**$_9$), 150.79(**C**$_7$), 149.20 (**C**$_{17}$), 144.51 (**C**$_4$), 137.07 (**C**$_{12}$), 134.27 (**C**$_{15}$), 132.02 (**C**$_{13}$), 126.48 (**C**$_5$), 122.07 (**C**$_3$), 120.35 (**C**$_{14}$), 118.92 (**C**$_{16}$), 109.30 (**C**$_6$), 107.55 (**C**$_{10}$), 97.69 (**C**$_8$), 60.25 (**C**$_{11}$), 44.97 ($N(\mathbf{C}H_2CH_3)_2$), 27.81 (**C**$_{18}$), 22.78 (**C**$_{19}$), 20.93 (**C**$_{22}$), 13.94 (**C**$_{20}$), 12.59 ($N(CH_2\mathbf{C}H_3)_2$).

HRMS ESI *m/z*: calc for $C_{27}H_{30}N_4O_4$ $[M+H]^+$ 475.2340, $[M+Na]^+$ 497.2159; Obs $[M+H]^+$ 497.2159, $[M+Na]^+$ 497.2159

The synthesis of (43)

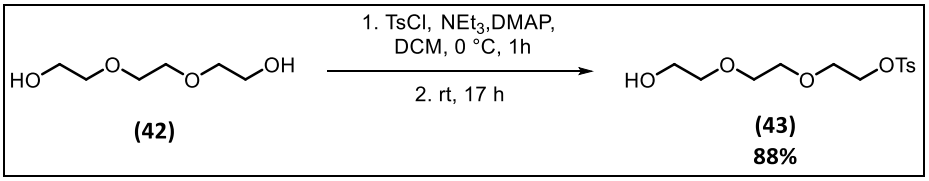

NEt_3 (3.07 mL, 22.0 mmol, 1.1 eq.) was added to a stirred solution of DMAP (122 mg, 1.0 mmol, 0.05 eq.) and triethylene glycol (13.4 mL, 100.0 mmol, 5.0 eq.) in dry CH_2Cl_2 (110 mL) at rt under Ar. The resulting solution was cooled to 0 °C and a solution of tosyl chloride (3.81 g, 20.0 mmol, 1.0 eq.) in dry CH_2Cl_2 (10 mL) was added dropwise over 30 min. The resulting solution was stirred at 0 °C for 1 h then warmed to rt over 2 h. The reaction mixture was washed sequentially with aqueous HCl (1 M) (2 x 80 mL), H_2O (3 x 40 mL) and brine (40 mL) before being dried over $MgSO_4$, filtered and concentrated *in vacuo* to afford the product as a colourless oil with a yield of 5.3 g, 17.4 mmol, (88%).

^{1}H NMR (400 MHz, $CDCl_3$) δ 7.67 (d, *J* = 8.3 Hz, 2H, OTsPh**H**), 7.24 (d, *J* = 8.3 Hz, 2H, OTsPh**H**), 4.06 – 4.01 (m, 2H, C**H**$_2$), 3.58 – 3.54 (m, 4H, C**H**$_2$), 3.48 – 3.41 (m, 6H, C**H**$_2$), 3.20 – 3.08 (Broad, 1H, O**H**), 2.32 (s, 3H, OTsC**H**$_3$).

Spectroscopic data were in agreement with [46]

The synthesis of (40)

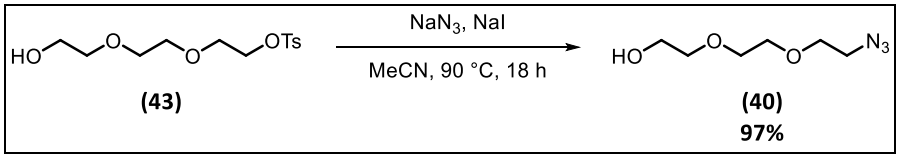

(43) **(40)** **97%**

Monotosyl triethylene glycol **(43)** (5.33 g, 17.5 mmol, 1.0 eq.), cat. NaI (10 mol%) and NaN_3 (2.28 g, 35.1 mmol, 2.0 eq.) were dissolved in MeCN (44 mL) at rt. The resulting solution was stirred and heated at 85 °C for 16 h. After being allowed to cool to rt, the reaction mixture was evaporated under reduced pressure. The residue was dissolved in CH_2Cl_2 (80 ml), and H_2O (40 ml) and the two layers were separated. The aqueous layer was extracted with CH_2Cl_2 (3 x 160 ml), and the combined organics were washed with brine (40 ml), dried (Na_2SO_4), filtered and concentrated *in vacuo*. The crude product was purified by flash column chromatography (10-60% EtOAc: petrol) and pure fractions were combined and concentrated to afford the desired product as a colourless oil with a yield of 2.9 g, 16.6 mmol, (97%).

^{1}H NMR (400 MHz, $CDCl_3$) δ 3.76 (broad, 1H, O**H**), 3.63 – 3.59 (m, 2H, C**H**$_2$), 3.56 (overlapping, 6H, C**H**$_2$), 3.51 – 3.46 (m, 2H, C**H**$_2$), 3.31 – 3.25 (m, 2H, C**H**$_2$).

Spectroscopic data were in agreement with [47]

The Synthesis of **(4)**

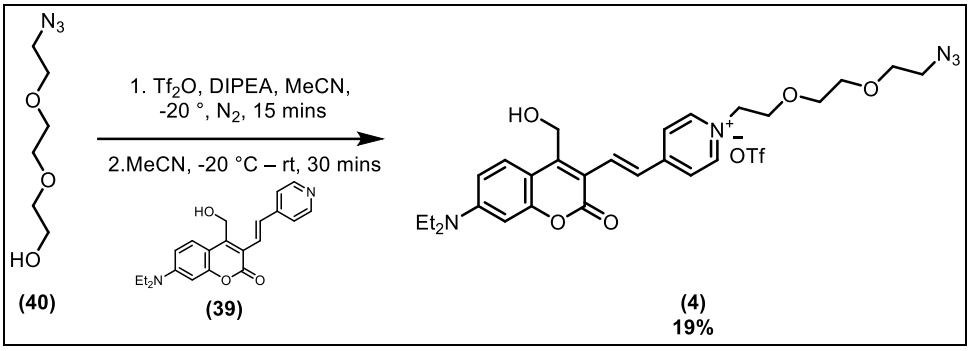

A solution of **(40)** (228 mg, 1.30 mmol, 3 eq.) in anhydrous MeCN (5 ml) was cooled to -20 °C and purged with N_2 for 5 mins. At this point triflic anhydride (219 µL, 1.30 mmol, 3 eq.) was added in a dropwise fashion. Upon full addition, the reaction mixture was stirred for a further 15 mins at -20 °C. A solution of **(39)** (150 mg, 0.42 mmol, 1 eq.) in anhydrous MeCN (10 ml) under N_2 atmosphere was then added dropwise to the initial reaction mixture. Upon complete addition the reaction mixture was warmed to rt and allowed to stir for a further 30 mins. The reaction was then quenched using sat. $NaHCO_3$ solution (20 ml) which was added in a dropwise fashion. Upon quenching, a colour change from colourless to intense red/purple was observed. The quenched reaction mixture was extracted with EtOAc (3 × 20 ml). The combined organic layers were washed with brine (30 ml) before being dried over $MgSO_4$, filtered and concentrated *in vacuo*. The residue was redissolved in EtOAc (10 ml) and added dropwise to cold diethyl ether (90ml) to precipitate the product, which was then pelleted by centrifugation (4,000 rpm, 6 mins) and the supernatant removed, affording the purified product as red solid with a yield of 54 mg, 0.08 mmol, (19%).

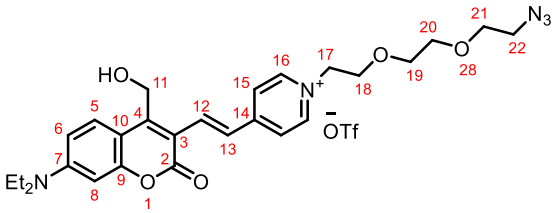

^{1}H NMR (400 MHz, MeCN-d_3) δ 8.46 (d, *J* = 7.0 Hz, 2H, H_{16}), 8.06 – 7.93 (overlapping, 4H, $H_{12,13,15}$), 7.77 (d, *J* = 9.3 Hz, Ar**H**$_5$), 6.78 (dd, *J* = 9.3, 2.6 Hz, 1H, Ar**H**$_6$), 6.53 (d, *J* = 2.6 Hz, 1H, Ar**H**$_8$), 4.94 (d, *J* = 5.2 Hz, 2H, C**H**$_2$OH, H_{11}), 4.58 – 4.49 (m, 2H, H_{17}), 3.94 – 3.87 (m, 2H, H_{18}), 3.72 (t, *J* = 5.6 Hz, 1H, PEGH), 3.59 (ddd, *J* = 6.6, 3.2, 1.5 Hz, 2H, H_{19}) 3.57 – 3.53 (m, 3H, PEGH), 3.49 (q, *J* = 7.1 Hz, 4H, N(C**H**$_2$CH$_3$)$_2$), 3.36 – 3.31 (m, 2H, PEGH), 1.19 (t, *J* = 7.1 Hz, 6H, N(CH$_2$C**H**$_3$)$_2$).

^{13}C NMR (101 MHz, MeCN-d_3) δ 160.26 (**C**$_2$), 156.46(**C**$_9$), 155.20 (**C**$_{14}$), 154.14 (**C**$_4$), 152.12 (**C**$_7$), 144.09 (**C**$_{16}$), 134.81 (**C**$_{12}$), 128.11 (**C**$_5$), 124.94 (**C**$_{13}$), 123.53 (**C**$_{15}$), 112.72 (**C**$_3$), 109.95 (**C**$_6$), 108.15 (**C**$_{10}$), 96.66 (**C**$_8$), 70.36 (**C**$_{19}$), 69.96 (**C**$_{20}$), 69.61 (**C**$_{21}$), 68.86 (**C**$_{18}$), 60.12 (**C**$_{17}$), 55.67 (**C**$_{11}$), 50.52 (**C**$_{22}$), 44.65 (N(**C**H$_2$CH$_3$)$_2$), 11.87 (N(CH$_2$**C**H$_3$)$_2$).

^{19}F NMR (376 MHz, CD_3CN) δ -79.23 (Triflate).

HRMS ESI *m/z*: calc for $C_{27}H_{33}N_5O_5$ $[M+H]^+$ 508.2554; Obs: 508.2554

The synthesis of **(44)**

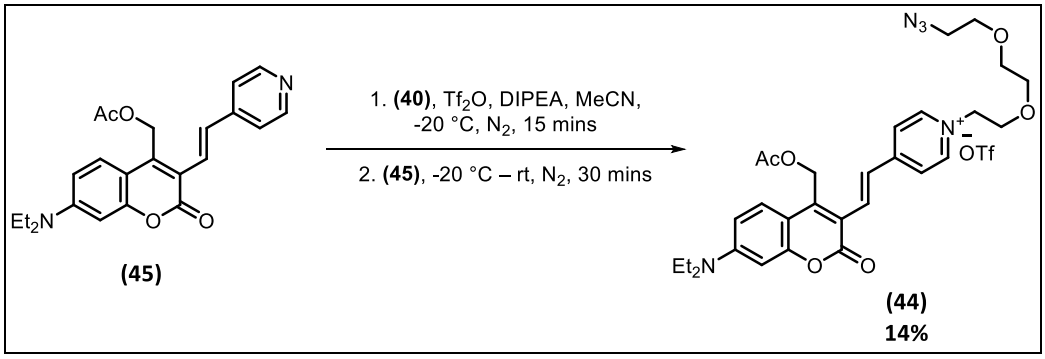

(40) (158 mg, 0.90 mmol, 3 eq.) was added to a 100 ml RBF. Anhydrous MeCN (5 ml) was added, and the solution was cooled to -20 °C and purged with N_2 for 5 mins. At this point triflic anhydride (150 µL, 0.90 mmol, 3 eq.) was added in a dropwise fashion. Upon full addition, the reaction mixture was stirred for a further 15 mins at -20 °C.

In the meantime **(45)** (116 mg, 0.30 mmol, 1 eq.) was dissolved in anhydrous MeCN (10 ml) and placed under N_2 atmosphere. Upon completion of step 1, this **(45)** solution was added dropwise to the initial reaction mixture. As the drops were added a localised colour change from colourless to red was observed where the drop made contact. However, this change was temporary and upon complete addition the reaction mixture was colourless. Upon complete addition the reaction mixture was warmed to rt and allowed to stir for a further 30 mins. Excess triflic anhydride was then quenched using sat. $NaHCO_3$ solution (20 ml) which was added in a dropwise fashion. Upon quenching, a colour change from colourless to intense red/purple was observed. The quenched reaction mixture was diluted with EtOAc (20 ml) and the product was extracted with EtOAc (3 × 20 ml). The combined organic layers were washed with brine before being dried over $MgSO_4$, filtered and concentrated *in vacuo*. The crude product was redissolved in EtOAc (10 ml) and added dropwise to cold diethyl ether (90ml) in two 50 ml falcon tubes, to precipitate the product, which was then pelleted by centrifugation (4,000 rpm, 6 mins) and the supernatant removed, affording the purified product as red solid with a yield of 28 mg, 0.04 mmol, (14%).

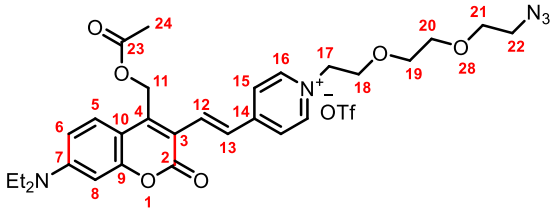

^{1}H NMR (400 MHz, MeCN-d_3) δ 8.50 (d, *J* = 7.0 Hz, 2H, Pyr**H**, H_{16}), 7.98 (d, *J* = 7.0 Hz, 2H, Pyr**H**, H_{15}), 7.94 (d, *J* = 15.9 Hz, 1H, Alkene, H_{12}/H_{13}), 7.89 (d, *J* = 15.9 Hz, 1H, Alkene, H_{12}/H_{13}), 7.64 (d, *J* = 9.3 Hz, 1H, Ar**H**$_5$), 6.75 (dd, *J* = 9.3, 2.6 Hz, 1H, Ar**H**$_6$), 6.49 (d, *J* = 2.6 Hz, 1H, Ar**H**$_8$), 5.46 (s, 2H, C**H**$_2$OAc, H_{11}), 4.59 – 4.53 (m, 2H, PEG**H**, H_{17}), 3.94 – 3.88 (m, 2H, PEG**H**, H_{18}), 3.72 –

3.62 (m, 1H, PEG**H**), 3.61 – 3.57 (m, 2H, H_{19}), 3.57 – 3.52 (m, 3H, PEG**H**), 3.45 (q, *J* = 7.1 Hz, 4H, $N(C\mathbf{H}_2CH_3)_2$), 3.36 – 3.30 (m, 2H, PEG**H**), 2.04 (s, 3H, $OCOC\mathbf{H}_3$, H15), 1.17 (t, *J* = 7.1 Hz, 6H, $N(CH_2C\mathbf{H}_3)_2$,).

^{13}C NMR (101 MHz, MeCN-d_3) δ 170.47 ($\mathbf{C}_{23}$), 159.81 ($\mathbf{C}_2$), 156.17 ($\mathbf{C}_9$), 154.85 ($\mathbf{C}_{14}$), 152.17 ($\mathbf{C}_7$), 148.85 ($\mathbf{C}_4$), 144.23 ($\mathbf{C}_{16}$), 133.97 ($\mathbf{C}_{12}$/$\mathbf{C}_{13}$), 127.85 ($\mathbf{C}_5$), 125.73 ($\mathbf{C}_{12}$/$\mathbf{C}_{13}$), 123.65 ($\mathbf{C}_{15}$), 122.66 ($\mathbf{C}F_3$), 119.47($\mathbf{C}F_3$) , 113.76 ($\mathbf{C}_3$), 110.18 ($\mathbf{C}_6$), 108.10 ($\mathbf{C}_{10}$), 96.65 ($\mathbf{C}_8$), 70.33 (PEG), 69.93 (PEG), 69.60 (PEG), 68.86 (PEG), 60.16 (PEG), 57.41 (C_{11}), 50.52 (PEG), 44.71 ($N(\mathbf{C}H_2CH_3)_2$), 20.09 (C_{24}), 11.90 ($N(CH_2\mathbf{C}H_3)_2$).

^{19}F NMR (376 MHz, CD_3CN) δ -79.20 (Triflate).

HRMS ESI *m/z*: calc for $C_{29}H_{36}N_5O_6$ $[M]^+$ 550.2660; Obs $[M]^+$ 550.2671

3.10.3 NMR Spectra of Novel Compounds

NMR Spectra of **(15)**

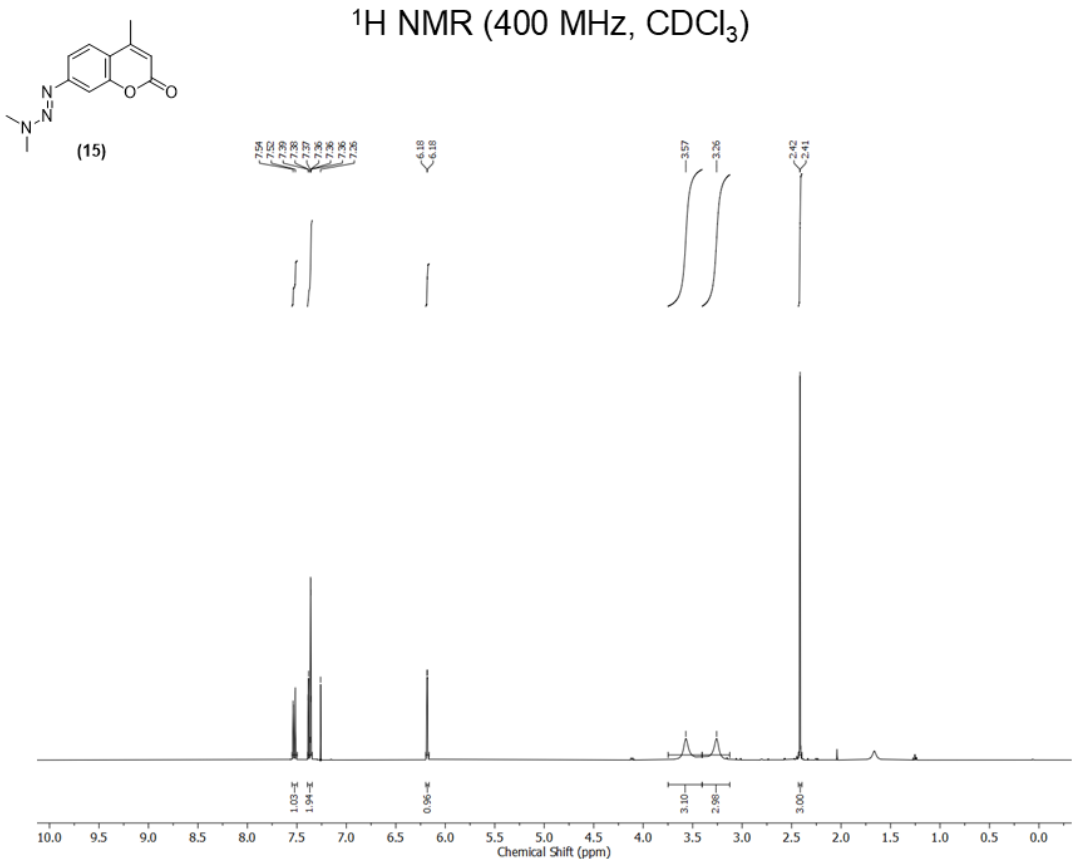

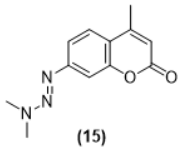

(15)

^{13}C NMR (100 MHz, $CDCl_3$)

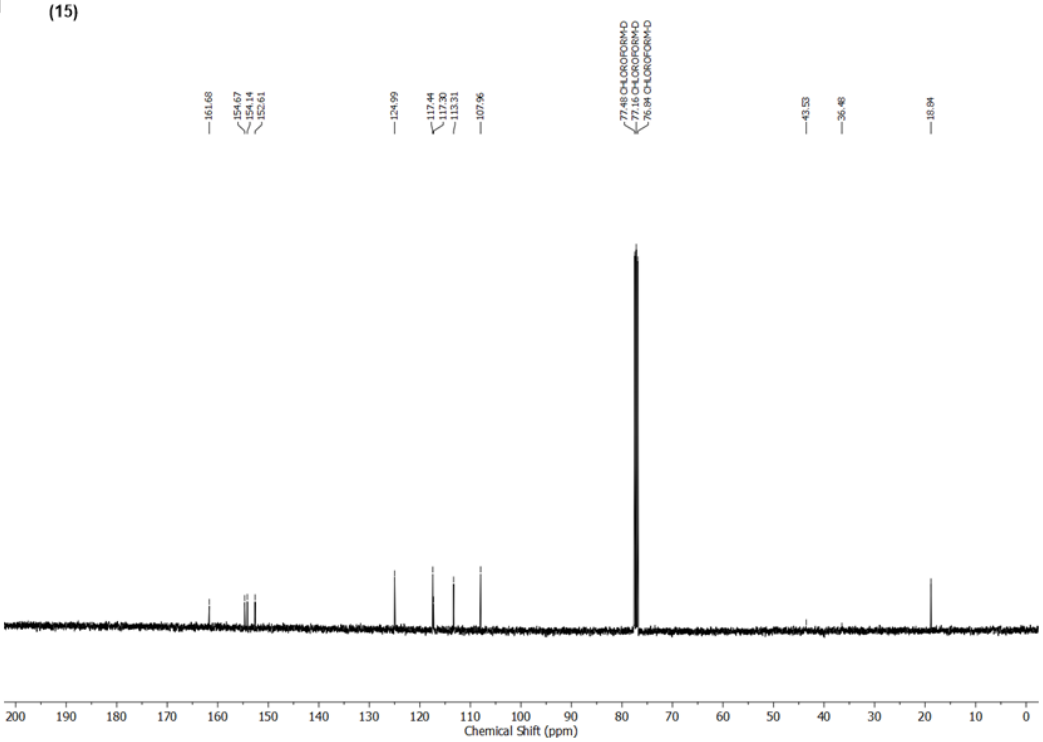

NMR Spectra of **(14)**

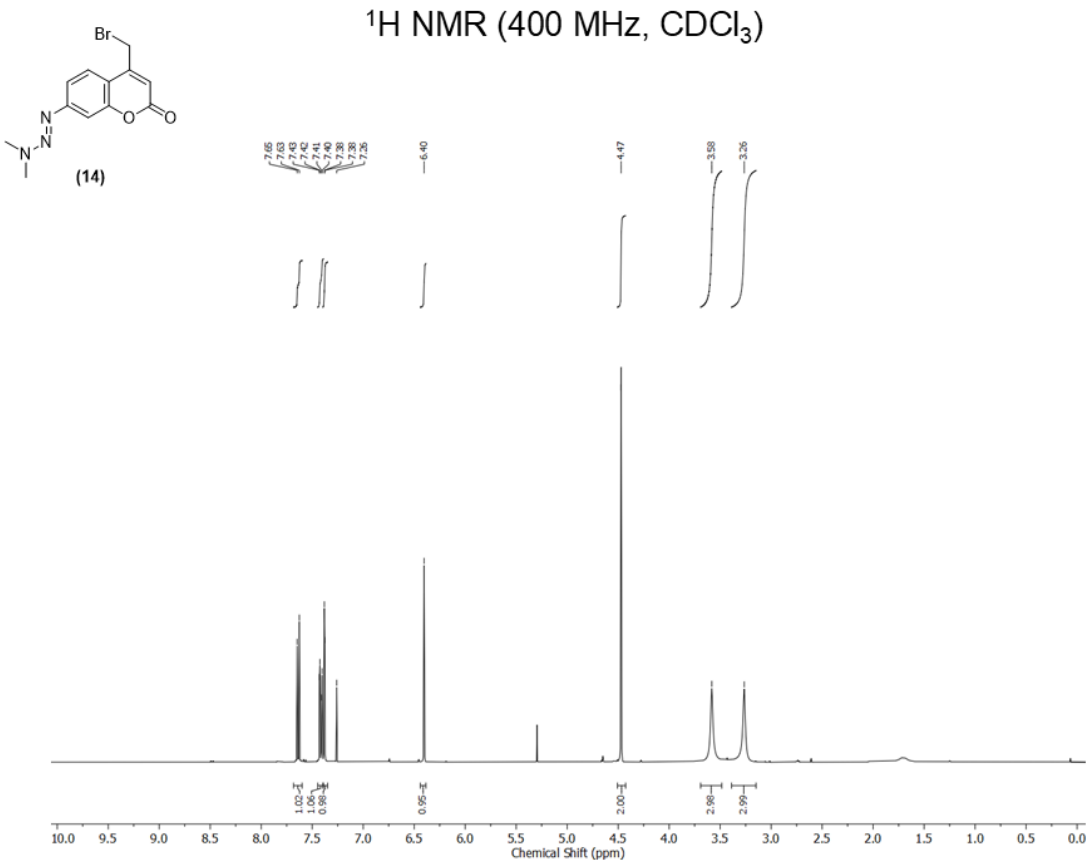

^{13}C NMR (100 MHz, $CDCl_3$)

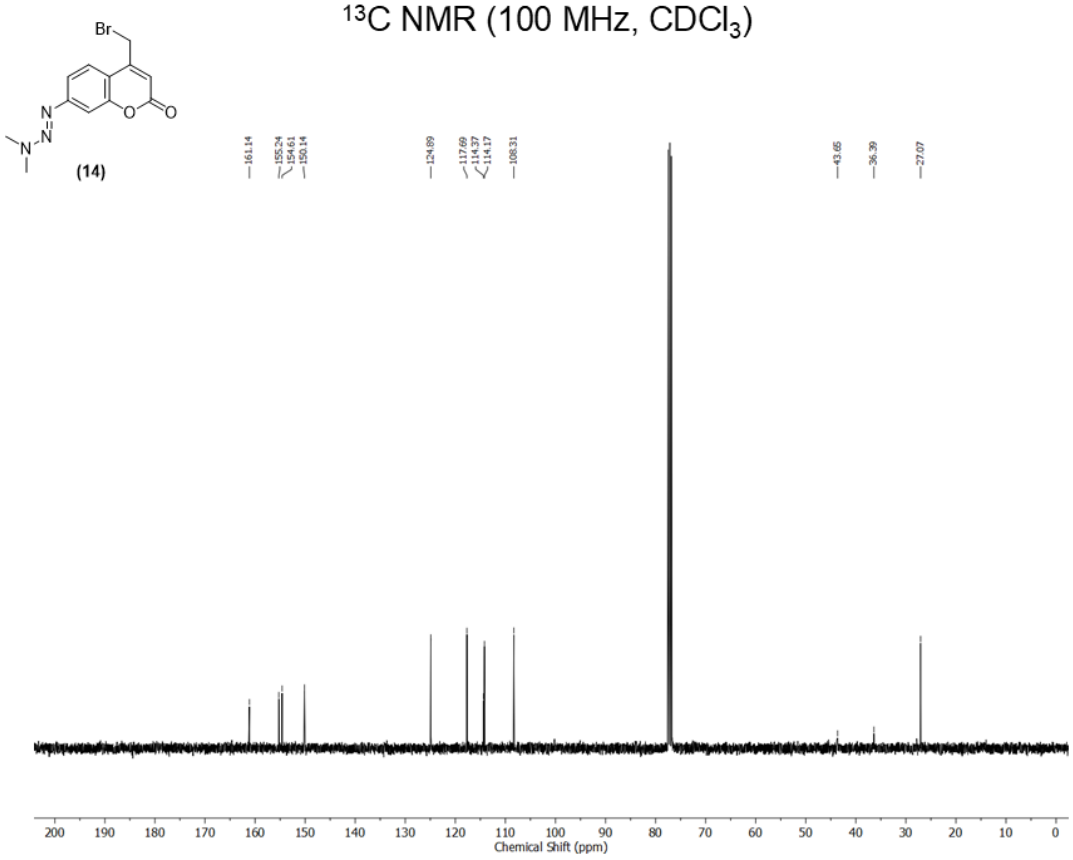

NMR Spectra of **(13)**

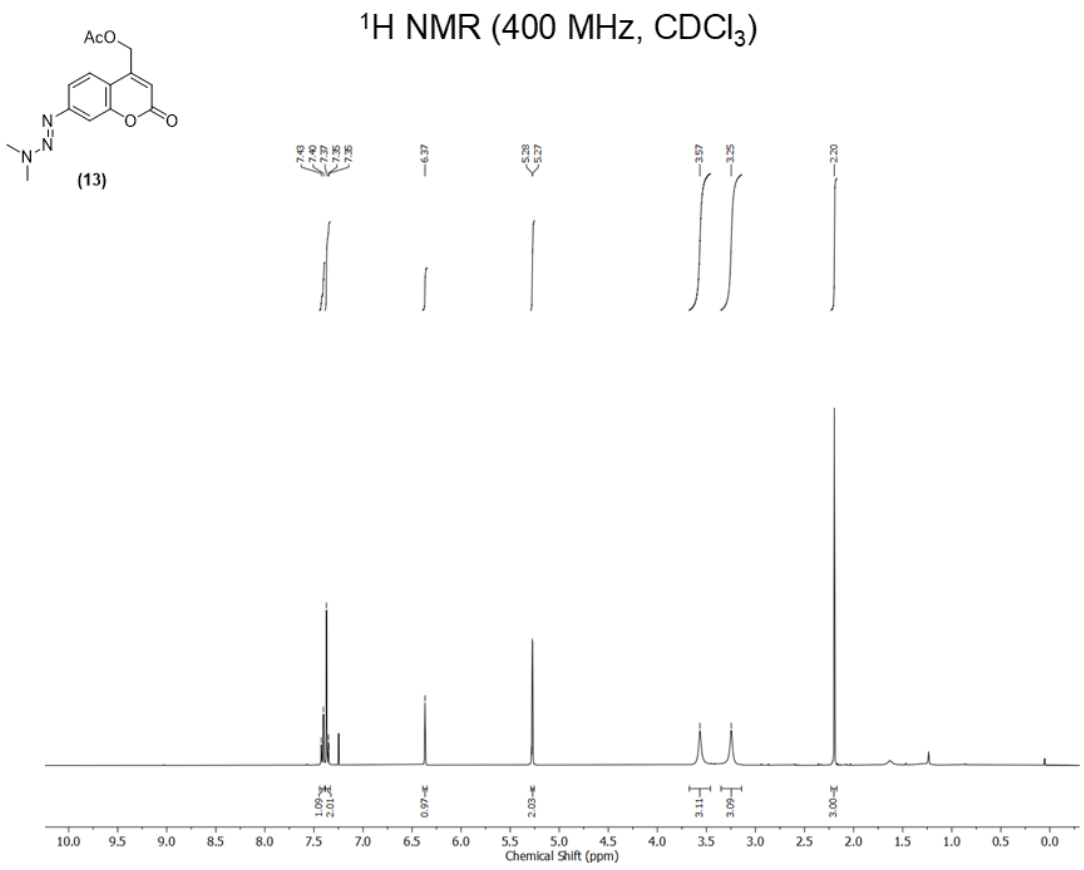

^{13}C NMR (100 MHz, $CDCl_3$)

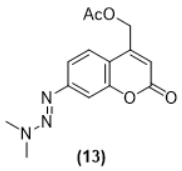

(13)

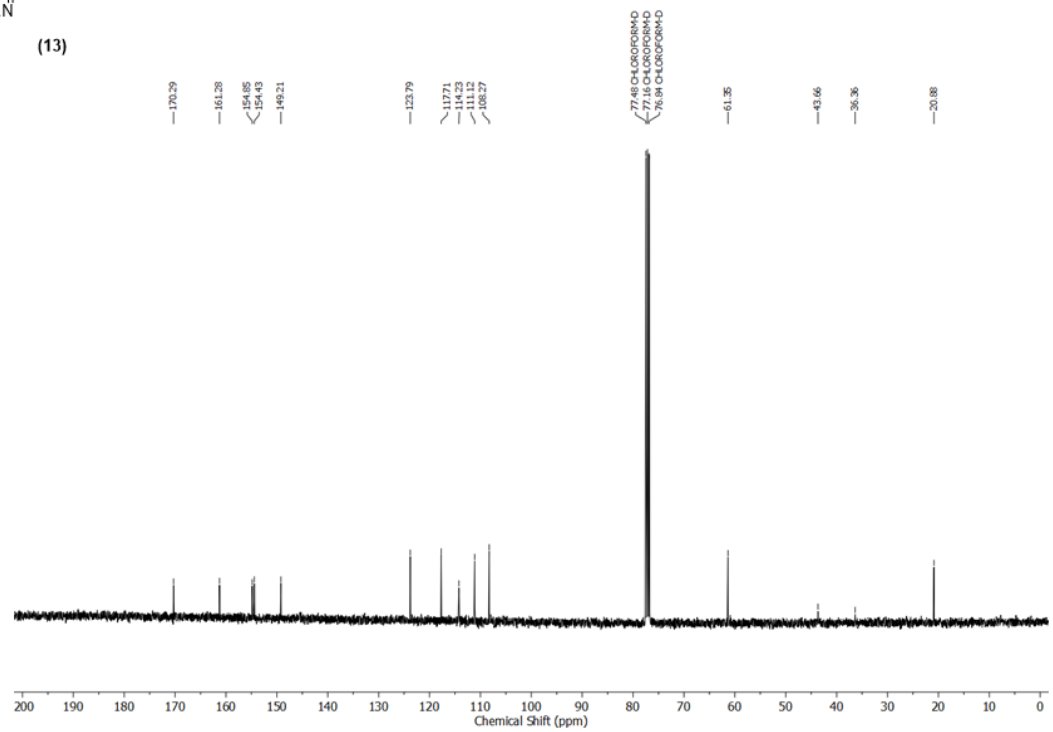

NMR Spectra of **(12)**

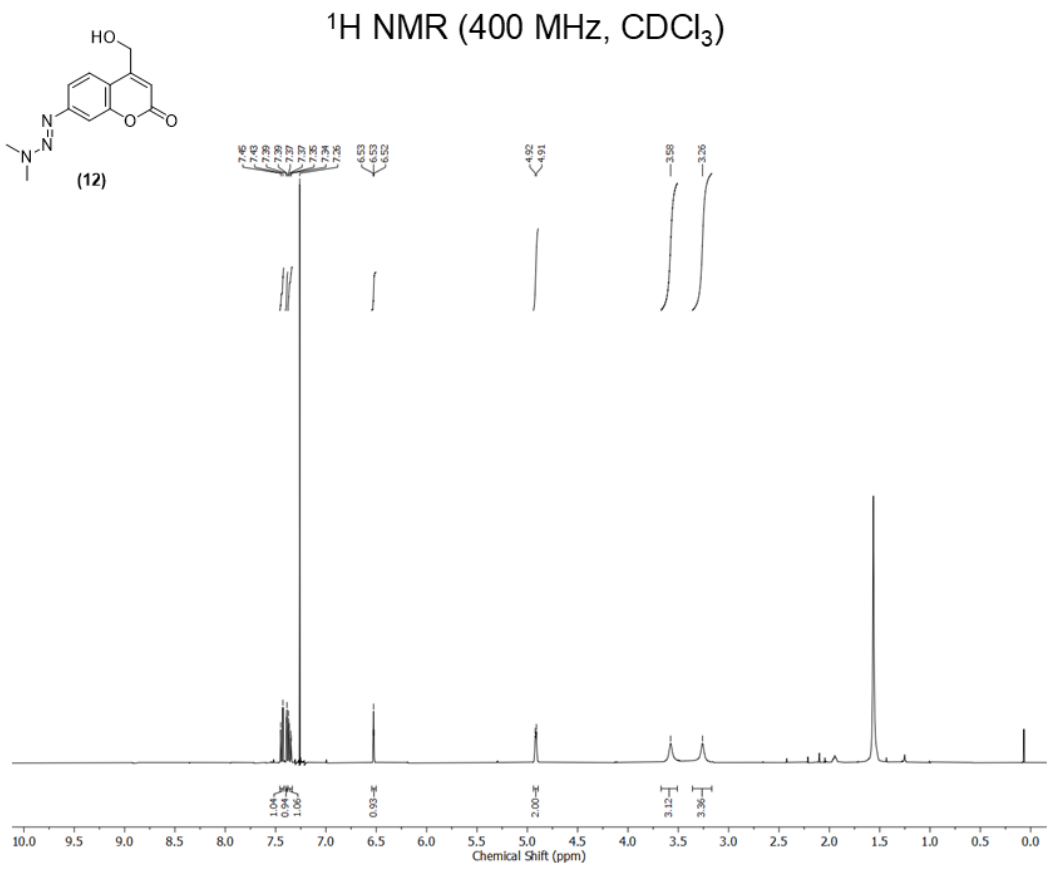

NMR Spectra of **(16)**

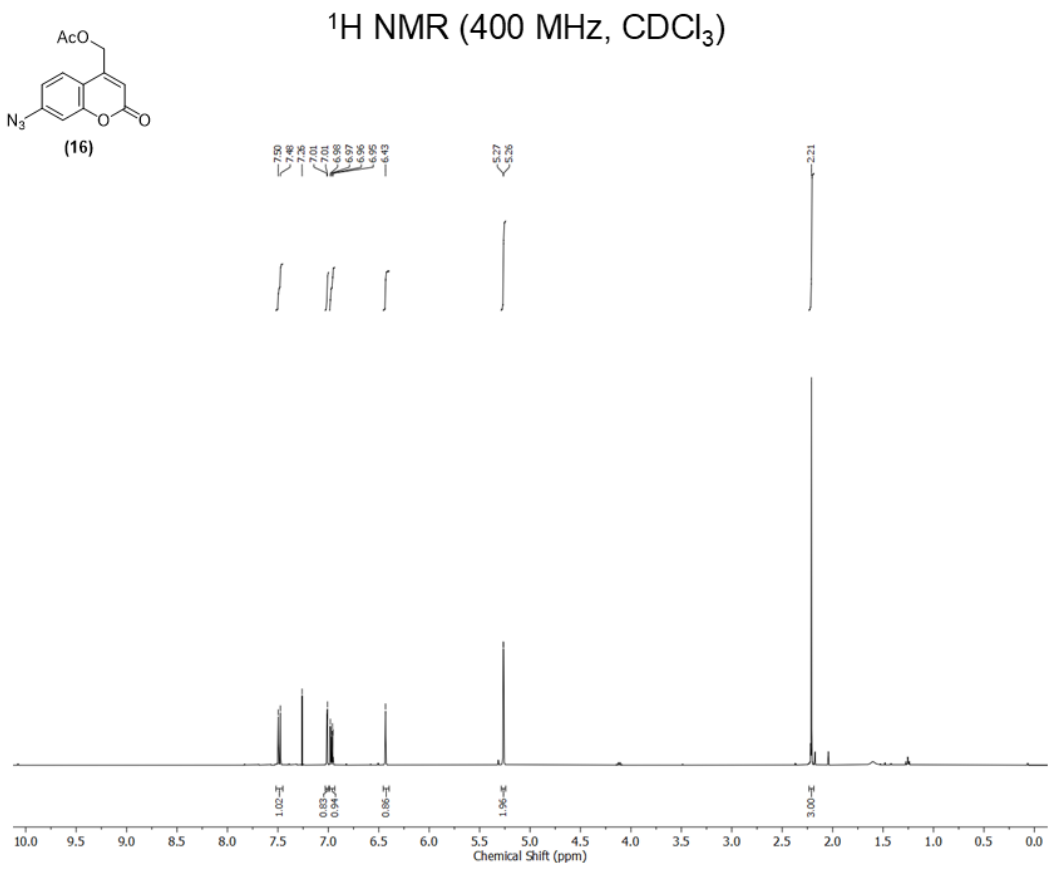

^{13}C NMR (100 MHz, $CDCl_3$)

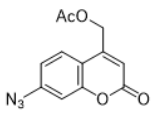

(16)

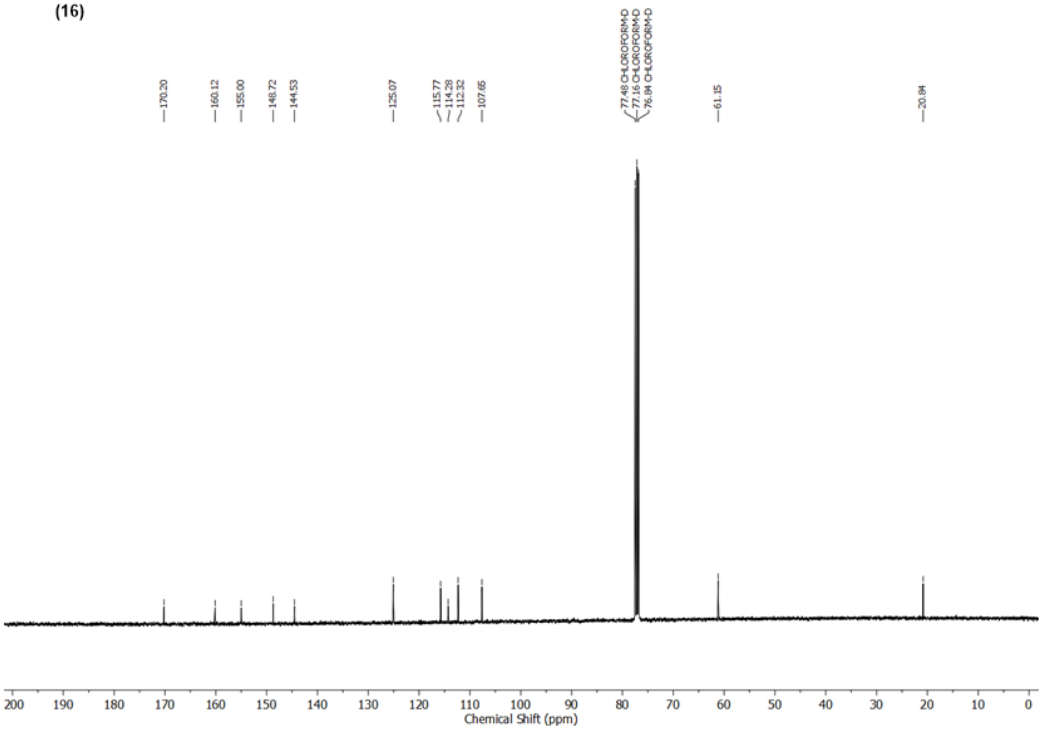

NMR Spectra of **(17)**

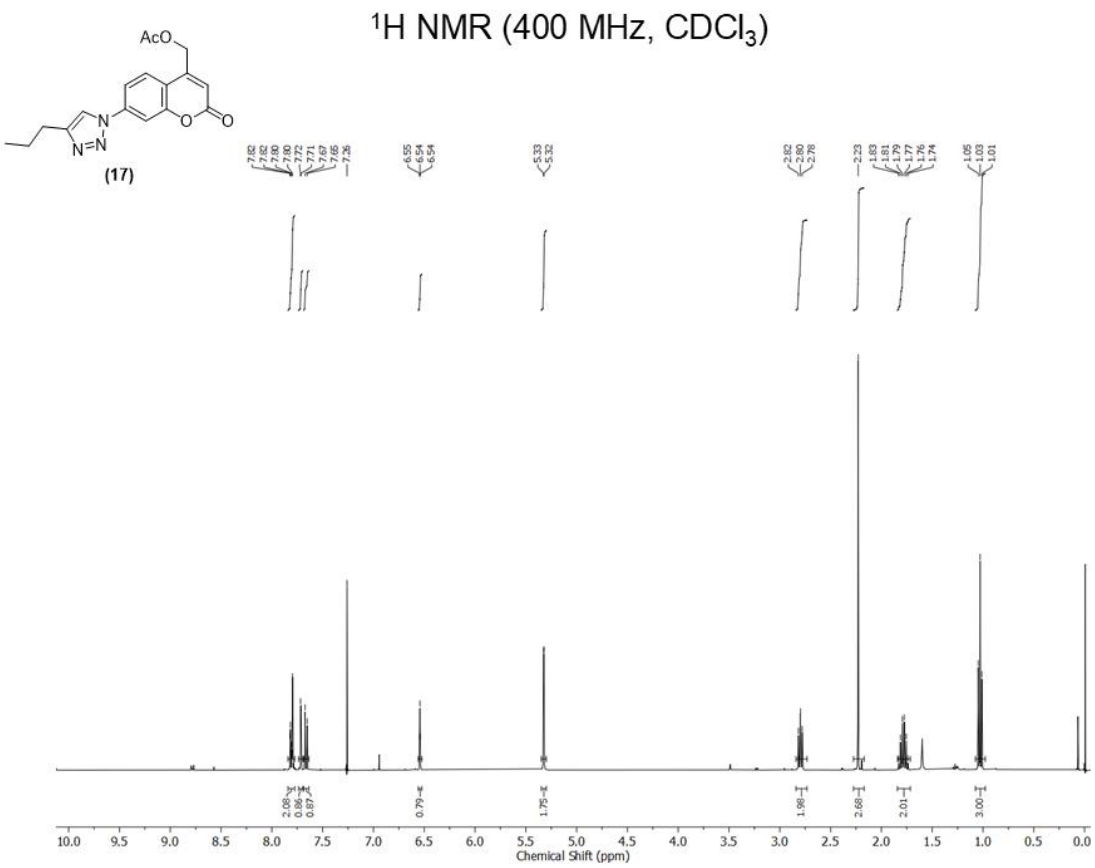

^{13}C NMR (100 MHz, $CDCl_3$)

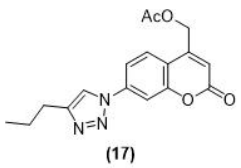

(17)

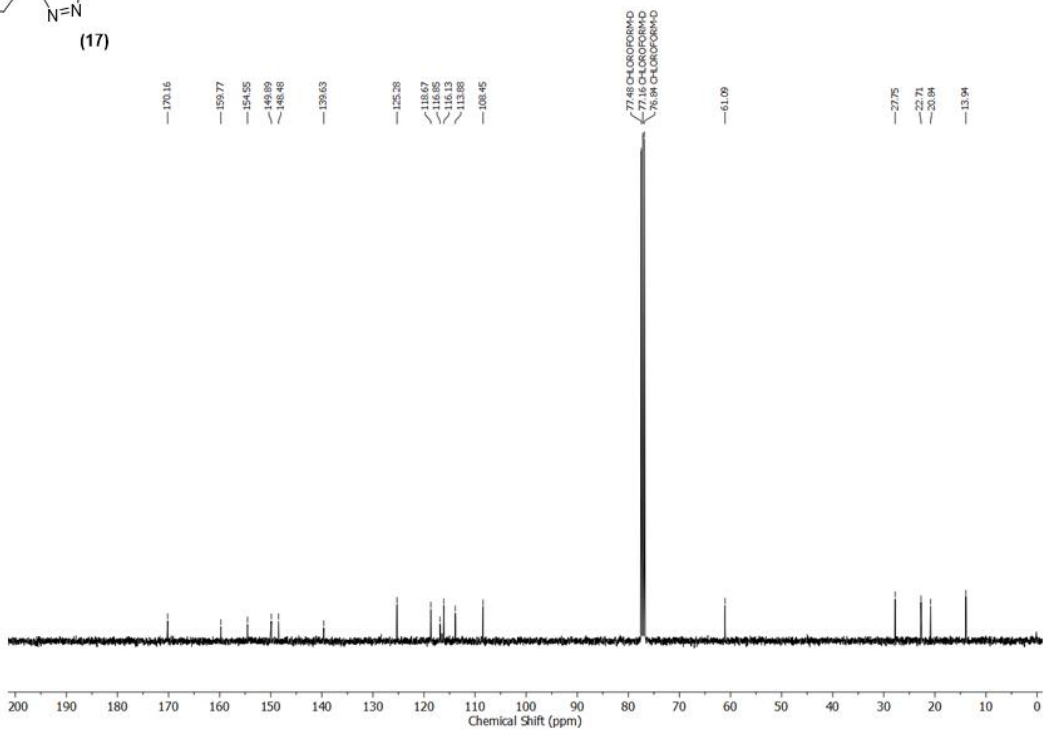

NMR Spectra of **(34)**

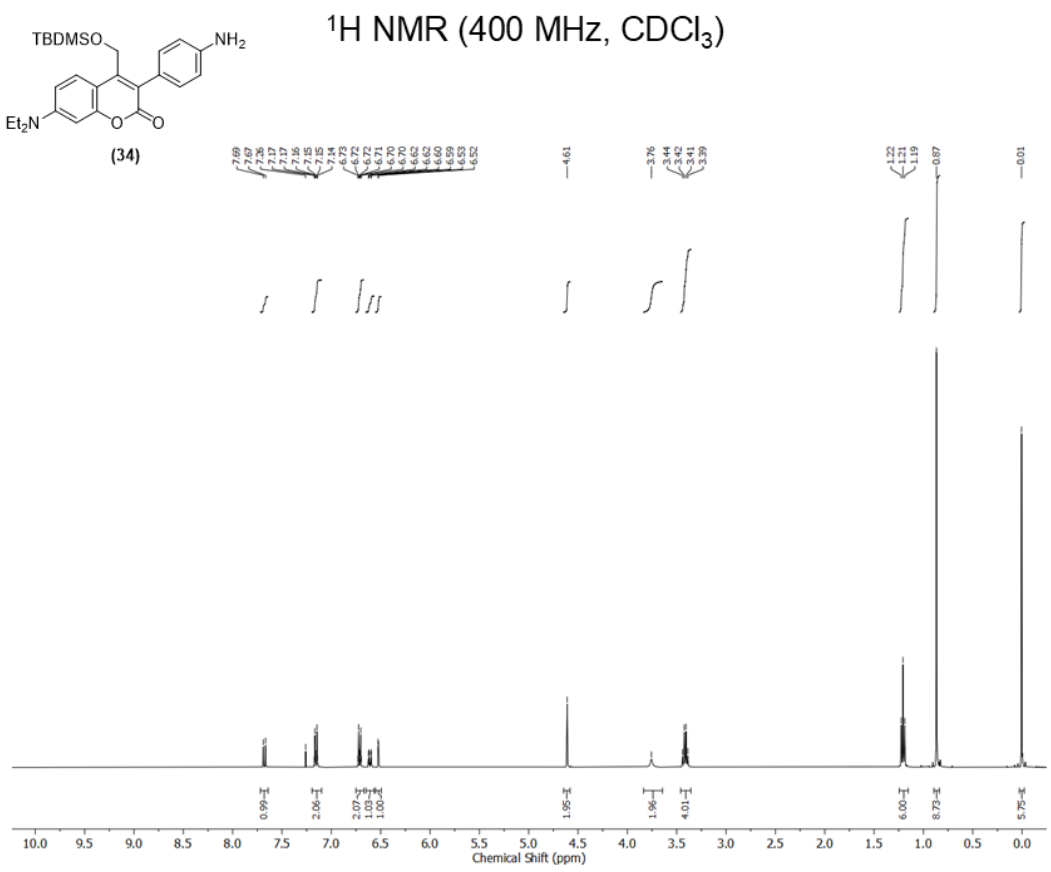

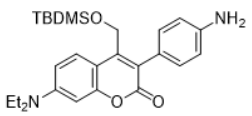

(34)

^{13}C NMR (100 MHz, $CDCl_3$)

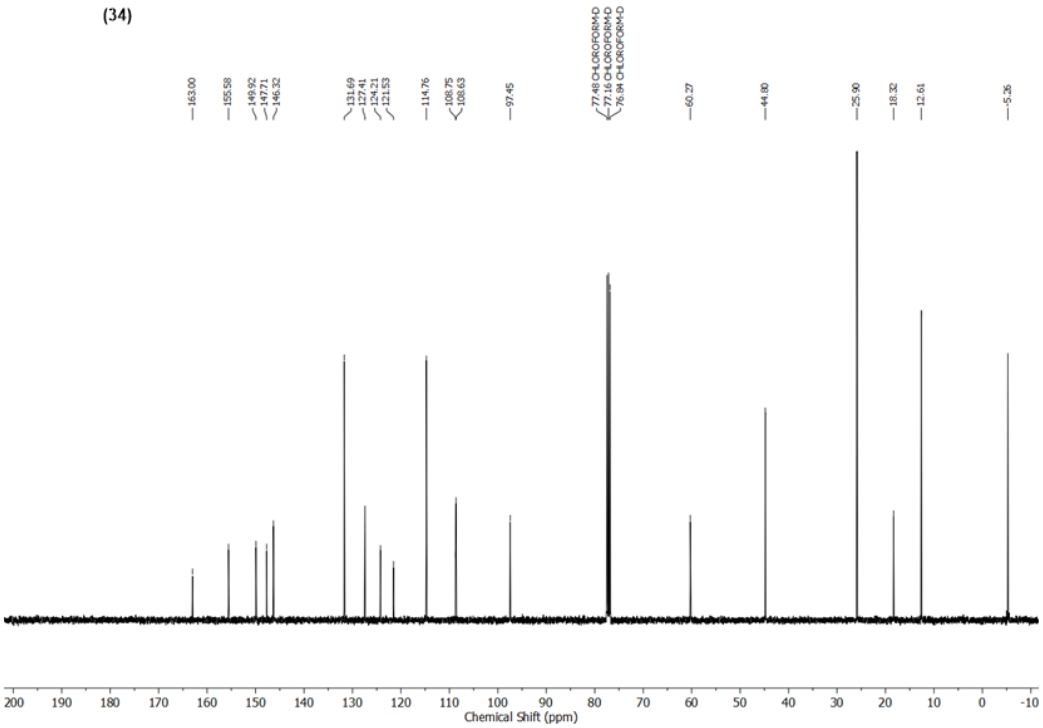

NMR Spectra of **(35)**

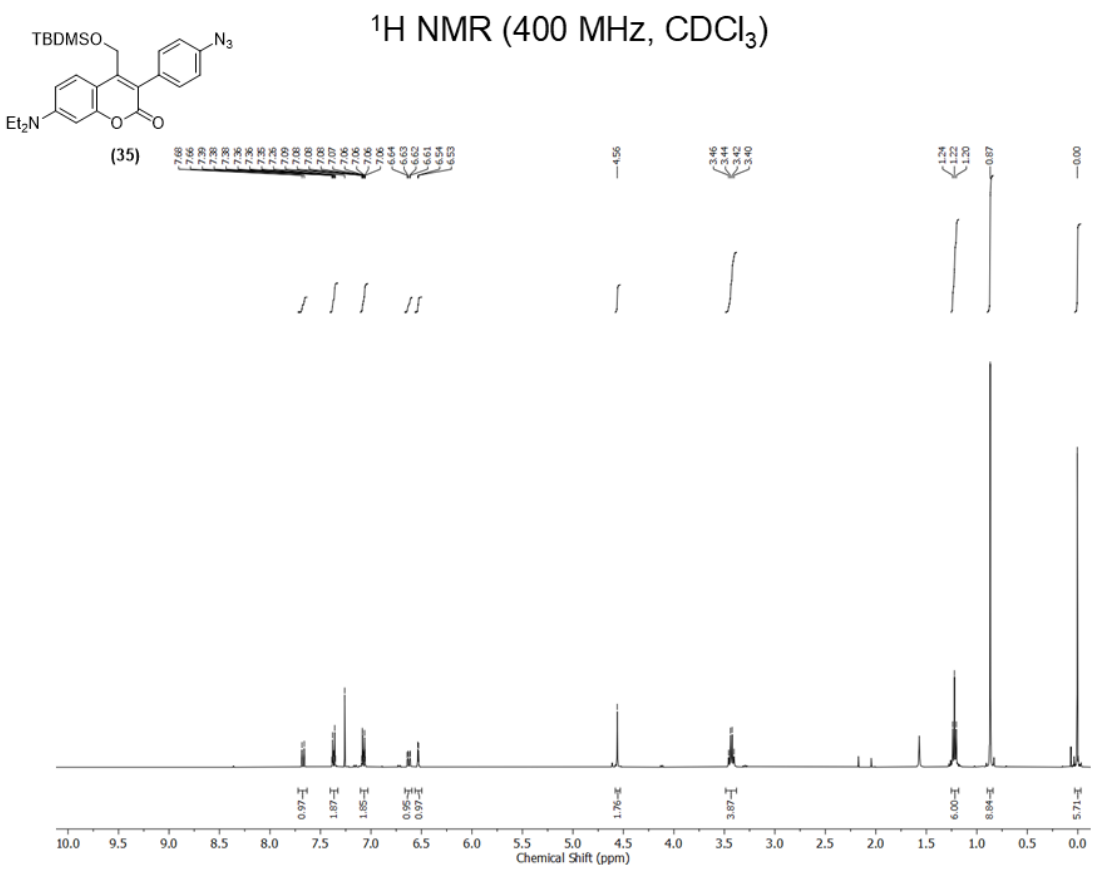

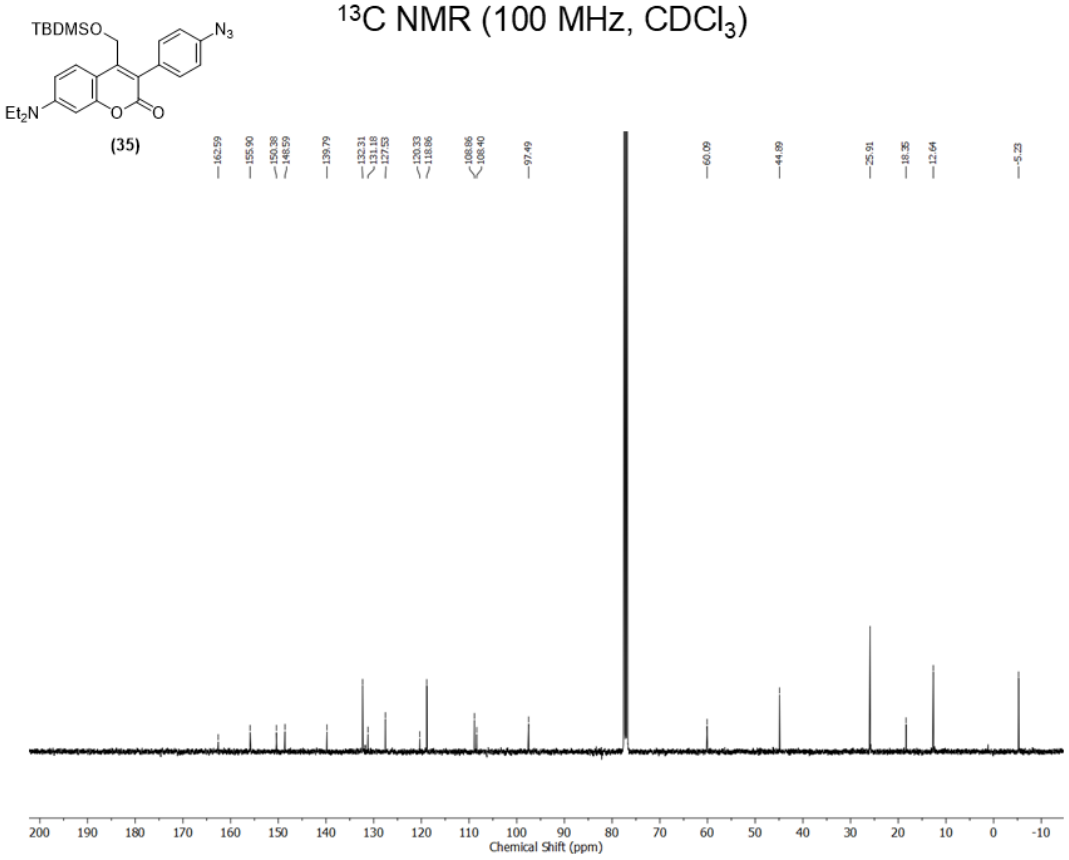
TBDMSO
N3
Et2N
O
O
(35)
13C NMR (100 MHz, CDCl3)
162.59
155.90
150.38
148.59
139.79
132.31
131.18
127.53
120.33
118.86
108.86
108.40
97.49
60.09
44.89
25.91
18.35
12.64
-5.23
200 190 180 170 160 150 140 130 120 110 100 90 80 70 60 50 40 30 20 10 0 -10
Chemical Shift (ppm)

NMR Spectra of **(31)**

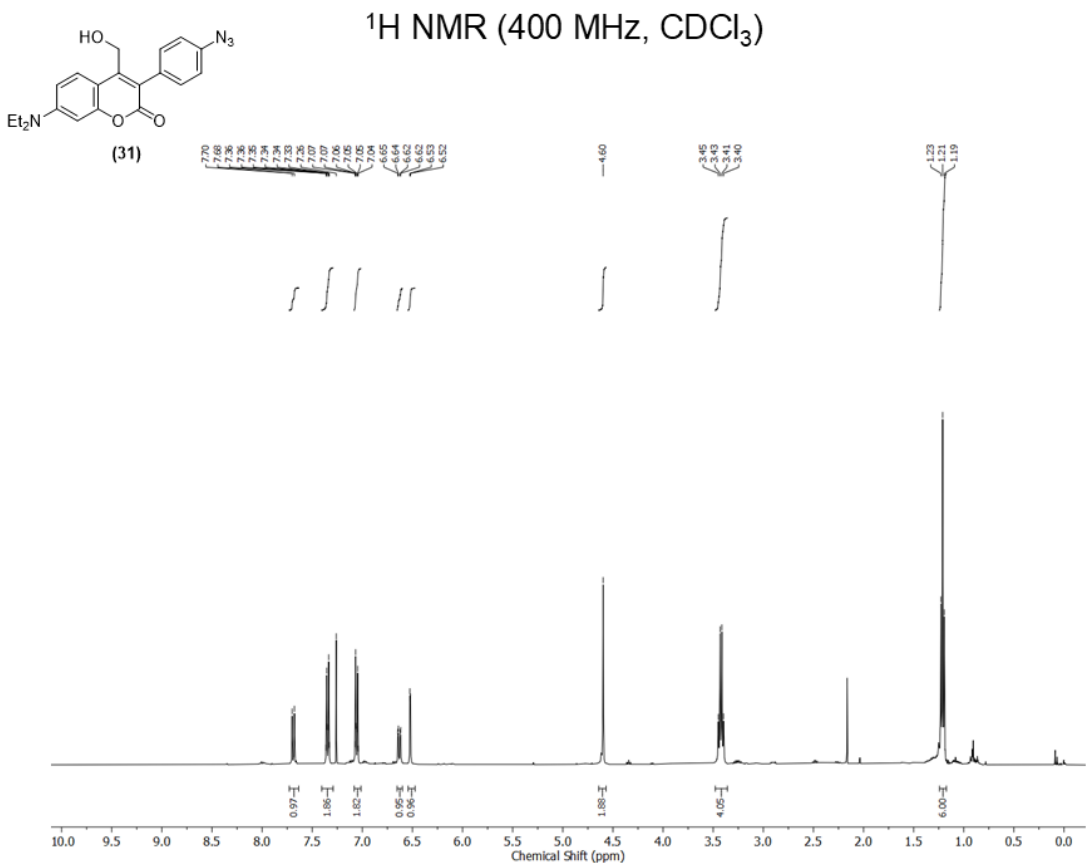

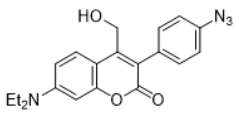

(31)

^{13}C NMR (100 MHz, $CDCl_3$)

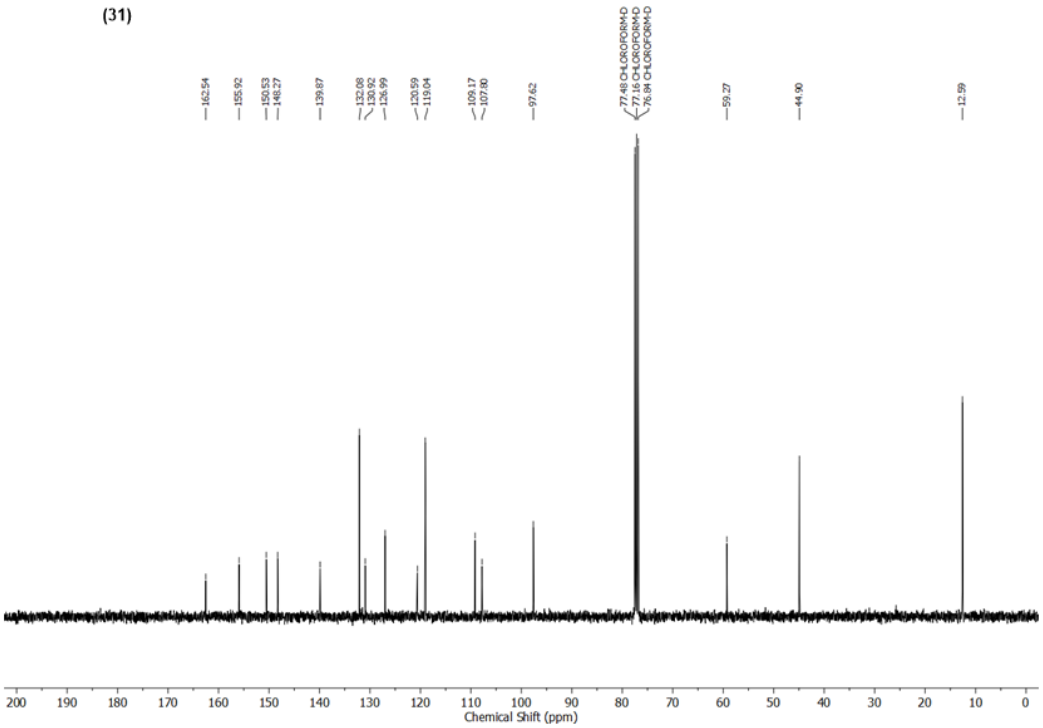

NMR Spectra of **(37)**

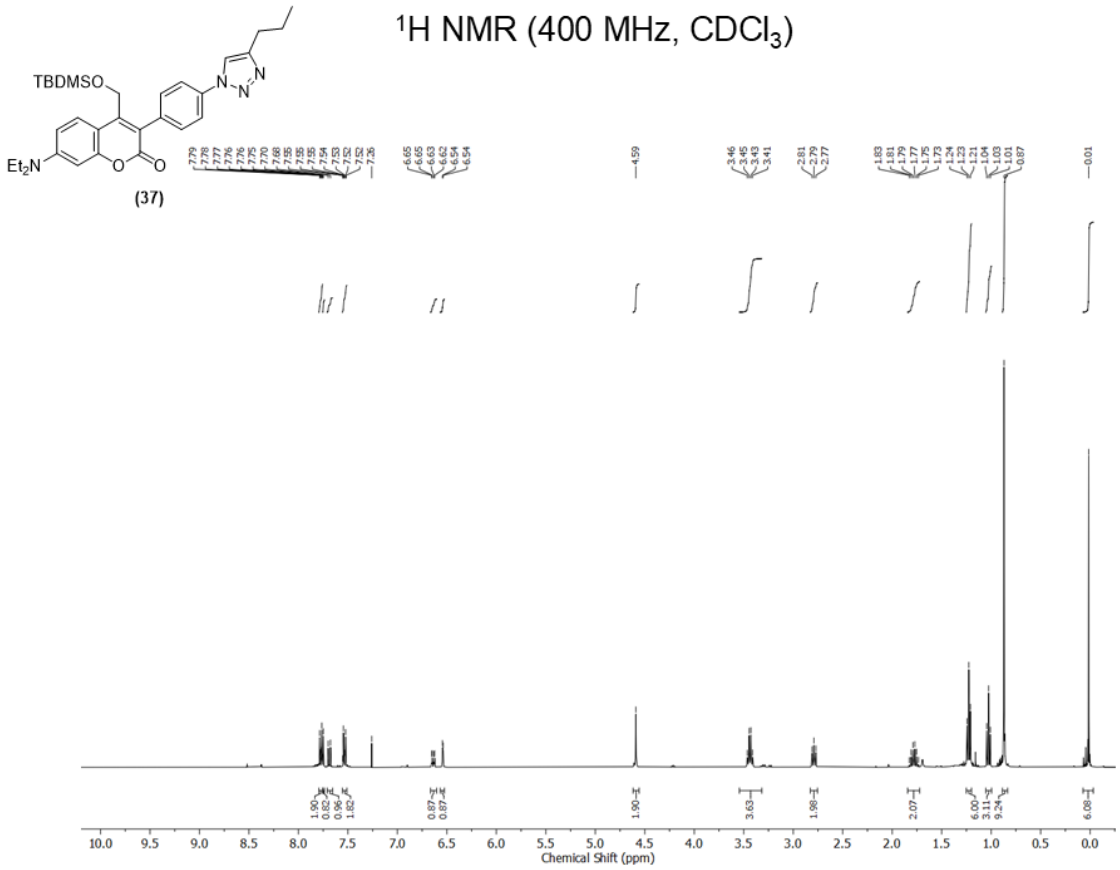

^{13}C NMR (100 MHz, $CDCl_3$)

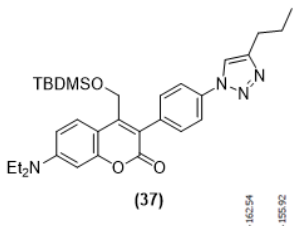

(37)

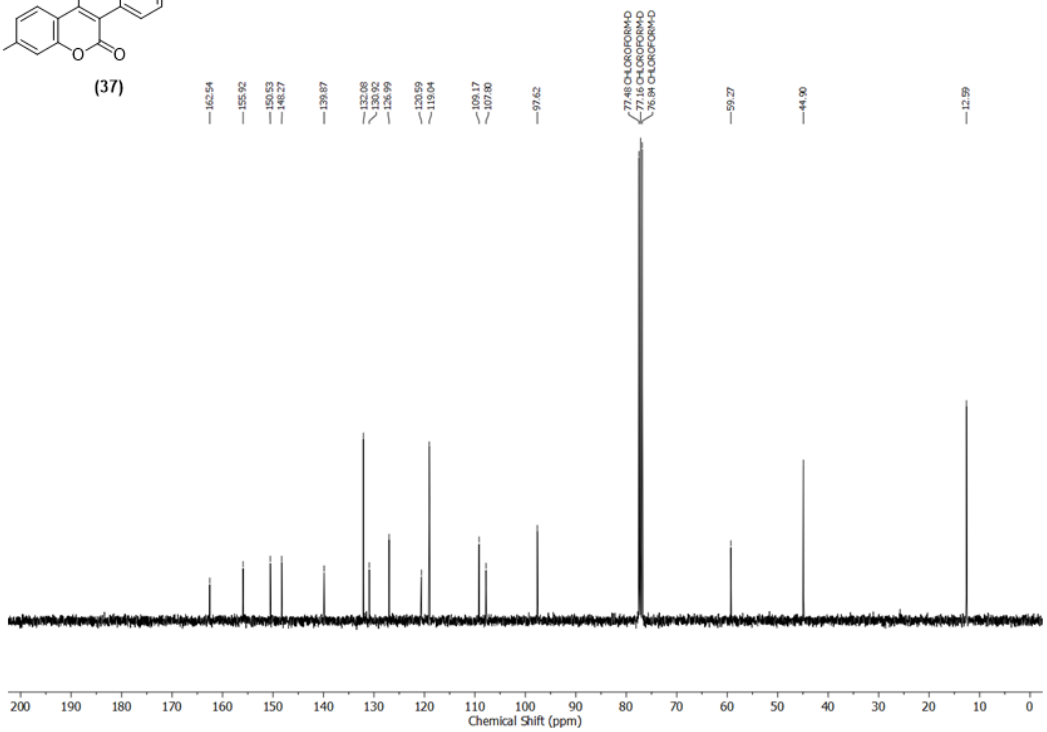

NMR Spectra of **(38)**

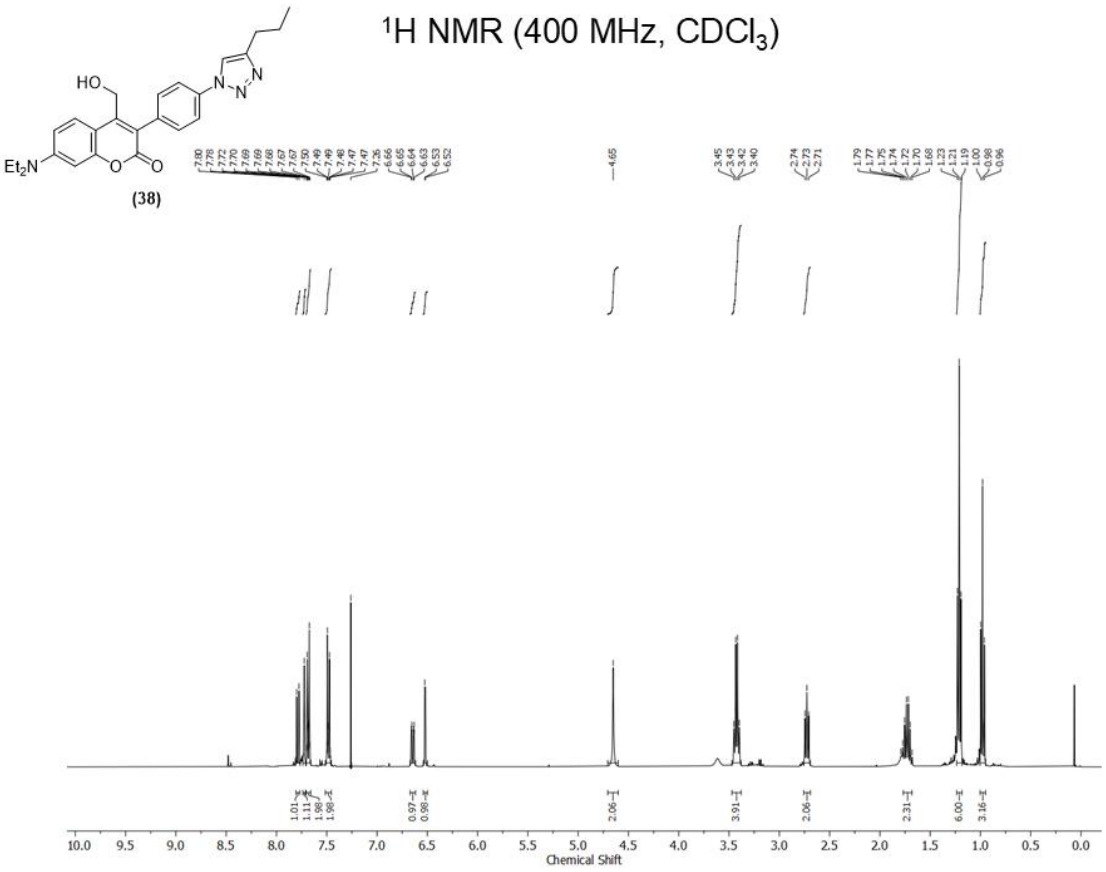

^{13}C NMR (100 MHz, $CDCl_3$)

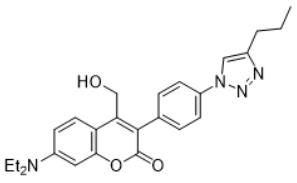

(38)

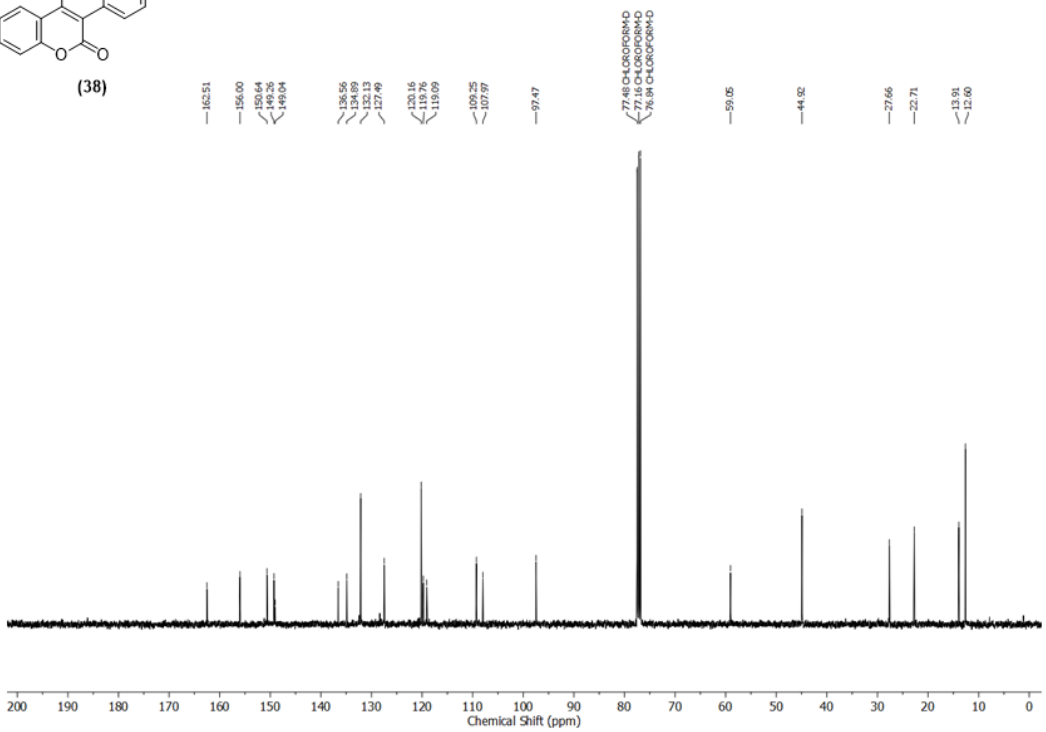

NMR Spectra of **(36)**

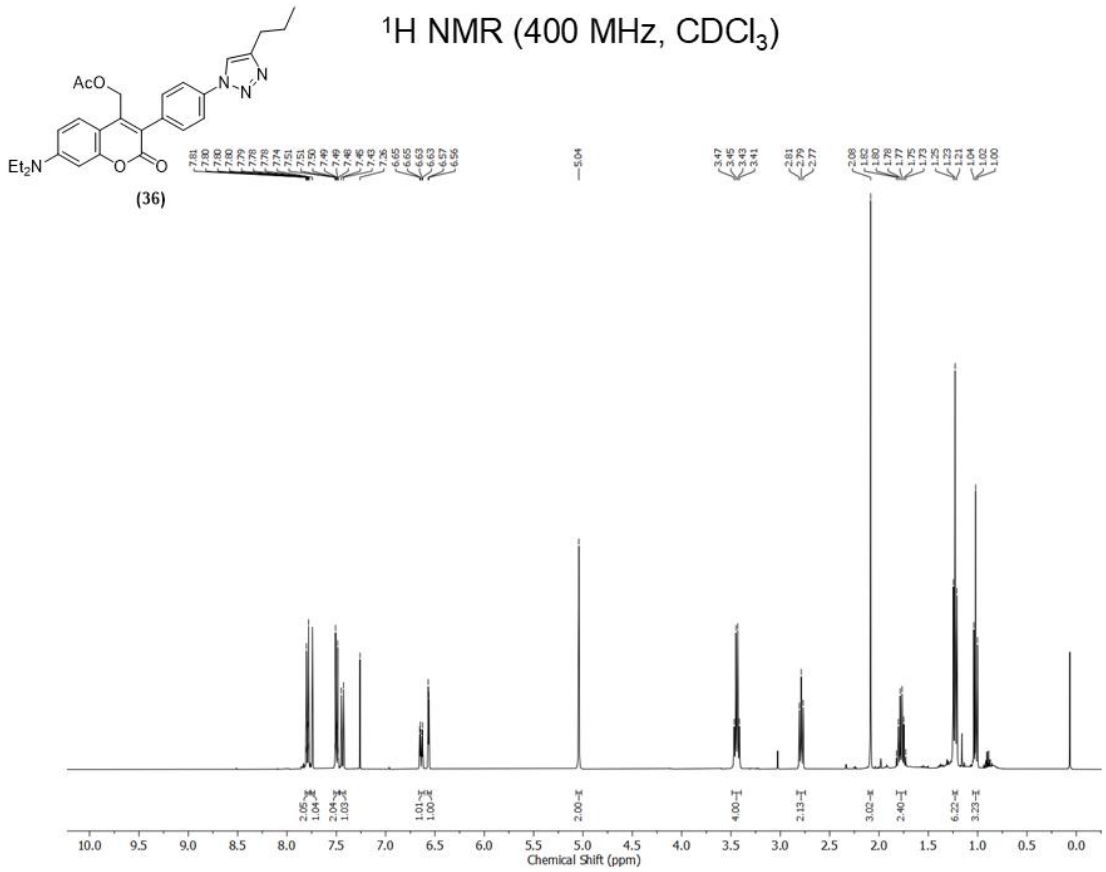

^{13}C NMR (100 MHz, $CDCl_3$)

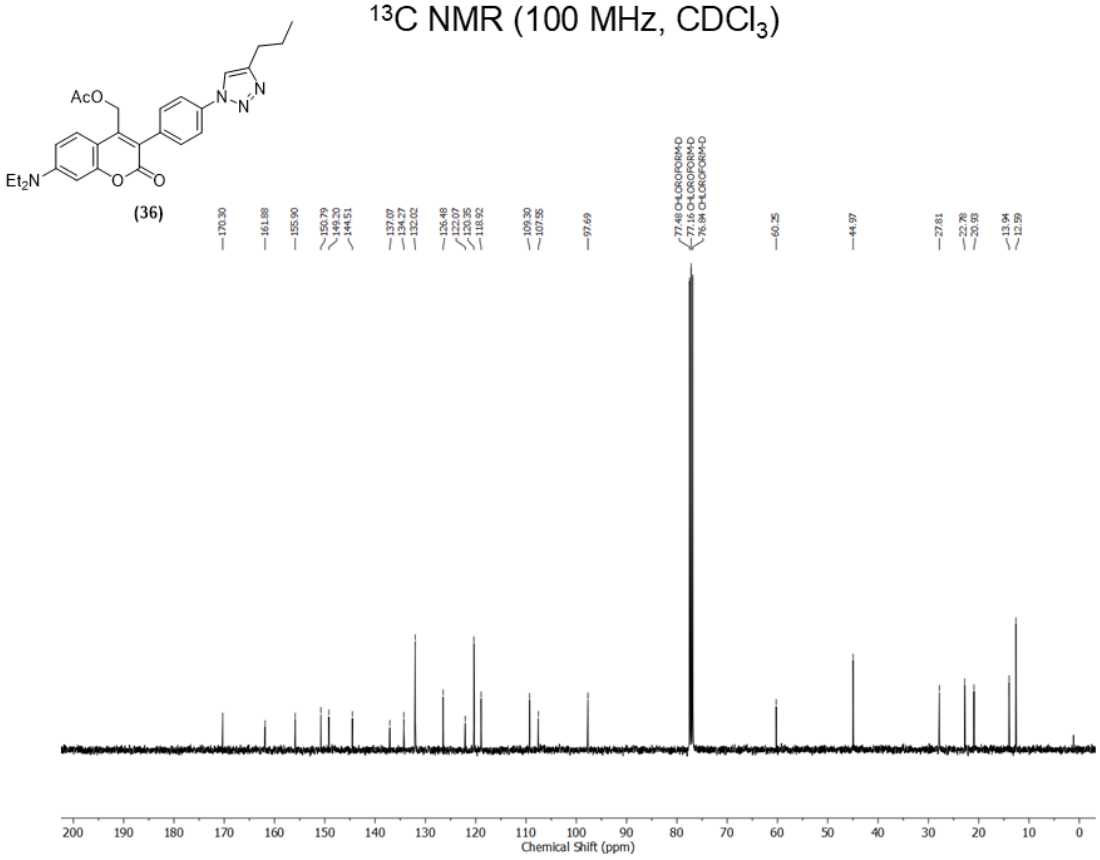

NMR Spectra of **(4)**

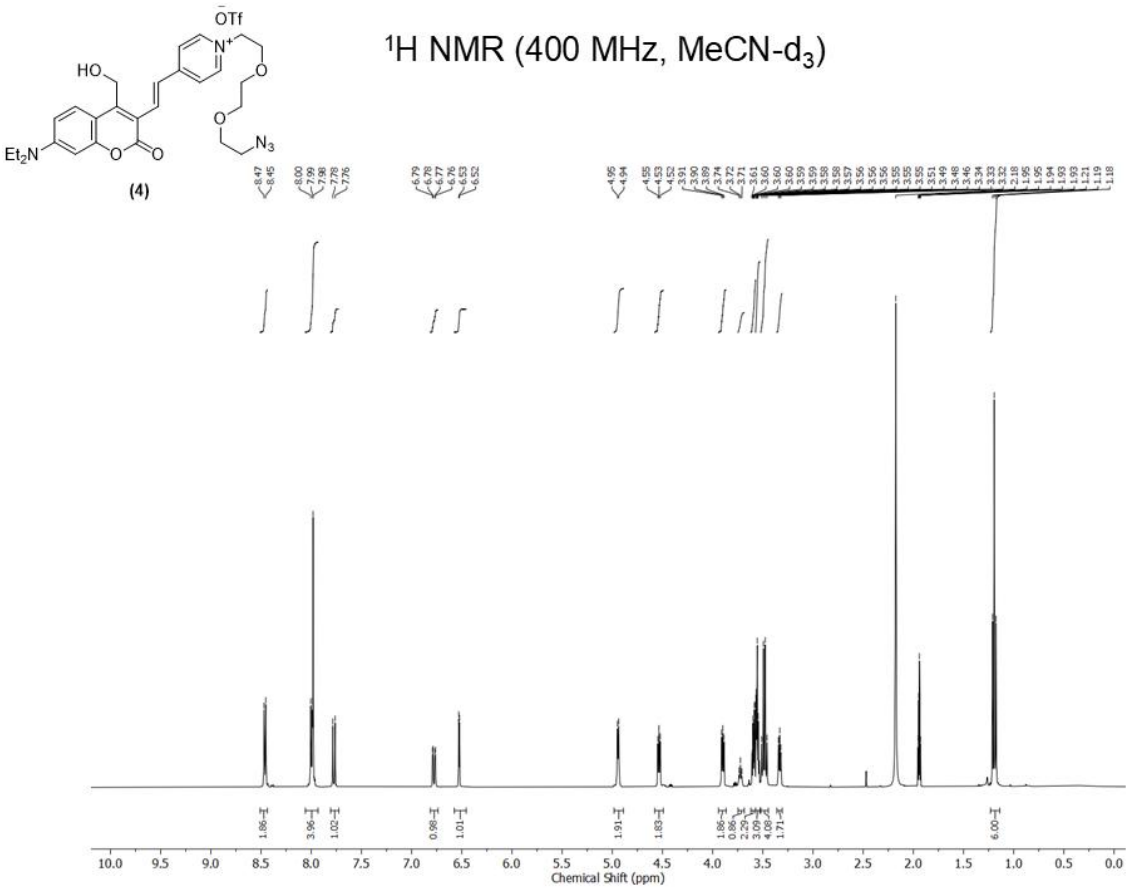

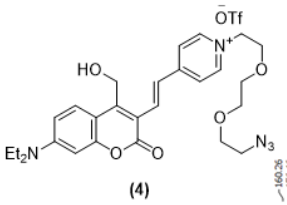

(4)

^{13}C NMR (100 MHz, MeCN-d_3)

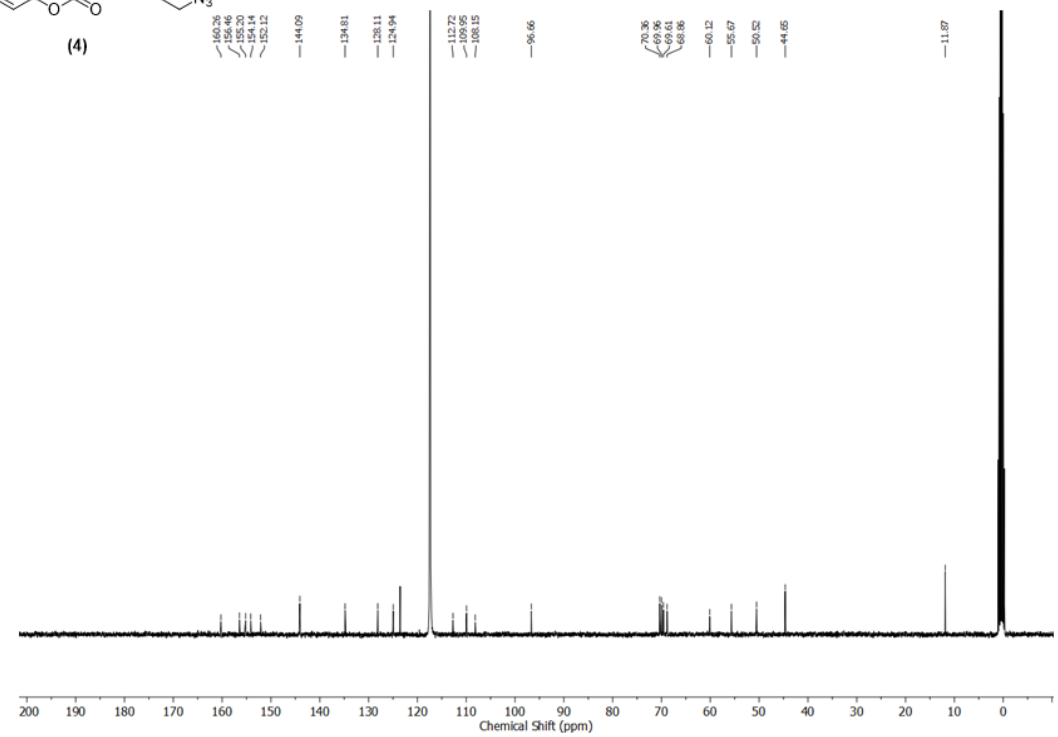

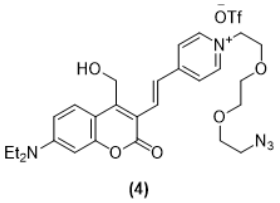

(4)

^{19}F NMR (400 MHz, MeCN-d_3)

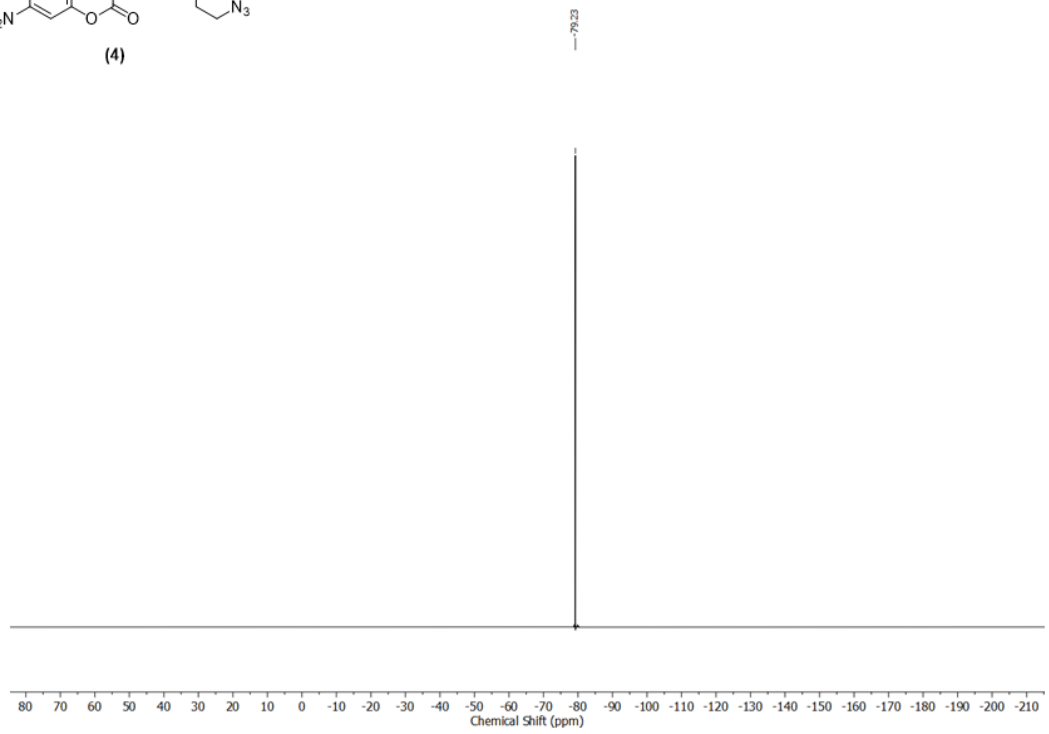

NMR Spectra of **(44)**

^{1}H NMR (400 MHz, MeCN-d_3)

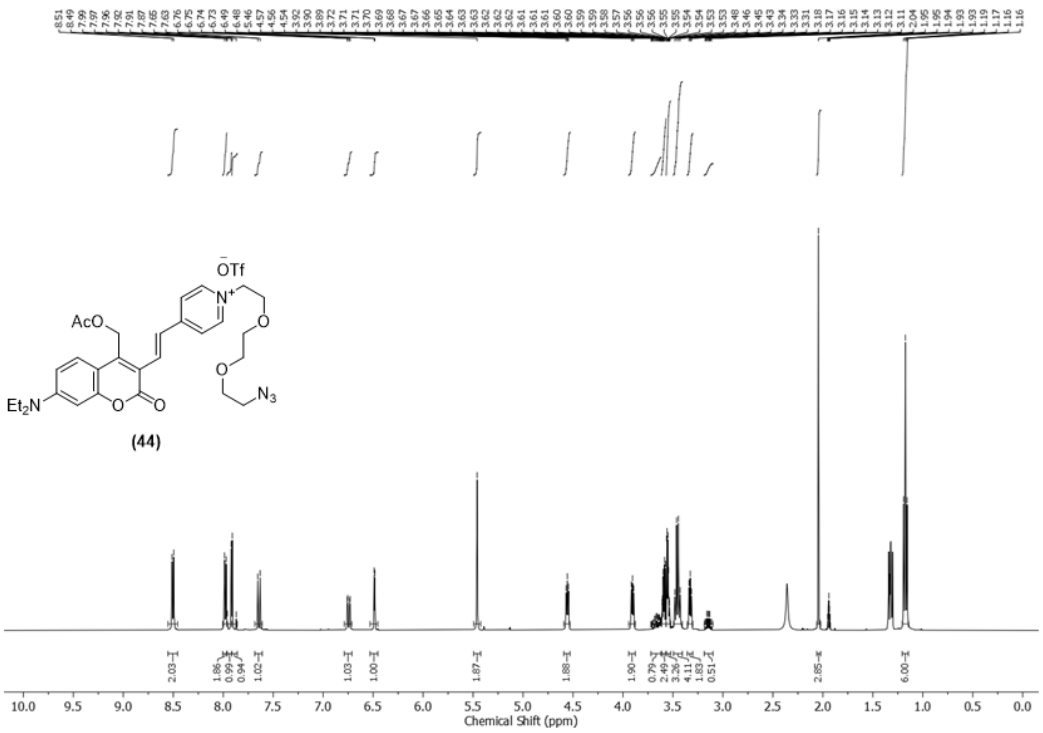

^{13}C NMR (100 MHz, MeCN-d_3)

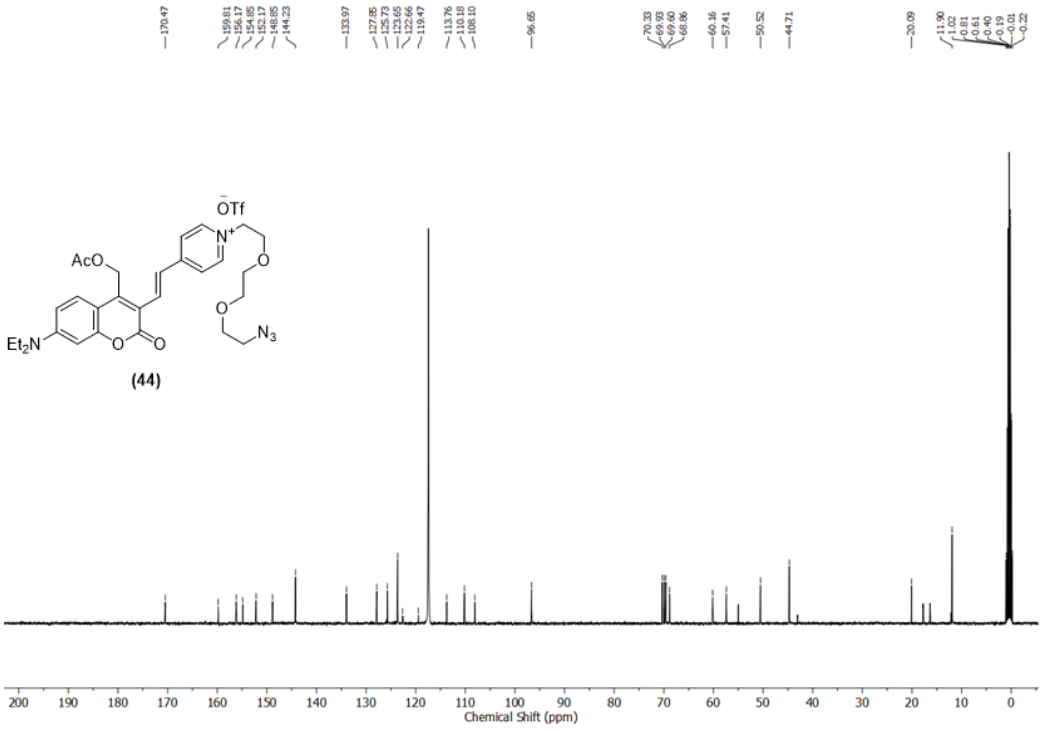

---

^{19}F NMR (400 MHz, MeCN-d_3)

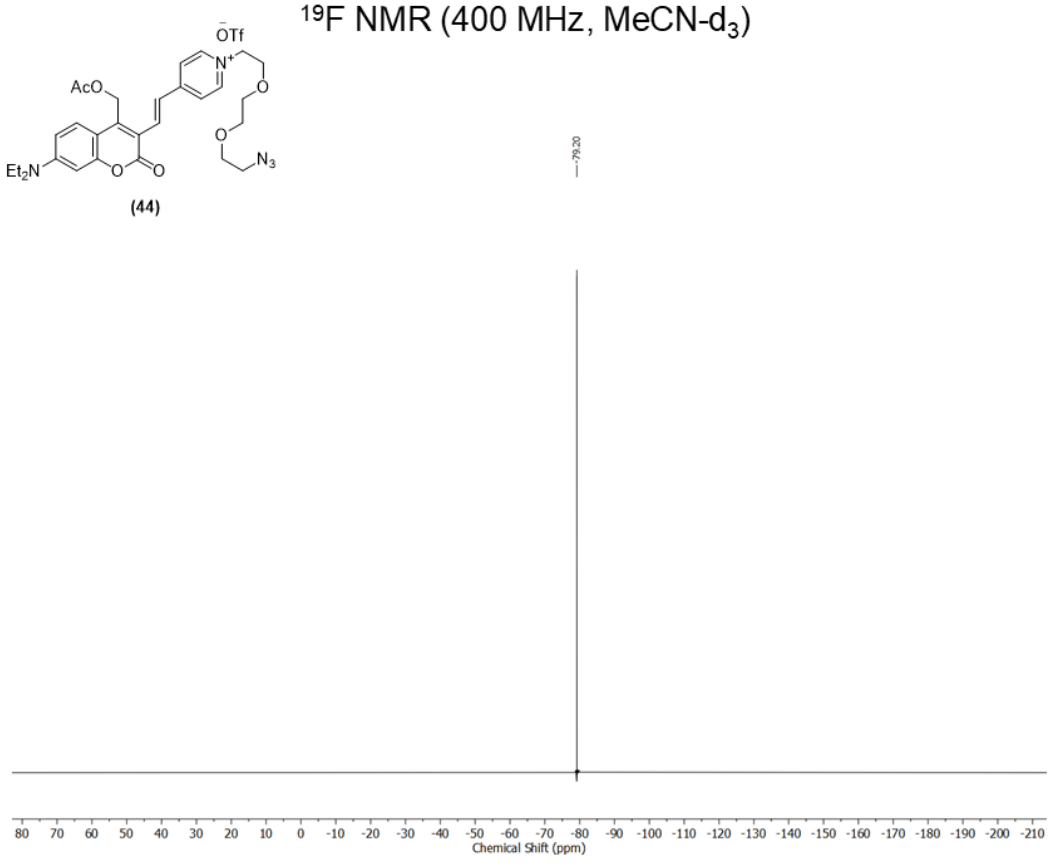

3.11 References

1. Peterson, J. A.; Yuan, D.; Winter, A. H. Multiwavelength Control of Mixtures Using Visible Light-Absorbing Photocages. *J. Org. Chem.* **2021**, *86* (14), 9781–9787.
2. Azagarsamy, M. A.; Anseth, K. S. Wavelength-Controlled Photocleavage for the Orthogonal and Sequential Release of Multiple Proteins. *Angew. Chem. Int. Ed.* **2013**, *52* (51), 13803–13807.
3. Kolb, H. C.; Finn, M. G.; Sharpless, K. B. Click Chemistry: Diverse Chemical Function from a Few Good Reactions. *Angew. Chem. Int. Ed.* **2001**, *40* (11), 2004–2021.
4. Agard, N. J.; Prescher, J. A.; Bertozzi, C. R. A Strain-Promoted [3 + 2] Azide-Alkyne Cycloaddition for Covalent Modification of Biomolecules in Living Systems. *J. Am. Chem. Soc.* **2004**, *126* (46), 15046–15047.
5. DeForest, C. A.; Sims, E. A.; Anseth, K. S. Peptide-Functionalized Click Hydrogels with Independently Tunable Mechanics and Chemical Functionality for 3D Cell Culture. *Chem. Mater.* **2010**, *22* (16), 4783–4790.
6. Chen, F.; Le, P.; Fernandes-Cunha, G. M.; Heilshorn, S. C.; Myung, D. Bio-Orthogonally Crosslinked Hyaluronate-Collagen Hydrogel for Suture-Free Corneal Defect Repair. *Biomaterials* **2020**, *255*, 120176.
7. Jewett, J. C.; Bertozzi, C. R. Cu-Free Click Cycloaddition Reactions in Chemical Biology. *Chem. Soc. Rev.* **2010**, *39* (4), 1272–1279.
8. Bojtár, M.; Kormos, A.; Kis-Petik, K.; Kellermayer, M.; Kele, P. Green-Light Activatable, Water-Soluble Red-Shifted Coumarin Photocages. *Org. Lett.* **2019**, *21* (23), 9410–9414.
9. Ullrich, R.; Grewer, T. Decomposition of Aromatic Diazonium Compounds. *Thermochim. Acta* **1993**, *225* (2), 291–299.
10. Weinrich, T.; Gränz, M.; Grünewald, C.; Prisner, T. F.; Göbel, M. W. Synthesis of a Cytidine Phosphoramidite with Protected Nitroxide Spin Label for EPR Experiments with RNA. *Eur. J. Org. Chem.* **2017**, *2017* (3), 515–523.
11. Gross, M. L.; Blank, D. H.; Welch, W. M. The Triazene Moiety as a Protecting Group for Aromatic Amines. *J. Org. Chem.* **1993**, *58* (8), 2127–2133.
12. Liu, C. Y.; Knochel, P. Preparation of Polyfunctional Aryl Azides from Aryl Triazenes. A New Synthesis of Ellipticine, 9-Methoxyellipticine, Isoellipticine, and 7-Carbethoxyisoellipticine. *J. Org. Chem.* **2007**, *72* (19), 7108–7114.
13. Kimball, D. B.; Haley, M. M. Triazenes: A Versatile Tool in Organic Synthesis. *Angew. Chem. Int. Ed.* **2002**, *41* (18), 3338–3351.
14. Zhang, X.; Zhang, R.; Wu, S.; Sun, Y.; Yang, H.; Lin, B. Physically and Chemically Dual-Crosslinked Hydrogels with Superior Mechanical Properties and Self-Healing Behavior. *New J. Chem.* **2020**, *44* (23), 9903–9911.
15. Bassolino, G.; Nançoz, C.; Thiel, Z.; Bois, E.; Vauthey, E.; Rivera-Fuentes, P. Photolabile Coumarins with Improved Efficiency through Azetidinyl Substitution. *Chem. Sci.* **2018**, *9* (2), 387–391.
16. Chen, J.; Xie, X.; Liu, J.; Yu, Z.; Su, W. Revisiting Aromatic Diazotization and Aryl Diazonium Salts in Continuous Flow: Highlighted Research during 2001–2021. *React. Chem. Eng.* **2022**, *7* (6), 1247–1275.
17. Hagen, V.; Bendig, J.; Frings, S.; Eckardt, T.; Helm, S.; Reuter, D.; Kaupp, U. B. Highly Efficient and Ultrafast Phototriggers for cAMP and cGMP by Using Long-Wavelength UV/Vis Activation. *Angew. Chem. Int. Ed.* **2001**, *40* (6), 1045–1048.

18. Hagen, V.; Frings, S.; Wiesner, B.; Helm, S.; Kaupp, U. B.; Bendig, J. [7-(Dialkylamino)Coumarin-4-yl]Methyl-Caged Compounds as Ultrafast and Effective Long-Wavelength Phototriggers of 8-Bromo-Substituted Cyclic Nucleotides. *ChemBioChem* **2003**, *4* (5), 434–442.
19. Schmidt, R.; Geissler, D.; Hagen, V.; Bendig, J. Mechanism of Photocleavage of (Coumarin-4-yl)Methyl Esters. *J. Phys. Chem. A* **2007**, *111* (26), 5768–5774.
20. Singh, A.; Thornton, E. R.; Westheimer, F. H. The Photolysis of Diazoacetylchymotrypsin. *J. Biol. Chem.* **1962**, *237* (9), PC3006–PC3008.
21. Wilson, D. F.; Miyata, Y.; Erecińska, M.; Vanderkooi, J. M. An Aryl Azide Suitable for Photoaffinity Labeling of Amine Groups in Proteins. *Arch. Biochem. Biophys.* **1975**, *171* (1), 104–107.
22. Zhang, Y.; Tan, J.; Chen, Y. Visible-Light-Induced Protein Labeling in Live Cells with Aryl Azides. *Chem. Commun.* **2023**, *59* (17), 2413–2420.
23. Karaj, E.; Sindi, S. H.; Viranga Tillekeratne, L. M. Photoaffinity Labeling and Bioorthogonal Ligation: Two Critical Tools for Designing “Fish Hooks” to Scout for Target Proteins. *Bioorg. Med. Chem.* **2022**, *62*, 116721.
24. Popova, T. V.; Reinbolt, J.; Ehresmann, B.; Shakirov, M. M.; Serebriakova, M. V.; Gerassimova, Y. V.; Knorre, D. G.; Godovikova, T. S. Why Do P-Nitro-Substituted Aryl Azides Provide Unintended Dark Reactions with Proteins? *J. Photochem. Photobiol. B* **2010**, *100* (1), 47–54.
25. Zhao, Y. R.; Zheng, Q.; Dakin, K.; Xu, K.; Martinez, M. L.; Li, W. H. New Caged Coumarin Fluorophores with Extraordinary Uncaging Cross Sections Suitable for Biological Imaging Applications. *J. Am. Chem. Soc.* **2004**, *126* (14), 4653–4663.
26. Bao, C.; Fan, G.; Lin, Q.; Li, B.; Cheng, S.; Huang, Q.; Zhu, L. Styryl Conjugated Coumarin Caged Alcohol: Efficient Photorelease by Either One-Photon Long Wavelength or Two-Photon NIR Excitation. *Org. Lett.* **2012**, *14* (2), 572–575.
27. Klausen, M.; Dubois, V.; Clermont, G.; Tonnelé, C.; Castet, F.; Blanchard-Desce, M. Dual-Wavelength Efficient Two-Photon Photorelease of Glycine by π-Extended Dipolar Coumarins. *Chem. Sci.* **2019**, *10* (15), 4209–4219.
28. Schulte, A. M.; Smid, L. M.; Alachouzos, G.; Szymański, W.; Feringa, B. L. Cation Delocalization and Photo-Isomerization Enhance the Uncaging Quantum Yield of a Photocleavable Protecting Group. *Chem. Commun.* **2024**, *60* (5), 578–581.
29. Andersen, J.; Madsen, U.; Björkling, F.; Liang, X. Rapid Synthesis of Aryl Azides from Aryl Halides under Mild Conditions. *Synlett* **2005**, (14), 2209–2213.
30. Tkach, I. I.; Mikhailova, T. A.; Reznichenko, V. A.; Savvina, L. P.; Luk’yanets, E. A. Synthesis and Spectral-Luminescence Properties of Azomethines in the Coumarin Series. *Chem. Heterocycl. Compd.* **1990**, *26* (3), 327–332.
31. Yan, Z.; Deng, J.; Tian, J.; Luo, G. A Safer, Greener and Faster Synthesis Process of Sodium Azide by Simply Altering the Alcohol Reactant. *Green Chem.* **2024**, *26* (10), 6139–6149.
32. Joshi, S. R.; Kataria, K. L.; Sawant, S. B.; Joshi, J. B. Kinetics of Oxidation of Benzyl Alcohol with Dilute Nitric Acid. *Ind. Eng. Chem. Res.* **2005**, *44* (2), 325–333.
33. Calvo, R.; Zhang, K.; Passera, A.; Katayev, D. Facile Access to Nitroarenes and Nitroheteroarenes Using N-Nitrosaccharin. *Nat. Commun.* **2019**, *10* (1), 3410.
34. Alhaj Zen, A.; Aylott, J. W.; Chan, W. C. An Appraisal of the Suzuki Cross-Coupling Reaction for the Synthesis of Novel Fluorescent Coumarin Derivatives. *Tetrahedron Lett.* **2014**, *55* (40), 5550–5553.

35. Olson, J. P.; Kwon, H. B.; Takasaki, K. T.; Chiu, C. Q.; Higley, M. J.; Sabatini, B. L.; Ellis-Davies, G. C. R. Optically Selective Two-Photon Uncaging of Glutamate at 900 Nm. *J. Am. Chem. Soc.* **2013**, *135* (16), 6842–6845.
36. Bhalla, V.; Singh, H.; Kumar, M. Facile Cyclization of Terphenyl to Triphenylene: A New Chemodosimeter for Fluoride Ions. *Org. Lett.* **2010**, *12* (3), 628–631.
37. Mangione, M. I.; Spanevello, R. A.; Anzardi, M. B. Efficient and Straightforward Click Synthesis of Structurally Related Dendritic Triazoles. *RSC Adv.* **2017**, *7* (75), 47681–47688.
38. Cicco, L.; Perna, F. M.; Falcicchio, A.; Altomare, A.; Messa, F.; Salomone, A.; Capriati, V.; Vitale, P. 1,3-Dipolar Cycloaddition of Alkanone Enolates with Azides in Deep Eutectic Solvents for the Metal-Free Regioselective Synthesis of Densely Functionalized 1,2,3-Triazoles. *Eur. J. Org. Chem.* **2022**, *2022* (36), e202200843.
39. Gillis, R. G. The Mechanism of Diazotization. *J. Chem. Educ.* **1954**, *31* (7), 344–347.
40. Troian-Gautier, L.; Valkenier, H.; Mattiuzzi, A.; Jabin, I.; Van den Brande, N.; Van Mele, B.; Hubert, J.; Reniers, F.; Bruylants, G.; Lagrost, C.; Leroux, Y. Extremely Robust and Post-Functionalizable Gold Nanoparticles Coated with Calix[4]Arenes via Metal–Carbon Bonds. *Chem. Commun.* **2016**, *52* (69), 10493–10496.
41. Yates, N. D. J.; Hudson, L.; Schwabe, O.; Parkin, A. Using Triazabutadienes as a Protected Source of Diazonium Cations to Facilitate Electrografting to a Variety of Conductive Surfaces. *Langmuir* **2025**, *41* (11), 7386–7395.
42. Mele, L.; El Bekri Saudain, R.; Pirat, J.-L.; Tomás-Mendivil, E.; Martin, D.; Virieux, D.; Ayad, T. Benchmarking Methanophosphocines as Versatile PIII/PV Redox Organocatalysts. *Adv. Synth. Catal.* **2024**, *366* (17), 3636–3645.
43. Pain, P. K.; Palit, D.; Shegane, M.; Singh, R. P.; Manna, D. Optochemical Control of Cu(I) Homeostasis in Mammalian Cells. *Chem. Commun.* **2023**, *59* (16), 2419–2422.
44. Kamatham, N.; Da Silva, J. P.; Givens, R. S.; Ramamurthy, V. Melding Caged Compounds with Supramolecular Containers: Photogeneration and Miscreant Behavior of the Coumarylmethyl Carbocation. *Org. Lett.* **2017**, *19* (13), 3378–3381.
45. Hartmann, D.; Chowdhry, R.; Smith, J. M.; Booth, M. J. Orthogonal Light-Activated DNA for Patterned Biocomputing within Synthetic Cells. *J. Am. Chem. Soc.* **2023**, *145* (17), 7449–7457.
46. Billamboz, M.; Mangin, F.; Drillaud, N.; Chevrin-Villette, C.; Banaszak-Léonard, E.; Len, C. Micellar Catalysis Using a Photochromic Surfactant: Application to the Pd-Catalyzed Tsuji–Trost Reaction in Water. *J. Org. Chem.* **2014**, *79* (2), 493–500.
47. Dakanali, M.; Do, T. H.; Horn, A.; Chongchivivat, A.; Jarusreni, T.; Lichlyter, D.; Guizzunti, G.; Haidekker, M. A.; Theodorakis, E. A. Self-Calibrating Viscosity Probes: Design and Subcellular Localization. *Bioorg. Med. Chem.* **2012**, *20* (14), 4443–4450.

Chapter 4: Decaging studies and peptide functionalisation

4.1 Introduction

The previous two chapters detailed the design and synthesis of BODIPY and coumarin photocages. Now that these photocages had been synthesised, decaging studies were required in order to verify their photoreactivity. These studies aimed not only to confirm the decaging ability of these compounds, but also to provide kinetic data on the decaging process. This kinetic information is crucial to the future applications of these compounds, allowing us to predict release profiles of differentially caged cargo molecules upon irradiation with different wavelengths of light. This would ultimately provide enhanced spatiotemporal control over any photoresponsive materials developed, facilitating improved control over any biological signalling pathways to be mimicked.

With a view to our ultimate goal of caging peptide activity, preliminary work on these substrates was also carried out. This involved the synthesis of model peptides using automated solid phase peptide synthesis (SPPS), followed by subsequent functionalisation using photocages. This required the use of selective deprotection strategies, capable of unveiling a single amino acid residue of interest, followed by a coupling reaction to allow for the installation of the desired photocage. Following the synthesis of a caged peptide, a decaging study was also performed on this substrate in order to provide insight into how these photocages would behave in a biologically relevant context, with future scope for developing photoresponsive materials.

4.2 Decaging follows first order kinetics

The decaging of (coumarin-4-yl)methyl esters is a multi-step process, with several competing reaction pathways.[1] Upon irradiation with light, the coumarin-cargo complex (CM-C), absorbs a photon, promoting an electron to the LUMO and forming the excited singlet state ^{1}[CM-C]*. This excited state can decay *via* fluorescence and other non-radiative processes returning the complex to the ground state ^{1}[CM-C]. However, the excited state can also dissipate energy *via* heterolytic bond cleavage, forming the singlet ion pair ^{1}[CM^+ C^-]. At this point these ions can recombine to form the original CM-C ground state. However, they can also proceed to escape their solvent cage forming the solvent separated ions CM^+ and C^-. The positively charged CM^+ then reacts rapidly with a surrounding water molecule forming the hydroxymethyl coumarin CM-OH.[1] These processes are illustrated in scheme 1 below.

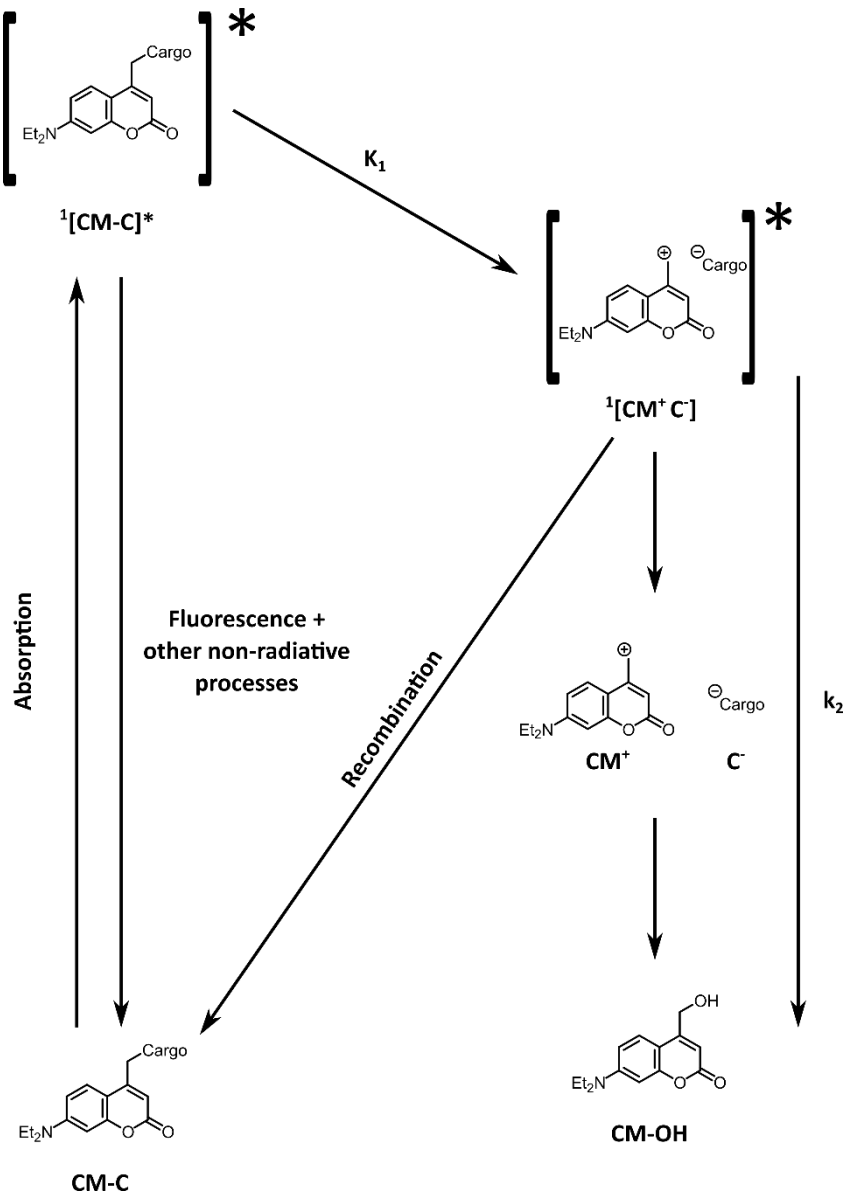

Scheme 1: A schematic of the proposed decaging mechanism of coumarin photocages. Absorption of a photon causes the coumarin-cargo complex to enter the excited state. This excited state can then dissipate energy by heterolytic bond cleavage leading to the formation of the coumarin cargo ion pair. The coumarin cation is then rapidly quenched by surrounding water to form the alcohol coumarin CM-OH.[1]

Although the decaging mechanism comprises three steps, photon absorption, heterolytic bond cleavage and finally solvolysis of the methyl cation, the chemically decisive step is the

cleavage of the coumarin-cargo bond. As the solvolysis step is rapid, and not rate-limiting it can be excluded from the kinetic description in order to simplify the analysis. Under these conditions, a steady state approximation can be applied where the first order rate constant k_1, describes both the absorption capability of the photocage and the quantum efficiency of heterolytic bond cleavage, upon formation of the excited state. Accordingly, plotting ln[CM-C] *vs* time should yield a linear fit, with the slope corresponding to $-k_1$ as illustrated in figure 1 below.

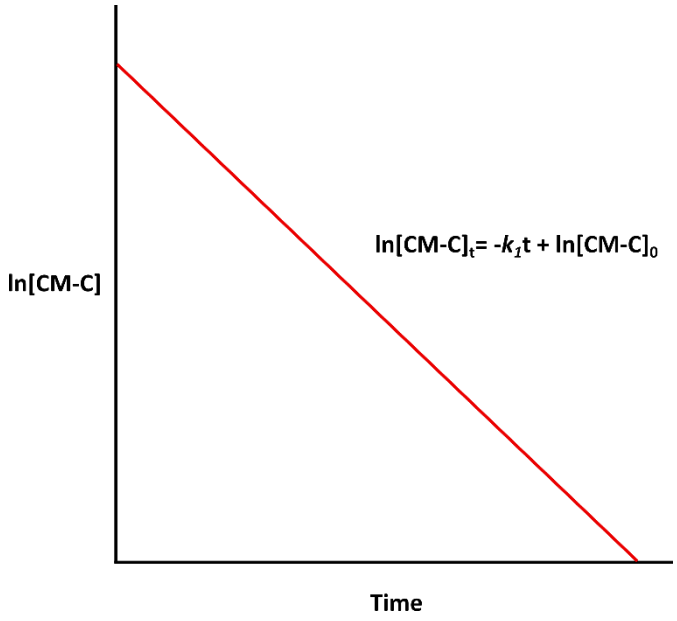

Figure 1: An example of a kinetic plot for a 1st order chemical reaction. The slope of the linear line produced is equal to the negative of the rate constant (k_1).

4.3 Decaging study of **(1)**

4.3.1Experimental design

In section 3.5 of the previous chapter, photocage **(1)** was used as a standard in the decaging studies performed on several of the photocleavable linkers which had been synthesised, on

the basis of its well documented decaging ability in literature [2–4] However, we did not previously attempt to elucidate any kinetic information about the decaging process from this study. Additionally, this experiment was performed in a mixture of MeOH: H_2O (1: 4), whereas future applications are intended for biologically relevant conditions. For this reason, phosphate-buffered saline (**PBS**) was adopted as a solvent for the studies described in this chapter.

Acetic acid was chosen as the model cargo molecule, due to its low molecular weight (60 g mol^{-1}), which was well separated from the mass of **(1)** and thereby simplified mass spectrometric analysis. Additionally, its minimal absorbance in the 210 – 400 nm region would avoid chromatographic interference. Additionally, acetate groups were commonly used to protect the 4-hydroxyl group throughout the synthesis of other coumarin photocages described in the previous chapters. As such, many of the derivatives required for the decaging studies to be discussed during this chapter had already been synthesised, negating the need for additional synthesis. The proposed decaging reaction upon the irradiation of **(1)** with light can be seen in figure 2 below.

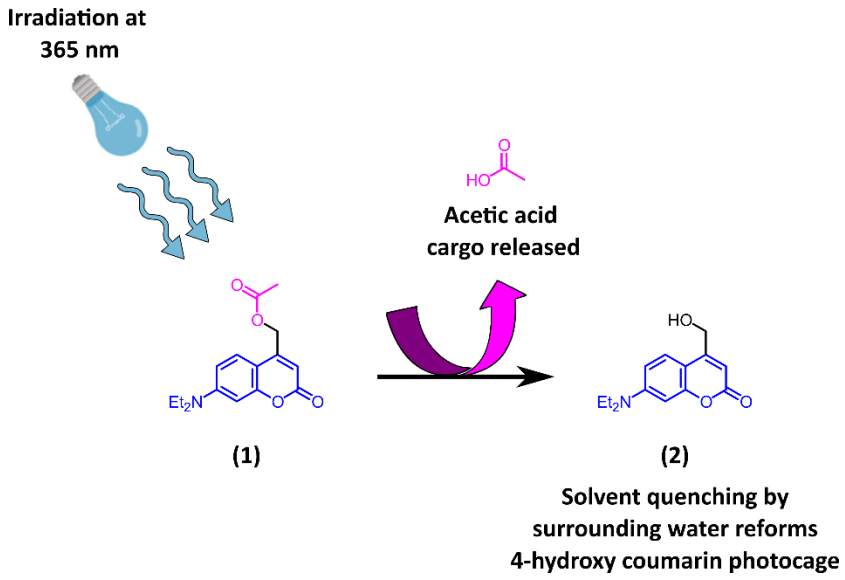

*Figure 2: A schematic of the proposed decaging reaction upon irradiation of **(1)** at 365 nm. Photolysis occurs releasing the acetic acid cargo and forming hydroxycoumarin **(2)**.*

Due to limited solubility in PBS, a 1 mM stock solution of **(1)** was prepared in MeCN, which was then diluted with PBS to afford a final concentration of 0.1 mM in (PBS: MeCN, 9:1). 2 ml of this solution was placed in a glass vial and irradiated using a 365 nm LED light source, within an EvoluChem PhotoRedOx Box. Aliquots were taken every 20 seconds, and analysed using LC-MS.

4.3.2 Kinetic analysis

A representative UV 210 – 400 nm chromatogram can be seen in figure 3 below, on which two peaks (A & B) are clearly observed. The corresponding mass spectra of these peaks identified them as being the decaging product **(2)**, and unreacted starting material **(1)** respectively.

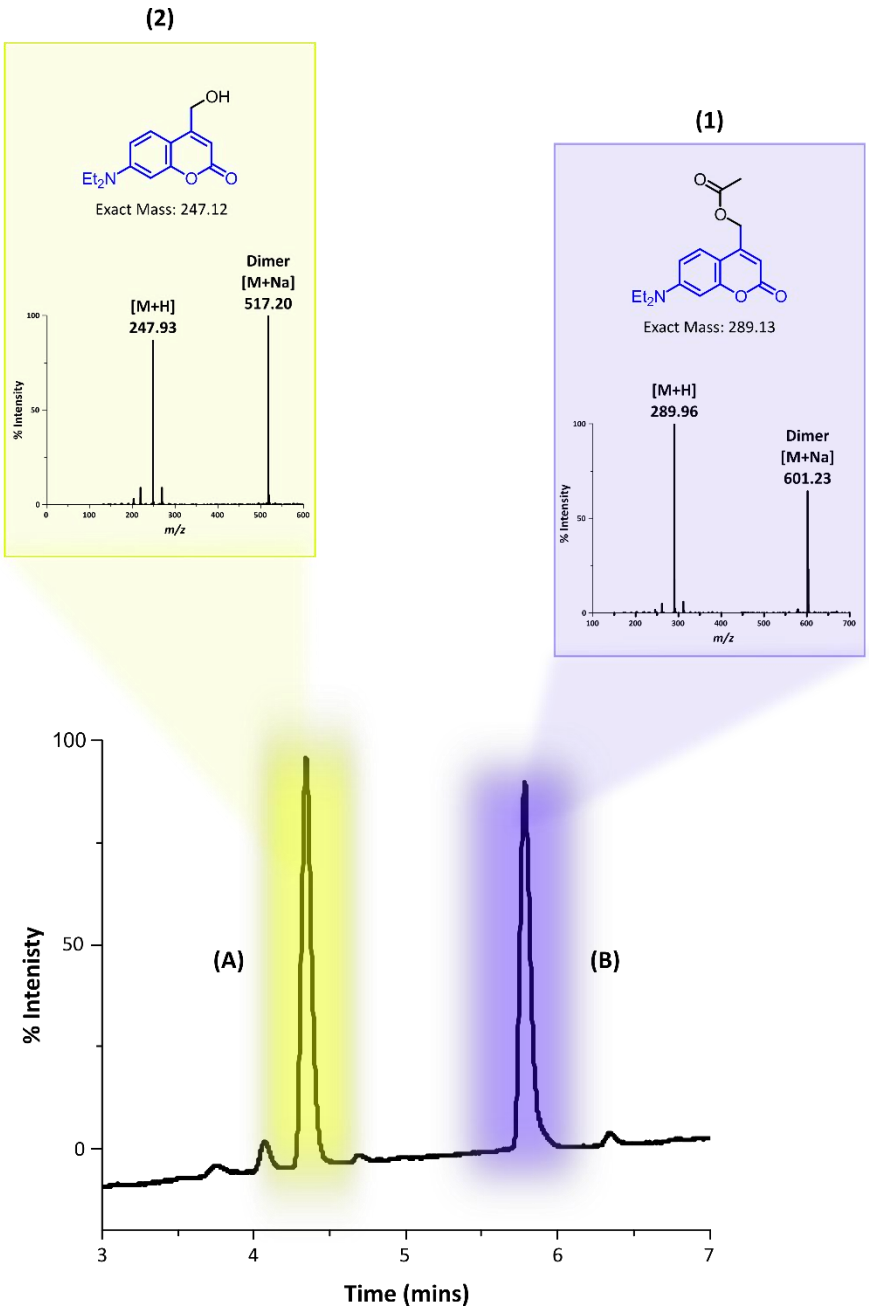

*Figure 3: A representative LC-MS chromatogram after irradiation of **(1)** at 365 nm for 2 mins. Two peaks (A and B) are present, with the corresponding mass spectra confirming their identity as decaged coumarin **(2)** and unreacted starting material **(1)** respectively.*

During our study, conversion was determined by integrating the peaks corresponding to product and starting material on the UV 210 – 400 nm chromatograms and calculating their area ratio. This approach was appropriate due to the fact that **(1)** and **(2)** contain the same 7-

diethylamino coumarin chromophore, meaning that their absorption can be expected to be comparable in this region.

Although decaging quantum yield (Φ), which is defined as the number of decaging events that occur for every photon absorbed,[5] is conventionally utilised to determine decaging efficiency,[2,6,7] Its accurate determination typically requires specialist methods such as chemical actinometry which is used to calibrate photon flux,[8,9] making it less practical for routine measurements. Furthermore, this parameter does not account for the influence of factors such as irradiance and path length, therefore limiting its predictive power for working systems. As such, in this work we decided to restrict our analysis to pseudo-first-order rate constants (k_1). These constants were not only more convenient to calculate but also provided a direct measure of decaging kinetics under the specific irradiation conditions employed. As our experimental set-up was designed with future application to photo-responsive materials, the use of k_1 values offered a practical means of predicting how such systems will respond to light exposure under comparable conditions in the future.

Following the calculation of conversion across the course of the experiment, first-order kinetics were evaluated by plotting Ln**([1])** *vs* time as seen in figure 4 below. The dataset produced a linear fit ($R^2 = 0.99$) which was consistent with a first-order decaging process. The slope of this line corresponded to $-k_1$, providing us with a value for k_1 of 6.88×10^{-3} s^{-1}.

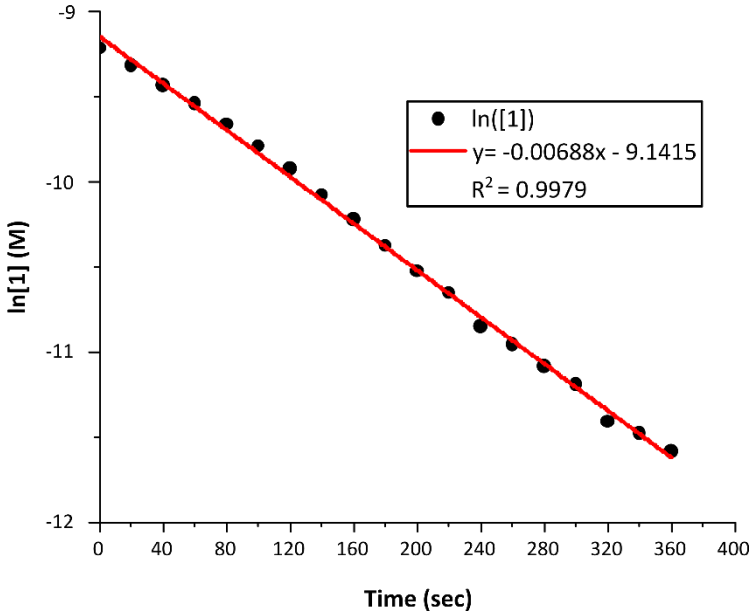

*Figure 4: A plot of Ln[1] vs time illustrating the decaging kinetics of **(1)** upon photolysis at 365 nm. The linear nature of the plot is consistent with 1st order reaction behaviour.*

Following the successful decaging of **(1)** upon irradiation at 365 nm, we decided to repeat the experiment but instead irradiating at 405 nm. This wavelength is further into the visible range meaning that it is lower in energy and thus provides greater biocompatibility.[10] Consequently it would be beneficial if **(1)** exhibited more efficient decaging at this wavelength. Once again, a 0.1 mM solution of **(1)** in PBS: MeCN (9:1) was irradiated at 405 nm for 6 mins, with an aliquot taken every 20 seconds. The plot of Ln**(1)** *vs* time obtained for this experiment can be seen in figure 5 below. A linear fit was obtained ($R^2 = 0.96$) the slope of which gave us a value for k_1 of $1.06 \times 10^{-2}\ s^{-1}$.

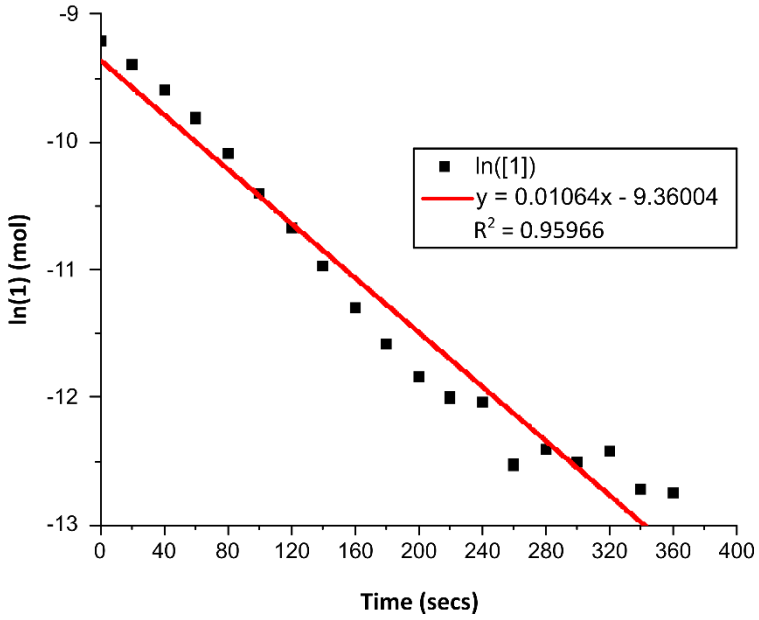

Figure 5: Plot of ln[1] vs time illustrating the decaging kinetics of compound ***(1)*** *upon irradiation at 405 nm. The linearity of the plot is consistent with first-order reaction behaviour, indicative of a unimolecular photolysis pathway.*

Conversion *vs* time plots provide a clear visual representation of the decaging progress over the course of the experiment and allow for direct comparison of decaging process at both 365 and 405 nm. These plots, together with their corresponding logarithmic fits modelled in COPASI can be seen in figure 6 below.

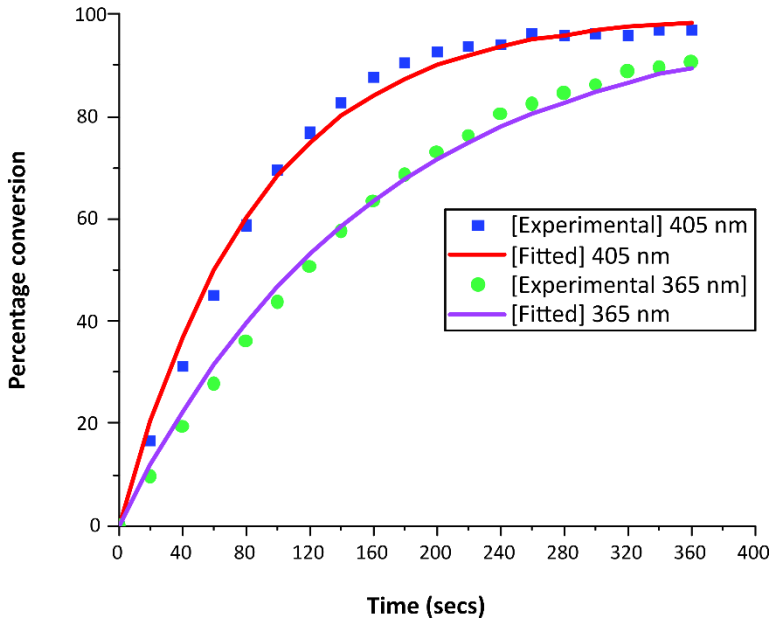

Figure 6: Plots of conversion vs time for the decaging of ***(1)*** *at 365 and 405 nm with the corresponding COPASI fits overlaid.*

4.3.3 Discussion

Under continuous irradiation, **(1)** underwent efficient decaging at both 365 nm and 405 nm, releasing 93% and 96% of the acetic acid cargo within 6 mins respectively. Kinetic analysis indicated that decaging proceeded approximately 1.5 times faster at 405 nm. The LED light sources used had irradiance values of 190 mW cm^{-2} (365 nm) and 201 mW cm^{-2} (405 nm), and thus the 405 nm bulb was slightly more powerful. However, this difference was not sufficient to account for the ~59% increase in k_1 observed during our experiment, meaning that the decaging of **(1)** at 405 nm was definitively faster than at 365 nm under our experimental conditions, which was in agreement with literature reports.[2,3] In the initial development of 7-diethylamino coumarin as a photocage, Kaupp et al. employed this photocage in the caging of cyclic GMP,[2] and in the caging of 8-bromo-substituted cyclic nucleotides.[3] In both reports the studied compounds were dissolved in aqueous buffer and exhibited efficient decaging at both

365 nm and 405 nm. Consistent with our results, conversion after 6 mins was almost identical but decaging at 405 nm proceeded more rapidly. Notably, their decaging progressed at a significantly faster rate, with up to 80% conversion and up to 98% conversion observed after 60 seconds at 365 and 405 nm respectively, compared to just 28% and 45% recorded during our study. However, this can be accounted for by the fact that they utilised high power LASER pulses rather than the low power LEDs which were used during our study. This highlighted the relevance of calculating rate constants rather than quantum yields for our study, as these provided a more representative measure of decaging efficiency under our specific experimental conditions, thus allowing us to more conveniently predict how future photo-responsive materials would behave. Furthermore, the calculated k_1 values for the decaging of **(1)** at 365 and 405 nm would serve as a suitable benchmark for future decaging studies, due to the fact that identical experimental conditions would be employed throughout.

4.4 Decaging study of (4)

4.4.1 Experimental considerations

In section 3.7 of the previous chapter, novel photocleavable linker **(3)**, was successfully synthesised. In order to allow for direct comparison to the cleavage of **(1)** discussed above, acetic acid was once again selected as a model cargo. Additionally, due to the inherent photosensitivity of aryl azides, the azido moiety was subjected to a click reaction prior to the decaging study. This not only provided a more representative model of the photophysical properties of **(3)** once tethered to a material, but it also prevented the formation of any undesired side products related to the photodegradation of the aryl azide which would otherwise complicate the study. Consequently, compound **(4)**, the clicked, acetate version of **(3)** was utilised during this decaging study. The structures of **(3)** and **(4)**, alongside the predicted decaging product **(5)** can be seen in figure 7 below.

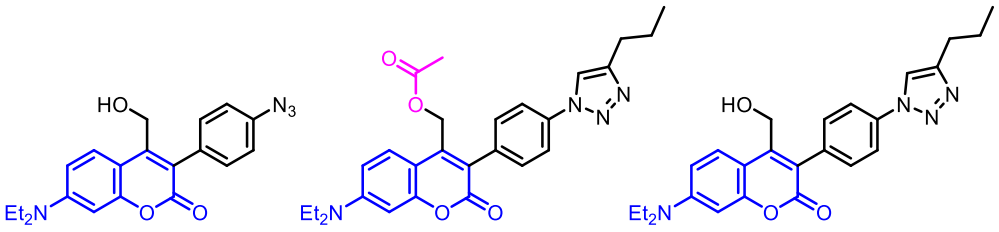

*Figure 7: The structures of novel photocleavable linker **(3)**, its clicked acetate counterpart **(4)** and the predicted decaging product **(5).***

A 0.1 mM solution of **(4)** was created in PBS: MeCN (9:1), and a 2 ml aliquot was placed in a glass vial for irradiation within an EvoluChem PhotoRedOx Box. During irradiation at 365 nm, timepoint samples were collected every 20 seconds over the course of 6 mins. However, irradiation at 405 nm resulted in almost full decaging within 40 seconds. Consequently, this experiment was repeated over a shortened time period of 45 seconds with aliquots taken at 5 second intervals. Once again, all samples were analysed using LC-MS, and the extent of conversion was determined by integrating the starting material and product peaks observed in the UV 210 – 400 nm chromatograms.

4.4.2 Kinetic Analysis

A representative UV 210 – 400 nm chromatogram following irradiation at 365 nm can be seen in figure 8 below, on which two peaks (A & B) are clearly observed. The corresponding mass spectra of these peaks identified them as being the decaging product **(5)**, and unreacted starting material **(4)** respectively, indicating that decaging had successfully occurred. By integrating these peaks for each collected timepoint and calculating the ratio of their areas, we were able to calculate conversion across the course of the experiment.

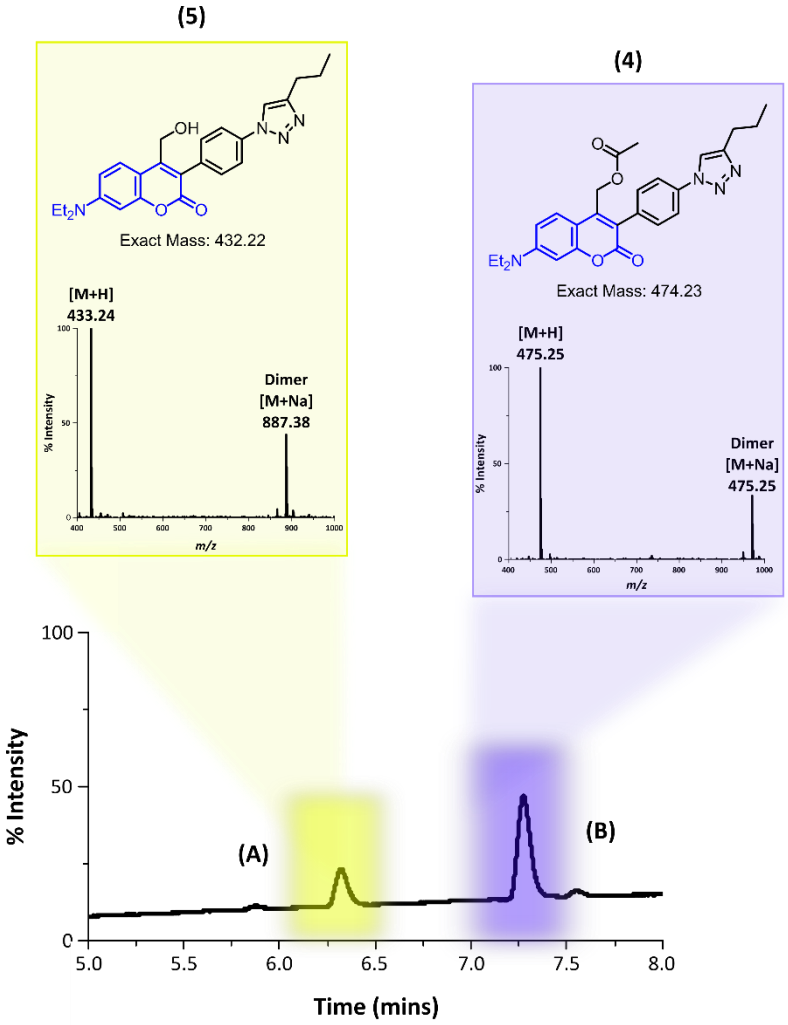

Figure 8: A representative UV 210 400 nm chromatogram generated during the decaging of ***(4)*** *at 365 nm.*

Following confirmation that decaging had successfully occurred, ln**([4])** *vs* time was plotted in order to evaluate the decaging kinetics of this reaction as seen in figure 9. A linear fit (R^2 = 0.99) was obtained which was once again consistent with a first-order process. The slope of this line provided us with a value of 1.20×10^{-2} s^{-1} for k_1.

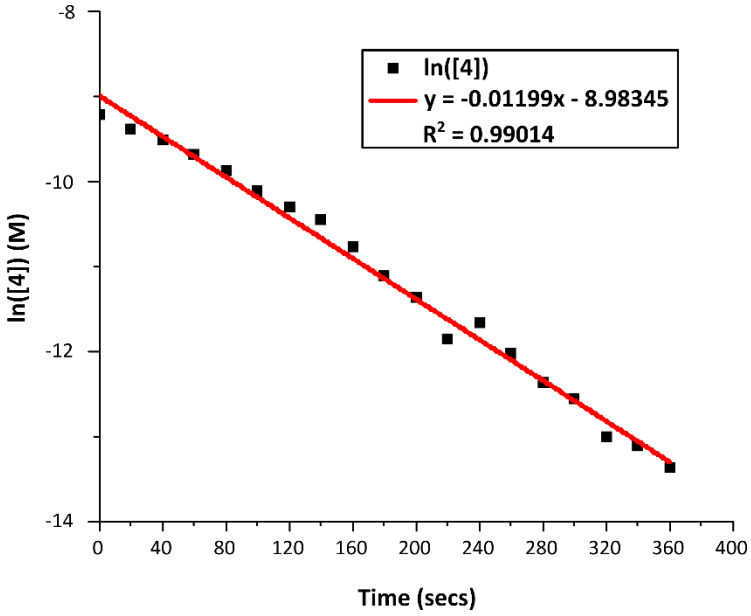

*Figure 9: The 1st order kinetic plot obtained for the decaging of **(4)** at 365 nm.*

The above experiment was then repeated, but this time irradiating at 405 nm rather than 365 nm. Additionally, due to the rapid nature of this reaction, the experiment was carried out over a time period of 45 seconds with aliquots taken every 5 seconds. Ln**([4])** vs time was plotted as seen below and a linear fit (R^2 = 0.98) was obtained as seen in figure 10. The slope of this line gave us a value of 9.00×10^{-2} s^{-1} for k_1.

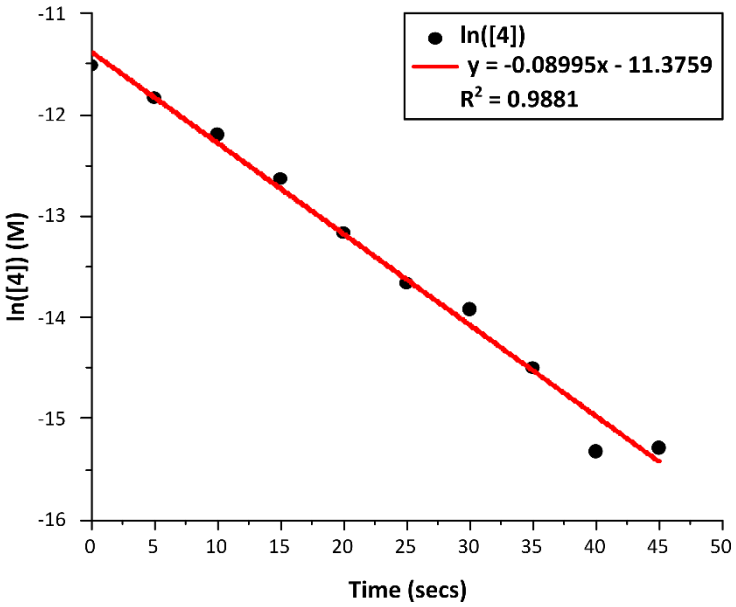

*Figure 10: The 1st order kinetic plot obtained for the decaging of **(4)** at 405 nm.*

Conversion *vs* time for both experiments was then plotted alongside their corresponding logarithmic fits modelled in COPASI, as can be seen in figure 11 below.

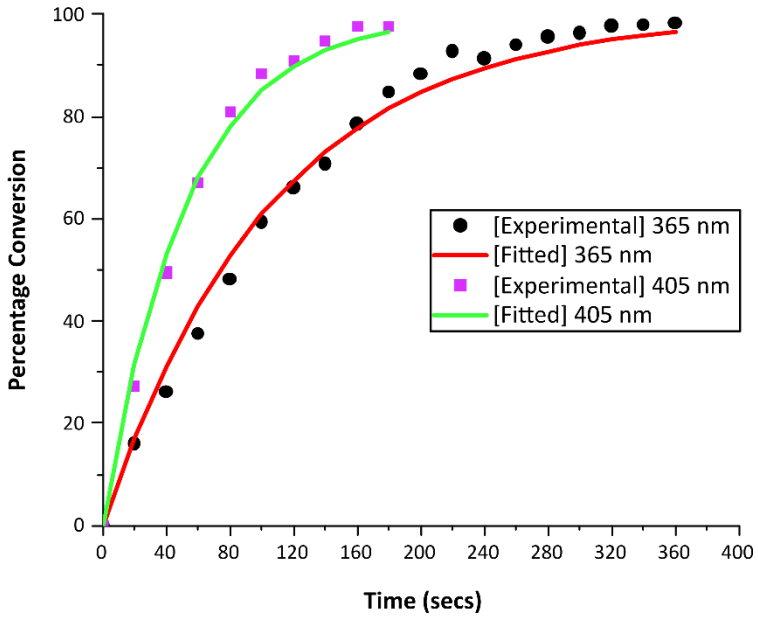

*Figure 11: Plots of conversion vs time obtained during the irradiation of **(4)** at 365 and 405 nm with the corresponding COPASI fits overlaid.*

4.4.3 Discussion

In the previous chapter, photocleavable linker **(6)** was synthesised based on the work of Anseth & Azagarsamy.[11] In section 3.5, decaging studies revealed that this compound failed to exhibit decaging at 365 nm under our experimental conditions. Whilst Anseth & Azagarsamy hypothesised the successful release of Boc-β-alanine, they relied on UV-Vis spectroscopy to monitor conversion, meaning that the photoproducts were not fully characterised. In contrast to this, our study utilised LC-MS analysis allowing for MS characterisation of any products formed. Although we did observe almost full consumption of **(6)**, upon MS analysis it was found that no decaging products could be detected. Instead, the species that were formed could be attributed to photodegradation of the aryl azide.[12] A subsequent study of **(7)**, the "clicked" analogue of this compound, confirmed the absence of photorelease, and this compound was shown to be stable to irradiation at 365 nm for at least 2 h. It was these results

that motivated the design and synthesis of **(3)**, with the aim of developing a photocleavable linker capable of efficient photorelease at 365 nm. Not only was the "clicked" analogue of this compound **(4)** shown to efficiently decage at 365 nm, but also at 405 nm, representing a significant improvement over the previous system.

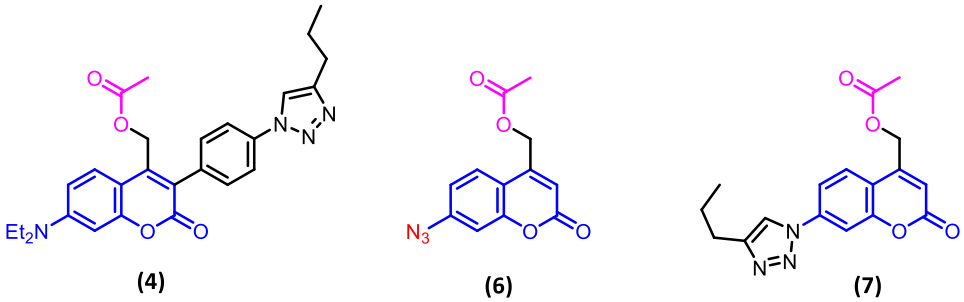

(4) **(6)** **(7)**

*Figure 12: The structures of novel, clicked photocleavable linker **(4)**, the photocleavable linker developed by Anseth & Azagarsamy **(6)**, and its clicked counterpart **(7).***

Our experiments indicated that the decaging of **(4)** was approximately 7.5 times faster at 405 nm than 365 nm. From a biological perspective, this finding had several important implications. First, the use of 405 nm light represents a significant advantage for both *in vitro* and *in vivo* applications, as it is generally less damaging to biomolecules and cells than higher energy UV light.[10] Additionally, the substantially faster rate of photorelease at this wavelength would facilitate considerably shorter irradiation times, limiting the amount of light exposure required. Both of these factors contribute to improved biocompatibility, which is a critical consideration for the development of photocages intended for biological applications.

In section 4.3, a decaging study was performed on **(1)** under identical experimental conditions, enabling a direct comparison of its rate constants with those obtained for **(4)**. A summary of these values is presented in Table 1. From this comparison, it is evident that **(4)** underwent more efficient decaging at both 365 and 405 nm. At 365 nm, the rate constant was

approximately 1.7-fold higher than that of **(1)**, while at 405 nm the enhancement was even more pronounced, with decaging proceeding ~8.5 times faster.

This marked increase in efficiency at 405 nm can be rationalised by considering the photophysical properties of **(4)**. The introduction of the 3-aryl substituent resulted in a slight red-shift in the absorption profile, increasing the λ_{max} to 403 nm. The λ_{max} of **(1)** on the other hand was 380 nm, which was further toward the UV region. As outlined in section 1.3.2 of the introductory chapter, decaging efficiency is governed primarily by two factors, the decaging quantum yield, and the absorption capabilities of the photocage at the irradiation wavelength.[13] While quantum yields were not determined in this study, the absorption spectra provide valuable insight. Interestingly, **(4)** also performed better at 365 nm despite exhibiting weaker absorption at this wavelength than **(1)**. This suggested that the decaging quantum yield of **(4)** was also superior, although this could not be confirmed directly using the data generated during our experiment.

Property	(1)	(4)	Relative Change
λ_{max}	380 nm	403 nm	+ 23 nm
k_{365}	6.88×10^{-3} s^{-1}	1.20×10^{-2} s^{-1}	1.7-fold faster
k_{405}	1.06×10^{-2} s^{-1}	9.00×10^{-2} s^{-1}	8.5-fold faster

*Table 1: Photophysical and kinetic parameters for compounds **(1)** and **(4)** under irradiation at 365 and 405 nm.*

4.5 Decaging study of **(7)**

4.5.1 Experimental considerations

Following the successful decaging of **(1)** and **(4)** above, it was time to attempt the decaging of **(7)**. This compound was synthesised based on the work of Kele et al.,[7] who had previously successfully released 3,5-dimethyl benzoic acid (DMBA) from the related compound **(7-I)** compound using a green light LED. Although our version of this compound featured a triflate counterion and was used to cage acetic acid rather than (DMBA), we postulated that this would have a minimal effect on the performance of **(7)**, due to the fact that it would be dissolved in PBS, leading to dissociation of the counterion and that acetic acid would be released under an identical decaging mechanism. The structure of these compounds can be seen in figure 13 below.

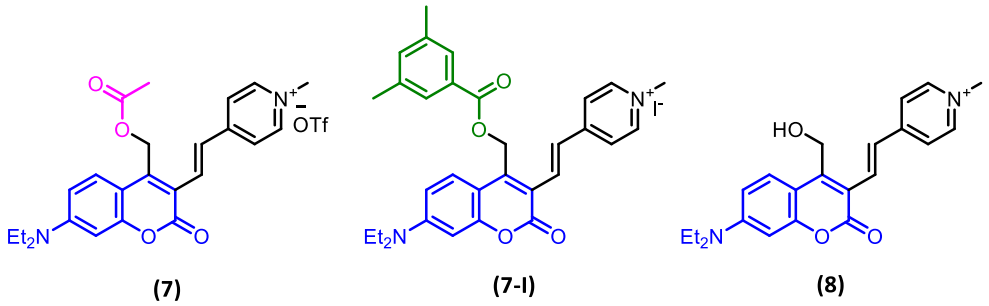

*Figure 13: The structures of **(7)** and **(7-I)** alongside the predicted decaging product **(8).***

As with the decaging studies discussed above, **(7)** was initially dissolved in PBS: MeCN (9: 1) and a 2 ml aliquot was placed in a glass vial for irradiation at 525 nm within an EvoluChem PhotoRedOx Box. However, upon analysis of this compound by LC-MS it was found that a concentration of 0.1 mM, absorbed too strongly and saturated the UV-detector, making for difficult analysis. Consequently, we opted to use a concentration of 0.01 mM for this study, in order to aid analysis. As a result, the final solution was composed of PBS: MeCN (99: 1), due

to the additional dilution, which afforded the benefit of reducing the amount of organic solvent required for this study.

4.5.2 Kinetic analysis

An aliquot of the 0.01 mM of solution was irradiated at 525 nm for 6 mins, with a 20 µl aliquot taken every 30 seconds. However, after analysis of these timepoint samples using LC-MS, it was found that decaging had not occurred successfully. The UV 210 – 400 nm chromatograms recorded at $t_{0,}$ and t = 6 mins are depicted in figure 14 below. Looking at these chromatograms, two peaks (A & B) are observed, indicating that consumption of **(7)** was occurring. However, upon looking at the resulting mass spectra it can be seen that these peaks were of the same mass. This indicated that peak A was likely arising as a result of isomerisation of the alkene, rather than successful decaging. In their experiment Kele et al. had performed an NMR study which did in fact confirm that photoisomerisation of the alkene did take place upon irradiation of **(7-I)** with green light, and so this result was consistent with their work.[7] Interestingly, the t_0 chromatogram also had two peaks present, despite the sample of **(7)** that was used being confirmed to be diastereomerically pure by NMR prior to the experiment. However, the sample was stored for approximately 12 h following the recording of the spectrum and as such it is possible that some of the sample isomerised to form the *Z* isomer, prior to the decaging experiment. It is also possible that isomerisation resulted from dissolving the sample in PBS.

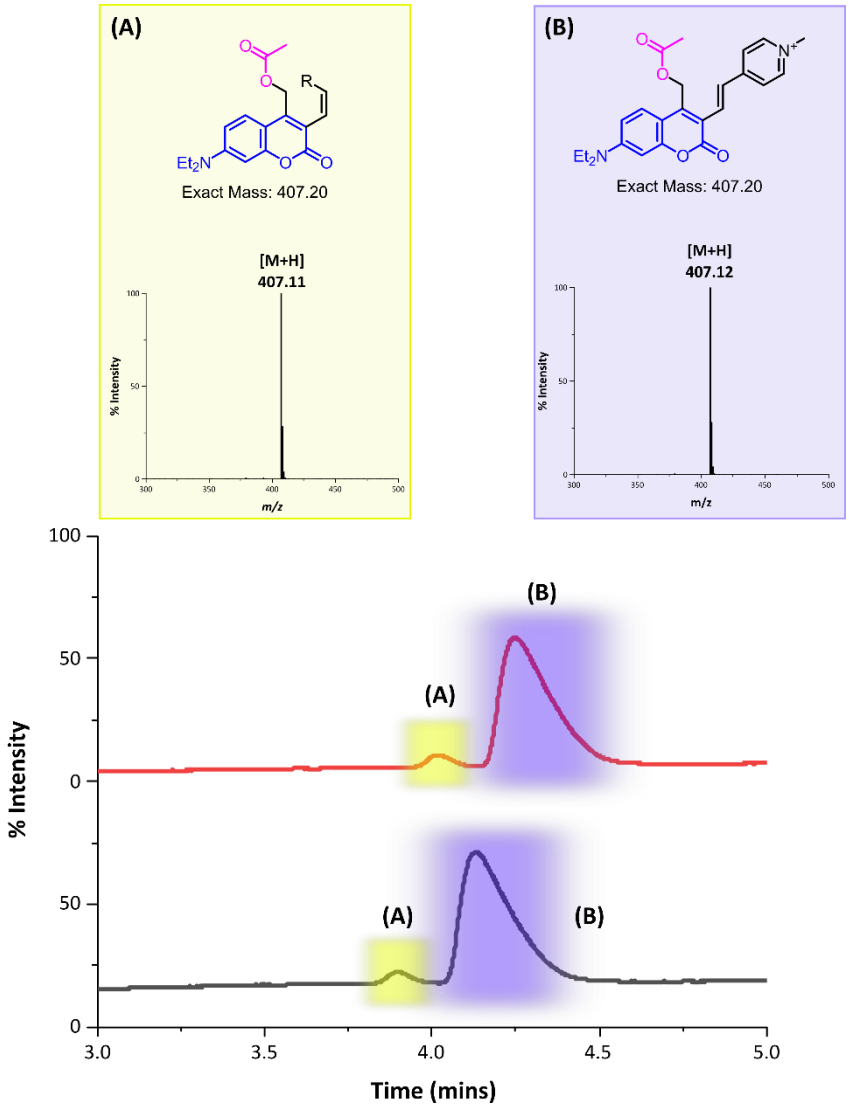

*Figure 14: The UV 210 – 400 nm chromatograms obtained at t_0 and t= 6 mins following the irradiation of **(7)** at 525 nm.*

Following the unsuccessful decaging of **(7)** above, we decided to increase the irradiation time to 90 mins. The resulting UV 210 – 400 nm chromatograms at t_0 and t = 90 mins can be seen in figure 15 below. Looking at this figure it can be seen that in addition to peaks (A & B), which were previously suspected to be the *E* and Z isomers of **(7)**, there is a 3rd peak (C) present at t = 90 mins. MS analysis confirmed that this peak was in fact the expected decaging product **(8)**, indicating that decaging had successfully occurred. However, integrating the areas of the

peaks on the UV 210 – 400 nm chromatograms indicated that only 5% conversion had occurred within this time period. Additionally, the ratio of (A):(B) was also shown to change over the course of the experiment. At t_0, approximately 4% of the sample existed in the *Z* form. This increased to 11% at t = 90 mins indicating that irradiation at 525 nm was also resulting in isomerisation.

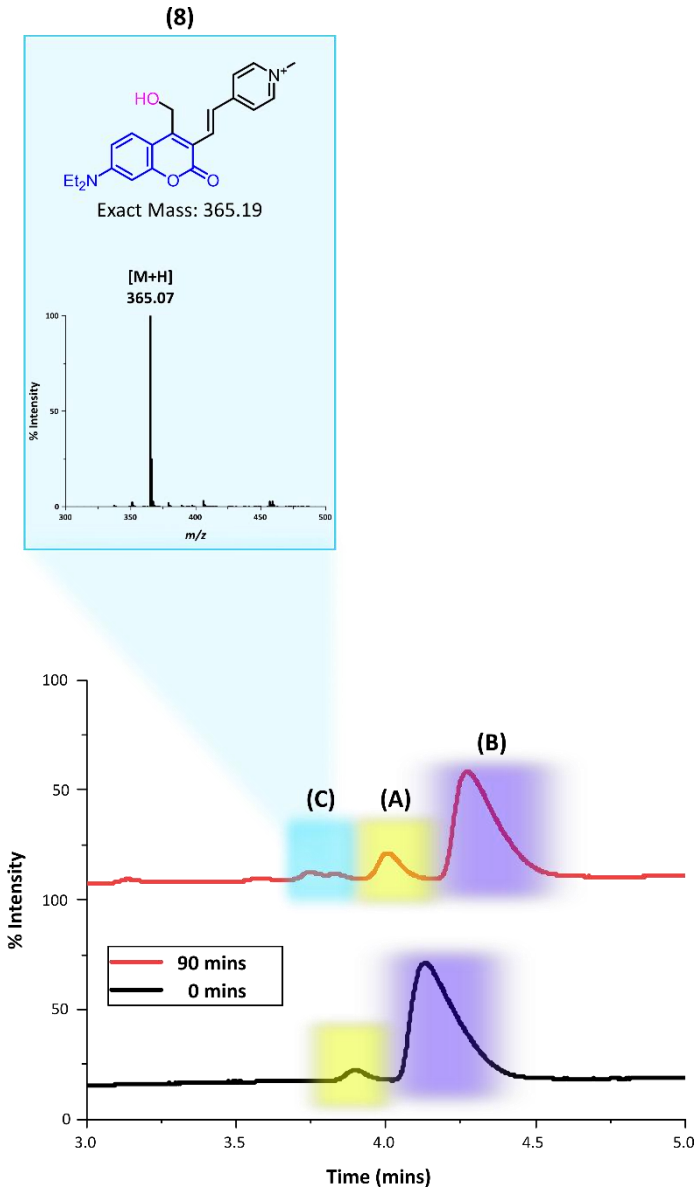

*Figure 15: The UV 210 – 400 nm chromatograms obtained at t_0 and t= 90 mins following the irradiation of **(7)** at 525 nm.*

4.5.3 Discussion

From the above results, it could be seen that **(7)** did not decage successfully upon irradiation at 525 nm under our experimental conditions. This was unexpected as in their work, Kele et al. reported efficient decaging of its related compound using a broad-emission LED centred around 544 nm, where a 0.1 mM solution of **(7-I)** in H2O: MeCN (95:5) achieved full photorelease within 20 – 25 mins.[7] However, there were several differences between their study and ours which may account for this discrepancy.

Firstly, although both studies employed broad emission green LEDs, their setup utilised three 10 W LED chips with emission centred at 544 nm. Whilst the emission range was comparable to ours, it is possible that their light source delivered higher irradiance, thereby enhancing photolysis efficiency. However, a more likely explanation is the choice of cargo molecule. Kele et al. studied the photorelease of 3,5-dimethyl benzoic acid,[7] whereas in our study **(7)** was employed in the caging of acetic acid. The influence of the leaving group on decaging efficiency is well documented in the literature.[14,15] Although comparisons are typically drawn across different classes of compound (e.g. halides *vs* carboxylates), 3,5-dimethylbenzoic acid (pK_a = 4.32) is more acidic than acetic acid (pK_a = 4.76). Consequently, its conjugate base is more stable, rendering it a more effective leaving group. Although this difference is not dramatic enough to warrant the dramatic difference in decaging efficiency observed between **(7)** and **(7-I)**.

Notably, towards the conclusion of our work Feringa et al. studied the photorelease of acetic acid from **(7-1)**.[16] They recorded a quantum yield of 0.2% for the release of acetic acid from **(7-I)** which was approximately 5-fold lower than the quantum yield reported for the photorelease of 3,5-dimethyl benzoic acid reported by Kele et al.[7] They attributed this to the

fact that higher water contents typically have a positive effect on decaging efficiency,[17] as they utilised a solvent system of D_2O/DMSO-d_6 (1:1) rather than the H_2O: MeCN (95: 5) utilised by Kele et al. However, it nonetheless underlined the poor decaging efficiency for the release of acetic acid from **(7-I)**.

They built on this poor efficiency by attempting to design and develop a photocage which maintained the red-shifted absorbance of **(7-I)**, whilst simultaneously improving the decaging quantum yield. As mentioned in section 4.2 above, the decaging of coumarin photocages proceeds *via* two key steps.[1] Heterolytic cleavage of the coumarin-cargo bond results in the formation of the coumarin-cargo ion pair, followed by the escape of these ions from the solvent cage resulting in photorelease. Up to this point the solvolysis step has been considered to be effectively instantaneous. However, if the coumarin methyl cation which forms as a result of heterolytic cleavage is unstable, recombination with the cargo anion can occur, diminishing decaging efficiency. In a previous study, Feringa et al. had reported that substitution of the 4-methyl group with a prenyl substituent enhanced decaging efficiency by facilitating delocalisation of the positive charge generated upon heterolytic cleavage.[18] They postulated that the electron-withdrawing effect of the 3-vinylpyridinium substituent of **(7-I)** destabilised the intermediate carbocation, contributing to the observed decaging inefficiency. Thus, they substituted the 4-methyl group with a prenyl moiety in the hope of improving efficiency. Upon irradiation at 530 nm, they noted that prenyl substituted photocage **(9)** had a quantum yield which was 7.4-fold greater than **(7)** for the release of acetic acid.

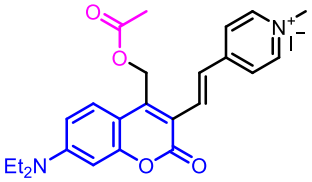

(7-I)
Φ_D= 0.2%

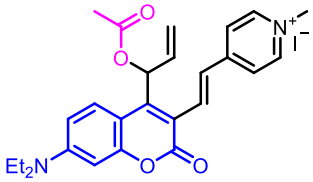

(9)
Φ_D= 1.5%

*Figure 16: The decaging quantum yields for the photorelease of acetic acid from **(7-I)** and **(9)** as reported by Feringa et al.*[16]

The above study by Feringa et al. was particularly significant in the context of this thesis, as it highlighted that carbocation stability can be critical to decaging efficiency. As such, analogues of **(9)** present themselves as a useful photocages for the future applications of this project, although time constraints did not allow for their syntheses.

4.6 Decaging study of (10)

4.6.1 Experimental considerations

Following the decaging study performed of **(7)** above, we set out to perform a decaging study on **(10)**, its corresponding photocleavable linker which had been synthesised in section 3.12 of the previous chapter. A 0.01 mM solution of **(10)** in PBS: MeCN (99: 1) was created and a 2ml aliquot placed in a glass vial equipped with a stirrer bar for irradiation within an EvoluChem PhotoRedOx Box. The solution was irradiated at 525 nm and 10 µl aliquots were taken at regular intervals and analysed using LC-MS. The ratio of decaging product **(11)** to unreacted starting material **(10)** present on the UV 210 – 400 nm chromatograms was then used to calculate conversion over time. A schematic of the proposed decaging reaction of **(10)** upon irradiation at 525 nm can be seen in figure 17 below.

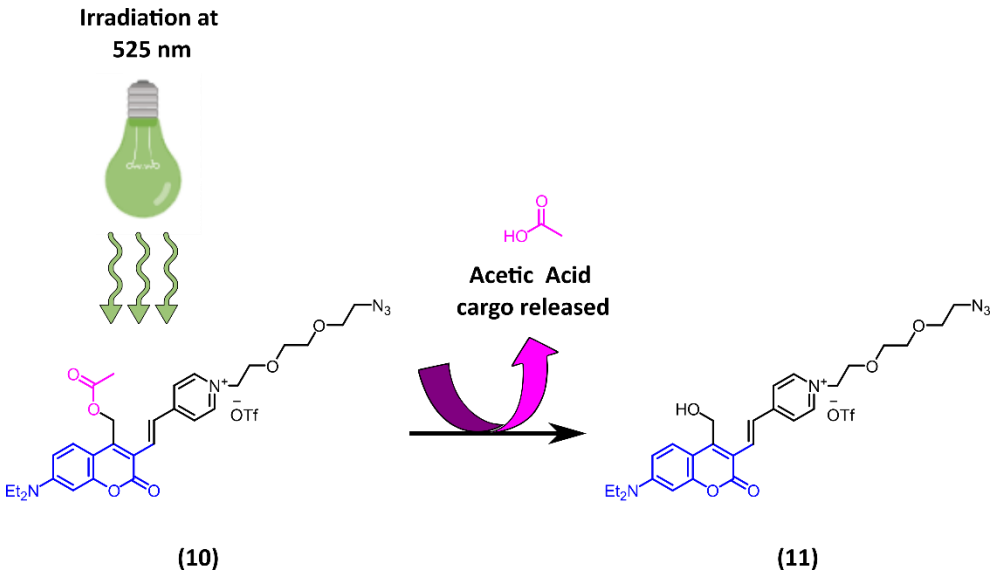

*Figure 17: The proposed decaging reaction that occurs upon the irradiation of **(10)** at 525 nm.*

4.6.2 Kinetic Analysis

Initially, a 0.01 mM solution of **(10)** was irradiated at 525 nm for 10 mins, with a timepoint sample taken every 60 seconds. The UV 210 – 400 nm chromatograms for t_0 and the t = 10 mins timepoints can be seen in figure 18 below. Looking at these chromatograms it can be seen that peak **(A)** converts to form peak **(B)** over the course of the experiment. However, upon examination of the accompanying mass spectra it is discernible that peak **(B)** does not arise from decaging, but rather from suspected photoisomerisation of the alkene from *E* to *Z*, as had previously been observed for **(7)** in section 4.5.2 above. Consequently, it was clear that decaging had not occurred within the 10-minute timeframe of the experiment.

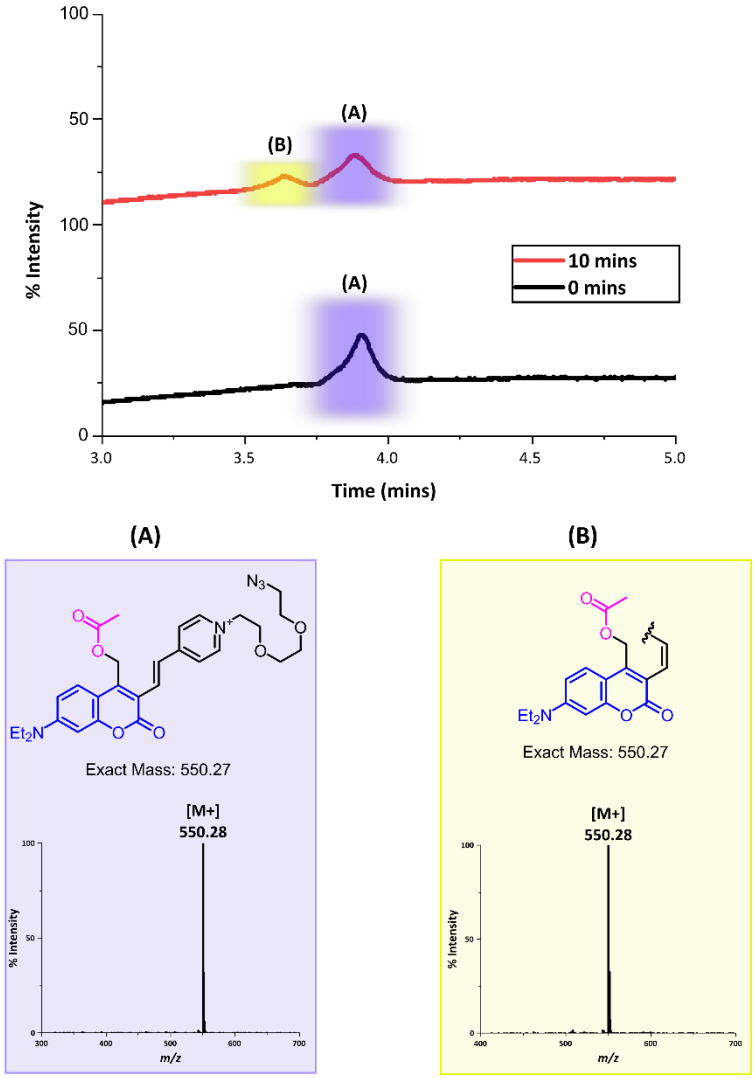

*Figure 18: The UV 210 – 400 nm chromatograms obtained for t_0 and t= 10 mins following the irradiation of **(10)** at 525 nm.*

Following the failure of the above experiment, it was decided that it would be repeated over a longer time period in the hope that some decaging could be observed. As such, we decided to replicate the above conditions but instead irradiating the sample for 3 h rather than 10 mins. The resulting chromatograms at t_0 and t = 3 h can be seen in figure 19 below. Once again it can be seen that isomerisation was the preferred process with the starting material peak **(A)** degrading to form peak **(B)**. However, on this occasion a smaller product peak **(C)** was also

observed. Upon examination of its corresponding mass spectrum a mass of 540.25 was found which was equal to the expected mass of a methanol adduct of the decaging product **(11)**.

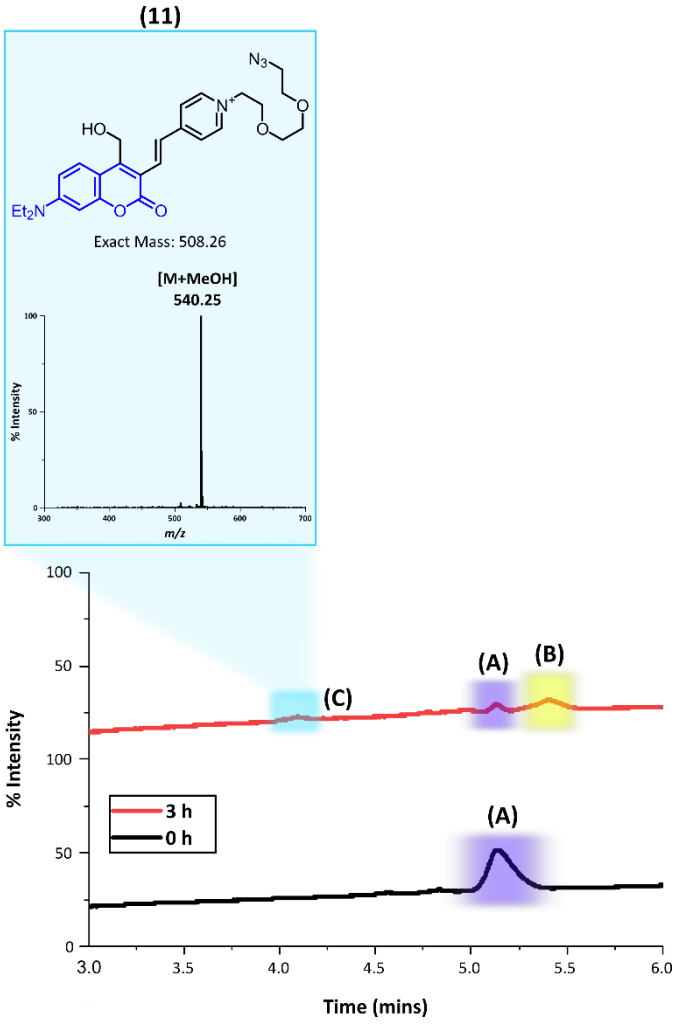

*Figure 19: The UV 210 – 400 nm chromatograms obtained at t0 and t= 3h following the irradiation of **(10)** at 525 nm.*

Although, the above experiment did result in decaging, the small amount of conversion observed made it difficult to track conversion. As mentioned in section 4.5.3 above, Kele et al. had utilised 3,5-dimethyl benzoic acid as a model cargo during their decaging study of **(7-I)**. As such, we decided to synthesise **(12)** which replaced the acetic acid cargo of **(10)**, with 3,5-dimethyl benzoic acid, in the hope that this cargo molecule would undergo more efficient

photolysis and allow us to elucidate kinetic information about the decaging process. The structure of **(12)** can be seen in figure 20 below.

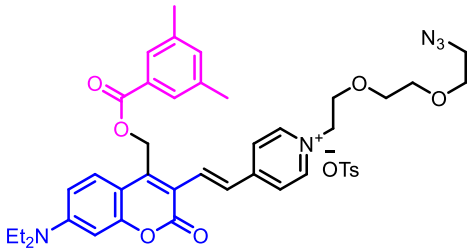

(12)

*Figure 20: The structure of **(12)***

Following the successful synthesis of **(12)** a 0.01 mM solution of it was created in PBS:MeCN (99:1). 2 ml of this solution was added to a glass vial equipped with a magnetic stirrer bar. The previous experiment had achieved minimal conversion within 3 h. As we hoped to obtain kinetic information about the decaging process we decided to once again extend the irradiation time, this time to 6 h with a timepoint aliquot taken every 30 mins. The UV 210 – 400 nm chromatograms for t_0 and the aliquot t = 6 h can be seen in figure 32 below. Once again, it was suspected that isomerisation had taken place as peak **(A)** on the t_0 chromatogram was converted into two overlapping peaks of equal mass at 6 h. However, on this occasion two additional product peaks are observed on the 6 h chromatogram. Peak **(B)** had a mass of 540.23, which matched the expected mass of the decaged product +32, suggesting that it was a methanol adduct of **(11)**. Peak **(C)** on the other hand had a mass of 508.25 which exactly matched the expected mass of the decaged product **(11)**. As such, it was clear that **(12)** had indeed successfully decaged within the timeframe of the experiment, albeit at a lesser rate than had been observed previously during the decaging studies of **(1)** and **(4)** above.

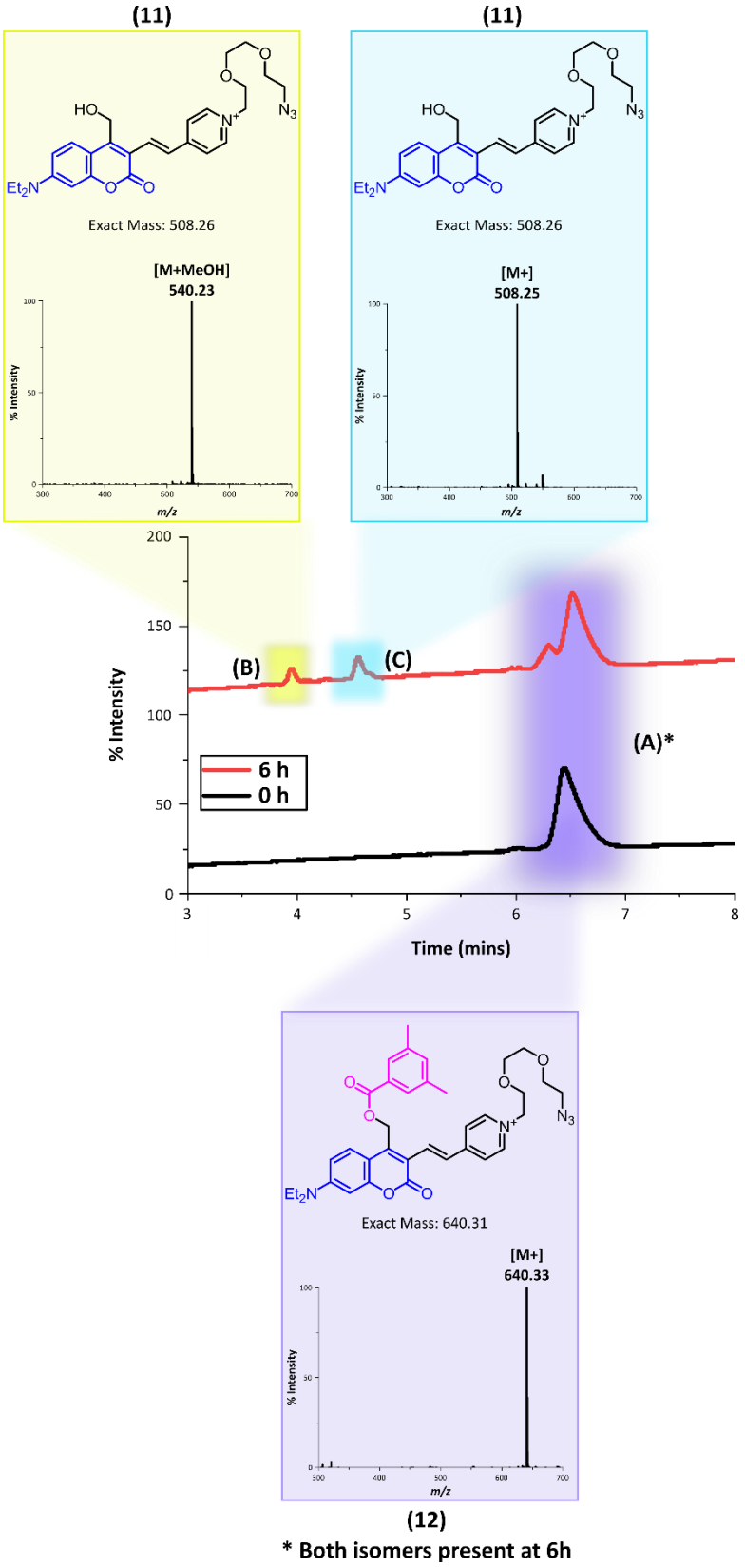

*Figure 21: The UV 210 – 400 nm chromatograms at t_0 and t= 6 h obtained following the irradiation of **(12)** at 525 nm*

A plot of ln([**12**]) was then plotted *vs* time in order to evaluate the decaging kinetics of this reaction as seen in figure 22. A linear fit (R^2 = 0.99) was produced which was consistent with a first-order process. The slope of this line provided us with a value of 7.13×10^{-6} s^{-1} for k_1.

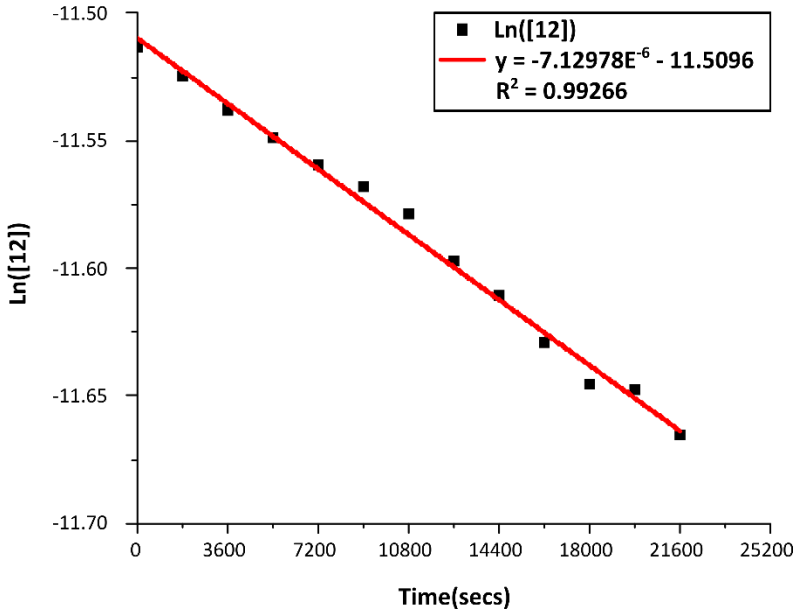

Figure 22: The 1st order kinetic plot obtained for ***(13)*** *upon irradiation at 525 nm*

We then plotted conversion *vs* time, alongside the corresponding fit modelled using COPASI as can be seen in figure 23 below.

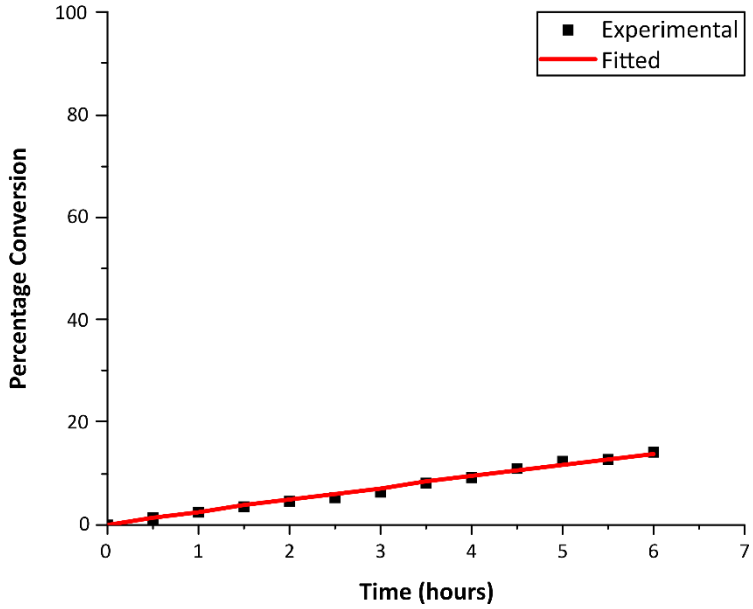

*Figure 23: A plot of conversion vs time for the decaging of **(12)** upon irradiation at 525 nm.*

4.6.3 Discussion

Although replacing the acetic acid cargo molecule of **(10)** with 3,5-dimethyl benzoic acid did lead to an observed increase in decaging efficiency, the calculated rate constant of 7.13×10^{-6} s^{-1} for the decaging of **(12)** was extremely slow in comparison to the rate constants calculated for the decaging of **(1)** and **(4)** above. To contextualise these results the half-lives for these reactions can be calculated using equation 1 below.

$$t_{\frac{1}{2}} = \frac{ln2}{k_1}$$

Equation 1

Using this equation, a half-life of 27.01 h was obtained for the photolysis of **(12)** at 525 nm, meaning that this reaction would require this length of irradiation to reach 50% conversion. In contrast, the fastest decaging process studied during this work (the decaging of **(4)** at 405 nm) had a half-life of just 7.7 seconds. This difference in timescales spans over four orders of

magnitude, highlights the dramatic disparity in decaging efficiency between these two compounds.

The calculated rate constants and half-lives for **(1)**, **(4)** and **(12)** are summarised in table 2 below. From this data, it is evident that the decaging of **(12)** at 525 nm was by far the slowest process, with all of the previously studied processes being at least three orders of magnitude faster. As such, although **(12)** did decage successfully upon irradiation at 525 nm, the timescale of this process was too slow for our intended application. Consequently, further tuning of its photophysical properties in order to enhance its decaging rate will be required before this compound can be incorporated into a future photo-responsive materials

Compound	Wavelength	k_1 (s^{-1})	$t_{1/2}$ (s)	Rate enhancement vs (12)
(1)	365 nm	6.88×10^{-3}	101	10^3
(1)	365 nm	1.06×10^{-2}	65.4	1.5×10^3
(4)	405 nm	1.20×10^{-2}	57.8	1.7×10^3
(4)	405 nm	9.00×10^{-2}	7.7	1.3×10^4
(12)	525 nm	7.13×10^{-6}	9.72×10^4	-

*Table 2: First-order rate constants, half-lives, and relative rate enhancements for the decaging of compounds **(1)** and **(4)** vs **(12)***

Similar to the decaging study performed on **(7)** in the previous section, the poor decaging rate of (**10)**, highlights the relevance of the work of Feringa et al. to this project, as the introduction of a 4-prenyl substituent to **(10)** could potentially enhance its decaging rate, to an acceptable level for our intended applications.[16,18]

4.7 Peptide functionalisation

Now that decaging studies had been performed on the synthesised photocages, preliminary peptide work could begin. All peptide syntheses conducted throughout the course of this work were performed using solid-phase peptide synthesis (SPPS). First developed by Robert Merrifield, this technique involves the attachment of an amino acid to an insoluble resin support and subsequent assembly of the peptide chain through a series of stepwise additions.[19] There are several different methodologies that can be used during solid phase peptide synthesis, but the most common, and the one which was employed by us is Fmoc solid phase peptide synthesis. Fmoc or 9-fluorenylmethyloxycarbonyl, is a base-labile protecting group which is used to protect the N-terminus of an amino acid. Peptides are synthesised from C terminus to N terminus and so the C terminal amino acid is coupled to the solid support prior to deprotection of the Fmoc protected N terminus with piperidine in DMF. Fmoc deprotection occurs *via* base-induced β-elimination which generates a reactive intermediate, dibenzofulvene. This species is highly electrophilic and so it rapidly reacts with excess piperidine to form a piperidine-dibenzofulvene adduct.[20] Removal of these species is essential to allow for subsequent coupling steps and as such a DMF wash is completed to remove them. The next amino acid in the sequence is then added (with its N-terminus Fmoc protected) and an amide bond is formed between its free carboxylic acid and the now deprotected amine of the previous amino acid in the chain. Upon completion of this step, another wash is performed removing the coupling reagents and any excess unreacted amino acid, followed by another Fmoc deprotection. In this way a peptide chain can be assembled using these repeating cycles. Upon synthesis of the desired peptide, it can be cleaved from the solid support under acidic conditions. The side chains of many amino acids can interfere with the peptide synthesis process. Consequently, they are typically protected during the

synthesis, to prevent any undesirable side reactions. Typically, amino acid side chains are protected by acid-labile protecting groups such as tert-butyl (tBu) or tert-butyloxycarbonyl (Boc) as these groups can be removed during the TFA cleavage at the conclusion of the peptide synthesis process, negating the need for additional steps. A schematic, providing an overview of the peptide synthesis process can be seen in figure 36 below.[21] Synthesis on rink amide resin is depicted in this schematic, meaning that upon TFA mediated cleavage at the end of the peptide synthesis process, the C-terminus exists as an amide rather than carboxylic acid.

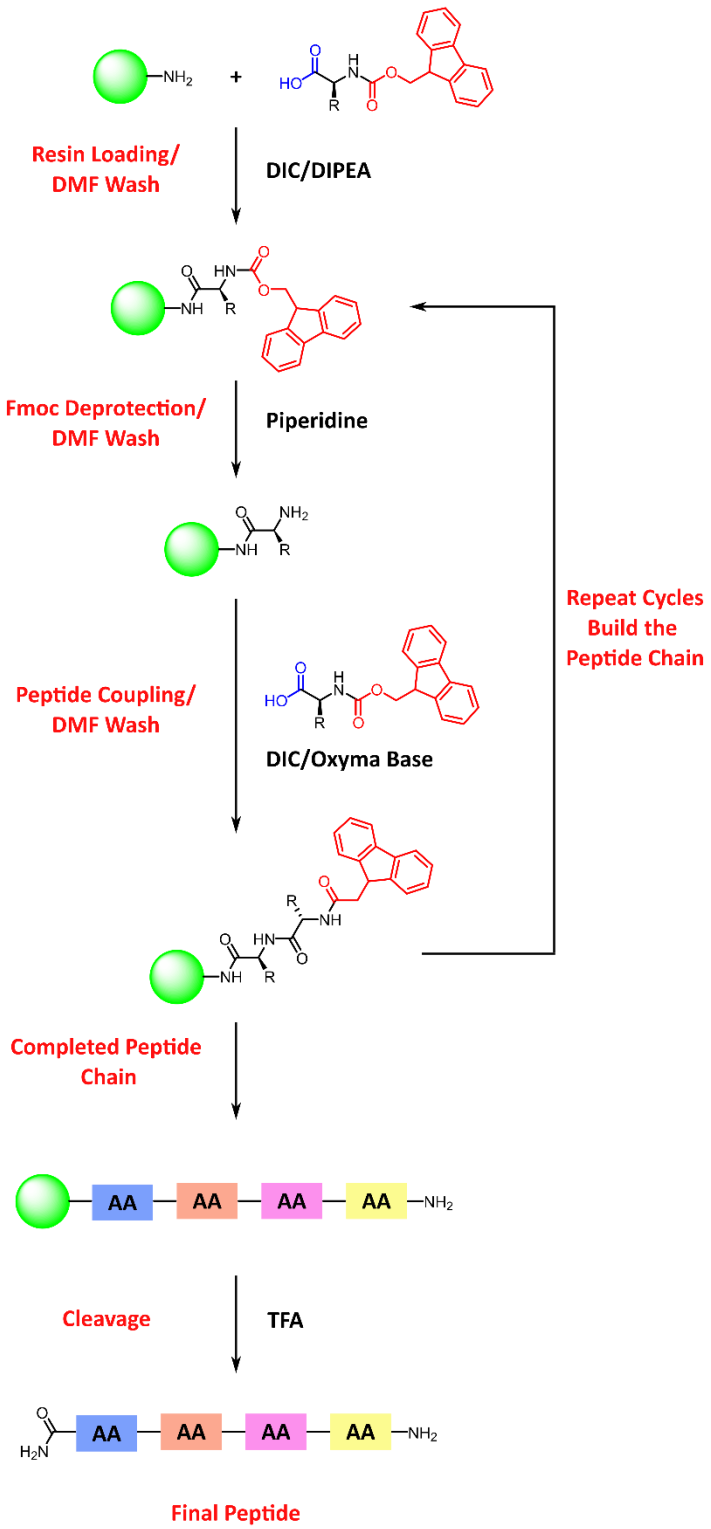

Figure 24: A schematic describing the process of automated SPPS. [21]

When attempting to functionalise a peptide that is synthesised using the above methodology with a photocage there are several potential strategies that could be employed. One method involves the synthesis of an unnatural amino acid building block. The side chain of an Fmoc protected amino acid can be modified, creating an unnatural amino acid which can then be used during the peptide synthesis process.[21] This method allows for the direct installation of the desired modification, without the need for additional steps post-peptide synthesis. However, the automated SPPS synthesiser that we wished to employ during our work utilised harsh microwave conditions, in order to enhance the rate of the coupling steps. As such, any unnatural amino acid produced in this manner would have to be stable under these conditions. Coumarin-caged Fmoc-protected building blocks have previously been synthesised and incorporated into peptide sequences, such as the phosphoamino acids produced by Imperiali et al.,[22] and the aspartic acid derivative produced by Marchán et al.,[23] as seen in figure 25.

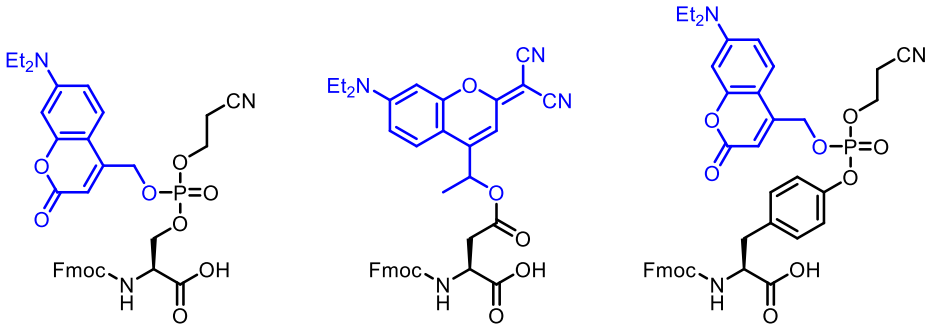

Coumarin-Caged Phosphoserine | **Coumarin-Caged Aspartic Acid** | **Coumarin-Caged Phosphotyrosine**

Figure 25: The Fmoc-protected coumarin-caged amino acids produced by Imperiali et al., and Márchan et al.[22,23]

The other strategy, which we opted to employ during our work, was the use of selective side-chain deprotection. As mentioned previously, the side chains of many amino acids are reactive under peptide synthesis conditions, requiring them to be protected during the peptide synthesis process. Typically, acid sensitive protecting groups such as boc or tert-butyl are used,[24] as these can be removed after peptide assembly during the TFA mediated resin cleavage. However, other protecting groups, which are selectively cleavable prior to peptide cleavage are also available.[21,24] These selective conditions leave other protecting groups intact whilst deprotecting an amino acid side chain of interest. This side chain can then be functionalised without the risk of functionalisations occurring at other sites on the peptide. Additionally, selective deprotection allows the subsequent functionalisation reaction to be performed whilst the peptide remains resin bound. This allows for the easy removal of any soluble impurities simply by performing a wash step. Following the installation of the desired modification, TFA cleavage removes any protecting groups remaining on the other amino acid residues and liberates the functionalised peptide from the resin. An overview of this process can be seen in figure 26 below.

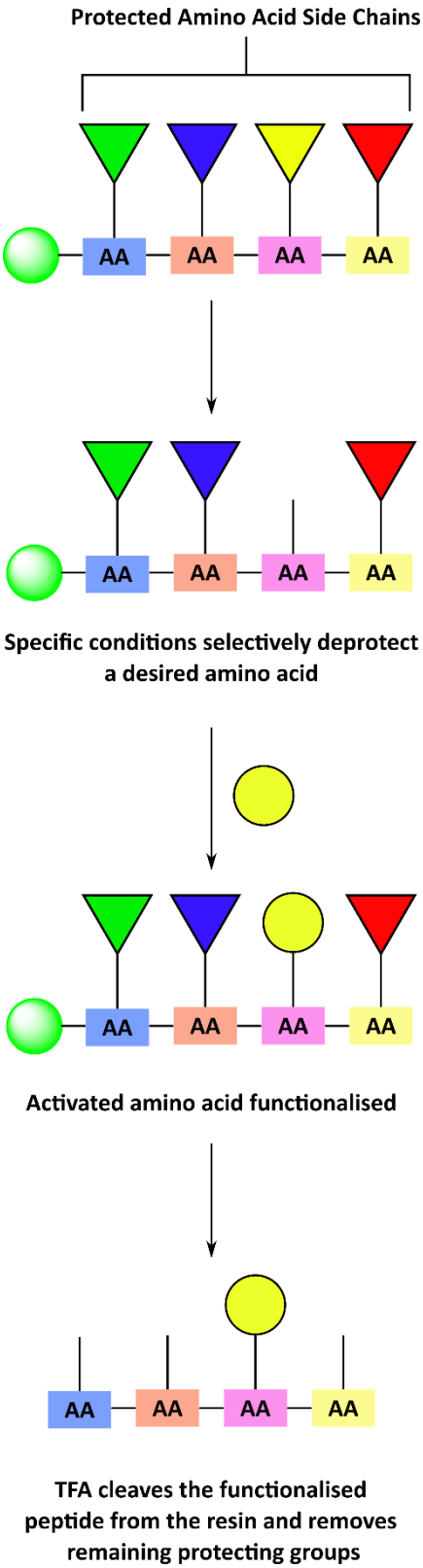

Figure 26: A schematic describing the selective deprotection method of peptide functionalistation.

4.8 The selective deprotection and functionalisation of lysine

When deciding on an amino acid to functionalise there were several important factors to consider. Firstly, the side chain needed to be reactive and capable of undergoing a coupling reaction in order to install the desired photocage. Secondly, it was desirable that a derivative of this amino acid, capable of orthogonal deprotection was commercially available. Finally, the chosen amino acid needed to be prevalent in bioactive peptide sequences, thereby ensuring that the methodology developed would be broadly applicable to the photocaging of a diverse array of peptide substrates.

With these factors in mind, we decided to focus our initial efforts upon lysine. Lysine accounts for approximately 6% of all amino acid residues within the human proteome,[25] meaning that the vast majority of human proteins contain at least one lysine residue. Not only this, but the nucleophilic nature of its amine side chain means that lysine often plays an important functional role such as in enzyme active sites.[26,27] Consequently, not only is this residue common, but it is also likely to play a key role in the function of a bioactive peptide making it an attractive target for photocaging.

During solid phase peptide synthesis this amino group is typically protected using a Boc group, as this can be easily cleaved during the TFA mediated cleavage of the peptide from the resin.[24] However, an alternative lysine derivative, with its side chain protected by 1-(4,4-dimethyl-2,6-dioxocyclohex-1-ylidene)ethyl (Dde) is also commercially available. This protecting group can be selectively cleaved using a mixture of hydroxylamine and imidazole in *N*-methyl-2-pyrrolidinone,[28] providing access to the free amine and providing a route toward selective functionalisation. Fmoc-Lys(Boc)-OH and its selectively cleavable counterpart Fmoc-Lys(Dde)-OH can be seen in figure 27 below.

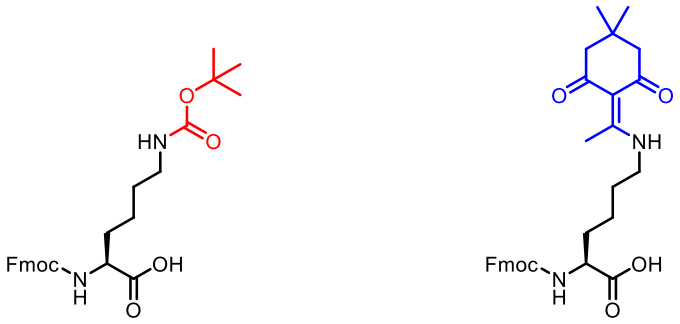

Fmoc-Lys(Boc)-OH **Fmoc-Lys(Dde)-OH**

Figure 27: The structures of the typical SPPS building block Fmoc-Lys(Boc)-OH and its alternative derivative Fmoc-Lys(Dde)-OH. [24]

We chose peptide **(13)** with a sequence of G-Y-A-K-K-E-D as a model for this work. We selected this sequence, as it was hoped that the glutamic and aspartic acid residues would aid water solubility. Within this sequence, all side chains were protected using their typical, acid-labile protecting groups,[24] with the exception of the first lysine residue which was protected with Dde, in the hope that we could demonstrate that our functionalisation technique was selective for Dde-protected lysine residues only. Additionally, the N-terminus of this peptide was protected with a Boc group, in order to avoid unwanted modification at this site. This peptide was synthesised using automated SPPS, before the resulting peptide on resin was subjected to the Dde deprotection conditions outlined previously, as seen in figure 28 below.

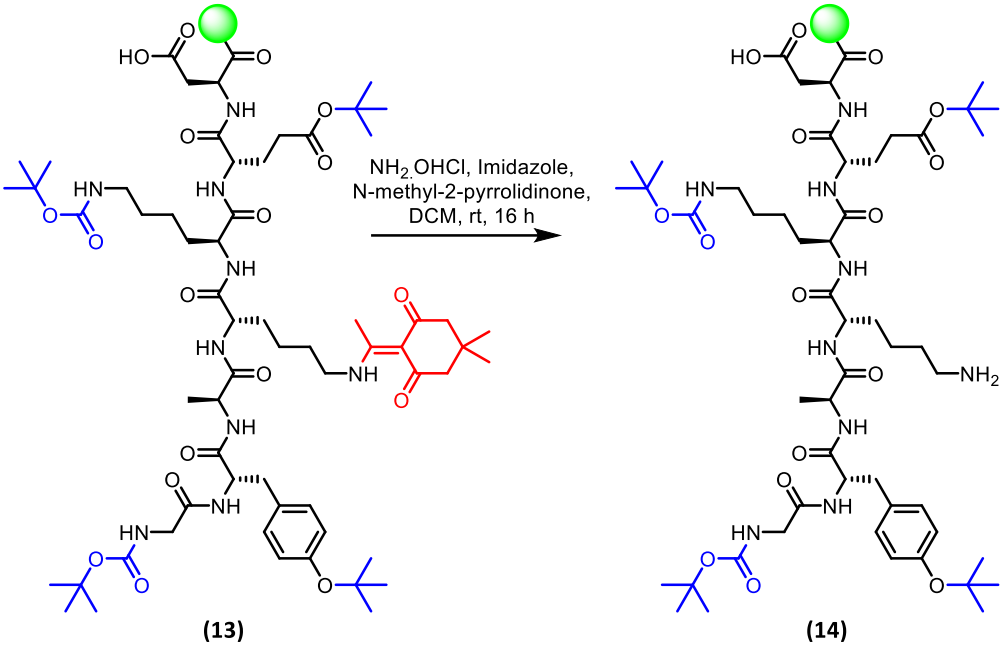

Figure 28: The conditions employed for the selective deprotection of Lys(Dde).

Now that, the amine side chain of the lysine residue had been selectively deprotected, it was time to install a photocage. Photocage **(2)** was chosen for this purpose, and it was first reacted with 4-nitrophenyl chloroformate in order to create an electrophilic site for amine addition to facilitate attachment to the peptide.

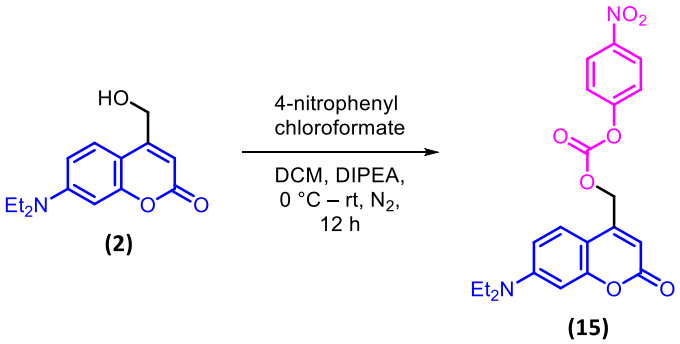

*Figure 29: The synthesis of activated photocage **(15).***

Activated photocage **(15)** was then coupled to **(14)** in the presence of DIPEA as seen in figure 30 below. The photocaged peptide on resin was then subjected to TFA cleavage conditions in

order to remove the additional side chain protecting groups, as well as liberate the final photocaged peptide **(17)** from the resin.

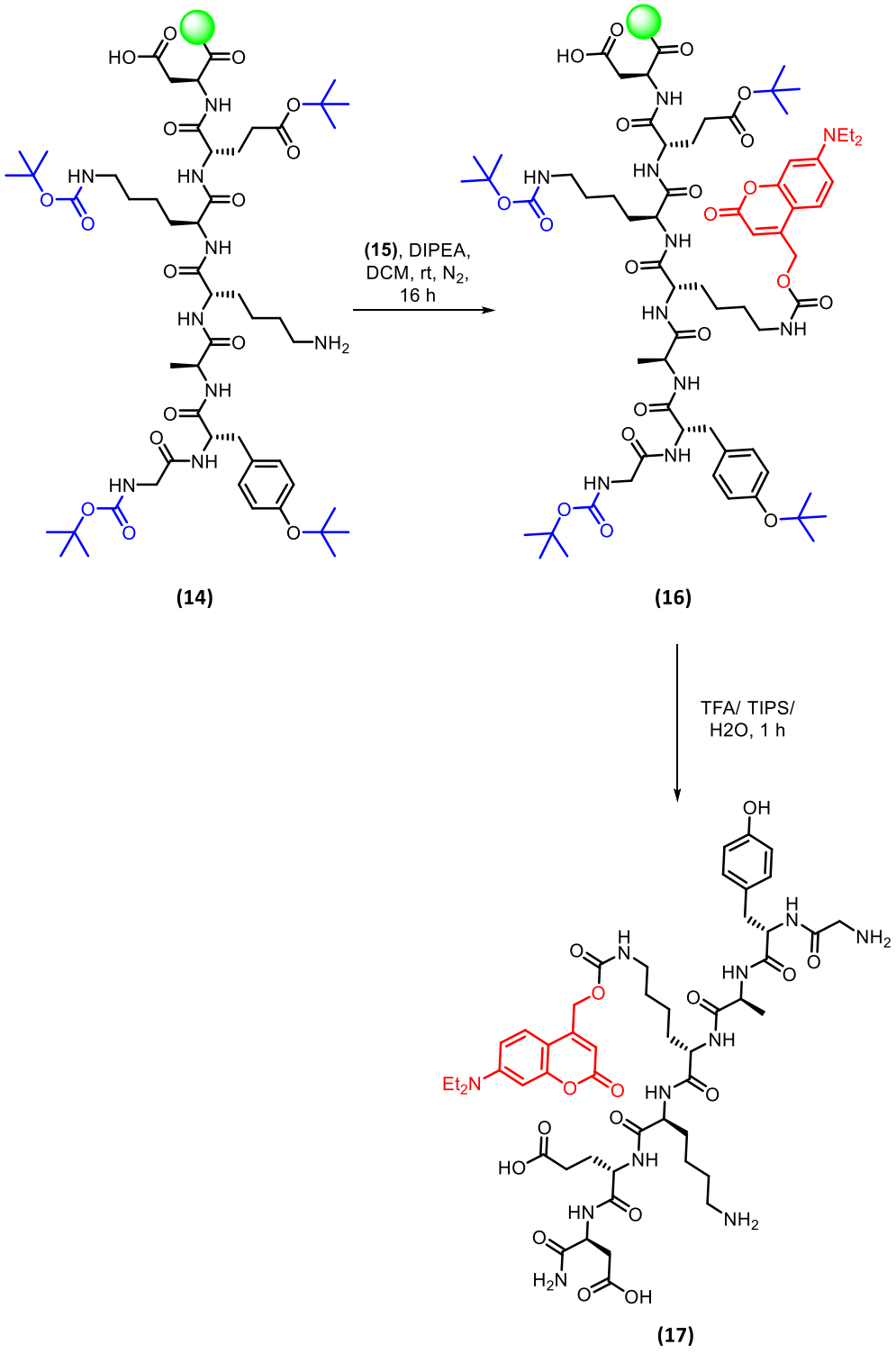

*Figure 30: A schematic of the modification strategy used to selectively install **(2)***

(17) was then analysed by LC-MS in order to verify that only the desired, single-modified product had been formed. The resulting UV 210 – 400 nm chromatogram is pictured in figure 31 below. Looking at this chromatogram, only a singular peak is observed, the corresponding mass spectrum of which matched the expected mass of **(17)** confirming that only the desired peptide had been formed.

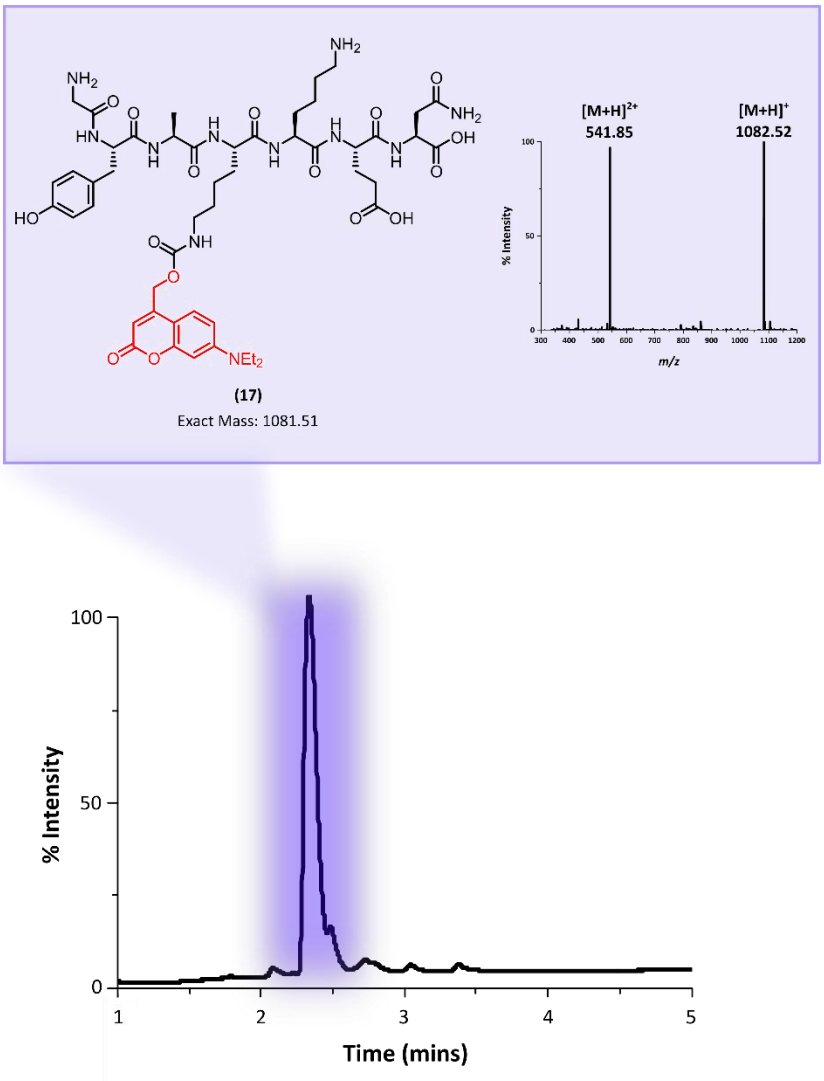

*Figure 31: The UV 210 – 400 nm chromatogram and corresponding mass spectrum confirmed that **(17)** had been successfully synthesised.*

4.9 Decaging study of **(17)**

4.9.1 Mechanistic considerations

Previously in this chapter, decaging studies were performed on the photocages synthesised during this work in order to elucidate kinetic information about their respective decaging processes. Now that the photocaged peptide **(17)** had been successfully synthesised, it was time to perform a decaging study, in order to investigate the kinetics of the decaging process when a photocage is applied to a peptide. As described in section 4.8 above, the photocage was installed on one of the lysine residues of this model peptide which was facilitated by a carbamate linker. This linker molecule means that the decaging mechanism of this reaction differs slightly to the photolysis mechanism when acetic acid is released. Although the heterolytic cleavage occurs through a similar mechanism, the carbamate linker facilitates the concomitant release of carbon dioxide alongside the peptide as seen in figure 32.[29]

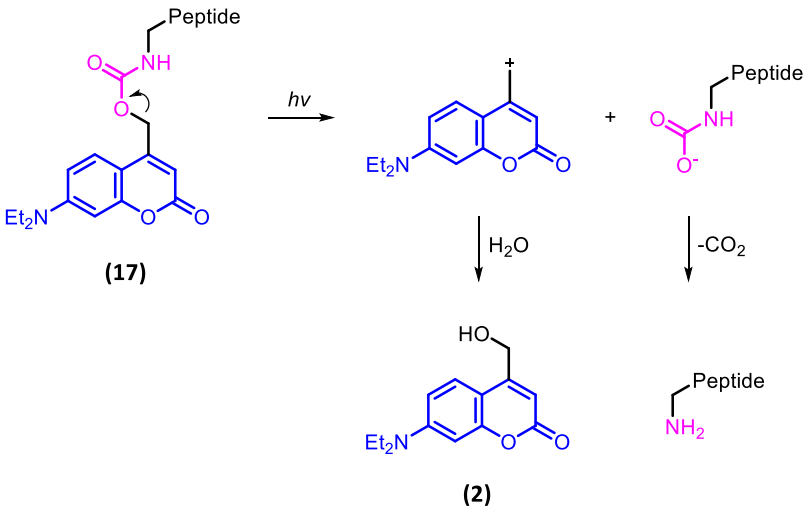

*Figure 32: The contrasting decaging mechanisms of **(1)** vs **(17)**.* [29]

4.9.2 Experimental considerations

Although the small molecule decaging studies utilised PBS, this study was performed in H2O as it was actually performed in advance of these studies, a limitation which will be resolved in future work. A 92.5 µM (0.1 mg/ml) solution of **(17)** in deionised water was created and placed in a glass vial equipped with a stirrer bar for irradiation within an EvoluChem PhotoRedOx Box. This solution was irradiated at 365 nm for 6 mins with a 10 µl aliquot taken every 30 seconds. The timepoint aliquots were then analysed using LCMS in order to determine conversion over time. Due to the strong UV 210 – 400 nm absorbance of photocage **(2)**, the ratio of the area under peaks of caged peptide **(17)** *vs* cleaved photocage **(2)**, in the UV 210 – 400 nm chromatograms were used to determine conversion, as both of these species contained the same 7-diethylamino coumarin chromophore. The proposed decaging reaction that occurred upon irradiation of **(17)** at 365 nm is depicted in figure 33 below.

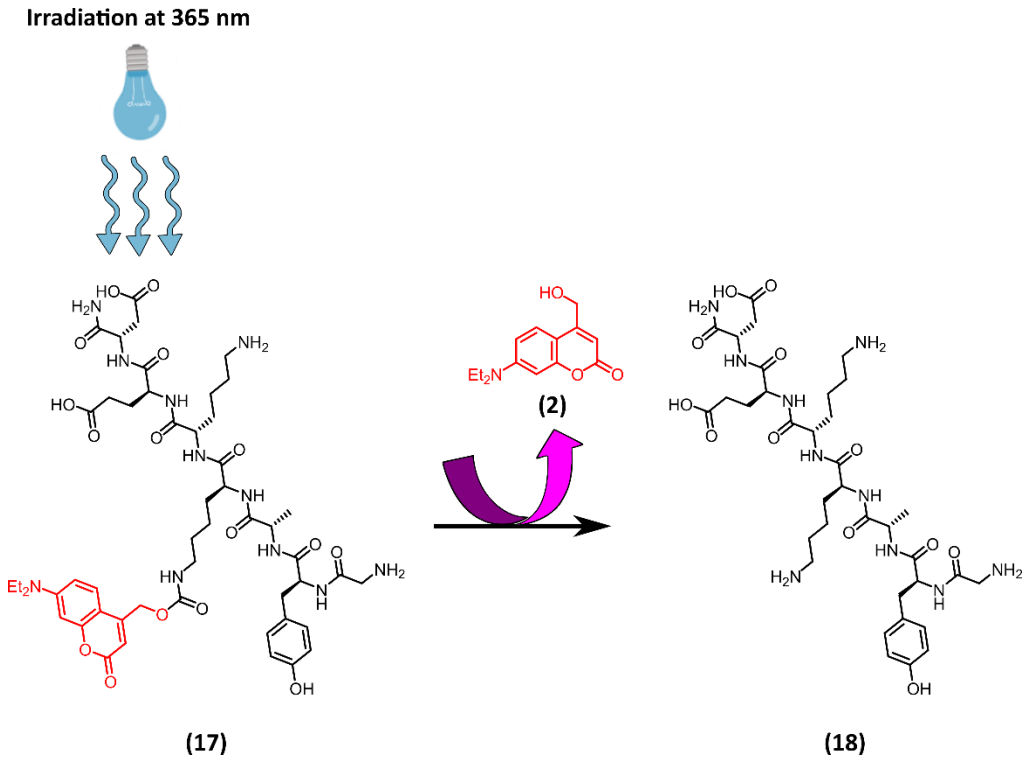

*Figure 33: The proposed decaging reaction that occurs upon the irradiation of **(17)** at 365 nm.*

4.9.3 Kinetic analysis

(17) was irradiated at 365 nm for 6 mins and conversion was determined by analysing the UV 210 – 400 nm chromatograms as described above. From this data we plotted Ln([**17**]) *vs* time in order to evaluate the decaging kinetics of this reaction as seen in figure 34 below. A linear fit (R^2 = 0.95) was obtained which confirmed that the decaging reaction was again a first-order process. The slope of this line gave us an experimental value for k_1 of 1.05 × 10^{-2} s^{-1}.

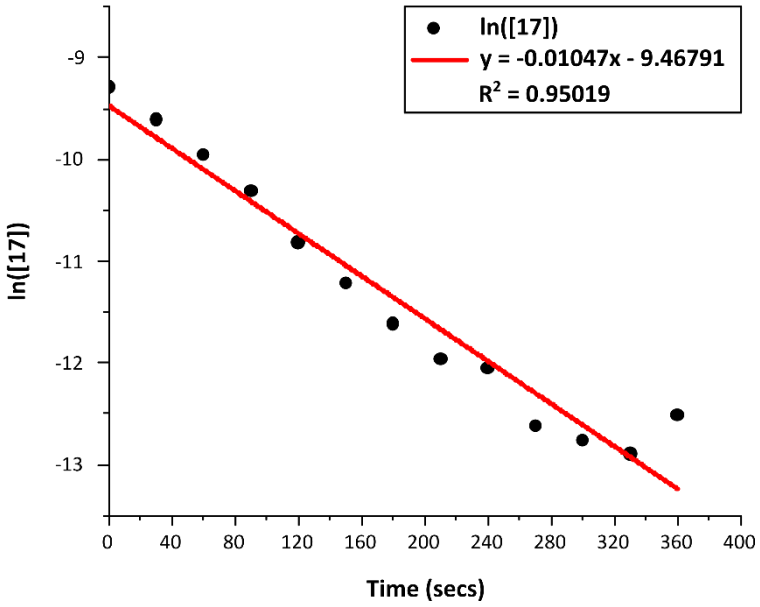

*Figure 34: The 1st order kinetic plot obtained for the decaging of **(17)** at 365 nm.*

We then plotted conversion *vs* time, alongside the corresponding fit modelled using COPASI as can be seen in figure 35 below.

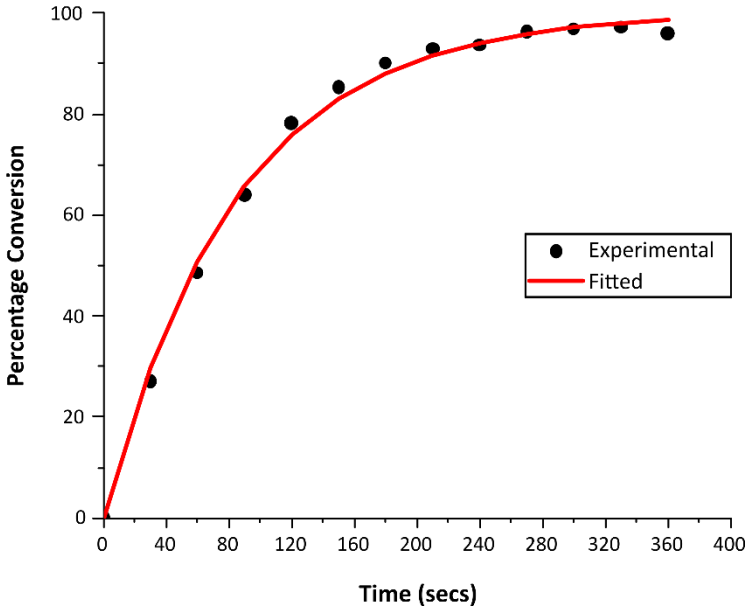

Figure 35: A plot conversion vs time obtained for the decaging of (17) upon irradiation at 365 nm.

4.9.4 Discussion

Coumarin photocages tethered to their cargo molecules *via* carbamate linkers have previously been shown to undergo rapid photolysis under near-UV irradiation, and thus the efficient decaging observed upon the irradiation of **(17)** at 365 nm was consistent with expectations.[29,30] As discussed in Section 4.3.2, first-order rate constants were calculated in this work to enable meaningful comparisons of decaging efficiency across different photocages under identical experimental conditions. As such the calculated rate constant of 6.88×10^{-3} s^{-1} for the release of acetic acid from **(1)** at 365 nm served as a useful benchmark for decaging efficiency. The photorelease of **(18)** from **(17)** was approximately 1.5-fold faster than this process, despite both of these species containing an identical 7-diethylamino coumarin photocage **(2)**. This observed increase in rate was likely due to the concomitant

release of CO_2 during the decaging of **(17)** leading to an increase in entropy, thus providing a thermodynamic driving force for faster photolysis.

4.10 The selective deprotection and functionalisation of glutamic acid

In section 4.8, the selective deprotection and subsequent functionalisation of lysine was discussed. Although this was successful, not every peptide sequence contains a lysine residue and so, having alternative functionalisable amino acids would be beneficial to the scope of this work. Once again, we preferred a commercially available amino acid with a side chain capable of undergoing a selective deprotection. With this in mind we decided upon glutamic acid. Typically, the carboxylic acid side chain of this amino acid is protected using a tert-butyl group,[24] which is cleaved during the global TFA deprotection at the end of the peptide synthesis process. However, another derivative, with its side chain protected by an allyl group is also commercially available.[24,31] This group can be cleaved using a palladium-mediated deprotection allowing for the selective activation of the glutamic acid side chain.[32] The structures of these two commercially available derivatives can be seen in figure 36 below.

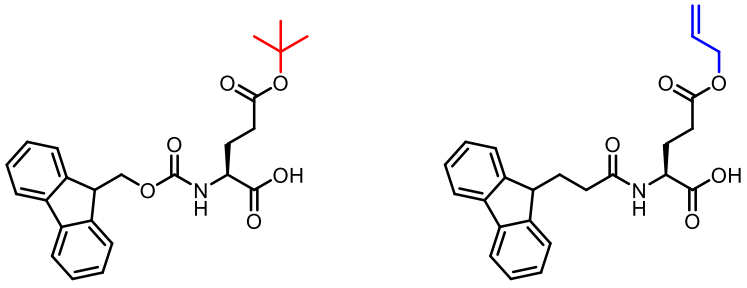

Fmoc-Glu(OtBu)-OH **Fmoc-Glu(OAll)-OH**

Figure 36: The structures of Fmoc-Glu(OtBu)-OH and its alternative derivative Fmoc-Glu(OAll)-OH. [24]

Model peptide **(19)** with the sequence BocNH-G-G-Y-Glu(OAll)-G was synthesised using automated solid phase peptide synthesis. Once again, the peptide was left uncleaved from the resin so that subsequent selective deprotection of glutamic acid and photocage installation could be performed, with the N-terminus being protected with a Boc group to prevent it from participating in unwanted side reactions. The structure of this peptide can be seen in figure 37 below.

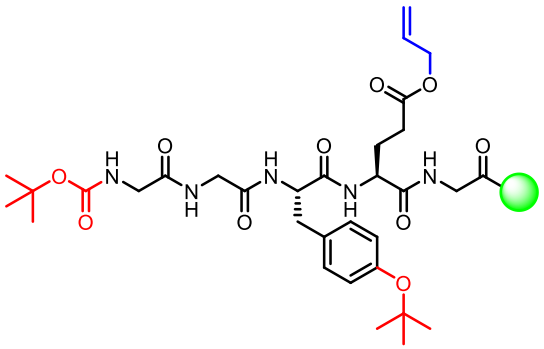

(19)

*Figure 37: The structure of resin-bound, fully protected model peptide **(19).***

Deprotection of the O-allyl, as seen in figure 38 below, was achieved by incubating **(19)** with $Pd(PPh_3)_4$ and phenyl silane in DMF for 1 h. Prior to use, the $Pd(PPh_3)_4$ was washed with methanol to remove any palladium oxide impurities which may have impacted the reaction, with a colour change from brown to bright yellow observed upon washing. Notably it was found, that if this wash step was not performed, the deprotection did not go to completion.

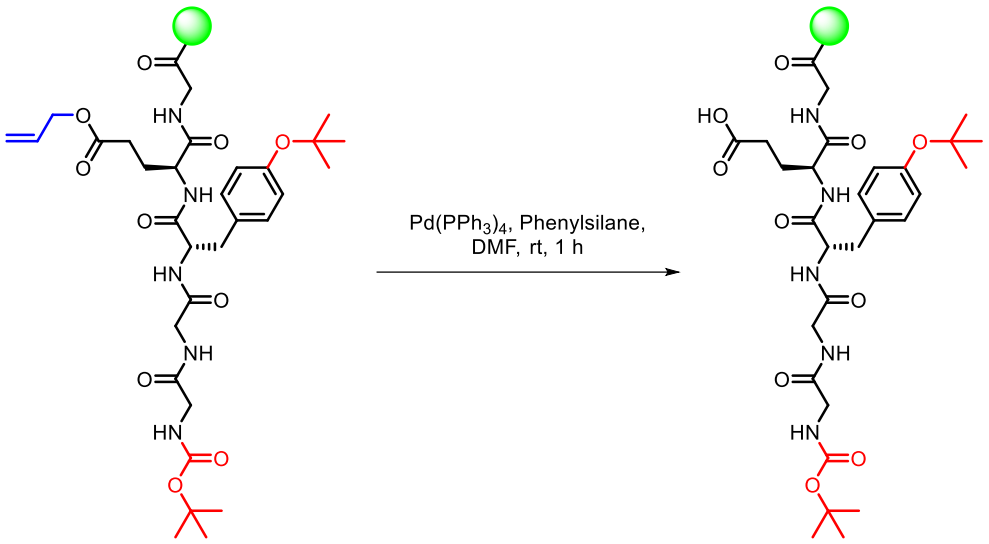

(19) **(20)**

Figure 38: The conditions utilised for the selective deprotection of Glu(OAll).

Following selective deprotection of the glutamic acid residue, it was time to attempt to install a photocage at this site. When selecting a suitable coupling reaction, there were several factors to consider. Primarily, a reliable coupling strategy, capable of producing the desired product in high yields was required. Additionally, due to the resin bound nature of the peptide, it was desirable that any by-products of the reaction be soluble, so that they could simply be removed by washing. Consequently, we decided to employ a Steglich esterification.[33] This reaction involves the activation of a carboxylic acid with a coupling reagent such as DCC and a catalytic quantity of DMAP, in order to form a reactive intermediate which then undergoes nucleophilic attack by an alcohol to form the corresponding ester. Additionally, the photocages synthesised in the previous chapters all contained hydroxyl groups, meaning that additional synthesis was not required in preparation for peptide coupling. Brominated coumarin derivative **(22)** was selected as a model photocage for this reaction, as we had ample quantities of this compound available to us at the time. The conditions used can be seen in figure 39 below. The coupling reagent diisopropylcarbodiimide (DIC) was employed rather

than the aforementioned DCC, as this reagent, and its byproducts are liquids and soluble in organic solvents, in contrast to DCC, making them easy to remove at the conclusion of the reaction by washing with organic solvent.

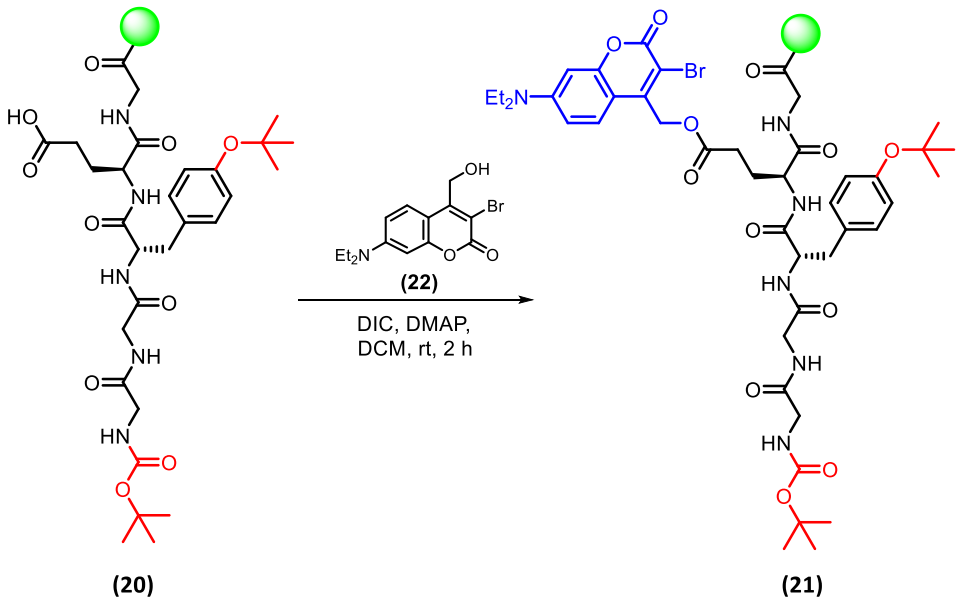

*Figure 39: The conditions employed to selectively couple **(22)** to the exposed glutamic acid side chain of **(20)**.*

Following the installation of **(22)**, a global TFA-mediated cleavage was performed in order to cleave the peptide from the resin and remove any remaining protecting groups. This afforded the final photocaged peptide **(23)**, as seen in figure 40 below.

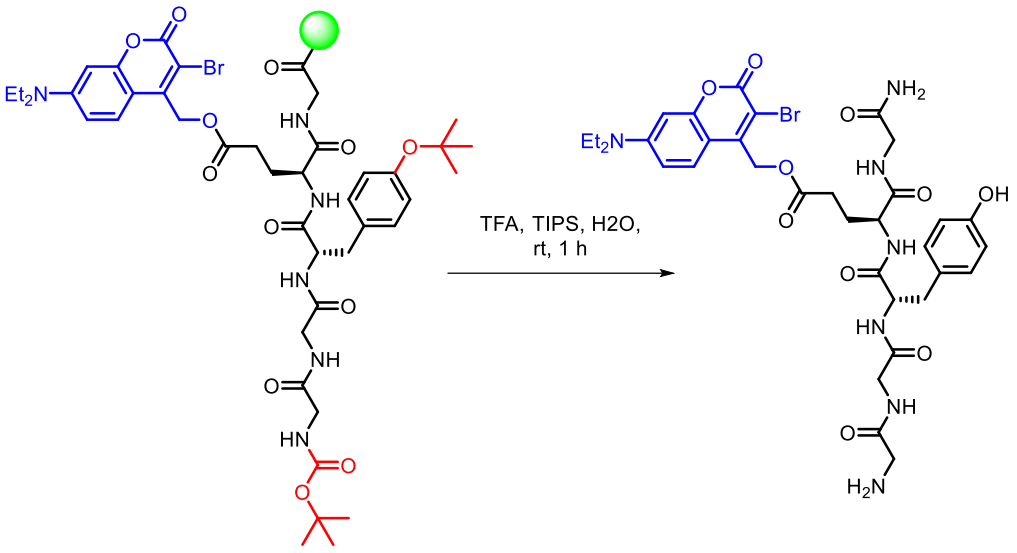

(21) **(23)**

*Figure 40: The TFA cleavage conditions utilised to afford final photocaged peptide **(23).***

Following TFA cleavage, **(23)** was dissolved in 10% acetic acid solution, frozen and lyophilised. This ensured that the peptide was isolated as the acetate salt,[34] which improves its water solubility and improves biocompatibility compared to the trifluouroacetate salt which is considerably more acidic.[35,36] LC-MS analysis confirmed that the major peak A was indeed **(23)** indicating that this peptide had been caged successfully, as can be seen in figure 41 below. Two additional peaks **(B)** and **(C)**, were also present, with **(B)** corresponding to coumarin photocage **(22)**. The identity of peak **(C)** could not be elucidated as its corresponding mass did not match that of the starting material nor any of the predicted products. Although peak **(A)** was the largest by area, it is important to note that the presence of its photocage **(22)** means it absorbs strongly in this region. Meaning that we could not determine what percentage of the sample consisted of the desired product vs. the unmodified product **(24)**. Nonetheless, the large difference in retention times meant that that purification by reverse phase

chromatography would likely have been easy to achieve. However, due to time constraints neither purification nor a decaging study were performed.

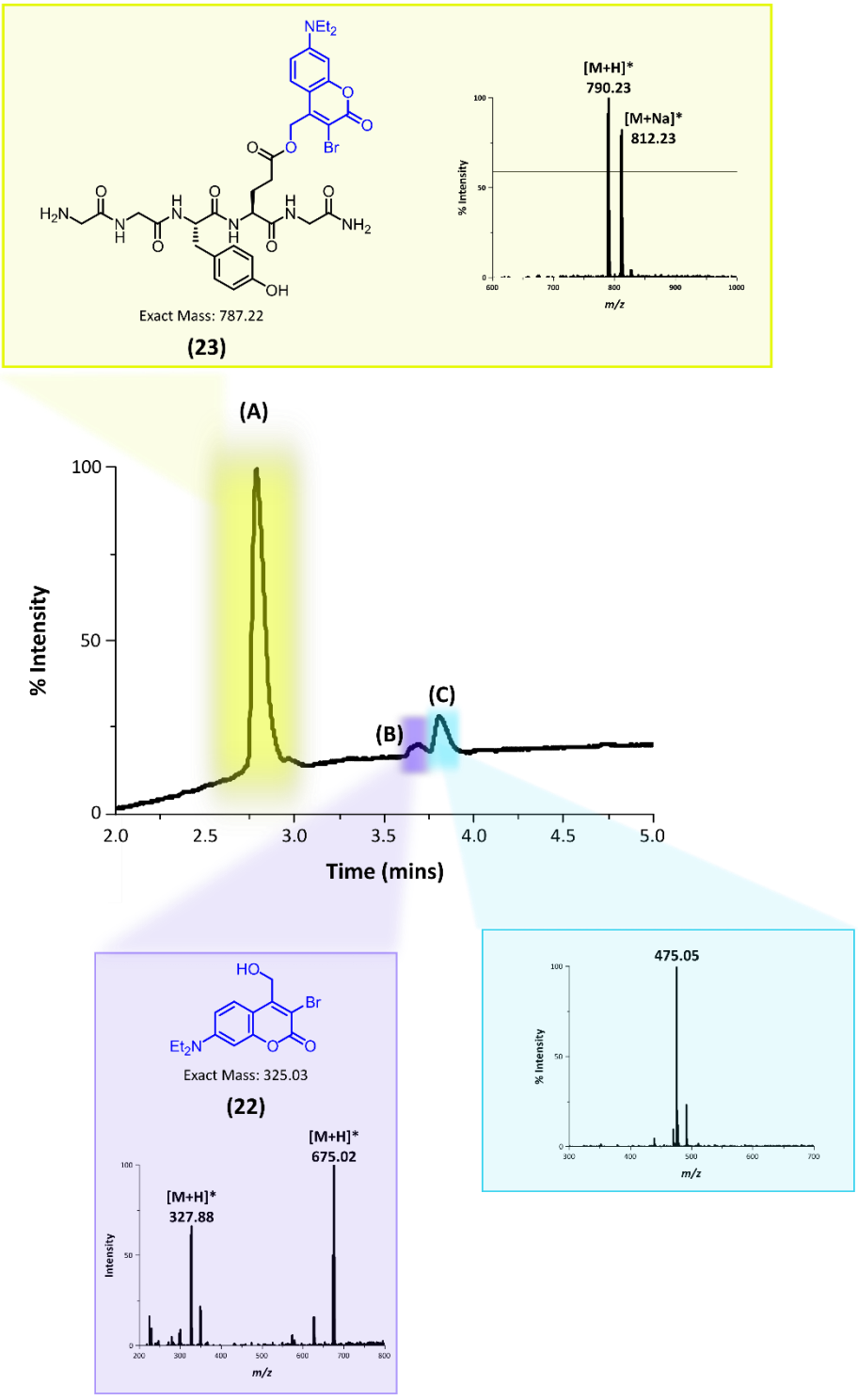

*Figure 41: The 210 – 400 nm and corresponding mass spectra obtained for **(23)**.*

4.11 Conclusions

In this chapter, decaging studies were conducted on the photocages synthesised in the previous chapters in order to determine their efficiencies. Conventionally, decaging quantum yields are reported,[2,6,7] however, their determination requires the use of specialised techniques such as actinometry making them more difficult to calculate.[8,9] As such, we decided to calculate first-order rate constants (k_1) as not only is this parameter more accessible, but it would also give us direct measure of decaging performance under our exact irradiation conditions, thereby improving the predictive value for future photoresponsive materials tested with the same setup.

Our initial decaging study was performed on **(1)**, as its decaging ability at both 365 and 405 nm had previously been well characterised in literature.[2,3] As such, calculating first-order rate constants for these processes would serve as useful benchmarks, with which to compare the other photocages. **(1)** was shown to efficiently release acetic acid at both 365 and 405 nm with values of 6.88×10^{-3} and 1.06×10^{-2} s^{-1} calculated for k_1 for these processes respectively. These values indicated that decaging at 405 nm was approximately 1.5-fold faster than the corresponding process at 365 nm. This was in agreement with literature and was significant to the biocompatibility of this photocage as 405 nm is lower in energy and thus less cytotoxic than 365 nm.[2,3,10]

We then assessed photocleavable linker **(4)** which had been designed and synthesised to overcome the limitations of **(6)**, which had previously been developed by Anseth & Azagarsamy and had failed to exhibit any decaging activity under our experimental conditions.[11] Not only was **(4)** shown to efficiently decage at 365 and 405 nm, but the calculated 1st order rate constants of k_{365}= 1.20×10^{-2} s^{-1} and k_{405}= 9.00×10^{-2} s^{-1} indicated

that this photocleavable linker outperformed **(1)** at both wavelengths, with the decaging processes being 1.7 and 8.5-fold faster respectively. The large gain at 405 nm is particularly valuable for envisioned biological use, enabling shorter irradiation times and reducing risks such as photobleaching.[37,38]

We then turned our attention to **(7)**, which had been synthesised based on the work of Kele et al.,[7] and its novel photocleavable linker analogue **(10)**. Unlike the aforementioned blue-light absorbing photocages, these compounds did not exhibit efficient decaging under our experimental conditions at the desired wavelength of 525 nm. This was initially unexpected as Kele et al., had previously reported that the related compound **(7-I)** exhibited full photorelease of 3,5-dimethyl benzoic acid within 20 – 25 mins of irradiation at a similar wavelength.[7] However, during our decaging studies, Feringa et al. reported that the decaging of **(7-I)** was 5-fold less efficient than had been previously reported when the cargo molecule was replaced with acetic acid.[16] This corroborated our finding that the photorelease of acetic acid by **(7)** upon irradiation with green light was inefficient. In fact, we did notice an improvement in efficiency when the cargo molecule of **(10)** was exchanged for 3,5-dimethyl benzoic acid, which allowed us to calculate a k_1 of 7.13×10^{-6} s^{-1} for the photorelease of this molecule. However, this rate was at least three orders of magnitude slower than the values calculated for the decaging of **(1)** and **(4)** rendering **(10)** too slow for our desired application. However, Feringa et al. did report that substituting the external carbon of the 4-methyl group of **(7-I)** with a prenyl substituent allowed for the stabilisation of the positive charge formed during the decaging process, allowing for a 7.4-fold increase in decaging efficiency.[16] Thus, it is likely that if we introduced this substituent to **(10)** we would observe a significant enhancement to the rate of decaging, making this compound more suitable for incorporation into photoresponsive materials.

We then developed and demonstrated solid-phase strategies for peptide photocaging. For model peptide **(13)**, we chose lysine as the caging site based on its prevalence[25] (makes up approximately 6% of residues in the human proteome) and frequent functional importance in locations such as active sites.[26,27] We decided to employ a strategy of orthogonal deprotection on the solid phase, as this methodology would allow us to specifically target desired residues of interest, as well as facilitate easy purification as any reagents could be removed by performing a wash step at the conclusion of the reaction. Lysine(DDe) was incorporated into model peptide **(13)** and selectively deprotected with a mixture of hydroxylamine and imidazole in *N*-methyl-2-pyrrolidinone.[28] Following this, the free amine was coupled to activated photocage **(15)**. The resulting photocaged peptide **(17)**, was then decaged at 365 nm and a value for k_1 of 1.05×10^{-2} s^{-1} was obtained within the range spanned by **(1)** and **(4)** at this wavelength. This demonstrated the practicality of performing the small molecule decaging studies prior to peptide studies.

We also targeted the side chain of glutamic acid in model peptide **(19)**. Once again, we decided to employ an orthogonal deprotection strategy to achieve this. An O-Ally protected glutamic acid residue was incorporated into **(19)** and selectively deprotected using $Pd(PPh3)_4$ and $PhSiH_3$.[32] Following this photocage **(22)** was successfully coupled using a Steiglich esterification. Although the resulting photocaged peptide **(23)** was not fully purified, this was largely due to time constraints, and it is likely that reverse-phase chromatography would have been successful.

In summary, the blue-light-absorbing photocages **(1)** and **(4)** delivered robust, efficient decaging at 365 and 405 nm, enabling both photoactivation (through the use of **(1)**) and photodeactivation (through the use of **(4)**) of peptides within a material. The green-light-

absorbing photocages **(7)** and **(10)** were inefficient at 525 nm under our conditions, however, literature-guided structural modification (4-prenyl substitution) offers a plausible path to significantly increasing decaging rates.[16,18] Once improved, we have laid out successful strategies for the photocaging of both lysine and glutamic acid residues, ensuring that we can successfully photocage a wide array of bioactive peptide substrates in the future.

4.12 Experimental

4.12.1 General Considerations

Proton nuclear magnetic resonance (^{1}H NMR) spectra were recorded on a Jeol ECX-400 (400 MHz) or Bruker AVIIIHD (500 MHz) spectrometer. Carbon nuclear magnetic resonance (^{13}C NMR) spectra were recorded on a Jeol ECX-400 (100 MHz) spectrometer. NMR shifts were assigned using COSY, HSQC and HMBC spectra. All chemical shifts are quoted on the δ scale in ppm using residual solvent as the internal standard (^{1}H NMR: $CDCl_3$ = 7.26; MeOD = 3.31; D_2O = 4.69; DMSO-d_6 = 2.50 and ^{13}C NMR: $CDCl_3$ = 77.16, MeOD = 49.00, DMSO-d_6 = 39.52). Coupling constants (*J*) are reported in Hz with the following splitting abbreviations: s = singlet, d = doublet, t = triplet, q = quartet, sept = septet, m = multiplet, app = apparent, br = broad. High resolution electrospray ionisation (ESI) mass spectra (HRMS) were recorded on a Bruker Campact TOF-MS or a Jeol AccuTOF GCx-plus spectrometer. Nominal and exact *m/z* values are reported in Daltons.

Thin layer chromatography (TLC) was carried out using aluminium backed sheets coated with 60 F_{254} silica gel (Merck). Visualization of the silica plates was achieved using a UV lamp (λ_{max} = 254, 302, or 366 nm), and/or ammonium molybdate (5% in 2M H_2SO_4), and/or potassium permanganate (5% $KMnO_4$ in 1M NaOH with 5 % potassium carbonate), and/or ninhydrin (1.5% ninhydrin, 3% AcOH in *n*-butanol), and/or bromocresol green (0.4% bromocresol green

in ethanol, basified till blue with 0.1 M NaOH). Flash column chromatography was carried out using Geduran Si 60 (40 – 63 µm) (Merck). Mobile phases are reported as % volume of more polar solvent in less polar solvent.

Anhydrous solvents were dried using a PureSolv MD 7 Solvent Purification System. Deionised water was used for chemical reactions. All other solvents were used as supplied (Analytical or HPLC grade), without prior purification. Reagents were purchased from Sigma-Aldrich and used as supplied, unless otherwise indicated. Brine refers to a saturated solution of sodium chloride. Petrol refers to the fraction of petroleum ether boiling in the range 40-60 °C. Anhydrous magnesium sulfate ($MgSO_4$) was used as the drying agent after reaction workup unless otherwise stated.

4.12.2 Small molecule synthesis

The synthesis of (26)

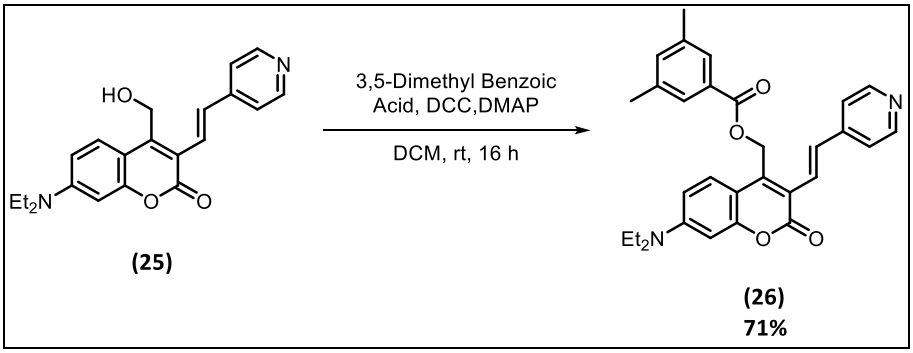

(25) (100 mg, 0.29 mmol, 1 eq.) was dissolved in DCM (15 ml). 3,5-Dimethylbenzoic acid (53 mg, 0.35 mmol, 1.2 eq.), DCC (72 mg, 0.35 mmol, 1.2 eq.) and DMAP (43 mg, 0.35 mmol, 1.2 eq.) were added and the reaction was stirred at rt for 16 h. The reaction mixture was then diluted with brine (20 ml) and the product was extracted with DCM (3 × 20 ml). The combined organics were concentrated *in vacuo*, and the residue redissolved in MeCN (10 ml) before being left in the freezer for 1 h in order to precipitate any residual DCU. This solution was then

filtered under vacuum, and the filtrate was concentrated *in vacuo*. The residue was then purified using flash column chromatography (20-100% EtOAc: petrol), and pure fractions were concentrated *in vacuo* affording the product as an orange solid with a yield of 99 mg, 0.21 mmol (71%).

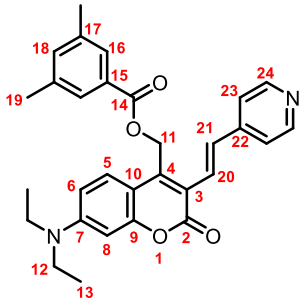

^{1}H NMR (400 MHz, C*D*Cl$_3$) δ 8.56-8.48 (m, 2H, H$_{24}$), 7.66 (d, *J* = 16.1 Hz, 1H, H$_{21}$/H$_{22}$), 7.62 (m, 2H, H$_5$, H$_{16}$), 7.52 (d, *J* = 16.1 Hz, 1H, H$_{21}$/H$_{22}$), 7.38-7.32 (m, 2H, H$_{23}$), 7.17 (s, 1H, H$_{18}$), 6.64 (dd, *J* = 9.2, 2.6 Hz, 1H, H$_6$), 6.51 (d, *J* = 2.6 Hz, 1H, H$_8$), 5.61 (s, 2H, C**H**$_2$OR, H$_{11}$), 3.42 (q, *J* = 7.1 Hz, 4H, N(C**H**$_2$CH$_3$)$_2$, H$_{12}$), 2.28 (s, 6H, H$_{19}$), 1.21 (t, *J* = 7.1 Hz, 6H, N(CH$_2$C**H**$_3$)$_2$ H$_{13}$).

Spectroscopic data were in agreement with [7]

The synthesis of **(27)**

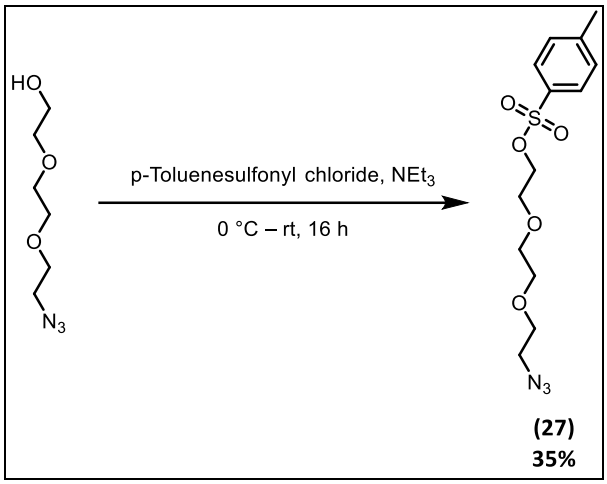

2-[2-(2-azidoethoxy)ethoxy]ethan-1-ol (100 mg, 0.57 mmol, 1 eq.), was dissolved in DCM (5 ml). NEt_3 (240 µl, 1.71 mmol, 3 eq.) was added and the reaction mixture was cooled to 0 °C. In the meantime, a solution of *p*-toluene sulfonyl chloride (163 mg, 1.14 mmol, 1.5 eq.) in DCM (5 ml) was created. and added dropwise over the course of 5 mins. Upon complete addition, the reaction was warmed to room temperature and stirred for an additional 16 h. At this point the reaction mixture was diluted with aqueous HCl solution (1 M, 10 ml) and extracted with DCM (3 × 15 ml). The combined organics were washed with $NaHCO_3$ (20 ml) followed by brine (20 ml), before being dried over $MgSO_4$, filtered and concentrated *in vacuo*. The crude product was purified by flash column chromatography (0 – 60% EtOAc: petrol) affording the product as a colourless oil with a yield of 66 mg, 0.2 mmol (35%).

^{1}H NMR (400 MHz, C*D*Cl_3) δ 7.83 – 7.75 (m, 2H, Ar**H**), 7.33 (d, *J* = 7.8 Hz, 2H, Ar**H**), 4.19 – 4.14 (m, 2H, PEG**H**), 3.71 – 3.67 (m, 2H, PEG**H**), 3.63 (dd, *J* = 5.6, 4.5 Hz, 2H, PEG**H**), 3.59 (s, 4H, PEG**H**), 3.40 – 3.30 (m, 2H, PEG**H**), 2.43 (s, 3H, C**H**$_3$).

HRMS ESI *m/*z: calc for $C_{13}H_{19}N_3O_5S$ $[M+Na]^+$ 352.0938, $[M+K]^+$ 368.0677; Obs $[M+Na]^+$ 352.0935, $[M+K]^+$ 368.0679

Spectroscopic data were in agreement with [39]

The synthesis of **(12)**

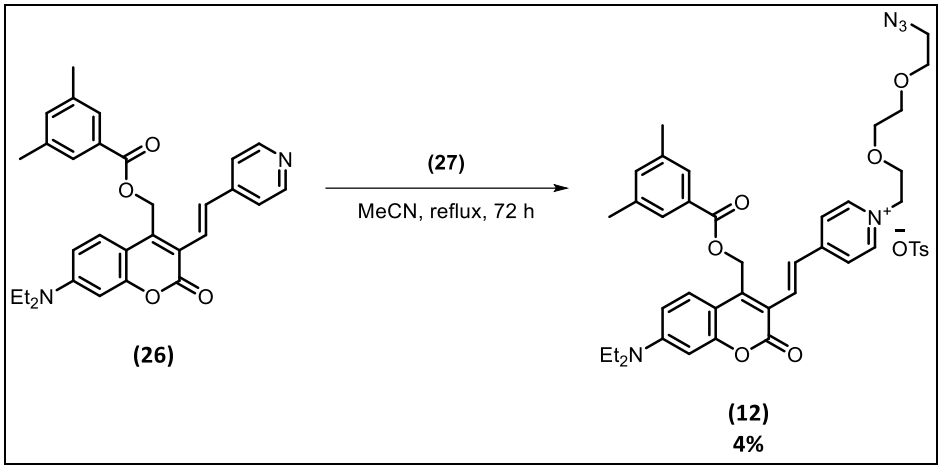

(26) (29 mg, 0.06 mmol, 1 eq.) was dissolved in MeCN (10 ml). **(27)** (60 mg, 0.09 mmol, 3 eq.) was added and the reaction mixture was refluxed for 72 h. After cooling to rt, the solvent was removed *in vacuo* and the residue was redissolved in EtOAc (2 ml). This solution was added dropwise to ice-cold diethyl ether (8 ml) to precipitate the product, which was then pelleted by centrifugation (4000 rpm, 6 mins) and the supernatant removed, affording a red solid, which was further purified by flash column chromatography (5-100% MeOH:DCM) to afford the product as a dark red solid with a yield of 2 mg, 2.5 µmol (4%).

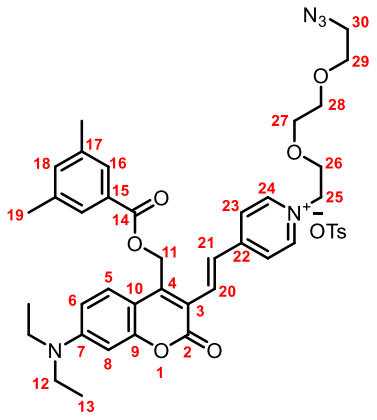

^{1}H NMR (400 MHz, MeCN-d_3) δ 8.46 (d, *J* = 7.0 Hz, 2H, Pyr**H**$_{24}$), 8.04 (d, *J* = 15.7 Hz, 1H, Alkene**H**), 8.01-7.95 (m, 3H, Alkene**H**, Pyr**H**$_{23}$), 7.78 (d, *J* = 9.3 Hz, 1H, Ar**H**$_5$), 7.60 – 7.53(overlapping, 4H, Tosylate/ Ar**H**$_{16}$), 7.22 (s, 1H, Ar**H**$_{18}$), 7.11 (d, *J* = 7.7 Hz, 2H, Tosylate,), 6.78 (dd, *J* = 9.3, 2.6 Hz, 1H, Ar**H**$_6$), 6.54 (d, *J* = 2.6 Hz, 1H, Ar**H**$_8$), 5.72 (s, 2H, C**H**$_2$OR, H$_{11}$), 4.54 – 4.49 (m, 2H, PEG), 3.89 – 3.84 (m, 2H, PEG), 3.57 –3.43 (Overlapping, 10H, PEG/H$_{12}$), 3.29 – 3.24(m, 2H, PEG), 2.29 (s, 3H, CH_3, Tosylate), 2.25 (s, 6H, CH_3, H$_{19}$), 1.17 (t, *J* = 7.1 Hz, 6H, H$_{13}$).

HRMS ESI *m/z*: calc for $C_{36}H_{42}N_5O_6$ $[M]^+$ 640.3130; Obs $[M]^+$ 640.3161

The synthesis of (15)

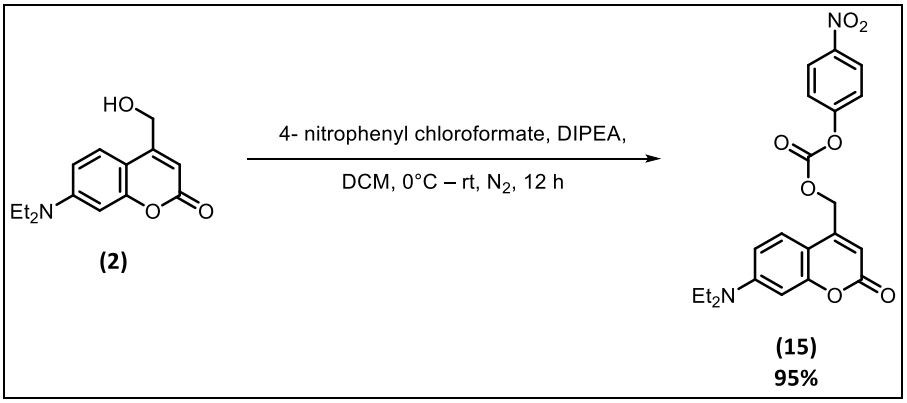

A solution of **(2)** (500 mg, 2.02 mmol, 1 eq.) and 4-nitrophenyl chloroformate (814 mg, 4.04 mmol, 2 eq.) in DCM (50 ml) was placed under N_2 and protected from light prior at 0 °C. DIPEA (700 µL, 4.04 mmol, 2 eq.) was added dropwise and the resulting solution was stirred at 0 °C for 15 mins. The reaction mixture was then allowed to warm to room temperature and stirred for an additional 16 h. At this point the precipitate that had formed was dissolved with additional DCM (50 ml) before stirring for a further 1 h. The crude reaction mixture was concentrated *in vacuo*, yielding a brown solid. which was purified by flash column chromatography (DCM), with the pure fractions being combined and concentrated to afford the product as a yellow solid with a yield of 792 mg, 1.92 mmol (95%).

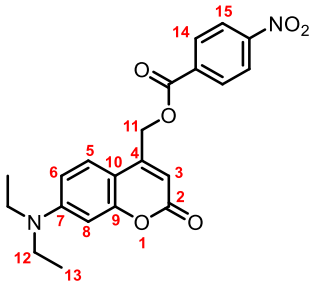

^{1}H NMR (400 MHz, $CDCl_3$) δ 8.30 (d, *J* = 9.2 Hz, 2H, $NO_2Ar\mathbf{H}_{15}$), 7.41 (d, *J* = 9.2 Hz, 2H, $NO_2Ar\mathbf{H}_{14}$), 7.30 (d, *J* = 9.0 Hz, 1H, Ar**H**$_5$), 6.60 (dd, *J* = 9.0, 2.6 Hz, 1H, Ar**H**$_6$), 6.53 (d, *J* = 2.6 Hz, 1H, Ar**H**$_8$), 6.22 (s, 1H, Ar**H**$_3$), 5.39 (s, 2H, C**H**$_2$OR, H_{11}), 3.42 (q, *J* = 7.1 Hz, 4H, $N(C\mathbf{H}_2CH_3)_2$), H_{12}), 1.21 (t, *J* = 7.1 Hz, 6H, $N(CH_2C\mathbf{H}_3)_2$, H_{13}).

HRMS ESI *m/z*: calc for $C_{21}H_{20}N_2O_7$ $[M+Na]^+$ 435.1163, $[M+K]^+$ 451.0902; Obs $[M+Na]^+$ 435.1177, $[M+K]^+$ 451.0914

Spectroscopic data were in agreement with [40]

4.12.3.1 General peptide synthesis

Peptide synthesis was carried out *via* Fmoc SPPS using a CEM Liberty Lite Automated Microwave Peptide Synthesiser, according to the manufacturer's standard protocols. Briefly, Fmoc-protected amino acids (5.5 equiv., 0.2 M in DMF) were coupled in the presence of DIC (15 equiv.) and Oxyma Pure (6 equiv.), as coupling agent and base respectively, under microwave irradiation at a temperature of 90 °C for 2 minutes. Where required, the amino acids Fmoc-Lys(Dde)-OH, Fmoc-Glu(OAll)-OH, were installed for peptide functionalisation and Boc-Gly-OH at peptide N-termini to prevent side reactions at the *N*-terminus. Fmoc deprotection was performed using 20% piperidine in DMF at 90 °C for 60 seconds. Syntheses were performed on a 0.1 mmol scale, using Rink Amide MBHA resin (*C*-terminal amide, 0.5 mmol/g, 1% DVB, 100-200 mesh, Fluorochem). Following synthesis, the resin was washed

sequentially using DMF (3 × 15 ml), followed by DCM (3 × 15 ml), and finally methanol (3 × 15 ml). Following these washes, the peptides were retained on resin and stored in the freezer, in order to allow for subsequent functionalisation with photocages.

4.12.3.2 Lys(Dde) Deprotection

The following procedure describes the selective deprotection of a single Lys(Dde) residue within a peptide sequence retained on rink amide resin, performed on a 0.1 mmol scale. $NH_2OH.HCl$ (166 mg, 2.4 mmol, 24 eq.) and imidazole (130 mg, 2.0 mmol) were dissolved in *N*-methyl-2-pyrrolidinone (3 ml). The mixture was sonicated until complete dissolution prior to its addition to a suspension of peptide on resin (200 mg, 0.1 mmol) in DCM (2 ml). The resulting mixture was stirred for 16 h to allow for full Dde deprotection. At the end of this period, the resin was filtered in order to remove any soluble impurities before being washed with DCM (3 × 10 ml), dried under vacuum and stored at -20 °C ready for use.

4.12.3.3 Glu(OAll) Deprotection

The following procedure describes the selective deprotection of a single Glu(OAll) residue within a peptide sequence retained on rink amide resin, performed on a 0.1 mmol scale. $Pd(PPh_3)_4$ (29 mg, 0.025 mmol, 0.25 eq.) was washed with methanol (25 ml) under a flow of nitrogen in order to remove palladium oxide from its surface which was indicated by a colour change from brown to bright yellow. The washed palladium was then transferred to a stirring solution of phenyl silane (308 µl, 2.5 mmol, 25 eq.) in DMF (2 ml), prior to the addition of peptide on resin (0.1 mmol, 1 eq.). The reaction mixture was stirred at rt for 1 h after which point it was filtered in order to remove any soluble impurities. The resin was washed with DCM (3 × 10 ml), dried under vacuum and stored at -20 °C ready for use.

4.12.3.4 TFA Global Deprotection

The following procedure details the global deprotection of acid labile protecting groups present on the side chains of a peptide. Additionally, this procedure results in the cleavage of the peptide from rink amide resin, liberating its C terminus in the form of an amide.

Peptide on resin (0.1 mmol, 1 eq.) was suspended in a cleavage cocktail of (90% TFA, 5% H_2O, 5% Triisopropyl silane, 20 ml) and stirred at rt for 2 h. The resin was then filtered and washed with DCM (3 x 50 mL). The filtrate was concentrated *in vacuo* to a volume of approximately 2 ml, which was then added dropwise into ice cold diethyl ether (50 ml) to precipitate the peptide. The precipitate was pelleted by centrifugation (4000 rpm, 6 mins) and the supernatant removed. The pellets were then resuspended in cold diethyl ether (50 ml), and centrifuged again, affording a solid which was allowed to air dry for 15 mins. This solid was then dissolved in 20% acetic acid in water (25 ml) and flash frozen using liquid N_2, before being dried by lyophilisation.

4.12.4 The synthesis of photocaged peptides

4.12.4.1 The synthesis of **(17)**

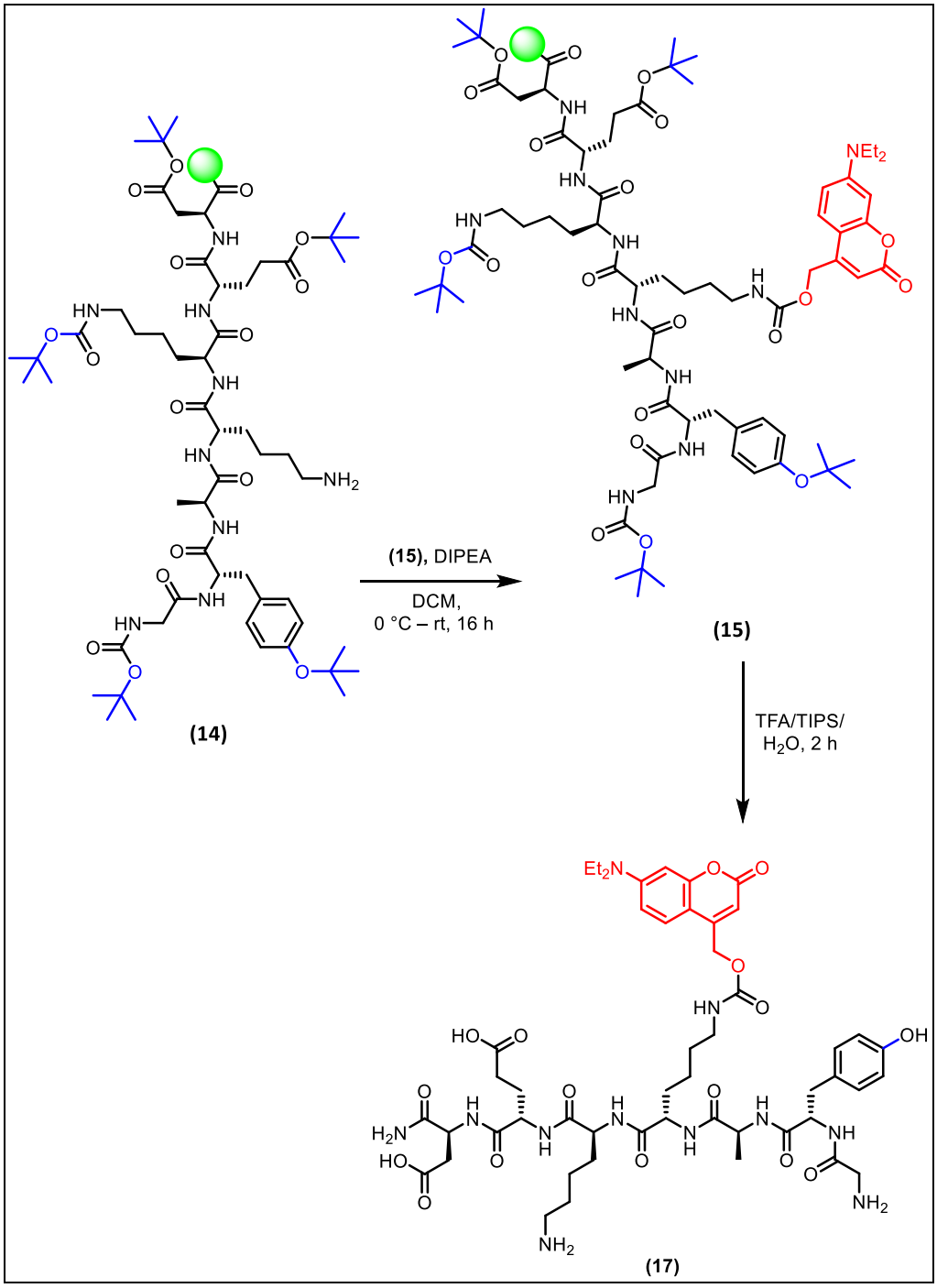

A peptide of the sequence Boc-NH-G-Y-A-K(Dde)-K-E-D was synthesised according to the protocol outlined in section 14.12.1 above. 50 mg (0.025 mmol) was subjected to the Lys(Dde) deprotection conditions described in 4.12.2 activating the side chain of its lysine residue. The resin was then suspended in DCM (5ml), protected from light and cooled to 0 °C. **(15)** (170

mg, 0.4 mmol, 16 eq.) was then added prior to dropwise addition of DIPEA (49 µL, 0.28 mmol, 11 eq.). The reaction mixture was the allowed to warm to rt and stirred for a further 16 h in the dark. The resin was then filtered and washed with DCM (3 x 25 ml) before being subjected to the global TFA deprotection outlined in section 4.12.4 above. Following lyophilisation, the desired product was obtained as a yellow solid with a yield of 11 mg, 0.01 mmol (40%)

m/z: $[M+2H]^{2+}$ 541.85, $[M+H]^{+}$ 1082.52

4.12.4.2 The synthesis of **(23)**

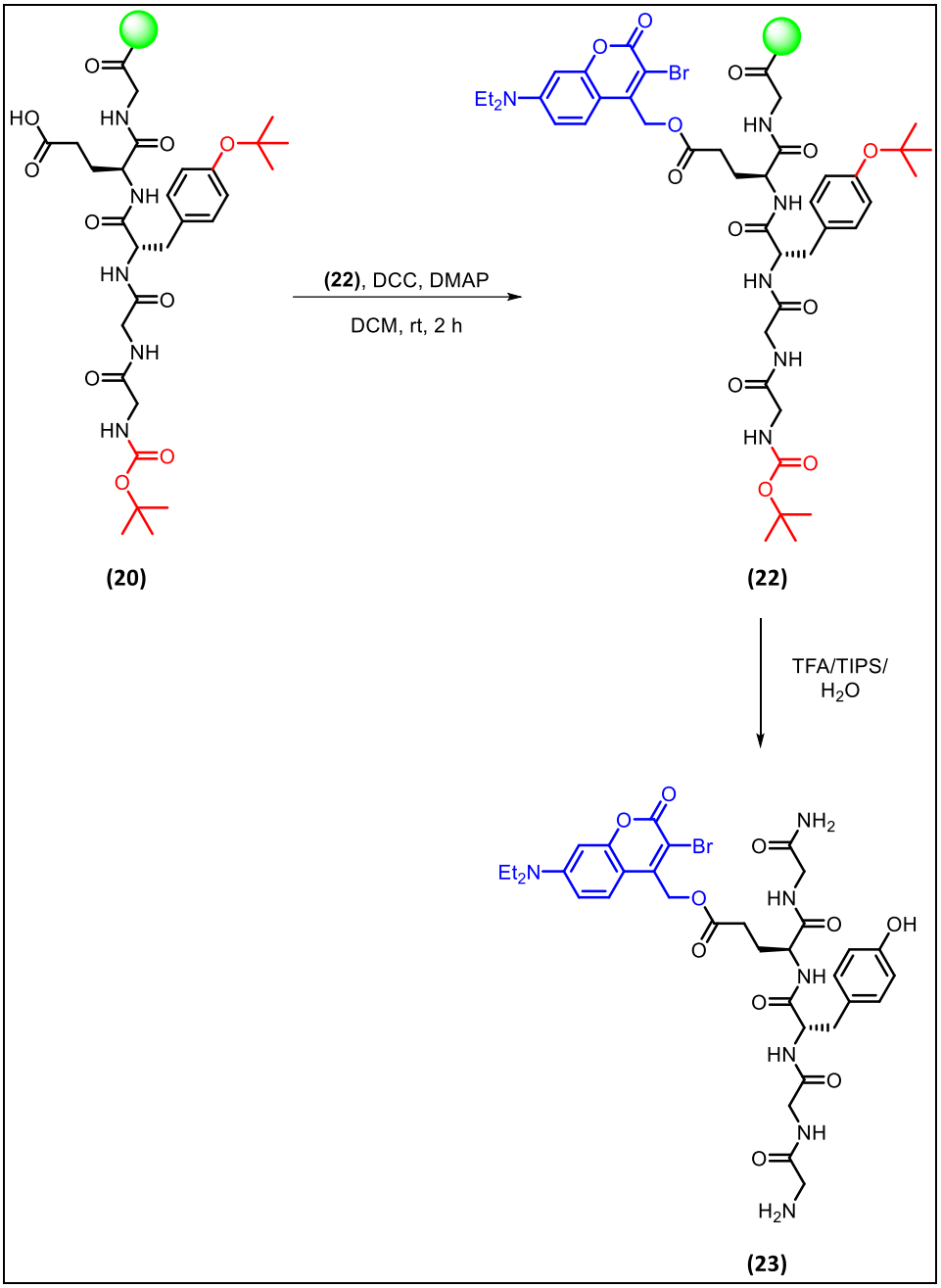

A peptide of the sequence Boc-N(H)-G-G-Y-E(OAll)-G was synthesised according to the protocol outlined in section 14.12.1 above and subjected to the Glu(OAll) deprotection conditions described in section 4.12.3 50 mg (0.02 mmol, 1 eq.) of the resulting resin was suspended in DCM (5 ml) alongside DIC (15 µl, 0.1 mmol, 5 eq.) and DMAP (2.5 mg, 0.02 mmol, 1 eq.) and the resulting mixture was protected from light and stirred at rt for 5 mins to ensure

full dissolution. At this point a solution of **(22)** (33 mg, 0.1 mmol, 5 eq.) in DCM (3 ml) was added and the reaction mixture was stirred at rt in darkness for 2 h. The resin was then filtered and washed with DCM (3 x 25 ml) before being subjected to the global TFA deprotection outlined in section 4.13.2.3 above. Following lyophilisation, the desired product was obtained as a yellow solid with a yield of 12.3 mg, 0.016 mmol, (78%).

m/z: $[M+H]^+$ 790.23, $[M+Na]^+$ 812.33

4.12.5 Decaging studies

The decaging studies carried out during this work were performed using the EvoluChem PhotoRedOx Box™ from Hepatochem. 2 ml solutions of the studied compounds were prepared as indicated in table 3 below and placed in 2.7 ml glass vials. These vials were then stirred and irradiated with the stated light source and protected from external light using aluminium foil. The light sources used during these experiments were LED PF non-dimmable 110-220 V bulbs also produced by Hepatochem. The irradiance (light energy per unit area per unit time) of the bulbs used were as follows. 365 nm (190 mW/cm^2), 405 nm (201 mW/cm^2), 525 nm (163 mW/cm^2). During irradiation of the studied compounds timepoint aliquots (10 µl) were taken at regular intervals as indicated, transferred to an LC-MS vial and protected from light until LC-MS characterisation could be performed.

Compound	λ (nm)	Concentration	Total Time	Timepoints
(1)	365	0.1 mM	6 mins	20 s
(1)	365	0.1 mM	6 mins	20 s
(4)	405	0.1 mM	6 mins	20 s
(4)	405	0.1 mM	45 s	5 s
(7)	525	0.01 mM	90 mins	10 mins
(10)	525	0.01 mM	3 h	30 mins
(12)	525	0.01 mM	6 h	30 mins
(17)	365	92.4 µM	6 mins	30 s

Table 3: The experimental conditions used during the decaging experiments

4.12.6 LC-MS Characterisation

Liquid chromatography-mass spectrometry (LC-MS) was performed on a HCTultra ETD II ion trap spectrometer, coupled to an Ultimate300 HPLC using an Accucore C18 column (150 × 2.1 mm, 2.6 µm particle size). Water (solvent A) and acetonitrile (solvent B), both containing 0.1% formic acid, were used as the mobile phase at a flow rate of 0.3 mL min^{-1}. LC traces were measured via UV absorption at 220, 270, and 280. The LC-MS Gradients utilised for small molecules and peptide characterisation can be seen in figures 42 and 43 below respectively.

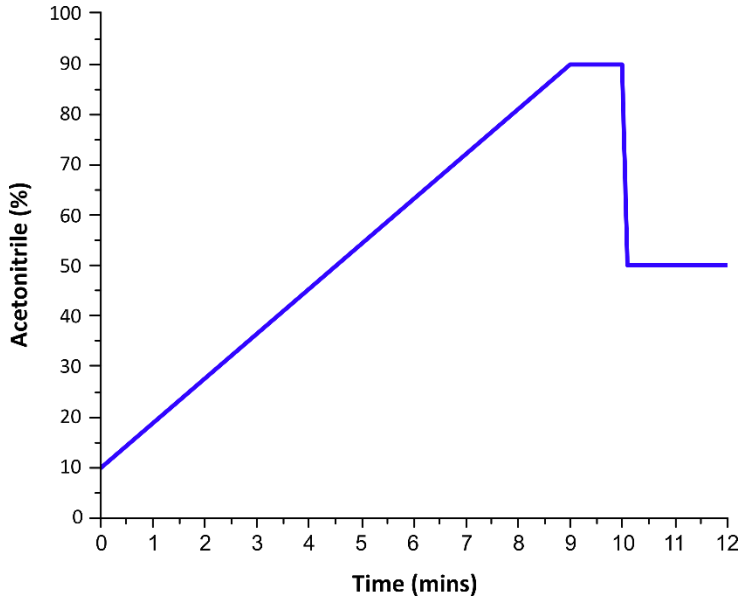

Figure 42: The LC-MS method used for small molecule characterisation.

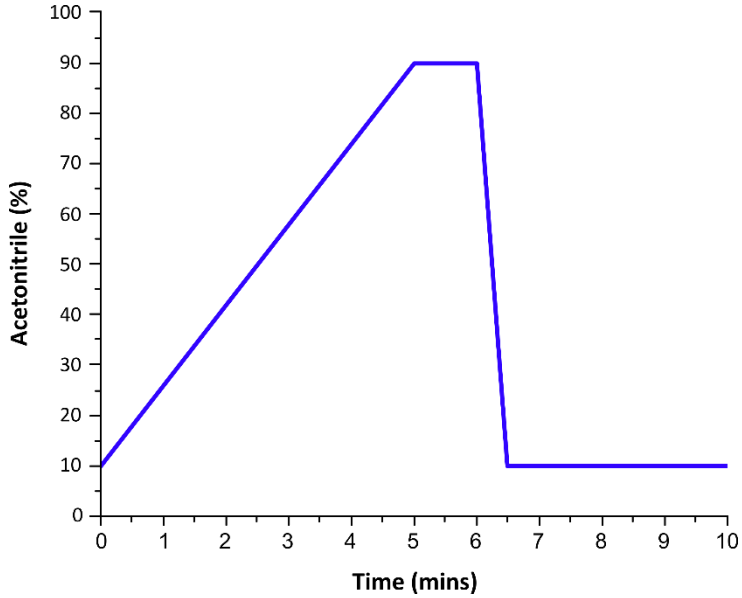

Figure 43: The LC-MS method used for peptide characterisation.

4.12.7 NMR Spectra of Novel Compounds

NMR Spectra of **(12)**

^{1}H NMR (400 MHz, MeCN-d_3)

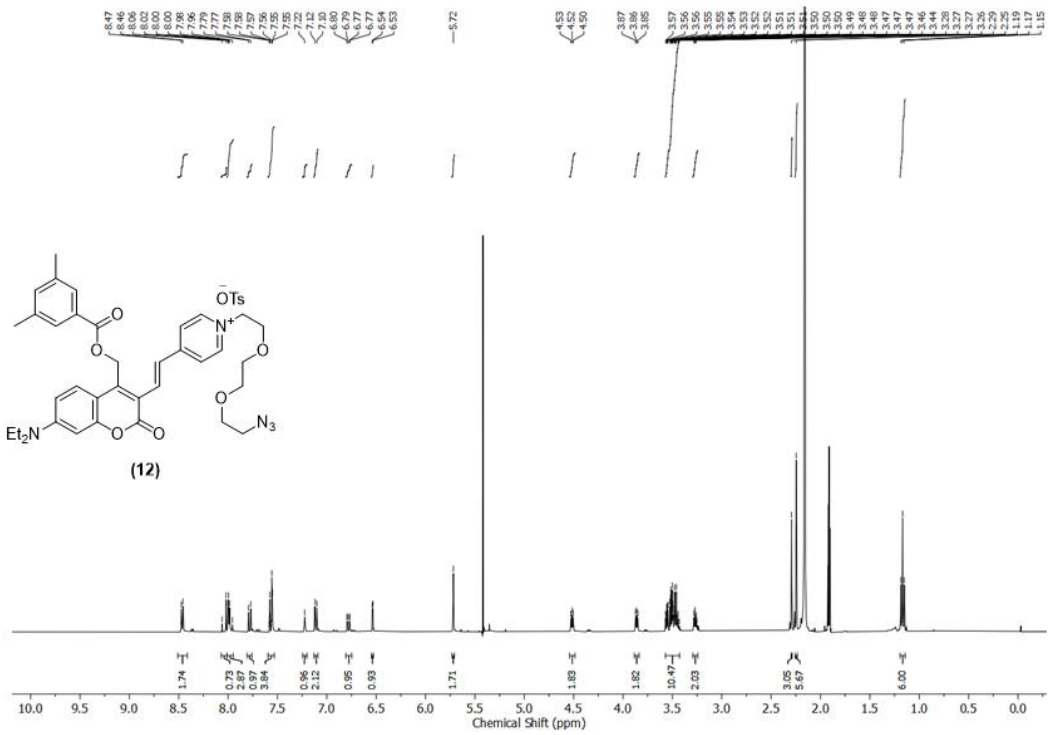

4.13 References

1. Schmidt, R.; Geissler, D.; Hagen, V.; Bendig, J. Mechanism of photocleavage of (coumarin-4-yl)methyl esters. *J. Phys. Chem. A* **2007**, *111* (27), 5768–5774.
2. Hagen, V.; Bendig, J.; Frings, S.; Eckardt, T.; Helm, S.; Reuter, D.; Kaupp, U. B. Highly efficient and ultrafast phototriggers for cAMP and cGMP by using long-wavelength UV/Vis activation. *Angew. Chem., Int. Ed.* **2001**, *40* (6), 1045–1048.
3. Hagen, V.; Frings, S.; Wiesner, B.; Helm, S.; Kaupp, U. B.; Bendig, J. [7-(Dialkylamino)coumarin-4-yl]methyl-caged compounds as ultrafast and effective long-wavelength phototriggers of 8-bromo-substituted cyclic nucleotides. *ChemBioChem* **2003**, *4* (5), 434–442.
4. Peterson, J. A.; Yuan, D.; Winter, A. H. Multiwavelength control of mixtures using visible light-absorbing photocages. *J. Org. Chem.* **2021**, *86* (14), 9655–9664.
5. Stadler, E.; Eibel, A.; Fast, D.; Freißmuth, H.; Holly, C.; Wiech, M.; Moszner, N.; Gescheidt, G. A versatile method for the determination of photochemical quantum yields via online UV–Vis spectroscopy. *Photochem. Photobiol. Sci.* **2018**, *17* (5), 660–669.

6. Peterson, J. A.; Wijesooriya, C.; Gehrmann, E. J.; Mahoney, K. M.; Goswami, P. P.; Albright, T. R.; Syed, A.; Dutton, A. S.; Smith, E. A.; Winter, A. H. Family of BODIPY photocages cleaved by single photons of visible/near-infrared light. *J. Am. Chem. Soc.* **2018**, *140* (23), 7343–7346.
7. Bojtár, M.; Kormos, A.; Kis-Petik, K.; Kellermayer, M.; Kele, P. Green-light activatable, water-soluble red-shifted coumarin photocages. *Org. Lett.* **2019**, *21* (23), 9410–9414.
8. Kuhn, H. J.; Braslavsky, S. E.; Schmidt, R. Chemical actinometry (IUPAC technical report). *Pure Appl. Chem.* **2004**, *76* (12), 2105–2146.
9. Rabani, J.; Mamane, H.; Pousty, D.; Bolton, J. R. Practical chemical actinometry—A review. *Photochem. Photobiol.* **2021**, *97* (5), 873–902.
10. Klak, M.; Gomółka, M.; Dobrzański, T.; Tymicki, G.; Cywoniuk, P.; Kowalska, P.; Kosowska, K.; Bryniarski, T.; Berman, A.; Dobrzyń, A.; Idaszek, J.; Święszkowski, W.; Wszoła, M. Irradiation with 365 nm and 405 nm wavelength shows differences in DNA damage of swine pancreatic islets. *PLoS One* **2020**, *15* (6), e0235052.
11. Azagarsamy, M. A.; Anseth, K. S. Wavelength-controlled photocleavage for the orthogonal and sequential release of multiple proteins. *Angew. Chem., Int. Ed.* **2013**, *52* (51), 13803–13807.
12. Popova, T. V.; Reinbolt, J.; Ehresmann, B.; Shakirov, M. M.; Serebriakova, M. V.; Gerassimova, Y. V.; Knorre, D. G.; Godovikova, T. S. Why do p-nitro-substituted aryl azides provide unintended dark reactions with proteins? *J. Photochem. Photobiol., B* **2010**, *100* (1), 40–45.
13. Zhao, Y. R.; Zheng, Q.; Dakin, K.; Xu, K.; Martinez, M. L.; Li, W.-H. New caged coumarin fluorophores with extraordinary uncaging cross sections suitable for biological imaging applications. *J. Am. Chem. Soc.* **2004**, *126* (14), 4653–4663.
14. Slanina, T.; Shrestha, P.; Palao, E.; Kand, D.; Peterson, J. A.; Dutton, A. S.; Rubinstein, N.; Weinstain, R.; Winter, A. H.; Klán, P. In search of the perfect photocage: Structure–reactivity relationships in meso-methyl BODIPY photoremovable protecting groups. *J. Am. Chem. Soc.* **2017**, *139* (42), 15168–15175.
15. Shrestha, P.; Mukhopadhyay, A.; Dissanayake, K. C.; Winter, A. H. Efficiency of functional group caging with second-generation green- and red-light-labile BODIPY photoremovable protecting groups. *J. Org. Chem.* **2022**, *87* (21), 14334–14341.
16. Schulte, A. M.; Smid, L. M.; Alachouzos, G.; Szymański, W.; Feringa, B. L. Cation delocalization and photo-isomerization enhance the uncaging quantum yield of a photocleavable protecting group. *Chem. Commun.* **2023**, *60* (5), 673–676.
17. Egyed, A.; Németh, K.; Molnár, T. Á.; Kállay, M.; Kele, P.; Bojtár, M. Turning red without feeling embarrassed—Xanthenium-based photocages for red-light-activated phototherapeutics. *J. Am. Chem. Soc.* **2023**, *145* (7), 4026–4034.
18. Schulte, A. M.; Alachouzos, G.; Szymański, W.; Feringa, B. L. Strategy for engineering high photolysis efficiency of photocleavable protecting groups through cation stabilization. *J. Am. Chem. Soc.* **2022**, *144* (27), 12105–12115.
19. Merrifield, R. B. Solid phase peptide synthesis. I. The synthesis of a tetrapeptide. *J. Am. Chem. Soc.* **1963**, *85* (14), 2149–2154.
20. Eissler, S.; Kley, M.; Bächle, D.; Loidl, G.; Meier, T.; Samson, D. Substitution determination of Fmoc-substituted resins at different wavelengths. *J. Pept. Sci.* **2017**, *23* (10), 757–762.
21. Palomo, J. M. Solid-phase peptide synthesis: An overview focused on the preparation of biologically relevant peptides. *RSC Adv.* **2014**, *4* (62), 32658–32672.

22. Goguen, B. N.; Aemissegger, A.; Imperiali, B. Sequential activation and deactivation of protein function using spectrally differentiated caged phosphoamino acids. *J. Am. Chem. Soc.* **2011**, *133* (29), 11038–11041.
23. Gandioso, A.; Cano, M.; Massaguer, A.; Marchán, V. A green light-triggerable RGD peptide for photocontrolled targeted drug delivery: Synthesis and photolysis studies. *J. Org. Chem.* **2016**, *81* (23), 11556–11564.
24. Isidro-Llobet, A.; Álvarez, M.; Albericio, F. Amino acid-protecting groups. *Chem. Rev.* **2009**, *109* (6), 2455–2504.
25. Tekaia, F.; Yeramian, E.; Dujon, B. Amino acid composition of genomes, lifestyles of organisms, and evolutionary trends: A global picture with correspondence analysis. *Gene* **2002**, *297* (1), 51–60.
26. Patricelli, M. P.; Szardenings, A. K.; Liyanage, M.; Nomanbhoy, T. K.; Wu, M.; Weissig, H.; Aban, A.; Chun, D.; Tanner, S.; Kozarich, J. W. Functional interrogation of the kinome using nucleotide acyl phosphates. *Biochemistry* **2007**, *46* (2), 350–358.
27. Hacker, S. M.; Backus, K. M.; Lazear, M. R.; Forli, S.; Correia, B. E.; Cravatt, B. F. Global profiling of lysine reactivity and ligandability in the human proteome. *Nat. Chem.* **2017**, *9* (12), 1181–1190.
28. Díaz-Mochón, J. J.; Bialy, L.; Bradley, M. Full orthogonality between Dde and Fmoc: The direct synthesis of PNA–peptide conjugates. *Org. Lett.* **2004**, *6* (7), 1127–1129.
29. Herzig, L.-M.; Elamri, I.; Schwalbe, H.; Wachtveitl, J. Light-induced antibiotic release from a coumarin-caged compound on the ultrafast timescale. *Phys. Chem. Chem. Phys.* **2017**, *19* (22), 14835–14844.
30. Takaoka, K.; Tatsu, Y.; Yumoto, N.; Nakajima, T.; Shimamoto, K. Synthesis of carbamate-type caged derivatives of a novel glutamate transporter blocker. *Bioorg. Med. Chem.* **2004**, *12* (13), 3687–3694.
31. Loffet, A.; Zhang, H. X. Allyl-based groups for side-chain protection of amino acids. *Int. J. Pept. Protein Res.* **1993**, *42* (4), 346–351.
32. Grieco, P.; Gitu, P. M.; Hruby, V. J. Preparation of “side-chain-to-side-chain” cyclic peptides by allyl and alloc strategy: Potential for library synthesis. *J. Pept. Res.* **2001**, *57* (3), 250–256.
33. Neises, B.; Steglich, W. Simple method for the esterification of carboxylic acids. *Angew. Chem., Int. Ed. Engl.* **1978**, *17* (7), 522–524.
34. Adelhorst, K.; Hedegaard, B. B.; Knudsen, L. B.; Kirk, O. Structure–activity studies of glucagon-like peptide-1. *J. Biol. Chem.* **1994**, *269* (9), 6275–6278.
35. López-Sánchez, A. G.; Rodríguez-Mejía, K. G.; Cuero-Amu, K. J.; Ardila-Chantré, N.; Reyes-Calderón, J. E.; González-López, N. M.; Huertas-Ortiz, K. A.; Fierro-Medina, R.; Rivera-Monroy, Z. J.; García-Castañeda, J. E. A new methodology for synthetic peptides purification and counterion exchange in one step using solid-phase extraction chromatography. *Processes* **2025**, *13* (1), 27.
36. Sikora, K.; Jaśkiewicz, M.; Neubauer, D.; Migoń, D.; Kamysz, W. The role of counter-ions in peptides—An overview. *Pharmaceuticals* **2020**, *13* (12), 442.
37. Clydesdale, G. J.; Dandie, G. W.; Muller, H. K. Ultraviolet light induced injury: Immunological and inflammatory effects. *Immunol. Cell Biol.* **2001**, *79* (6), 547–568.
38. McMillan, T. J.; Leatherman, E.; Ridley, A.; Shorrocks, J.; Tobi, S. E.; Whiteside, J. R. Cellular effects of long wavelength UV light (UVA) in mammalian cells. *J. Pharm. Pharmacol.* **2008**, *60* (8), 969–976.

39. Mahía, A.; Kiib, A. E.; Nisavic, M.; Svenningsen, E. B.; Palmfeldt, J.; Poulsen, T. B. α-Lactam electrophiles for covalent chemical biology. *Angew. Chem., Int. Ed.* **2023**, *62* (26), e202304142.
40. Becker, B.; Englert, S.; Schneider, H.; Yanakieva, D.; Hofmann, S.; Dombrowsky, C.; Macarrón Palacios, A.; Bitsch, S.; Elter, A.; Meckel, T.; Kugler, B.; Schirmacher, A.; Avrutina, O.; Diederichsen, U.; Kolmar, H. Multivalent dextran hybrids for efficient cytosolic delivery of biomolecular cargoes. *J. Pept. Sci.* **2021**, *27* (4), e3298.

Chapter 5
Future Work

5.1 Project summary

The work presented in this thesis has established a foundation for achieving spatiotemporal control over the function of bioactive peptides within hydrogel matrices through the use of photocages and photocleavable linkers. The initial chapter of this work focused on the optimisation of the synthesis of pre-existing photocages, enabling their preparation in consistently high yields and facilitating their bulk incorporation into materials in the future. These compounds will be employed to inhibit the biological function of target molecules, thus placing their activity under the control of light. Photocages based upon both the coumarin and BODIPY scaffolds were synthesised, and these photocages were shown to have distinct absorption profiles, maximising the potential for orthogonal, sequential activation. However, it was later discovered that the acid sensitive nature of the BODIPY scaffold, prevented this class of compound from being incorporated into peptides synthesised by SPPS, meaning that we chose to focus on coumarin photocages **(1)** and **(2)**, the structures of which can be seen in figure 1 below.

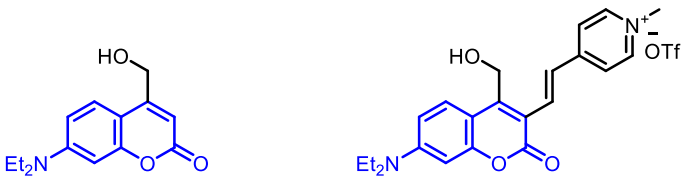

Figure 1: The structures of the coumarin photocages produced during this work.

Building on this work, novel photocleavable linkers were designed and synthesised. A novel synthetic route was developed for **(3)**, which had previously been developed by Anseth & Azagarsamy,[1] which facilitated more reliable production of this compound. However, a subsequent decaging study revealed that **(3)** did not undergo photolysis under our

experimental conditions when irradiated at 365 nm, likely due to its absorption profile being too far shifted into the UV region. This motivated the design and synthesis of novel photocleavable linker **(4)**, which incorporated a 7-diethylamino group. The inclusion of this electron donating substituent resulted in a red-shift in the absorption profile of this photocleavable linker, which we hoped would enable efficient photocleavage in the visible range. Following this, novel, photocleavable linker **(5)** was designed and synthesised based on the work of Kele et al.[2] This compound had an absorption profile centred around the green region of the visible light spectrum, which we hoped would allow for orthogonal photocleavage with **(2)**.

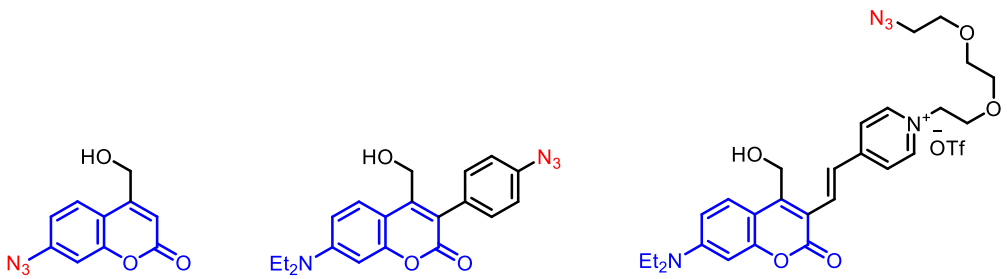

Figure 2: The structures of the photocleavable linkers synthesised during this work.

Following the synthetic efforts outlined in chapters 1 and 2, we set out to perform decaging studies in order to verify the photoreactivity of the produced compounds. During these studies it was found that blue-light absorbing compounds **(1)** and **(4)**, performed well, undergoing efficient photorelease at both 365 and 405 nm. Notably, novel photocleavable linker **(4)**, displayed markedly improved kinetics, undergoing photolysis 1.7 and 8.5-fold faster than **(1)** at 365 nm and 405 nm respectively. In contrast, the green-light absorbing compounds **(2)** and **(5)** were considerably less effective. Compound **(2)** achieved just 5% acetic acid release following 90 mins of irradiation at 525 nm, while its corresponding linker **(5)**, released 3,5-

dimethyl benzoic acid at a rate that was at least three orders of magnitude slower than the photorelease of acetic acid from **(1)** and **(4)**. These decaging studies highlighted that the photophysical properties of **(2)** and **(5)** would need to be optimised before they could be used for our desired application.

5.2 Synthetic development of red-shifted photocages and photocleavable linkers

5.2.1 Improving quantum yield through 4-methyl substitution

A key finding of the decaging studies presented in chapter 4, was that the green-light absorbing compounds **(2)** and **(5)**, did not undergo efficient photocleavage upon irradiation at 525 nm. These compounds absorbed well within the green-light region, meaning that if their decaging efficiencies were to be improved, efforts should be focused on improving the decaging quantum yields of these compounds. As discussed in the previous chapter, towards the conclusion of our work, Feringa et al. reported a significant improvement in the quantum yield of related coumarin photocage **(6-I)**, by incorporating an additional prenyl substituent at the 4-methyl position, the structure of which is seen in figure 3 below.[3,4]

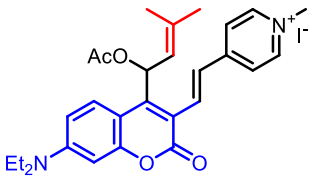

(6-I)

Figure 3: The structure of (6-I) developed by Feringa et al. which exhibited an improved quantum yield due to the substitution of its 4-methyl group with a prenyl substituent.[4]

The synthesis of **(6-I)** was analogous to the synthesis of **(2)** discussed in Chapter 2 of this work. However, rather than performing a Heck coupling on 7-diethylamino-3-bromo-4-

hydroxymethyl coumarin, Feringa et al. instead utilised 3-bromo-4-formyl coumarin derivative **(7)**, which facilitated the later incorporation of the prenyl substituent *via* a Grignard reaction, forming **(8)**. Final alkylation of the pyridine ring with methyl iodide then produced **(6-I)**. In our work, the use of methyl triflate proved advantageous for this transformation, as the resulting triflate salt displayed greater solubility in organic solvents compared to the corresponding iodide, which facilitated easier purification and characterisation of compound **(2)**. Additionally, alkylating agent **(9)** was synthesised in chapter 3, which facilitated the synthesis of photocleavable linker **(5)** *via* an identical route. The proposed synthetic routes for the production of the potential improved-quantum-yield photocage **(10)** and its corresponding photocleavable linker **(11)** can be seen in scheme 1 below.

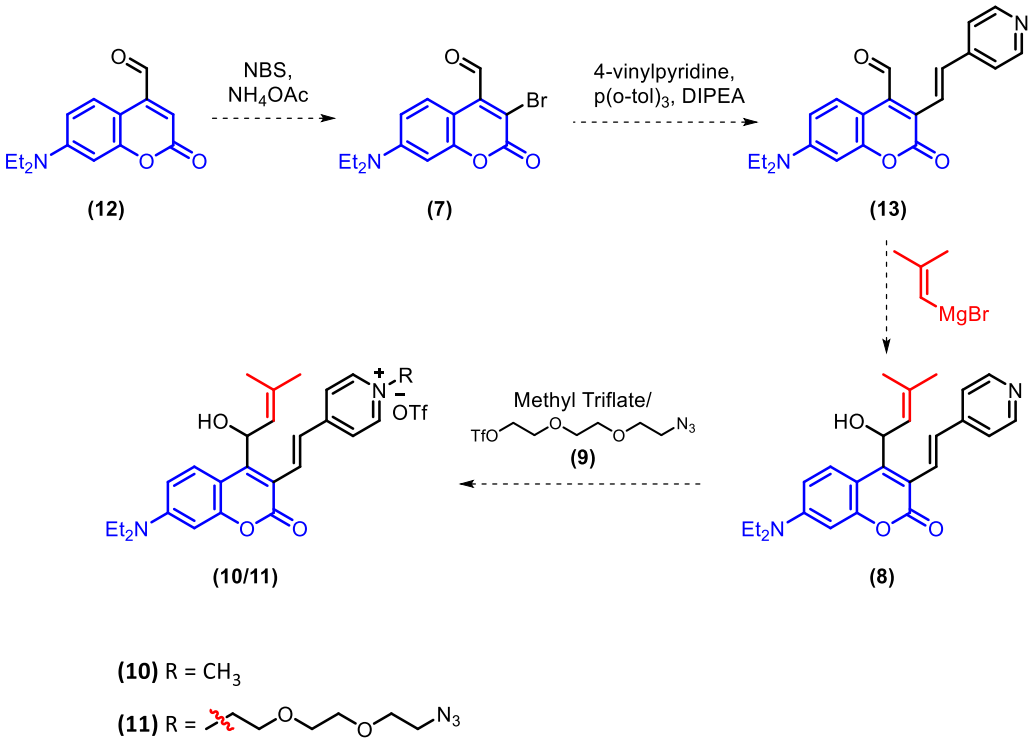

*Scheme 1: Schematic of the proposed synthetic route for the production of **(10)** and **(11)**.*

5.2.2 Improving quantum yield through restricted ring systems

Another proven strategy of improving the decaging quantum yield of coumarin photocages is through the introduction of a restricted ring system at the 7-position of the scaffold. As discussed in section 1.4.2.6 of the introductory chapter, Heckel et al. demonstrated that this modification improved the decaging quantum yield of blue-light absorbing coumarin photocages by up to five-fold relative to **(1)**.[5] This improvement was attributed to the prevention of rotation around the C-N bond upon formation of the excited state, thus limiting competitive non-radiative decay pathways.[5] Although the synthesis of these derivatives is demanding, involving challenging multi-step syntheses, Rivera-Fuentes et al. reported an analogous improvement in decaging quantum yield, through the incorporation of an azetidinyl substituent at the 7-position.[6] In addition to restricting C-N bond rotation this modification offers the practical advantage of being accessible from commercially available coumarin precursor **(14).** Following the synthesis of azetidinyl coumarin derivative **(15)**, we propose that a route analogous to that employed for compound **(2)** described in Chapter 2 could be used in order to produce novel 7-azetidinyl coumarin photocage **(16)**, together with its corresponding photocleavable linker **(17)** as seen in scheme 2 below.

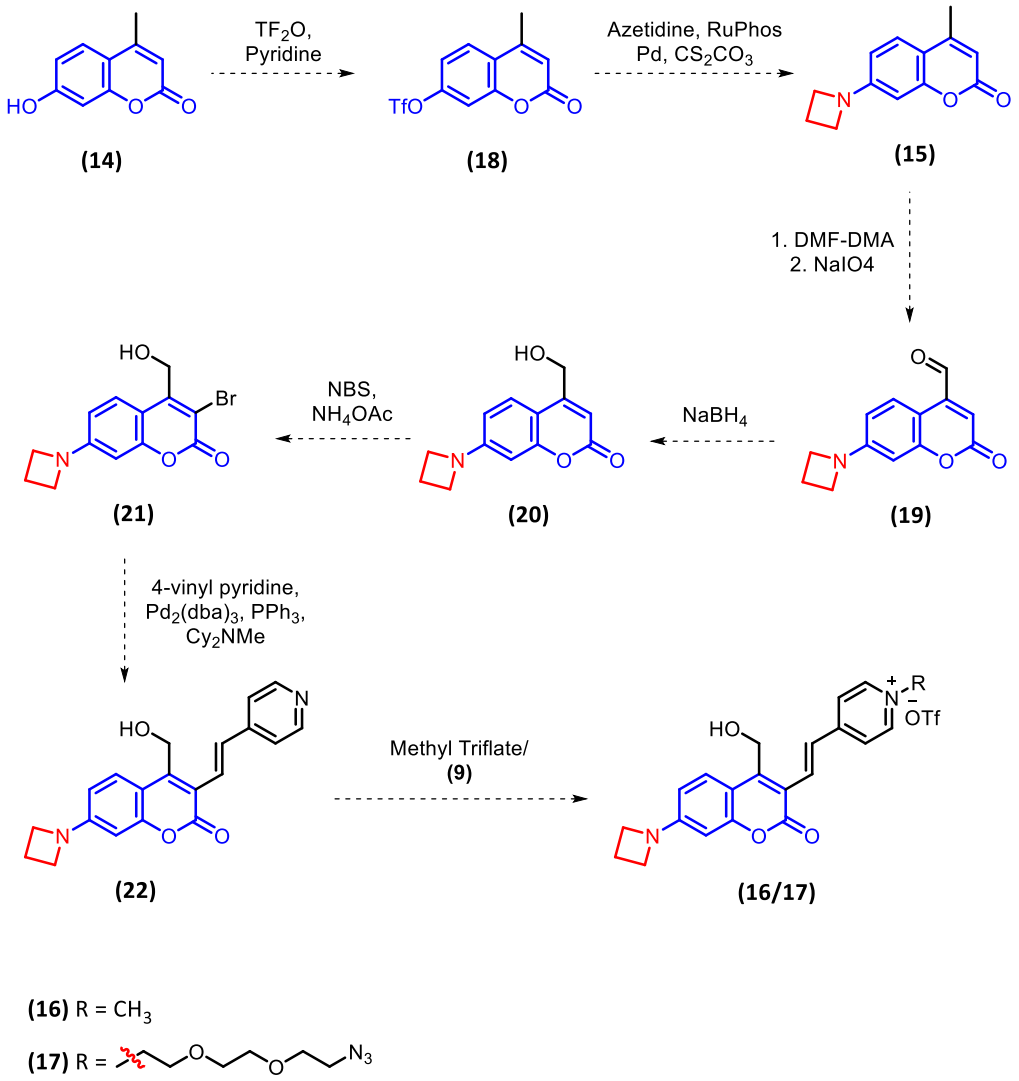

Scheme 2: Schematic of the proposed synthetic route for the production of ***(16)*** *and* ***(17).***

In Chapter 3, the synthesis of **(3)** was optimised with the incorporation of a triazene moiety at the 7-position of the coumarin scaffold being key to the success of this route. At the conclusion of this route, **(23)** was diazotised allowing for the installation of an azido group *via* a Sandmeyer-type reaction. Importantly, the scope of the Sandmeyer-type reaction is large, allowing for the installation of wide array of nucleophiles.[7] Of particular relevance to the future development of this project, is the installation of a bromine atom, which can be achieved by treatment of the diazonium with HBr. The resulting 7-bromo coumarin derivative **(24)** could then undergo a Buchwald-Hartwig reaction with azetidine,[8] as depicted in scheme

3 below. This would provide an alternative means of installing this moiety, which would circumvent the need for the subsequent oxidation steps required in the route shown in scheme 2 above, which had previously presented challenges with the synthesis of other coumarin derivatives.

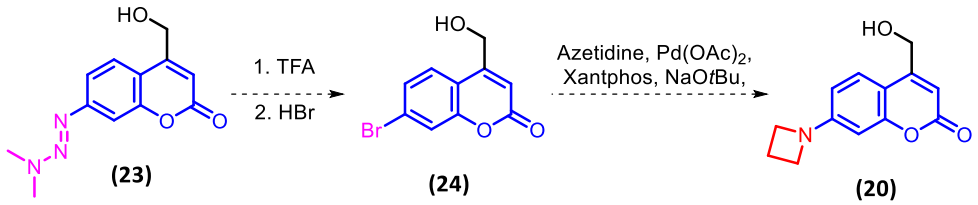

Scheme 3: Schematic of a proposed route for the installation of an azetidine moiety from previously synthesised ***(23).***

5.2.3 Substituent effects can be additive

The 4-prenyl and azetidine substituents described above have both previously been shown to enhance the decaging quantum yields of coumarin photocages.[4,6] However, it is important to note that these moieties achieve this through different mechanisms. The 4-prenyl group employed by Feringa et al. improved the decaging quantum yield through stabilisation of the methyl coumarin carbocation formed as a result of heterolytic bond cleavage.[4] In contrast to this the azetidine moiety utilised by Rivera-Fuentes et al. inactivated competitive decay pathways upon formation of the excited state, through restriction of the C-N bond.[6] Thus it is likely that if both of these modifications, could be incorporated into a single molecule, their effects would be additive, dramatically improving the decaging quantum yield, through both cation stabilisation and the inactivation of competitive excited state decay pathways. The proposed structures of future optimised photocage **(25)**, and its corresponding photocleavable linker **(26)** can be seen in figure 4 below.

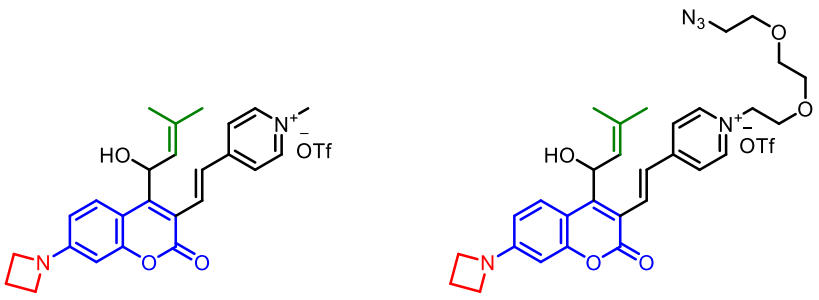

*Figure 4: The structures of potential future photoresponsive molecules **(25)** and **(26).***

5.3 Hydrogel Scaffold Applications

5.3.1 Validation of photorelease from **(4)** within hydrogel matrices

Although the decaging study performed on **(4)** in section 4.4 of the previous chapter, confirmed that this photocleavable linker efficiently released acetic acid upon irradiation at 365 and 405 nm, further studies are required to evaluate how this compound will perform when incorporated into a hydrogel scaffold. Demonstrating controlled photorelease in a material context is a crucial next step, as the decaging activity of a compound in solution is not directly transferable to performance within a hydrogel matrix, where light penetration, diffusion, and local microenvironmental effects can all influence reaction efficiency. We propose to confirm the photoreactivity of **(4)**, within a material setting by tracking the release of a fluorescent probe using fluorescence spectroscopy.

This form of validation experiment is prevalent in literature and has been utilised on numerous occasions to monitor the photolysis of photocleavable linkers within hydrogel matrices. For example, Anseth & Azagarsamy conjugated coumarin based linker **(3)** and o-nitrobenzyl based photocleavable linker **(27)** to Rhodamine B isothiocyanate and fluorescein respectively, thereby enabling photorelease to be tracked by fluorescence spectroscopy at both 365 and 405 nm.[1] Although based on the decaging experiment performed in section 3.5 of Chapter 3,

we suspect that photorelease of Rhodamine B isothiocyanate may have been facilitated by the broad spectral output of the LED light source, this methodology remains sound for the monitoring of photolysis of the linker-cargo bond. The release of fluorescein from **(27)** within a hydrogel matrix is depicted in figure 5 below.

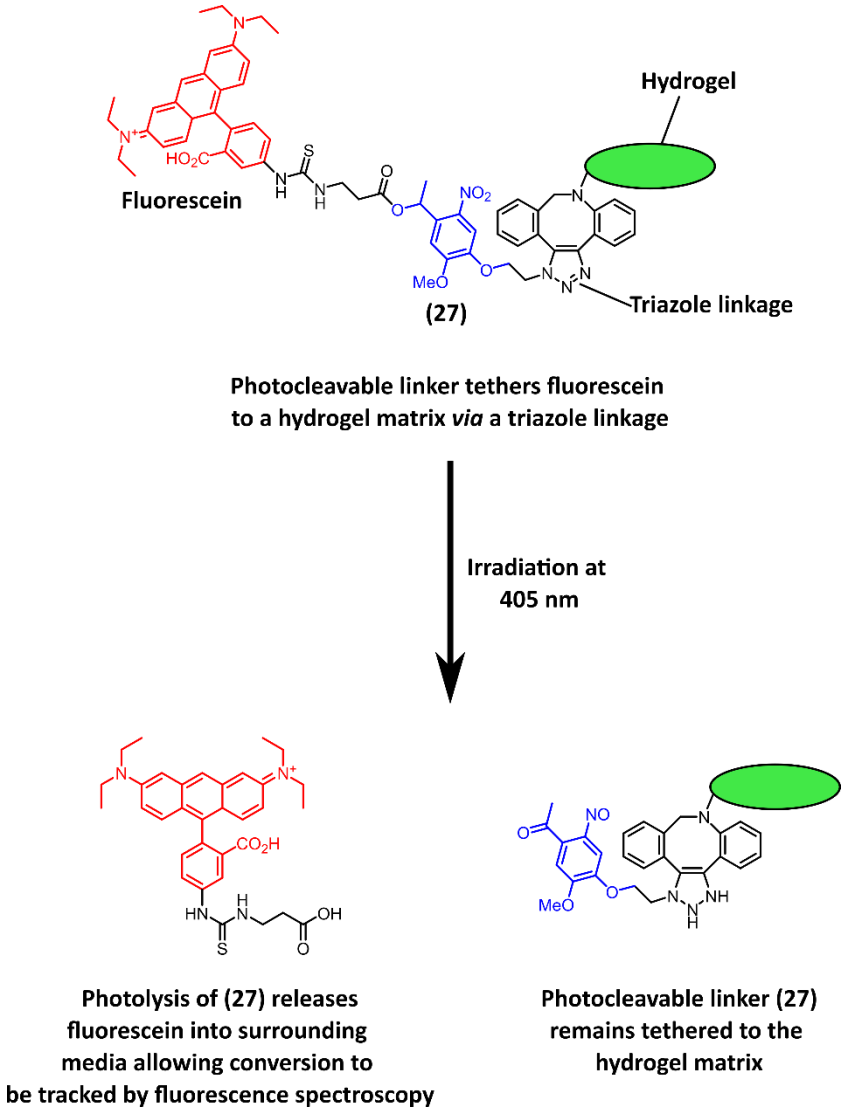

Figure 5: Schematic representation of the experiment performed by Anseth & Azagarsamy demonstrating the photorelease of fluorescein from ***(27)*** *within a hydrogel matrix.*

To validate the photoreactivity of **(4)**, we propose attaching it to the *N*-terminus of a fluorescently labelled peptide using a carbamate linker, employing the same strategy used to

photocage lysine in section 4.8 of the previous chapter. The azido group of **(4)** can then undergo SPAAC with a suitably functionalised hydrogel, tethering the fluorescent peptide to the matrix. Upon irradiation, photolysis of **(4)** would release the peptide into the surrounding media and this process could be monitored using fluorescence spectroscopy. This experiment would not only confirm that **(4)** functions effectively in a materials context but would also provide a convenient platform for quantifying release kinetics from hydrogels. It is essential for this proposed experiment that the fluorescent label present on the peptide has minimal spectral overlap with **(4)**, in order to allow for clear monitoring of photorelease. Cy5, a fluorescent dye based on the cyanine scaffold presents itself as a useful candidate for this role as it exhibits intense absorption and emission in the far-red region (≈650 nm), which is far removed from the λ_{max} of **(4)** which occurs at approximately 400 nm. Furthermore, Fmoc-Lys(Cy5)-OH is a commercially available SPPS-compatible building block, simplifying the incorporation of this dye into a model peptide sequence. A schematic view of this proposed experiment is provided in figure 6 below.

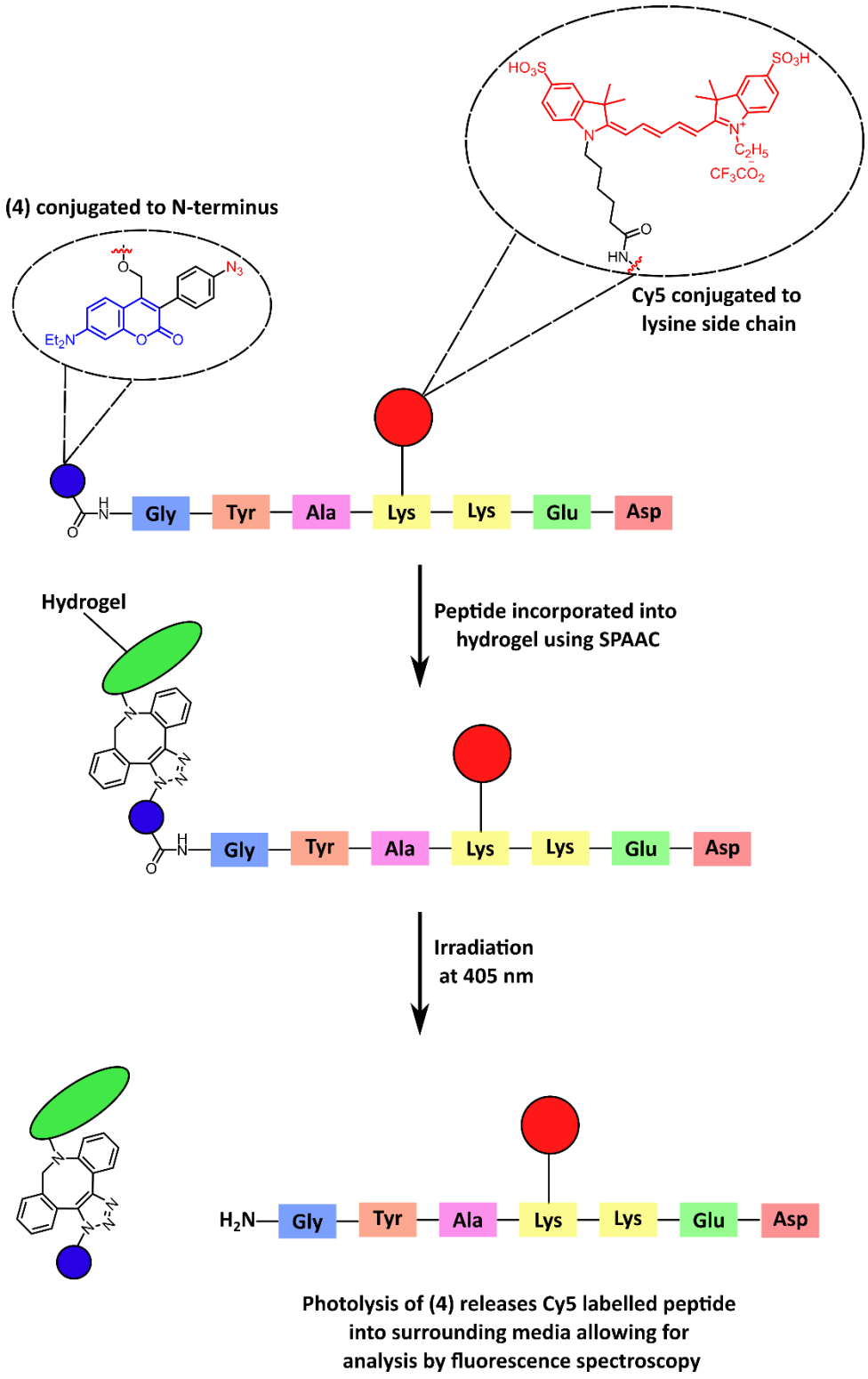

*Figure 6: Proposed experiment for validating the photoreactivity of **(4)** within a hydrogel matrix. **(4)** is conjugated to the N-terminus of a Cy5-labelled peptide via a carbamate linker, followed by SPAAC coupling to a functionalised hydrogel. Upon irradiation at 405 nm,*

*photolysis of **(4)** results in peptide release, which can be monitored by fluorescence spectroscopy.*

5.3.2 Validation of the decaging of (1) from within hydrogel matrices

The decaging ability of **(1)**, must also be validated within a hydrogel environment, in order to confirm that this compound performs effectively when applied in a materials context. In contrast to **(4)**, which functions as a photocleavable linker, tethering a peptide of interest to a material scaffold, **(1)** is conjugated to the cargo molecule only. Thus, decaging upon irradiation with an appropriate wavelength, releases **(1)** into the surrounding media, activating the peptide. This distinction simplifies experimental design, as the decaging of (**1)** can be followed by exploiting the inherent fluorescence of the coumarin chromophore. Although we have previously highlighted the limitations of relying solely on spectroscopy to quantify decaging kinetics, in the case of **(1)** these limitations are mitigated by the decaging study performed in section 4.3 of the previous chapter which comprehensively identified the products of photorelease.

In our proposed experiment, **(1)** will be conjugated to the amino group of the side chain of a lysine residue within a model peptide *via* a carbamate linker as previously described. The resulting caged peptide will then be anchored to a hydrogel scaffold *via* its *N*-terminus. Upon irradiation with an appropriate wavelength of light, the decaging of **(1)** will result in its release into the surrounding media, which can then be tracked in real time using fluorescence spectroscopy. Thus, providing us with a better understanding of the decaging kinetics of **(1)** in a material setting. A schematic of the proposed experiment can be seen in figure 7 below.

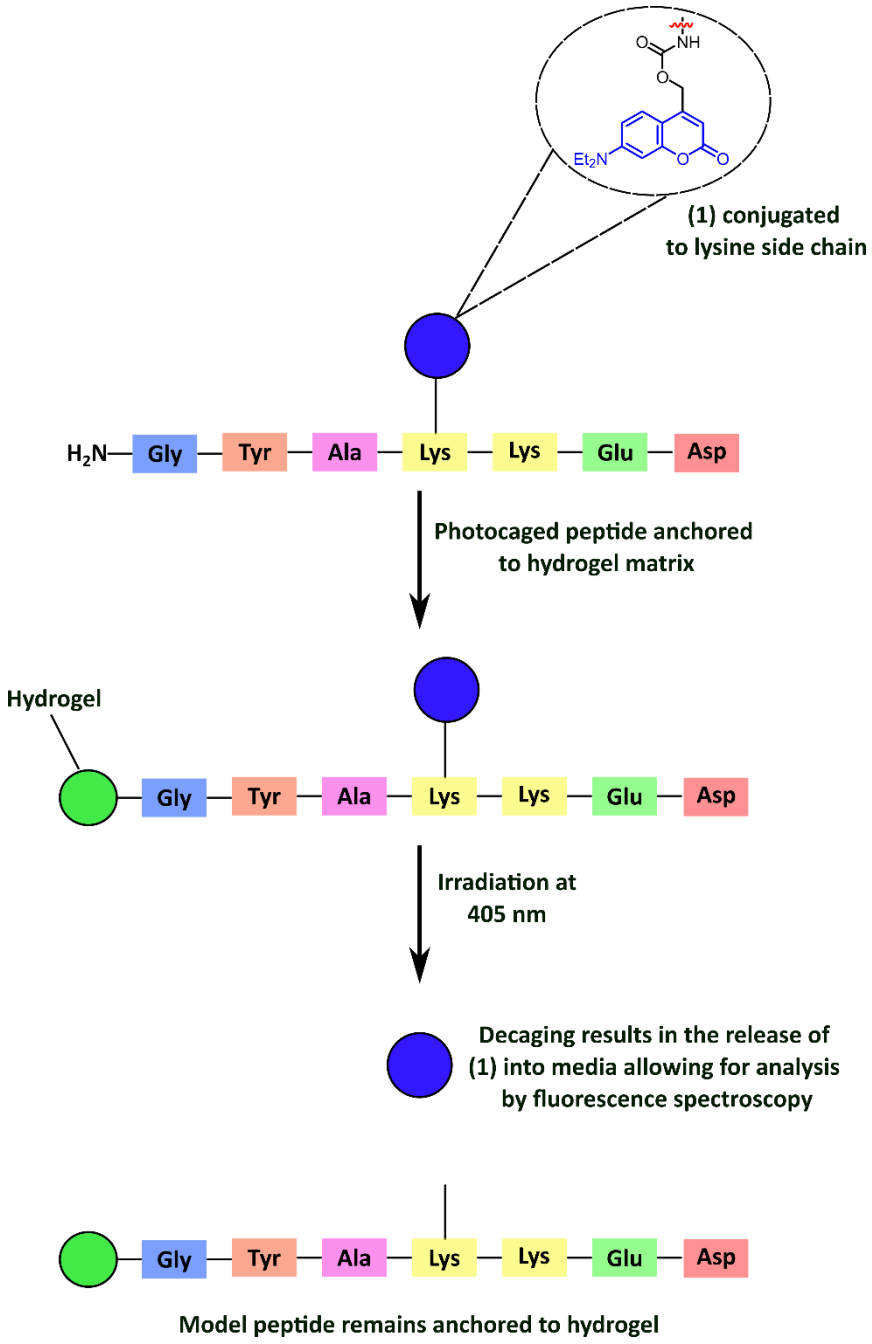

Figure 7: A schematic of the proposed experiment designed to verify the effective decaging of ***(1)*** *within a material setting.*

5.3.3 Multiplexing photorelease

Once the ability of **(1)** and **(4)** to undergo efficient photolysis within a hydrogel matrix has been confirmed, their potential for multiplexed photorelease will be investigated. Achieving multiplexed control is key to the success of this work, as the ability to activate and deactivate

biological signalling pathways in a desired sequence would provide a means of mimicking the dynamic nature of biological signalling cascades. As mentioned in section 5.1, the ultimate goal of this work is to develop multiple, orthogonally cleavable photoresponsive molecules, thereby allowing for the modulation of multiple biological signalling pathways. Although **(1)** and **(4)** are not orthogonally cleavable, their distinct modes of action still offer the potential for sequential control over biological signalling.

We propose tethering a GF sequestering peptide to a hydrogel matrix using photocleavable linker **(4).** A second peptide, with its activity inhibited by photocage **(1)** could be simultaneously anchored to the same surface, *via* its *N*-terminus. Initially, the first peptide is active, and capable of sequestering its desired GF, whereas the second peptide remains inactive due to the presence of **(1)**. Irradiation with an appropriate wavelength of light would then simultaneously cleave both molecules, inactivating the first peptide by releasing it from the surface, whilst also activating the second peptide via the removal of its photocage. This process would allow for the sequential enrichment of two distinct GFs at the surface of a hydrogel, thus providing a simple but effective means of multiplexed control. A schematic view of the proposed multiplexing experiment is provided in figure 8 below.

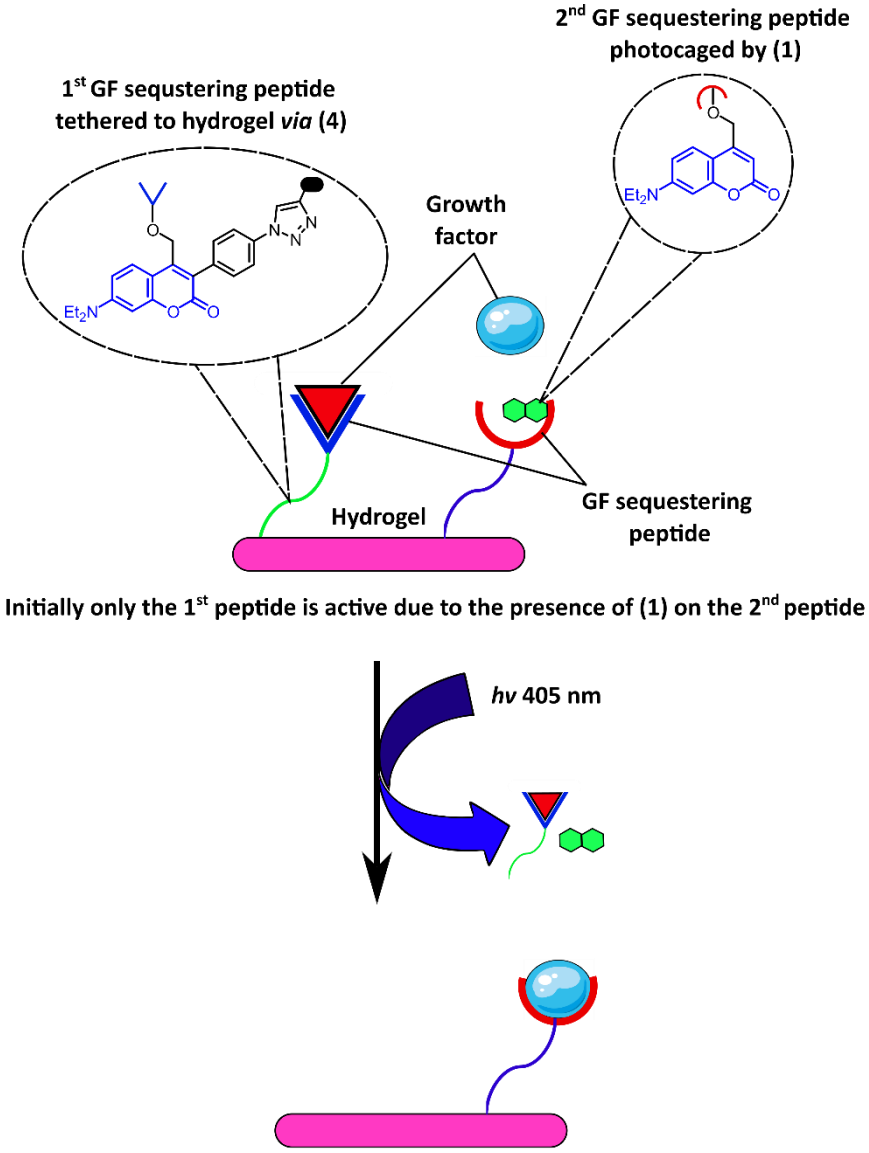

*Figure 8: A schematic view of the proposed multiplexed application of **(1)** and **(4)** when applied in tandem.*

5.4 Driving stem cell differentiation

Once the potential for sequential activation has been demonstrated, we can begin to apply this technology to living systems. Although, the scope of our approach is broad, and could in principle be utilised to modulate virtually any GF signalling pathway of interest, we propose

driving chondrogenesis, the formation of cartilage, as a proof-of-concept system. Sequential GF signalling has previously been reported to be key to driving this process, making it an ideal proof-of-concept system. Additionally, driving chondrogenesis within hMSCs is a research interest of a collaborator, allowing for interdisciplinary work.

The importance of sequential GF enrichment to driving hMSC chondrogenic differentiation has been reported on several occasions. Caplan et al. sequentially exposed hMSCs to Fibroblast Growth Factor (FGF) 2, 9 and 18 in the hopes of driving this process.[9] During this study, it was found that exposure to FGF-2 at the beginning of development, enhanced cell proliferation, building an initial cell population. Sequential exposure to FGF-9 and FGF-18 then amplified ECM production and facilitated chondrogenic differentiation. Similarly, both Rives-Estilla et al. and Nixon et al. have reported the advantages of sequentially exposing hMSCs to TGF- β1 and IGF-1 for driving chondrogenesis.[10,11]

The above examples of sequential exposure all rely on the timed addition of GFs to the culture medium. Whilst this has proven to be effective so far, this approach lacks spatial resolution and requires careful manipulation of the media conditions. In contrast, the photoresponsive hydrogel system proposed in this work, would provide an additional level of spatiotemporal control by enabling light-triggered activation and deactivation of GF sequestering peptides with high precision, allowing for more delicate control over the tissue development process.

An obvious limitation of our strategy is the requirement for peptides which are capable of sequestering a GF at the surface of a material without rendering them inactive. Whilst a peptide sequence capable of sequestering of TGF-β1, has been reported by Stupp et al,[12] peptides capable of sequestering the other GFs of interest are not currently known. However, this limitation could be overcome by implementing a display technology such as phage or

mRNA display which could be utilised to identify a sequestering peptide for virtually any GF of interest.[13]

5.5 References

1. Azagarsamy, M. A.; Anseth, K. S. Wavelength-controlled photocleavage for the orthogonal and sequential release of multiple proteins. *Angew. Chem. Int. Ed.* **2013**, *52* (51), 13803–13807.
2. Bojtár, M.; Kormos, A.; Kis-Petik, K.; Kellermayer, M.; Kele, P. Green-light activatable, water-soluble red-shifted coumarin photocages. *Org. Lett.* **2019**, *21* (23), 9410–9414.
3. Schulte, A. M.; Alachouzos, G.; Szymański, W.; Feringa, B. L. Strategy for engineering high photolysis efficiency of photocleavable protecting groups through cation stabilization. *J. Am. Chem. Soc.* **2022**, *144* (27), 12421–12430.
4. Schulte, A. M.; Smid, L. M.; Alachouzos, G.; Szymański, W.; Feringa, B. L. Cation delocalization and photo-isomerization enhance the uncaging quantum yield of a photocleavable protecting group. *Chem. Commun.* **2024**, *60* (5), 578–581.
5. Klimek, R.; Asido, M.; Hermanns, V.; Junek, S.; Wachtveitl, J.; Heckel, A. Inactivation of competitive decay channels leads to enhanced coumarin photochemistry. *Chem.—Eur. J.* **2022**, *28* (35), e202200647.
6. Bassolino, G.; Nançoz, C.; Thiel, Z.; Bois, E.; Vauthey, E.; Rivera-Fuentes, P. Photolabile coumarins with improved efficiency through azetidinyl substitution. *Chem. Sci.* **2018**, *9* (2), 387–391.
7. Akhtar, R.; Zahoor, A. F.; Rasool, N.; Ahmad, M.; Ali, K. G. Recent trends in the chemistry of Sandmeyer reaction: A review. *Mol. Divers.* **2022**, *26* (3), 1837–1873.
8. Witulski, B.; Senft, S.; Bonet, J.; Jost, O. Palladium-catalyzed N-arylation reactions with aziridine and azetidine. *Synthesis* **2007**, *2007* (2), 243–250.
9. Correa, D.; Somoza, R. A.; Lin, P.; Greenberg, S.; Rom, E.; Duesler, L.; Welter, J. F.; Yayon, A.; Caplan, A. I. Sequential exposure to fibroblast growth factors (FGF) 2, 9 and 18 enhances hMSC chondrogenic differentiation. *Osteoarthritis Cartilage* **2015**, *23* (3), 443–453.
10. Garcia-Ruiz, A.; Sánchez-Domínguez, C. N.; Moncada-Saucedo, N. K.; Pérez-Silos, V.; Lara-Arias, J.; Marino-Martínez, I. A.; Camacho-Morales, A.; Romero-Diaz, V. J.; Peña-Martinez, V.; Ramos-Payán, R.; Castro-Govea, Y.; Tuan, R. S.; Lin, H.; Fuentes-Mera, L.; Rivas-Estilla, A. M. Sequential growth factor exposure of human Ad-MSCs improves chondrogenic differentiation in an osteochondral biphasic implant. *Exp. Ther. Med.* **2021**, *22* (5), 1282.
11. Worster, A. A.; Brower-Toland, B. D.; Fortier, L. A.; Bent, S. J.; Williams, J.; Nixon, A. J. Chondrocytic differentiation of mesenchymal stem cells sequentially exposed to transforming growth factor-β1 in monolayer and insulin-like growth factor-I in a three-dimensional matrix. *J. Orthop. Res.* **2001**, *19* (4), 738–749.
12. Shah, R. N.; Shah, N. A.; Lim, M. M. D. R.; Hsieh, C.; Nuber, G.; Stupp, S. I. Supramolecular design of self-assembling nanofibers for cartilage regeneration. *Proc. Natl. Acad. Sci. U.S.A.* **2010**, *107* (8), 3293–3298.

13. Jaroszewicz, W.; Morcinek-Orłowska, J.; Pierzynowska, K.; Gaffke, L.; Węgrzyn, G. Phage display and other peptide display technologies. *FEMS Microbiol. Rev.* **2022**, *46* (2), fuab052.